LAPPEENRANTA-LAHTI UNIVERSITY OF TECHNOLOGY LUT

Arthur Sousa de Sena

INTELLIGENT REFLECTING SURFACES AND ADVANCED MULTIPLE ACCESS TECHNIQUES FOR MULTI-ANTENNA WIRELESS COMMUNICATION SYSTEMS

ACTA UNIVERSITATIS LAPPEENRANTAENSIS 1042

Arthur Sousa de Sena

INTELLIGENT REFLECTING SURFACES AND ADVANCED MULTIPLE ACCESS TECHNIQUES FOR MULTI-ANTENNA WIRELESS COMMUNICATION SYSTEMS

Dissertation for the degree of Doctor of Science (Technology) to be presented with due permission for public examination and criticism in the Auditorium 1316 at Lappeenranta–Lahti University of Technology LUT, Lappeenranta, Finland on the 24th of October, 2022, at noon.

Acta Universitatis
Lappeenrantaensis 1042

Supervisors Associate Professor Pedro Henrique Juliano Nardelli
LUT School of Energy Systems
Lappeenranta–Lahti University of Technology LUT
Finland

Dr. Daniel Benevides da Costa
AI and Digital Science Research Center
Technology Innovation Institute (TII)
United Arab Emirates

Professor Petar Popovski
Department of Electronic Systems
Aalborg University
Denmark

Reviewers Dr. Himal A. Suraweera
Department of Electrical and Electronic Engineering
University of Peradeniya
Sri Lanka

Associate Professor Telex Magloire N. Ngatched
Faculty of Engineering and Applied Science
Memorial University
Canada

Opponent Dr. Himal A. Suraweera
Department of Electrical and Electronic Engineering
University of Peradeniya
Sri Lanka

ISBN 978-952-335-859-1
ISBN 978-952-335-860-7 (PDF)
ISSN 1456-4491 (Print)
ISSN 2814-5518 (Online)

Lappeenranta–Lahti University of Technology LUT
LUT University Press 2022

Abstract

Arthur Sousa de Sena

Intelligent Reflecting Surfaces and Advanced Multiple Access Techniques for Multi-Antenna Wireless Communication Systems

Lappeenranta 2022
136 pages
Acta Universitatis Lappeenrantaensis 1042
Diss. Lappeenranta-Lahti University of Technology LUT
ISBN 978-952-335-859-1, ISBN 978-952-335-860-7 (PDF), ISSN 1456-4491 (Print), ISSN 2814-5518 (Online)

Multiple-input multiple-output (MIMO) is an indispensable technology for deploying the pervasive connectivity sought for fifth-generation (5G) and beyond communication systems. By relying on a large number of antennas, massive MIMO schemes can implement space division multiple access (SDMA) to serve spatially separated users with a single frequency–time resource block, thus, leading to incredible spectral and latency enhancements. Nevertheless, there are certain communication scenarios, such as ultra-dense deployments or environments with users sharing overlapping angular positions, where spatial multiplexing becomes unrealizable through SDMA alone. These challenging scenarios motivate the exploitation of different domains and technologies. In particular, power-domain non-orthogonal multiple access (NOMA) and rate-splitting multiple access (RSMA) have appeared as strong candidates for extending the capabilities of MIMO systems and enabling resource-efficient simultaneous transmissions even to overlapping users. In parallel development, a disruptive concept of an intelligent reflecting surface (IRS) has arisen as a method to manipulate electromagnetic propagation through reconfigurable, low-power, subwavelength reflecting elements. As their main feature, the properties of IRSs can be dynamically tuned and harnessed to attack harsh phenomena of wireless channels and accomplish diverse objectives, enabling communication environments with optimized signal radiation. Driven by the promising capabilities of the above-mentioned technologies, this doctoral dissertation focuses on studying and developing novel transmission schemes based on the synergy between NOMA, RSMA, and IRSs, and their application to next-generation multiuser MIMO communication networks.

This research work starts by investigating practical issues of imperfect successive interference cancellation (SIC) on a downlink multicluster massive MIMO-NOMA network. Through an in-depth theoretical analysis, exact closed-form expressions are derived for the outage probability and ergodic rates observed by each user. By exploiting the Karush–Kuhn–Tucker conditions, efficient dynamic power allocation strategies are also implemented for improving rate fairness within each cluster in the network. Motivated by the performance limitations identified in our seminal investigations, our research is continued on the MIMO-NOMA topic by exploiting the powerful capabilities of IRSs to tackle the interference issues of SIC. To broaden our optimization opportunities, a novel disruptive dual-polarized IRS is proposed to harness the additional degree of freedom offered by the polarization domain. By manipulating wave polarization with these promising IRSs through interior-point and conditional gradient methods, advanced dual-polarized transmission strategies are implemented, which can effectively mitigate SIC-related problems and remarkably improve the data rates of all users, both in the downlink and uplink of dual-polarized MIMO-NOMA networks. Among our contributions for the downlink, besides optimizing the IRS reflecting elements, a closed-form expression is derived for the ergodic rates considering large IRSs, whereas for the uplink, also a low-complexity alternate power allocation policy is proposed for balancing uplink data rates.

Next, motivated by the impressive broader region of achievable rates possible with RSMA, this research is advanced and the advantages of the amalgamation between IRSs and MIMO-RSMA are investigated, showing that SIC issues can also degrade the performance of RSMA-based schemes. To solve the limitations introduced with SIC once and for all, in our last results, a novel high-performance dual-polarized massive MIMO-RSMA scheme is proposed that does not require SIC, thereby eliminating all associated problems. As a practical tool for assisting the design of the proposed system, a deep neural network (DNN) model is implemented for predicting the ergodic sum-rates observed in the network with high accuracy. Last, an intelligent DNN-aided adaptive power allocation strategy is developed, which maximizes the sum-rate of the dual-polarized MIMO-RSMA even under high levels of cross-polar interference and imperfect channel state information. Our contributions and all novel transmission schemes proposed in this doctoral dissertation are supported with extensive simulation results and fair performance comparisons with state-of-the-art baseline communication systems.

Keywords: Massive MIMO, non-orthogonal multiple access, rate-splitting multiple access, intelligent reflecting surfaces, performance analysis, resource optimization, deep neural networks

Acknowledgments

The research reported in this doctoral dissertation was carried out at the Department of Electrical Engineering, LUT School of Energy Systems, Lappeenranta–Lahti University of Technology LUT, Finland, from September 2019 to October 2022. This work was mainly part of the research project ee-IoT n.319009, funded by the Academy of Finland, and partly related to the projects FIREMAN consortium n.326270 of the CHIST-ERA grant CHIST-ERA-17-BDSI-003 and EnergyNet Research Fellowship n.321265/ n.328869, also funded by the Academy of Finland. During the period of this research, I had the privilege to receive the prestigious Nokia Foundation Award and the LUT Research Foundation Award for outstanding doctoral studies.

Firstly, I would like to express my deepest gratitude to my principal supervisor, and good friend, Associate Professor Pedro Henrique Juliano Nardelli, for giving me the opportunity of pursuing my doctoral studies with the School of Energy Systems at LUT. Many thanks for the continual support, patience, and friendship since the very start of this journey.

I would like to extend my gratitude to my supervisor Dr. Daniel Benevides da Costa, from the Technology Innovation Institute (TII), the United Arab Emirates, for his invaluable guidance and friendship throughout my master's and doctoral studies. His technical expertise, wise comments, and constant encouragement have been essential to my academic and personal achievements. Many thanks to my supervisor Professor Petar Popovski from Aalborg University, Denmark, for his meticulous comments, inspiring ideas, and invaluable contributions to this research work. I am also grateful for the warm welcoming at his research group in 2020, where I had the opportunity to make a short but fruitful research visit. I also want to express my sincere gratitude to Professor Francisco Rafael M. Lima, from the Federal University of Ceará, Brazil, and Professor Constantinos B. Papadias, from the American College of Greece, Greece, for their collaboration, ideas, and always pertinent comments, which, for sure, have been crucial for the development of this doctoral dissertation.

Special thanks to the reviewers of this dissertation, Dr. Himal A. Suraweera from the University of Peradeniya, Sri Lanka, and Professor Telex M. N. Ngatched from Memorial University, Canada, for their valuable time spent on reading this dissertation and for the constructive comments. I wish to express my deepest gratitude also to Associate Professor Hanna Niemelä for her meticulous language revision, which has greatly improved the text of this dissertation.

With all my heart, my deepest gratitude to my beloved wife, Ana Jéssica Sousa de Sena, my life partner and my everything, the one who is always by my side, providing me endless support, encouragement, and love. You are, have been, and always will be the sunshine that lights up my days. During this doctoral journey, your love and care have inspired me and given me the strength to go through even the coldest and darkest Finnish days.

My deepest gratitude to my father (in memoriam), José Pereira de Sena, my mother, Mirian Pereira de Sousa, my sister, Aline Maria Sousa de Sena, and my aunts, Antonia Miraci de Sousa and Erotildes Pereira Paiva, for their unceasing love, caring, and moral values that shaped me into the person I am today.

Not least important, many thanks to all my friends for so many good memories, which have made my doctorate days easier, more joyful, and unforgettable. Specially, to my friends Daniel Gutiérrez, Majid Hussain, Mehar Ullah, Arun Narayanan, Dick Carrillo, Marcelo Hamaguchi, Clara Mendoza, and Olimar Borges.

Arthur Sousa de Sena
October 2022
Lappeenranta, Finland

To my love,
my wife Jéssica

Contents

Publications

List of Publications

The reported research work is based on the collection of papers listed below, cited in the text as Publications [I]–[VI] and appended to the end of this dissertation. The rights to include the papers in this dissertation have been granted by the publishers.

[I] **A. S. de Sena**, F. R. M. Lima, D. B. da Costa, Z. Ding, P. H. J. Nardelli, U. S. Dias, and C. B. Papadias, "Massive MIMO-NOMA Networks with Imperfect SIC: Design and Fairness Enhancement," *IEEE Transactions on Wireless Communications*, vol. 19, no. 9, pp. 6100–6115, Sep. 2020.

[II] **A. S. de Sena**, D. Carrillo, F. Fang, P. H. J. Nardelli, D. B. da Costa, U. S. Dias, Z. Ding, C. B. Papadias, and W. Saad, "What Role Do Intelligent Reflecting Surfaces Play in Multi-Antenna Non-Orthogonal Multiple Access?" *IEEE Wireless Communications*, vol. 27, no. 5, pp. 24–31, Oct. 2020.

[III] **A. S. de Sena**, P. H. J. Nardelli, D. B. da Costa, F. R. M. Lima, L. Yang, P. Popovski, Z. Ding, and C. B. Papadias,"IRS-Assisted Massive MIMO-NOMA Networks: Exploiting Wave Polarization," *IEEE Transactions on Wireless Communications*, vol. 20, no. 11, pp. 7166–7183, May 2021.

[IV] **A. S. de Sena**, P. H. J. Nardelli, D. B. d. Costa, U. S. Dias, P. Popovski, and C. B. Papadias, "Dual-Polarized IRSs in Uplink MIMO-NOMA Networks: An Interference Mitigation Approach," *IEEE Wireless Communications Letters*, vol. 10, no. 10, pp. 2284–2288, Jul. 2021.

[V] **A. S. de Sena**, P. H. J. Nardelli, D. B. da Costa, P. Popovski, and C. B. Papadias, "Rate-Splitting Multiple Access and Its Interplay with Intelligent Reflecting Surfaces," *IEEE Communications Magazine*, vol. 60, no. 7, pp. 52–57, Jul. 2022.

[VI] **A. S. de Sena**, P. H. J. Nardelli, D. B. da Costa, P. Popovski, C. B. Papadias, and M. Debbah, "Dual-Polarized RSMA for Massive MIMO Systems" *IEEE Wireless Communications Letters*, vol. 11, no. 9, pp. 2000–2004, Sep. 2022.

Arthur Sousa de Sena is the leading author and responsible for the original ideas proposed in Publications [I]–[VI]. He carried out extensive literature reviews, performed theoretical studies, formulated and solved the optimization problems, and implemented the simulation algorithms. The co-authors provided invaluable criticism and supporting ideas for improving the writing and contributions of the referred publications.

Other Related Publications

Interested readers are also encouraged to consult our other 11 related publications, listed below, which have been developed during the period of this doctoral research in collaboration with our reputed partners, but are not included in the base articles of this dissertation.

- D. C. Melgarejo, C. Kalalas, **A. S. de Sena**, P. H. J. Nardelli, and G. Fraidenraich, "Reconfigurable intelligent surface-aided grant-free access for uplink URLLC," in *Proc. 2nd 6G Wireless Summit (6G SUMMIT)*, Mar. 2020, Levi, Finland.

- **A. S. de Sena**, D. B. da Costa, Z. Ding, P. H. J. Nardelli, U. S. Dias, and C. B. Papadias, "Successive Sub-Array Activation for Massive MIMO-NOMA Networks," in *Proc. IEEE International Conference on Communications (ICC 2020)*, Jun. 2020, Dublin, Ireland.

- A. Narayanan, **A. S. de Sena**, D. Gutierrez-Rojas, D. C. Melgarejo, H. M. Hussain, M. Ullah, S. Bayhan, and P. H. J. Nardelli, "Key Advances in Pervasive Edge Computing for Industrial Internet of Things in 5G and Beyond," *IEEE Access*, 8, pp. 206734–206754, Nov. 2020.

- **A. S. de Sena**, P. H. J. Nardelli, D. B. da Costa, F. R. M. Lima, L. Yang, P. Popovski, Z. Ding, and C. B. Papadias, "IRS-Assisted Massive MIMO-NOMA Networks with Polarization Diversity," in *Proc. IEEE International Conference on Communications Workshops (ICC Workshops)*, Jun. 2021, Montreal, Canada.

- R. C. Moioli, P. H. J. Nardelli, M. T. Barros, W. Saad, A. Hekmatmanesh, P. E. G. Silva, **A. S. de Sena**, M. Dzaferagic, H. Siljak, W. V. Leekwijck, D. C. Melgarejo, and S. Latré, "Neurosciences and Wireless Networks: The Potential of Brain-Type Communications and Their Applications," *IEEE Communications Surveys & Tutorials*, vol. 23, no. 3, pp. 1599–1621, Jun. 2021.

- S. K. Taskou, M. Rasti, P. H. J. Nardelli, and **A. S. de Sena**, "Distributed joint power and rate control for NOMA/OFDMA in 5G and beyond," in *Proc. IEEE Global Communications Conference (GLOBECOM)*, Dec. 2021, Madrid, Spain.

- **A. S. de Sena**, M. Ullah, and P. H. J. Nardelli, "Edge Computing in Smart Grids," in *Handbook of Smart Energy Systems*, Springer, Cham, Switzerland, Mar. 2022.

- B. K. S. Lima, **A. S. de Sena**, R. Dinis, D. B. da Costa, M. Beko, R. Oliveira, and M. Debbah, "Aerial intelligent reflecting surfaces in MIMO-NOMA networks: Fundamentals, potential achievements, and challenges," *IEEE Open Journal of the Communications Society*, vol. 3, pp. 1007–1024, Jun. 2022.

- A. Narayanan, M. S. Korium, D. C. Melgarejo, H. M. Hussain, **A. S. de Sena**, P. E. G. Silva, D. Gutierrez-Rojas, M. Ullah, A. E. Nezhad, M. Rasti, E. Pournaras, P. H. J. Nardelli, "Collective intelligence using 5G: Concepts, applications, and challenges in sociotechnical environments," *IEEE Access*, vol. 10, pp. 70394–70417, Jun. 2022.

- **A. S. de Sena**, P. H. J. Nardelli, D. B. da Costa, P. Popovski, and C. B. Papadias, and M. Debbah, "RSMA for Dual-Polarized Massive MIMO Networks: A SIC-Free Approach," in *Proc. IEEE Global Communications Conference (GLOBECOM)*, 2022, Rio de Janeiro, Brazil, (accepted for publication).

- **A. S. de Sena**, P. H. J. Nardelli, D. B. da Costa, P. Popovski, and C. B. Papadias, and M. Debbah, "Dual-Polarized Massive MIMO-RSMA Networks: Tackling Imperfect SIC," *IEEE Transactions on Wireless Communications*, (submitted).

Nomenclature

Acronyms

3GPP	3rd Generation Partnership Project
5G	Fifth generation
6G	Sixth generation
ADAM	Adaptive moment estimation
BPCU	Bits per channel use
BS	Base station
CDF	Cumulative distribution function
CSI	Channel state information
DNN	Deep neural network
DoF	Degrees of freedom
FDD	Frequency division duplex
GPU	Graphics processing unit
IRS	Intelligent reflecting surface
iXPD	Inverse cross-polar discrimination
JSDM	Joint spatial division and multiplexing
KKT	Karush–Kuhn–Tucker
LOS	Line-of-sight
LTE-A	Long-Term Evolution Advanced
MA	Multiple access
MF	Matched filter
MIMO	Multiple-input multiple-output
MSE	Mean-squared error
NLOS	Non-line-of-sight
NOMA	Non-orthogonal multiple access
NR	New Radio
OFDM	Orthogonal frequency division multiplexing
OFDMA	Orthogonal frequency division multiple access
OMA	Orthogonal multiple access
PDF	Probability density function
QAM	Quadrature amplitude modulation
ReLU	Rectified linear unity

RMSE	Root mean squared error
RSMA	Rate-splitting multiple access
SC	Superposition coding
SDMA	Space-division multiple access
SER	Symbol error rate
SIC	Successive interference cancellation
SINR	Signal-to-interference-plus-noise ratio
SISO	Single-input single-output
SNR	Signal-to-noise ratio
SVD	Singular value decomposition
SWIPT	Simultaneous wireless information and power transfer
TDD	Time division duplex
TDMA	Time division multiple access
TPU	Tensor processing unit
UAV	Unmanned aerial vehicle
VWN	Virtualized wireless network

Notation and Special Functions

a	Scalar
$\mathbf{a}$	Column vector
$\mathbf{A}$	Matrix
$\|a\|$	Magnitude of a
$\|\|\mathbf{a}\|\|$	Euclidean norm of $\mathbf{a}$
$[\mathbf{a}]_i$	ith entry of $\mathbf{a}$
$[\mathbf{A}]_{i,j}$	(i,j) entry of $\mathbf{A}$
$[\mathbf{A}]_{i:j}$	Submatrix of $\mathbf{A}$ containing its columns from i to j
$[\mathbf{A}]_{:j}$	jth column of $\mathbf{A}$
$\mathbf{A}^T$	Transpose of $\mathbf{A}$
$\mathbf{A}^H$	Hermitian transpose of $\mathbf{A}$
$\mathbf{A}^{-1}$	Inverse of $\mathbf{A}$
$\mathbf{A}^\dagger$	Moore–Penrose pseudo-inverse of $\mathbf{A}$
$\mathrm{tr}\{\mathbf{A}\}$	Trace of $\mathbf{A}$
$\mathrm{vec}\{\mathbf{A}\}$	Transforms $\mathbf{A}$ into a column vector
$\mathrm{vecd}\{\mathbf{A}\}$	Converts the diagonal elements of a square matrix $\mathbf{A}$ into a column vector

$\mathrm{diag}\{\mathbf{a}\}$	Transforms a vector $\mathbf{a}$ of length M into an $M \times M$ diagonal matrix
$\mathbf{I_M}$	Identity matrix of dimension $M \times M$
$\mathbf{0}_{M,N}$	Matrix of dimension $M \times N$ with all zero entries
$\mathbf{1}_{M,N}$	Matrix of dimension $M \times N$ with all one entries
$\circledcirc$	Hadamard product
$\otimes$	Kronecker product
$\odot$	Khatri–Rao product [1]
$\Re\{a\}$	Real part of a complex number a
$a^{'}$	Complex conjugate of a complex number a
$\lvert\mathscr{A}\rvert$	Cardinality of a set $\mathscr{A}$
$\circ$	Function composition
$\mathrm{E}\{\cdot\}$	Expectation
$\Gamma(\cdot)$	Gamma function [2, eq. (8.310.1)]
$\gamma(\cdot,\cdot)$	Lower incomplete Gamma function [2, eq. (8.350.1)]
$G_{p,q}^{m,n}\left({\mathbf{a} \atop \mathbf{b}} \,\middle\vert\, x\right)$	Meijer's G-function [2, eq. (9.301)]
$\mathrm{Ei}(\cdot)$	Exponential integral
$\mathbb{R}$	Field of real numbers
$\mathbb{C}$	Field of complex numbers

1 Introduction

1.1 Context and Motivation

While fifth-generation (5G) wireless systems are still gaining momentum worldwide, both academia and industry have started the race to develop the sixth-generation (6G) [3]. Once 5G is completely deployed, it should support demanding applications from diverse verticals, such as automotive, energy, manufacturing, healthcare, and entertainment, to name but a few. In turn, 6G should extend the range of capabilities and boost the performance of the applications already supported by 5G. Unforeseen services and use cases should also emerge as the 6G era approaches [4]. In order to enable such an unprecedented range of applications, a multitude of stringent requisites must be met, including ultra-dense connectivity, ultra-low latency, extreme data rates, and high spectral and energy efficiencies. In this regard, multi-antenna technologies such as massive multiple-input multiple-output (MIMO) shall play a central role [5]. By employing a large number of antennas at the base station (BS), a massive MIMO system is able to communicate with multiple users simultaneously (in the same frequency and time slot) and deliver near-optimal performance by simple linear precoding (or beamforming) techniques. Such features provide impressive connectivity and spectrum improvements that are augmented further with the increase of transmit and receive antennas. As a result, massive MIMO systems are capable of remarkably outperforming classical single-input single-output (SISO) schemes and multiuser small-scale MIMO.

Nevertheless, antenna elements cannot be installed indiscriminately in size-constrained arrays. Reducing the interantenna space to increase the number of antennas is also not the best option because channel correlation is amplified, which can degrade the performance of massive MIMO. A clever solution for relaxing such a constraint is achieved by fabricating antenna arrays with pairs of co-located dual-polarized antennas, e.g., with vertical and horizontal orientations. The strategy enables the construction of compact arrays with twice the number of antennas of single-polarized counterparts with identical physical dimensions. In addition to the efficient space utilization, dual-polarized antenna arrays are standard in commercial communication systems [6], implying that the polarization domain is a practical and abundant extra resource that can be exploited for performance optimization. As demonstrated in [7], by employing proper transmission strategies, dual-polarized massive MIMO systems can enable polarization diversity for users, leading to more reliable communication and spectral gains that considerably outperform conventional single-polarized schemes. Motivated by the above-mentioned features, this dissertation focuses on both single-polarized and dual-polarized MIMO systems, as more details will be provided later.

Despite the undeniable advantages of single and dual-polarized massive MIMO systems, in scenarios where users are located in a similar angular sector or sharing the same scattering environment, it can become infeasible to establish reliable noninterfering communication by counting solely on linear precoding. To overcome this issue and ensure zero inter-beam interference, orthogonal multiple access (OMA) techniques, such as time-division multiple access (TDMA), are conventionally employed in massive MIMO networks. Even though classical OMA techniques are able to avoid interuser interference effectively, they provide a low spectral efficiency and a high communication latency, which worsens as the number of scheduled users grows [6]. Therefore, MIMO-OMA schemes are not suited for meeting the demanding requirements of future 6G communication systems.

The limitations of OMA techniques motivate the use of more sophisticated multiple access (MA) strategies. In particular, power-domain non-orthogonal multiple access (NOMA) is one promising candidate technique for future-generation MIMO systems so that MIMO-NOMA can serve multiple users simultaneously even when located in overlapping spatial directions and sharing highly correlated channels [8]. When operating in the downlink mode, NOMA superimposes the data symbols of different users in the power domain using superposition coding (SC) at the base station (BS) and executes successive interference cancellation (SIC) at the users' side for recovering the transmitted information. On the other hand, in the uplink, the BS is the entity that carries out SIC for decoding the data messages coming from multiple users [9]. These features provide MIMO-NOMA systems with attractive connectivity, latency, and spectral improvements, which can significantly outperform conventional MIMO-OMA counterparts [6, 8, 9].

Rate-splitting multiple access (RSMA) has recently appeared as another robust next-generation MA technique for the downlink of MIMO systems with the potential for remarkable performance improvements [10, 11]. RSMA is based on the concept of rate splitting proposed in [12], which was motivated by the goal of expanding the region of achievable rates. At the BS, RSMA encodes the data messages of different users into common and private symbols. The common symbol is transmitted via a common precoder intended for all uses, whereas the private symbols are sent via private precoders designed and intended for individual users. In the reception, users carry out SIC to retrieve common and private symbols from the received superimposed data stream. This approach enables RSMA to smartly adjust the amount of interference to be decoded and the amount to be considered noise. Because of the flexible interference management, RSMA can offer higher data rates and robustness to scenarios with imperfect channel state information (CSI) [10]. Moreover, recent results have shown that RSMA, when combined with massive MIMO, can outperform all conventional MA techniques, including NOMA, TDMA, space-division multiple access (SDMA), and orthogonal frequency-division multiple access (OFDMA) [11, 13].

Regardless of the above advantages, both massive MIMO-NOMA and MIMO-RSMA systems still have unsolved issues that need to be thoroughly investigated and solved. As already discussed, NOMA and RSMA require SIC to separate the transmitted superimposed symbols, which, despite introducing benefits, also brings drawbacks. First, because of the sequential decoding concept implemented by SIC, the first symbols in the decoding order, i.e., the first SIC layers, will always experience interference from higher layers [14, 7]. In RSMA, for instance, this implies that the common message will always be detected with interference from private messages, whereas in NOMA, all users, except the last one in the decoding order, will recover their messages under interference. This detrimental performance behavior can hamper the achievable data rates of the two techniques. Second, the majority of existing works take for granted that SIC can be carried out without introducing decoding errors. Such an assumption, however, is idealistic and difficult to be realized in practice. In real-world implementations, even if users are capable of estimating the CSI accurately, hardware imperfections can cause error propagation during the SIC decoding process [15, 16]. Third, MIMO-NOMA and MIMO-RSMA, like any other wireless communication technology, are susceptible to the harmful uncontrollable phenomena of the wireless propagation environment. Specifically, the stochastic nature of wireless channels, deep fading, blockages, and signal absorption can severely degrade the performance of such schemes. Thus, innovative strategies and technologies are needed to mitigate these issues and further enhance the capabilities of MIMO-NOMA and MIMO-RSMA.

Fortunately, advances in electromagnetic metamaterials have recently brought to light a disruptive new concept of an intelligent reflecting surface (IRS), which should pave the way to smart propagation environments in next-generation communication networks [17, 18]. An IRS is an engineered two-dimensional thin structure comprising multiple reconfigurable reflecting elements, also called meta-atoms or unity cells, with the size within the subwavelength range. The reflecting elements are made of nearly passive conductive materials and can be implemented with diverse technologies and designs. PIN diodes, varactors, liquid crystals, and graphene are among the most popular choices [18]. Independently of the design of technology, a low-power control layer smartly adjusts the electrical currents flowing through the IRS, which enables the reflecting elements to collectively forward impinging electromagnetic waves with exotic radiation patterns that are not found in nature. This capability allows IRSs to mitigate detrimental wireless phenomena and contribute to optimized (and potentially energy-efficient) signal propagation, which unlocks countless opportunities. For instance, it is possible to improve the signal reception in a particular user and mitigate deep fading, assist interference cancellation, or even manipulate wave polarization [19]. All in all, the impressive features of IRSs hold great potential for tackling the discussed limitations and unleashing the true capabilities of MIMO-NOMA and MIMO-RSMA.

Although a number of technical contributions on the topics of IRS, MIMO-NOMA, and MIMO-RSMA have appeared recently, most of the prior works have addressed these technologies independently, with the majority limiting their studies only to single-polarized system models. As a result, when starting this research work, the full improvement opportunities achievable by the synergy between these promising subjects were unclear. Furthermore, no attempts had been made to solve practical issues of imperfect SIC in MIMO-NOMA and MIMO-RSMA networks through the extra degree of freedom (DoF) offered by the polarization domain. Driven by these major literature gaps and the promising features of the referred technologies, this dissertation provides a complete and in-depth understanding of attractive performance gains offered by the combinations IRS-MIMO-

NOMA and IRS-MIMO-RSMA. Furthermore, in this work, by manipulating wave polarization with promising dual-polarized IRSs, advanced transmissions strategies are implemented, which can effectively mitigate SIC-related problems in both the downlink and uplink of dual-polarized MIMO-NOMA networks. A disruptive novel SIC-free dual-polarized MIMO-RSMA scheme is also proposed.

1.2 Related Works

In this section, a literature review of the most relevant recent works is presented related to the contributions of this dissertation.

1.2.1 NOMA-Related Works

First, the focus is on works that study the effects of SIC error propagation in MIMO-NOMA schemes, from which all consider only single-polarized system models. For instance, the work in [15] investigated SIC issues in the downlink of a massive MIMO-NOMA system. The authors implemented a single-cell communication scenario comprising one multi-antenna BS and multiple single-antenna users. The work investigated a non-orthogonal channel estimation scheme and derived a lower bound expression for the system spectral efficiency. Iterative optimization algorithms for maximizing the weighted sum-spectral efficiency were also proposed. Simulation results were provided to validate the theoretical analysis and algorithms. The work in [20] proposed a suboptimal iterative algorithm for maximizing the sum-rate of a downlink MIMO-NOMA network. In the proposed scenario, the authors equipped both users and the BS with two antennas and investigated two very specific scenarios, considering only two values for the SIC error factor. The authors of [21] studied the outage probability and minimized the total transmit power of a multicarrier NOMA system by modeling the SIC error propagation as a complex Gaussian random variable. Complementary geometric programming and arithmetic–geometric mean approximation techniques were employed to solve the formulated optimization problems. In turn, the work in [22] concentrated on the study of heterogeneous networks. The authors modeled various sources of interference, such as intercell interference, power disparity, and imperfect SIC, and proposed user clustering, power, and bandwidth optimization algorithms.

The detrimental effects of imperfect SIC in the uplink of MIMO-NOMA systems were investigated in [23], where the concept of virtualized wireless networks (VWN) was exploited. This work proposed algorithms based on successive convex approximation and complementary geometric programming for implementing subcarrier and power allocation policies. The work in [24] studied a massive MIMO-NOMA system with distributed antenna arrays, in which the authors derived a closed-form expression for the ergodic sum-rate. The presented numerical results showed that MIMO-OMA can still outperform MIMO-NOMA if the number of users in the network is low. The authors of [25] proposed a full-duplex relaying MIMO-NOMA system and investigated the impacts of both imperfect SIC and in-phase and quadrature-phase imbalance. A full-duplex relaying MIMO-NOMA system was also considered in [26], in which the authors optimized the BS precoders and proposed two user selection strategies by considering inter-user interference and self-interference. The case of α-μ fading channels in cooperative NOMA networks under hardware imperfections was studied in [27], and in [28], the authors tackled imperfect SIC in MIMO-NOMA systems with deep learning techniques.

The vast majority of NOMA works consider that SIC can be perfectly executed. For instance, the work in [29] assumed perfect SIC decoding and investigated fairness issues in a simple system with a single-antenna BS serving multiple single-antenna users. The authors proposed low-complexity bisection-based iterative algorithms to solve the formulated power allocation optimization problem. The authors of [30] proposed a user clustering strategy for MIMO-NOMA networks, also considering perfect SIC. This work implemented bisection algorithms for power allocation and presented three suboptimal algorithms for performing user clustering. The work in [31] proposed a NOMA protocol for ensuring that users achieve data rates that are at least the same as those achieved with OMA. For implementing the strategy near and cell-edge single-antenna, the users were paired to form NOMA groups. The authors also investigated the outage probability experienced with the proposed approach. In [32] and [33], user clustering algorithms were proposed based on proportional fairness to balance throughput and fairness. The work in [32] derived an optimal power allocation policy for maximizing the system sum-rate so that the rates of weak users are at least equal to those achieved with OMA. In [34], the authors developed dynamic resource allocation policies, which are optimally obtained by Lagrangian dual decomposition. The millimeter-wave MIMO-NOMA case was addressed in [35], in which spatial sparsity was exploited to propose suboptimal power allocation protocols. However, to the present author's knowledge, [7] was the only dual-polarized MIMO-NOMA-related work reported before starting this research. Specifically, the authors of [7] proposed polarization diversity and multiplexing strategies for a dual-polarized MIMO-NOMA network. The developed dual-polarized transmission schemes significantly outperformed conventional single-polarized counterparts in the presented simulation results.

1.2.2 RSMA-Related Works

Although the concept of splitting rates into two data streams dates back to 1978 [12], the modern RSMA technique for MIMO systems has appeared very recently, making this research area still little explored. As a result, to the best of the present author's knowledge, all existing MIMO-RSMA-related works prior to Publication [VI] consider only single-polarized system models. For instance, the work in [10] studied a single-polarized MIMO network, with a single BS communicating in the downlink mode with multiple single-antenna users. Simulation results demonstrated that MIMO-RSMA remarkably outperforms conventional multiuser MIMO and MIMO-NOMA schemes considering both underloaded and overloaded scenarios. The authors of [11] investigated harmful issues of high user mobility in single-polarized massive MIMO-RSMA networks, where lower bound expressions for the ergodic sum-rates were derived. This work also implemented a suboptimal allocation policy for adjusting the power coefficients of common and private symbols. The authors provided link-level simulations, which revealed that the proposed massive MIMO-RSMA scheme is significantly more robust to high-mobility scenarios than conventional massive MIMO systems. The work in [36] addressed MIMO-RSMA cooperative user-relaying networks. This work proposed an algorithm based on successive convex approximations for jointly optimizing precoders, message split, and time slot allocation, aiming at max-min fairness. The MIMO-RSMA multibeam satellite case was investigated in [37]. The authors of this work characterized the system DoF and developed a transmit power optimization strategy, also aiming at max-min data rate fairness. The proposed MIMO-RSMA satellite transmission scheme delivered attractive performance improvements against baseline systems. The application of RSMA to visible-light communications was studied in [38], where authors considered a simple two-user scenario. The work in [39] investigated the benefits of MIMO-RSMA in a cloud radio access network, and multicarrier MIMO-RSMA schemes were considered in [40].

1.2.3 IRS-Related Works

Most of the recent works on the IRS-MIMO subject are focused on investigating single-polarized point-to-point or OMA-based schemes. For instance, point-to-point IRS-MIMO systems with both frequency-flat and frequency-selective fading operating with orthogonal frequency division multiplexing (OFDM) were investigated in [41]. The authors of this work optimized the BS precoders and IRS reflecting elements to maximize the ergodic data rates. Simulation results confirmed the effectiveness of the implemented optimization algorithms and showed that the proposed IRS-assisted scheme outperforms conventional MIMO systems with and without IRSs. The work in [42] addressed the minimization of symbol error rate (SER) for a point-to-point IRS-MIMO system. The authors proposed four alternate methods for optimizing the BS precoding matrix and IRS-reflecting elements. All proposed strategies were able to deliver significantly lower SER curves than those achieved with the considered baseline MIMO systems without an IRS. The proposed schemes also outperformed MIMO systems assisted by full-duplex relays. In [43], the authors minimized the total transmit power of a single-cell multiuser IRS-MIMO network under users' signal-to-interference-plus-noise ratio (SINR) constraints. The authors also performed an asymptotic analysis for large IRSs. It was found through simulations that, with fewer transmit antennas, the proposed IRS-MIMO system can reach the same rate performance of massive MIMO-OMA systems without an IRS. The work in [44] investigated the multicell IRS-MIMO communication scenario. The authors exploited one IRS to assist transmission to cell-edge users. To this end, two algorithms based on majorization-minimization and the complex circle manifold methods were implemented to optimize the reflecting elements. Multiuser IRS-MIMO cognitive radio systems were addressed in [45]. In this work, a block coordinate descent algorithm was proposed to maximize the achievable weighted sum rates of the system. Furthermore, the study of simultaneous wireless information and power transfer (SWIPT) in IRS-MIMO systems was considered in [46], and [47] investigated the security issues of IRS-MIMO schemes.

A few recent papers have studied the application of IRSs to MIMO-NOMA schemes. For example, the authors of [48] considered a simple IRS-MIMO-NOMA network with two users per NOMA group. The authors performed a theoretical analysis and derived a closed-form expression for the outage probability observed by each user. The performance of the proposed scheme was investigated through simulation examples, where hardware impairments were also taken into account. The work in [49] investigated a two-user IRS-MIMO-NOMA network. The deployed IRS and the BS precoding vectors were jointly optimized to minimize the total power consumption of the proposed system. In the simulation results, the proposed system outperformed conventional MIMO-NOMA and MIMO-OMA schemes in terms of energy efficiency. The impacts of employing continuous and discrete reflecting coefficients were investigated in [50]. This work proposed algorithms to maximize the sum rate of a multiuser IRS-MIMO-NOMA network, which remarkably outperformed conventional MIMO-NOMA and MIMO-OMA baseline systems. Moreover, results showed that 3-bit phase shifters were enough to reach almost the same performance as the ideal case with infinity resolution. The multicluster IRS-MIMO-NOMA case was investigated in [51]. By relying solely on the deployed IRS, the authors implemented an efficient algorithm for canceling intercluster interference. Closed-form expressions for the outage probability and ergodic rates were derived. The proposed system achieved a better performance than zero-forcing and signal-alignment-based schemes in all presented simulation examples. The work in [52] studied the application of IRSs to millimeter-wave MIMO-NOMA systems. The authors of this work developed an algorithm for optimizing the transmit power coefficients, reflecting elements, and active BS precoding matrices aiming at sum-rate maximization. The authors of [53] investigated the application of unmanned aerial vehicles (UAV) employing IRSs to MIMO-NOMA networks, and the work in [54] studied and implemented a prototype of a dual-polarized IRS to transmit quadrature amplitude modulation (QAM) symbols in a simple two-antenna MIMO system.

With the exception of Publication [V], until the moment of writing this dissertation, only the four works in [55], [56], [57], and [58], investigate the combination of IRS and RSMA schemes. Specifically, the conference paper [55] maximized the energy efficiency of a downlink multiuser MIMO-RSMA network assisted by multiple IRSs under minimum rate constraints. To this end, the authors jointly optimized the reflecting coefficients of all RISs, the BS precoding vectors, and the rate allocation at the BS. The presented simulation results showed that the proposed IRS-MIMO-RSMA scheme delivers a higher energy efficiency than the conventional IRS-MIMO-NOMA IRS-MIMO-OFDMA schemes. The authors of [56] also investigated a scenario with multiple IRSs. However, the IRSs were deployed to assist only single-antenna cell-edge users in a two-layer hierarchical MIMO-RSMA network. By applying an on–off optimization strategy for configuring the IRSs, the authors derived closed-form expressions for the outage probability of both near and cell-edge users. The proposed scheme outperformed all considered baseline systems and significantly improved the performance of cell-edge users. The same authors investigated a simplified version of the scenario introduced in [56], in [57], where both the users and the BS employed a single antenna. In this IRS-assisted SISO-RSMA network, an on–off approach was also employed to optimize the reflecting elements of the IRSs. The authors presented extensive simulation results to demonstrate the superior performance of their scheme. Last, the report in [58] deployed one IRS with fully connected reflecting elements to assist multiple single-antenna users in a MIMO-RSMA network. The continuous reflecting coefficients of the IRS were optimized to maximize the system sum-rate, leading to attractive spectral efficiency improvements.

1.3 Overall Objectives and Dissertation Outline

This dissertation investigates and develops promising multi-antenna and MA techniques of great potential for enabling massive access in future beyond-5G and 6G communication systems. In particular, the contributions of this dissertation provide solid answers to the following fundamental research questions:

Q1: What are the impacts of imperfect SIC on the performance of MIMO-NOMA systems, and how can the related issues be mitigated?

Q2: What are the fundamental performance limits in terms of spectral and energy efficiencies achievable with the amalgamation of IRS technology and MIMO-NOMA systems?

Q3: With the help of IRSs, can future wireless communication systems become energy-neutral, and what are the minimum necessary conditions to accomplish this feature?

Q4: Can IRSs truly control all propagation phenomena experienced in wireless channels, e.g., even change the signal polarization, and how to implement this capability?

Q5: Can dual-polarized IRSs harness wave polarization to mitigate degrading interference issues of imperfect SIC in MIMO-NOMA schemes?

Q6: What benefits can IRSs offer to MIMO-RSMA and, reciprocally, how can MIMO-RSMA improve the performance of IRSs?

Q7: Are MIMO-RSMA schemes also vulnerable to imperfect SIC decoding, and how to avoid this harmful issue definitively?

The answers to the above research questions are provided sequentially in the remainder of this dissertation, which is structured into five chapters and can be outlined as follows:

- Chapter 1 provides a comprehensive introduction to the covered topics, giving context and motivation for the development of this dissertation. A literature review of the most relevant state-of-the-art related works is also given, followed by the fundamental research questions and the outline of the dissertation.

- Chapter 2 provides readers with the essential background of concepts and techniques exploited throughout this research work. First, an introduction to the basics of MIMO communication is given, where the correlated and uncorrelated and single and dual-polarized channel models adopted in Publications [I]–[VI] are explained. Then, standard CSI estimation strategies are discussed in brief, and a channel model for characterizing imperfect CSI is introduced. Two important precoding strategies for downlink and uplink communication are also presented. Last, the working principles of NOMA, RSMA, and IRSs are explained.

- Chapters 3 and 4 concentrate on the primary results of this dissertation and answer all the above research questions. Chapter 3, specifically, overviews the contributions provided in Publications [I]–[IV], which are focused on MIMO-NOMA and IRS-assisted MIMO-NOMA schemes. In brief:

    - Section 3.1 presents the results of Publication [I] and addresses question *Q1*, where it is shown that SIC decoding errors can severely degrade the performance of MIMO-NOMA.
    - Section 3.2 introduces the contributions of Publication [II], where IRSs are applied to MIMO-NOMA and the potential achievable spectral and energy efficiency gains are investigated. This section aims to answer questions *Q2* and *Q3*.
    - Sections 3.3 and 3.4 answer questions *Q4* and *Q5* with the results from Publications [III] and [IV]. In these sections, a novel dual-polarized IRS is proposed and its capabilities are exploited to tackle SIC issues in both the downlink and uplink of MIMO-NOMA networks.

- Chapter 4 focuses on the MIMO-RSMA-based schemes proposed in Publications [V] and [VI], as follows:

    - Section 4.1 studies the mutual benefits generated by the synergy between IRS technology and MIMO-RSMA, which clarifies question *Q6*.
    - Last, Section 4.2 answers question *Q7* with a novel dual-polarized MIMO-RSMA scheme proposed in Publication [VI], which is free from SIC problems.

- Chapter 5 finishes this dissertation by summarizing the main scientific contributions of the work, presenting concluding thoughts, and shedding light on promising future research directions.

The complete details of the contributions reported in Publications [I]–[VI] are presented in Chapters 3 and 4.

2 Background

2.1 MIMO Communication Systems

Scattering objects present in wireless networks induce electromagnetic signals to propagate via different paths toward receivers. This phenomenon is known as multipath propagation and can be highly detrimental to the performance of communication systems if not properly addressed. Fortunately, by employing multiple antennas for transmitting and receiving information, the MIMO technology can harness and transform this unavoidable issue into an advantage. More specifically, with the help of preprocessing and decoding strategies, multipath propagation can be exploited to introduce data redundancy or convey simultaneously distinct data streams via the space domain using the same time and frequency resources, which enables MIMO systems to achieve impressive diversity, multiplexing, and spectral gains.

The first patent for the MIMO technology dates back to 1993 [59], which led other works in subsequent years to study further the features of multi-antenna schemes [60, 61]. However, in most of these seminal systems, only point-to-point communication with a small number of antennas was considered. In 2010, by relying on the law of large numbers, the work in [62] investigated the advantages of employing a massive number of antennas for serving multiple spatially distributed users. Specifically, in the asymptotic case, when the number of transmit antennas goes to infinity, two appealing propagation properties can be achieved, which are known as favorable propagation and channel hardening properties. Favorable propagation comes from the well-known property from random matrix theory, which states that

$$\lim_{M\to\infty} \frac{1}{M}\mathbf{h}^H\mathbf{g} \to 0, \quad \text{almost surely,} \tag{2.1}$$

where $\mathbf{h} \in \mathbb{C}^M$ and $\mathbf{g} \in \mathbb{C}^M$ are two mutually independent random vectors with the variances σ_h^2 and σ_g^2, respectively, and whose entries are independent and identically distributed (i.i.d.). On the other hand, channel hardening comes from a second property that ensures

$$\lim_{M\to\infty} \frac{1}{M}\mathbf{h}^H\mathbf{h} \to \sigma_h^2, \quad \text{almost surely.} \tag{2.2}$$

In the context of MIMO systems, if it is assumed that $\mathbf{h}$ and $\mathbf{g}$ are the channel vectors of two distinct single-antenna users, the properties (2.1) and (2.2) reveal, respectively, that the propagation channels of different users approach the orthogonality, and the channel gains of individual users become nearly deterministic as the number of transmit antennas increases. These performance behaviors are illustrated in Figure 2.1. The main implication of such properties is that interuser interference is naturally mitigated by increasing the number of transmit antennas, which enables simple linear precoding techniques, such as zero-forcing, regularized zero-forcing, and matched filter precoding, to achieve near-optimal performance [63, 64]. Moreover, channel hardening also helps to improve chan-

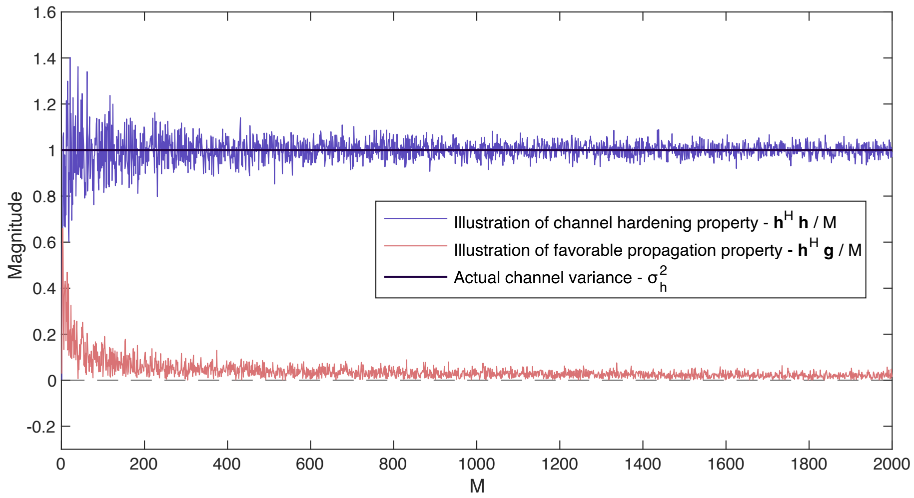

Figure 2.1: Favorable propagation and channel hardening properties. The entries of $\mathbf{h} \in \mathbb{C}^M$ and $\mathbf{g} \in \mathbb{C}^M$ are drawn from the complex standard Gaussian distribution.

nel estimation [65]. As a result, the practical implementation of massive MIMO systems can be greatly simplified. These attractive features, combined with the high spectral efficiency and the massive connectivity capabilities, made the massive MIMO technology an indispensable component of 5G communication systems [66, 67], and it should continue to play a central role in beyond-5G generations.

2.1.1 Single-Polarized MIMO Channel Models

In this subsection, the fundamental background of single-polarized channel models and estimation strategies suited for both multiuser small-scale MIMO and massive MIMO systems is provided. For illustration purposes, let us consider a simple scenario where one BS with M antennas communicates with U users employing N antennas. By assuming that the MIMO system operates in a rich isotropic scattering environment with non-line-of-sight (NLOS) propagation, each antenna will receive a superposition of several wavefronts coming from different scatterers due to multipath phenomena [68]. As a result, the central limit theorem can be exploited to model the wireless channels observed by the uth user by the following random matrix:

$$\mathbf{H}_u = \begin{bmatrix} h_{11,u} & h_{12,u} & \cdots & h_{1N,u} \\ h_{21,u} & h_{22,u} & \cdots & h_{2N,u} \\ \vdots & \cdots & \ddots & \vdots \\ h_{M1,u} & h_{M2,u} & \cdots & h_{MN,u} \end{bmatrix} \in \mathbb{C}^{M \times N}, \tag{2.3}$$

where the entries of $\mathbf{H}_u$ consist of i.i.d. complex Gaussian random variables with zero mean and variance ζ_u, in which ζ_u denotes the large-scale fading coefficient. Each element of $\mathbf{H}_u$, i.e., $h_{mn,u}$, models the complex baseband fast-fading channel response between the mth BS antenna and the nth antenna of the uth user. This channel representation is known as the uncorrelated Rayleigh fading model and is widely employed in the literature because of its simplicity. It is noteworthy that when users have line-of-sight (LOS) channels, the Rayleigh model is no longer valid. In this case, other channel models should be employed, such as the Rician and Nakagami fading models [69]. In particular, in this dissertation, only NLOS scenarios are studied.

Considering wireless channels to have i.i.d. coefficients can be useful for obtaining fundamental performance insights. However, it is an idealistic assumption. In practical MIMO channels, the tight separation between antenna elements, nonuniform electromagnetic radiation caused by the scattering environment, and other propagation phenomena make the entries of $\mathbf{H}_u$ correlated. In other words, signals transmitted from different antennas tend to propagate through a reduced number of spatial directions and common paths. Mathematically, these phenomena make the spatial correlation matrix of $\mathbf{H}_u$ to become rank deficient, i.e., the matrix $\mathbf{R}_u = \mathrm{E}\{\mathbf{H}_u\mathbf{H}_u^H\} \in \mathbb{C}^{M \times M}$ will have a rank $r_u < M$. In such correlated scenarios, modeling the channel matrix $\mathbf{H}_u$ with i.i.d. random variables can lead to unrealistic results. Therefore, it is important to take into account channel correlation issues when designing a MIMO system. To this end, the Karhunen–Loeve decomposition [65, 70] is recalled for incorporating the correlation characteristics into $\mathbf{H}_u$, as follows:

$$\mathbf{H}_u = \mathbf{U}_u \mathbf{\Lambda}_u^{\frac{1}{2}} \mathbf{G}_u \in \mathbb{C}^{M \times N}, \tag{2.4}$$

where $\mathbf{\Lambda}_u \in \mathbb{R}_{>0}^{r_u^\star \times r_u^\star}$ is a real-valued diagonal matrix comprising $r_u^\star < r_u$ nonzero eigenvalues of $\mathbf{R}_u$ sorted in a descending order, $\mathbf{U}_u \in \mathbb{C}^{M \times r_u^\star}$ collects the corresponding $r_u^\star$ left eigenvectors of $\mathbf{R}_u$, which can be obtained from its singular value decomposition (SVD), and $\mathbf{G}_u \in \mathbb{C}^{r_u^\star \times N}$ is a reduced-dimension matrix comprising the nonredundant fast-fading channel coefficients, whose entries follow the complex Gaussian distribution with zero mean and unity variance. Note that the model in (2.4) is also valid in the case in which users employ a single antenna, with the only difference that instead of a matrix $\mathbf{G}_u$, each user would be associated with a reduced dimension fast-fading vector $\mathbf{g}_u \in \mathbb{C}^{r^\star}$. As explained in Subsection 2.1.4, the possibility of decomposing the channels like in (2.4) brings benefits to massive MIMO systems, such as a reduction in feedback overhead and simplification of channel estimation and the precoding design.

2.1.2 Spatial Correlation Model and User Clustering

In (2.4), a generative model was introduced based on the Karhunen–Loeve decomposition for incorporating correlation properties into the channel matrices $\mathbf{H}_u$, which depends on the eigenvalues and eigenvectors of $\mathbf{R}_u$. Now, details are provided on the spatial cor-

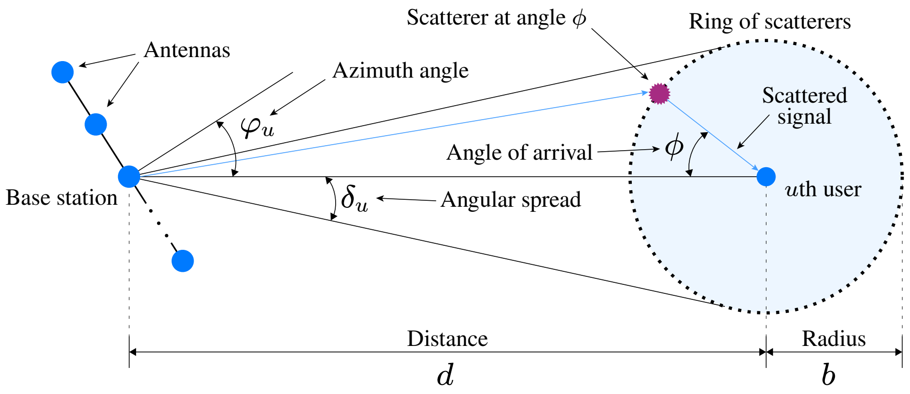

Figure 2.2: Illustration of the one-ring geometrical model.

relation model used for generating the correlation matrices $\mathbf{R}_u$, which was employed in Publications [I], [II], [III], and [VI]. More specifically, the one-ring geometrical model is adopted [70, 71, 72], also known as the local scattering model [65], which is adequate for modeling NLOS-correlated Rayleigh fading channels. The one-ring model characterizes the scenario where one BS employing isotropic antennas is elevated in relation to the users and does not observe scatterers in its near-field. In addition, the transmitted signals are bounced toward users once by a large number of diffuse scattering objects, in which the actual objects are modeled by a cluster of virtual scatterers uniformly distributed in a circumference centered at the users [72]. The model is valid for different array arrangements. However, for simplicity, the BS is equipped with a uniform linear array in this dissertation. Under such assumptions, the correlation between the channels of antennas m and m', from the BS to the uth user, can be calculated by [70, 71]

$$[\mathbf{R}_u]_{m,m'} = \frac{1}{2\delta_u}\int_{-\delta_u}^{\delta_u} e^{-j\frac{2\pi}{\lambda}[\cos(\phi+\varphi_u),\sin(\phi+\varphi_u)](\mathbf{a}_m-\mathbf{a}_{m'})}d\phi, \tag{2.5}$$

where λ is the carrier wavelength, φ_u denotes the azimuth angle corresponding to the center of the ring of scatterers that surrounds the uth user, which has a radius b and a distance of d from the BS. The parameter ϕ represents the angle of arrival of incoming waves, δ_u is the angular spread, such that $\delta_u \approx \mathrm{atan}(b/d)$, and $\mathbf{a}_m$ and $\mathbf{a}_{m'}$ are the coordinate vectors in the two-dimensional plane of antennas m and m', for $m, m' = 1, \cdots, M$. The geometrical scenario characterized by the one-ring model is illustrated in Figure 2.2.

The impact of the interantenna space on channel correlation is illustrated in Figure 2.3, which plots the eigenvalues of $\mathbf{R}_u$ sorted in a descending order. In this example, $\mathbf{R}_u$ is generated with (2.5) considering a uniform linear array of $M = 100$ antennas and a carrier frequency of 3 GHz. Moreover, the cluster of scatterers is located at the azimuth angle of 30° and has an angular spread of 15°. As can be seen, by decreasing the interantenna space, the number of nonzero eigenvalues decreases, which implies that the rank of $\mathbf{R}_u$ also decreases, and the channel correlation intensifies. Therefore, when designing antenna arrays, the number of antennas and the physical space utilization should be carefully optimized in order to achieve satisfactory levels of correlation for the system needs. In particular, the spacing of $\lambda/2$ between antennas is adopted as the standard in Publications [I], [II], [III], and [VI].

In overloaded scenarios or in situations where multiple users are located in overlapping spatial directions, possibly sharing (approximately) the same cluster of scatterers there is a high likelihood of experiencing a strong interuser channel correlation. This phenomenon can hamper the favorable propagation property and make MIMO precoding techniques alone incapable of separating users in space. In these situations, the application of MA techniques is necessary for avoiding severe interuser interference. Nevertheless, as anticipated in Section 1.1, MA techniques also have limitations. In the case of NOMA, for instance, when the number of served users grows, the interference observed in the SIC process and the chances of experiencing decoding errors increase. In its turn, in RSMA, the design of a single common precoder able to satisfy the requirements of a large number of users becomes quite challenging. Therefore, an indiscriminate number of users cannot be served relying solely on MA techniques. Fortunately, user clustering strategies, in which users are organized into smaller clusters, have been proposed to cope with the above-mentioned limitations. In these approaches, MIMO precoding schemes are responsible for multiplexing the different user clusters, and MA techniques have the role of serving users within each cluster separately. As a result, because of the smaller number of users, the complexity of precoding and MA techniques can be considerably reduced.

Employing efficient user clustering strategies becomes then an important concern for MA schemes in massive MIMO networks. In fact, user clustering is an active research area, and several approaches have been provided in the literature [22, 71]. However, the study of this subject goes beyond the scope of this dissertation. Nevertheless, one effective strategy, which is particularly important for sustaining the assumptions made in this dissertation, consists of clustering users based on the similarity of the subspace spanned by users' channel correlation matrices. The authors of [71], for instance, proposed a K-means-based algorithm to partition users into G disjoint spatial groups so that the spatial correlation matrices of users within each group have approximately similar dominant eigenspaces. The proposed algorithm gave as the output G unitary matrices, each one comprising the mean of dominant eigenvectors of users within the given group. These unitary matrices were used for constructing the precoders for multiplexing different groups in space. This possibility makes it reasonable to assume that users receiving signals from a common cluster of scatters share approximately a single effective correlation matrix, as assumed in [14, 7, 70]. More specifically, if the gth spatial group comprises U_g users, it can be assumed that $\mathbf{R}_{g1} \approx \mathbf{R}_{g2} \approx \cdots \approx \mathbf{R}_{gU_g} \approx \mathbf{R}_g$, where $\mathbf{R}_g$ is the effective channel correlation matrix for the gth group. For mathematical tractability, this approximation has been adopted in Publications [I]–[III] and [VI].

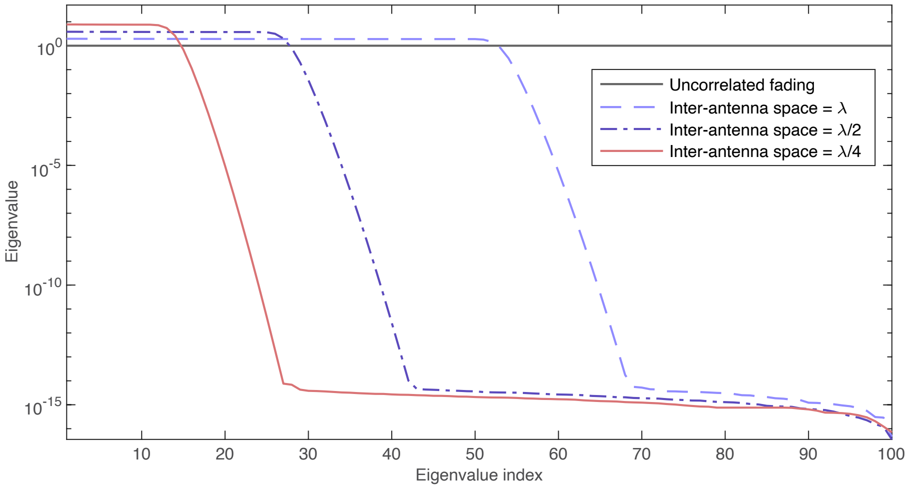

Figure 2.3: Impact of the interantenna space separation on the eigenvalues of the channel correlation matrix $\mathbf{R}_u$ generated with the one-ring geometrical model considering a uniform linear array with $M = 100$ antennas and a cluster of scatterers located at an azimuth angle of $30°$, an angular spread of $15°$, and a carrier frequency of 3 GHz.

2.1.3 Dual-Polarized MIMO Channel Models

As previously discussed, by increasing the number of transmit antennas at the BS, the channels of different users (with nonoverlapping spatial directions) become nearly orthogonal because of the favorable propagation property. Deploying more antennas also helps to boost the antenna array gain and improve signal reception. However, it is not possible to deploy an unlimited number of antennas because of physical space constraints or excessively reduce the interantenna space, as it is illustrated in Subsection 2.1.2. Fortunately, by exploiting the polarization dimension, this limitation can be efficiently mitigated. That is, orthogonal dual-polarized antennas can be implemented, e.g., with vertical and horizontal ($0°$ and $90°$) or slant ($\pm 45°$) orientations, arranged into co-located pairs, thus, leading to compact antenna arrays and attractive performance improvements, as anticipated in Section 1.1. Owing to the above-mentioned advantages, dual-polarized antenna arrays are the preferred architecture deployed in current commercial cellular systems and the standard adopted in the Long-Term Evolution Advanced (LTE-A) and 5G New Radio (NR) specifications of the 3rd Generation Partnership Project (3GPP). [73, 74].

The channel model for a dual-polarized MIMO system is slightly more complicated than the models for the single-polarized counterpart. To explain, let us consider the scenario where one BS with $M/2$ pairs of co-located dual-polarized antennas transmits information to U users employing $N/2$ pairs of dual-polarized antennas. Moreover, let us assume that the antenna pairs are installed with vertical polarization (represented by v throughout this dissertation) and horizontal polarization (represented by h). The dual-polarized channel for the uth user can be represented by a matrix that models the input–output relation between transmit and receive polarizations, i.e., v to v, v to h, h to v, and h to h, as follows [75]:

$$\mathbf{H}_u = \begin{bmatrix} \mathbf{H}_u^{vv} & \mathbf{H}_u^{vh} \\ \mathbf{H}_u^{hv} & \mathbf{H}_u^{hh} \end{bmatrix} \in \mathbb{C}^{M \times N}, \tag{2.6}$$

where $\mathbf{H}_u^{ab} \in \mathbb{C}^{\frac{M}{2} \times \frac{N}{2}}$ is a matrix that models the channels from transmit polarization a to receive polarization b, in which $a, b \in \{v, h\}$. In ideal environments with no cross-polarization transmissions, the channel coefficients of the off-diagonal blocks in (2.6) should be zero, i.e., $\mathbf{H}_u^{vh} = \mathbf{H}_u^{hv} = \mathbf{0}_{\frac{M}{2}, \frac{N}{2}}$. However, in real-world scenarios, this condition does not hold. In practice, as a result of scattering phenomena, such as reflection, diffraction, diffuse scattering, and others, the radiated energy can leak from one polarization to another. Furthermore, even in scenarios without scattering, practical antennas have a nonzero radiation pattern in the cross-polar electromagnetic field [73], which makes antennas incapable of transmitting perfectly polarized signals. The combination of these scattering and antenna fabrication issues causes cross-polar interference, i.e.,$\mathbf{H}_u^{vh} \neq \mathbf{H}_u^{hv} \neq \mathbf{0}_{\frac{M}{2}, \frac{N}{2}}$, which can be modeled by the following power imbalance matrix:

$$\mathbf{X} = \begin{bmatrix} 1 & \sqrt{\chi} \\ \sqrt{\chi} & 1 \end{bmatrix}, \tag{2.7}$$

where $\chi \in [0, 1]$ denotes the inverse cross-polar discrimination (iXPD) that measures the ratio of cross-polar to co-polar signal powers observed at receivers, i.e., the higher the value of χ, the more cross-polar interference is experienced in the system. By recalling the Karhunen–Loeve decomposition [65, 70] and incorporating the matrix from (2.7) in (2.6), the full dual-polarized channel matrix for the uth user can be structured as [7, 76, 73]

$$\begin{aligned} \mathbf{H}_u &= \left(\mathbf{I}_2 \otimes \left(\bar{\mathbf{U}}_u \bar{\mathbf{\Lambda}}_u^{\frac{1}{2}}\right)\right) \left(\begin{bmatrix} \mathbf{G}_u^{vv} & \mathbf{G}_u^{vh} \\ \mathbf{G}_u^{hv} & \mathbf{G}_u^{hh} \end{bmatrix} \circledcirc \left(\begin{bmatrix} 1 & \sqrt{\chi} \\ \sqrt{\chi} & 1 \end{bmatrix} \otimes \mathbf{1}_{\bar{r}^\star \times \frac{N}{2}} \right) \right) \\ &= \left(\mathbf{I}_2 \otimes \left(\bar{\mathbf{U}}_u \bar{\mathbf{\Lambda}}_u^{\frac{1}{2}}\right)\right) \begin{bmatrix} \mathbf{G}_u^{vv} & \sqrt{\chi}\mathbf{G}_u^{vh} \\ \sqrt{\chi}\mathbf{G}_u^{hv} & \mathbf{G}_u^{hh} \end{bmatrix}, \end{aligned} \tag{2.8}$$

and the corresponding dual-polarized correlation matrix can be expressed as

$$\mathbf{R}_u = \mathrm{E}\{\mathbf{H}_u \mathbf{H}_u^H\} = \begin{bmatrix} (1+\chi)\bar{\mathbf{R}}_u & \mathbf{0} \\ \mathbf{0} & (1+\chi)\bar{\mathbf{R}}_u \end{bmatrix} \in \mathbb{C}^{M \times M}, \tag{2.9}$$

where $\bar{\mathbf{R}}_u \in \mathbb{C}^{\frac{M}{2} \times \frac{M}{2}}$ is the channel correlation matrix for each polarization with a rank

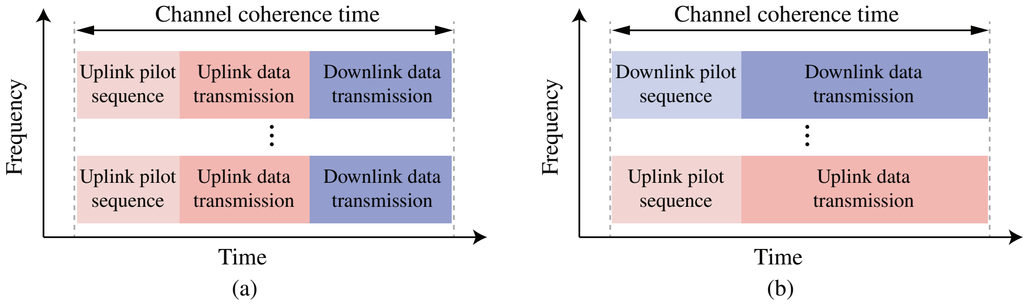

Figure 2.4: Simplified coherence block for: (a) TDD, and (b) FDD.

denoted by $\bar{r}_u$, $\bar{\mathbf{\Lambda}}_u$ is the $\bar{r}_u^\star \times \bar{r}_u^\star$ diagonal matrix with the $\bar{r}_u^\star$ nonzero eigenvalues of $\bar{\mathbf{R}}_u$, $\bar{\mathbf{U}}_u \in \mathbb{C}^{\frac{M}{2} \times \bar{r}_u^\star}$ comprises the left eigenvectors of $\bar{\mathbf{R}}_u$ associated with its nonzero eigenvalues, and $\mathbf{G}_u^{ab} \in \mathbb{C}^{\bar{r}_u^\star \times \frac{N}{2}}$ is the reduced-dimension fast-varying channel matrix from polarization a to b, with $a, b \in \{v, h\}$, whose entries follow the complex Gaussian distribution with zero mean and unit variance.

2.1.4 Channel Estimation Strategies and Imperfect CSI Model

Channel estimation in MIMO systems can be carried out following both FDD and time division duplex (TDD) approaches. TDD systems rely on channel reciprocity to estimate downlink channels by uplink pilot training. To this end, the total time spent for uplink and downlink transmissions must be shorter than the channel coherence interval, which makes the TDD protocol more suited for low-mobility scenarios [65]. In contrast, FDD systems separate uplink and downlink transmissions in the frequency domain. Consequently, channel reciprocity cannot be exploited by FDD. Specifically, pilot sequences are required to be transmitted in both directions, uplink and downlink, and users need to feed back a quantized version of the downlink channel estimate to the BS for precoding [76]. The number of downlink pilot sequences in FDD systems scale with the number of BS antennas. As a result, the uplink feedback overhead can become overwhelming when large antenna arrays are employed at the BS (mainly when considering i.i.d. channel coefficients [77]). On the other hand, in TDD systems, the duration of the uplink pilot training phase is independent of the number of BS antennas and depends only on the number of connected users. For this reason, TDD is the most common protocol employed in massive MIMO systems. Simplified diagrams for TDD and FDD protocols are provided in Figure 2.4.

Nevertheless, for commercial reasons, there is still a huge interest in developing massive MIMO systems with the FDD protocol. Most notable strategies aim to reduce the complexity of the FDD protocol by exploiting the spatial correlation structure of the channels in (2.4) [70, 78, 77]. More specifically, because the correlation matrix $\mathbf{R}_u$ captures slowly varying characteristics of the channel, they can be accurately estimated by long-term measurements after several coherence intervals. Thus, only the reduced-dimension fast-fading channel $\mathbf{G}_u$ (or $\mathbf{G}_u^{ab}$ in the case of dual-polarized schemes) needs to be estimated frequently, which is less demanding than estimating the full channel $\mathbf{H}_u$ that has a higher dimension. As demonstrated in [70], this strategy can significantly simplify the channel estimation and reduce the feedback overhead and precoding design, which makes FDD also feasible to be employed in massive MIMO systems. It is noteworthy that the MIMO schemes proposed in Publications [I]–[VI] are generic enough to operate under both TDD and FDD protocols. Furthermore, the study of channel estimation strategies is beyond the scope of this dissertation, arising thus as a potential future research direction.

Regardless of the channel estimation strategy and the operation mode (TDD or FDD), because of quantization errors, outdated CSI, pilot contamination, and other issues, the acquisition of $\mathbf{G}_u$ at the BS is imperfect in practice. Following the work in [76], the corrupted estimate of $\mathbf{G}_u$ can be modeled by

$$\hat{\mathbf{G}}_u = \sqrt{1-\tau_u^2}\mathbf{G}_u + \tau_u\mathbf{Z}_u, \tag{2.10}$$

where $\mathbf{Z}_u$ is a complex standard Gaussian random matrix independent of $\mathbf{G}_u$, and τ_u is a factor that informs the quality of the CSI estimation for the uth user, in which $\tau_u = 0$ represents the scenario with perfect CSI, and $\tau_u = 1$ corresponds to the extreme case where $\hat{\mathbf{G}}_u$ is statistically independent of $\mathbf{G}_u$.

The channel models adopted in Publications [I], [II], and [III] are based on the correlated Rayleigh fading model in (2.4), where the performance of massive MIMO systems is studied in combination with different multiple access techniques in scenarios where the BS has perfect knowledge of the CSI. The imperfect CSI case is studied in Publication [VI], where the model in (2.10) is adopted for capturing the imperfect estimation of the reduced-dimension fast-varying fading channels. In turn, small-scale MIMO systems are investigated in Publications [IV] and [V], in which the propagation channels are assumed to follow the uncorrelated Rayleigh fading model in (2.3). Furthermore, Publications [I], [II], and [V] consider single-polarized channels, whereas Publications [III], [IV], and [VI] investigate dual-polarized MIMO schemes.

2.1.5 MIMO Precoding Strategies

There is a plethora of precoding strategies for MIMO systems available in the literature, each one with its own characteristics, advantages, and drawbacks. However, providing an extensive survey of all these strategies goes beyond the objectives of this dissertation. Instead, in this subsection, the focus is only on the main precoding techniques that have been proposed in Publications [I]–[VI].

Precoding for Downlink Spatial Multiplexing

First, the concepts of the precoders used for downlink transmissions in Publications [I], [II], [III], and [VI] are introduced. These concepts are inspired by the joint spatial division and multiplexing (JSDM) technique proposed in [70] and its extension to dual-polarized systems in [7] and [76]. Specifically, JSDM consists of a multistage precoding technique of the form $\mathbf{B}_g\mathbf{v}_{gu} = \mathbf{P}_g\mathbf{W}_g\mathbf{v}_{gu}$, where $\mathbf{P}_g$ is a precoding matrix responsible for nulling out the interference of groups $g' \neq g$, $\mathbf{W}_g$ is an eigen-beamforming matrix designed to maximize the dominant effective channel gains in the intended group g, and $\mathbf{v}_{gu}$ is an inner precoding vector usually designed to separate and further improve the performance of users within each group. The design of $\mathbf{P}_g$ and $\mathbf{W}_g$ only depends on long-term statistical information of the channels, i.e., on the spatial correlation matrices $\mathbf{R}_g$. In turn, $\mathbf{v}_{gu}$ can be constructed based (or not) on the reduced-dimension fast-fading channel matrices $\mathbf{G}_{gu}$, whose design depends on the implemented MA strategy and the specific goals of the communication system. Thus, more details of $\mathbf{v}_{gu}$ will be provided in later chapters. As discussed in [70], this multistage structure is beneficial to massive MIMO systems and can help to reduce the complexity and overhead of channel estimation, making JSDM suitable for both the TDD and FDD modes. Next, the construction of $\mathbf{P}_g$ and $\mathbf{W}_g$ is explained.

Let us start with the design of $\mathbf{P}_g$. In order to explain, let us consider a downlink network where one BS with M antennas wishes to multiplex G groups in space, and within each group there are U users. Following the model in (2.4), the channel matrix for the uth user in the gth group can be expressed by

$$\mathbf{H}_{gu} = \mathbf{U}_{gu}\mathbf{\Lambda}_{gu}^{\frac{1}{2}}\mathbf{G}_{gu}. \tag{2.11}$$

It can be noticed in the above channel structure that intergroup interference can be canceled if $\mathbf{P}_g$ can null out the dominant eigenmodes of interfering channels $g' \neq g$. Mathematically, we must achieve

$$\big[\mathbf{U}_1, \cdots, \mathbf{U}_{g-1}, \mathbf{U}_{g+1}, \cdots, \mathbf{U}_G\big]^H\mathbf{P}_g = (\mathbf{U}_g^-)^H\mathbf{P}_g = \mathbf{0}, \quad \forall g = 1, \cdots, G, \tag{2.12}$$

where $\mathbf{U}_g^- \in \mathbb{C}^{M\times\sum_{g'=1,g'\neq g}^{G} r_{g'}^\star}$ is a tall matrix containing the dominant eigenvectors of the interfering channels observed by the gth group. Therefore, $\mathbf{P}_g$ should be constructed from the null space of $\mathbf{U}_g^-$. In particular, the eigendecomposition of $\mathbf{U}_g^-$ can be exploited to compute the desired null space. More specifically, the interference matrix for the gth group can be decomposed as $\mathbf{U}_g^- = \mathbf{E}_g\mathbf{\Delta}_g\mathbf{E}_g^H$, where $\mathbf{E}_g$ comprises the eigenvectors of $\mathbf{U}_g^-$. Given that the last $M - \sum_{g'\neq g} r_{g'}^\star$ columns of $\mathbf{E}_g$ form an orthonomal basis for the null space of $\mathbf{U}_g^-$, the precoding matrix for interference cancellation can be computed by

$$\mathbf{P}_g = [\mathbf{E}_g]_{\left(1+\sum_{g'\neq g} r_{g'}^\star\right):M} \in \mathbb{C}^{M\times\left(M-\sum_{g'\neq g} r_{g'}^\star\right)}, \tag{2.13}$$

where the constraint $M > \sum_{g'\neq g} r_{g'}^\star$ must be satisfied. As long as the spatial directions of different groups are not overlapping, the precoder in (2.13) can effectively cancel the intergroup interference.

Further, in order to maximize the signal reception at the gth intended group, $\mathbf{W}_g$ should be projected onto the direction of its dominant transformed eigenmodes, i.e, after precoded by $\mathbf{P}_g$. To this end, the eigenvectors of the transformed covariance matrix $(\mathbf{\Lambda}_g^{\frac{1}{2}}\mathbf{U}_g^H\mathbf{P}_g)^H\mathbf{\Lambda}_g^{\frac{1}{2}}$ $\mathbf{U}_g^H\mathbf{P}_g = \mathbf{P}_g^H\mathbf{\Sigma}_g\mathbf{P}_g = \bar{\mathbf{\Sigma}}_g \in \mathbb{C}^{\left(M-\sum_{g'\neq g} r_{g'}^{\star}\right)\times\left(M-\sum_{g'\neq g} r_{g'}^{\star}\right)}$ must be computed. Specifically, by applying the eigendecomposition, we achieve $\bar{\mathbf{\Sigma}}_g = \bar{\mathbf{E}}_g\bar{\mathbf{\Delta}}_g\bar{\mathbf{E}}_g^H$, where $\bar{\mathbf{E}}_g$ and $\bar{\mathbf{\Delta}}_g$ are, respectively, the matrices of eigenvectors and eigenvalues of $\bar{\mathbf{\Sigma}}_g$. Because the eigenvectors in $\bar{\mathbf{E}}_g$ form the basis for the column space of $\bar{\mathbf{\Sigma}}_g$, the eigen-beamforming matrix for the gth group can be constructed from the first $\bar{M}$ columns of $\bar{\mathbf{E}}_g$, as follows

$$\mathbf{W}_g = [\bar{\mathbf{E}}_g]_{1:\bar{M}} \in \mathbb{C}^{\left(M-\sum_{g'\neq g} \bar{r}_{g'}\right)\times\bar{M}}, \tag{2.14}$$

where $\bar{M}$ is a design parameter that, because of the dimensions of $\mathbf{P}_g$ and $\bar{\mathbf{E}}_g$, should satisfy $G \leq \bar{M} \leq \left(M - \sum_{g'\neq g} r_{g'}^{\star}\right)$ and $\bar{M} \leq r_g^{\star}$. In our studies, $\bar{M}$ is configured so that all the constraints are satisfied. The above precoding design can be easily extended to dual-polarized systems. Thus, the dual-polarized case is not explained in this dissertation. Interested readers are referred to Publications [III]–[IV] and references therein for a full explanation.

Precoding for Uplink Signal Alignment

Precoding for signal alignment is explained in this subsection, which has been proposed for uplink communication in Publication [IV]. Signal alignment techniques are efficient methods for mitigating interference in multicluster and multicell networks [9, 79, 80]. The concept allows us to design precoders capable of aligning the propagation channels of different users from a given group into a common interference subspace. In the uplink mode, these strategies enable the BS to maintain interfering transmissions coming simultaneously from multiple users at tolerable levels through simple detection techniques. More specifically, once the channels of different users are aligned, linear reception techniques such as zero-forcing can effectively eliminate intergroup interference, which facilitates the BS to employ MA techniques, like uplink NOMA, to decode the messages from users within a given group [9].

For illustration purposes, let us consider an uplink scenario where one BS with M antennas is receiving signals from users within G groups, so that in each group there are U users employing N antennas. For aligning the propagation channels from the gth group into a common subspace, the uth user should employ a precoder $\mathbf{p}_{gu}$ capable of achieving the following:

$$\mathbf{H}_{g1}\mathbf{p}_{g1} = \mathbf{H}_{g2}\mathbf{p}_{g2} = \cdots = \mathbf{H}_{gU}\mathbf{p}_{gU}, \tag{2.15}$$

where $\mathbf{H}_{gu} \in \mathbb{C}^{M\times N}$ is the channel matrix for the uth user in the gth group, which in Publication [IV] is modeled as uncorrelated Rayleigh fading, as in (2.3). The objective in

(2.15) can be accomplished by solving the following matrix problem

$$\begin{bmatrix} \mathbf{I}_M & -\mathbf{H}_{g1} & \mathbf{0}_{M,N} & \dots & \mathbf{0}_{M,N} \\ \mathbf{I}_M & \mathbf{0}_{M,N} & -\mathbf{H}_{g2} & \dots & \mathbf{0}_{M,N} \\ \vdots & \vdots & \vdots & \ddots & \vdots \\ \mathbf{I}_M & \mathbf{0}_{M,N} & \mathbf{0}_{M,N} & \dots & -\mathbf{H}_{gU} \end{bmatrix} \begin{bmatrix} \bar{\mathbf{h}}_g \\ \mathbf{p}_{g1} \\ \vdots \\ \mathbf{p}_{gU} \end{bmatrix} = \mathbf{0}_{(UM),1}, \tag{2.16}$$

where $\bar{\mathbf{h}}_g \in \mathbb{C}^M$ is the effective aligned channel vector that is observed at the BS from users in the gth group, i.e., $\bar{\mathbf{h}}_g = \mathbf{H}_{gu}\mathbf{p}_{gu}, \forall u = 1, \cdots, U$. Because the matrix in the leftmost side of (2.16) has the dimension $(MU) \times (M + NU)$, the condition $NU > M(U-1)$ must be satisfied. Note that for addressing intergroup interference, the BS only requires the knowledge of the aligned channels $\bar{\mathbf{h}}_g$, for $g = 1, \cdots, G$. As a result, channel acquisition and signal detection can be greatly simplified at the BS. This concept of signal alignment is extended to dual-polarized channels in Publication [IV].

2.2 Basics of Power-Domain NOMA

In this section, the NOMA technique is presented in more detail. Let us start by considering a downlink scenario where one BS employing M antennas communicates with U single-antenna users. Let us assume that the BS wishes to deliver the data symbol x_u to the uth user by allocating a transmit power coefficient α_u. Further, let $\mathbf{h}_u \in \mathbb{C}^M$ denote the uncorrelated channel vector, and $\mathbf{p}_u \in \mathbb{C}^M$ an arbitrary precoder employed at the BS for the uth user. As mentioned in Section 1.1, the relying concept of downlink NOMA consists of applying SC to the data symbols of different users at the BS and executing SIC on the users' side. By convention, to implement this transmission strategy, the users are first sorted in an ascending order by the BS based on their effective channel gains achieved after precoding, so that $|\mathbf{h}_1^H\mathbf{p}_1|^2 \leq |\mathbf{h}_2^H\mathbf{p}_2|^2 \leq \cdots |\mathbf{h}_U^H\mathbf{p}_U|^2 \leq$, which implies that the 1st user experiences the worst channel conditions, and the Uth user the best conditions. Then, when fixed power allocation is employed, the BS allocates to lower order users a larger power coefficient and to higher order users a smaller coefficient, resulting in $\alpha_1 \geq \alpha_2 \geq \cdots \geq \alpha_U$. Finally, after applying SC to the users' symbols, the BS achieves the following superimposed symbols

$$\mathbf{x} = \sum_{u=1}^{U} \mathbf{p}_u \sqrt{\alpha_u} x_u, \tag{2.17}$$

which are then transmitted to all users. After the superimposed data stream $\mathbf{x}$ propagates through $\mathbf{h}_u$, the uth user receives

$$y_u = \mathbf{h}_u^H \sum_{u=1}^{U} \mathbf{p}_u \sqrt{\alpha_u} x_u + n_u \in \mathbb{C}, \tag{2.18}$$

where n_u is the noise observed by the uth user. Before the u user retrieves its own message, it detects the symbol for the nth lower order user, i.e., $n = 1, \cdots, u-1$, while treating the symbols intended for higher order users $m > n$ as interference. The detected symbol of the nth user is then subtracted through SIC from the composite signal in (2.18), and the decoding process continues. Only after all the symbols of the users $n < u$ have been canceled by SIC, the uth user can decode its intended data symbol. Under ideal conditions, this sequential decoding can be carried out perfectly, and the uth user is able to recover its symbol without interference from users $n < u$. In practice, however, hardware sensibility, imperfect CSI, feedback errors, and other issues can cause decoding errors, resulting in residual SIC interference, which can be modeled by a linear function of lower order decoded symbols. More specifically, the uth user receives

$$\hat{x}_u = \underbrace{\mathbf{h}_u^H \mathbf{p}_u \sqrt{\alpha_u} x_u}_{\text{Desired symbol}} + \underbrace{\mathbf{h}_u^H \sum_{m=u+1}^{U} \mathbf{p}_m \sqrt{\alpha_m} x_m}_{\text{Interference of higher order users}} + \underbrace{\sqrt{\mu} \mathbf{h}_u^H \sum_{n=1}^{u-1} \mathbf{p}_n \sqrt{\alpha_n} x_n}_{\text{Residual SIC interference}} + \underbrace{n_u}_{\text{Noise}}, \tag{2.19}$$

where $\mu \in [0, 1]$ represents the SIC error propagation factor, in which $\mu = 1$ models the extreme scenario of maximum decoding errors, and $\mu = 0$ represents the ideal case where SIC can be executed perfectly. The above model is employed in Publications [I], [III], [V], and [VI] to capture the degrading effects of imperfect SIC. Note that for enabling correct decoding, the users need to feedback their observed effective channel gains to the BS, and the BS is required to inform the resulting user ordering.

For the case of uplink communication, the BS executes a similar decoding procedure. However, the symbols transmitted simultaneously by different users are superimposed naturally at the BS, i.e., users do not need to apply SC. Moreover, the symbols coming from different users are detected following the opposite order employed in the downlink. Specifically, users are sorted in a descending order based on their channel gains observed at the BS, and SIC is executed to decode the received symbols starting from the user with the best channel conditions to the user with the worst conditions. A more in-depth explanation of the decoding process for uplink NOMA is provided in Section 3.4, which presents the results of Publication [IV].

2.3 Basics of RSMA

To explain RSMA, let us consider the same downlink communication scenario from the previous section, with one BS equipped with M antennas and U single-antenna users. When employing the simplest version of RSMA, the messages intended for each individual user are split by the BS into two parts. The first parts of each message are encoded into a common supersymbol, which can be denoted by x^c. In turn, the second parts of each data message are encoded independently, resulting in U private symbols, represented by x_u^p, for $u = 1, \cdots, U$. Then, the symbol x^c is mapped to the BS antennas through a common precoder $\mathbf{w}^c$, which should be designed to deliver the common symbol to all users, while the symbols x_u^p are multiplied by private precoders $\mathbf{w}_u^p$, constructed to deliver the corresponding private symbol only to the intended uth user. Next, the two obtained data streams are superimposed in the power domain, resulting in the following signal

$$\mathbf{x} = \sum_{u=1}^{U} \mathbf{w}_u^p \sqrt{\alpha_u^p} x_u^p + \mathbf{w}^c \sqrt{\alpha^c} x^c, \tag{2.20}$$

which is then transmitted toward the users, with α^c and α_u^p representing the power coefficients for the common and private symbols, respectively. After the transmitted symbols have been filtered through the wireless channel, the uth user observes

$$y_u = \mathbf{h}_u^H \left(\underbrace{\mathbf{w}_u^p \sqrt{\alpha_u^p} x_u^p}_{\text{Desired private data}} + \underbrace{\sum_{n=1, n\neq u}^{U} \mathbf{w}_n^p \sqrt{\alpha_n^p} x_n^p}_{\substack{\text{Private data}\\ \text{intended to other users}}} + \underbrace{\mathbf{w}^c \sqrt{\alpha^c} x^c}_{\substack{\text{Common stream}\\ \text{to be decoded through SIC}}} \right) + \underbrace{n_u}_{\text{Noise}}. \tag{2.21}$$

Upon reception, the common stream is decoded first while treating the private streams as interference. Next, the users execute SIC to subtract the recovered common symbol from the received superimposed data stream in (2.21). After the SIC decoding is finalized, the uth should be able to recover its private symbol successfully, ideally, interference-free. However, because of practical issues, SIC can also be carried out imperfectly in RSMA, which can be modeled as in the previous section. Specifically, the performance impacts of imperfect SIC is investigated in our two RSMA-related publications, [V] and [VI], further details of which will be provided later.

Due to the fact that part of the users' messages are encoded into a single common stream, and users execute SIC only once, the technique explained above is called single-layer RSMA. Altough it is a relatively simple technique, single-layer RSMA has the potential to outperform all classical MA techniques, including NOMA, TDMA, OFDMA, and SDMA, as reported in recent works [81]. RSMA strategies with multiple layers of SIC have also been proposed recently, such as the generalized RSMA [10] and the hierarchical RSMA [56]. Nevertheless, the focus of this dissertation is only on single-layer RSMA. These more intricate schemes are left for future work.

2.4 Basics of an IRS and its Standard Channel Model

As introduced in Section 1.1, an IRS consists of a thin planar structure comprising multiple reflecting elements, each one with a size smaller than the signal wavelength and with reconfigurable electromagnetic properties. Each element operates as a subwavelength scatterer, which can induce phases and amplitude changes in impinging electromagnetic signals, as illustrated in Figure 2.5. Collectively, these small tunable elements enable

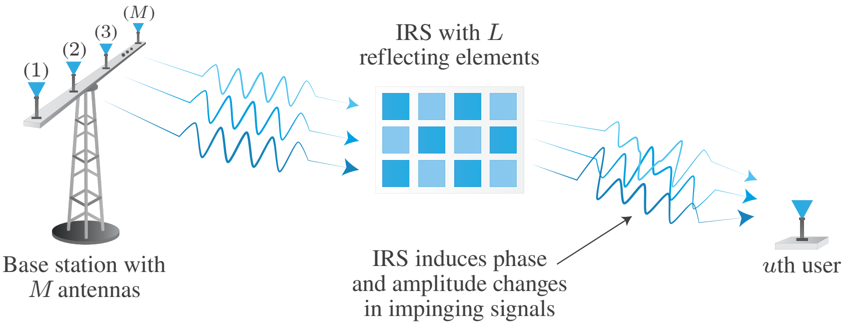

Figure 2.5: Illustration of the capabilities of an IRS considering only a reflected link.

an IRS to generate reflections with an optimized radiation pattern. Specifically, if we consider one IRS with L reflecting elements, the transformations induced by lth element can be represented by a complex number $\omega_l e^{j\phi_l}$, in which ω_l models the amplitude of the reflected signal, and ϕ_l denotes the induced phase change. As a result, the collective responses for one IRS can be represented by the following diagonal matrix

$$\boldsymbol{\Theta} = \begin{bmatrix} \omega_1 e^{j\phi_1} & 0 & 0 & \cdots & 0 \\ 0 & \omega_2 e^{j\phi_2} & 0 & \cdots & 0 \\ \vdots & \vdots & \ddots & \cdots & \vdots \\ 0 & 0 & 0 & \cdots & \omega_L e^{j\phi_L} \end{bmatrix} \in \mathbb{C}^{L\times L}. \tag{2.22}$$

The reflection matrix in (2.22), combined with the channel matrices for the links between the BS and the IRS, and the IRS and users, compose the standard channel representation adopted in IRS-assisted communication systems, known as the multiplicative dyadic channel model [17]. More specifically, by considering the scenario with one BS with M antennas, U single-antenna users, and one IRS with L elements, the full channel that characterizes all propagation links can be represented by

$$\mathbf{h}_u^H = \mathbf{s}_u^H \boldsymbol{\Theta} \mathbf{G} + \mathbf{d}_u^H, \tag{2.23}$$

where $\boldsymbol{\Theta}$ is defined in (2.22), and $\mathbf{G} \in \mathbb{C}^{L\times M}$, $\mathbf{s}_u \in \mathbb{C}^{L}$, and $\mathbf{d}_u \in \mathbb{C}^{M}$ denote the channel responses between the BS and the IRS, the IRS and the uth user, and the BS and the uth user, respectively.

The IRS channel representation in (2.23) is used for generating the results in Publications [II] and [V], which investigate IRS-MIMO-NOMA and IRS-MIMO-RSMA schemes, respectively. It is noteworthy that this model is unaware of signal polarization. In Publication [III], this model is extended to also incorporate polarization aspects of electromagnetic propagation and a novel dual-polarized IRS with appealing capabilities is proposed.

3 Overview of Publications on MIMO-NOMA Networks

This chapter provides a comprehensive overview of the novel contributions achieved for MIMO-NOMA networks, with and without the aid of IRSs, which are proposed in Publications [I]–[IV].

3.1 Massive MIMO-NOMA Networks with Imperfect SIC

This section focuses on the findings and original contributions proposed in Publication [I], which is the starting point of this study and has provided motivation for developing the subsequent works. Specifically, it is shown that imperfect SIC is highly detrimental to the performance of MIMO-NOMA schemes and that individual users experience unbalanced and unfair data rates under fixed power allocation. These important findings and the results reported next answer the first research question *Q1*.

3.1.1 Motivation and Contributions

The majority of existing MIMO-NOMA-related works are underpinned by the assumption of perfect SIC decoding, which is idealistic and difficult to realize in practice. Moreover, no previous works have proposed power allocation strategies aiming at rate fairness in massive MIMO-NOMA networks considering SIC error propagation. These major literature gaps motivated the development of Publication [I], which, in summary, designs, investigates, and optimizes multicluster massive MIMO-NOMA networks undergoing practical issues of imperfect SIC decoding. More specifically:

- A downlink scenario is considered where multiple users employing multiple antennas are located in different spatial clusters. Within each cluster, the users are divided by the BS into multiple NOMA groups, each one containing two users so that the computational complexity of SIC is maintained at manageable levels. At the BS, a multistage precoder like the one presented in Subsection 2.1.5 is employed. Specifically, outer precoders, which are responsible for canceling out intercluster interference and focusing transmissions on the clusters of interest, are constructed based only on the users' slowly varying correlation matrices. On the other hand, inner precoders, which play the role of assigning the superimposed data symbols to intended NOMA groups, are designed to be independent of users' CSI.

- An analytical framework for multicluster massive MIMO-NOMA networks under imperfect SIC is derived considering fixed power allocation policies. First, the expression for the SINR is determined, based on which the effective channel gains and interference terms are statistically characterized. Next, based on the achieved SINR expression and its statistical properties, an exact closed-form expression is derived for the outage probability. The users' ergodic rates are also derived in closed-form. Our novel analytical framework can be exploited as a practical tool for assisting the design of massive MIMO-NOMA networks under imperfect SIC.

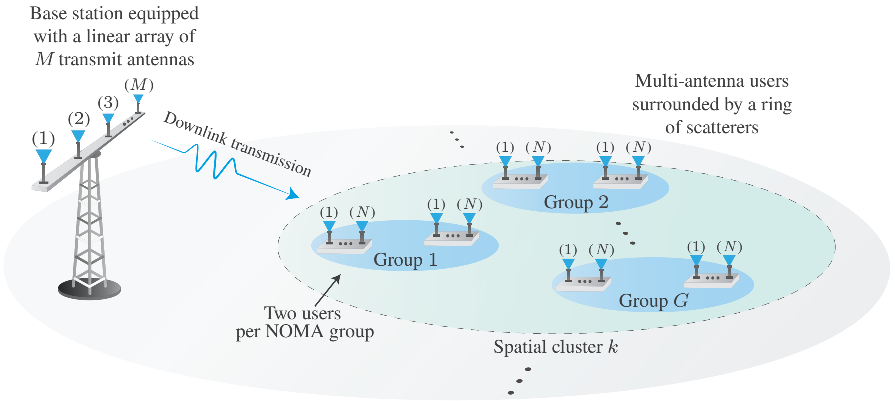

Figure 3.1: System model studied in Publication [I]. Multiantenna users within each spatial cluster are divided into multiple two-user NOMA groups.

- An adaptive power allocation policy is proposed for maximizing the minimum observed instantaneous users' data rates within each NOMA group. Our power optimization problem ensures that weak users (those experiencing the worst channel conditions) can achieve at least the same data rate levels observed by strong users. The optimal solution for the formulated problem is obtained in closed-form by the Karush–Kuhn–Tucker (KKT) conditions [82]. To extend data rate fairness across different NOMA groups, a simple but effective iterative algorithm is proposed for balancing the power budget between groups so that all users within each cluster can experience similar data rate levels, i.e., maximum fairness is provided for users within each spatial cluster.

- Comprehensive discussions are presented alongside insightful simulation results. In particular, the detrimental effects of imperfect SIC on the outage probability and ergodic rate performance are revealed. The effectiveness and advantages of the proposed fair power allocation policy also become evident in the results. Among other insights, it is shown that, when operating with fixed power allocation, the implemented baseline MIMO-OMA scheme outperforms the MIMO-NOMA counterpart when the SIC error propagation factor is high. It is also confirmed that our fair power allocation policy can achieve remarkable outage probability improvements over the MIMO-NOMA system under fixed power allocation.

3.1.2 System Model, Precoding, and Reception

Now, more details are provided on the system model studied in Publication [I]. Specifically, a single-cell multicluster downlink communication network is considered, comprising one unobstructed elevated BS and several multi-antenna users surrounded by a large number of scattering objects so that correlated Rayleigh fading is achieved. The BS is equipped with a uniform linear array with M single-polarized antennas separated by half of the wavelength, i.e., $\lambda/2$, and at each user, N single-polarized receive antennas are employed, where $M \gg N$, which represents a massive MIMO system. Moreover, the users are assumed to be distributed within different geographical regions forming K spatial clusters, following the one-ring geometrical model explained in Subsection 2.1.2. As depicted in Figure 3.1, to reduce the complexity of NOMA, the users within each spatial cluster are organized by the BS into G two-user groups. Then, MIMO precoding is used to multiplex different clusters in space, and NOMA is exploited to serve users within the groups via the power domain. As a result, after applying SC and transmitting the precoded data symbols via the wireless medium, the users receive the following superimposed signal

$$\mathbf{y}_{kgu} = \mathbf{H}_{kgu}^{H} \sum_{q=1}^{K} \mathbf{B}_q \sum_{m=1}^{G} \mathbf{v}_{qm} \sum_{n=1}^{2} \sqrt{\alpha_{qmn}} x_{qmn} + \mathbf{n}_{kgu}, \tag{3.1}$$

where $\mathbf{H}_{kgu} = \sqrt{\Phi d_{kg}^{-\eta}} \mathbf{U}_k \mathbf{\Lambda}_k^{\frac{1}{2}} \mathbf{G}_{kgu}$ denotes the correlated channel matrix for the uth user in the gth group in the kth cluster, which has an effective correlation matrix given by $\mathrm{E}\{\mathbf{H}_{kgu}\mathbf{H}_{kgu}^{H}\} = \Phi d_{kg}^{-\eta} \mathbf{R}_k \in \mathbb{C}^{M \times M}$, with a rank given by r_k, and $r_k^{\star} \leq r_k$ nonzero eigenvalues. The matrices $\mathbf{G}_{kgu}$, $\mathbf{\Lambda}_k$, and $\mathbf{U}_k$ are defined as in (2.4), which comprise, respectively, the fast-varying channel coefficients, the $r_k^{\star}$ nonzero eigenvalues of $\mathbf{R}_k$, and the corresponding dominant eigenvectors. In turn, the parameter d_{kg} represents the distance of the gth NOMA group from the BS, η is the path-loss exponent, and Φ is an array gain parameter adjusted according to the desired users' SINR [83]. Furthermore, note that the users within the kth cluster are assumed to share a common effective correlation matrix $\mathbf{R}_k$, which has been generated using (2.5). The vector $\mathbf{n}_{kgu} \in \mathbb{C}^{N}$ models the additive noise, whose entries follow the complex Gaussian distribution with zero mean and variance σ^2. The parameter α_{qmn} represents the power allocation coefficient, and x_{qmn} denotes the data symbol for the nth user in the mth group in the qth spatial cluster. $\mathbf{B}_q \in \mathbb{C}^{M \times \bar{M}}$ is the precoding matrix responsible for multiplexing the spatial clusters, which is constructed similarly as in Subsection 2.1.5, and $\mathbf{v}_{qm} \in \mathbb{C}^{\bar{M}}$ is the precoding vector that assigns the superimposed symbols to the corresponding NOMA groups, which is designed as follows

$$\mathbf{v}_{kg} = [\, \mathbf{0}_{1,(g-1)} \ , \ 1 \ , \ \mathbf{0}_{1,(\bar{M}-g)} \,]^T, \quad \forall g = 1, \cdots, G. \tag{3.2}$$

Observe that the only capability of the precoder in (3.2) is to forward the gth effective data stream to the gth group without applying any further processing on the data symbols. The main advantage of such a strategy is that the BS will only need to estimate the channel correlation matrices for constructing the precoding matrices, which is much less demanding than acquiring the full CSI. Moreover, because $\mathbf{B}_k$ is built based on the correlation matrices $\mathbf{R}_k$, which can be estimated with a high degree of accuracy, it is assumed in Publication [I] that the intercluster interference can be canceled perfectly. Nevertheless, the users are still required to employ a detection technique to cope with the remaining intergroup interference within each spatial cluster. To this end, at each user, a zero-forcing receiver is implemented, which can be computed by

$$\mathbf{H}_{gu}^{\dagger} = [(\mathbf{H}_{gu}^{H}\mathbf{B})^{H}\mathbf{H}_{gu}^{H}\mathbf{B}]^{-1}(\mathbf{H}_{gu}^{H}\mathbf{B})^{H}, \tag{3.3}$$

where $\mathbf{H}_{gu}^{\dagger}$ is the Moore–Penrose pseudoinverse of users' effective channels. Note that, because the intercluster interference can be perfectly nulled out by $\mathbf{B}_k$, for simplicity, the cluster subscript is dropped. It is also noteworthy that for constructing the above detection matrices, the BS needs to feed back the matrices $\mathbf{B}$ to the users, which can be realized by imposing a low overhead.

Following the convention used in downlink NOMA explained in Section 2.2, it is assumed that the BS sorts users within each group in an ascending order according to the magnitude of the observed effective channel gains. Upon reception, the users employ SIC to separate the transmitted superimposed data symbols, so that the user with the worst channel condition (the weak user) recovers its data symbol directly from the received signal while treating the symbol intended for the user with the best channel condition (the strong user) as interference. In its turn, the strong user first decodes the message for the weak user, subtracts it from the superimposed symbol, and only then recovers its own message. In ideal conditions, only the weak user, the first user in the decoding order, experiences interference, whereas the strong one receives information interference-free. However, as anticipated, in practice, even if the CSI can be estimated with precision, hardware imperfections and other issues can generate SIC decoding errors, which deteriorates the performance of the strong users. Consequently, after multiplying the signal in (3.1) by $\mathbf{H}_{gu}^{\dagger}$, the users in the gth group will retrieve the following corrupted data symbol

$$\hat{x}_{gu} = \begin{cases} \underset{\substack{\uparrow \\ \text{symbol of interest}}}{\sqrt{\alpha_{g1}}x_{g1}} + \underset{\substack{\uparrow \\ \text{interference}}}{\sqrt{\alpha_{g2}}x_{g2}} + \underset{\substack{\uparrow \\ \text{noise}}}{[\mathbf{H}_{g1}^{\dagger}\mathbf{n}_{g1}]_g}, & \text{if } u = 1, \\ \underset{\substack{\uparrow \\ \text{symbol of interest}}}{\sqrt{\alpha_{g2}}x_{g2}} + \underset{\substack{\uparrow \\ \text{residual SIC interference}}}{\sqrt{\mu\alpha_{g1}}x_{g1}} + \underset{\substack{\uparrow \\ \text{noise}}}{[\mathbf{H}_{g2}^{\dagger}\mathbf{n}_{g2}]_g}, & \text{if } u = 2, \end{cases} \tag{3.4}$$

where $\mu \in [0, 1]$ denotes the SIC error propagation factor, such that $\mu = 0$ represents the ideal scenario with perfect SIC, and $\mu = 1$ models an extreme case with a maximum SIC error.

3.1.3 Performance Analysis

In this subsection, the main mathematical results achieved in Publication [I] are presented; the results are valid for massive MIMO-NOMA systems operating with fixed power allocation and undergoing SIC error propagation. First, the SINR expression observed by each user is introduced. Then, based on the statistical distribution of the SINR gains, closed-form expressions for the outage probabilities are derived. Last, the ergodic rates are also calculated in closed-form.

SINR Analysis

By exploiting the expressions for the recovered symbols in (3.4), the SINR achieved by the two users within a given NOMA group is provided in the following lemma.

Lemma 3.1: When users within each NOMA group are sorted by the BS in an ascending order based on their effective channel gains, the SINR observed by the uth user, $1 \leq u \leq 2$, while decoding the symbol intended to the ith user, $1 \leq i \leq 2$, can be expressed by

$$\gamma_{gu}^{i} = \frac{\rho \varrho_{gu} \alpha_{gi}}{\rho \varrho_{gu} \alpha_{gi}^{\star} + 1}, \qquad \text{for} \quad 1 \leq i \leq k \leq 2, \tag{3.5}$$

where $\varrho_{gu} = \frac{1}{[\mathbf{H}_{gu}^{\dagger} \mathbf{H}_{gu}^{\dagger H}]_{g,g}}$ denotes the effective channel gain, $\rho = 1/\sigma^2$ is the signal-to-noise ratio (SNR), and $\alpha_{gi}^{\star}$ models the interference power, which is defined by

$$\alpha_{gi}^{\star} = \begin{cases} \alpha_{g2}, & \text{for} \quad i = 1, \\ \mu \alpha_{g1}, & \text{for} \quad i = u = 2, \end{cases} \tag{3.6}$$

Proof: The reader is referred to Appendix A in Publication [I]. ■

A crucial step for deriving the closed-form expressions of the desired performance metrics is determining the statistical distribution of the effective channel gains $\varrho_{gu} = \frac{1}{[\mathbf{H}_{gu}^{\dagger} \mathbf{H}_{gu}^{\dagger H}]_{g,g}}$. To this end, a statistical characterization is carried out on ϱ_{gu}. Specifically, by first considering that the gains are unordered random variables, ϱ_{gu} can be characterized by a Gamma distribution with the shape parameter $N - V + 1$ and the scale parameter given by $\Phi d_g^{-\eta} [(\mathbf{B}^H \mathbf{R} \mathbf{B})^{-1}]_{g,g}$. However, because the users are ordered by the BS in an ascending order, it is required to apply the theory of order statistics [84] to accurately model the referred channel gains. More specifically, the probability density function (PDF) of the ordered effective channel gains for user 1 (the weak user) can be expressed by

$$f_{\varrho_{g1}}(x) = \frac{2\beta_g^{\vartheta}}{\Gamma(\vartheta)} \left[x^{\vartheta - 1} e^{-\beta_g x} - x^{\vartheta - 1} e^{-\beta_g x} \frac{\gamma(\vartheta, \beta_g x)}{\Gamma(\vartheta)} \right], \tag{3.7}$$

and for user 2 (the strong user) by

$$f_{\varrho_{g2}}(x) = \frac{2\beta_g^{\vartheta}}{\Gamma(\vartheta)} x^{\vartheta - 1} e^{-\beta_g x} \frac{\gamma(\vartheta, \beta_g x)}{\Gamma(\vartheta)}, \tag{3.8}$$

where, for notation simplicity, it is defined that $\vartheta = N - V + 1$ and $\beta_g = \Phi d_g^{-\eta}$ $[(\mathbf{B}^H \mathbf{R} \mathbf{B})^{-1}]_{g,g}$. For the complete details of this statistical characterization, interested readers are encouraged to go through Subsection III-B of Publication [I]. The expressions in (3.7) and (3.8) are used for deriving the next results.

Outage Probability

A given user is considered to be in an outage state when its instantaneous data rate is less than the target rate required for decoding its received symbol. For the considered system model, this implies that the weak user (user 1) will experience an outage event when $\log_2(1+\gamma_{g1}^1) < T_{g1}$ and the strong user (user 2) either when $\log_2(1+\gamma_{g2}^1) < T_{g1}$ or when $\log_2(1+\gamma_{g2}^2) < T_{g2}$, where T_{gu} denotes the target data rates. As a result, the outage probability observed by the uth user in the gth NOMA group can be computed by [14, 7]

$$P_{gu} = P[\log_2(1+\gamma_{gu}^i) < T_{gi}], \quad \forall i = 1, \cdots, u. \tag{3.9}$$

Note that the SIC error propagation term in (3.6) will deteriorate the outage probability performance of the strong user. Proposition 3.1, next, derives closed-form expressions for the outage probability achieved by weak and strong users within each group.

Proposition 3.1: When users within each NOMA group are sorted in an ascending order, i.e., $\varrho_{g1} < \varrho_{g2}$, and the strong user is susceptible to SIC error propagation, the outage probability can be derived in closed-form as follows:

- Weak user:

$$P_{g1} = \begin{cases} \frac{2\gamma(\vartheta,\rho^{-1}\beta_g\mathscr{L}_{g1})}{\Gamma(\vartheta)} - \left[\frac{\gamma(\vartheta,\rho^{-1}\beta_g\mathscr{L}_{g1})}{\Gamma(\vartheta)}\right]^2, & \text{if} \quad \mathscr{L}_{g1} \geq 0, \\ 1, & \text{otherwise.} \end{cases} \tag{3.10}$$

- Strong user:

$$P_{g2} = \begin{cases} \left[\frac{\gamma(\vartheta,\rho^{-1}\beta_g \max\{\mathscr{L}_{g1},\mathscr{L}_{g2}\})}{\Gamma(\vartheta)}\right]^2, & \text{if} \quad \min\{\mathscr{L}_{g1}, \mathscr{L}_{g2}\} \geq 0, \\ 1, & \text{otherwise,} \end{cases} \tag{3.11}$$

where $\mathscr{L}_{g1} = \frac{2^{T_{g1}}-1}{\alpha_{g1}-\alpha_{g2}(2^{T_{g1}}-1)}$, and $\mathscr{L}_{g2} = \frac{2^{T_{g2}}-1}{\alpha_{g2}-\mu\alpha_{g1}(2^{T_{g2}}-1)}$.

Proof: The reader is referred to Appendix B in Publication [I]. ■

Ergodic Rate

For deriving the ergodic rates experienced by users within each NOMA group, it is assumed that the strong user is unable to decode perfectly the message intended for the weak user as a result of imperfect SIC. Consequently, the instantaneous data rate of the strong user, which is computed based on the SINR achieved when decoding its own symbol, is degraded by residual SIC errors. Under such assumptions, their data rates can be expressed by

$$R_{g1} = \log_2(1+\gamma_{g1}^1) = \log_2\left(1 + \frac{\rho\varrho_{g1}\alpha_{g1}}{\rho\varrho_{g1}\alpha_{g2}+1}\right), \tag{3.12}$$

and

$$R_{g2} = \log_2(1+\gamma_{g2}^2) = \log_2\left(1+\frac{\rho\varrho_{g2}\alpha_{g2}}{\rho\varrho_{g2}\mu\alpha_{g1}+1}\right). \tag{3.13}$$

By calculating the statistical expectation of (3.12) and (3.13), Proposition 3.2 provides exact closed-form expressions for the ergodic rates of the two users.

Proposition 3.2: Closed-form expressions for the ergodic rates observed by weak and strong users, when the strong user experiences SIC error propagation, can be derived by:

- Weak user:

$$\bar{R}_{g1} = \xi_1(\kappa_{g1}) - \xi_1(\tilde{\kappa}_{g1}), \tag{3.14}$$

where $\kappa_{g1} = \rho(\alpha_{g1}+\alpha_{g2})$, $\tilde{\kappa}_{g1} = \rho\alpha_{g2}$, and

$$\xi_1(\kappa) = \begin{cases} \sum_{i=0}^{\vartheta-1} \frac{1}{2^{\vartheta+i-1}\ln(2)\Gamma(\vartheta)i!} \sum_{m=0}^{\vartheta+i-1} \frac{(\vartheta+i-1)!}{(\vartheta+i-m-1)!} \left[\frac{(-1)^{\vartheta+i-m-2}}{\left(\frac{\kappa}{2\beta_g}\right)^{\vartheta+i-m-1}} e^{\frac{2\beta_g}{\kappa}} \mathrm{Ei}\left(-\frac{2\beta_g}{\kappa}\right)\right. \\ \quad \left. + \sum_{n=1}^{\vartheta+i-m-1} \frac{(n-1)!}{\left(-\frac{\kappa}{2\beta_g}\right)^{\vartheta+i-m-n-1}}\right], \qquad \textit{if} \quad \vartheta > 1, \\ -\frac{1}{\ln(2)} e^{\frac{2\beta_g}{\kappa}} \mathrm{Ei}\left(-\frac{2\beta_g}{\kappa}\right), \qquad \textit{if} \quad \vartheta = 1. \end{cases}$$

- Strong user:

$$\bar{R}_{g2} = \begin{cases} \xi_2(\kappa_{g2}) - \xi_2(\tilde{\kappa}_{g2}), & \textit{if} \quad \mu > 0, \\ \xi_2(\kappa_{g2}), & \textit{if} \quad \mu = 0, \end{cases} \tag{3.15}$$

where $\kappa_{g2} = \rho(\mu\alpha_{g1}+\alpha_{g2})$, $\tilde{\kappa}_{g2} = \rho\mu\alpha_{g1}$, and

$$\xi_2(\kappa) = \begin{cases} \frac{2}{\ln(2)} \sum_{m=0}^{\vartheta-1} \frac{1}{(\vartheta-m-1)!} \left[\frac{(-1)^{\vartheta-m-2}}{\left(\frac{\kappa}{\beta_g}\right)^{\vartheta-m-1}} e^{\frac{\beta_g}{\kappa}} \mathrm{Ei}\left(-\frac{\beta_g}{\kappa}\right)\right. \\ \quad \left. + \sum_{n=1}^{\vartheta-m-1} \frac{(n-1)!}{\left(-\frac{\kappa}{\beta_g}\right)^{\vartheta-m-n-1}}\right] - \xi_1(\kappa), \qquad \textit{if} \quad \vartheta > 1, \\ -\frac{2}{\ln(2)} e^{\frac{\beta_g}{\kappa}} \mathrm{Ei}\left(-\frac{\beta_g}{\kappa}\right) - \xi_1(\kappa), \qquad \textit{if} \quad \vartheta = 1. \end{cases}$$

Proof: The reader is referred to Appendix C in Publication [I]. ■

3.1.4 Fair Power Allocation

To satisfactorily meet the data rate requirements of multiple users in wireless communication networks, limited resources such as transmit power need to be allocated with fairness. Several recent NOMA-related works have employed fixed power allocation policies following the convention of assigning more power to weak users and less to strong ones as an attempt to provide a certain degree of fairness to the network [85, 14, 7]. However, fixed strategies cannot cope with the dynamic behavior of wireless propagation. Moreover, weak users under fixed power allocation will always experience limited data rates as a result of interference from strong users, which causes unbalanced and unfair rate performance that is undesirable in applications with strict fairness requirements. This limitation motivated us to develop in Publication [I] fair dynamic policies for allocating the transmit power both within and among different groups.

First, within each NOMA group, an optimization problem is formulated to maximize the rate of the strong user under the constraint that the weak user achieves a data rate not less than the observed by the strong one. In practice, this approach ensures that the two users will obtain the same data rate. More specifically, the power allocation for providing fair data rates to users within each group is achieved by solving the following problem:

$$\max_{\alpha_{g1},\alpha_{g2}} \; \{R_{g2}\} \tag{3.16a}$$

$$\text{s.t.} \;\; R_{g1} \geq R_{g2}, \tag{3.16b}$$

$$\alpha_{g1} + \alpha_{g2} = \bar{\alpha}_g, \tag{3.16c}$$

$$\alpha_{g1} \geq 0, \alpha_{g2} \geq 0, \tag{3.16d}$$

in which $\bar{\alpha}_g$ is defined as the transmit power budget available for the gth NOMA group. After some manipulations, (3.16) can be simplified to a convex problem, which allows us to apply the KKT conditions. The optimal solution for the problem in (3.16) is then provided in closed-form in Proposition 3.3, as shown next.

Proposition 3.3: The optimization problem in (3.16) can be transformed into an equivalent convex problem, which has a global optimal solution given in closed-form by

$$\alpha_{g2}^{*} = \begin{cases} \frac{-(\varrho_{g1}\rho^{-1}+\varrho_{g2}\rho^{-1}+2\mu\varrho_{g1}\varrho_{g2}\bar{\alpha}_g)}{2(\varrho_{g1}\varrho_{g2}-\mu\varrho_{g1}\varrho_{g2})} \\ +\frac{\sqrt{(\varrho_{g1}\rho^{-1}+\varrho_{g2}\rho^{-1}+2\mu\varrho_{g1}\varrho_{g2}\bar{\alpha}_g)^2+4\varrho_{g1}\varrho_{g2}(1-\mu)(\varrho_{g1}\rho^{-1}\bar{\alpha}_g+\mu\varrho_{g1}\varrho_{g2}\bar{\alpha}_g^2)}}{2(\varrho_{g1}\varrho_{g2}-\mu\varrho_{g1}\varrho_{g2})}, & \text{if} \quad \mu \in [0,1), \\ \frac{\varrho_{g1}\rho^{-1}\bar{\alpha}_g+\mu\varrho_{g1}\varrho_{g2}\bar{\alpha}_g^2}{\varrho_{g1}\rho^{-1}+\varrho_{g2}\rho^{-1}+2\mu\varrho_{g1}\varrho_{g2}\bar{\alpha}_g}, & \text{if} \quad \mu = 1, \end{cases} \tag{3.17}$$

for the strong user, and

$$\alpha_{g1}^{*} = \bar{\alpha}_g - \alpha_{g2}^{*}, \tag{3.18}$$

for the weak user.
Proof: The reader is referred to Appendix D in Publication [I]. ■

Observe that, for carrying out the above power allocation, the BS needs to have access to the users' channel gains ϱ_{gu} and the SIC error factor μ. Recall that the effective gains ϱ_{gu} are exploited by the BS for sorting users and implementing NOMA. Thus, no additional complexity is added for using ϱ_{gu} in the power allocation policy. On the other hand, as explained in Publication [I], the error factor μ can be estimated by users by long-term

Algorithm 1: Iterative Algorithm for Enabling Fairness Among NOMA Groups

```
Input: $\epsilon, \rho, \varrho_{g1}, \varrho_{g2}$.
Set the initial available power to $\bar{\alpha}_g = 1, \forall g$;
do
    for $g = 1$ to $G$ do
        Calculate $\alpha^*_{g2}$ and $\alpha^*_{g1}$ using (3.17) and (3.18), respectively;
        Calculate the subgroup's sum-rate by $\mathcal{R}_g = R_{g1} + R_{g2}$;
    end
    $\hat{g} = \mathbf{argmax}(\mathcal{R}_g : \forall g \in \{1, 2, \cdots, G\})$;
    $\check{g} = \mathbf{argmin}(\mathcal{R}_g : \forall g \in \{1, 2, \cdots, G\})$;
    Calculate $\Delta_\alpha$ using (3.19);
    Update $\bar{\alpha}_{\hat{g}} = \bar{\alpha}_{\hat{g}} - \Delta_\alpha$;
    Update $\bar{\alpha}_{\check{g}} = \bar{\alpha}_{\check{g}} + \Delta_\alpha$;
    $\epsilon^* = \mathcal{R}_{\hat{g}} - \mathcal{R}_{\check{g}}$;
while $\epsilon^* > \epsilon$;
```

measurements and informed back to the BS, imposing a small additional feedback overhead.

For enabling rate fairness also across different NOMA groups, i.e., in order for all users in all groups within a spatial cluster to achieve the same data rate, an iterative algorithm is also proposed to redistribute the transmit power budgets among different groups. The underlying idea of the algorithm is to iteratively transfer part of the power budget, represented by Δ_α, from the best to the worst NOMA group, and to exploit the adaptive power allocation in (3.17) and (3.18) to readjust the rates of each user. The proposed iterative intergroup allocation strategy is presented in Algorithm 1, and the power fraction Δ_α is computed in Proposition 3.4, as follows.

Proposition 3.4: The power fraction Δ_α required to be transferred from the group with the highest sum-rate to the group with the lowest sum-rate is given by

$$\Delta_\alpha = \frac{-A_2 \pm \sqrt{A_2^2 - 4A_1A_3}}{2A_1}, \tag{3.19}$$

where

$$A_1 = 4\varrho^2_{\check{g}1}\varrho_{\check{g}2}\rho^{-1} + 4K_1, \qquad A_2 = 2A_1K_3 + 16K_2K_1,$$
$$A_3 = K_3^2 - 4K_2\frac{\varrho^2_{\check{g}1}}{\varrho^2_{\hat{g}1}}(\varrho_{\hat{g}1}\rho^{-1} + \varrho_{\hat{g}2}\rho^{-1})^2 - 16K_2K_1\bar{\alpha}_{\hat{g}},$$

and

$$K_1 = \frac{\varrho^2_{\check{g}1}}{\varrho^2_{\hat{g}1}}\varrho^2_{\hat{g}1}\varrho_{\hat{g}2}\rho^{-1}, \qquad K_2 = (\varrho_{\check{g}1}\rho^{-1} + \varrho_{\check{g}2}\rho^{-1} - \frac{\varrho_{\check{g}1}}{\varrho_{\hat{g}1}}(\varrho_{\hat{g}1}\rho^{-1} + \varrho_{\hat{g}2}\rho^{-1}))^2,$$

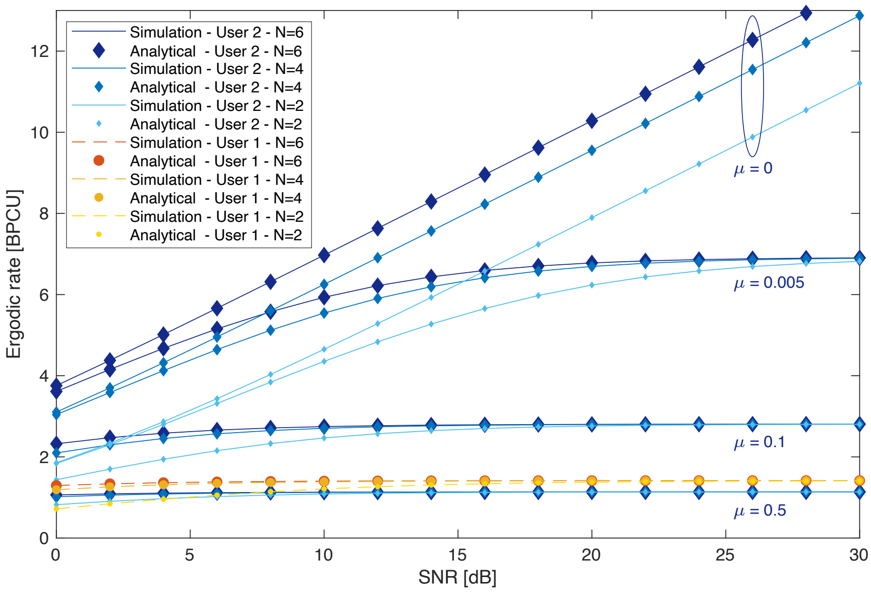

Figure 3.2: Impact of imperfect SIC on the users' ergodic rates for different numbers of receive antennas [I], ©2020 IEEE.

$$K_3 = (\varrho_{\check{g}1}\rho^{-1} + \varrho_{\check{g}2}\rho^{-1})^2 + 4\varrho_{\check{g}1}^2\varrho_{\check{g}2}\rho^{-1}\bar{\alpha}_{\check{g}} - K_2 - \frac{\varrho_{\check{g}1}^2}{\varrho_{\hat{g}1}^2}(\varrho_{\check{g}1}\rho^{-1} + \varrho_{\check{g}2}\rho^{-1})^2 - 4K_1\bar{\alpha}_{\hat{g}}.$$

Proof: The reader is referred to Appendix E in Publication [I]. ■

For the complete description and complexity analysis of Algorithm 1, interested readers are referred to Subsection IV-B of Publication [I].

3.1.5 Main Results

This subsection focuses on the main simulation and numerical results presented in Publication [I], which are the most relevant ones for this dissertation. The implemented massive MIMO-NOMA network comprises one BS equipped with a uniform linear array of $M = 90$ antennas and multiple multi-antenna users uniformly distributed across $K = 4$ spatial clusters, with each cluster having 50 m of diameter. The simulation results are generated considering the first cluster, which has a center located at a distance of 141 m from the BS and an azimuth angle of $\varphi = 7°$, corresponding to an angular spread of $\delta = 10°$. In addition, within the spatial cluster of interest there are $G = \bar{M} = 2$ NOMA groups, where each group contains $U = 2$ users. The focus is on the performance of users from the first group that is located at 115 m from the BS. The path-loss exponent is adjusted to $\eta = 2$, and the gain parameter to $\Phi = 40^4$. In the results with fixed power allocation, the power coefficients of users 1 and 2 are set to $\alpha_1 = 5/8$ and $\alpha_2 = 3/8$, respectively. The presented results are generated by averaging a large number of Monte Carlo iterations.

Figure 3.2 presents simulated and analytical ergodic rates (generated with (3.14) and

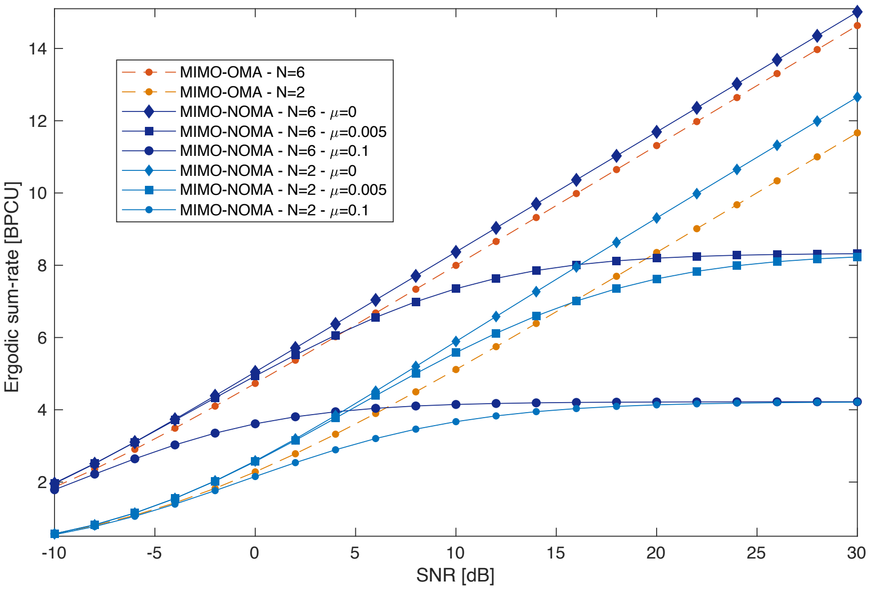

Figure 3.3: Simulated ergodic sum-rate curves for a massive MIMO-NOMA system with imperfect SIC and the conventional massive MIMO-OMA counterpart [I], ©2020 IEEE.

(3.15)), measured in bits per channel use (BPCU), experienced by the weak and strong users under fixed power allocation, where different SIC error factors and numbers of receive antennas are considered. As can be seen, independent of the system parameters, a perfect agreement between simulated and analytical curves is achieved, which validates the ergodic rate analysis. This result also reveals that imperfect SIC can be very harmful to the performance of the strong user, such that when $\mu = 0.5$, its ergodic rate becomes inferior to the one achieved by the weak user. Another important insight that can be observed in Figure 3.2 is that the rate performance of the two users is highly unbalanced, so that independently of the number of transmit antennas, the rate of the weak user is always limited to moderate to high SNR values, which confirms that fixed power allocation in NOMA leads to unfair performance.

In Figure 3.3, the performance of MIMO-NOMA under imperfect SIC is put into perspective with conventional MIMO-OMA, which implements TDMA. As can be noticed, even for a low value of SIC error propagation factor, e.g., $\mu = 0.005$, the MIMO-NOMA scheme is outperformed by the MIMO-OMA counterpart in the high-SNR regime, regardless of the number of receive antennas. Such a performance behavior sheds light on a serious issue, which implies that, in real-world conditions where users are experiencing a considerable number of SIC decoding errors, MIMO-NOMA alone may not be the best option. In fact, we can see that when $\mu = 0.1$, for both $N = 2$ and $N = 6$, the adoption of OMA always delivers the highest performance.

Our theoretical analysis is further corroborated in Figure 3.4, where the analytical outage probability curves match perfectly the simulated ones. The detrimental effects of imper-

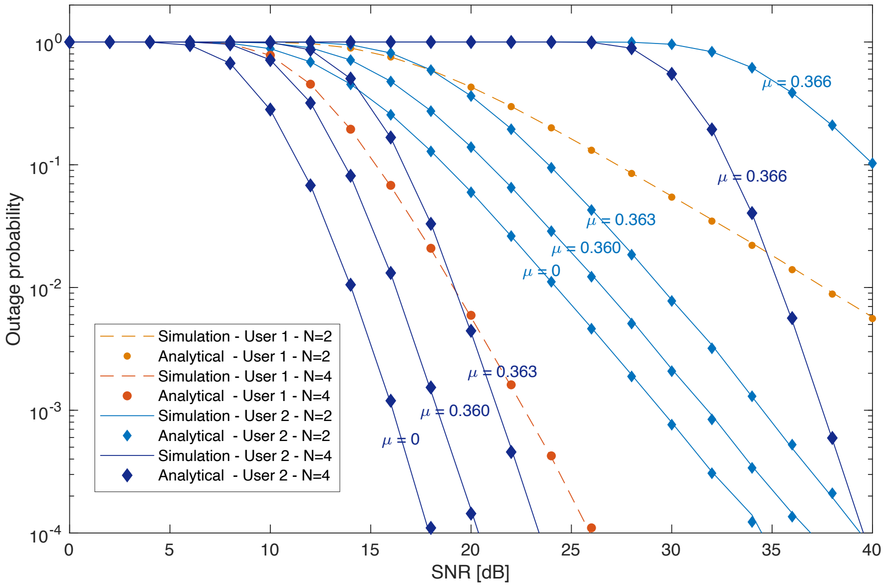

Figure 3.4: Impact of imperfect SIC on the outage probability for different numbers of receive antennas ($T_1 = T_2 = 1.4$ BPCU) [I], ©2020 IEEE.

fect SIC on the users' outage performance become evident in this figure. As can be seen, when the SIC error factor reaches values superior to 0.36, the outage probability curve for the strong user rapidly deteriorates. For instance, when the strong user employs $N = 4$ antennas and the SIC error grows to $\mu = 0.366$, even the weak user employing $N = 2$ receive antennas achieves the best performance for SNRs less than 36 dB. This accentuated performance degradation is explained by the fact that when the SIC error propagation becomes elevated, the data rate achieved by the strong user becomes limited, as revealed in Figure 3.2, which increases the probability of experiencing outage events.

Previous results have shown that fixed power allocation hampers the performance of both the data rate and outage probability of weak users, confirming unfair resource sharing. Figures 3.5 and 3.6 reveal the potential of our dynamic power allocation strategy proposed in Subsection 3.1.4 to overcome such a limitation and enhance fairness within the NOMA groups. Specifically, Figure 3.5 shows that the fair power allocation balances the data rate of the two users at the cost of decreasing the rate of the strong user. This dynamic approach allows the weak user to achieve a data rate considerably higher than that achievable with the fixed policy, which results in a lower but still satisfactory performance for the strong user. For example, under perfect SIC, the fair power allocation policy delivers an ergodic rate of 4.82 BPCU to the two users when the SNR is 22dB, which is an impressive improvement of more than 3.4 BPCU to the weak user when compared with 1.39 BPCU achieved with the fixed policy counterpart.

Last, Figure 3.6 presents the remarkable improvements offered by the fair power allocation to the outage probability of the two users. As it was observed in Figure 3.5, despite

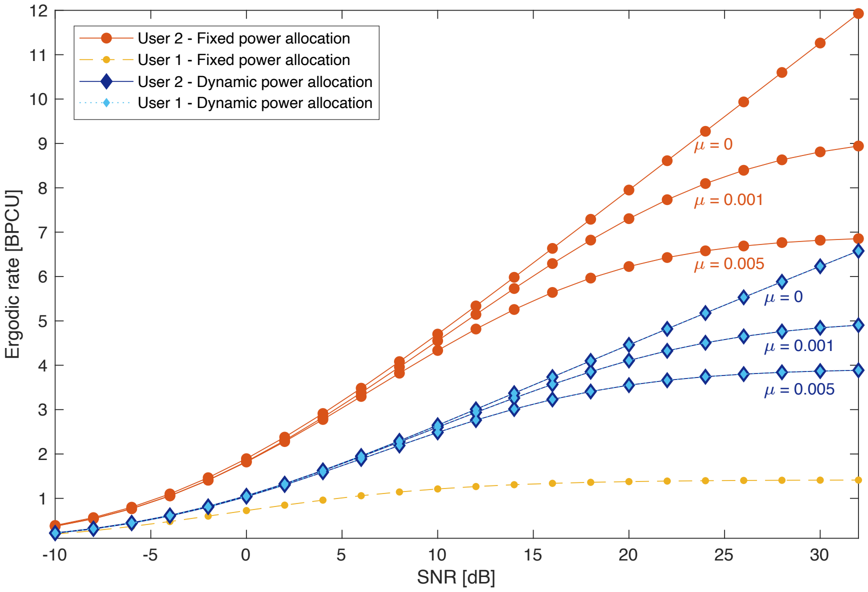

Figure 3.5: Ergodic rates for strong and weak users in a massive MIMO-NOMA system with dynamic and fixed power allocation policies ($N = 2$) [I], ©2020 IEEE.

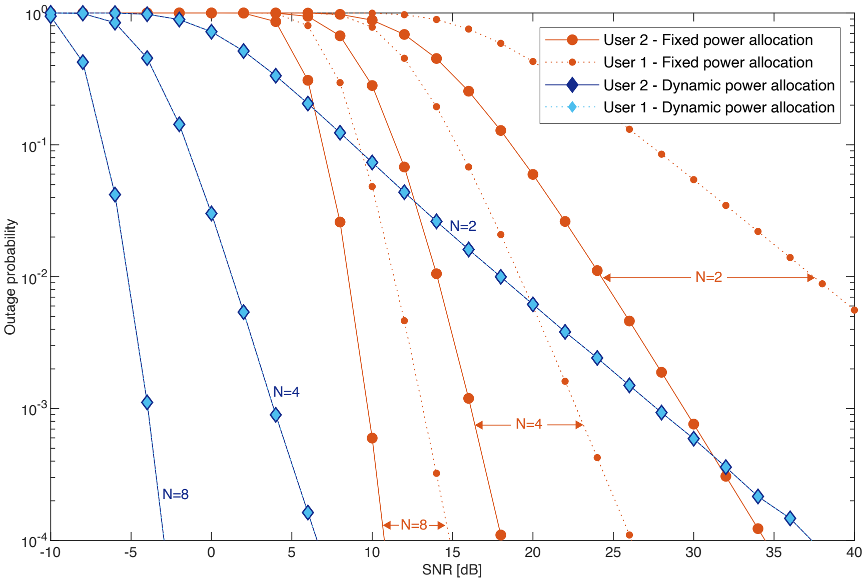

Figure 3.6: Outage probabilities achieved with dynamic and fixed power allocation policies in massive MIMO-NOMA systems ($T_1 = T_2 = 1.4$ BPCU; $\mu = 0$) [I], ©2020 IEEE.

the fact that the ergodic rate of the strong user is decreased to improve the performance of the weak one, the outage probability of the strong user is significantly improved when operating under the fair policy. For instance, when the strong user employs $N = 4$ antennas and is served with the fair power allocation, it can achieve an outage probability performance that is approximately the same as the one observed with the fixed policy but with 12 dB less SNR. The performance improvements delivered to the weak user by the fair allocation are even more expressive, where a gain of more than 20dB in terms of SNR can be achieved when $N = 4$. For the full list of results and further discussions, readers are referred to Section V in Publication [I].

3.1.6 Summary

This section presented a comprehensive overview of the main results and important discoveries of Publication [I]. Specifically, for the first time in the literature, the impact of practical issues of imperfect SIC on the performance of multicluster massive MIMO-NOMA networks was investigated, considering both fixed and dynamic power allocation policies (aiming at enhancing rate fairness). Furthermore, a novel analytical framework with closed-form expressions for the outage probability and ergodic rates was derived, which provides practical tools for assisting the design of MIMO-NOMA systems. Representative simulation results validate the proposed analytical and power allocation frameworks. In particular, our results show that fair power allocation enables remarkable performance improvements for the weak user. Among other important insights, Publication [I] also confirms that imperfect SIC is highly detrimental to the data rates and outage probabilities of MIMO-NOMA schemes, so that when SIC error propagation is high, classical MIMO-OMA outperforms MIMO-NOMA. Such a limitation calls for innovative solutions and provided motivation for developing our subsequent Publications [II], [III], and [IV], which are described in the following sections.

3.2 Roles of IRSs in Massive MIMO-NOMA Networks

In the previous section, it was demonstrated that despite the numerous advantages of massive MIMO-NOMA systems, they still have certain limitations. Furthermore, like any wireless communication system, MIMO-NOMA schemes are also susceptible to the degrading effects of wireless propagation, such as fast-varying channels, blocking, atmospheric absorption, deep fading, and more. Fortunately, as introduced in Section 2.4, IRSs have arisen as disruptive devices for harnessing and tuning these harsh wireless phenomena. The appealing capabilities of IRSs have motivated us to investigate their application to massive MIMO-NOMA systems and led us to write the magazine article in Publication [II], which is our seminal work on the IRS subject, the focus of this section. Specifically, this section answers questions *Q2* and *Q3* by revealing that IRSs can deliver attractive spectral and energy efficiency improvements to MIMO-NOMA schemes.

3.2.1 Motivation and Contributions

At the moment of writing Publication [II], the roles that IRSs are able to play in MIMO-NOMA networks were still not completely clarified. Moreover, surveys and tutorials studying the combination of the subjects IRS and massive MIMO-NOMA were, until then, nonexistent. This lacuna has driven the development of Publication [II], where a thorough investigation is performed and the true potential of the amalgamation of these featured technologies is unveiled. Specifically, an insightful report is provided on promising energy and spectral improvements that can be enabled by massive IRS-MIMO-NOMA systems in future 5G and 6G wireless networks. Light is also shed on important challenges that need to be solved before these systems can be deployed in practice. Further details and our key contributions can be summarized as follows:

- An introduction to the IRS subject is provided. The working principles of IRSs and present typical architectures, materials, and the main technologies used for their fabrication are explained. The standard dyadic channel representation used in IRS-assisted communication is also presented, which is followed by an illustrative comparison between the main features of IRSs and other related technologies.

- Four promising potential performance improvements offered by IRS-MIMO-NOMA systems are identified and comprehensively discussed, supported with insightful simulation examples generated by extensive Monte Carlo iterations. As the main results, it is demonstrated that IRSs can enable MIMO-NOMA to achieve more flexible control of the channel gains and order of connected users. Further, it is shown that the performance of the fair power allocation, proposed in Publication [I], can be further enhanced and that signal coverage to cell-edge users served with NOMA can be improved. It is also shown that if the IRS hardware has a neutral or low energy consumption, IRS-MIMO-NOMA networks can contribute to remarkable energy efficiency gains.

- Potential use case scenarios that IRS-MIMO-NOMA can enable in beyond-5G systems are presented and discussed. The pervasive coverage is proposed through mul-

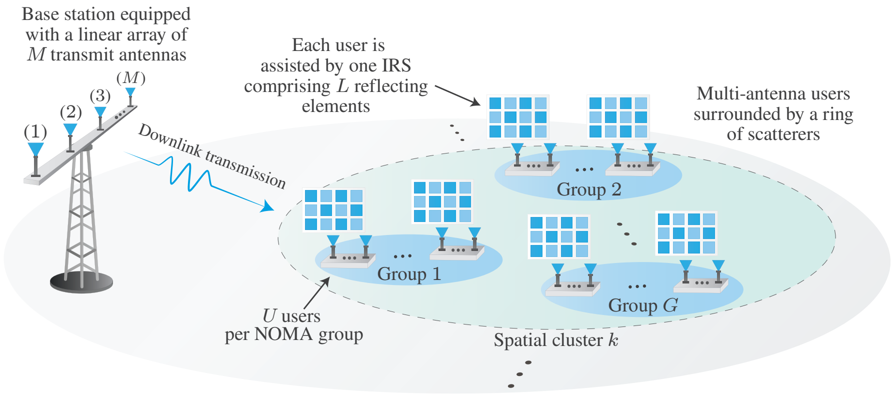

Figure 3.7: System model studied in Publication [II]. Each user is assisted by one IRS comprising L reflecting elements.

tiple IRSs, 3D coverage in UAV networks, and massive grant-free transmissions as three promising applications that can be unlocked by IRS-MIMO-NOMA in the future.

- Last, discussions on unsolved issues, technological challenges, and future research directions related to IRS-MIMO-NOMA networks are provided to conclude the article.

In this section, the focus is on presenting the four above-mentioned performance improvements enabled by IRS-MIMO-NOMA, which are related to spectral efficiency, signal coverage, and energy consumption.

3.2.2 System Model

The system model implemented in Publication [II] is based on the one proposed in the previous section. However, it is assumed that SIC is carried out perfectly in the presented simulation examples. More specifically, the focus of study is on a single-cell network containing one BS equipped with a uniform linear array of M transmit antennas, separated by half of the carrier wavelength, i.e., by $\lambda/2$. The BS communicates in the downlink mode with multiple users equipped with N receive antennas, which are distributed among K spatial clusters, where, within each cluster, the users are organized by the BS into G NOMA groups containing U users each. Furthermore, to enable the anticipated performance improvements, in the vicinity of each user, one IRS comprising L reflecting elements is deployed, as illustrated in Figure 3.7. Under this communication scenario, following the model introduced in Section 2.4, the full composite channel matrix is represented for the uth user in the gth group in the kth cluster by

$$\mathbf{H}_{kgu}^{H} = \mathbf{S}_{kgu}^{H}\boldsymbol{\Theta}_{kgu}\sqrt{\Phi d_{kgu}^{-\eta}}\mathbf{G}_{kgu} + \sqrt{\Phi d_{kgu}^{-\eta}}\mathbf{D}_{kgu}^{H}, \tag{3.20}$$

where $\mathbf{\Theta}_{kgu} \in \mathbb{C}^{L\times L}$ is the diagonal matrix modeling the reflections induced by the L reflecting elements of the IRS serving the uth user, and the matrices $\mathbf{G}_{kgu} \in \mathbb{C}^{L\times M}$, $\mathbf{S}_{kgu} \in \mathbb{C}^{L\times N}$, and $\mathbf{D}_{kgu} \in \mathbb{C}^{M\times N}$ denote the channel responses between the BS and the IRS, the IRS and the users, and the BS and the users, respectively. The parameter d_{kgu} represents the distance from the BS to the uth user, which is the same distance configured to its serving IRS, η is the path-loss exponent, and Φ is the gain parameter adjusted based on the desired performance of the receivers. Note that because the IRSs are considered to be close to their connected user, path-loss in the link between IRSs and users is not modeled, and the channel matrix $\mathbf{S}_{kgu}$ is assumed to be uncorrelated. However, because of the scattering environment and the closely spaced antennas, the channels between the BS and the users and the BS and the IRSs are considered to be correlated, where the correlation matrices of $\mathbf{G}_{kgu}$ and $\mathbf{D}_{kgu}$ are generated following the one-ring geometrical model explained in Subsection 2.1.2.

After the superimposed signal transmitted by the BS has propagated through the wireless channels, the uth user in the gth group in the kth cluster observes the following

$$\mathbf{y}_{kgu} = \mathbf{H}_{kgu}^{H} \sum_{q=1}^{K} \mathbf{B}_q \sum_{m=1}^{G} \mathbf{v}_{qm} \sum_{n=1}^{U} \sqrt{\alpha_{qmn}} x_{qmn} + \mathbf{n}_{kgu}, \tag{3.21}$$

where $\mathbf{n}_{kgu} \in \mathbb{C}^{N}$ is the noise vector with entries following the complex Gaussian distribution with zero mean and variance σ^2. The variable α_{qmn} denotes the power coefficient, and x_{qmn} is the symbol intended for the nth user in the mth NOMA group at the qth cluster. $\mathbf{B}_q \in \mathbb{C}^{M\times \bar{M}}$ is the beamforming matrix responsible for eliminating the intercluster interference, which is designed based on the null space spanned by the nonzero eigenmodes of the correlation matrices of interfering clusters like in Subsection 2.1.5, and $\mathbf{v}_{qm} \in \mathbb{C}^{\bar{M}}$ is the precoding vector for assigning the superimposed symbols to corresponding NOMA groups designed as in (3.2).

By assuming that the beamforming matrix $\mathbf{B}_q$ can successfully null out all intercluster interference, the superposed signal observed by the uth user in the gth group can be rewritten as

$$\mathbf{y}_{kgu} = \mathbf{H}_{kgu}^{H} \mathbf{B}_k \sum_{m=1}^{G} \mathbf{v}_{kn} \sum_{n=1}^{U} \sqrt{\alpha_{knm}} x_{knm} + \mathbf{n}_{kgu}. \tag{3.22}$$

To eliminate the remaining intergroup interference, as in (3.3), the users employ the following zero-forcing receiver

$$\begin{aligned}\mathbf{H}_{kgu}^{\dagger} =&[(\mathbf{H}_{kgu}^{H}\mathbf{B}_k)^H\mathbf{H}_{kgu}^{H}\mathbf{B}_k]^{-1}(\mathbf{H}_{kgu}^{H}\mathbf{B}_k)^H\\ =&\Bigg[\left(\left(\mathbf{S}_{kgu}^{H}\mathbf{\Theta}_{kgu}\sqrt{\Phi d_{kgu}^{-\eta}}\mathbf{G}_{kgu}+\sqrt{\Phi d_{kgu}^{-\eta}}\mathbf{D}_{kgu}^{H}\right)\mathbf{B}_k\right)^H\\ &\times\left(\mathbf{S}_{kgu}^{H}\mathbf{\Theta}_{kgu}\sqrt{\Phi d_{kgu}^{-\eta}}\mathbf{G}_{kgu}+\sqrt{\Phi d_{kgu}^{-\eta}}\mathbf{D}_{kgu}^{H}\right)\mathbf{B}_k\Bigg]^{-1}\\ &\times\left(\left(\mathbf{S}_{kgu}^{H}\mathbf{\Theta}_{kgu}\sqrt{\Phi d_{kgu}^{-\eta}}\mathbf{G}_{kgu}+\sqrt{\Phi d_{kgu}^{-\eta}}\mathbf{D}_{kgu}^{H}\right)\mathbf{B}_k\right)^H. \end{aligned}\tag{3.23}$$

After the received signal in (3.21) has been filtered through the zero-forcing receiver in (3.23), the uth user in the gth group at the kth cluster will recover the following corrupted data vector

$$\hat{\mathbf{x}}_{kgu}=\begin{bmatrix}\sum_{n=1}^{U}\sqrt{\alpha_{k1n}}x_{k1n}\\ \vdots\\ \sum_{n=1}^{U}\sqrt{\alpha_{kGn}}x_{kGn}\end{bmatrix}+\mathbf{H}_{kgu}^{\dagger}\mathbf{n}_{kgu}.\tag{3.24}$$

Observe that each element in the vector in (3.24) is intended for a distinct NOMA group. Thus, users within the gth NOMA group carry out SIC on the gth element of the detected data vector. As a result, by assuming that the users are sorted in an ascending order based on their effective channel gains, the SINR observed at the uth user when decoding the symbol belonging to the ith user, $1\le i\le u\le U$, can be expressed as follows

$$\gamma_{kgu}^{i}=\frac{\rho\varrho_{kgu}\alpha_{kgi}}{\rho\varrho_{kgu}\alpha_{kgi}^{\star}+1},\qquad \text{for}\quad 1\le i\le u\le U,\tag{3.25}$$

where $\varrho_{kgu}=\frac{1}{[\mathbf{H}_{kgu}^{\dagger}\mathbf{H}_{kgu}^{\dagger H}]_{g,g}}$, $\rho=1/\sigma^2$, and the interference $\alpha_{kgi}^{\star}$ is defined by

$$\alpha_{kgi}^{\star}=\begin{cases}\sum_{j=i+1}^{U}\alpha_{kgj}, & \text{for}\quad 1\le i\le u<U,\\ 0, & \text{for}\quad i=u=U.\end{cases}\tag{3.26}$$

The above expression is obtained similarly as in Lemma 3.1, in Subsection 3.1.3, and thus, the proof is omitted.

3.2.3 IRS Optimization

For generating the simulation results in Publication [II], IRSs are implemented considering both fixed and optimized reflection coefficients. In the simulation examples where IRSs are claimed to be optimized, at each channel coherence interval, the reflecting elements are dynamically tuned to either maximize or attenuate the instantaneous data rates achieved by each user so that different system objectives can be achieved. In order to implement such capabilities, an exhaustive search is carried out to find the best set of reflection coefficients. In contrast, when fixed reflecting elements are deployed, all phase coefficients are adjusted to $0°$, and all reflection amplitudes are set to the maximum, i.e., to 1. Even though these configuration strategies are straightforward, they can satisfactorily illustrate the desired performance capabilities. More sophisticated optimization techniques are proposed and implemented in Publications [III], [IV], and [V].

3.2.4 Performance Metrics

Two important performance metrics are presented and discussed in the provided simulation results. First, the achievable data rates observed by each user, which are measured in BPCU, are studied, and second, the energy efficiency curves, in BPCU/Watts, achieved by the considered NOMA group, are plotted. More specifically, the achievable rate for the uth user in the gth group at the kth cluster is calculated by

$$R_{kgu} = \log_2(1 + \gamma_{kgu}^{u}), \tag{3.27}$$

with γ_{kgu}^{u} given in (3.25). In turn, the energy efficiency for the gth group in the kth cluster is defined by the ratio between sum-rate and the total energy consumption, as follows

$$\mathcal{E}_{kg} = \frac{\sum_{n=1}^{U} R_{kgn}}{\bar{\alpha}_{\text{T}} + \bar{\alpha}_{\text{S}} + UL\bar{\alpha}_{\text{IRS}}}, \tag{3.28}$$

where $\bar{\alpha}_{\text{T}}$ denotes the total power budget available at the BS, $\bar{\alpha}_{\text{S}}$ is a static power dissipated in the system, and $\bar{\alpha}_{\text{IRS}}$ is the power consumed by each IRS reflecting element.

3.2.5 Main Results

Now that the essential details for the considered system model have been provided, the four most relevant improvements identified in Publication [II] delivered by IRS-MIMO-NOMA networks are presented. To this end, a BS is implemented employing $M = 80$ transmit antennas and multiple users employing $N = 4$ receive antennas, which are distributed in different regions forming $K = 4$ spatial clusters, so that within each cluster, the users are divided into $G = 4$ NOMA groups. In Figures 3.8, 3.9, and 3.11, each group is formed containing two users, whereas in Figure 3.10, it is assumed that there are three users per group, and nearby each user, and one IRS with $L = 20$ reflecting elements is installed. Moreover, in Figures 3.8, 3.10, and 3.11, the users are served only with fixed power allocation. On the other hand, in Figure 3.9, the users are served with both fixed and the dynamic fair power allocation policy from Publication [I]. Other specific simulation parameters are informed in the legends of the corresponding figure, and without loss of generality, the presented results are generated focusing on the first NOMA group in the first cluster.

Figure 3.8 illustrates the first interesting property that IRSs can enable in MIMO-NOMA systems, which is related to the improved control of users' effective channel gains. As

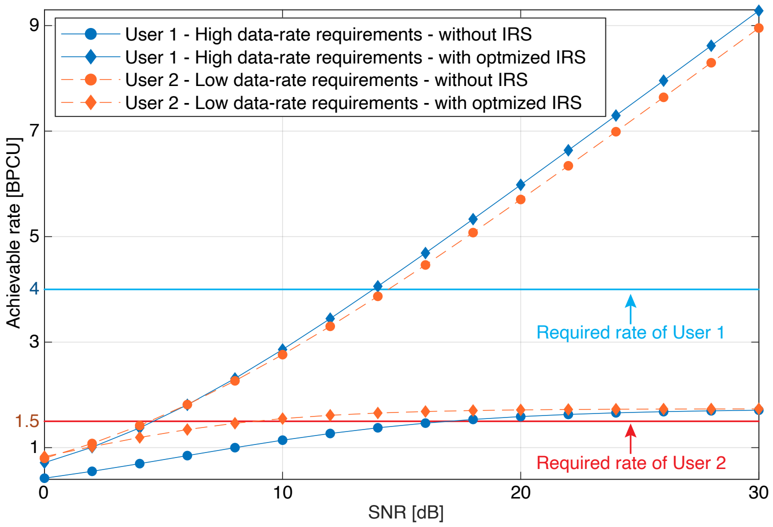

Figure 3.8: Achievable rates versus SNR for MIMO-NOMA and IRS-NOMA systems under fixed power allocation where user 1 is located at 200 m and user 2 at 100 m from the BS. The power allocation coefficients of users 1 and 2 are $7/10$ and $3/10$, respectively [II], ©2020 IEEE.

explained, the knowledge of the channel strengths of individual users is crucial for executing SIC successfully in NOMA, as users are ordered based on this information by the BS. Moreover, the way user ordering is performed influences the level of interference experienced by each user. However, in classical wireless environments, users' channel gains are highly stochastic and difficult to be controlled, which has a direct impact on the performance of MIMO-NOMA systems. In this regard, Figure 3.8 shows that IRSs can help to smartly adjust the propagation environment and change the effective strengths of users' channels, which enables a more flexible user ordering and new opportunities for performance improvements. For instance, as can be seen, user 1, located 200 m from the BS, is served as the weak user in the conventional MIMO-NOMA, which, because of the SIC protocol, has a rate limited to a value way below its required target data rate as a result of interference from user 2. Consequently, user 1 faces a high outage probability under the conventional MIMO-NOMA. In turn, by deploying IRSs close to the users and properly optimizing the reflecting elements, the order of the user's effective channel gains can be changed, which allows the user 1 (previously achieving low data rates) to surpass its target rate of 4 BPCU and, at the same time, user 2 can still satisfy its requirements.

The dynamic power allocation strategy proposed in Subsection 3.1.4 enabled users with different channel conditions to experience the same data rates in the considered MIMO-NOMA network. However, it also became clear that, in order to achieve this property, the data rates of strong users need to be decreased. Such a characteristic is detrimental to the system sum-rate and can lead to unsatisfactory network-wide performance in situations where the weak user is undergoing severe channel attenuation. Figure 3.9 shows

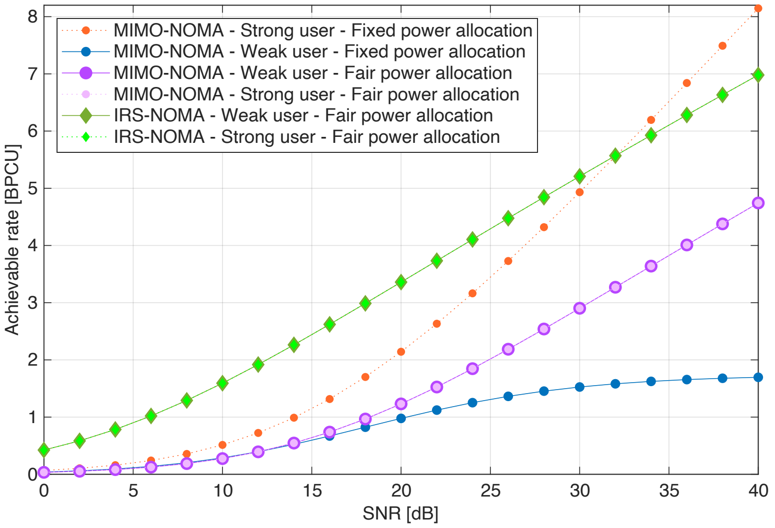

Figure 3.9: Achievable rates versus SNR for MIMO-NOMA and IRS-NOMA systems under fixed and fair power allocation, where the weak user is located at 200 m and the strong one at 100 m from the BS. When fixed allocation is employed, the power coefficients for the weak and strong users are $7/10$ and $3/10$, respectively [II], ©2020 IEEE.

that IRSs are highly beneficial for mitigating such an issue. This figure presents the users' achievable rates achieved with fixed and fair power allocation policies, and in the IRS-assisted results, only fixed reflecting coefficients are implemented. As can be seen, in the conventional MIMO-NOMA, the dynamic policy can successfully bring the data rates of the two users to similar levels. However, the curve for the strong one is significantly lowered for achieving fairness, a limitation not observed in the IRS-MIMO-NOMA counterpart. Specifically, it can be seen that both users under IRS-MIMO-NOMA can achieve higher data rates than that observed by the strong user in the conventional MIMO-NOMA scheme, almost in the entire SNR range.

In conventional MIMO-NOMA networks, users with excessively low SINRs are commonly disconnected to avoid heavy losses in the network sum rate, which is particularly detrimental to cell-edge users and limits the practical communication range. Figure 3.10 illustrates the capability of IRSs for overcoming this problem and extending signal coverage in MIMO-NOMA systems, where fixed power allocation and an SNR value of 26 dBm are considered. As informed in the referred figure, there are three users in the studied NOMA group, in which one of the users is at a far 1500 m distance from the BS. It is depicted that, because of the high path-loss, the distant user can achieve only 0.188 BPCU of data rate when served with MIMO-NOMA alone. On the other hand, when deploying an IRS, the same user can achieve an impressive rate of 1.185 BPCU, which is nearly the same performance observed by the second closest user and represents a rate improvement of more than six times.

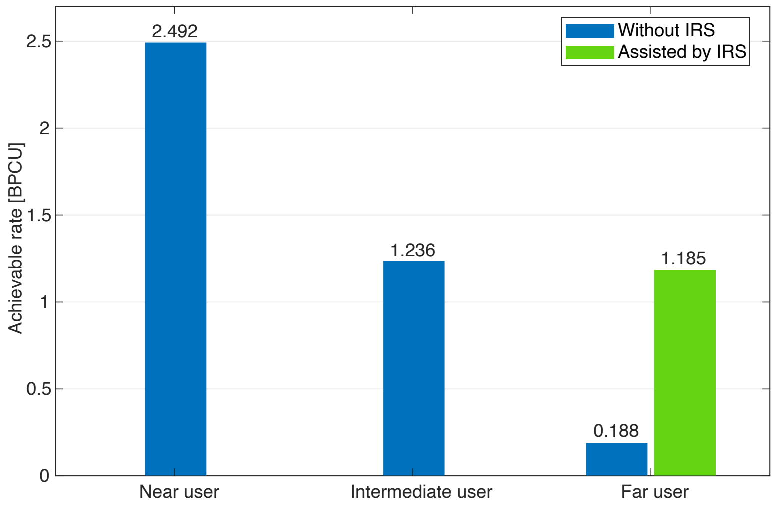

Figure 3.10: Achievable rates when the SNR is 26 dBm for MIMO-NOMA and IRS-NOMA systems serving three users with fixed power allocation. The near user is located at 100 m, the intermediate user at 200 m, and the far user at 1500 m from the BS. The power coefficients for the near, intermediate, and far users are $1/10$, $3/10$, and $6/10$, respectively [II], ©2020 IEEE.

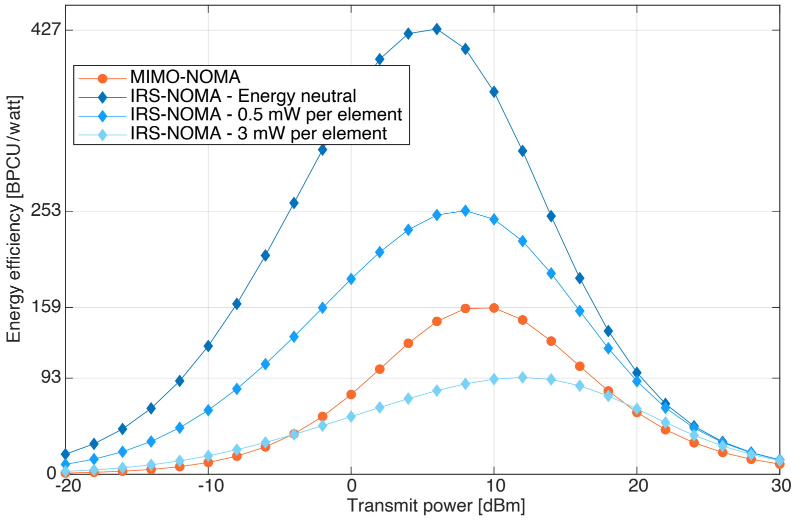

Figure 3.11: Energy efficiency versus transmit power for MIMO-NOMA and IRS-NOMA systems under fixed power allocation. Two users are considered in this simulation, one located at 100 m and another at 200 m from the BS. The power coefficients for the far and near users are $7/10$ and $3/10$, respectively [II], ©2020 IEEE.

As illustrated in the previous result, the performance of weak users can be improved with the aid of IRSs without directly requiring the BS to allocate a higher transmit power. If the hardware components of the IRSs are efficient enough so that the additional energy consumption required for their configuration is maintained at moderate levels, the energy efficiency of the network can be considerably improved. This potential benefit is depicted in the curves in Figure 3.11, which compares the energy efficiencies of both conventional MIMO-NOMA and IRS-MIMO-NOMA systems under fixed power allocation and considering different energy consumption behaviors for elements of the IRSs. For instance, under the assumption of energy neutrality, the proposed IRS-MIMO-NOMA system requires almost 20 dBm less transmit power than the conventional MIMO-NOMA counterpart requires to achieve its maximum energy efficiency of only 159.6 BPCU/Watt. To put into perspective, the maximum efficiency value of the energy-neutral IRS-assisted scheme is incredibly 427.2 BPCU/Watt. However, as can be seen, if the energy consumption of the reflecting elements is increased, the energy efficiency improvements diminish. By considering that each element consumes 0.5 mW, for instance, the maximum energy efficiency reaches only 253 BPCU/Watt, whereas with 3 mW per element, the IRS-MIMO-NOMA scheme outperforms the conventional MIMO-NOMA system only in the low or very high transmit power regime.

3.2.6 Summary

This section focused on the contributions of Publication [II], covering four main performance improvements that the IRS technology should enable in future massive MIMO-NOMA networks. Specifically, an extension of the massive MIMO-NOMA system model proposed in Section 3.1 was implemented, where the users were assisted with multiple IRSs. The increased control of the users' effective channel gains, high-performance adaptive fair power allocation, enhanced cell-edge NOMA user performance, and (possibly) high energy efficiency were identified and comprehensively discussed as promising improvement oppotunities. Readers are invited to go through our complete work in Publication [II], where further discussions are provided and promising use case scenarios foreseen for 6G are presented.

It is noteworthy that perfect SIC was assumed in all the scenarios studied in Publication [II]. However, it was found that imperfect SIC is also an important detrimental issue in MIMO-NOMA networks, which deserves to be studied and tackled. Such a task is performed in Publications [III], and [IV], where the polarization domain is exploited with the help of IRSs to mitigate SIC error propagation.

3.3 IRSs for Downlink Dual-Polarized Massive MIMO-NOMA Networks

In previous sections, the studies were limited to single-polarized system models only. Moreover, the reflecting elements of the IRSs were optimized through exhaustive search strategies for illustrative purposes. In this section, our contributions to the IRS-MIMO-NOMA topic are further elaborated. Our studies are extended to more general dual-polarized models, and more sophisticated optimization algorithms are developed to unleash the full potential of IRS technology. The results presented in this section were proposed in Publication [III] and are dedicated to answering the research questions *Q4* and *Q5*.

3.3.1 Motivation and Contributions

Our seminal work in Publication [II] has enlightened us on a few major improvements that can be enabled in massive MIMO-NOMA systems with the aid of IRSs. However, the detrimental issue of imperfect SIC identified in Publication [I] remained unsolved. Furthermore, all related technical works were limited to single-polarized systems, and there were no works exploiting the capabilities of IRSs for harnessing the extra DoF offered by the polarization domain in dual-polarized MIMO-NOMA networks undergoing SIC error propagation. These literature gaps were identified as a great research opportunity and provided motivation for developing the innovative ideas proposed in Publication [III]. In this section, the properties of disruptive dual-polarized IRSs are optimized for unlocking users to enjoy polarization diversity and mitigating the degrading effects of imperfect SIC decoding in a massive dual-polarized MIMO-NOMA network. Additional details and main contributions of Publication [III] can be summarized as follows:

- By modeling imperfect SIC decoding as in Publication [I], a multicluster downlink communication network is implemented where users and the BS are equipped with multiple co-located pairs of dual-polarized antennas. In this scenario, multiple NOMA groups within different spatial clusters are reorganized by the BS into two subsets. Then, we rely on IRSs with appealing polarization manipulation capabilities and propose a novel transmission approach for multiplexing the two subsets of users in the polarization domain. More specifically, at the BS, antennas with vertical polarization are assigned to serve one subset and antennas with horizontal polarization to serve the other subset. Because each subset counts with a lower number of users, our strategy offers a simplified SIC decoding process and reduced levels of interference. Furthermore, cross-polar transmissions, which usually are a source of interference in conventional dual-polarized MIMO systems, are harnessed by the proposed IRSs to unleash polarization diversity and further mitigate the detrimental effects of imperfect SIC on users.

- Each user is assisted with one dual-polarized IRS. Moreover, it is assumed that users and their serving IRSs within a given geographical region are receiving signals propagating through a common cluster of scatterers. Then, inspired by our previous publications, multistage precoders are proposed based on the spatial correlation information of the multiple clusters for multiplexing both users and IRSs in space. The precoding matrices for canceling intercluster interference are then concatenated with precoders of low computational complexity for performing the polarization multiplexing of user subsets.

- With the objective of nulling out interfering polarized transmissions arriving at unintended subsets, a generalized least squares problem for matrix equations is formulated for optimizing the reflecting coefficients of the dual-polarized IRSs. Achieving a solution for the original problem is challenging because of its complicated form. After some transformations, the formulated problem is simplified into convex quadratic constrained quadratic subproblems. By performing an analysis, it is confirmed that the simplified problems are convex and thus have global optimal solutions that can be computed iteratively. To find the desired solutions, the interior-points method is implemented, which counts with polynomial time complexity.

- By taking practical issues into consideration, such as cross-polar transmissions and SIC error propagation, an in-depth theoretical study is performed on the proposed dual-polarized IRS-MIMO-NOMA network. First, after determining expressions for the SINR observed by each user, a comprehensive statistical characterization of the achieved channel gains is performed. Due to the fact that the IRS reflecting coefficients are optimized dynamically at each coherence interval of the fast-varying channels, determining their statistical properties for arbitrary IRS sizes turns out to be a convoluted task. To overcome this mathematical challenge, asymptotic scenarios where large IRSs comprise massive numbers of reflecting elements are studied. The asymptotic statistical distributions of the effective channel gains are determined, which are then exploited for deriving closed-form expressions for the users' ergodic rates. The developed analytical framework can be used to achieve important insights on fundamental performance limits when large IRSs are employed in the considered dual-polarized scheme.

- To conclude our contributions in Publication [III], illustrative numerical and simulation examples are provided that confirm the accuracy of our theoretical analysis and demonstrate impressive performance capabilities of the proposed dual-polarized massive IRS-MIMO-NOMA system. It is revealed that in the asymptotic case when the number of reflecting elements is large, our novel dual-polarized system is capable of outperforming the considered massive MIMO-NOMA and MIMO-OMA baseline schemes even in scenarios with significant levels of SIC decoding errors. The attractive capabilities of dual-polarized IRSs for recycling cross-polar transmissions and transforming them into polarization diversity for users are also demonstrated.

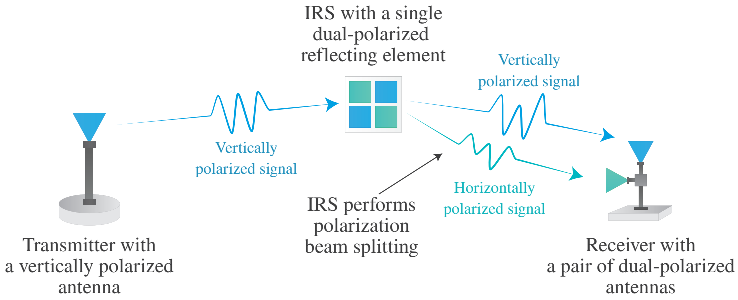

Figure 3.12: Toy example with one IRS employing a single dual-polarized reflecting element. A vertically polarized signal is split into two beams with orthogonal polarizations.

3.3.2 Fundamentals of a Dual-Polarized IRS

Before introducing the actual system model studied in Publication [III], it is important to understand the working principles and fundamental capabilities of a dual-polarized reflecting element. It was explained in Section 2.4 that one element of a conventional IRS can induce phase and amplitude changes in impinging signals, which can be modeled by a complex number $\omega e^{-j\phi}$, with ω representing the reflection amplitude and ϕ the induced phase shift. A dual-polarized reflecting element can perform the same capabilities and be modeled in an analogous fashion. However, more than phase and amplitude control, reflecting elements with polarization manipulation capabilities can realize functions such as independent control of impinging polarizations, polarization conversion, and polarization beam splitting [86]. For example, when considering a linear scheme with vertical and horizontal polarizations, signals impinging at a dual-polarized IRS with vertical polarization can be converted and forwarded in the horizontal polarization (or vice versa) or just forwarded without changing impinging polarizations [87, 88]. More specifically, the functionalities of a single dual-polarized reflecting element can be characterized by the following matrix:

$$\mathbf{\Psi} = \begin{bmatrix} \omega^{vv} e^{-j\phi^{vv}} & \omega^{hv} e^{-j\phi^{hv}} \\ \omega^{vh} e^{-j\phi^{vh}} & \omega^{hh} e^{-j\phi^{hh}} \end{bmatrix}, \tag{3.29}$$

where the coefficients $\omega^{ab} \in [0, 1]$ and $\phi^{ab} \in [0, 2\pi]$ model the reflection amplitude and phase change, respectively, induced in impinging signals from the polarization a to b, in which $a, b \in \{v, h\}$.

To better illustrate the proposed concept, consider the following toy example. Assume an idealistic scenario with no depolarization phenomena where one transmitter employing one antenna, installed with vertical polarization, communicates with one receiver employing one co-located pair of dual-polarized antennas, i.e., two antenna elements installed with vertical and horizontal orientations. In the scenario without an IRS, the vertically polarized transmitted signals only reach the receiver in its matching antenna of vertical polarization, and this disables the receiver to exploit diversity. In contrast, in a scenario with a dual-polarized IRS, transmitted signals with vertical polarization can be transformed into two independent beams with vertical and horizontal polarizations, as illustrated in Figure 3.12. This implies that a dual-polarized IRS can enable polarization diversity in the receiver, which can be exploited for improving the communication performance in practical systems. For illustration purposes, assume that the IRS deployed in this example comprises a single dual-polarized element. Then, by recalling the reflection matrix in (3.29), and considering only the reflected link via the IRS, the dual-polarized noiseless signal observed by the receiver can be expressed by:

$$\begin{aligned}\begin{bmatrix} y^v \\ y^h \end{bmatrix} &= \frac{1}{\sqrt{2}} \begin{bmatrix} (s^{vv})' & 0 \\ 0 & (s^{hh})' \end{bmatrix} \begin{bmatrix} \omega^{vv} e^{-j\phi^{vv}} & \omega^{hv} e^{-j\phi^{hv}} \\ \omega^{vh} e^{-j\phi^{vh}} & \omega^{hh} e^{-j\phi^{hh}} \end{bmatrix} \begin{bmatrix} g^{vv} \\ 0 \end{bmatrix} x \\ &= \begin{bmatrix} \frac{1}{\sqrt{2}}(s^{vv})' \omega^{vv} e^{-j\phi^{vv}} g^{vv} x \\ \frac{1}{\sqrt{2}}(s^{hh})' \omega^{vh} e^{-j\phi^{vh}} g^{vv} x \end{bmatrix}, \end{aligned} \tag{3.30}$$

where x represents the data message intended for the receiver, g^{vv} denotes the channel gain for the link between the transmitter and the IRS, and s^{ab} is the channel gain for the link between the IRS and the receiver, which models the propagation path of signals reflected with the polarization a and received with the polarization b, with $a, b \in \{v, h\}$. For ensuring only passive transformations at the IRS, the normalization factor $\frac{1}{\sqrt{2}}$ is introduced. The signal in (3.30) shows that, through polarization beam splitting, the dual-polarized IRS can enable the delivery of the data message (originally from the vertical polarization) to the two receive polarizations. This example illustrates an interesting feature, but it also makes evident that a number of other possibilities can be realized by optimizing the polarization properties of dual-polarized IRSs. As we will see, by combining multiple reflecting elements in a larger IRS, countless more advanced capabilities are unleashed.

Given that the amplitude and phase changes induced by one dual-polarized reflecting element can be represented by a 2×2 reflection matrix as in (3.29), one IRS with L dual-polarized reflecting elements can be modeled by a $2L \times 2L$ reflection matrix, with a block structure containing four $L \times L$ matrices, each one consisting of a diagonal matrix modeling a distinct polarization transformation, as follows:

$$\boldsymbol{\Theta} = \begin{bmatrix} \boldsymbol{\Phi}^{vv} & \boldsymbol{\Phi}^{hv} \\ \boldsymbol{\Phi}^{vh} & \boldsymbol{\Phi}^{hh} \end{bmatrix} \in \mathbb{C}^{2L \times 2L}, \tag{3.31}$$

where $\boldsymbol{\Phi}^{ab} = \mathrm{diag}\{[\omega_1^{ab} e^{-j\phi_1^{ab}}, \omega_2^{ab} e^{-j\phi_2^{ab}}, \cdots, \omega_L^{ab} e^{-j\phi_L^{ab}}]\} \in \mathbb{C}^{L \times L}$, in which ω_l^{ab} and ϕ_l^{ab} denote, respectively, the reflection amplitude and phase-shift coefficients for the lth element from the polarization a to b, with $a, b \in \{v, h\}$, so that $|\omega_l^{ab}|^2 \leq 1$ must be satisfied for modeling passive IRSs. The representation in (3.31) is the base model used to derive the results in Publication [III], where a more complex scenario with multiple

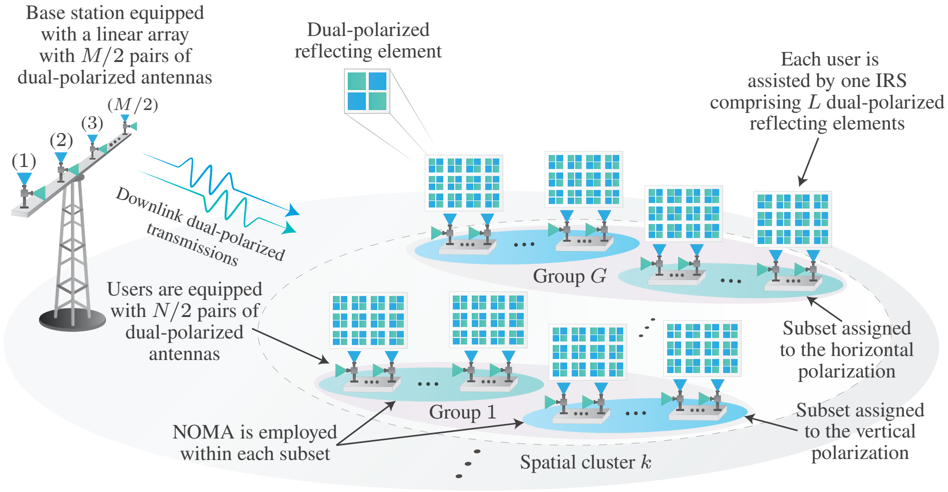

Figure 3.13: System model investigated in Publication [III]. Users within different groups are organized into two polarization subsets with the aid of dual-polarized IRSs.

dual-polarized IRSs across several clusters and large numbers of reflecting elements is studied.

3.3.3 System Model

Here, a single-cell MIMO-NOMA network is considered, containing one BS that carries out downlink transmissions to multiple users, where the BS and users employ multiple co-located pairs of linearly polarized vertical/horizontal antennas. The BS is equipped with a uniform linear array with $M/2$ pairs of dual-polarized antennas, each pair spaced by $\lambda/2$, and the users employ $N/2$ pairs of dual-polarized receive antennas. In this work, a spatially correlated scenario is also implemented where users are uniformly distributed across K different spatial clusters. Moreover, within each cluster, the users are partitioned by the BS into G groups of U users, and each user is assisted by one dual-polarized IRS comprising L reflecting elements, as depicted in Figure 3.13.

In classical NOMA schemes (considered in our previous works), when the u user within any gth NOMA group executes SIC, this user is required to cope with interference from all remaining $U-1$ users in the given group. This characteristic makes SIC an interference-limited technique and can result in performance degradation if the number of users within the group is increased. Moreover, imperfect SIC can make such a limitation even more prominent. Our novel dual-polarized IRS-assisted transmission strategy efficiently mitigates this problem by harnessing the polarization domain, which can be explained as follows. First, each group is further partitioned into two subsets, called *vertical subset* and *horizontal subset*, with each polarization subset comprising U^a users, where $a \in \{v, h\}$ and $U^v + U^h = U$. Then, the BS is configured to serve the U^v users within the vertical subset with vertically polarized antennas and the remaining U^h users within the horizontal subset with horizontally polarized antennas. To reduce the probability of signals coming from one polarization causing interference at users in subsets assigned to the orthogonal polarization, the appealing properties of dual-polarized IRSs are optimized to minimize unwanted transmissions. For example, all IRSs connected to users in vertical subsets are configured to null out incoming transmissions from BS antennas of horizontal polarization and vice versa. With our IRS-MIMO-NOMA scheme, users are enabled to experience a reduced interference load when carrying out SIC, less impact from imperfect SIC, and exploit polarization diversity, imposing a low computational complexity on users.

For implementing the above scheme, the BS applies SC to the data symbols of users from each subset separately and transmits the superimposed data streams through their respective polarizations, resulting in the following signal

$$\mathbf{x} = \sum_{k=1}^{K} \mathbf{P}_k \begin{bmatrix} \mathbf{x}^v \\ \mathbf{x}^h \end{bmatrix} = \sum_{k=1}^{K} \mathbf{B}_k \sum_{g=1}^{G} \sum_{u=1}^{U} \mathbf{v}_{kgu} \sqrt{\alpha_{kgu}} x_{kgu} \in \mathbb{C}^{M}, \tag{3.32}$$

where the vector $\mathbf{x}^a$ comprises the superimposed symbols transmitted in antennas with polarization $a \in \{v, h\}$, α_{kgu} denotes the power allocation coefficient, and x_{kgu} is the symbol intended for the uth user in the gth group in the kth cluster. The matrix $\mathbf{B}_k \in \mathbb{C}^{M \times \bar{M}}$ is the precoder for multiplexing the spatial clusters, which has the following structure

$$\mathbf{B}_k = \begin{bmatrix} \tilde{\mathbf{B}}_k & \mathbf{0}_{\frac{M}{2}, \frac{\bar{M}}{2}} \\ \mathbf{0}_{\frac{M}{2}, \frac{\bar{M}}{2}} & \tilde{\mathbf{B}}_k \end{bmatrix} \in \mathbb{C}^{M \times \bar{M}}, \tag{3.33}$$

in which $\tilde{\mathbf{B}}_k \in \mathbb{C}^{\frac{M}{2} \times \frac{\bar{M}}{2}}$ is the precoding matrix for each polarization designed based on the correlation matrices of spatial clusters, following the same steps of Subsection 2.1.5, and $\mathbf{v}_{kgu}$ is the precoding vector for assigning the data symbols to the corresponding polarization subsets, which will be explained later.

By using the reflection model for a dual-polarized IRS introduced in (3.31), we can express the full dual-polarized channel matrix for the uth user in the gth group in the kth cluster by

$$\begin{aligned} \mathbf{H}_{kgu}^{H} = {} & \sqrt{\zeta_{kgu}^{\text{BS-IRS}} \zeta_{kgu}^{\text{IRS-U}}} \frac{1}{\sqrt{2}} \begin{bmatrix} \bar{\mathbf{S}}_{kgu}^{vv} & \mathbf{0}_{L, \frac{N}{2}} \\ \mathbf{0}_{L, \frac{N}{2}} & \bar{\mathbf{S}}_{kgu}^{hh} \end{bmatrix}^{H} \begin{bmatrix} \mathbf{\Phi}_{kgu}^{vv} & \mathbf{\Phi}_{kgu}^{hv} \\ \mathbf{\Phi}_{kgu}^{vh} & \mathbf{\Phi}_{kgu}^{hh} \end{bmatrix} \begin{bmatrix} \bar{\mathbf{G}}_{kgu}^{vv} & \sqrt{\chi^{\text{BS-IRS}}} \bar{\mathbf{G}}_{kgu}^{hv} \\ \sqrt{\chi^{\text{BS-IRS}}} \bar{\mathbf{G}}_{kgu}^{vh} & \bar{\mathbf{G}}_{kgu}^{hh} \end{bmatrix} \\ & + \sqrt{\zeta_{kgu}^{\text{BS-U}}} \begin{bmatrix} \bar{\mathbf{D}}_{kgu}^{vv} & \sqrt{\chi^{\text{BS-U}}} \bar{\mathbf{D}}_{kgu}^{vh} \\ \sqrt{\chi^{\text{BS-U}}} \bar{\mathbf{D}}_{kgu}^{hv} & \bar{\mathbf{D}}_{kgu}^{hh} \end{bmatrix}^{H} \in \mathbb{C}^{N \times M}, \end{aligned} \tag{3.34}$$

where the matrices $\bar{\mathbf{S}}_{kgu}^{pq} \in \mathbb{C}^{L \times \frac{N}{2}}$, $\bar{\mathbf{G}}_{kgu}^{pq} \in \mathbb{C}^{L \times \frac{M}{2}}$, and $\bar{\mathbf{D}}_{kgu}^{pq} \in \mathbb{C}^{\frac{M}{2} \times \frac{N}{2}}$ comprise the channel coefficients, respectively, for the links between the given IRS and its connected user (link IRS-U), the BS and the IRS (link BS-IRS), and the BS and the user (link BS-U), from the polarization a to b, with $a, b \in \{v, h\}$. Moreover, $\chi^{\text{BS-U}}$ and $\chi^{\text{BS-IRS}} \in [0, 1]$ denote the iXPD parameters that inform the levels of cross-polar transmissions experienced in the links BS-U and BS-IRS, $\frac{1}{\sqrt{2}}$ is the normalization factor for ensuring passive polarization transformations, and $\zeta^{\text{BS-U}}_{kgu}$, $\zeta^{\text{IRS-U}}_{kgu}$, and $\zeta^{\text{BS-IRS}}_{kgu}$ model, respectively, the large-scale fading observed in the links BS-U, IRS-U, and BS-IRS.

Note in (3.34) that depolarization phenomena in the link IRS-U are not considered. This implies that the cross-polar interference experienced in the channels between users and their serving IRSs is zero. Although such a condition cannot be exactly verified in practice, it was necessary in order to avoid a more intricate mathematical formulation and to ease the interpretation of our results. Nevertheless, it is noteworthy that our contributions can be easily extended to the more general case with depolarization in all propagation links.

The matrices $\bar{\mathbf{D}}^{pq}_{kgu}$ and $\bar{\mathbf{G}}^{pq}_{kgu}$ are assumed to be correlated. Thus, they are generated following the model in (2.4). On the other hand, the matrix $\bar{\mathbf{S}}^{pq}_{kgu}$ is considered to be uncorrelated, i.e., full rank. With such considerations, we can express the correlation matrices of $\bar{\mathbf{D}}^{pq}_{kgu}$ and $\bar{\mathbf{G}}^{pq}_{kgu}$ by

$$\mathbf{R}^{\text{BS-IRS}}_{k} = \zeta^{\text{BS-IRS}}_{kgu}(\chi^{\text{BS-IRS}} + 1)\mathbf{I}_2 \otimes \mathbf{R}_k, \tag{3.35}$$

$$\mathbf{R}^{\text{BS-U}}_{k} = \zeta^{\text{BS-U}}_{kgu}(\chi^{\text{BS-U}} + 1)\mathbf{I}_2 \otimes \mathbf{R}_k, \tag{3.36}$$

where $\mathbf{R}_k$ represents the spatial correlation matrix for each polarization, with a rank denoted by r_k. Note that, with the models in (3.35) and (3.36), it is assumed that the links BS-U and BS-IRS share the same correlation matrices. Such a condition is achievable when users and IRSs are irradiated by identical scattering clusters, which is a reasonable assumption in Publication [III], given that IRSs and connected users are close by in the implemented communication model.

By applying the Karhunen–Loeve decomposition to (3.34), the full channel for the uth user in the gth group in the kth cluster can be restructured as

$$\begin{aligned}
\mathbf{H}^{H}_{kgu} &= \begin{bmatrix} \mathbf{S}^{vv}_{kgu} & \mathbf{0}_{L,\frac{N}{2}} \\ \mathbf{0}_{L,\frac{N}{2}} & \mathbf{S}^{hh}_{kgu} \end{bmatrix}^{H} \begin{bmatrix} \mathbf{\Phi}^{vv}_{kgu} & \mathbf{\Phi}^{hv}_{kgu} \\ \mathbf{\Phi}^{vh}_{kgu} & \mathbf{\Phi}^{hh}_{kgu} \end{bmatrix} \begin{bmatrix} \mathbf{G}^{vv}_{kgu} & \mathbf{G}^{hv}_{kgu} \\ \mathbf{G}^{vh}_{kgu} & \mathbf{G}^{hh}_{kgu} \end{bmatrix} \left(\mathbf{I}_2 \otimes \left(\mathbf{\Lambda}^{\frac{1}{2}}_{k} \mathbf{U}^{H}_{k}\right)\right) \\
&\quad + \begin{bmatrix} \mathbf{D}^{vv}_{kgu} & \mathbf{D}^{vh}_{kgu} \\ \mathbf{D}^{hv}_{kgu} & \mathbf{D}^{hh}_{kgu} \end{bmatrix}^{H} \left(\mathbf{I}_2 \otimes \left(\mathbf{\Lambda}^{\frac{1}{2}}_{k} \mathbf{U}^{H}_{k}\right)\right) \\
&= \left(\mathbf{S}^{H}_{kgu} \mathbf{\Theta}_{kgu} \mathbf{G}_{kgu} + \mathbf{D}^{H}_{kgu}\right) \left(\mathbf{I}_2 \otimes \left(\mathbf{\Lambda}^{\frac{1}{2}}_{k} \mathbf{U}^{H}_{k}\right)\right),
\end{aligned} \tag{3.37}$$

where the matrices $\boldsymbol{\Lambda}_k \in \mathbb{R}_{>0}^{r_k^\star \times r_k^\star}$, and $\mathbf{U}_k \in \mathbb{C}^{\frac{M}{2} \times r_k^\star}$ are defined similarly as in (2.4), with $\boldsymbol{\Lambda}_k$ collecting the $r_k^\star$ nonzero eigenvalues of $\mathbf{R}_k$, and $\mathbf{U}_k$ the corresponding dominant eigenvectors. In turn, $\mathbf{S}_{kgu}^{ab} \in \mathbb{C}^{L \times \frac{N}{2}}$, $\mathbf{D}_{kgu}^{ab} \in \mathbb{C}^{r_k^\star \times \frac{N}{2}}$ and $\mathbf{G}_{kgu}^{ab} \in \mathbb{C}^{L \times r_k^\star}$ denote the full rank fast-fading channel matrices for the links IRS-U, BS-U, and BS-IRS, respectively, from the polarization a to b, in which $a, b \in \{v, h\}$, with entries following the complex Gaussian distribution with zero mean and unit variance. For the sake of simplicity, the normalization factor, path-loss, and iXPD have been incorporated into the channel matrices. Thus, from now on, these coefficients are omitted. As a result, after the transmitted data streams have traveled through both direct and reflected propagation links, the uth user in the gth group in the kth cluster receives the following signal

$$\begin{aligned} \mathbf{y}_{kgu} = {} & \left(\mathbf{S}_{kgu}^{H} \boldsymbol{\Theta}_{kgu} \mathbf{G}_{kgu} + \mathbf{D}_{kgu}^{H}\right) \left(\mathbf{I}_2 \otimes \left(\boldsymbol{\Lambda}_k^{\frac{1}{2}} \mathbf{U}_k^{H}\right)\right) \\ & \times \sum_{q=1}^{K} \mathbf{B}_q \sum_{m=1}^{G} \sum_{n=1}^{U} \mathbf{v}_{qmn} \sqrt{\alpha_{qmn}} x_{qmn} + \begin{bmatrix} \mathbf{n}_{kgu}^{v} \\ \mathbf{n}_{kgu}^{h} \end{bmatrix} \in \mathbb{C}^{N}, \end{aligned} \tag{3.38}$$

where $\mathbf{n}_{kgu}^{a} \in \mathbb{C}^{\frac{N}{2}}$ is the noise vector achieved in the polarization $a \in \{v, h\}$, with zero mean complex Gaussian distributed entries and variance σ^2.

3.3.4 Precoding, IRS Optimization, and Reception Matrices

Polarization Assignment and Formation of Subsets

This subsection explains the strategy proposed for creating and multiplexing the subset of users in the polarization domain as well as the design of the precoder $\mathbf{v}_{kgu}$. As the first step executed at the BS, the users within each group are sorted in an ascending order based on the path-loss coefficients of the direct link BS-U, i.e., $\zeta_{kg1}^{\text{BS-U}} < \zeta_{kg2}^{\text{BS-U}} < \cdots < \zeta_{kgU}^{\text{BS-U}}$. Next, based on the ordered list of users, and supposing that U is even, the users with odd indices are assigned to vertically polarized antennas, and the users with even indices to horizontally polarized antennas. As the output, the BS achieves two disjoint polarization subsets: $\mathcal{U}^v = \{1, 3, \cdots, U-1\}$, with $U^v = U/2$ users, defined as the vertical subset, and $\mathcal{U}^h = \{2, 4, \cdots, U\}$, with $U^h = U - U^v = U/2$ users, defined as the horizontal subset. Last, in order to transmit the superimposed data symbols for users in their corresponding polarization subsets, the BS implements the following precoder

$$\mathbf{v}_{kgu} = \begin{bmatrix} \mathbf{v}_{kgu}^{v} \\ \mathbf{v}_{kgu}^{h} \end{bmatrix} = \begin{bmatrix} \left[\mathbf{0}_{1,g-1}, \mathbf{1}_{\mathcal{U}^v}(u), \mathbf{0}_{1,\frac{\bar{M}}{2}-g}\right]^T \\ \left[\mathbf{0}_{1,g-1}, \mathbf{1}_{\mathcal{U}^h}(u), \mathbf{0}_{1,\frac{\bar{M}}{2}-g}\right]^T \end{bmatrix}, \tag{3.39}$$

where $\mathbf{1}_{\mathcal{A}}(i)$ is the indicator function of a subset $\mathcal{A}$, which is defined by

$$\mathbf{1}_{\mathcal{A}}(i) = \begin{cases} 1 & \text{if} \quad i \in \mathcal{A}, \\ 0 & \text{if} \quad i \notin \mathcal{A}. \end{cases} \tag{3.40}$$

Because of the dimension of the precoding vector $\mathbf{v}_{kgu}$, $G \leq \bar{M}/2$ must be satisfied.

IRS Optimization

By relying on the effectiveness of the precoders $\mathbf{B}_k$, it is assumed from this point onward that the intercluster interference has been perfectly eliminated. As a result, by focusing on the first cluster, the cluster subscript is omitted and (3.38) is expanded as follows

$$\begin{aligned}
\mathbf{y}_{gu} = &\left(\begin{bmatrix} \left[(\mathbf{S}_{gu}^{vv})^H \boldsymbol{\Phi}_{gu}^{vv} \mathbf{G}_{gu}^{vv} + (\mathbf{S}_{gu}^{vv})^H \boldsymbol{\Phi}_{gu}^{hv} \mathbf{G}_{gu}^{vh}\right] & \left[(\mathbf{S}_{gu}^{vv})^H \boldsymbol{\Phi}_{gu}^{vv} \mathbf{G}_{gu}^{hv} + (\mathbf{S}_{gu}^{vv})^H \boldsymbol{\Phi}_{gu}^{hv} \mathbf{G}_{gu}^{hh}\right] \\ \left[(\mathbf{S}_{gu}^{hh})^H \boldsymbol{\Phi}_{gu}^{vh} \mathbf{G}_{gu}^{vv} + (\mathbf{S}_{gu}^{hh})^H \boldsymbol{\Phi}_{gu}^{hh} \mathbf{G}_{gu}^{vh}\right] & \left[(\mathbf{S}_{gu}^{hh})^H \boldsymbol{\Phi}_{gu}^{vh} \mathbf{G}_{gu}^{hv} + (\mathbf{S}_{gu}^{hh})^H \boldsymbol{\Phi}_{gu}^{hh} \mathbf{G}_{gu}^{hh}\right] \end{bmatrix} \right. \\
&\left. + \begin{bmatrix} (\mathbf{D}_{gu}^{vv})^H & (\mathbf{D}_{gu}^{hv})^H \\ (\mathbf{D}_{gu}^{vh})^H & (\mathbf{D}_{gu}^{hh})^H \end{bmatrix} \right) \begin{bmatrix} \boldsymbol{\Lambda}^{\frac{1}{2}} \mathbf{U}^H \tilde{\mathbf{B}} & \mathbf{0}_{r_k^\star, \frac{\bar{M}}{2}} \\ \mathbf{0}_{r_k^\star, \frac{\bar{M}}{2}} & \boldsymbol{\Lambda}^{\frac{1}{2}} \mathbf{U}^H \tilde{\mathbf{B}} \end{bmatrix} \\
&\times \sum_{m=1}^{G} \sum_{n=1}^{U} \begin{bmatrix} \mathbf{v}_{mn}^v \\ \mathbf{v}_{mn}^h \end{bmatrix} \sqrt{\alpha_{mn}} x_{mn} + \begin{bmatrix} \mathbf{n}_{gu}^v \\ \mathbf{n}_{gu}^h \end{bmatrix}.
\end{aligned} \tag{3.41}$$

It can be seen that the data streams transmitted from vertically polarized antennas at the BS, indented for vertical subsets, propagate through the left channel blocks in (3.41), whereas transmissions from horizontally polarized BS antennas, intended for horizontal subsets, propagate via the right channel blocks. This implies that the IRSs for the users within vertical subsets should be configured to eliminate the right blocks, and the IRSs for the users within horizontal subsets should cancel out the left channel blocks. To this end, optimization problems should be formulated so that, for the users within vertical subsets, we can achieve:

$$\begin{bmatrix} (\mathbf{S}_{gu}^{vv})^H \boldsymbol{\Phi}_{gu}^{vv} \mathbf{G}_{gu}^{hv} + (\mathbf{S}_{gu}^{vv})^H \boldsymbol{\Phi}_{gu}^{hv} \mathbf{G}_{gu}^{hh} \\ (\mathbf{S}_{gu}^{hh})^H \boldsymbol{\Phi}_{gu}^{vh} \mathbf{G}_{gu}^{hv} + (\mathbf{S}_{gu}^{hh})^H \boldsymbol{\Phi}_{gu}^{hh} \mathbf{G}_{gu}^{hh} \end{bmatrix} + \begin{bmatrix} (\mathbf{D}_{gu}^{hv})^H \\ (\mathbf{D}_{gu}^{hh})^H \end{bmatrix} \approx \begin{bmatrix} \mathbf{0}_{\frac{N}{2}, r_k^\star} \\ \mathbf{0}_{\frac{N}{2}, r_k^\star} \end{bmatrix}, \tag{3.42}$$

and in users within horizontal subsets:

$$\begin{bmatrix} (\mathbf{S}_{gu}^{vv})^H \boldsymbol{\Phi}_{gu}^{vv} \mathbf{G}_{gu}^{vv} + (\mathbf{S}_{gu}^{vv})^H \boldsymbol{\Phi}_{gu}^{hv} \mathbf{G}_{gu}^{vh} \\ (\mathbf{S}_{gu}^{hh})^H \boldsymbol{\Phi}_{gu}^{vh} \mathbf{G}_{gu}^{vv} + (\mathbf{S}_{gu}^{hh})^H \boldsymbol{\Phi}_{gu}^{hh} \mathbf{G}_{gu}^{vh} \end{bmatrix} + \begin{bmatrix} (\mathbf{D}_{gu}^{vv})^H \\ (\mathbf{D}_{gu}^{vh})^H \end{bmatrix} \approx \begin{bmatrix} \mathbf{0}_{\frac{N}{2}, r_k^\star} \\ \mathbf{0}_{\frac{N}{2}, r_k^\star} \end{bmatrix}. \tag{3.43}$$

For accomplishing the above goals, the IRSs from both vertical and horizontal subsets should be configured similarly, that is, the reflecting elements of the IRSs must be optimized aiming at eliminating cross-polar and co-polar interfering transmissions. Because of the similar objectives, without loss of generality, the optimization problem is next formulated only for IRSs within vertical subsets. More specifically, the goal in (3.42) can be achieved by solving the following problem

$$\min_{\substack{\boldsymbol{\Phi}_{gu}^{vv},\boldsymbol{\Phi}_{gu}^{vh},\\ \boldsymbol{\Phi}_{gu}^{hv},\boldsymbol{\Phi}_{gu}^{hh}}} \left\| \begin{bmatrix} (\mathbf{S}_{gu}^{vv})^H \boldsymbol{\Phi}_{gu}^{vv} \mathbf{G}_{gu}^{hv} \\ (\mathbf{S}_{gu}^{hh})^H \boldsymbol{\Phi}_{gu}^{vh} \mathbf{G}_{gu}^{hv} \end{bmatrix} + \begin{bmatrix} (\mathbf{S}_{gu}^{vv})^H \boldsymbol{\Phi}_{gu}^{hv} \mathbf{G}_{gu}^{hh} \\ (\mathbf{S}_{gu}^{hh})^H \boldsymbol{\Phi}_{gu}^{hh} \mathbf{G}_{gu}^{hh} \end{bmatrix} + \begin{bmatrix} (\mathbf{D}_{gu}^{hv})^H \\ (\mathbf{D}_{gu}^{hh})^H \end{bmatrix} \right\|^2 \tag{3.44a}$$

$$\text{s.t. } |\omega_{gu,l}^{ab}|^2 \leq 1, \ \ \forall l \in [1, L], \forall a, b \in \{v, h\}, \tag{3.44b}$$

$$\boldsymbol{\Phi}_{gu}^{vv}, \boldsymbol{\Phi}_{gu}^{vh}, \boldsymbol{\Phi}_{gu}^{hv}, \boldsymbol{\Phi}_{gu}^{hh} \text{ diagonal.} \tag{3.44c}$$

where the constraint in (3.44b) ensures passive reflections. The problem in (3.44) consists of a generalized least squares problem for matrix equations, in which some results have been provided in [89] for simpler cases. However, because of the elementwise quadratic constraint in (3.44b), and the constraint for diagonal matrices in (3.44c), solving (3.44) with its original formulation becomes highly complicated. To overcome this mathematical challenge, a series of transformations are applied and simplified (3.44) into equivalent convex problems. In short, the Khatri–Rao identity $(\mathbf{C}^T \odot \mathbf{A})\text{vecd}\{\mathbf{B}\} = \text{vec}\{\mathbf{ABC}\}$ [1] is used to define:

$$\boldsymbol{\theta}_{gu}^{ab} = \text{vecd}\{\boldsymbol{\Phi}_{gu}^{ab}\} \in \mathbb{C}^{L}, \tag{3.45}$$

$$\mathbf{d}_{gu}^{hv} = \text{vec}\left\{(\mathbf{D}_{gu}^{hv})^H\right\} \in \mathbb{C}^{\frac{N}{2} r_k^\star}, \tag{3.46}$$

$$\mathbf{d}_{gu}^{hh} = \text{vec}\left\{(\mathbf{D}_{gu}^{hh})^H\right\} \in \mathbb{C}^{\frac{N}{2} r_k^\star}, \tag{3.47}$$

$$\mathbf{K}_{gu}^{hv,vv} = [(\mathbf{G}_{gu}^{hv})^T \odot (\mathbf{S}_{gu}^{vv})^H] \in \mathbb{C}^{\frac{N}{2} r_k^\star \times L}, \tag{3.48}$$

$$\mathbf{K}_{gu}^{hh,vv} = [(\mathbf{G}_{gu}^{hh})^T \odot (\mathbf{S}_{gu}^{vv})^H] \in \mathbb{C}^{\frac{N}{2} r_k^\star \times L}, \tag{3.49}$$

$$\mathbf{K}_{gu}^{hv,hh} = [(\mathbf{G}_{gu}^{hv})^T \odot (\mathbf{S}_{gu}^{hh})^H] \in \mathbb{C}^{\frac{N}{2} r_k^\star \times L}, \tag{3.50}$$

$$\mathbf{K}_{gu}^{hh,hh} = [(\mathbf{G}_{gu}^{hh})^T \odot (\mathbf{S}_{gu}^{hh})^H] \in \mathbb{C}^{\frac{N}{2} r_k^\star \times L}. \tag{3.51}$$

Then, after some simplifications and expansions, the original problem in (3.44) is transformed into the following two subproblems

$$\min_{\boldsymbol{\theta}_{gu}^{vv},\boldsymbol{\theta}_{gu}^{hv}} \left\{ \begin{bmatrix} \boldsymbol{\theta}_{gu}^{vv} \\ \boldsymbol{\theta}_{gu}^{hv} \end{bmatrix}^H \bar{\mathbf{C}}_{gu} \begin{bmatrix} \boldsymbol{\theta}_{gu}^{vv} \\ \boldsymbol{\theta}_{gu}^{hv} \end{bmatrix} + 2\Re \left\{ (\mathbf{d}_{gu}^{hv})^H \bar{\mathbf{K}}_{gu} \begin{bmatrix} \boldsymbol{\theta}_{gu}^{vv} \\ \boldsymbol{\theta}_{gu}^{hv} \end{bmatrix} \right\} + (\mathbf{d}_{gu}^{hv})^H \mathbf{d}_{gu}^{hv} \right\} \tag{3.52a}$$

$$\text{s.t. } \begin{bmatrix} \boldsymbol{\theta}_{gu}^{vv} \\ \boldsymbol{\theta}_{gu}^{hv} \end{bmatrix}^H \mathbf{B}_l \begin{bmatrix} \boldsymbol{\theta}_{gu}^{vv} \\ \boldsymbol{\theta}_{gu}^{hv} \end{bmatrix} \leq 1, \tag{3.52b}$$

$$\min_{\boldsymbol{\theta}_{gu}^{vh},\boldsymbol{\theta}_{gu}^{hh}} \left\{ \begin{bmatrix} \boldsymbol{\theta}_{gu}^{vh} \\ \boldsymbol{\theta}_{gu}^{hh} \end{bmatrix}^H \tilde{\mathbf{C}}_{gu} \begin{bmatrix} \boldsymbol{\theta}_{gu}^{vh} \\ \boldsymbol{\theta}_{gu}^{hh} \end{bmatrix} + 2\Re\left\{ (\mathbf{d}_{gu}^{hh})^H \tilde{\mathbf{K}}_{gu} \begin{bmatrix} \boldsymbol{\theta}_{gu}^{vh} \\ \boldsymbol{\theta}_{gu}^{hh} \end{bmatrix} \right\} + (\mathbf{d}_{gu}^{hh})^H \mathbf{d}_{gu}^{hh} \right\} \tag{3.53a}$$

$$\text{s.t.} \quad \begin{bmatrix} \boldsymbol{\theta}_{gu}^{vh} \\ \boldsymbol{\theta}_{gu}^{hh} \end{bmatrix}^H \mathbf{B}_l \begin{bmatrix} \boldsymbol{\theta}_{gu}^{vh} \\ \boldsymbol{\theta}_{gu}^{hh} \end{bmatrix} \leq 1. \tag{3.53b}$$

where $\mathbf{B}_l = \operatorname{diag}\{\mathbf{e}_l\}, l = 1, \cdots, L$, in which $\mathbf{e}_l$ represents the standard basis vector computed as

$$\mathbf{e}_l = [\, \mathbf{0}_{1,(l-1)} \;,\; 1 \;,\; \mathbf{0}_{1,(L-l)} \,]^T, \quad l = 1, \cdots, L, \tag{3.54}$$

and the following have been defined:

$$\bar{\mathbf{K}}_{gu} = \begin{bmatrix} \mathbf{K}_{gu}^{hv,vv} & \mathbf{K}_{gu}^{hh,vv} \end{bmatrix}, \tag{3.55}$$

$$\tilde{\mathbf{K}}_{gu} = \begin{bmatrix} \mathbf{K}_{gu}^{hv,hh} & \mathbf{K}_{gu}^{hh,hh} \end{bmatrix}, \tag{3.56}$$

$$\bar{\mathbf{C}}_{gu} = \bar{\mathbf{K}}_{gu}^H \bar{\mathbf{K}}_{gu}, \tag{3.57}$$

$$\tilde{\mathbf{C}}_{gu} = \tilde{\mathbf{K}}_{gu}^H \tilde{\mathbf{K}}_{gu}. \tag{3.58}$$

It can be checked that the problems in (3.52) and (3.53) consist of quadratically constrained quadratic problems. Due to the fact that the entries of the matrices $\bar{\mathbf{K}}_{gu}$ and $\tilde{\mathbf{K}}_{gu}$ are independent and identically distributed complex Gaussian random variables, the matrices $\bar{\mathbf{C}}_{gu}$ and $\tilde{\mathbf{C}}_{gu}$ will be positive semidefinite matrices almost surely. In addition, given that $\mathbf{z}^H \mathbf{B}_l \mathbf{z} = |[\mathbf{z}]_l|^2 \geq 0, \forall \mathbf{z} \in \mathbb{C}^L$, $\mathbf{B}_l$ is also a positive semidefinite matrix. These properties confirm that (3.52) and (3.53) are convex optimization problems. As result, their global optimal solutions exist and can be computed through interior-point methods iteratively in polynomial time [90]. Specifically, by representing the vector solutions of problems (3.52) and (3.53) by $\dot{\boldsymbol{\theta}}_{gu}^{ab}$, the diagonal matrices with the optimal set of reflection coefficients that minimize (3.44) are computed by $\boldsymbol{\Phi}_{gu}^{ab} = \operatorname{diag}\left\{\dot{\boldsymbol{\theta}}_{gu}^{ab}\right\}, \forall a, b \in \{v, h\}$.

Signal Reception

For notation simplicity, the channels of the links BS-U, BS-IRS, and IRS-U are absorbed into a single matrix, which allows us to simplify (3.37) into the following compact channel representation

$$\mathbf{H}_{gu}^H = \begin{bmatrix} \tilde{\mathbf{H}}_{gu}^{vv} & \tilde{\mathbf{H}}_{gu}^{vh} \\ \tilde{\mathbf{H}}_{gu}^{hv} & \tilde{\mathbf{H}}_{gu}^{hh} \end{bmatrix}^H, \tag{3.59}$$

where $\tilde{\mathbf{H}}_{gu}^{ab}$ comprises the effective channel coefficients resulting from the superposition of transmissions propagating via direct and reflected links from the polarization a at the BS to the polarization b on the users' side, in which $a, b \in \{v, h\}$. To exemplify, the channel matrix comprising effective vertical-to-vertical channel coefficients is computed by $\tilde{\mathbf{H}}_{gu}^{vv} = \mathbf{U}_k \mathbf{\Lambda}_k^{\frac{1}{2}} \left[(\mathbf{S}_{gu}^{vv})^H \mathbf{\Phi}_{gu}^{vv} \mathbf{G}_{gu}^{vv} + (\mathbf{S}_{gu}^{vv})^H \mathbf{\Phi}_{gu}^{hv} \mathbf{G}_{gu}^{vh} \right]^H + \mathbf{U}_k \mathbf{\Lambda}_k^{\frac{1}{2}} \mathbf{D}_{gu}^{vv}$. By using this simplified notation, the signal in (3.41) can be rewritten as

$$\mathbf{y}_{gu} = \begin{bmatrix} (\tilde{\mathbf{H}}_{gu}^{vv})^H \tilde{\mathbf{B}} & (\tilde{\mathbf{H}}_{gu}^{hv})^H \tilde{\mathbf{B}} \\ (\tilde{\mathbf{H}}_{gu}^{vh})^H \tilde{\mathbf{B}} & (\tilde{\mathbf{H}}_{gu}^{hh})^H \tilde{\mathbf{B}} \end{bmatrix} \sum_{m=1}^{G} \sum_{n=1}^{U} \begin{bmatrix} \mathbf{v}_{mn}^{v} \\ \mathbf{v}_{mn}^{h} \end{bmatrix} \sqrt{\alpha_{mn}} x_{mn} + \begin{bmatrix} \mathbf{n}_{gu}^{v} \\ \mathbf{n}_{gu}^{h} \end{bmatrix}. \tag{3.60}$$

To explain the employed detection strategy, in this subsection, the focus continues to be on the vertical subsets. Recall that the IRSs of users in vertical subsets are configured to cancel transmissions from horizontally polarized BS antennas. By knowing this, we rely on the IRSs to address interference between subsets of different polarizations and design our detection matrices to cancel the remaining interference between subsets assigned to the same polarization. To this end, the users in vertical subsets exploit the left blocks of the channel matrix in (3.60) to build the desired detection matrix, as follows

$$\mathbf{H}_{gu}^{\dagger} = \begin{bmatrix} \mathbf{H}_{gu}^{\dagger v} & \mathbf{0}_{\frac{\bar{M}}{2}, \frac{N}{2}} \\ \mathbf{0}_{\frac{\bar{M}}{2}, \frac{N}{2}} & \mathbf{H}_{gu}^{\dagger h} \end{bmatrix} = \begin{bmatrix} [(\underline{\mathbf{H}}_{gu}^{vv})^H \underline{\mathbf{H}}_{gu}^{vv}]^{-1} (\underline{\mathbf{H}}_{gu}^{vv})^H & \mathbf{0}_{\frac{\bar{M}}{2}, \frac{N}{2}} \\ \mathbf{0}_{\frac{\bar{M}}{2}, \frac{N}{2}} & [(\underline{\mathbf{H}}_{gu}^{vh})^H \underline{\mathbf{H}}_{gu}^{vh}]^{-1} (\underline{\mathbf{H}}_{gu}^{vh})^H \end{bmatrix}, \tag{3.61}$$

where $\underline{\mathbf{H}}_{gu}^{vv} = (\tilde{\mathbf{H}}_{gu}^{vv})^H \tilde{\mathbf{B}}$ and $\underline{\mathbf{H}}_{gu}^{vh} = (\tilde{\mathbf{H}}_{gu}^{vh})^H \tilde{\mathbf{B}}$ denote the virtual channels for the uth user in the gth vertical subset, with $\mathbf{H}_{gu}^{\dagger a}$ representing left Moore–Penrose pseudoinverse for the polarization a, such that $N \geq \bar{M}$ must be satisfied. By filtering the signal in (3.60) with $\mathbf{H}_{gu}^{\dagger}$, the uth user in the gth vertical subset recovers the following vector

$$\hat{\mathbf{x}}_{gu} = \begin{bmatrix} \hat{\mathbf{x}}_{gu}^{v} \\ \hat{\mathbf{x}}_{gu}^{h} \end{bmatrix} = \begin{bmatrix} \mathbf{x}^v + \mathbf{H}_{gu}^{\dagger v} \underline{\mathbf{H}}_{gu}^{hv} \mathbf{x}^h \\ \mathbf{x}^v + \mathbf{H}_{gu}^{\dagger h} \underline{\mathbf{H}}_{gu}^{hh} \mathbf{x}^h \end{bmatrix} + \begin{bmatrix} \mathbf{H}_{gu}^{\dagger v} \mathbf{n}_{gu}^{v} \\ \mathbf{H}_{gu}^{\dagger h} \mathbf{n}_{gu}^{h} \end{bmatrix}, \tag{3.62}$$

with $\mathbf{x}^v$ obtained as

$$\mathbf{x}^v = \begin{bmatrix} \sum_{n \in \mathcal{U}^v} \sqrt{\alpha_{1n}} x_{1n} \\ \vdots \\ \sum_{n \in \mathcal{U}^v} \sqrt{\alpha_{Gn}} x_{Gn} \end{bmatrix}. \tag{3.63}$$

As can be seen in (3.62), as a result of our transmission and detection strategies, the users are able to recover in both polarization replicas of their intended superimposed data symbols, which have been transmitted from the vertically polarized antennas of the BS. More specifically, the users within the gth vertical subset can recover their transmitted messages by executing SIC on the gth element of either $\hat{\mathbf{x}}_{gu}^{v}$ or $\hat{\mathbf{x}}_{gu}^{h}$, which allows users to exploit diversity. In particular, users are configured to retrieve their symbol from the polarization with the highest effective channel gain, which is represented as the polarization $\ddot{a}$. With this approach, before executing SIC, the uth user in the gth vertical subset will achieve

$$[\hat{\mathbf{x}}^{\ddot{a}}_{gu}]_g = \sum_{n\in\mathcal{U}^v} \sqrt{\alpha_{gn}}x_{gn} + [\mathbf{H}^{\dagger\ddot{a}}_{gu}\underline{\mathbf{H}}^{h\ddot{a}}_{gu}\mathbf{x}^h]_g + [\mathbf{H}^{\dagger\ddot{a}}_{gu}\mathbf{n}^{\ddot{a}}_{gu}]_g. \tag{3.64}$$

The same strategy is implemented for the users in the horizontal subsets. However, in contrast to the detection matrices for vertical subsets, $\mathbf{H}^{\dagger}_{gu}$ is built by exploiting the right blocks of the effective channel matrix in (3.60).

Now that the main details of our proposed IRS-MIMO-NOMA scheme have been explained, we are ready to dive into the main results provided in Publication [III], starting with the primary outcomes of our theoretical studies in the next subsection.

3.3.5 Performance Analysis

To start our contributions in this section, first, all sources of interference are modeled, including the standard interference from the SIC decoding process, error propagation resulting from imperfect SIC, and polarization interference, and an expression is determined for the SINR experienced by users. Then, through a thorough statistical characterization, the asymptotic distributions are derived for the SINR effective gains in the regime where $L \to \infty$. Finally, based on the determined PDFs, a closed-form expression for the users' asymptotic ergodic rate is derived.

SINR Analysis

In order to finally retrieve the indented individual messages, each user carries out SIC on the detected superimposed data symbol in (3.64). More specifically, as a result of the scheme proposed for the formation of subsets presented in Subsection 3.3.4, the users in vertical subsets are ordered as $\zeta^{\text{BS-U}}_{kg1} < \zeta^{\text{BS-U}}_{kg3} < \cdots < \zeta^{\text{BS-U}}_{kg(U-1)}$, and in horizontal subsets as $\zeta^{\text{BS-U}}_{kg2} < \zeta^{\text{BS-U}}_{kg4} < \cdots < \zeta^{\text{BS-U}}_{kgU}$. Then, the uth user within the subset $\mathcal{U}^a$, with $a \in \{v, h\}$, first decodes the symbol intended for the mth lower order user, $\forall m < u,\, m \in \mathcal{U}^a$, while considering symbols intended for the nth higher order user as interference, $\forall n > u, n \in \mathcal{U}^a$. Because of practical issues, it is assumed that SIC cannot be carried out perfectly, which implies that the uth user also experiences residual interference from the users $m < u$, following the imperfect SIC model proposed in Publication [I]. Consequently, at the end of the SIC process, the uth user in the gth group in the subset $\mathcal{U}^a$, recovers the following corrupted data symbol

$$\begin{aligned}\hat{x}_{gu} = {} & \underbrace{\sqrt{\alpha_{gu}}x_{gu}}_{\text{Desired symbol}} + \underbrace{\sum_{m\in\{i|\,i>u,\,i\in\mathcal{U}^a\}} \sqrt{\alpha_{gm}}x_{gm}}_{\text{Interference of stronger users}} + \underbrace{\sqrt{\xi}\sum_{n\in\{j|\,j<u,\,j\in\mathcal{U}^a\}} \sqrt{\alpha_{gn}}x_{gn}}_{\text{Residual SIC interference}} \\ & + \underbrace{[\mathbf{H}^{\dagger\ddot{a}}_{gu}\underline{\mathbf{H}}^{t\ddot{a}}_{gu}\mathbf{x}^t]_g}_{\text{Polarization interference}} + \underbrace{[\mathbf{H}^{\dagger\ddot{a}}_{gu}\mathbf{n}^{\ddot{a}}_{gu}]_g}_{\text{Noise}},\end{aligned} \tag{3.65}$$

where $\xi \in [0,1]$ denotes the error factor that models imperfect SIC, and t informs the polarization that causes interference, which is computed as $t = h$, if $u \in \mathcal{U}^v$, or $t = v$, if $u \in \mathcal{U}^h$. The SINR experienced by users within each subset is derived in the following lemma.

Lemma 3.2: Under the proposed IRS-MIMO-NOMA scheme, when the uth user in the gth group within the subset $\mathcal{U}^a$ detects the symbol intended for the ith user, $\forall i \leq u$, $i \in \mathcal{U}^a$, it observes the following SINR

$$\gamma_{gu}^{i} = \frac{\rho \ddot{\hslash}_{gu} \alpha_{gi}}{\rho \ddot{\hslash}_{gu} \mathfrak{I}_{gi} + \rho \ddot{\hslash}_{gu} \mathfrak{X}_{gu} + 1}, \tag{3.66}$$

where $\rho = 1/\sigma^2$ is the SNR, $\ddot{\hslash}_{gu} = \max\{\hslash_{gu}^{v}, \hslash_{gu}^{h}\}$ denotes the effective channel gain, with $\hslash_{gu}^{a} = [1/\mathbf{H}_{gu}^{\dagger a}(\mathbf{H}_{gu}^{\dagger a})^H]_{g,g}$ corresponding to the gain achieved in polarization $a \in \{v,h\}$, the term $\mathfrak{X}_{gu} = \left|[\mathbf{H}_{gu}^{\dagger \ddot{a}} \underline{\mathbf{H}}_{gu}^{t\ddot{a}} \mathbf{x}^{t}]_g\right|^2$ accounts for the polarization interference not canceled by the IRS, so that if $u \in \mathcal{U}^v$, $t = h$, and if $u \in \mathcal{U}^h$, $t = v$. In turn, $\mathfrak{I}_{gi}$ is the total interference resulting from the SIC process, which is defined by

$$\mathfrak{I}_{gi} = \begin{cases} \sum_{m=i+1}^{\max\{\mathcal{U}^a\}} \alpha_{gm}, & \text{if } i = \min\{\mathcal{U}^a\}, \\ \sum_{m=i+1}^{\max\{\mathcal{U}^a\}} \alpha_{gm} + \xi \sum_{n=\min\{\mathcal{U}^a\}}^{i-1} \alpha_{gn}, & \text{if } \min\{\mathcal{U}^a\} < i \leq u < \max\{\mathcal{U}^a\}, \\ \xi \sum_{n=1}^{i-1} \alpha_{gn}, & \text{if } i = u = \max\{\mathcal{U}^a\}, \end{cases} \tag{3.67}$$

Proof: The reader is referred to Appendix A in Publication [III]. ■

Statistical Characterization of Channel Gains

This subsection presents the statistical characterization performed for the SINR interference and channel gains. To this end, the focus is on the gains for the uth in the gth group assigned to the vertical subset, i.e., $\ddot{\hslash}_{gu} = \max\{1/[\mathbf{H}_{gu}^{\dagger v}(\mathbf{H}_{gu}^{\dagger v})^H]_{g,g}, 1/[\mathbf{H}_{gu}^{\dagger h}(\mathbf{H}_{gu}^{\dagger h})^H]_{g,g}\}$ and $\mathfrak{X}_{gu} = \left|[\mathbf{H}_{gu}^{\dagger \ddot{a}} \underline{\mathbf{H}}_{gu}^{t\ddot{a}} \mathbf{x}^{h}]_g\right|^2$. First, the matrices in $[\mathbf{H}_{gu}^{\dagger v}(\mathbf{H}_{gu}^{\dagger v})^H]_{g,g}$ are expanded as follows

$$\begin{aligned} \mathbf{H}_{gu}^{\dagger v}(\mathbf{H}_{gu}^{\dagger v})^H &= [\tilde{\mathbf{B}}^H \tilde{\mathbf{H}}_{gu}^{vv} (\tilde{\mathbf{H}}_{gu}^{vv})^H \tilde{\mathbf{B}}]^{-1} \\ &= \Big(\tilde{\mathbf{B}}^H \mathbf{U} \mathbf{\Lambda}^{\frac{1}{2}} (\mathbf{G}_{gu}^{vv})^H (\mathbf{\Phi}_{gu}^{vv})^H \mathbf{S}_{gu}^{vv} (\mathbf{S}_{gu}^{vv})^H \mathbf{\Phi}_{gu}^{vv} \mathbf{G}_{gu}^{vv} \mathbf{\Lambda}^{\frac{1}{2}} \mathbf{U}^H \tilde{\mathbf{B}} \\ &+ \tilde{\mathbf{B}}^H \mathbf{U} \mathbf{\Lambda}^{\frac{1}{2}} (\mathbf{G}_{gu}^{vh})^H (\mathbf{\Phi}_{gu}^{hv})^H \mathbf{S}_{gu}^{vv} (\mathbf{S}_{gu}^{vv})^H \mathbf{\Phi}_{gu}^{hv} \mathbf{G}_{gu}^{vh} \mathbf{\Lambda}^{\frac{1}{2}} \mathbf{U}^H \tilde{\mathbf{B}} \\ &+ \tilde{\mathbf{B}}^H \mathbf{U} \mathbf{\Lambda}^{\frac{1}{2}} \mathbf{D}_{gu}^{vv} (\mathbf{D}_{gu}^{vv})^H \mathbf{\Lambda}^{\frac{1}{2}} \mathbf{U}^H \tilde{\mathbf{B}} \Big)^{-1}. \end{aligned} \tag{3.68}$$

Because S_{gu}^{pq} is full rank, its covariance matrix is the identity matrix, i.e., $\mathrm{E}\{\mathbf{S}_{gu}^{vv}(\mathbf{S}_{gu}^{vv})^H\} =$

$\zeta_{gu}^{\text{IRS-U}}\mathbf{I}_{L,L}$. With this property, and recalling (3.34), (3.68) can be simplified as follows

$$\begin{aligned}\mathbf{H}_{gu}^{\dagger v}(\mathbf{H}_{gu}^{\dagger v})^{H} = \Big(&\frac{1}{2}\zeta_{gu}^{\text{BS-IRS}}\zeta_{gu}^{\text{IRS-U}}\tilde{\mathbf{B}}^{H}(\bar{\mathbf{G}}_{gu}^{vv})^{H}(\mathbf{\Phi}_{gu}^{vv})^{H}\mathbf{\Phi}_{gu}^{vv}\bar{\mathbf{G}}_{gu}^{vv}\tilde{\mathbf{B}}\\ &+\frac{1}{2}\zeta_{gu}^{\text{BS-IRS}}\zeta_{gu}^{\text{IRS-U}}\tilde{\mathbf{B}}^{H}(\bar{\mathbf{G}}_{gu}^{vh})^{H}(\mathbf{\Phi}_{gu}^{hv})^{H}\mathbf{\Phi}_{gu}^{hv}\bar{\mathbf{G}}_{gu}^{vh}\tilde{\mathbf{B}}\\ &+\zeta_{gu}^{\text{BS-U}}\tilde{\mathbf{B}}^{H}\bar{\mathbf{D}}_{gu}^{vv}(\bar{\mathbf{D}}_{gu}^{vv})^{H}\tilde{\mathbf{B}}\Big)^{-1}.\end{aligned} \tag{3.69}$$

It can be noticed that the entries of the matrix in (3.69) result from the inverse of the superposition of the channel matrices of the three propagation links, which are statistically independent. This implies that $\mathbf{H}_{gu}^{\dagger v}(\mathbf{H}_{gu}^{\dagger v})^{H}$ can be completely characterized if we can determine the individual distributions of $\tilde{\mathbf{B}}^{H}\bar{\mathbf{D}}_{gu}^{vv}$, $\tilde{\mathbf{B}}^{H}(\bar{\mathbf{G}}_{gu}^{vv})^{H}(\mathbf{\Phi}_{gu}^{vv})^{H}$, and $\tilde{\mathbf{B}}^{H}(\bar{\mathbf{G}}_{gu}^{hv})^{H}(\mathbf{\Phi}_{gu}^{hv})^{H}$, which, unfortunately, turns out to be a challenging task. Specifically, because the entries of $\mathbf{\Phi}_{gu}^{vv}$ and $\mathbf{\Phi}_{gu}^{hv}$ change rapidly with the fast-varying channels as a result of the complicated problem in (3.52), identifying the exact statistical distribution of (3.69) for arbitrary values of L becomes infeasible.

Alternatively, by relying on the asymptotic property of $(\mathbf{\Phi}_{gu}^{ab})^{H}\mathbf{\Phi}_{gu}^{ab}$ exhibited when $L \to \infty$, which is revealed in Lemma 3.3, we will continue our analysis by focusing on the scenario where IRSs comprise arbitrarily large numbers of reflecting elements. Lemma 3.3 is presented next.

Lemma 3.3: When the matrices $\mathbf{\Phi}_{gu}^{ab}$, $a, b \in \{v, h\}$ are tuned based on the optimization problem in (3.44), the magnitude of their entries becomes arbitrarily small as the number of reflecting elements L grows toward infinity, so that

$$(\mathbf{\Phi}_{gu}^{ab})^{H}\mathbf{\Phi}_{gu}^{ab} \to \mathbf{0}_{L,L} \qquad \text{as} \qquad L \to \infty, \qquad \forall a, b \in \{v, h\}. \tag{3.70}$$

Proof: The reader is referred to Appendix B in Publication [III]. ■

Lemma 3.3 reveals that the channel matrices for the links BS-IRS and IRS-U present in (3.69) vanish for a number sufficiently large of reflecting elements. As a result, in the asymptotic regime with $L \to \infty$, the matrix in (3.69) can be approximately given by

$$\mathbf{H}_{gu}^{\dagger v}(\mathbf{H}_{gu}^{\dagger v})^{H} \approx \left(\zeta_{gu}^{\text{BS-U}}\tilde{\mathbf{B}}^{H}\bar{\mathbf{D}}_{gu}^{vv}(\bar{\mathbf{D}}_{gu}^{vv})^{H}\tilde{\mathbf{B}}\right)^{-1}, \tag{3.71}$$

in which its statistics properties are easier to determine. Specifically, it is shown in Publication [III] that when L grows to infinity, the matrix $\mathbf{H}_{gu}^{\dagger v}(\mathbf{H}_{gu}^{\dagger v})^{H}$ converges in distribution to the inverse Wishart distribution with $\frac{N}{2}$ degrees of freedom, and the covariance matrix computed by $\mathrm{E}\{\mathbf{H}_{gu}^{\dagger v}(\mathbf{H}_{gu}^{\dagger v})^{H}\} = \left(\zeta_{gu}^{\text{BS-U}}\tilde{\mathbf{B}}^{H}\mathbf{R}\tilde{\mathbf{B}}\right)^{-1}$. Consequently, the effective channel gain $1/[\mathbf{H}_{gu}^{\dagger v}(\mathbf{H}_{gu}^{\dagger v})^{H}]_{g,g}$ follows approximately the Gamma distribution with the shape parameter $(N - \bar{M})/2 + 1$ and the rate parameter $(\zeta_{gu}^{\text{BS-U}}[\tilde{\mathbf{B}}^{H}\mathbf{R}\tilde{\mathbf{B}}]_{g,g})^{-1}$, for L sufficiently large. Then, we rely on the independence of the channel gains achieved in the two polarizations and derive the cumulative distribution function (CDF) of $\ddot{\hbar}_{gu}$ for users in vertical subsets as follows

$$F_{\ddot{\hbar}_{gu}}(x) = F_{\hbar^v_{gu}}(x) F_{\hbar^h_{gu}}(x) = \frac{\gamma\left(\kappa, (\chi^{\text{BS-U}})^{-1}\lambda_{gu}x\right)\gamma\left(\kappa, \lambda_{gu}x\right)}{\Gamma\left(\kappa\right)^2}, \tag{3.72}$$

Thus, the PDF of $\ddot{\hbar}_{gu}$ is achieved by calculating the derivative of $F_{\ddot{\hbar}_{gu}}(x)$, which results in

$$\begin{aligned} f_{\ddot{\hbar}_{gu}}(x) = \frac{(\lambda_{gu})^{\kappa} x^{\kappa-1}}{\Gamma\left(\kappa\right)^2} \Big[& e^{-\lambda_{gu}x}\gamma\left(\kappa, (\chi^{\text{BS-U}})^{-1}\lambda_{gu}x\right) \\ & + (\chi^{\text{BS-U}})^{-\kappa} e^{-(\chi^{\text{BS-U}})^{-1}\lambda_{gu}x}\gamma\left(\kappa, \lambda_{gu}x\right)\Big], \end{aligned} \tag{3.73}$$

where we have defined $\lambda_{gu} = (\zeta^{\text{BS-U}}_{gu}[\tilde{\mathbf{B}}^H\mathbf{R}\tilde{\mathbf{B}}]_{g,g})^{-1}$ and $\kappa = (N - \bar{M})/2 + 1$.

Users within horizontal subsets share identical CDFs and PDFs as the ones derived above. Thus, their expressions are not provided in this dissertation to avoid redundancy. It is noteworthy that when L is large enough, Lemma 3.3 ensures that the matrices $\mathbf{\Phi}^{ab}_{gu}$, $a, b \in \{v, h\}$, have entries with amplitude always less than one. This implies that the constraints in (3.52b) and (3.53b) are always satisfied when $L \to \infty$, and the solutions of (3.52) and (3.53) approach that achievable with a standard unconstrained least-squares problem. As a result, the polarization interference in the denominator of the SINR in (3.66) can be eliminated for large values of L, i.e., $\lim_{L\to\infty} \mathfrak{X}_{gu} \to 0$. This property is exploited in the next subsection for deriving a closed-form asymptotic expression for the ergodic rate.

Ergodic Rates for Arbitrarily Large IRSs

This subsection presents the closed-form asymptotic expression for the users' ergodic rates, which is the main result of the theoretical analysis derived in Publication [III]. To this end, we rely on Lemma 3.3 and consider that IRSs with a sufficiently large number of reflecting elements are deployed so that all polarization interference is canceled. Consequently, the SINRs of users are degraded only by SIC error propagation. With these assumptions, the ergodic rates are derived in the following proposition.

Proposition 3.5: When an IRS with an arbitrarily large number of reflecting elements, i.e., $L \to \infty$, is deployed to assist the uth user in the gth group within the polarization subset $\mathcal{U}^a, a \in \{v, h\}$, which is undergoing SIC error propagation, this user achieves the following ergodic rate

$$\begin{aligned}\bar{R}_{gu} = \frac{1}{\ln(2)\Gamma(\kappa)} \Bigg\{ & G_{3,2}^{1,3}\left(\begin{smallmatrix} 1-\kappa,1,1 \\ 1,0 \end{smallmatrix} \,\middle|\, \frac{\bar{\alpha}_{gu}}{\lambda_{gu}} \right) + G_{3,2}^{1,3}\left(\begin{smallmatrix} 1-\kappa,1,1 \\ 1,0 \end{smallmatrix} \,\middle|\, \frac{\chi^{\text{BS-U}}\bar{\alpha}_{gu}}{\lambda_{gu}} \right) \\ & - G_{3,2}^{1,3}\left(\begin{smallmatrix} 1-\kappa,1,1 \\ 1,0 \end{smallmatrix} \,\middle|\, \frac{\tilde{\alpha}_{gu}}{\lambda_{gu}} \right) - G_{3,2}^{1,3}\left(\begin{smallmatrix} 1-\kappa,1,1 \\ 1,0 \end{smallmatrix} \,\middle|\, \frac{\chi^{\text{BS-U}}\tilde{\alpha}_{gu}}{\lambda_{gu}} \right) \\ & - \sum_{n=0}^{\kappa-1} \frac{(\chi^{\text{BS-U}})^{\kappa} + (\chi^{\text{BS-U}})^{n}}{n!(\chi^{\text{BS-U}}+1)^{\kappa+n}} \left[G_{3,2}^{1,3}\left(\begin{smallmatrix} 1-\kappa-n,1,1 \\ 1,0 \end{smallmatrix} \,\middle|\, \frac{\chi^{\text{BS-U}}\bar{\alpha}_{gu}}{(\chi^{\text{BS-U}}+1)\lambda_{gu}} \right) \right. \\ & \left. - G_{3,2}^{1,3}\left(\begin{smallmatrix} 1-\kappa-n,1,1 \\ 1,0 \end{smallmatrix} \,\middle|\, \frac{\chi^{\text{BS-U}}\tilde{\alpha}_{gu}}{(\chi^{\text{BS-U}}+1)\lambda_{gu}} \right) \right] \Bigg\}, \qquad 1 \leq u \leq U, \end{aligned} \tag{3.74}$$

where $\bar{\alpha}_{gu} = \rho(\alpha_{gu}^2 + \mathfrak{I}_{gu})$, and $\tilde{\alpha}_{gu} = \rho\mathfrak{I}_{gu}$.

Proof: The reader is referred to Appendix C in Publication [III]. ■

The expression in (3.74) seems complicated, but by knowing the behavior of the achieved Meijer's G-functions, some insights can be obtained. More specifically, it has been verified through numerical simulations that the terms with Meijer's G-functions consist of monotone increasing functions of the SNR ρ. The first implication of this characteristic is that the negative terms in (3.74) will likely contribute to performance degradation. This insight is reinforced by the fact that the Meijer's G terms that have $\tilde{\alpha}_{gu}$ as the input are negative, and such terms model only interference. In contrast, positive terms that are functions of $\chi^{\text{BS-U}}$ and $\bar{\alpha}_{gu}$, suggest that cross-polar transmissions have a positive contribution to the users' ergodic rates. These performance behaviors are expected given that our proposed IRS-MIMO-NOMA scheme recycles cross-polar transmissions to enable polarization diversity at users. These insights are also confirmed in our simulation results, which are presented next.

3.3.6 Main Results

The main performance improvements unlocked by our dual-polarized IRS-MIMO-NOMA scheme are now revealed. Specifically, this section introduces relevant simulation results from Publication [III], where insightful performance comparisons with the proposed IRS-assisted system and other conventional communication schemes are performed. As the baseline schemes, the traditional MIMO-OMA employing the TDMA technique, the single-polarized MIMO-NOMA scheme based on the implementation of Publication [I], and the dual-polarized MIMO-NOMA scheme proposed in [7] are considered. Numerical results validating our mathematical analysis are also presented.

To ensure fair comparisons in the results, the BS is equipped in all systems with a uniform linear array comprising the same number of transmit antennas. To be specific, the

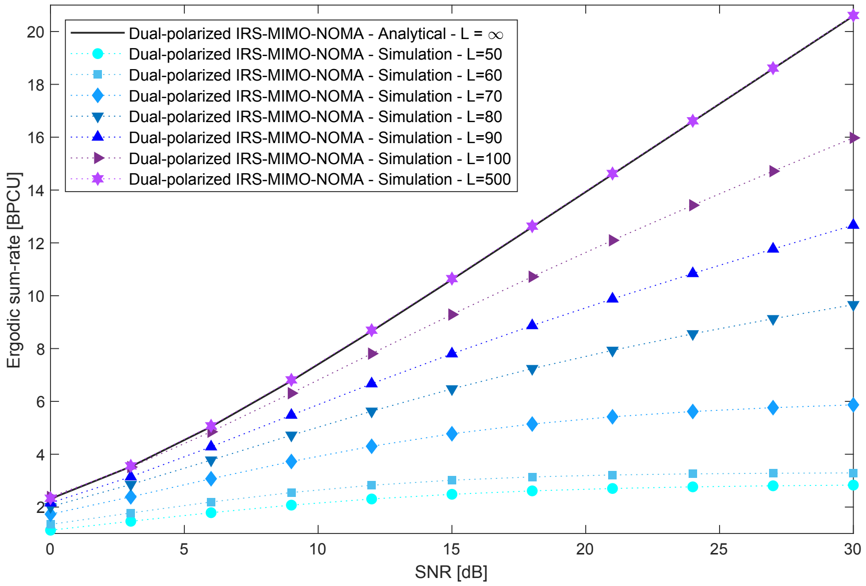

Figure 3.14: Simulated and analytical ergodic sum-rates considering perfect SIC. Effect of the increase in the number of dual-polarized reflecting elements ($N = 4, \chi = 0.5, \xi = 0$) [III], ©2021 IEEE.

dual-polarized schemes are configured with $\frac{M}{2} = 45$ pairs of dual-polarized antennas, i.e., $M = 90$ antenna elements in total, which is the same number configured for the single-polarized counterparts. The spatial clusters and their corresponding correlation matrices in (3.35) and (3.36) are generated using the one-ring correlation model as in Subsection 2.1.2. To this end, $K = 4$ spatial clusters are implemented with 30 m of radius. In the simulated scenario, the clusters are spatially distributed in a circumference surrounding the BS at a distance of 120 m to their center and positioned at different azimuth angles. Within each cluster, the users are organized into $G = \bar{M} = 4$ groups, with $U = 4$ users each. Moreover, for generating our results, the focus is on the first group within the first cluster, which is located at the azimuth angle of $30°$. Within the group of interest, users 1, 2, 3 and 4 are located at $d_1 = 135$ m, $d_2 = 125$ m, $d_3 = 115$ m, and $d_4 = 105$ m, respectively, from the BS, in which their serving IRSs are considered to be nearby. Thus, it is assumed that IRSs 1, 2, 3, and 4 are deployed at the same distances d_1, d_2, d_3, and d_4. With these considerations, inspired by our previous publications, the path-loss coefficients of the links BS-IRS and BS-U for the uth user are adjusted as $\zeta_u^{\text{BS-IRS}} = \zeta_u^{\text{BS-U}} = \Phi d_u^{-\eta}$, setting $\Phi = 20^4$ and the path-loss exponent to $\eta = 2$. For the link IRS-U, because IRSs operate passively, the gain parameter Φ is not included in the path-loss model and compute $\zeta_{gu}^{\text{IRS-U}} = \tilde{d}^{-\eta}$, where $\tilde{d} = 20$ m for all IRSs, which implies that the IRSs and the connected users are separated by 20 m. Furthermore, in Publication [III] only fixed power allocation is considered, where the users' power coefficients are adjusted as $\alpha_1^2 = 0.4, \alpha_2^2 = 0.35, \alpha_3^2 = 0.2, \alpha_4^2 = 0.05$.

Figure 3.14 compares the analytical ergodic sum-rate curve (generated with (3.74)) and

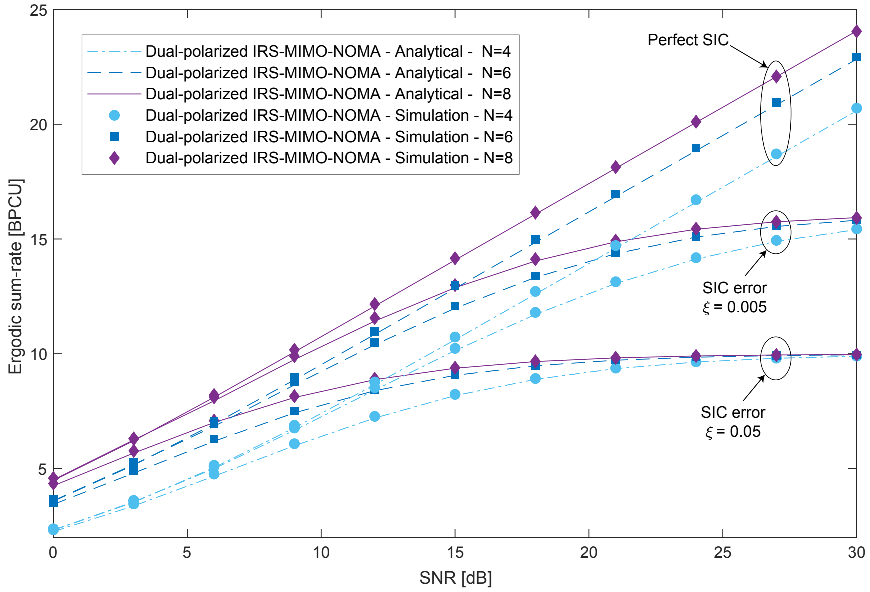

Figure 3.15: Simulated and analytical ergodic sum-rates for various levels of SIC error propagation ($L = 500, \chi = 0.5$) [III], ©2021 IEEE.

simulated ones for increasing values of L, in the ideal scenario with $\xi = 0$, i.e., under perfect SIC. This figure shows the impact of the number of reflecting elements on the capability of the IRSs to cancel polarization interference by solving (3.52) and (3.53). That is, for a small number of reflecting elements, the IRSs are unable to cancel the interference completely, which ends up limiting the sum-rates, as can be observed. In contrast, when L grows, the IRSs become capable to cope with the interference more effectively, which contributes to increasing the sum-rate, so that when $L = 500$, a perfect agreement between the simulated and asymptotic sum-rates is obtained. These results validate our theoretical analysis and satisfy the performance behavior described by Lemma 3.3.

To consolidate the accuracy of our asymptotic theoretical analysis, the number of reflecting elements is fixed to $L = 500$; the analytical and simulated ergodic sum-rates are plotted in Figure 3.15 and the analytical and simulated individual ergodic rates considering various interference parameters in Figure 3.16. For instance, different values of the SIC error factor ξ are tested in Figure 3.15. As can be observed, the performance of the proposed IRS-MIMO-NOMA scheme is also deteriorated by SIC error propagation. However, as shown in the following figures, our scheme can still remarkably outperform the baseline counterparts. Further, Figure 3.16 reveals the performance effects generated by increasing the levels of cross-polar transmissions χ when considering perfect SIC. This figure shows that our dual-polarized IRS-MIMO-NOMA scheme can indeed transform depolarization phenomena into an advantage, where we can see users significantly improving their performance with the increase of χ. Moreover, the IRS-MIMO-NOMA scheme can remarkably outperform the single-polarized MIMO-NOMA counterpart. These results also confirm that our analytical expression derived in (3.74)

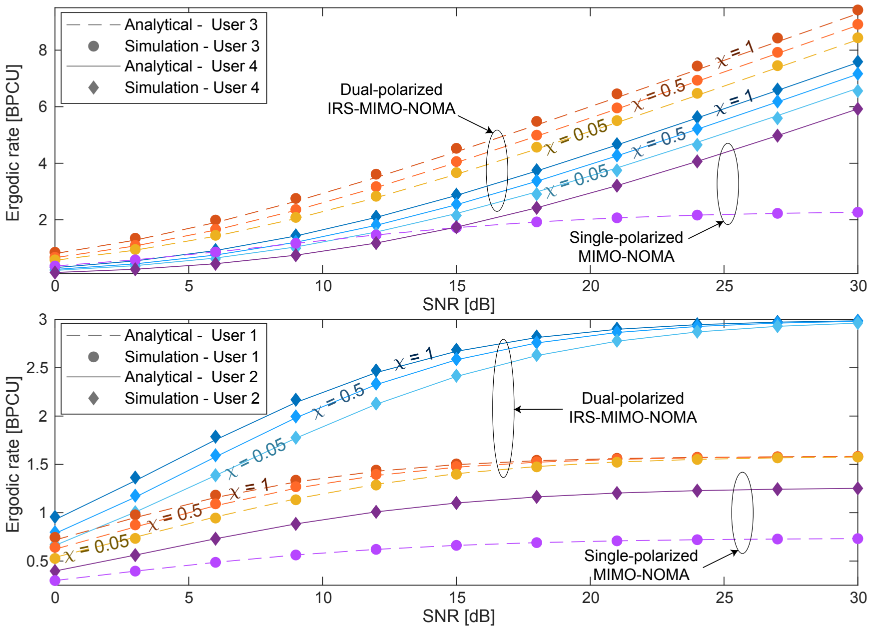

Figure 3.16: Simulated and analytical ergodic rates for different values of iXPD ($L = 500, N = 4, \xi = 0$) [III], ©2021 IEEE.

is capable of modeling with high fidelity the ergodic rates of the proposed scheme when $L \to \infty$, which, once again, validates our analysis.

Figure 3.17 plots the simulated ergodic sum-rates achieved with the proposed scheme and baseline systems, considering different numbers of reflecting elements and a high level of cross-polar interference. For instance, Figure 3.17 shows that when $L = 80$ reflecting elements are employed, the IRS-MIMO-NOMA scheme can be outperformed even by the classical MIMO-OMA in the high-SNR regime. Nevertheless, by adding ten additional elements, i.e., by setting $L = 90$, our proposed scheme outperforms all baseline systems in the entire SNR range. Last, Figure 3.18 confirms the performance superiority of the proposed IRS-MIMO-NOMA scheme over the baseline systems in practical scenarios with high levels of SIC decoding errors. These results reaffirm that all NOMA-based systems are susceptible to the degrading effects of imperfect SIC. However, it is also demonstrated that the dual-polarized IRS-MIMO-NOMA scheme shows more robustness to the issue, so that from $L = 90$ elements onward, our scheme can outperform all benchmark systems even with a moderate SIC error factor.

3.3.7 Summary

In Publication [I], it was found that imperfect SIC has the potential to severely degrade the performance of MIMO-NOMA networks, making them less spectrally efficient than MIMO-OMA. In Publication [III], the focus of this section, this major problem was tack-

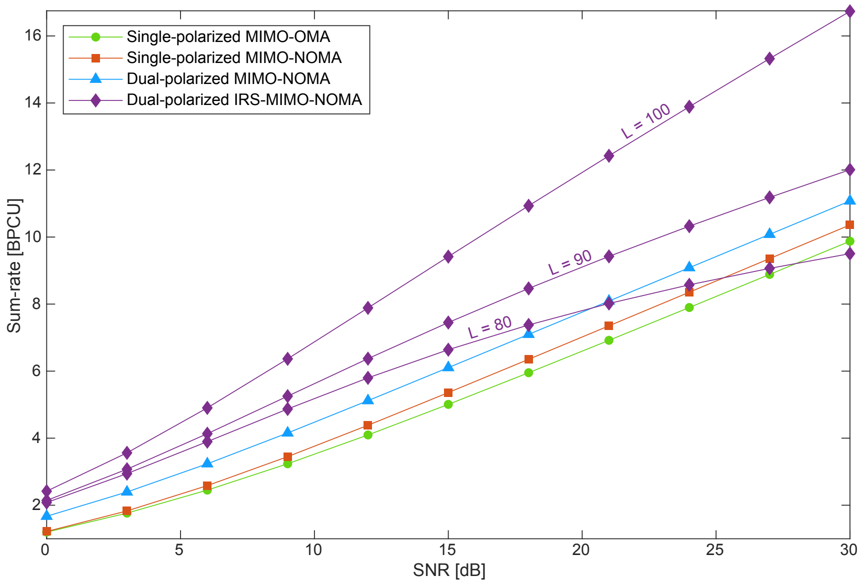

Figure 3.17: Simulated ergodic sum-rates. Comparison between proposed dual-polarized IRS-MIMO-NOMA and conventional schemes ($N = 4, \chi = 0.5, \xi = 0$) [III], ©2021 IEEE.

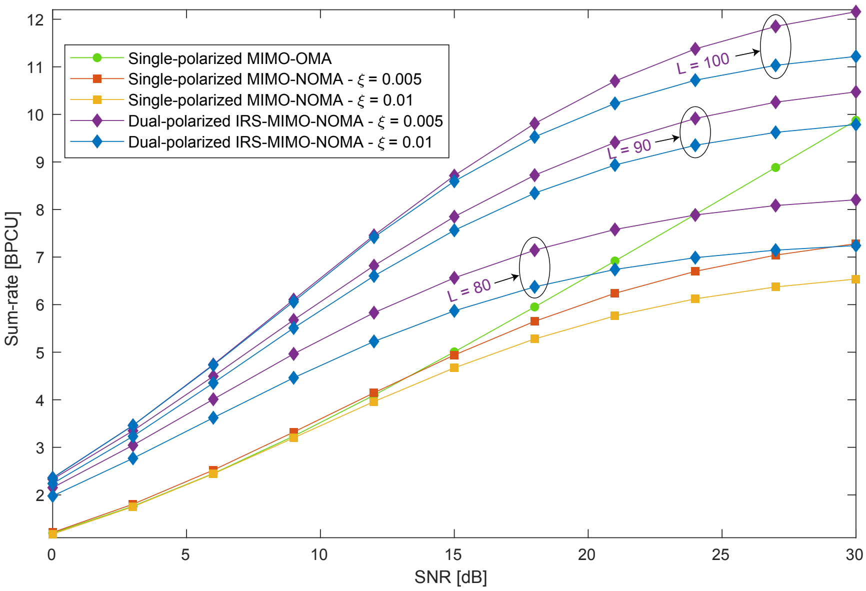

Figure 3.18: Simulated ergodic sum-rates. Comparison between proposed dual-polarized IRS-MIMO-NOMA and conventional schemes under imperfect SIC ($N = 4, \chi = 0.5$) [III], ©2021 IEEE.

led from a perspective that was still missing in the literature. The additional DoF offered by the polarization domain via appealing dual-polarized IRSs was exploited to mitigate the degrading effects of imperfect SIC in dual-polarized massive MIMO-NOMA networks. Publication [III] proposed, optimized, and thoroughly studied a novel dual-polarized downlink transmission strategy that enabled users to exploit diversity and experience reduced levels of interference, leading them to achieve attractive improvements. In our theoretical studies, the statistical behaviors of users' channel matrices were identified and a closed-form asymptotic expression was derived for the ergodic rates considering arbitrarily large IRSs. To wrap up, insightful results were presented, which validated the mathematical analysis and confirmed the effectiveness of the optimization algorithm implemented for configuring the IRSs. Among other important insights, the presented numerical results demonstrated that our dual-polarized IRS-MIMO-NOMA scheme provides impressive performance gains to users, which remarkably outperforms conventional dual-polarized and single-polarized MIMO-NOMA and MIMO-OMA systems. In the next section, our studies are extended and the features of dual-polarized IRSs are exploited to mitigate the limitations of SIC also in the uplink of MIMO-NOMA networks.

3.4 IRSs for Uplink Dual-Polarized MIMO-NOMA Networks

From Publications [I] to [III], MIMO-NOMA schemes operating only in the downlink mode were investigated. However, it is equally important to understand the limitations experienced in the uplink of MIMO-NOMA as well as to develop strategies to solve related problems. Publication [IV] presents promising results toward this goal, which are now discussed. Specifically, this section overviews the main outcomes of Publication [IV], which is focused on the study of uplink IRS-MIMO-NOMA networks and complements the answers to questions *Q4* and *Q5*.

3.4.1 Motivation and Contributions

It was demonstrated in Publication [I] that, under fixed power allocation, downlink NOMA always limits the rate of weak users because of interference from strong ones. In the uplink, the opposite performance behavior is observed. As explained in Section 2.2, in the uplink, the BS is the entity that executes SIC, with the convention of decoding first the data symbols of strong users and considering symbols from weak ones interference. As a consequence, the strong users are the ones to have their data rates limited, which has an even greater impact on the network sum-rate. Furthermore, the rates of individual users end up unequal, a characteristic not desired in applications that demand a balanced performance.

In Publication [II], it was demonstrated that IRSs can help to implement robust dynamic power allocation strategies for balancing user data rates, whereas in Publication [III], it was shown that dual-polarized IRSs can be exploited to mitigate SIC limitations in downlink MIMO-NOMA networks. It is clear that these attractive opportunities can be combined and harnessed to address also the issues experienced in the uplink MIMO-NOMA described above, and this has motivated the development of Publication [IV]. More specifically, in this section, the capabilities of dual-polarized IRSs are exploited for minimizing interference levels experienced by the BS when executing SIC in a dual-polarized uplink MIMO-NOMA network. Other specific details and main contributions are summarized as follows:

- Differently from previous works, in Publication [IV], a small-scale MIMO system is studied, where both users and the BS employ a small number of dual-polarized antennas, with users undergoing uncorrelated Rayleigh fading, following the model in (2.3). Moreover, the users are assumed to be organized into multiple uncorrelated groups. Then, inspired by the strategy proposed in Publication [III], the users within each group are partitioned into two disjoint subsets so that incoming transmissions from users in a given subset are detected only in one of the receive polarizations preassigned by the BS, i.e., using either vertically polarized or horizontally polarized BS antennas.
- To enable our proposed strategy, each group is assisted with one dual-polarized IRS. The reflecting elements of the IRSs are optimized to ensure that transmissions com-

ing from a given subset impinge only antennas with the predetermined polarization at the BS. After some transformations, the original formulated problem is simplified into least squares subproblems with ℓ_∞ norm constraints. Then, it is proven that the achieved problems are convex, and an iterative algorithm is proposed based on the Conditional Gradient method to compute their optimal solutions.

- Based on the concept of signal alignment introduced in Subsection 2.1.5, precoding and detection strategies are developed to project the channels of users within each subset into a common interference subspace. The approach enables the BS to efficiently cope with the remaining intergroup interference observed in each polarization.

- Inspired by Publication [I], an efficient dynamic power allocation strategy is also proposed for balancing the uplink data rates of the users within each subset. To this end, a low-complexity alternate approach is proposed to compute the users' power coefficients adaptively.

- To conclude our contributions, numerical results are presented together with comprehensive discussions. Among other insightful remarks, it is shown that the proposed dual-polarized IRS-MIMO-NOMA scheme can remarkably improve the uplink data rates of all users and outperform the considered baseline systems.

3.4.2 System Model

Here, we consider a single-cell communication scenario where one BS, employing $M/2$ co-located pairs of dual-polarized antennas, receives uplink transmissions simultaneously from multiple users equipped with $N/2$ pairs of dual-polarized antennas, in which M and N are even and satisfy $M \geq 2$ and $N \geq 2$. In contrast to our previous publications, spatial correlation is not modeled. However, for employing NOMA and implementing our uplink transmission strategy, it is assumed that the users are organized into G groups, with each group containing U users. As illustrated in Figure 3.19, to assist the BS coping with polarization interference, each group of users is associated with one dual-polarized IRS, so that a total of G IRSs are deployed in the network. To reduce the interference levels experienced in the SIC decoding process, like in Publication [III], instead of implementing NOMA considering the entire group, the BS subdivides each group into two subsets and applies NOMA to each subset separately. To this end, the BS sets its vertically polarized antennas to receive information signals from one subset, called the vertical subset, which comprises U^v users, and its horizontally polarized antennas to receive signals from the other subset, called the horizontal subset, with U^h users, in which $U^v + U^h = U$. To enable our reduced-interference MIMO-NOMA scheme, IRSs are configured associated with each group to mitigate all transmissions arriving at unsigned polarizations at the BS. Note that imperfect SIC is not tackled in Publication [IV] but only problems related to the uplink NOMA technique itself under ideal decoding conditions are addressed.

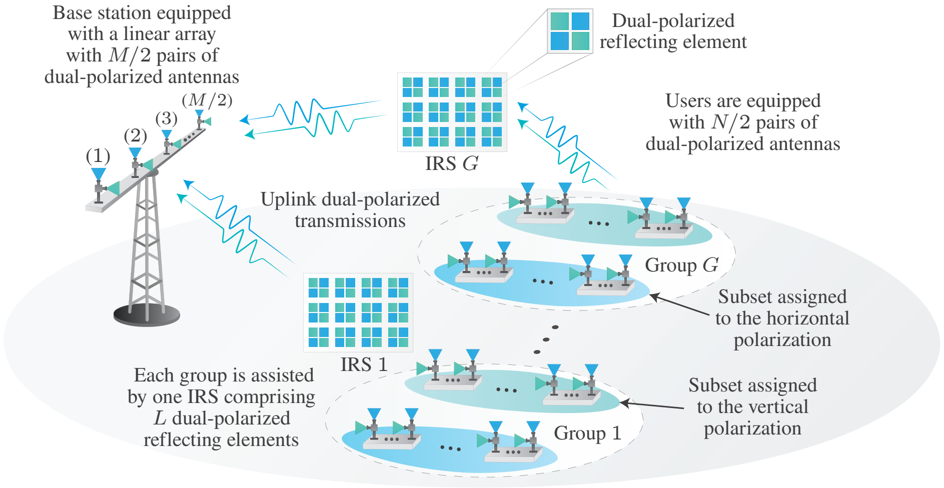

Figure 3.19: Uplink scenario investigated in Publication [IV]. Each dual-polarized IRS serves one group of users. IRSs mitigate polarization interference and assist the BS to multiplex user subsets in the polarization domain.

With the described system model, and recalling the model proposed in Publication [III], the reflection matrix for the dual-polarized IRS associated with the gth group can be written as

$$\boldsymbol{\Theta}_g = \begin{bmatrix} \boldsymbol{\Phi}_g^{vv} & \boldsymbol{\Phi}_g^{hv} \\ \boldsymbol{\Phi}_g^{vh} & \boldsymbol{\Phi}_g^{hh} \end{bmatrix} \in \mathbb{C}^{2L \times 2L}, \tag{3.75}$$

where $\boldsymbol{\Phi}_g^{ab}$ represents the diagonal matrix with the IRS coefficients that model the reflections from the polarization a to the polarization b, with $a, b \in \{v, h\}$, defined identically as in (3.31). As a result, the full dual-polarized channel matrix achieved by the BS can be represented by

$$\begin{aligned} \mathbf{H}_{gu} = & \begin{bmatrix} \mathbf{F}_g^{vv} & \mathbf{0}_{L,\frac{M}{2}} \\ \mathbf{0}_{L,\frac{M}{2}} & \mathbf{F}_g^{hh} \end{bmatrix}^H \begin{bmatrix} \boldsymbol{\Phi}_g^{vv} & \boldsymbol{\Phi}_g^{hv} \\ \boldsymbol{\Phi}_g^{vh} & \boldsymbol{\Phi}_g^{hh} \end{bmatrix} \begin{bmatrix} \mathbf{G}_{gu}^{vv} & \sqrt{\chi^{\text{U-IRS}}}\mathbf{G}_{gu}^{hv} \\ \sqrt{\chi^{\text{U-IRS}}}\mathbf{G}_{gu}^{vh} & \mathbf{G}_{gu}^{hh} \end{bmatrix} \\ & + \begin{bmatrix} \mathbf{D}_{gu}^{vv} & \sqrt{\chi^{\text{U-BS}}}\mathbf{D}_{gu}^{hv} \\ \sqrt{\chi^{\text{U-BS}}}\mathbf{D}_{gu}^{vh} & \mathbf{D}_{gu}^{hh} \end{bmatrix} \in \mathbb{C}^{M \times N}, \end{aligned} \tag{3.76}$$

where $\mathbf{D}_{gu}^{ab} = \sqrt{\varsigma_{gu}^{\text{U-BS}}}\tilde{\mathbf{D}}_{gu}^{ab} \in \mathbb{C}^{\frac{M}{2} \times \frac{N}{2}}$, $\mathbf{G}_{gu}^{ab} = \sqrt{\frac{\varsigma_{gu}^{\text{U-IRS}}}{2}}\tilde{\mathbf{G}}_{gu}^{ab} \in \mathbb{C}^{L \times \frac{N}{2}}$, and $\mathbf{F}_g^{ab} = \sqrt{\varsigma_{gu}^{\text{IRS-BS}}}\tilde{\mathbf{F}}_g^{ab} \in \mathbb{C}^{L \times \frac{M}{2}}$, with $\tilde{\mathbf{D}}_g^{ab}$, $\tilde{\mathbf{G}}_g^{ab}$ and $\tilde{\mathbf{F}}_g^{ab}$ representing, respectively, the full-rank channel matrices for the links between the uth user and the BS (link U-BS), the uth user and the gth IRS (link U-IRS), and the gth IRS and the BS (link IRS-BS), from the polarization a to b. Moreover, the channel coefficients in the matrices $\tilde{\mathbf{D}}_g^{ab}$, $\tilde{\mathbf{G}}_g^{ab}$ and $\tilde{\mathbf{F}}_g^{ab}$ follow the complex Gaussian distribution with zero mean and unity variance, and the coefficients $\zeta_{gu}^{\text{U-BS}}$, $\zeta_{gu}^{\text{U-IRS}}$, and $\zeta_{gu}^{\text{IRS-BS}}$ denote the path-loss observed in the links U-BS, U-IRS, and IRS-BS, respectively. The normalization factor $\frac{1}{\sqrt{2}}$ is introduced for ensuring a passive polarization beam splitting, as explained in Subsection 3.3.2, and $\chi^{\text{U-IRS}}$, and $\chi^{\text{U-BS}} \in [0, 1]$ are the iXPD parameters that model the power imbalance between polarizations in the corresponding propagation link. For mathematical simplicity, like in Publication [III], depolarization in the link IRS-BS is not modeled.

Under the above considerations, after the data streams transmitted by the users have traveled through all propagation links, the BS receives the following superimposed signal

$$\mathbf{y} = \sum_{m=1}^{G} \sum_{n=1}^{U} \mathbf{H}_{mn} \mathbf{x}_{mn} + \mathbf{n} \in \mathbb{C}^M, \tag{3.77}$$

where $\mathbf{x}_{mn} = \mathbf{p}_{mn} \sqrt{P \beta_{mn}} x_{mn} \in \mathbb{C}^N$ represents the precoded data stream transmitted by the nth user within the mth group, with $\mathbf{p}_{mn}$ representing the precoding vector for signal alignment, P denotes the total transmit power available at the user, $\beta_{mn} \in [0, 1]$ denotes the power allocation coefficient, x_{mn} is the user data message, and the vector $\mathbf{n} = [(\mathbf{n}^v)^T, (\mathbf{n}^h)^T]^T \in \mathbb{C}^M$ models the thermal noise experienced by the BS, with entries following the complex Gaussian distribution with zero mean and variance σ^2.

3.4.3 IRS Optimization, Precoding, and Reception

IRS Optimization

This subsection explains the strategy for optimizing the dual-polarized reflecting elements of IRSs proposed in Publication [IV]. First, to achieve a more compact channel representation, we make the following definitions:

$$\begin{aligned} \mathbf{G}_{gu}^v &= \left[\mathbf{G}_{gu}^{vv} \; \sqrt{\chi^{\text{U-IRS}}} \mathbf{G}_{gu}^{hv}\right], \; \mathbf{G}_{gu}^h = \left[\sqrt{\chi^{\text{U-IRS}}} \mathbf{G}_{gu}^{vh} \; \mathbf{G}_{gu}^{hh}\right] \\ \mathbf{D}_{gu}^v &= \left[\mathbf{D}_{gu}^{vv} \; \sqrt{\chi^{\text{U-IRS}}} \mathbf{D}_{gu}^{hv}\right], \; \mathbf{D}_{gu}^h = \left[\sqrt{\chi^{\text{U-IRS}}} \mathbf{D}_{gu}^{vh} \; \mathbf{D}_{gu}^{hh}\right]. \end{aligned}$$

With the above notation, we can rewrite the superimposed signal in (3.77) as follows

$$\begin{aligned} \mathbf{y} = \sum_{m=1}^{G} \Bigg[\sum_{n=1}^{U} & \left(\begin{bmatrix} (\mathbf{F}_m^{vv})^H \boldsymbol{\Phi}_m^{vv} \mathbf{G}_{mn}^v \\ (\mathbf{F}_m^{hh})^H \boldsymbol{\Phi}_m^{vh} \mathbf{G}_{mn}^v \end{bmatrix} + \begin{bmatrix} (\mathbf{F}_m^{vv})^H \boldsymbol{\Phi}_m^{hv} \mathbf{G}_{mn}^h \\ (\mathbf{F}_m^{hh})^H \boldsymbol{\Phi}_m^{hh} \mathbf{G}_{mn}^h \end{bmatrix} \right) \mathbf{x}_{mn} \\ & + \sum_{s \in \mathcal{G}_m^v} \begin{bmatrix} \mathbf{D}_{ms}^v \\ \mathbf{D}_{ms}^h \end{bmatrix} \mathbf{x}_{ms} + \sum_{t \in \mathcal{G}_m^h} \begin{bmatrix} \mathbf{D}_{mt}^v \\ \mathbf{D}_{mt}^h \end{bmatrix} \mathbf{x}_{mt} \Bigg] + \mathbf{n}, \end{aligned} \tag{3.78}$$

where the index sets $\mathcal{G}_g^a = \{1, 2, \cdots, U^a\}$, represent the subset of users assigned to the polarization $a \in \{v, h\}$ within the gth group.

It has been explained that to reduce the levels of interference in the SIC process, the BS employs NOMA to each subset separately. By analyzing the signal in (3.78), it becomes clear that for our strategy to be effective, the dual-polarized IRSs should ensure that messages transmitted by users in vertical subsets, $\mathcal{G}_g^v$, reach the BS only via the upper channel blocks of the matrices in (3.78), whereas messages from horizontal subsets, $\mathcal{G}_g^h$, should propagate through the lower channel blocks only. This implies that the IRS serving the gth group should eliminate signals transmitted from the subset $\mathcal{G}_g^v$ that arrive at horizontally polarized BS antennas and from the subset $\mathcal{G}_g^h$ that arrive at vertically polarized BS antennas. More specifically, for vertical subsets $\mathcal{G}_g^v$, the gth IRS has to be programmed in such a way that the following is achieved:

$$\sum_{n=1}^{U} \left[(\mathbf{F}_g^{hh})^H \mathbf{\Phi}_g^{vh} \mathbf{G}_{gn}^v + (\mathbf{F}_g^{hh})^H \mathbf{\Phi}_g^{hh} \mathbf{G}_{gn}^h \right] \mathbf{x}_{gn} + \sum_{s \in \mathcal{G}_g^v} \mathbf{D}_{gs}^h \mathbf{x}_{gs} \approx \mathbf{0}, \tag{3.79}$$

and for horizontal subsets $\mathcal{G}_g^h$:

$$\sum_{n=1}^{U} \left[(\mathbf{F}_g^{vv})^H \mathbf{\Phi}_g^{vv} \mathbf{G}_{gn}^v + (\mathbf{F}_g^{vv})^H \mathbf{\Phi}_g^{hv} \mathbf{G}_{gn}^h \right] \mathbf{x}_{gn} + \sum_{t \in \mathcal{G}_g^h} \mathbf{D}_{gt}^v \mathbf{x}_{gt} \approx \mathbf{0}. \tag{3.80}$$

The objectives in (3.79) and (3.80) can be accomplished by solving the following optimization problem

$$\underset{\mathbf{\Theta}_g}{\arg\min} \left\| \begin{bmatrix} (\mathbf{F}_g^{vv})^H \mathbf{\Phi}_g^{vv} \sum_{n=1}^{U} \mathbf{G}_{gn}^v \mathbf{x}_{gn} \\ (\mathbf{F}_g^{hh})^H \mathbf{\Phi}_g^{vh} \sum_{n=1}^{U} \mathbf{G}_{gn}^v \mathbf{x}_{gn} \end{bmatrix} + \begin{bmatrix} (\mathbf{F}_g^{vv})^H \mathbf{\Phi}_g^{hv} \sum_{n=1}^{U} \mathbf{G}_{gn}^h \mathbf{x}_{gn} \\ (\mathbf{F}_g^{hh})^H \mathbf{\Phi}_g^{hh} \sum_{n=1}^{U} \mathbf{G}_{gn}^h \mathbf{x}_{gn} \end{bmatrix} + \begin{bmatrix} \sum_{t \in \mathcal{G}_g^h} \mathbf{D}_{gt}^v \mathbf{x}_{gt} \\ \sum_{s \in \mathcal{G}_g^v} \mathbf{D}_{gs}^h \mathbf{x}_{gs} \end{bmatrix} \right\|^2 \tag{3.81a}$$

$$\text{s.t. } |\omega_{g,l}^{ab}|^2 \le 1, \ \forall l \in [1, L], \forall a, b \in \{v, h\}, \tag{3.81b}$$

$$\mathbf{\Phi}_g^{vv}, \mathbf{\Phi}_g^{vh}, \mathbf{\Phi}_g^{hv}, \mathbf{\Phi}_g^{hh} \text{ diagonal.} \tag{3.81c}$$

Because of the matrix objective function and the constraint for diagonal matrices, computing the solution for (3.81) in its current form is complicated. In order to simplify the above problem, we exploit the Khatri–Rao identity $(\mathbf{C}^T \odot \mathbf{A})\text{vecd}\{\mathbf{B}\} = \text{vec}\{\mathbf{ABC}\}$ and define:

$$\boldsymbol{\theta}_g^{ab} = \text{vecd}\{\mathbf{\Phi}_g^{ab}\}, \qquad \mathbf{z}_g^v = \sum_{t \in \mathcal{G}_g^h} \mathbf{D}_{gt}^v \mathbf{x}_{gt}, \qquad \mathbf{z}_g^h = \sum_{s \in \mathcal{G}_g^v} \mathbf{D}_{gs}^h \mathbf{x}_{gs},$$

$$\mathbf{W}_g^{vv} = \left[\sum_{n=1}^{U} \mathbf{G}_{gn}^v \mathbf{x}_{gn} \right]^T \odot (\mathbf{F}_g^{vv})^H, \qquad \tilde{\mathbf{W}}_g^{vv} = \left[\sum_{n=1}^{U} \mathbf{G}_{gn}^h \mathbf{x}_{gn} \right]^T \odot (\mathbf{F}_g^{vv})^H,$$

$$\mathbf{W}_g^{hh} = \left[\sum_{n=1}^{U} \mathbf{G}_{gn}^{h} \mathbf{x}_{gn}\right]^T \odot (\mathbf{F}_g^{hh})^H, \qquad \tilde{\mathbf{W}}_g^{hh} = \left[\sum_{n=1}^{U} \mathbf{G}_{gn}^{v} \mathbf{x}_{gn}\right]^T \odot (\mathbf{F}_g^{hh})^H.$$

With the above transformations, we can decompose (3.81) into two subproblems as follows

$$\underset{\boldsymbol{\theta}_g^{vv}, \boldsymbol{\theta}_g^{hv}}{\arg\min} \left\| \begin{bmatrix} \mathbf{W}_g^{vv} & \tilde{\mathbf{W}}_g^{vv} \end{bmatrix} \begin{bmatrix} \boldsymbol{\theta}_g^{vv} \\ \boldsymbol{\theta}_g^{hv} \end{bmatrix} + \mathbf{z}_g^{v} \right\|^2 \tag{3.82a}$$

$$\text{s.t.} \quad \left\| \begin{bmatrix} \boldsymbol{\theta}_g^{vv} \\ \boldsymbol{\theta}_g^{hv} \end{bmatrix} \right\|_\infty \leq 1, \tag{3.82b}$$

$$\underset{\boldsymbol{\theta}_g^{vh}, \boldsymbol{\theta}_g^{hh}}{\arg\min} \left\| \begin{bmatrix} \tilde{\mathbf{W}}_g^{hh} & \mathbf{W}_g^{hh} \end{bmatrix} \begin{bmatrix} \boldsymbol{\theta}_g^{vh} \\ \boldsymbol{\theta}_g^{hh} \end{bmatrix} + \mathbf{z}_g^{h} \right\|^2 \tag{3.83a}$$

$$\text{s.t.} \quad \left\| \begin{bmatrix} \boldsymbol{\theta}_g^{vh} \\ \boldsymbol{\theta}_g^{hh} \end{bmatrix} \right\|_\infty \leq 1. \tag{3.83b}$$

Note that the objective functions in (3.82) and (3.83) have the following form $f(\boldsymbol{\theta}) = \|\mathbf{W}\boldsymbol{\theta} + \mathbf{z}\|^2$. The gradient of $f(\boldsymbol{\theta})$ can be computed by $\nabla f(\boldsymbol{\theta}) = 2\mathbf{W}^H(\mathbf{W}\boldsymbol{\theta} + \mathbf{z})$, and thus, its Hessian can be expressed by $2\mathbf{W}^H\mathbf{W}$, which consists of a positive semidefinite matrix. As a result of this condition, it can be affirmed that the expressions in (3.82a) and (3.83a) are convex objective functions. Furthermore, it can be verified that the constraints with ℓ_∞ norms in (3.82b) and (3.83b) form convex compact subsets. These properties imply thay the optimal solutions of (3.82) and (3.83) exist, and can be efficiently computed by the Conditional Gradient method, which is implemented in Algorithm 2.

Precoding for Intragroup Channel Alignment

In Subsection 2.1.5, an uplink precoding technique was introduced that can align the channels of users from a given group into a common subspace, orthogonal to the channels from other groups, which, among other advantages, enables the BS to address intergroup interference more efficiently. In this subsection, this interesting capability is exploited and the precoders $\mathbf{p}_{gu}$ are built to align the channels of users within each subset into a common interference subspace. To this end, we rely on the effectiveness of the dual-polarized IRSs to tackle polarization interference, and, for users within each subset, we construct $\mathbf{p}_{gu}$ to align only the channels of the link U-BS corresponding to the polarization assigned to the given subset. For implementing this strategy, we first define $\tilde{\mathbf{D}}_{gu}^{v} = (\sqrt{\zeta_{gu}^{\text{U-BS}}})^{-1}\mathbf{D}_{gu}^{v}$

Algorithm 2: Algorithm for optimizing the dual-polarized IRSs based on the Conditional Gradient method

```
Input: $K, \mathbf{z}_g^v, \mathbf{z}_g^h, [\mathbf{W}_g^{vv}\ \tilde{\mathbf{W}}_g^{vv}], [\tilde{\mathbf{W}}_g^{hh}\ \mathbf{W}_g^{hh}]$.
Output: $\mathbf{\Phi}_g^{vv}, \mathbf{\Phi}_g^{hv}, \mathbf{\Phi}_g^{vh}, \mathbf{\Phi}_g^{hh}$.
Initialize $c = 1, \boldsymbol{\theta}_g^{(1)} = \mathbf{0}_{2L,1}, \tilde{\boldsymbol{\theta}}_g^{(1)} = \mathbf{0}_{2L,1}$;
for $k = 1$ to $K - 1$ do
    Compute the gradients of (3.82a) and (3.83a):
        $\nabla f\left(\boldsymbol{\theta}_g^{(k)}\right) = 2\left[\mathbf{W}_g^{vv}\ \tilde{\mathbf{W}}_g^{vv}\right]^H\left(\left[\mathbf{W}_g^{vv}\ \tilde{\mathbf{W}}_g^{vv}\right]\boldsymbol{\theta}_g^{(k)} + \mathbf{z}_g^v\right)$,
        $\nabla f\left(\tilde{\boldsymbol{\theta}}_g^{(k)}\right) = 2\left[\tilde{\mathbf{W}}_g^{hh}\ \mathbf{W}_g^{hh}\right]^H\left(\left[\tilde{\mathbf{W}}_g^{hh}\ \mathbf{W}_g^{hh}\right]\tilde{\boldsymbol{\theta}}_g^{(k)} + \mathbf{z}_g^h\right)$;
    Construct the direction-finding vectors $\mathbf{s}^{(k)}$ and $\tilde{\mathbf{s}}^{(k)}$ by computing:
        $\left[\mathbf{s}^{(k)}\right]_i = -c \cdot \nabla f\left(\boldsymbol{\theta}_g^{(k)}\right)$,
        $\left[\tilde{\mathbf{s}}^{(k)}\right]_i = -c \cdot \nabla f\left(\tilde{\boldsymbol{\theta}}_g^{(k)}\right)$;
    Compute the step size: $\nu^{(k)} = \frac{2}{2+k}$;
    Update the vectors of reflecting coefficients:
        $\boldsymbol{\theta}_g^{(k+1)} = \left(1 - \nu^{(k)}\right)\boldsymbol{\theta}_g^{(k)} + \nu^{(k)}\mathbf{s}^{(k)}$,
        $\tilde{\boldsymbol{\theta}}_g^{(k+1)} = \left(1 - \nu^{(k)}\right)\tilde{\boldsymbol{\theta}}_g^{(k)} + \nu^{(k)}\tilde{\mathbf{s}}^{(k)}$;
end
Obtain the final set of coefficients:
    $\mathbf{\Phi}_g^{vv} = \mathrm{diag}\left\{\left[\boldsymbol{\theta}_g^{(K)}\right]_{1:L}\right\}$, $\mathbf{\Phi}_g^{vh} = \mathrm{diag}\left\{\left[\tilde{\boldsymbol{\theta}}_g^{(K)}\right]_{1:L}\right\}$,
    $\mathbf{\Phi}_g^{hv} = \mathrm{diag}\left\{\left[\boldsymbol{\theta}_g^{(K)}\right]_{(L+1):2L}\right\}$, $\mathbf{\Phi}_g^{hh} = \mathrm{diag}\left\{\left[\tilde{\boldsymbol{\theta}}_g^{(K)}\right]_{(L+1):2L}\right\}$.
```

and $\tilde{\mathbf{D}}_{gu}^h = (\sqrt{\zeta_{gu}^{\text{U-BS}}})^{-1}\mathbf{D}_{gu}^h$, which correspond to the block channel matrices modeling, respectively, the signals impinging at vertically and horizontally polarized antennas at the BS. With this notation, the precoding vector $\mathbf{p}_{gu}$ for the uth user within the subset $\mathcal{G}_g^a$, where $a \in \{v, h\}$, is constructed such that:

$$\tilde{\mathbf{D}}_{g1}^a\mathbf{p}_{g1} = \tilde{\mathbf{D}}_{g2}^a\mathbf{p}_{g2} = \cdots = \tilde{\mathbf{D}}_{gU^a}^a\mathbf{p}_{gU^a}, \tag{3.84}$$

which can be accomplished identically as in Subsection (2.1.5) based on the matrices $\tilde{\mathbf{D}}_{gu}^a$, for $u = 1, 2, \cdots, U^a$. Thus, the detailed steps are omitted. As the output of the problem in (2.16), we achieve the precoding vectors $\mathbf{p}_{gu}$ and an aligned channel vector $\bar{\mathbf{d}}_g^a \in \mathbb{C}^{\frac{M}{2}}$, which is observed by the BS in its polarization a associated with users in the subset $\mathcal{G}_g^a$, i.e., $\bar{\mathbf{d}}_g^a = \tilde{\mathbf{D}}_{gu}^a\mathbf{p}_{gu}, \forall u \in \mathcal{G}_g^a$. Moreover, because of the dimensions of the channel matrices, the constraint $2NU^a > M\left(U^a - 1\right)$ must be satisfied.

Signal Reception

By employing the precoders designed in the previous subsection, users within each subset can effectively align their channels corresponding to the assigned polarization. This implies that all the users within the gth group in the subset $\mathcal{G}_g^a$ will achieve the same effective channel vector $\bar{\mathbf{d}}_g^a$ at the BS. As a result, the intergroup interference generated by subsets sharing the same polarization $a \in \{v, h\}$ can be efficiently tackled by the BS with the following detection vector

$$\mathbf{q}_g^a = \mathrm{null}\Big\{\big[\bar{\mathbf{d}}_1^a, \cdots, \bar{\mathbf{d}}_{(g-1)}^a, \bar{\mathbf{d}}_{(g+1)}^a, \cdots, \bar{\mathbf{d}}_G^a\big]^H\Big\} \in \mathbb{C}^{\frac{M}{2}}, \tag{3.85}$$

where, for the existence of the above null space, $M > 2(G-1)$ must be satisfied. By multiplying the superimposed signals in (3.78) received in the vertical and horizontal polarizations by $\mathbf{q}_g^v$ and $\mathbf{q}_g^h$, respectively, the inter-subset interference vanishes and the BS detects the following data vector

$$\hat{\mathbf{x}}_g = \begin{bmatrix} (\mathbf{q}_g^v)^H \bar{\mathbf{d}}_g^v \sum_{s \in \mathcal{G}_g^v} \sqrt{\zeta_{gs}^{\text{U-BS}} P \beta_{gs}}\, x_{gs} \\ (\mathbf{q}_g^h)^H \bar{\mathbf{d}}_g^h \sum_{t \in \mathcal{G}_g^h} \sqrt{\zeta_{gt}^{\text{U-BS}} P \beta_{gt}}\, x_{gt} \end{bmatrix} + \begin{bmatrix} I_g^v \\ I_g^h \end{bmatrix} + \begin{bmatrix} (\mathbf{q}_g^v)^H \mathbf{n}^v \\ (\mathbf{q}_g^h)^H \mathbf{n}^h \end{bmatrix} \in \mathbb{C}^2, \tag{3.86}$$

where the term I_g^a models the residual polarization interference leaked from the gth IRS, which is given by

$$\begin{aligned} \begin{bmatrix} I_g^v \\ I_g^h \end{bmatrix} &= \sum_{n=1}^{U} \begin{bmatrix} (\mathbf{q}_g^v)^H (\mathbf{F}_g^{vv})^H \mathbf{\Phi}_g^{vv} \mathbf{G}_{gn}^v \mathbf{x}_{gn} \\ (\mathbf{q}_g^h)^H (\mathbf{F}_g^{hh})^H \mathbf{\Phi}_g^{vh} \mathbf{G}_{gn}^v \mathbf{x}_{gn} \end{bmatrix} + \sum_{n=1}^{U} \begin{bmatrix} (\mathbf{q}_g^v)^H (\mathbf{F}_g^{vv})^H \mathbf{\Phi}_g^{hv} \mathbf{G}_{gn}^h \mathbf{x}_{gn} \\ (\mathbf{q}_g^h)^H (\mathbf{F}_g^{hh})^H \mathbf{\Phi}_g^{hh} \mathbf{G}_{gn}^h \mathbf{x}_{gn} \end{bmatrix} \\ &+ \begin{bmatrix} (\mathbf{q}_g^v)^H \sum_{t \in \mathcal{G}_g^h} \mathbf{D}_{gt}^v \mathbf{x}_{gt} \\ (\mathbf{q}_g^h)^H \sum_{s \in \mathcal{G}_g^v} \mathbf{D}_{gs}^h \mathbf{x}_{gs} \end{bmatrix}. \end{aligned} \tag{3.87}$$

Note that when the transmissions impinging in unintended polarizations are nulled out by the IRSs perfectly, the interference modeled by (3.87) disappears.

SINR Analysis

We can see in (3.86) that the combination of our transmission and detection strategies has enabled the BS to receive the superimposed symbols from the subsets $\mathcal{G}_g^v$ and $\mathcal{G}_g^h$ in the BS antennas with the matching polarizations v and h, respectively. As a result, the messages from users in each subset can be detected by executing SIC to each polarization separately. To implement this decoding approach, following the convention for uplink NOMA explained in Section 2.2, the users in each subset are sorted in a descending order based on their path-loss coefficients of the direct channel link U-BS, and SIC is carried out following the order $\zeta_{g1}^{\text{U-BS}} > \zeta_{g2}^{\text{U-BS}} > \cdots > \zeta_{gU^a}^{\text{U-BS}}$. More specifically, the BS decodes the data symbol transmitted by the uth user within the subset $\mathcal{G}_g^a$ considering the symbols coming from the $U^a - u$ higher-order users as interference, which results in

$$\begin{aligned}\hat{x}_{gu}^a = &\underbrace{(\mathbf{q}_g^a)^H \bar{\mathbf{d}}_g^a \sqrt{\zeta_{gu}^{\text{U-BS}} P \beta_{gu}}\, x_{gu}}_{\text{Desired symbol}} + \underbrace{(\mathbf{q}_g^a)^H \bar{\mathbf{d}}_g^a \sum_{n=u+1}^{U^a} \sqrt{\zeta_{gn}^{\text{U-BS}} P \beta_{gn}}\, x_{gn}}_{\text{Interference from weaker users}} \\ &+ \underbrace{I_g^a}_{\text{Polarization interference}} + \underbrace{(\mathbf{q}_g^a)^H \mathbf{n}^a}_{\text{Noise}}. \end{aligned} \tag{3.88}$$

Because the detection vector $\mathbf{q}_g^a$ is isotropically distributed on the unit sphere, we have that $|(\mathbf{q}_g^a)^H \mathbf{n}^a|^2 = (\mathbf{q}_g^a)^H \mathbf{n}^a (\mathbf{n}^a)^H \mathbf{q}_g^a = \sigma^2$. Consequently, the symbol from the uth user in the subset $\mathcal{G}_g^a$ is detected with the following the SINR:

$$\gamma_{gu}^a = \frac{|(\mathbf{q}_g^a)^H \bar{\mathbf{d}}_g^a|^2 \zeta_{gu}^{\text{U-BS}} \beta_{gu}}{|(\mathbf{q}_g^a)^H \bar{\mathbf{d}}_g^a|^2 \sum_{n=u+1}^{U^a} \zeta_{gn}^{\text{U-BS}} \beta_{gn} + |I_g^a|^2/P + 1/\rho}, \tag{3.89}$$

where $\rho = \frac{P}{\sigma^2}$ is defined as the SNR. Next, the expression in (3.89) is used for developing the power allocation strategy.

3.4.4 Power Allocation for Rate Fairness

In this section, the concept of fair power allocation proposed in Publication [I] is extended to uplink MIMO-NOMA communication. A low-complexity alternate adaptive strategy is developed for balancing the uplink data rates achieved by users in each polarization subset. Our main goal in implementing this strategy is to demonstrate that our uplink dual-polarized IRS-MIMO-NOMA scheme can deliver high performance even when operating with fair power allocation policies, corroborating the IRS improvements illustrated in Publication [II].

Because of the interference-limited behavior of SIC, small groups are preferred in practical NOMA systems. Under this motivation, our power allocation strategy is developed by considering $U = 4$ users per group, i.e., two users per subset. Moreover, it is assumed that only negligible polarization interference is left by the IRSs. As a result, the term in (3.88) is considered $I_g^a \approx 0$. With these assumptions, the symbol for the first user in the subset $\mathcal{U}_g^a$ is detected with the following data rate

$$R_{g1}^a = \log_2 \left(1 + \frac{|(\mathbf{q}_g^a)^H \bar{\mathbf{d}}_g^a|^2 \zeta_{g1}^{\text{U-BS}} \rho \beta_{g1}}{|(\mathbf{q}_g^a)^H \bar{\mathbf{d}}_g^a|^2 \zeta_{g2}^{\text{U-BS}} \rho \beta_{g2} + 1} \right), \tag{3.90}$$

and for the second user, with

$$R_{g2}^a = \log_2 \left(1 + |(\mathbf{q}_g^a)^H \bar{\mathbf{d}}_g^a|^2 \zeta_{g2}^{\text{U-BS}} \rho \beta_{g2} \right). \tag{3.91}$$

Given the above expressions, the power allocation for uplink rate fairness can be implemented with the following optimization problem:

$$\begin{aligned} \underset{\beta_{g1},\beta_{g2}}{\arg\max} \quad & R_{g1}^{a} && \text{(3.92a)} \\ \text{s.t.} \quad & R_{g2}^{a} \geq R_{g1}^{a}, && \text{(3.92b)} \\ & 0 \leq \beta_{g1} \leq 1, && \text{(3.92c)} \\ & 0 \leq \beta_{g2} \leq 1, && \text{(3.92d)} \end{aligned}$$

The above problem seeks to maximize the data rate for the user with the best channel conditions under the constraint that the user with the worst conditions achieves at least the same rate, i.e., the problem balances the data rates. Moreover, the constraints in (3.92c) and (3.92d) ensure the power coefficients to be within the unity range.

After analyzing and identifying some useful properties in (3.92), β_{g1} is assumed to be a constant and the original problem is reformulated considering β_{g2} as our only decision variable, as follows

$$\begin{aligned} \underset{\beta_{g2}}{\arg\max} \quad & \log_2\left(1+\frac{|(\mathbf{q}_g^a)^H\bar{\mathbf{d}}_g^a|^2\zeta_{g1}^{\text{U-BS}}\rho\beta_{g1}}{|(\mathbf{q}_g^a)^H\bar{\mathbf{d}}_g^a|^2\zeta_{g2}^{\text{U-BS}}\rho\beta_{g2}+1}\right) && \text{(3.93a)} \\ \text{s.t.} \quad & \left(|(\mathbf{q}_g^a)^H\bar{\mathbf{d}}_g^a|^2\zeta_{g2}^{\text{U-BS}}\rho\right)^2\beta_{g2}^2+\left(|(\mathbf{q}_g^a)^H\bar{\mathbf{d}}_g^a|^2\zeta_{g2}^{\text{U-BS}}\rho\right)\beta_{g2} \\ & -\left(|(\mathbf{q}_g^a)^H\bar{\mathbf{d}}_g^a|^2\zeta_{g1}^{\text{U-BS}}\rho\right)\beta_{g1}\geq 0, && \text{(3.93b)} \\ & 0\leq\beta_{g2}\leq 1. && \text{(3.93c)} \end{aligned}$$

Then, by further investigating the behaviors of the objective function and constraints in (3.93), the optimal power coefficients for balancing the user data rates are computed with the following low-complexity strategy:

- First, aiming the maximization of R_{g1}^{a}, β_{g1} is initialized with 1.
- Second, the positive root of (3.93b) is calculated as follows:

$$\begin{aligned} \Delta_{g2} = & \frac{\sqrt{\left(|(\mathbf{q}_g^a)^H\bar{\mathbf{d}}_g^a|^2\zeta_{g2}^{\text{U-BS}}\rho\right)^2+4\left(|(\mathbf{q}_g^a)^H\bar{\mathbf{d}}_g^a|^2\zeta_{g2}^{\text{U-BS}}\rho\right)^2|(\mathbf{q}_g^a)^H\bar{\mathbf{d}}_g^a|^2\zeta_{g1}^{\text{U-BS}}\rho\beta_{g1}}}{2\left(|(\mathbf{q}_g^a)^H\bar{\mathbf{d}}_g^a|^2\zeta_{g2}^{\text{U-BS}}\rho\right)^2} \\ & -\frac{1}{2|(\mathbf{q}_g^a)^H\bar{\mathbf{d}}_g^a|^2\zeta_{g2}^{\text{U-BS}}\rho}, \qquad \text{(3.94)} \end{aligned}$$

- Last, the optimal power coefficients are determined as follows:
  - If $\Delta_{g2} \leq 1$, then $\beta_{g2}^{*} = \Delta_{g2}$, and $\beta_{g1}^{*} = 1$;
  - Otherwise, $\beta_{g2}^{*} = 1$, and β_{g1}^{*} is computed with (3.94) by setting $\Delta_{g2} = 1$.

A complete explanation of the above development and how to reach the proposed solution is provided in Publication [IV].

3.4.5 Main Results

Now, the impressive performance improvements that can be achieved with our IRS-MIMO-NOMA uplink transmission strategy are illustrated. In particular, the sum-rates and individual user rates experienced with our scheme are compared with those of conventional single-polarized MIMO-NOMA and MIMO-TDMA baseline systems. Our results are generated with all systems configured with eight users organized into $G = 2$ groups, i.e., $U = 4$ users per group, and the BS and users equipped with the same number of antenna elements $M = N = 4$. The focus is only on one group where the distances from the BS to users 1, 2, 3, and 4 are set to $d_1 = 20$ m, $d_2 = 40$ m, $d_3 = 80$ m, and $d_4 = 120$ m, respectively. Then, following the proposed polarization multiplexing strategy, users 1 and 2 are paired into the vertical subset $\mathcal{U}^v$, and users 3 and 4 into the horizontal subset $\mathcal{U}^h$. In the simulated scenario, the IRS associated with the studied group close to the BS is deployed. As a result, it is assumed that the distances between the IRS and the connected users are identical to the distances of the BS to the respective users. In contrast, different distances between the IRS and the BS, represented by $\bar{d}$, are investigated for performance illustration purposes. Moreover, the path-loss coefficients observed in the links U-BS and U-IRS are computed as $\zeta_u^{\text{U-BS}} = \zeta_u^{\text{U-IRS}} = \Phi d_u^{-\eta}$, whereas in the link IRS-BS we model by $\zeta_u^{\text{IRS-BS}} = \bar{d}^{-\eta}$, with Φ denoting the gain parameter adjusted to 30 dB and η the path-loss exponent adjusted to 2. In all results, we consider $\chi^{\text{U-BS}} = \chi^{\text{U-IRS}} = 0.5$ and $P = 1$. Furthermore, when fixed power allocation is employed, we adjust $\beta_1 = \beta_2 = \beta_3 = \beta_4 = 1$, i.e., all users allocate their full transmit power.

In Figure 3.20(a), the distance from the IRS to the BS is fixed to 15 m, and the ergodic sum-rates of our proposed dual-polarized IRS-MIMO-NOMA scheme are investigated considering different numbers of reflecting elements. As can be seen, by implementing just $L = 10$ dual-polarized elements, our IRS-assisted scheme can already outperform both the conventional MIMO-NOMA and MIMO-TDMA baseline schemes in the entire considered SNR range. For $L = 30$, the gains are even more remarkable, so that an impressive improvement of almost 6 BPCU can be achieved over the single-polarized MIMO-NOMA counterpart when the SNR is 40 dB. In Figure 3.20(b), the SNR is set to 26 dB and the ergodic sum-rate is plotted versus different distances between the IRS and the BS. We can see that the sum-rate achieved by the IRS-MIMO-NOMA scheme is reduced by increasing the distance. This is indeed an expected behavior because a higher path-loss coefficient deteriorates the capability of the IRS to mitigate interfering transmissions, leading to lower data rates. Nevertheless, even when the IRS is $\bar{d} = 30$ m apart from the BS, the proposed scheme can still outperform all baseline systems, as long as the IRS is large enough.

By implementing $L = 30$ reflecting elements, Figure 3.21(a) confirms the capability of the IRS-MIMO-NOMA scheme to offer high sum-rate performance even when operating with fair power allocation. As can be seen, the fair policy causes a slight degradation on the sum-rate curve, but impressive performance gains can still be achieved. For example, when the SNR is 40 dB, the IRS-MIMO-NOMA system with fair power allocation

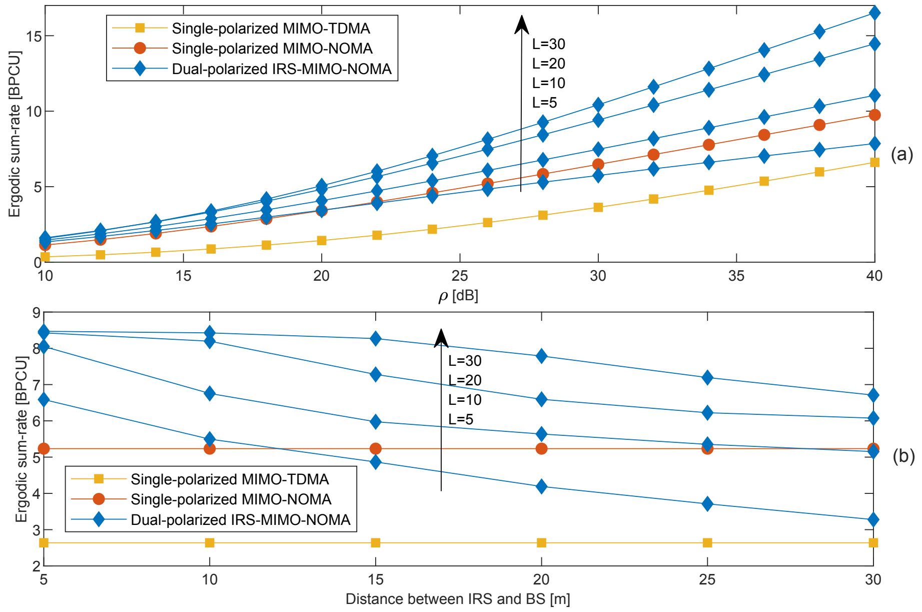

Figure 3.20: Ergodic sum-rates with fixed power allocation when the IRS is located at $\bar{d} = 15$ m from the BS (a), and when ρ is fixed to 26 dB (b) [IV], ©2021 IEEE.

still delivers a sum rate of more than 16 BPCU. Such a throughput represents a significant improvement of more than 6 BPCU over the single-polarized MIMO-NOMA and 9 BPCU over the MIMO-TDMA counterparts. Lastly, Figures 3.21(b) and 3.21(c) investigate more closely the performance behavior of individual users when operating with fixed and fair power allocation. As we can see, the IRS-MIMO-NOMA scheme enables all users within the two polarization subsets to achieve data rates considerably higher than those achievable with the conventional single-polarized MIMO-NOMA counterpart. The observed improvements mainly result from the reduced interference levels in the SIC process, which is enabled by multiplexing the subsets of users in the polarization domain. It is also shown that the adaptive power allocation benefits the users with the best channel conditions, i.e., user 1 within the subset $\mathcal{U}^v$ and user 3 within the subset $\mathcal{U}^h$. When the SNR is 40 dB, for instance, the IRS-MIMO-NOMA scheme with the fair policy unleashes a data rate of impressive 3.39 BPCU for user 3, who, with the fixed allocation, can achieve only 1.63 BPCU.

3.4.6 Summary

This section overviewed promising results provided in Publication [IV], focusing specifically on uplink communication. The ideas from Publication [III] were extended and a novel IRS-assisted dual-polarized transmission scheme was developed for mitigating uplink interference in dual-polarized MIMO-NOMA systems. To this end, the powerful

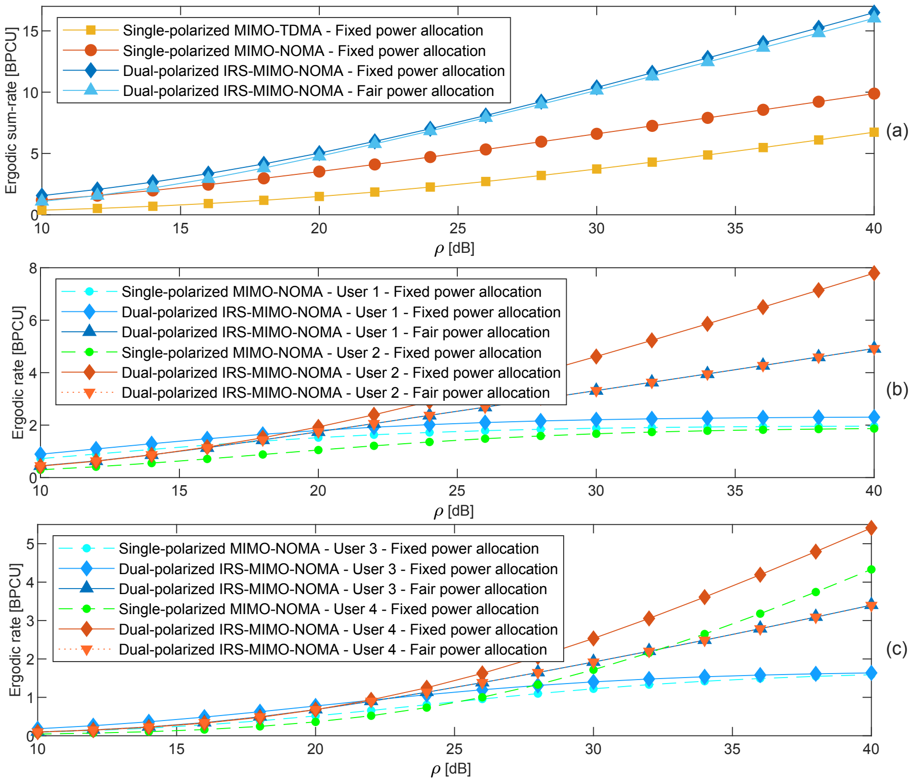

Figure 3.21: Ergodic sum-rates (a) and rates (b)–(c) with fixed and fair power allocation for $L = 30$ and $\bar{d} = 10$ m [IV], ©2021 IEEE.

capabilities of signal alignment techniques and dual-polarized IRSs were combined for multiplexing subsets of users in the polarization domain. Our innovative strategy significantly reduced the interference levels of the SIC decoding process at the BS, which led to impressive performance improvements. An adaptive power allocation strategy of low computational complexity was also developed for balancing the individual rates of users within each subset, thereby leading to enhanced levels of fairness within the network. Representative simulation examples were provided to illustrate the performance improvements enabled by our scheme. Among the discussed insights, it was demonstrated that our dual-polarized IRS-MIMO-NOMA uplink scheme can deliver a high data rate performance to all users even under the proposed fair power allocation regime.

Now that also MIMO-NOMA networks operating in the uplink mode have been studied, all the primary use cases and issues identified throughout the development of our Publications [I] to [IV] can be considered covered. Thus, this section concludes our results on the MIMO-NOMA topic, and we can head to our next chapter, which investigates novel RSMA-based schemes.

4 Overview of Publications on MIMO-RSMA Networks

This chapter is dedicated to overviewing our main results and findings on the promising RSMA technique presented in the last two papers included in this dissertation, Publications [V] and [VI]. Specifically, in Publication [V], the focus of study is on the synergy between the IRS technology and RSMA, and the paper identifies the attractive improvement opportunities offered by the combination of the two subjects, whereas in our final Publication [VI], a novel robust dual-polarized RSMA technique for massive MIMO networks is proposed, which can efficiently overcome some of the limitations unveiled in Publication [V]. Further details are provided in the two upcoming sections.

4.1 RSMA and its Interplay with IRSs

RSMA is a robust downlink MA technique for MIMO systems that counts with appealing advantages and can provide a broader region of achievable data rates not possible with other classical MA strategies. Despite the attractiveness of RSMA, the technique is also vulnerable to fast-varying wireless phenomena and SIC error propagation, like NOMA. In this regard, Publications [II]–[IV] have demonstrated that IRSs can be efficiently configured to mitigate channel and SIC-related problems in MIMO-NOMA networks, which implies that MIMO-RSMA can likewise benefit from the IRS capabilities. The promising improvements reported in our previous papers have encouraged us to investigate the application of IRS also to RSMA, which is the topic of our second magazine article of this dissertation, i.e., Publication [V], the focus of this section. The potential benefits enabled by the combination IRS-MIMO-RSMA presented in this section answer question *Q6*.

4.1.1 Motivation and Contributions

As explained in Section 2.3, by relying on SIC to decode common and private data streams on the receiver's side, RSMA unlocks new opportunities for optimizing interference mitigation, which provides the technique with optimal DoF and high spectral efficiency even in scenarios with imperfect CSI. Regardless of such robustness, wireless communication is nonreliable in essence, and its randomness can inevitably deteriorate the performance of RSMA. Moreover, even in ideal environments where the CSI is perfect, users can experience performance degradation due to SIC decoding errors. Fortunately, Publications [II]–[IV] have shown that the properties of IRSs can be tuned to alleviate these undesired issues. However, before writing Publication [V], only a few works on the topic of IRS-RSMA had been reported, and the full improvement opportunities of the synergy between IRS and RSMA were yet to be clarified. This research opportunity motivated the proposal of the ideas and contributions presented in this section, which are summarized as follows:

- First, light is shed on the basic background, operating principles, and features of the RSMA technique. The motivation for its development is explained and the main employed precoding strategies and the decoding process of the technique are introduced. The features and capabilities of the IRS technology are also addressed. Further, the main IRS functionalities, fabrication practices, and the standard channel model commonly employed by the wireless communication theory community are presented.

- In our studies, attractive potential enhancements are identified that IRSs can enable to RSMA and, reciprocally, that RSMA can bring to IRSs. Our insightful discussions are supported by illustrative simulation examples, which confirm our improvement hypotheses and demonstrate the performance superiority of IRS-MIMO-NOMA schemes over conventional MIMO-RSMA, MIMO-NOMA, and MIMO-TDMA systems.
- It is shown that IRSs can contribute to reducing the complexity of BS precoding and improving the reception of the common stream at all users, which is a design challenge in RSMA. As demonstrated in the previous chapter for MIMO-NOMA, it is also confirmed that IRSs can efficiently tackle the problems of imperfect SIC in RSMA. As our last potential improvement, it is shown that RSMA can make IRSs more robust to inaccurate CSI, contributing to less demanding IRS channel estimation and acquisition.
- Last, this section discusses three exciting communication scenarios foreseen in beyond-5G networks that IRS-MIMO-RSMA schemes can help to bring to reality, namely CSI-robust UAV networks, enhanced high-frequency communication (e.g., up to the terahertz spectrum), and seamless satellite communication. Publication [V] finishes by enlightening readers about important unsolved challenges and future research directions.

The content of this section is limited to the three main mutual benefits that IRS and MIMO-RSMA can achieve combined. For the full contributions, interested readers are encouraged to consult Publication [V].

4.1.2 System Model

Publication [V] addresses a single-cell scenario where one BS equipped with M antennas communicates in the downlink mode with two single-antenna users, each one assisted by one IRS comprising L reflecting elements. Similarly as assumed in our previous works, the users and their corresponding IRSs are deployed at a common distance from the BS. More specifically, user 1 and its IRS 1 are located at a distance denoted by d_1, and user 2 and IRS 2 at d_2, so that $d_1 > d_2$, i.e., user 2 has the best channel conditions and user 1 the worst. Moreover, the two IRSs are deployed close to their connected users separated by a distance $\bar{d}$. This communication scenario is presented in Figure 4.1, which, although simple, is enough to illustrate the fundamental performance gains offered by IRS-MIMO-NOMA. For implementing our simulations, it is assumed that all channels are uncorrelated and that the IRS from one user does not interfere with the other. To this

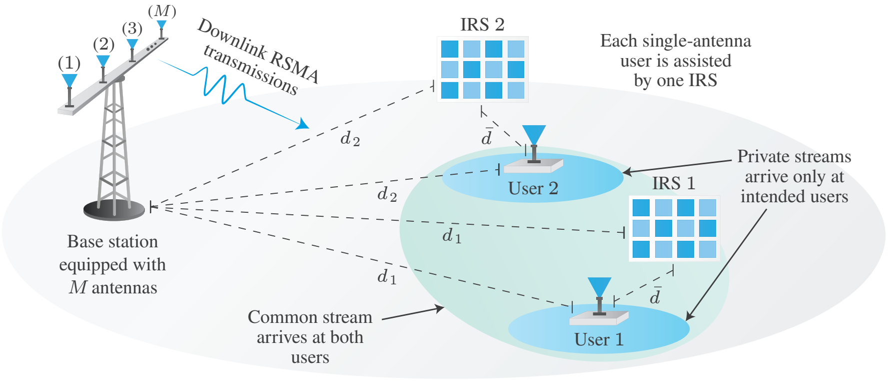

Figure 4.1: IRS-MIMO-RSMA scenario considered in Publication [V]. The IRSs assist two single-antenna users.

end, the composite channel for the uth user is modeled by

$$\mathbf{h}_u^H = \sqrt{\bar{\zeta}}\mathbf{s}_u^H \boldsymbol{\Theta}_u \sqrt{\zeta_u}\mathbf{G}_u + \sqrt{\zeta_u}\mathbf{d}_u^H, \tag{4.1}$$

where $\boldsymbol{\Theta}_u \in \mathbb{C}^{L\times L}$ is the diagonal matrix with reflection coefficients of the uth IRS with L reflecting elements, and $\mathbf{G}_u \in \mathbb{C}^{L\times M}$, $\mathbf{s}_u \in \mathbb{C}^{L}$, and $\mathbf{d}_u \in \mathbb{C}^{M}$ denote the channel responses between the BS and the IRS, the IRS and the users, and the BS and the users, respectively. Moreover, $\bar{\zeta} = \bar{d}^{-\eta}$ and $\zeta_u = \Phi d_u^{-\eta}$ model the path-loss coefficients of the links from the IRSs to the users and from the BS to the users and the IRSs, in which η is the path-loss exponent, and Φ is the array gain parameter adjusted at the BS.

Following the RSMA protocol explained in Section 2.3, after the transmitted signal has propagated through all wireless channels, the uth user receives

$$y_u = \mathbf{h}_u^H \left(\sum_{n=1}^{2} \mathbf{w}_n^p \sqrt{\alpha_n^p} x_n^p + \mathbf{w}^c \sqrt{\alpha^c} x^c \right) + n_u, \tag{4.2}$$

where x^c and x_n^p denote the common symbol intended to all users and the private symbol intended to the nth user, respectively, and α^c and α_n^p are the corresponding power allocation coefficients, satisfying $\alpha^c + \sum_{n=1}^{2} \alpha_n^p = 1$. In turn, $\mathbf{w}^c \in \mathbb{C}^M$ and $\mathbf{w}_n^p \in \mathbb{C}^M$ denote the precoding vectors responsible for conveying the common and private symbols, respectively, and $n_u \in \mathbb{C}$ is the complex Gaussian distributed noise observed by the uth user, which has zero mean and variance σ^2. In the upcoming subsections, the adopted precoding and IRS optimization strategies are presented.

4.1.3 Precoding for Common and Private Symbols

For illustration purposes, in all RSMA-based schemes implemented in this section, $\mathbf{w}^c$ is constructed as a random precoder with entries following the standard complex Gaussian distribution. On the other hand, for conveying the private messages, zero-forcing precoders constructed based only on the channel estimate of the direct link are employed. More specifically, by denoting the imperfect estimate of the channel vector $\mathbf{d}_u$ by $\hat{\mathbf{d}}_u$, modeled as in (4.7), we can define $\hat{\mathbf{D}} = [\hat{\mathbf{d}}_1, \hat{\mathbf{d}}_2] \in \mathbb{C}^{M\times 2}$. Then, the private precoder for the uth user is computed by

$$\mathbf{w}_u^p = \left[\hat{\mathbf{D}}\big(\hat{\mathbf{D}}^H\hat{\mathbf{D}}\big)^{-1}\right]_{:u}, \tag{4.3}$$

where $M \geq 2$ should be satisfied.

4.1.4 IRS Optimization

For achieving the simulation results in Publication [V], the IRS for each user was optimized based on the estimate of its effective channels of the direct and reflected links after precoding, using two main approaches. In the first approach, which was employed for generating Figure 4.2, the reflecting elements of the IRSs are optimized to add constructively the channel gains of the common stream in the reflected link with the gains of the direct link. Further, in Figures 4.3 and 4.4, the IRSs are optimized to boost the effective channel gains of private streams while mitigating interference. Following the steps of Publications [III] and [IV], the optimizations of the reflecting elements were implemented exploiting the Khatri–Rao property $(\mathbf{C}^T \odot \mathbf{A})\mathrm{vecd}\{\mathbf{B}\} = \mathrm{vec}\{\mathbf{ABC}\}$ and the constrained least-squares method from [82].

4.1.5 SNR Analysis

With the given IRS optimization and precoding strategies, the uth user detects the common symbol directly from the signal in (4.2) without any further processing. As a result, the following SINR is achieved

$$\gamma_u^c = \frac{|\mathbf{h}_u^H \mathbf{w}^c|^2 \rho \alpha^c}{\sum_{n=1}^{2} |\mathbf{h}_u^H \mathbf{w}_n^p|^2 \rho \alpha_n^p + 1}, \tag{4.4}$$

where $\rho = 1/\sigma^2$ represents the SNR, and the first term in the denominator models the interference generated by the private symbols, which are decoded only after SIC.

Following the model from Publication [I], it is considered that both users experience SIC error propagation. As a result, after the common message is detected and subtracted through SIC from the superimposed data stream, the uth user observes the following SNR when decoding its private message

$$\gamma_u^p = \frac{|\mathbf{h}_u^H \mathbf{w}_u^p|^2 \rho \alpha_u^p}{\xi |\mathbf{h}_u^H \mathbf{w}^c|^2 \rho \alpha^c + \sum_{n=1, n\neq u}^{2} |\mathbf{h}_u^H \mathbf{w}_n^p|^2 \rho \alpha_n^p + 1}. \tag{4.5}$$

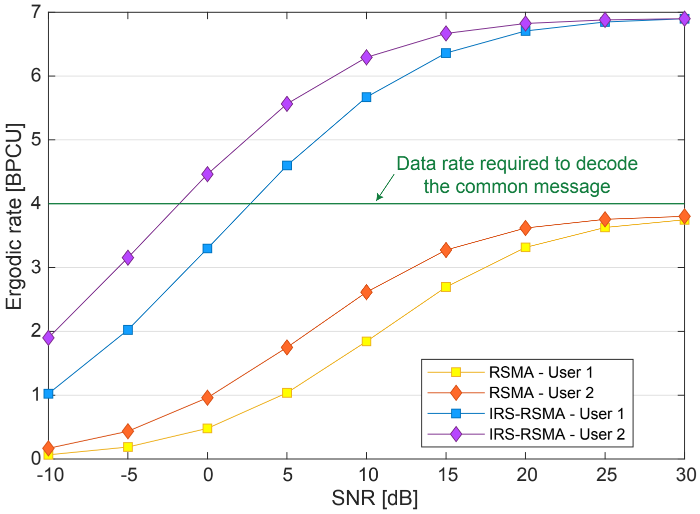

Figure 4.2: Ergodic rates vs. SNR for the common message in RSMA schemes ($\alpha_c = 0.9, \alpha_1 = \alpha_2 = 0.05$) [V], ©2022 IEEE.

where ξ is the SIC error propagation factor and the second term in the denominator models the residual interference from imperfect CSI. The above SINR expressions are used for computing the users' individual rates and sum-rates plotted in Figures 4.2 to 4.4, discussed in the next subsection.

4.1.6 Main Results

Now, the three main performance improvements unleashed by the combination of IRS and MIMO-RSMA are finally presented. To this end, the scenario described in Subsection 4.1.2 is implemented and the performance of our IRS-MIMO-RSMA scheme is compared with various baseline systems, including the conventional MIMO-TDMA, MIMO-NOMA, and MIMO-RSMA schemes. The distance for user 1 is adjusted to $d_1 = 50$ m and for user 2 to $d_2 = 30$ m. The number of BS antennas is set to $M = 4$, and each user is assisted by one IRS with $L = 50$ reflecting elements, where each IRS is deployed 10 m apart from its connected user. Moreover, in all simulation examples, only fixed power allocation policies are considered. Specifically, the power allocation coefficients for users 1 and 2 in the MIMO-NOMA schemes are set to $\alpha_1 = 7/8$ and $\alpha_2 = 1/8$, in the MIMO-TDMA we adjust $\alpha_1 = \alpha_2 = 1$, and in the MIMO-RSMA systems, the power coefficients for the private messages are computed by $\alpha_1 = \alpha_2 = (1 - \alpha_c)/2$, in which different values for α_c are tested in the simulation examples.

The strategy implemented by RSMA of splitting downlink transmissions into two data streams provides IRSs with new opportunities for improvements that are not achievable with other conventional communication schemes. More specifically, the reflecting elements of IRSs can be optimized to improve the performance and simplify the design of

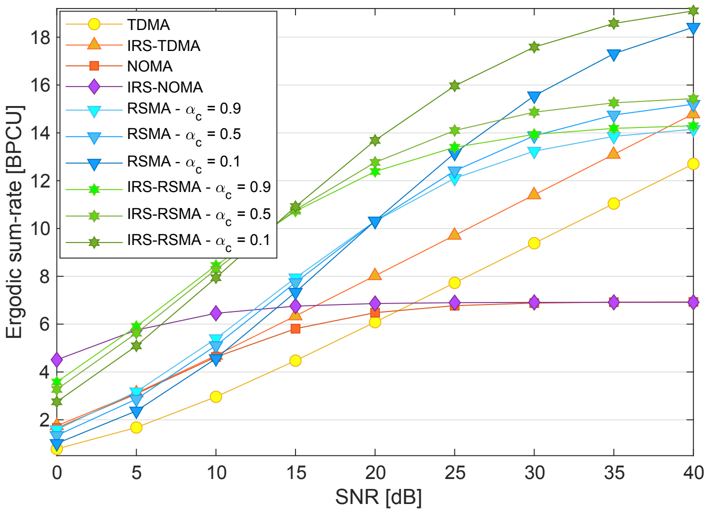

Figure 4.3: Impact of imperfect SIC on the ergodic sum-rates of various MA systems (SIC error factor $= 0.01$) [V], ©2022 IEEE.

precoders for common symbols, which is one of the challenges in MIMO-RSMA. Furthermore, designing a single precoder for satisfying the data rate requisites of all users in the network is not always possible. The capability of IRSs to cope with such an issue is depicted in Figure 4.2, which brings the individual ergodic rates for the common symbol observed with MIMO-RSMA and IRS-MIMO-RSMA. In this example, the conventional MIMO-RSMA is unable to deliver for the two users the minimum rate needed for recovering the common data symbol, leading users to experience rate outage. On the other hand, with the IRS-MIMO-RSMA scheme, users achieve improved data rates that can satisfy the requisites of the common message for SNR values above 5 dB. For instance, when users are in the high-SNR regime and are served with IRS-MIMO-RSMA, an impressive rate of nearly 7 BPCU can be obtained, representing a gain of more than 3 BPCU gainst that achieved with the baseline scheme in the same SNR regime.

As explained, conventional RSMA employs SIC to separate private and common symbols upon reception. However, even though effective, it has been demonstrated that SIC counts with interference limitations. Moreover, in practical conditions, the technique can lead to decoding error propagation, which certainly is detrimental to the performance of RSMA. In this regard, IRSs find a great opportunity for improvement. The benefits delivered by IRS-MIMO-RSMA under imperfect SIC are illustrated in Figure 4.3. As can be observed, the IRS-MIMO-RSMA system can achieve a high sum-rate even in a scenario with SIC error propagation. On the other hand, the two considered NOMA-based baseline schemes have their performance severely degraded by SIC errors, with sum-rate curves saturating at the low value of only 6.9 BPCU. It is also evident that the RSMA schemes are affected by imperfect SIC. Nevertheless, we can see that by properly allocating the power coefficient α_c, both IRS-MIMO-RSMA and MIMO-RSMA can outperform the other schemes. For instance, when allocating to the common message the coefficient $\alpha_c = 0.5$ and con-

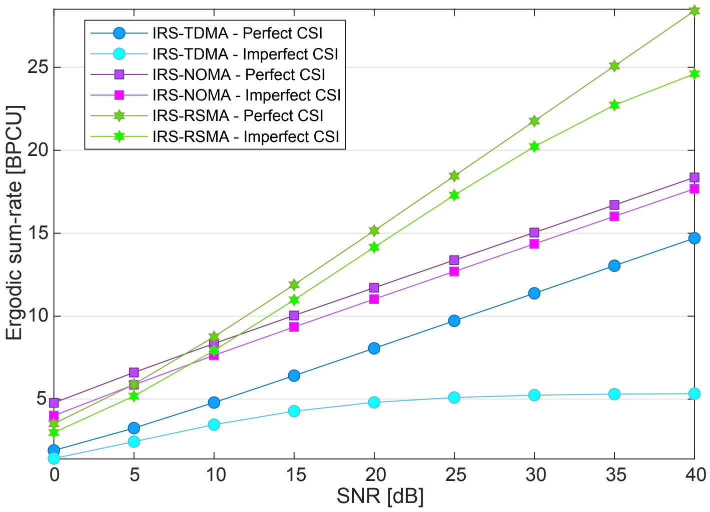

Figure 4.4: Ergodic sum-rate curves for various MA systems under imperfect CSI (channel error variance = 0.5, $\alpha_c = 0.9, \alpha_1 = \alpha_2 = 0.05$) [V], ©2022 IEEE.

sidering an SNR value of 25 dB, the IRS-MIMO-RSMA scheme can offer an impressive sum-rate of 14 BPCU, which outperforms the sum-rate achieved by the other baseline schemes, including the conventional MIMO-RSMA system for all considered power coefficients α_c.

The accurate acquisition of reflected channels remains a major challenge in IRS-assisted communication. Because IRSs are engineered solely with nearly passive electronic elements, channel estimation turns out to be a complicated task, making imperfect CSI almost unavoidable. Fortunately, the robustness to inaccurate CSI is one of the main advantages of RSMA, a feature that is of great help to IRS technology. This benefit is confirmed in Figure 4.4, our last result of Publication [V]. This simulation example demonstrates the ergodic sum-rates achieved with various IRS-assisted systems in scenarios with perfect and imperfect CSI. As can be seen, the IRS-MIMO-RSMA scheme can offer high sum-rates in the two CSI conditions, surpassing the performance of all other systems from moderate to high values of SNR. With 30 dB, for example, the proposed IRS-MIMO-RSMA scheme delivers a sum-rate of more than 20.2 BPCU despite undergoing imperfect CSI. This rate corresponds to a remarkable gain of more than 6 BPCU over the IRS-MIMO-NOMA counterpart under the same CSI conditions and 15 BPCU over the conventional IRS-TDMA.

4.1.7 Summary

This section presented our first results on the MIMO-RMSA subject. It was demonstrated that the synergy between the disruptive IRS technology and the robust RSMA technique can generate mutual benefits, in which three promising performance gains were identified.

Through illustrative simulation examples, it was shown that IRSs have the potential to improve the transmission performance of both common and private data streams even under adverse conditions, such as when undergoing imperfect CSI and SIC error propagation. Reciprocally, it was demonstrated that the flexible interference management framework enabled with RSMA can provide for IRSs robustness to imperfect CSI, an attractive and desired feature given that IRSs cannot estimate the reflected channels actively, which likely leads to inaccurate channel estimates.

Our results made evident that IRSs can bring further robustness and improve the data rates to RSMA, which can remarkably outperform classical systems. However, it also became clear that, even though IRSs can alleviate some performance degradation, imperfect SIC inevitably limits the data rates of even IRS-MIMO-RSMA schemes. It is crucial then to find more effective strategies to tackle this harmful limitation once and for all. In Publication [VI], more drastic measures are taken to completely remove the need for executing SIC in a novel dual-polarized RSMA transmission technique.

4.2 Dual-Polarized RSMA for Massive MIMO Systems

This section provides the last results of the dissertation, addressing our recent discoveries from Publication [VI] on a new promising dual-polarized MIMO-RSMA transmission strategy that does not rely on SIC. As a result, our dual-polarized MIMO-RSMA scheme is free from the harmful problems introduced by SIC, which addresses our last research question *Q7*.

4.2.1 Motivation and Contributions

The results from Publication [V] presented in the previous section revealed that even with the help of IRSs, the interference limitations and practical issues of SIC degrade the performance of MIMO-RSMA. More specifically, even if SIC is perfect, the common symbols are always detected with interference from the private ones. Moreover, imperfect SIC inevitably introduces errors that impair the decoding of private symbols. These two major SIC limitations saturate the achievable data rates of RSMA, which led us to investigate new innovative solutions. In particular, Publications [III] and [IV] showed that, with the help of IRSs, wave polarization can be exploited to mitigate the limitations of SIC and implement improved user multiplexing. Motivated by the extra DoF offered by the polarization domain, but differently from these two previous papers, in Publication [V], the IRSs are discarded and a novel RSMA technique is proposed for the downlink of dual-polarized massive MIMO networks, relying solely on the polarization domain and without requiring SIC. Specific details and our main contributions are summarized as follows:

- We rely on the strategy of splitting the rates into two data streams and propose a promising new dual-polarized RSMA technique. However, in contrast to the original RSMA concept, common and private symbols are multiplexed in the polarization domain with a simple dynamic approach for maximizing the instantaneous sum-rates of different user groups. Our dynamic polarization multiplexing strategy unlocks users to detect both symbols simultaneously from independent polarizations imposing low computational complexity and being SIC-free. As a result, with a slight additional cross-polar noise, users can experience an overall reduced interference without the degrading limitations of SIC.
- The proposed dynamic polarization multiplexing strategy complicates the statistical characterization of the users' fast-fading channel coefficients. Consequently, carrying out a classical theoretical performance analysis becomes an intricate task. As an alternative, to overcome the mathematical challenge, a deep neural network (DNN) model is implemented for predicting the ergodic sum-rates of the network. Our proposed DNN sum-rate framework is capable of providing accurate predictions. Thus, it provides an efficient alternative to conventional methods, which can be exploited to assist the practical implementation of the proposed dual-polarized RSMA scheme.

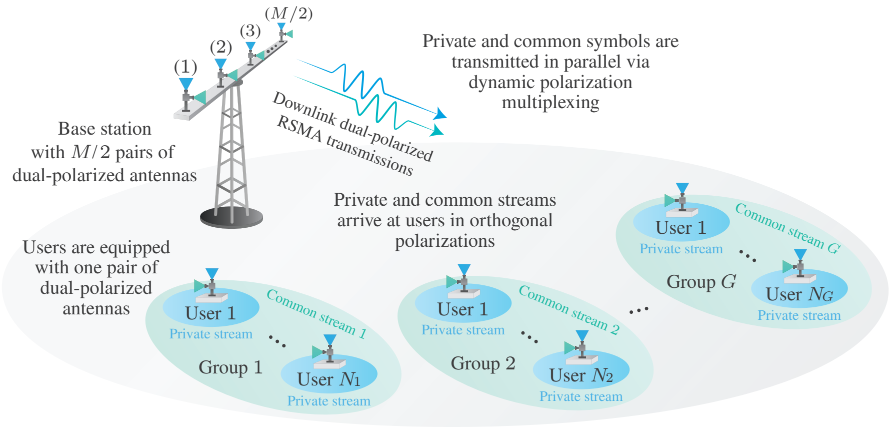

Figure 4.5: Dual-polarized massive MIMO network considered in Publication [VI]. The novel dual-polarized RSMA technique is employed to serve users within different spatial groups.

- To fully unleash the performance potentials of the proposed dual-polarized MIMO-RSMA scheme, our original DNN framework is extended and an efficient dynamic DNN-aided power allocation strategy is implemented, which adaptively allocates the power coefficients of common and private symbols based on observed system parameters.
- Last, extensive simulation results are presented that confirm the advantages of our novel dual-polarized MIMO-RSMA scheme. Our results show that the dual-polarized MIMO-RSMA can impressively outperform all conventional baseline systems, including single and dual-polarized MIMO-NOMA, MIMO-RSMA, MIMO-TDMA, and MIMO-SDMA schemes. The results also reveal that our DNN adaptive power allocation provides further improvements and robustness to both imperfect CSI and cross-polar interference.

4.2.2 System Model

For developing the new dual-polarized RSMA strategy, in Publication [VI] a geometrical scenario based on the one-ring model is implemented, like in Publications [I]–[III]. More specifically, as depicted in Figure 4.5, the target is to study a single-cell network with one BS carrying out downlink transmissions to multiple users organized into G spatial groups comprising N_g users each. Under this scenario, the BS is configured with a uniform linear array containing $M/2$ pairs of dual-polarized antennas, whereas each user employs a single pair of dual-polarized antennas. Moreover, it is assumed that users within a specific group share a common cluster of scatterers. Thus, each group shares a common spatial correlation matrix, which, in Publication [VI], is denoted by $\mathbf{R}_g = \mathbf{I}_2 \otimes \boldsymbol{\Sigma}_g = \mathbf{I}_2 \otimes (\mathbf{Q}_g \boldsymbol{\Delta}_g \mathbf{Q}_g^H)$, where $\boldsymbol{\Sigma}_g \in \mathbb{C}^{\frac{M}{2} \times \frac{M}{2}}$ is the correlation matrix with a rank r_g corresponding to one polarization, which is generated using (2.5). In turn, $\mathbf{\Delta}_g$ denotes the real-valued $\bar{r}_g \times \bar{r}_g$ diagonal matrix with $\bar{r}_g < r_g$ nonzero eigenvalues of $\mathbf{\Sigma}_g$, and $\mathbf{Q}_g$ is the matrix collecting the corresponding dominant eigenvectors.

By combining the correlated and dual-polarized channel representations in (2.4) and (2.6), a channel matrix is modeled for the nth user in the gth group as follows

$$\mathbf{H}_{gn} = \begin{bmatrix} \mathbf{h}_{gn}^{vv} & \mathbf{h}_{gn}^{vh} \\ \mathbf{h}_{gn}^{hv} & \mathbf{h}_{gn}^{hh} \end{bmatrix} = \left[\mathbf{I}_2 \otimes \left(\mathbf{Q}_g \mathbf{\Delta}_g^{\frac{1}{2}} \right) \right] \begin{bmatrix} \mathbf{g}_{gn}^{vv} & \sqrt{\chi} \mathbf{g}_{gn}^{vh} \\ \sqrt{\chi} \mathbf{g}_{gn}^{hv} & \mathbf{g}_{gn}^{hh} \end{bmatrix}, \tag{4.6}$$

where $\mathbf{g}_{gn}^{ab} \in \mathbb{C}^{\bar{r}_g}$ represents the reduced-dimension fast-varying channel vector from the polarization a to the polarization b, with $a, b \in \{v, h\}$, and $\chi \in [0, 1]$ is the inverse cross-polar discrimination.

CSI Estimation and Acquisition

We consider that the proposed MIMO system operates in the FDD mode. Thus, the reduced dimension fast-fading channels, $\mathbf{g}_{gn}^{ab}$, are estimated by downlink training and fed back to the BS through an uplink control link imposing a low overhead. However, as explained in Subsection 2.1.4, quantization errors and other issues make the acquisition of $\mathbf{g}_{gn}^{ab}$ imperfect at the BS. Following the model in (2.10), the imperfect channel estimation is characterized through

$$\hat{\mathbf{g}}_{gn}^{ij} = \sqrt{1 - \tau^2} \mathbf{g}_{gn}^{ij} + \tau \mathbf{z}_{gn}^{ij}, \tag{4.7}$$

where $\mathbf{z}_{gn}^{ab}$ is a complex standard Gaussian random vector independent of $\mathbf{g}_{gn}^{ab}$, and τ is the factor informing the CSI estimation quality.

On the other hand, because the correlation matrices are slowly varying, they can be estimated with accuracy by long-term measurements. Therefore, it is assumed that a perfect estimate of $\mathbf{\Sigma}_g$ is available at the BS.

4.2.3 Dual-Polarized Rate-Splitting Multiple Access

Now, the details of the proposed dual-polarized RSMA technique are introduced. First, following the encoding process of RSMA, the original data messages intended for users within each group are divided into two parts. The first parts of each user within the gth group are encoded into a common supersymbol, represented by x_g^c, whereas the second parts are encoded individually into private symbols, which are denoted by x_{gn}^p. For successful decoding, all users in the gth group should receive the common symbol x_g^c, while only the intended nth user should decode x_{gn}^p. In the conventional RSMA, after applying linear precoding techniques to x_g^c and x_{gn}^p, the achieved data streams are superimposed in

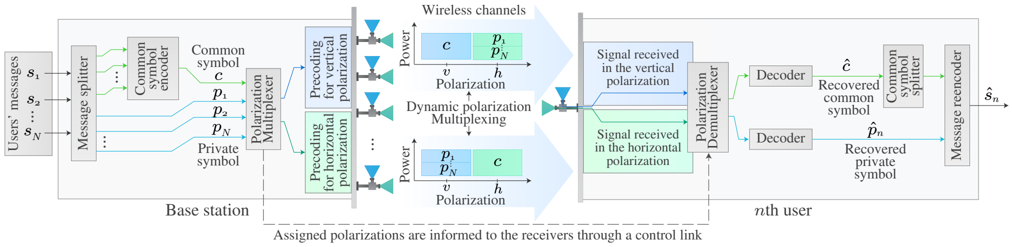

Figure 4.6: Dual-polarized MIMO-RSMA transceiver. Private and common streams are transmitted in parallel via the polarization domain [VI], ©2022 IEEE.

the power domain, which demands users to execute SIC, thereby introducing degrading issues. To avoid the limitations of RSMA revealed in our previous publication, a different approach is proposed, which relies on the polarization domain without requiring SIC. Specifically, common and private symbols are transmitted in parallel to linearly precoded data streams using orthogonal antenna polarizations. To this end, the following signal is transmitted

$$\mathbf{x} = \sum_{g=1}^{G} \mathbf{P}_g \left(\sum_{n=1}^{N_g} \mathbf{w}_{gn}^p \sqrt{P\zeta_{gn}\alpha_{gn}^p x_{gn}^p} + \mathbf{w}_g^c \sqrt{P\zeta_{gn}\alpha_g^c x_g^c} \right), \tag{4.8}$$

where P denotes the power budget available at the BS, ζ_{gn} represents the path-loss coefficient for the nth user within the gth group, and the coefficients α_g^c and α_{gn}^p represent the power coefficients for the common and private symbols, respectively, satisfying $\alpha_g^c + \sum_{n=1}^{N_g} \alpha_{gn}^p = 1$. The matrix $\mathbf{P}_g = \left(\mathbf{I}_2 \otimes \bar{\mathbf{P}}_g\right) \in \mathbb{C}^{M \times \bar{\bar{M}}}$ is the precoder for spatial multiplexing, with $\bar{\mathbf{P}}_g \in \mathbb{C}^{\frac{M}{2} \times \bar{M}}$ representing the precoding matrix for one polarization, such that $\bar{M} \triangleq \bar{\bar{M}}/2$ is the parameter that determines the dimension of the transformed channel. The matrix $\bar{\mathbf{P}}_g$ is constructed identically as the first stage precoder in (2.13), i.e., designed only to cancel spatial interference based on the correlation matrices of interfering groups. In turn, the vectors $\mathbf{w}_g^c \in \mathbb{C}^{\bar{\bar{M}}}$ and $\mathbf{w}_{gn}^p \in \mathbb{C}^{\bar{\bar{M}}}$ denote the precoders designed for multiplexing common and private symbols in polarizations i_g^c and i_g^p, with $i_g^c \neq i_g^p \in \{v, h\}$, having the following structure

$$\mathbf{w}_g^c = \begin{bmatrix} \mathbf{w}_g^{c,v} \\ \mathbf{0} \end{bmatrix}, \ \mathbf{w}_{gn}^p = \begin{bmatrix} \mathbf{0} \\ \mathbf{w}_{gn}^{p,h} \end{bmatrix}, \text{ if } i_g^c = v, \text{and } i_g^p = h, \tag{4.9}$$

$$\mathbf{w}_g^c = \begin{bmatrix} \mathbf{0} \\ \mathbf{w}_g^{c,h} \end{bmatrix}, \ \mathbf{w}_{gn}^p = \begin{bmatrix} \mathbf{w}_{gn}^{p,v} \\ \mathbf{0} \end{bmatrix}, \text{ if } i_g^c = h, \text{and } i_g^p = v. \tag{4.10}$$

The polarizations i_g^c and i_g^p at each channel coherence interval are determined through a dynamic strategy aiming at maximizing the instantaneous sum-rates of each group. More specifically, based on the imperfect CSI model in (4.7), the BS estimates the instantaneous rates of the common and private symbols observed at each user, defined by $\hat{R}^c_{gn}$ and $\hat{R}^p_{gn}$, and computes the polarizations i^c_g and i^p_g as follows

$$\underset{i^c_g, i^p_g}{\arg\max} \sum_{n=1}^{N_g} \left[\hat{R}^p_{gn} + \min_{l \in \{1, \cdots, N_g\}} \hat{R}^c_{gl} \right]. \tag{4.11}$$

Then, to enable the decoding of the transmitted symbols, the assigned polarizations i^c_g and i^p_g are informed back to the users. Upon reception, the uth user in the gth group recovers its private message from the predetermined polarization i^p_g and the common message from i^c_g. This strategy removes the need for SIC and, as we are going to see, leads to impressive performance improvements. A schematic diagram of the proposed dual-polarized RSMA scheme is presented in Figure 4.6.

SINR Analysis

By assuming that all intergroup interference has been cancelled by the precoders $\bar{\mathbf{P}}_g$, the signal received by the nth user in the gth group can be expressed by

$$\begin{aligned}\mathbf{y}_{gn} = &\begin{bmatrix} (\mathbf{g}^{vv}_{gn})^H \boldsymbol{\Delta}_g^{\frac{1}{2}} \mathbf{Q}_g^H \bar{\mathbf{P}}_g & \sqrt{\chi}(\mathbf{g}^{hv}_{gn})^H \boldsymbol{\Delta}_g^{\frac{1}{2}} \mathbf{Q}_g^H \bar{\mathbf{P}}_g \\ \sqrt{\chi}(\mathbf{g}^{vh}_{gn})^H \boldsymbol{\Delta}_g^{\frac{1}{2}} \mathbf{Q}_g^H \bar{\mathbf{P}}_g & (\mathbf{g}^{hh}_{gn})^H \boldsymbol{\Delta}_g^{\frac{1}{2}} \mathbf{Q}_g^H \bar{\mathbf{P}}_g \end{bmatrix} \\ &\times \left(\sum_{u=1}^{N_g} \mathbf{w}^p_{gu} \sqrt{P \zeta_{gu} \alpha^p_{gu}} x^p_{gu} + \mathbf{w}^c_g \sqrt{P \zeta_{gu} \alpha^c_g} x^c_g \right) + \begin{bmatrix} n^v_{gn} \\ n^h_{gn} \end{bmatrix},\end{aligned} \tag{4.12}$$

where n^a_{gn} represents noise achieved by the nth user in its antenna element with the polarization $a \in \{v, h\}$, following the complex Gaussian distribution with zero mean and variance σ^2.

With the above signal model, the SINR observed by the nth user within the gth group when detecting the common symbol can be expressed as follows

$$\gamma^c_{gn} = \frac{|(\mathbf{g}^{i^c i^c}_{gn})^H \boldsymbol{\Delta}_g^{\frac{1}{2}} \mathbf{Q}_g^H \bar{\mathbf{P}}_g \mathbf{w}_g^{c, i^c_g}|^2 \rho \zeta_{gn} \alpha^c_g}{\chi \sum_{u=1}^{N_g} |(\mathbf{g}^{i^p_g i^c_g}_{gn})^H \boldsymbol{\Delta}_g^{\frac{1}{2}} \mathbf{Q}_g^H \bar{\mathbf{P}}_g \mathbf{w}_{gu}^{p, i^p_g}|^2 \rho \zeta_{gn} \alpha^p_{gu} + 1}, \tag{4.13}$$

where $\rho = P/\sigma^2$ is the SNR, and the first denominator term corresponds to the cross-polar interference originating from the polarization i^p_g at the BS to polarization i^c_g at the user. In its turn, the SINR for the private message achieved by the uth user within the gth group can be given by

$$\gamma^p_{gn} = \frac{|(\mathbf{g}^{i^p_g i^p_g}_{gn})^H \boldsymbol{\Delta}_g^{\frac{1}{2}} \mathbf{Q}_g^H \bar{\mathbf{P}}_g \mathbf{w}_{gn}^{p, i^p_g}|^2 \rho \zeta_{gn} \alpha^p_{gn}}{\chi |(\mathbf{g}^{i^c i^p}_{gn})^H \boldsymbol{\Delta}_g^{\frac{1}{2}} \mathbf{Q}_g^H \bar{\mathbf{P}}_g \mathbf{w}_g^{c, i^c_g}|^2 \rho \zeta_{gn} \alpha^c_g + \Psi^{i^p_g}_{gn} + 1}. \tag{4.14}$$

where the first denominator term represents the cross-polar interference, and the factor $\Psi_{gn}^{i_g^p} = \sum_{u=1,u\neq n}^{N_g} |(\mathbf{g}_{gn}^{i_g^p i_g^p})^H \mathbf{\Delta}_g^{\frac{1}{2}} \mathbf{Q}_g^H \bar{\mathbf{P}}_g \mathbf{w}_{gu}^{p,i_g^p}|^2 \rho \zeta_{gn} \alpha_{gu}^p$ models the residual interference of imperfect CSI.

Precoding for the Common and Private Symbols

More information on the common and private precoders is provided in this subsection. First, the precoder $\mathbf{w}_{gn}^{p,i_g^p} \in \mathbb{C}^{\bar{M}}$ is explained, which is designed to tackle interuser interference of private streams within each spatial group in the polarization $i_g^p \in \{v, h\}$. For accomplishing this goal, the private precoder must ensure $\big[(\mathbf{g}_{gn'}^{i_g^p i_g^p})^H \mathbf{\Delta}_g^{\frac{1}{2}} \mathbf{Q}_g^H \bar{\mathbf{P}}_g\big] \mathbf{w}_{gn}^{p,i_g^p} \approx 0$, for $\forall n' \neq n \in \{1, \cdots, N_g\}$. To this end, first, we define

$$\hat{\mathbf{H}}_g^{i_g^p} = \big[\bar{\mathbf{P}}_g^H \mathbf{Q}_g \mathbf{\Delta}_g^{\frac{1}{2}} \hat{\mathbf{g}}_{g1}^{i_g^p i_g^p}, \cdots, \bar{\mathbf{P}}_g^H \mathbf{Q}_g \mathbf{\Delta}_g^{\frac{1}{2}} \hat{\mathbf{g}}_{gN_g}^{i_g^p i_g^p}\big] \in \mathbb{C}^{\bar{M} \times N_g}. \tag{4.15}$$

Then, we can construct $\mathbf{w}_{gn}^{p,i_g^p}$ as a zero-forcing precoder, as follows

$$\mathbf{w}_{gn}^{p,i_g^p} = \big[\hat{\mathbf{H}}_g^{i_g^p} \big((\hat{\mathbf{H}}_g^{i_g^p})^H \hat{\mathbf{H}}_g^{i_g^p} \big)^{-1} \big]_{:n}, \tag{4.16}$$

where $\bar{M} \geq N_g$ must be satisfied.

Now, the focus is on the design of the precoding vector $\mathbf{w}_g^{c,i_g^c} \in \mathbb{C}^{\bar{M}}$, which is responsible for broadcasting the common symbol in the polarization i_g^c. Because the common symbol should be delivered to all users within each group, $\mathbf{w}_g^{c,i_g^c}$ should be constructed as a multicast precoder. As stated in [91], the main issue that limits the sum-rate of multicast systems is the performance of the weakest users. Therefore, $\mathbf{w}_g^{c,i_g^c}$ should be designed aiming at maximizing the worst observed SINR, which can be achieved as follows:

$$\begin{aligned} \max_{{\mathbf{w}_g}^{c,i_g^c}} \quad & \min_{\forall l \in \{1, \cdots . N_g\}} \gamma_{gn}^c, \\ \text{s.t.} \quad & \|\mathbf{w}_g^{c,i_g^c}\|^2 = 1. \end{aligned} \tag{4.17}$$

However, for arbitrary numbers of antennas, (4.17) is a nonconvex NP-hard problem [91]. As a result, (4.17) can only be solved suboptimally through iterative methods, which usually have high computational complexity, e.g., semidefinite relaxation and successive convex approximation-based methods [92]. Fortunately, a low-complexity solution can be achieved when large antenna arrays are employed. Specifically, when $M \to \infty$, the asymptotic solution for the problem in (4.17) is given by a linear combination of the effective channel vectors of users within each group, which is given by [13]

$$\mathbf{w}_g^{c,i_g^c} = \sum_{n=1}^{N_g} \mu_{gn} \bar{\mathbf{P}}_g^H \mathbf{Q}_g \mathbf{\Delta}_g^{\frac{1}{2}} \hat{\mathbf{g}}_{gn}^{i^c i^c}, \tag{4.18}$$

which can be seen as a weighted matched filter (MF) precoding vector for the assigned polarization $i_g^c \in \{v, h\}$, with μ_{gn} representing the weight corresponding to the nth user in the gth group. In Publication [VI], equal weights are allocated to all users, i.e., $\mu_{g1} = \cdots = \mu_{gN_g} = \mu_g$. More specifically, the weight μ_g is computed by

$$\mu_g^2 = \frac{1}{N_g^2 \left(\boldsymbol{\omega}_g^H \bar{\mathbf{P}}_g^H \bar{\mathbf{P}}_g \boldsymbol{\omega}_g\right)}, \tag{4.19}$$

where $\boldsymbol{\omega}_g = \frac{1}{N_g} \sum_{n=1}^{N_g} \bar{\mathbf{P}}_g^H \mathbf{Q}_g \boldsymbol{\Delta}_g^{\frac{1}{2}} \hat{\mathbf{g}}_{gn}^{i^c i^c}$, which meets the magnitude constraint in (4.17).

4.2.4 Ergodic Sum-Rate and Power Allocation with DNNs

Ergodic Sum-Rate

The ergodic sum-rate is an important performance metric for designing a wireless communication system, as it informs the maximum throughput that can be transmitted with reliability, i.e., with a negligible error probability. For the proposed MIMO-RSMA scheme, the instantaneous rate achieved by the nth user within the gth group is defined by the sum of the common and private data rates, computed, respectively, by

$$R_{gn}^c = \min_{\forall l \in \{1, \cdots, N_g\}} \{\log_2(1 + \gamma_{gl}^c)\}, \tag{4.20}$$

and

$$R_{gn}^p = \log_2(1 + \gamma_{gn}^p). \tag{4.21}$$

As a result, the ergodic sum-rate for the gth group can be derived analytically by averaging the sum $\sum_{n=1}^{N_g}(R_{gn}^p + R_{gn}^c)$ as follows

$$\bar{R}_g = \sum_{n=1}^{N_g} \left(\int_0^\infty \log_2(1 + x) f_{\gamma_{gn}^p}(x) dx + \int_0^\infty \log_2(1 + y) f_{\gamma_{g(1)}^c}(y) dy \right), \tag{4.22}$$

where $f_{\gamma_{gn}^p}(x)$ represents the PDF of γ_{gn}^p, and $f_{\gamma_{g(1)}^c}(y)$ corresponds to the PDF of the first order statistic of the gain γ_{gn}^c, i.e., $\min_{\forall l}\{\gamma_{gl}^c\}$. The first challenge for solving (4.22) is to obtain these PDFs. Because of the imperfect CSI, the cross-polar interference, the employed precoders, and the correlated gains in the SINRs in (4.13) and (4.14), deriving exactly $f_{\gamma_{gn}^p}(x)$ and $f_{\gamma_{g(1)}^c}(y)$ is highly complicated. The incapability of obtaining these PDFs, combined with the dynamic policy employed for polarization multiplexing in (4.11), makes it impossible to solve (4.22). As an alternative, efficient DNNs are implemented to predict the ergodic sum-rates of the proposed system, more details of which are provided in the next subsection.

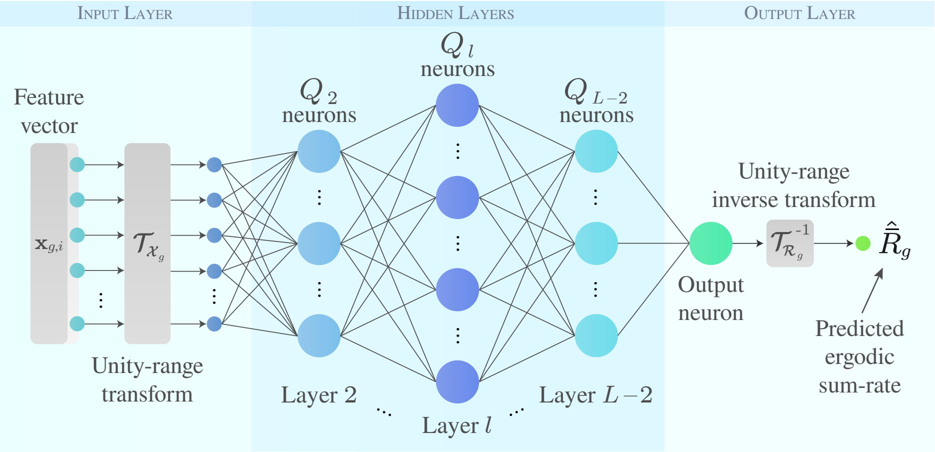

Figure 4.7: Illustration of the implemented DNN model for sum-rate prediction.

DNN for Ergodic Sum-Rate Prediction

For predicting the ergodic sum-rates, a DNN model containing L fully-connected layers, with Q_l neurons in the lth layer, is implemented. Moreover, the convention that the 1st layer represents the input layer is used, and the Lth layer corresponds to the output layer. To reduce the model complexity and speed up the training phase, the groups are addressed independently, i.e., one DNN is implemented for each group. Under such considerations, the training dataset for the gth spatial group is represented by $\mathcal{D}_g = \{(\mathbf{x}_{g,i}, \bar{R}_{g,i}) | \mathbf{x}_{g,i} \in \mathcal{X}_g, \bar{R}_{g,i} \in \mathbb{R}, i = 1, \cdots, |\mathcal{D}_g|\}$, where $\bar{R}_{g,i}$ denotes the target ergodic sum-rate in the ith sample of $\mathcal{D}_g$, and $\mathbf{x}_{g,i}$ represents the ith feature vector with $b_{\mathcal{X}_g} = 2N_g + 7$ parameters, which is organized as $\mathbf{x}_{g,i} = [M, \bar{M}, N_g, \chi, \tau, \alpha^c_g, [\alpha^p_{g1}, \cdots, \alpha^p_{gN_g}], [\zeta_{g1}, \cdots, \zeta_{gN_g}], \rho]^T$.

To avoid an unstable and slow convergence in the training phase, both input and output samples are scaled to the unity range. Specifically, for a data sample $\mathbf{x}_i \in \mathcal{X}$, the following entrywise transformation is applied:

$$\mathcal{T}_{\mathcal{X}}\{\mathbf{x}_i\} = \frac{\mathbf{x}_i - \min_{\forall j \in \{1,\cdots,|\mathcal{X}|\}}(\mathbf{x}_j)}{\max_{\forall j \in \{1,\cdots,|\mathcal{X}|\}}(\mathbf{x}_j) - \min_{\forall j \in \{1,\cdots,|\mathcal{X}|\}}(\mathbf{x}_j)}. \tag{4.23}$$

As a result, the underlying function of the DNN for ergodic sum-rate prediction for the gth group can be written as

$$\hat{\bar{R}}_g(\mathbf{x}_{g,i}) = \mathcal{T}^{-1}_{\mathcal{R}_g}\{\mathbf{r}_{L-1} \circ \mathbf{r}_{L-2} \circ \cdots \circ \mathbf{r}_1(\mathcal{T}_{\mathcal{X}_g}\{\mathbf{x}_{g,i}\})\}, \tag{4.24}$$

where $\mathcal{T}^{-1}_{\mathcal{R}_g}\{\cdot\}$ is the inverse of (4.23), with $\mathcal{R}_g$ and $\mathcal{X}_g$ denoting, respectively, the subsets of target outputs and input parameters for the gth group, and $\mathbf{r}_l(\cdot)$ models the transformation applied to the input data in the lth layer, which can be defined by

$$\mathbf{r}_l(\mathbf{x}) = \pi_l\left(\mathbf{W}_l\mathbf{x} + \mathbf{b}_l\right), \forall l \in \{1, \cdots, L-1\}, \tag{4.25}$$

with $\mathbf{x}$ representing the data input for the lth layer. Moreover, $\mathbf{W}_l \in \mathbb{R}^{Q_l \times Q_{l-1}}$ denotes the matrix of weights between the lth and $(l-1)$th layers, and $\mathbf{b}_l \in \mathbb{R}^{Q_l}$ and $\pi_l : \mathbb{R}^{Q_l} \to \mathbb{R}^{Q_l}$ are the bias vector and the activation function employed in the lth layer, respectively. Specifically, in the $L-2$ hidden layers, the rectified linear unity (ReLU) activation function is adopted, which is defined by $\pi_l(\mathbf{x}) = \max(0, \mathbf{x})$, $\forall l \in \{1, \cdots, L-2\}$, whereas in the output layer, a linear activation function is employed. The proposed DNN model is illustrated in Figure 4.7.

Furthermore, the mean-squared error (MSE) loss is adopted as our cost function, and the samples in the dataset $\mathcal{D}_g$ are partitioned into J random batches for training. Thus, the MSE loss function for the jth batch, $\forall j \in \{1, \cdots, J\}$, can be expressed by

$$\mathcal{L}_{\mathcal{D}_{g,j}}(\mathbf{\Lambda}_g) = \frac{1}{S}\sum_{s=1}^{S}\left|\hat{\bar{R}}_g(\mathbf{x}_{g,s}) - \bar{R}_{g,s}\right|^2, \tag{4.26}$$

where $\mathcal{D}_{g,j} = \{(\mathbf{x}_{g,s}, \bar{R}_{g,s}) | s = 1, \cdots, S\} \subseteq \mathcal{D}_g$ corresponds to the subset associated with the jth data batch, with S denoting the batch size, i.e., the carnality of $\mathcal{D}_{g,j}$.

DNN-Aided Adaptive Power Allocation

Following Publication [V], a uniform power allocation policy for the private symbols is employed, which is computed as a function of the coefficient for the common message, based on the formula $\alpha^p_{gu} = (1 - \alpha^c_g)/N_g$. With this approach, even though simple, it is still necessary to employ a strategy to determine the most suited power coefficient α^c_g. Because the target is to maximize the ergodic sum-rates observed within each group, α^c_g can be computed by solving the following optimization problem

$$\begin{aligned}&\underset{\alpha^c_g}{\arg\max} \sum_{n=1}^{N_g} \mathrm{E}\left[\log_2(1+\gamma^p_{gn}) + \min_{\forall l}\{\log_2(1+\gamma^c_{gl})\}\right], \\ &\text{s.t.} \quad \alpha^c_g \leq 1.\end{aligned} \tag{4.27}$$

However, owing to the complications in the SINR gains, as pointed out in Subsection (4.2.4), and the dynamic nature of the proposed scheme, solving optimally (4.27) is unwieldy. To overcome this challenge, in this subsection, once more, advantage is taken of the powerful capabilities of DNNs, and an intelligent framework is proposed for approximating the desired power allocation coefficient. More specifically, an adaptive power allocation strategy is implemented with a second DNN model comprising D fully-connected layers, with the dth layer containing V_d neurons.

The power allocation aided-DNN is trained using a new dataset $\mathcal{M}_g = \{(\mathbf{z}_{g,i}, \alpha_{g,i}^{c*}) | \mathbf{z}_{g,i} \in \mathcal{Z}_g, \alpha_{g,i}^{c*} \in \mathbb{R}, i = 1, \cdots, |\mathcal{M}_g|\}$, with $\alpha_{g,i}^{c*}$ representing the target optimal allocation coefficient, i.e., which maximizes the sum-rate, of the ith feature vector $\mathbf{z}_{g,i} \in \mathcal{Z}_g \subseteq \mathbb{R}^{b_{\mathcal{Z}_g}}$, structured as $\mathbf{z}_{g,i} = [M, \bar{M}, N_g, \chi, \tau, [\zeta_{g1}, \cdots, \zeta_{gN_g}], \rho]^T$. For determining the parameters in $\mathbf{z}_{g,i}$ and the associated optimal coefficients $\alpha_{g,i}^{c*}$, an exhaustive search is performed on the existing datasets $\mathcal{D}_g$. Moreover, the vectors $\mathbf{z}_{g,i}$ are scaled to the unity range. However, because the target outputs $\alpha_{g,i}^{c*}$ are already within the range $[0, 1]$, they are not scaled. With these specifications, the underlying function of the DNN for power allocation can be represented by

$$\hat{\Lambda}_g(\mathbf{z}_{g,i}) = \mathbf{r}_{D-1} \circ \mathbf{r}_{D-2} \circ \cdots \circ \mathbf{r}_1(\mathcal{T}_{\mathcal{Z}_g}\{\mathbf{z}_{g,i}\}), \tag{4.28}$$

where $\mathbf{r}_d(\cdot)$ models the transformations applied to the input data and is defined identically as in (4.25), so that ReLU activation functions are adopted in the hidden layers and a linear function in the output layer. Moreover, the MSE loss function is also employed in this DNN model. Thus, the optimal power allocation coefficient for the common message intended for the gth group is computed by

$$\hat{\alpha}_g^{c*} = \min\{1, \hat{\Lambda}_g(\mathbf{z}_{g,i})\}, \tag{4.29}$$

for satisfying the constraint in (4.27). After the training is properly performed, this DNN strategy should be able to accurately estimate the optimal power coefficient at each channel coherence interval. For more details on this power allocation strategy, readers are referred to Publication [VI].

Complexity Remarks

Our strategy of addressing each group of users in a separate manner removes the need for using as an input the high-dimensional $M \times M$ spatial correlation matrices in the implemented DNNs, which considerably reduces the complexity of the model design and training. Regarding computational complexity, however, the training phase of DNNs is usually more computationally intensive. However, highly efficient hardware oriented to artificial intelligence applications, such as tensor processing units (TPUs) and graphics processing units (GPUs), are available and can be used for training. As a result, the complexity of one forward pass after the DNNs have been trained becomes more relevant for practical implementations, which can be measured by floating-point operations [93]. In particular, the computational complexity of one forward pass for the DNN model implemented for sum-rate prediction can be given by $\mathcal{O}(\sum_{l=1}^{L} Q_{l-1} Q_l)$.

For the case of the DNN for power allocation, the computational complexity for generating the datasets $\mathcal{M}_g$ also deserves attention. Recall that $\mathcal{M}_g$ is generated through an exhaustive search on the samples of $\mathcal{D}_g$. Like any brute-force approach, performing such a search can be complex. Fortunately, this is not a frequent task because we need to construct (or update) $\mathcal{M}_g$ once before the training phase starts. After the DNN for power allocation has been properly trained, it is possible to efficiently predict the optimal power coefficients imposing a computational complexity of only $\mathcal{O}(\sum_{d=1}^{D} V_{d-1}V_d)$.

Datasets Generation and DNN Implementation

For achieving datasets of manageable sizes, the number of spatial groups is limited to $G = 3$ and the number of users is set to $N_1 = \cdots = N_g = 3$ in each group. As a result, the input vectors $\mathbf{x}_{g,i}$ and $\mathbf{z}_{g,i}$ with the lengths $b_{\mathcal{X}_g} = 13$ and $b_{\mathcal{Z}_g} = 9$, respectively, are achieved. Furthermore, a large number of Monte Carlo simulations were run for generating the data samples of $\mathcal{D}_g$ and $\mathcal{M}_g$, for $g = 1, \cdots, G$, so that, for each group, a total of $6,561,000$ samples for $\mathcal{D}_g$, and $72,900$ samples for $\mathcal{M}_g$ were obtained. To this end, the communication scenario and the dual-polarized RSMA scheme proposed in subsections 4.2.2 and 4.2.3, respectively, were implemented in the open-source high-performance Julia Programming Language [94].

The DNNs proposed in the two previous subsections were implemented and trained in Python 3.9.11 using Tensor Flow Metal 2.8.0 on a MacBook Pro computer with an M1 Max 10-core processor, 32-core GPU, and 32 GB of memory. The number of layers in the DNN for sum-rate prediction was adjusted to $L = 7$, in which the first and last hidden layers were configured with $Q_2 = Q_6 = 128$ neurons, and the rest of the hidden layers with $Q_3 = Q_4 = Q_5 = 256$ neurons each one. In the case of power allocation, a DNN model was implemented containing $D = 6$ layers in total, with the number of neurons in the first and last hidden layers set to $V_2 = V_5 = 128$ and, in the rest of the hidden layers, to $V_3 = V_4 = 256$. The adaptive moment estimation (ADAM) optimizer was adopted, where batch sizes of 1000 and 100 samples were adjusted for the sum-rate prediction and power allocation DNNs, respectively. Moreover, both DNNs were trained during 80 epochs. In this regard, Figure 4.8 shows the root mean squared error (RMSE) achieved over time during the training phase of the two DNNs. Because the learning rate of 0.001 provided the lowest RMSE, the value was configured as the standard in the results presented in the following subsection.

4.2.5 Main Results

The most relevant background now being explained, our main results can be presented. To illustrate the performance advantages of the proposed dual-polarized MIMO-RSMA transmission scheme, the conventional single-polarized MIMO-RSMA, MIMO-TDMA, MIMO-SDMA, MIMO-NOMA, and the dual-polarized MIMO-NOMA approach proposed in [7] are considered as our baseline systems. All simulated systems are configured with $M = 64$ BS antennas, meaning that the dual-polarized schemes employ $M/2 = 32$ pairs of dual-polarized antennas. Moreover, a total of $G = 3$ spatial groups are implemented, each one containing $N = 3$ users. The focus is on the first group, which exhibits an angular spread of 11° and is positioned at the azimuth angle of 20°. Within the group

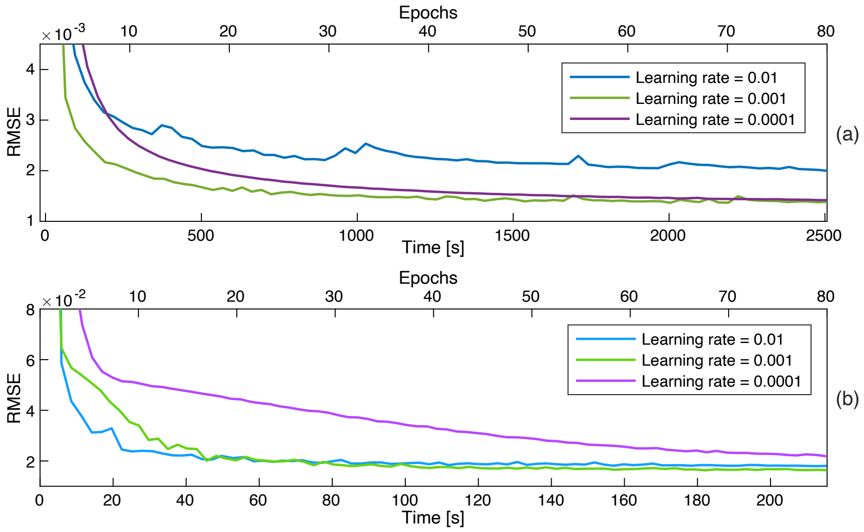

Figure 4.8: Training convergence behavior in terms of RMSE for: (a) DNN for ergodic sum-rate prediction, and (b) DNN for adaptive power allocation [VI], ©2022 IEEE.

of interest, users 1, 2, and 3 are located $d_1 = 115$ m, $d_2 = 100$ m, and $d_3 = 85$ m from the BS, and the path-loss coefficients is modeled similarly as in our previous publications, i.e., $\zeta_n = \Phi d_n^{-\eta}$, where the parameters δ and η are adjusted to 40 dB and 2.7, respectively. In addition, we set $\bar{M} = 6$, $P = 1$ W, and, when fixed power allocation is employed, $\alpha^c = 0.5$ and $\alpha_n^p = (1 - \alpha^c)/N \approx 0.17$ for the MIMO-RSMA schemes. In turn, the power coefficients of users $1, 2,$ and 3 are adjusted to $5/8, 2/8,$ and $1/8$,respectively, in the MIMO-NOMA systems, whereas a uniform allocation policy is used in the MIMO-SDMA schemes, and for the classical MIMO-TDMA counterpart, the full transmit power P is allocated to each user.

The effectiveness of the DNN model implemented for predicting the ergodic sum-rates is corroborated in Figure 4.9, where the users are served with fixed power allocation. As can be noticed, the DNN model can approximate the curves generated by the Monte Carlo simulations with high accuracy for all the tested parameters. These simulation examples also shed light on the important performance characteristics of the proposed system. For example, Figure 4.9(a) shows the performance influence of the power allocation coefficient for the common message in that, depending on the SNR value, a different power coefficient maximizes the sum-rate. In its turn, Figure 4.9(b) demonstrates the degrading effects of imperfect CSI on the performance of the dual-polarized RSMA scheme. We can see that the sum-rate diminishes by increasing the factor τ. Nevertheless, a high data rate can still be achieved even when $\tau = 0.4$, which shows that the robustness to imperfect CSI is maintained in the proposed strategy. In Figure 4.9(c), on the other hand, the ergodic sum-rates suffer severe degradation by increasing the cross-polar interference levels. However, it is noteworthy that such behavior is observed only under fixed power allocation, an issue efficiently addressed by our adaptive DNN power allocation strategy, as discussed next.

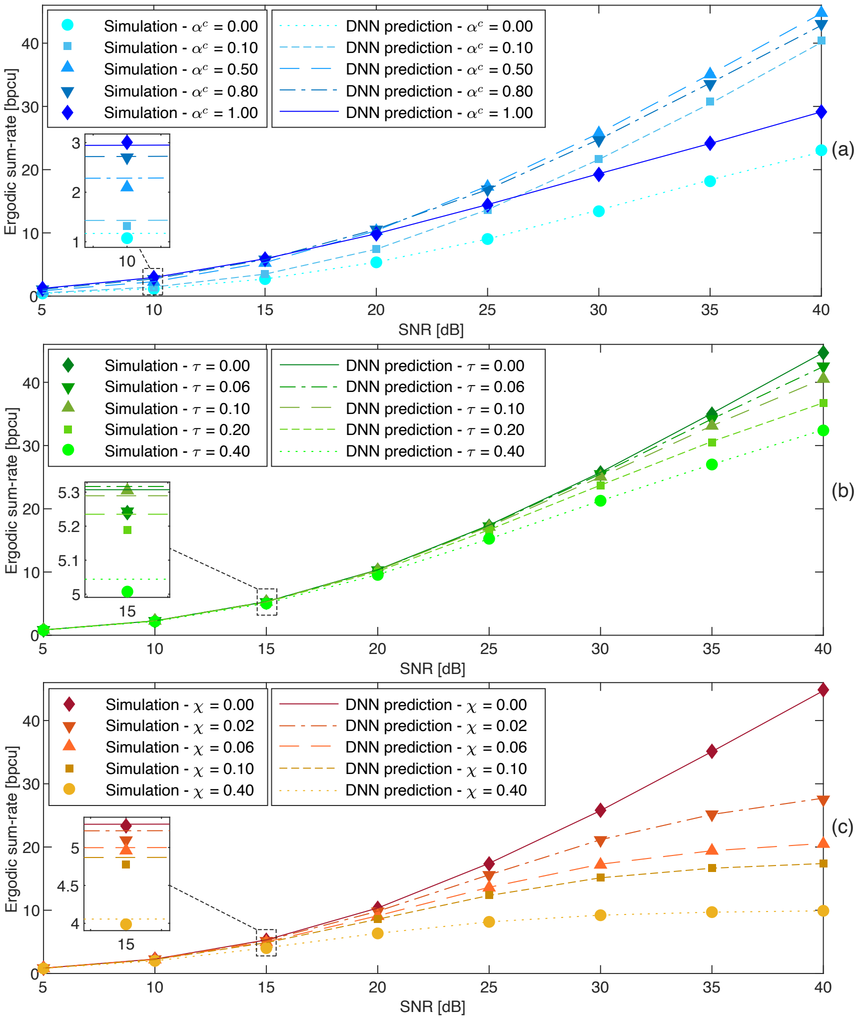

Figure 4.9: Simulated and predicted ergodic sum-rates: (a) for different values of α^c, with $\chi = 0$ and $\tau = 0$, (b) for different values of τ, with $\alpha^c = 0.5$ and $\chi = 0$, and (c) for different values of χ, with $\alpha^c = 0.5$ and $\tau = 0$ [VI], ©2022 IEEE.

The results in Figure 4.10 demonstrate that our dual-polarized MIMO-RSMA strategy can achieve impressive gains over the considered baseline schemes. For instance, in Figure 4.10(a), the sum-rate performance of our scheme is tested with both fixed and the DNN-aided power allocation methods. As can be seen, in the ideal scenario with zero cross-polar interference, the dual-polarized MIMO-RSMA can achieve a sum-rate of a remarkable 40 BPCU, which is more than twice the sum-rates provided by the conventional single-polarized MIMO-SDMA and MIMO-RSMA counterparts. Nevertheless, when the level of cross-polar transmissions is high, the dual-polarized MIMO-RSMA undergoes noticeable performance degradation, so that under fixed power allocation, the

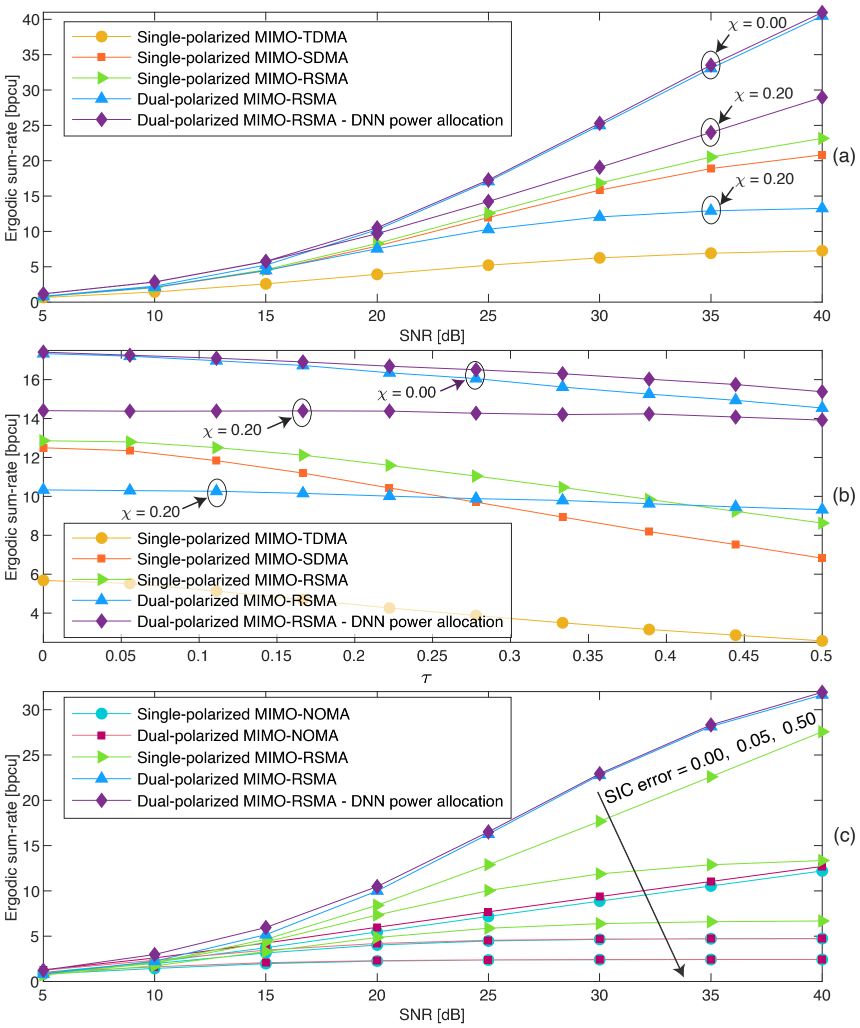

Figure 4.10: Simulated ergodic sum-rates: (a) versus SNR for different levels of χ, with $\tau = 0.1$, (b) versus τ for a SNR of 25 dB and different levels of χ, and (c) versus SNR for different levels of SIC error, with $\chi = 0.01$ and $\tau = 0$ [VI], ©2022 IEEE.

single-polarized MIMO-SDMA and MIMO-RSMA systems can outperform the proposed scheme. On the other hand, we can see that the DNN power allocation can smartly mitigate the limitations caused by cross-polar interference, enabling the dual-polarized MIMO-RSMA to achieve the best performance even with $\chi = 0.2$, which reinforces the efficiency of our DNN strategy.

The advantages of the proposed scheme are further revealed in Figure 4.10(b), where its robustness is tested against imperfect CSI considering different values of the quality factor τ. As can be noticed, the dual-polarized MIMO-RSMA employing the DNN approach can outperform the baseline systems even under high cross-polar interference in all the considered range of τ, which confirms another attractive advantage of our scheme. Last, Figure 4.10(c) shows the advantages of being free from detrimental SIC issues. This figure puts into perspective the sum-rates achieved with our dual-polarized MIMO-RSMA scheme and with conventional SIC-based systems considering different values of SIC error factors. As can be seen, the single-polarized MIMO-RSMA and the single and dual-polarized MIMO-NOMA schemes, which carry out SIC, have their sum-rate performance levels severely diminished by SIC error propagation. Meanwhile, in contrast, the novel dual-polarized MIMO-RSMA system is not impacted by SIC-related problems, which enables it to keep high sum-rates and remarkably outperform the baseline schemes for all the investigated error factors.

4.2.6 Summary

This section presented a novel low-complexity dual-polarized massive MIMO-RSMA scheme, which was proposed in our most recent Publication [VI]. Our promising transmission strategy unlocked users to detect common and private symbols from their orthogonally polarized antennas in parallel. As a beneficial consequence, the users were freed from the degrading effects of SIC-related issues, allowing them to operate under an overall reduced interference. Efficient DNN frameworks were also implemented for ergodic sum-rate prediction and adaptive power allocation, which provided further robustness to both imperfect CSI and cross-polar interference. Our insightful simulation results and discussions corroborated the capabilities of the dual-polarized MIMO-RSMA scheme and revealed its performance superiority. The effectiveness of the proposed DNNs was also validated. Among other highlighted remarks, our results showed that the dual-polarized MIMO-RSMA offers impressive performance gains that outperform all conventional baseline systems even when undergoing high cross-polar interference levels.

5 Conclusions and Future Directions

This doctoral dissertation investigated and implemented promising multi-antenna and MA techniques of great potential for enabling massive access in future beyond-5G and 6G communication systems. Our work generated six primary publications in prestigious journals of high impact factors, which provided answers to our seven research questions, from *Q1* to *Q7*. Our research started with Publication [I], where a major limiting issue of massive MIMO-NOMA systems was identified. Specifically, it was found that decoding errors generated by imperfect SIC can cause severe performance degradation in MIMO-NOMA systems, causing users in the network to experience limited data rates that are lower than those achievable with classical MIMO-OMA schemes. It was also shown that users can experience highly unbalanced data rates when the system operates under fixed power allocation policies, indicating an unfair performance of NOMA. This fairness problem was efficiently solved with a closed-form adaptive power allocation strategy achieved through KKT conditions. In the same work, the practical issues of imperfect SIC were modeled, and a new analytical framework with accurate closed-form expressions was developed for the users' outage probabilities and ergodic rates, composing an effective tool for assessing the performance of MIMO-NOMA.

The limitations of MIMO-NOMA schemes found in Publication [I] steered our research work toward the study of the featured IRS technology, resulting in three subsequent Publications [II]–[IV]. In our magazine article, Publication [II], in particular, by considering only scenarios with perfect SIC decoding, appealing performance improvements that IRS can offer to massive MIMO-NOMA were presented, including a more flexible ordering of users, fair power allocation protocols with enhanced performance, extended communication range, and potentially a better utilization of energy resources. These seminal findings were exploited and extended in Publication [III], where a more practical study case with users experiencing SIC error propagation was considered. More specifically, with the help of advanced dual-polarized IRSs, advantage was taken of the extra DoF offered by the polarization domain to mitigate the detrimental issues of imperfect SIC in a dual-polarized massive MIMO-NOMA network operating in the downlink mode. Through a clever collaborative strategy, dual-polarized IRSs were optimized by interior-point methods to assist the BS in multiplexing subsets of users in the polarization domain. The novel dual-polarized IRS-MIMO-NOMA scheme enabled users to detect transmitted symbols with the benefits of polarization diversity and experiencing reduced interference levels. A closed-form expression was also derived for the asymptotic ergodic rates considering large IRSs. Our results showed that the proposed dual-polarized IRS-MIMO-NOMA scheme is substantially more robust to imperfect SIC and can deliver remarkable spectral gains to all connected users.

In Publication [IV], the IRS-assisted polarization multiplexing concept from Publication [III] was further elaborated on and applied also to the uplink of MIMO-NOMA networks. To mitigate interference issues of SIC in the uplink, the powerful capabilities of dual-polarized IRSs and advanced signal alignment techniques were combined, which generated impressive performance improvements. To avoid unequal data rates and improve fairness in the MIMO-NOMA scheme, our ideas from Publication [I] were extended and a low-complexity alternate power allocation policy was developed, which efficiently balanced the uplink rates of individual users. Our insightful simulation results showed that our uplink IRS-MIMO-NOMA strategy can provide impressive data rate gains and that all users can experience a high uplink performance with the help of the proposed fair power allocation protocol. These contributions concluded Chapter 3.

In Chapter 4, our final two publications were presented, which focused on the promising RSMA technique. The chapter was started by presenting the mutual benefits that IRSs and RSMA can generate for one another, which were reported in Publication [V], our second magazine article. Attractive improvements enabled by the synergy IRS-RSMA were identified and discussed. For instance, on the one hand, it was shown that IRSs can contribute to improved transmissions of common and private data streams even under high levels of SIC error propagation and, on the other hand, that RSMA can enable IRSs to become more robust to imperfect CSI. The results provided in Publication [V] made clear that the combination IRS-MIMO-RSMA is highly advantageous and can remarkably outperform conventional systems, such as MIMO-TDMA, MIMO-SDMA, MIMO-NOMA, and MIMO-RSMA.

Nevertheless, the results from Publication [V] also showed that imperfect SIC can be detrimental even to IRS-MIMO-RSMA schemes. This undesirable characteristic motivated, instead of trying to mitigate SIC decoding errors, to develop in our last publication a novel RSMA-inspired technique that is SIC-free. Specifically, in Publication [VI], a promising dual-polarized MIMO-RSMA scheme was proposed with the potential to free users completely from the harmful SIC interference problems. An efficient DNN-aided power allocation policy was also implemented, which offered the technique with reliability even in scenarios with high cross-polar interference and imperfect CSI, remarkably outperforming the conventional baseline system. With the results reported in Publication [VI], we can conclude this dissertation and leave the readers with a few closing thoughts on our next research steps, as follows.

The performance improvements unleashed by the dual-polarized RSMA technique in Publication [VI] are clearly promising. The presented advantages give us the motivation to investigate the topic further and pave the way for numerous future research directions. For instance, it was discussed in Publication [VI] that a classical theoretical analysis has not been possible because of the complicated system model. However, what if we study a different system model or consider some simplification? Can we derive closed-form expressions of important performance metrics in these cases? Moreover, which benefits can we achieve by combining IRSs with dual-polarized RSMA? And how can we unlock further improvements? These still unsolved questions are exciting topics for our upcoming future works. Stay tuned.

References

[1] J. Brewer, “Kronecker products and matrix calculus in system theory,” *IEEE Trans. Circuits Syst.*, 1978.

[2] I. S. Gradshteyn and I. M. Ryzhik, *Table of Integrals, Series, and Products*, 7th ed. Academic Press, Amsterdam, 2007.

[3] G. Liu, Y. Huang, N. Li, J. Dong, J. Jin, Q. Wang, and N. Li, “Vision, requirements and network architecture of 6G mobile network beyond 2030,” *China Commun.*, vol. 17, no. 9, pp. 92–104, 2020.

[4] E.-K. Hong, I. Lee, B. Shim, Y.-C. Ko, S.-H. Kim, S. Pack, K. Lee, S. Kim, J.-H. Kim, Y. Shin, Y. Kim, and H. Jung, “6G R&D vision: Requirements and candidate technologies,” *J. Commun. Networks*, vol. 24, no. 2, pp. 232–245, 2022.

[5] J. Jeon, G. Lee, A. A. Ibrahim, J. Yuan, G. Xu, J. Cho, E. Onggosanusi, Y. Kim, J. Lee, and J. C. Zhang, “MIMO evolution toward 6G: Modular massive MIMO in low-frequency bands,” *IEEE Commun. Mag.*, vol. 59, no. 11, pp. 52–58, 2021.

[6] A. S. de Sena, P. H. J. Nardelli, D. B. da Costa, F. R. M. Lima, L. Yang, P. Popovski, Z. Ding, and C. B. Papadias, “IRS-assisted massive MIMO-NOMA networks: Exploiting wave polarization,” *IEEE Trans. Wireless Commun.*, vol. 20, no. 11, pp. 7166–7183, 2021.

[7] A. S. de Sena, D. B. da Costa, Z. Ding, and P. H. J. Nardelli, “Massive MIMO-NOMA networks with multi-polarized antennas,” *IEEE Trans. Wireless Commun.*, vol. 18, no. 12, pp. 5630–5642, Dec. 2019.

[8] A. S. de Sena, F. R. M. Lima, D. B. da Costa, Z. Ding, P. H. J. Nardelli, U. S. Dias, and C. B. Papadias, “Massive MIMO-NOMA networks with imperfect SIC: Design and fairness enhancement,” *IEEE Trans. Wireless Commun.*, vol. 19, no. 9, pp. 6100–6115, 2020.

[9] A. S. de Sena, P. H. J. Nardelli, D. B. d. Costa, U. S. Dias, P. Popovski, and C. B. Papadias, “Dual-polarized IRSs in uplink MIMO-NOMA networks: An interference mitigation approach,” *IEEE Wireless Commun. Lett.*, vol. 10, no. 10, pp. 2284–2288, 2021.

[10] Y. Mao, B. Clerckx, and V. O. Li, “Rate-splitting multiple access for downlink communication systems: bridging generalizing and outperforming SDMA and NOMA,” *EURASIP J. Wireless Commun. Networking*, 2018.

[11] O. Dizdar, Y. Mao, and B. Clerckx, “Rate-splitting multiple access to mitigate the curse of mobility in (massive) mimo networks,” *IEEE Trans. Commun.*, vol. 69, no. 10, pp. 6765–6780, 2021.

[12] A. Carleial, “Interference channels,” *IEEE Trans. Inf. Theory*, vol. 24, no. 1, pp. 60–70, 1978.

[13] M. Dai, B. Clerckx, D. Gesbert, and G. Caire, “A rate splitting strategy for massive MIMO with imperfect CSIT,” *IEEE Trans. Wireless Commun.*, vol. 15, no. 7, pp. 4611–4624, 2016.

[14] Z. Ding and V. Poor, “Design of massive-MIMO-NOMA with limited feedback,” *IEEE Signal Proces. Lett.*, vol. 23, no. 5, May 2016.

[15] X. Chen, Z. Zhang, C. Zhong, R. Jia, and D. W. K. Ng, “Fully non-orthogonal communication for massive access,” *IEEE Trans. Wireless Commun.*, vol. 66, no. 4, pp. 1717–1731, Apr. 2018.

[16] M. Zeng, N. Nguyen, O. A. Dobre, and H. V. Poor, “Securing downlink massive MIMO-NOMA networks with artificial noise,” *IEEE J. Sel. Topics Signal Process.*, vol. 13, no. 3, pp. 685–699, Jun. 2019.

[17] Y. Liang, R. Long, Q. Zhang, J. Chen, H. V. Cheng, and H. Guo, “Large intelligent surface/antennas (LISA): Making reflective radios smart,” *J. Commun. Inf. Networks*, vol. 4, no. 2, pp. 40–50, 2019.

[18] M. D. Renzo, A. Zappone, M. Debbah, M. Alouini, C. Yuen, J. D. Rosny, and S. Tretyakov, “Smart radio environments empowered by reconfigurable intelligent surfaces: How it works, state of research, and road ahead,” *IEEE J. Sel. Areas Commun.*, vol. 38, no. 11, pp. 2450–2525, 2020.

[19] Y. Li, Y. Wang, and Q. Cao, “Design of a multifunctional reconfigurable metasurface for polarization and propagation manipulation,” *IEEE Access*, vol. 7, pp. 129 183–129 191, 2019.

[20] H. Sun, B. Xie, R. Q. Hu, and G. Wu, “Non-orthogonal multiple access with SIC error propagation in downlink wireless MIMO networks,” in *Proc. IEEE Veh. Technol. Conf.*, Sep. 2016, pp. 1–5.

[21] S. Li, M. Derakhshani, and S. Lambotharan, “Outage-constrained robust power allocation for downlink MC-NOMA with imperfect SIC,” in *Proc. IEEE Int. Conf. Commun.*, 2018, pp. 1–7.

[22] A. Celik, M. Tsai, R. M. Radaydeh, F. S. Al-Qahtani, and M. Alouini, “Distributed cluster formation and power-bandwidth allocation for imperfect NOMA in DL-HetNets,” *IEEE Trans. Commun.*, vol. 67, no. 2, pp. 1677–1692, 2019.

[23] D. Tweed and T. Le-Ngoc, “Dynamic resource allocation for uplink MIMO NOMA VWN with imperfect SIC,” in *Proc. IEEE Int. Conf. Commun.*, May 2018, pp. 1–6.

[24] Y. Li and G. Amarasuriya, “NOMA-aided massive MIMO downlink with distributed antenna arrays,” in *Proc. IEEE Int. Conf. Commun.*, May 2019, pp. 1–7.

[25] X. Li, M. Liu, C. Deng, P. T. Mathiopoulos, Z. Ding, and Y. Liu, “Full-duplex cooperative NOMA relaying systems with I/Q imbalance and imperfect SIC,” *IEEE Wireless Commun. Lett.*, pp. 1–1, 2019.

[26] Z. Mobini, M. Mohammadi, B. K. Chalise, H. A. Suraweera, and Z. Ding, “Beamforming design and performance analysis of full-duplex cooperative NOMA systems,” *IEEE Trans. Wireless Commun.*, vol. 18, no. 6, pp. 3295–3311, 2019.

[27] X. Li, J. Li, Y. Liu, Z. Ding, and A. Nallanathan, “Residual transceiver hardware impairments on cooperative NOMA networks,” *IEEE Trans. Wireless Commun.*, pp. 1–1, 2019.

[28] J. Kang, I. Kim, and C. Chun, “Deep learning-based MIMO-NOMA with imperfect SIC decoding,” *IEEE Syst. J.*, pp. 1–4, 2019.

[29] S. Timotheou and I. Krikidis, “Fairness for non-orthogonal multiple access in 5G systems,” *IEEE Signal Proces. Lett.*, vol. 22, no. 10, pp. 1647–1651, Oct. 2015.

[30] Y. Liu, M. Elkashlan, Z. Ding, and G. K. Karagiannidis, “Fairness of user clustering in MIMO non-orthogonal multiple access systems,” *IEEE Wireless Commun. Lett.*, vol. 20, no. 7, pp. 1465–1468, Jul. 2016.

[31] J. A. Oviedo and H. R. Sadjadpour, “A fair power allocation approach to NOMA in multiuser SISO systems,” *IEEE Trans. Veh. Technol.*, vol. 66, no. 9, pp. 7974–7985, Sep. 2017.

[32] M. M. Al-Wani, A. Sali, N. K. Noordin, S. J. Hashim, C. Y. Leow, and I. Krikidis, “Robust beamforming and user clustering for guaranteed fairness in downlink NOMA with partial feedback,” *IEEE Access*, vol. 7, pp. 121 599–121 611, Aug. 2019.

[33] M. M. Al-Wani, A. Sali, B. M. Ali, A. A. Salah, K. Navaie, C. Y. Leow, N. K. Noordin, and S. J. Hashim, “On short term fairness and throughput of user clustering for downlink non-orthogonal multiple access system,” in *Proc. IEEE Veh. Technol. Conf.*, Apr. 2019, pp. 1–6.

[34] H. Xing, Y. Liu, A. Nallanathan, Z. Ding, and H. V. Poor, “Optimal throughput fairness tradeoffs for downlink non-orthogonal multiple access over fading channels,” *IEEE Trans. Wireless Commun.*, vol. 17, no. 6, pp. 3556–3571, Jun. 2018.

[35] Z. Xiao, L. Zhu, Z. Gao, D. O. Wu, and X. Xia, “User fairness non-orthogonal multiple access (NOMA) for millimeter-wave communications with analog beamforming,” *IEEE Trans. Wireless Commun.*, vol. 18, no. 7, pp. 3411–3423, Jul. 2019.

[36] Y. Mao, B. Clerckx, J. Zhang, V. O. K. Li, and M. A. Arafah, “Max-min fairness of K-user cooperative rate-splitting in MISO broadcast channel with user relaying,” *IEEE Trans. Wireless Commun.*, vol. 19, no. 10, pp. 6362–6376, 2020.

[37] L. Yin and B. Clerckx, “Rate-splitting multiple access for multigroup multicast and multibeam satellite systems,” *IEEE Trans. Commun.*, vol. 69, no. 2, pp. 976–990, 2021.

[38] S. Naser, P. C. Sofotasios, L. Bariah, W. Jaafar, S. Muhaidat, M. Al-Qutayri, and O. A. Dobre, “Rate-splitting multiple access: Unifying NOMA and SDMA in MISO VLC channels,” *IEEE Open J. Veh. Technol.*, vol. 1, pp. 393–413, 2020.

[39] A. A. Ahmad, Y. Mao, A. Sezgin, and B. Clerckx, “Rate splitting multiple access in C-RAN: A scalable and robust design,” *IEEE Trans. Commun.*, vol. 69, no. 9, pp. 5727–5743, 2021.

[40] L. Li, K. Chai, J. Li, and X. Li, “Resource allocation for multicarrier rate-splitting multiple access system,” *IEEE Access*, vol. 8, pp. 174 222–174 232, 2020.

[41] S. Zhang and R. Zhang, “Capacity characterization for intelligent reflecting surface aided MIMO communication,” *IEEE J. Sel. Areas Commun.*, vol. 38, no. 8, pp. 1823–1838, 2020.

[42] J. Ye, S. Guo, and M. S. Alouini, “Joint reflecting and precoding designs for SER minimization in reconfigurable intelligent surfaces assisted MIMO systems,” *IEEE Trans. Wireless Commun.*, vol. 19, no. 8, pp. 5561–5574, 2020.

[43] Q. Wu and R. Zhang, “Intelligent reflecting surface enhanced wireless network via joint active and passive beamforming,” *IEEE Trans. Wireless Commun.*, vol. 18, no. 11, pp. 5394–5409, 2019.

[44] C. Pan, H. Ren, K. Wang, W. Xu, M. Elkashlan, A. Nallanathan, and L. Hanzo, “Multicell MIMO communications relying on intelligent reflecting surfaces,” *IEEE Trans. Wireless Commun.*, vol. 19, no. 8, pp. 5218–5233, 2020.

[45] L. Zhang, Y. Wang, W. Tao, Z. Jia, T. Song, and C. Pan, “Intelligent reflecting surface aided MIMO cognitive radio systems,” *IEEE Trans. Veh. Technol.*, vol. 69, no. 10, pp. 11 445–11 457, 2020.

[46] C. Pan, H. Ren, K. Wang, M. Elkashlan, A. Nallanathan, J. Wang, and L. Hanzo, “Intelligent reflecting surface aided MIMO broadcasting for simultaneous wireless information and power transfer,” *IEEE J. Sel. Areas Commun.*, vol. 38, no. 8, pp. 1719–1734, 2020.

[47] W. Jiang, Y. Zhang, J. Wu, W. Feng, and Y. Jin, “Intelligent reflecting surface assisted secure wireless communications with multiple- transmit and multiple-receive antennas,” *IEEE Access*, vol. 8, pp. 86 659–86 673, 2020.

[48] Z. Ding and H. Vincent Poor, “A simple design of IRS-NOMA transmission,” *IEEE Commun. Lett.*, pp. 1119–1123, 2020.

[49] F. Fang, Y. Xu, Q. V. Pham, and Z. Ding, “Energy-efficient design of IRS-NOMA networks,” *IEEE Trans. Veh. Technol.*, vol. 69, no. 11, pp. 14 088–14 092, 2020.

[50] X. Mu, Y. Liu, L. Guo, J. Lin, and N. Al-Dhahir, “Exploiting intelligent reflecting surfaces in NOMA networks: Joint beamforming optimization,” *IEEE Trans. Wireless Commun.*, vol. 19, no. 10, pp. 6884–6898, 2020.

[51] T. Hou, Y. Liu, Z. Song, X. Sun, and Y. Chen, “MIMO-NOMA networks relying on reconfigurable intelligent surface: A signal cancellation-based design,” *IEEE Trans. Commun.*, vol. 68, no. 11, pp. 6932–6944, 2020.

[52] J. Zuo, Y. Liu, E. Basar, and O. A. Dobre, “Intelligent reflecting surface enhanced millimeter-wave NOMA systems,” *IEEE Commun. Lett.*, vol. 24, no. 11, pp. 2632–2636, 2020.

[53] S. Jiao, F. Fang, X. Zhou, and H. Zhang, “Joint beamforming and phase shift design in downlink UAV networks with IRS-assisted NOMA,” *J. Commun. Inf. Networks*, vol. 5, no. 2, pp. 138–149, 2020.

[54] X. Chen, J. C. Ke, W. Tang, M. Z. Chen, J. Y. Dai, E. Basar, S. Jin, Q. Cheng, and T. J. Cui, “Design and implementation of mimo transmission based on dual-polarized reconfigurable intelligent surface,” *IEEE Wireless Commun. Lett.*, vol. 10, no. 10, pp. 2155–2159, 2021.

[55] Z. Yang, J. Shi, Z. Li, M. Chen, W. Xu, and M. Shikh-Bahaei, “Energy efficient rate splitting multiple access (RSMA) with reconfigurable intelligent surface,” in *Proc. IEEE Int. Conf. Commun. Workshops (ICC Workshops)*, 2020, pp. 1–6.

[56] A. Bansal, K. Singh, and C.-P. Li, “Analysis of hierarchical rate splitting for intelligent reflecting surfaces-aided downlink multiuser MISO communications,” *IEEE Open J. Commun. Soc.*, vol. 2, pp. 785–798, 2021.

[57] A. Bansal, K. Singh, B. Clerckx, C.-P. Li, and M.-S. Alouini, “Rate-splitting multiple access for intelligent reflecting surface aided multi-user communications,” *IEEE Trans. Veh. Technol.*, vol. 70, no. 9, pp. 9217–9229, 2021.

[58] T. Fang, Y. Mao, S. Shen, Z. Zhu, and B. Clerckx, “Fully connected reconfigurable intelligent surface aided rate-splitting multiple access for multi-user multi-antenna transmission,” 2022. [Online]. Available: https://arxiv.org/abs/2201.07048

[59] A. J. Paulraj and T. Kailath, “Increasing capacity in wireless broadcast systems using distributed transmission/directional reception (DTDR),” U.S. Patent US5 345 599A, Sep., 1994.

[60] E. Telatar, “Capacity of multi-antenna gaussian channel,” *Bell Laboratories Technical Report*, 1995.

[61] G. J. Foschini, “Layered space-time architecture for wireless communication in a fading environment when using multi-element antennas,” *Bell Labs Technical Journal*, vol. 1, no. 2, pp. 41–59, 1996.

[62] T. L. Marzetta, “Noncooperative cellular wireless with unlimited numbers of base station antennas,” *IEEE Trans. Wireless Commun.*, vol. 9, no. 11, pp. 3590–3600, Nov. 2010.

[63] J. Hoydis, S. Ten Brink, and M. Debbah, “Massive MIMO in the UL/DL of Cellular Networks: How Many Antennas Do We Need?” *IEEE Journal on Selected Areas in Communications*, vol. 31, no. 2, pp. 160–171, Feb. 2013.

[64] M. Roy, S. Paquelet, L. L. Magoarou, and M. Crussiere, “MIMO Channel Hardening for Ray-based Models,” in *Proc. Int. Conf. Wireless Mobile Comput. Networking Commun. (WiMob)*, Oct. 2018, pp. 1–7.

[65] E. Bjornson, J. Hoydis, and L. Sanguinetti, *Massive MIMO Networks: Spectral, Energy, and Hardware Efficiency*. NOW, 2017.

[66] S. Lien, S. Shieh, Y. Huang, B. Su, Y. Hsu, and H. Wei, “5G New Radio: Waveform, Frame Structure, Multiple Access, and Initial Access,” *IEEE Communications Magazine*, vol. 55, no. 6, pp. 64–71, Jun. 2017.

[67] X. Xia, K. Xu, Y. Wang, and Y. Xu, “A 5G-enabling technology: Benefits, feasibility, and limitations of in-band full-duplex mMIMO,” *IEEE Veh. Technol. Mag.*, vol. 13, no. 3, pp. 81–90, 2018.

[68] T. L. Marzetta, E. G. Larsson, H. Yang, and H. Q. Ngo, *Fundamentals of massive MIMO*. Cambridge University Press, 2016.

[69] N. S. Kumar and D. Vakula, “Performance analysis of equalizers for MIMO in Rician-K and Nakagami-m fading channels,” in *Proc. Int. Conf. Electron., Commun. Aerosp. Tech. (ICECA)*, vol. 2, 2017, pp. 381–385.

[70] A. Adhikary, J. Nam, J. Ahn, and G. Caire, “Joint spatial division and multiplexing - The large-scale array regime,” *IEEE Trans. Inf. Theory*, vol. 59, no. 10, pp. 6441–6463, Oct. 2013.

[71] J. Nam, A. Adhikary, J.-Y. Ahn, and G. Caire, “Joint spatial division and multiplexing: Opportunistic beamforming, user grouping and simplified downlink scheduling,” *IEEE J. Sel. Top. Signal Process.*, vol. 8, no. 5, pp. 876–890, 2014.

[72] S. Yoo, J. Lee, and K. Kim, “Geometry-based one-ring models for MIMO systems: Modeling accuracy assessment and improvement,” *IEEE Trans. Wireless Commun.*, vol. 15, no. 7, pp. 4583–4597, 2016.

[73] B. Clerckx and C. Oestges, *MIMO Wireless Networks: Channels, Techniques and Standards for Multi-Antenna, Multi-User and Multi-Cell Systems*, 2nd ed. Orlando, FL, USA: Academic Press, Inc., 2013.

[74] F. Zheng, Y. Chen, B. Pang, C. Liu, S. Wang, D. Fan, and J. Zhang, “An efficient CSI feedback scheme for dual-polarized massive MIMO,” *IEEE Access*, vol. 6, pp. 23 420–23 430, 2018.

[75] T. Kim, B. Clerckx, D. J. Love, and S. J. Kim, “Limited feedback beamforming systems for dual-polarized MIMO channels,” *IEEE Trans. Wireless Commun.*, vol. 9, no. 11, Nov. 2010.

[76] J. Park and B. Clerckx, “Multi-user linear precoding for multi-polarized massive MIMO system under imperfect CSIT,” *IEEE Trans. Wireless Commun.*, vol. 14, no. 05, May 2015.

[77] Z. Jiang, A. F. Molisch, G. Caire, and Z. Niu, “Achievable rates of FDD massive MIMO systems with spatial channel correlation,” *IEEE Trans. Wireless Commun.*, vol. 14, no. 5, pp. 2868–2882, 2015.

[78] J. Flordelis, F. Rusek, F. Tufvesson, E. G. Larsson, and O. Edfors, “Massive MIMO performance-TDD versus FDD: What do measurements say?” *IEEE Trans. Wireless Commun.*, vol. 17, no. 4, pp. 2247–2261, 2018.

[79] W. Shao, S. Zhang, H. Li, N. Zhao, and O. A. Dobre, “Angle-domain NOMA over multicell millimeter wave massive MIMO networks,” *IEEE Trans. Commun.*, vol. 68, no. 4, pp. 2277–2292, 2020.

[80] J. Ma, S. Zhang, H. Li, N. Zhao, and V. C. M. Leung, “Interference-alignment and soft-space-reuse based cooperative transmission for multi-cell massive MIMO networks,” *IEEE Trans. Wireless Commun.*, vol. 17, no. 3, pp. 1907–1922, 2018.

[81] B. Clerckx, Y. Mao, R. Schober, E. A. Jorswieck, D. J. Love, J. Yuan, L. Hanzo, G. Y. Li, E. G. Larsson, and G. Caire, “Is noma efficient in multi-antenna networks? a critical look at next generation multiple access techniques,” *IEEE Open J. Commun. Soc.*, vol. 2, pp. 1310–1343, 2021.

[82] S. Boyd and L. Vandenberghe, *Convex Optimization*. New York, NY, USA: Cambridge University Press, 2004.

[83] H. Yin, D. Gesbert, and L. Cottatellucci, “Dealing with interference in distributed large-Scale MIMO systems: A statistical approach,” *IEEE J. Sel. Topics Signal Process.*, vol. 8, no. 5, pp. 942–953, Oct. 2014.

[84] H. A. David and H. N. Nagaraja, *Order Statistics*, 3rd ed. Wiley Series in Probability and Statistics, Aug. 2003.

[85] Z. Ding, F. Adachi, and H. V. Poor, “The application of MIMO to non-orthogonal multiple access,” *IEEE Trans. Wireless Commun.*, vol. 15, no. 1, pp. 537–552, Jan. 2016.

[86] H. F. Ma, G. Z. Wang, G. S. Kong, and T. J. Cui, “Independent controls of differently-polarized reflected waves by anisotropic metasurfaces,” *Scientific Reports*, vol. 5, no. 1, p. 1, 2015.

[87] S. Sun, W. Jiang, S. Gong, and T. Hong, “Reconfigurable linear-to-linear polarization conversion metasurface based on pin diodes,” *IEEE Antennas Wirel. Propag. Lett.*, vol. 17, no. 9, pp. 1722–1726, 2018.

[88] J. Wang, R. Yang, R. Ma, J. Tian, and W. Zhang, “Reconfigurable multifunctional metasurface for broadband polarization conversion and perfect absorption,” *IEEE Access*, vol. 8, pp. 105 815–105 823, 2020.

[89] S.-Y. Shim and Y. Chen, “Least squares solution of matrix equation AXB* + CYD* = E,” *SIAM Journal on Matrix Analysis and Applications*, vol. 24, no. 3, pp. 802–808, 2003.

[90] Z. Luo, W. Ma, A. M. So, Y. Ye, and S. Zhang, “Semidefinite relaxation of quadratic optimization problems,” *IEEE Signal Process Mag.*, vol. 27, no. 3, pp. 20–34, 2010.

[91] Z. Xiang, M. Tao, and X. Wang, “Massive MIMO multicasting in noncooperative cellular networks,” *IEEE J. Sel. Areas Commun.*, vol. 32, no. 6, pp. 1180–1193, 2014.

[92] A. Konar and N. D. Sidiropoulos, “Fast approximation algorithms for a class of non-convex QCQP problems using first-order methods,” *IEEE Trans. Signal Process.*, vol. 65, no. 13, pp. 3494–3509, 2017.

[93] Y. Yang, F. Gao, Z. Zhong, B. Ai, and A. Alkhateeb, “Deep transfer learning-based downlink channel prediction for FDD massive MIMO systems,” *IEEE Trans. Commun.*, vol. 68, no. 12, pp. 7485–7497, 2020.

[94] J. Bezanson, A. Edelman, S. Karpinski, and V. B. Shah, “Julia: A fresh approach to numerical computing,” *SIAM Review*, vol. 59, no. 1, pp. 65–98, 2017.

Publication I

de Sena, A. S., Lima, F. R. M., da Costa, D. B., Ding, Z., Nardelli, P. H. J.,
Dias, U. S., and Papadias, C. B.
Massive MIMO-NOMA Networks with Imperfect SIC: Design and Fairness Enhancement

Reprinted with permission from
IEEE Transactions on Wireless Communications
Vol. 19, no. 9, pp. 6100–6115, Sep. 2020

Massive MIMO-NOMA Networks With Imperfect SIC: Design and Fairness Enhancement

Arthur Sousa de Sena, *Student Member, IEEE*, Francisco Rafael Marques Lima, *Member, IEEE*,
Daniel Benevides da Costa, *Senior Member, IEEE*, Zhiguo Ding, *Fellow, IEEE*,
Pedro H. J. Nardelli, *Senior Member, IEEE*, Ugo Silva Dias, *Senior Member, IEEE*,
and Constantinos B. Papadias, *Fellow, IEEE*

***Abstract*— This paper addresses multi-user multi-cluster massive multiple-input-multiple-output (MIMO) systems with non-orthogonal multiple access (NOMA). Assuming the downlink mode, and taking into consideration the impact of imperfect successive interference cancellation (SIC), an in-depth analytical analysis is carried out, in which closed-form expressions for the outage probability and ergodic rates are derived. Subsequently, the power allocation coefficients of users within each sub-group are optimized to maximize fairness. The considered power optimization is simplified to a convex problem, which makes it possible to obtain the optimal solution via Karush-Kuhn-Tucker (KKT) conditions. Based on the achieved solution, we propose an iterative algorithm to provide fairness also among different sub-groups. Simulation results alongside with insightful discussions are provided to investigate the impact of imperfect SIC and demonstrate the fairness superiority of the proposed dynamic power allocation policies. For example, our results show that if the residual error propagation levels are high, the employment of orthogonal multiple access (OMA) is always preferable than NOMA. It is also shown that the proposed power allocation outperforms conventional massive MIMO-NOMA setups operating with fixed power allocation strategies in terms of outage probability.**

***Index Terms*— Fairness maximization, imperfect SIC, massive MIMO, NOMA.**

I. Introduction

Advances in technologies and the rise of new applications, such as unmanned vehicles, smart homes, smart grid, and massive sensor networks, are triggering an accelerated growth in the number of devices connected to communication systems. As an attempt to support this explosive trend, the 5th generation of wireless networks (5G) is being developed, and the first commercial systems have been deployed worldwide. 5G and beyond networks are expected to support a variety of demanding requisites, going from massive connectivity and ultra-low latency to improved user fairness [1]. Massive multiple-input-multiple-output (MIMO) is being credited as one of the key enabling components of 5G [2]. In particular, by employing a very large number of antennas and exploiting the space domain to multiplex different users, the massive MIMO technology has the potential to reduce system latency and to provide remarkable connectivity gains. Power-domain non-orthogonal multiple access (NOMA) is another promising technology for the future-generation wireless systems that allow multiple users to be served in parallel within the same frequency and time slot. The relying concept of NOMA consists of superposing the data symbols of different users in the power domain at the base station (BS) and employing successive interference cancellation (SIC) at the receivers. With such features, NOMA can also provide massive connectivity capabilities and a reduction in latency to the network.

If the NOMA technique is applied to massive MIMO, the achievable spectral and connectivity improvements are shown to be even greater [3]–[5]. However, if the transmission power is not well allocated within the MIMO-NOMA network, the performance of some users can be severely compromised.

Manuscript received December 1, 2019; revised April 14, 2020; accepted June 2, 2020. Date of publication June 11, 2020; date of current version September 10, 2020. The work of D. B. da Costa was supported in part by the Brazilian Research, Development, and Innovation Agency, CNPq, under Grant 302863/2017-6, in part by the Ceará Council of Scientific and Technological Development (FUNCAP) (Edital PRONEM) under Grant 01/2016, and in part by the Nokia Foundation through the Nokia Visiting Professors Program under Grant Project 201900134. The work of P. H. J. Nardelli was supported in part by the Academy of Finland via ee-IoT Project under Grant 319009, in part by the Framework for the Identification of Rare Events via Machine Learning and IoT Networks (FIREMAN) consortium under Grant CHIST-ERA/n.326270, and in part by the EnergyNet Research Fellowship under Grant 321265 and Grant 328869. The work of Ugo Silva Dias was supported in part by the Brazilian Research, Development, and Innovation Agency, CNPq, under Grant 311796/2018-4 and in part by the Ministry of Justice and Public Security, Government of Brazil, under Grant TED UnB-SENACON/MJSP 01/2019. The work of Constantinos B. Papadias was supported in part by the FIREMAN consortium under Grant CHIST-ERA/n.326270. Part of this article has been submitted at the IEEE International Symposium on Personal, Indoor, and Mobile Radio Communications (PIMRC 2020), London, U.K. The associate editor coordinating the review of this article and approving it for publication was S. Buzzi. *(Corresponding author: Daniel Benevides Da Costa.)*

Arthur Sousa de Sena and Pedro H. J. Nardelli are with the Department of Electrical Engineering, Lappeenranta University of Technology, 53850 Lappeenranta, Finland (e-mail: arthurssena@ieee.org; pedro.nardelli@lut.fi).

Francisco Rafael Marques Lima is with the Department of Computer Engineering, Federal University of Ceará (UFC), Sobral 62010-560, Brazil, and also with the Wireless Telecom Research Group (GTEL), Pici campus, UFC, Fortaleza 60416-200, Brazil (e-mail: rafaelm@gtel.ufc.br).

Daniel Benevides da Costa is with the Department of Computer Engineering, Federal University of Ceará (UFC), Sobral 62010-560, Brazil (e-mail: danielbcosta@ieee.org).

Zhiguo Ding is with the Department of Electrical and Electronic Engineering, The University of Manchester, Manchester M1 9BB, U.K. (e-mail: zhiguo.ding@manchester.ac.uk).

Ugo Silva Dias is with the Department of Electrical Engineering, University of Brasília, Brasília 70910-900, Brazil (e-mail: ugodias@ieee.org).

Constantinos B. Papadias is with the Research, Technology and Innovation Network (RTIN), The American College of Greece, Athens 15342, Greece (e-mail: cpapadias@acg.edu).

Color versions of one or more of the figures in this article are available online at http://ieeexplore.ieee.org.

Digital Object Identifier 10.1109/TWC.2020.3000192

For instance, the adoption of fixed power allocation policies in NOMA can be very beneficial to users with good channel conditions, however, it can be extremely disadvantageous to users that suffer from strong channel attenuation [6]. To improve the average performance of the weaker users, one could decrease as much as possible the power allocated to the strong ones so that a certain degree of fairness could be achieved [7]. However, such a strategy can severely impact the system sum-rate, and, due to the random behavior of the wireless channels, it will also result in unequal data rates. This characteristic can be detrimental to certain emerging applications. For example, in the upcoming industrial internet of things, it can be very important that all terminals experience similar data rates [8]. In such scenarios, the employment of fixed allocation policies can make some of the terminals not able to meet their minimum requirements and result in a poor network performance. Besides, 5G and beyond are expected to support the concept of network slicing, which is to create isolated logical networks, i.e., slices, each dedicated to a subset of terminals with specific requirements [9]. Since within each slice users are expected to share identical requisites, it will be crucial to perform a fair distribution of resources, which is a feature that fixed power allocation is not capable of providing. Therefore, more sophisticated and adaptive power allocation strategies are important and necessary to guarantee fairness in future MIMO-NOMA networks. In addition, the majority of existing works make the strong assumption that SIC can be carried out perfectly, which is idealistic and difficult to hold in practice. In real-world deployments, various impairments such as fast varying channels, atmospheric absorption, strong channel correlation, and hardware issues, can degrade the signal reception and introduce errors during the detection of transmitted symbols [10], [11]. As a result, since the recovery of each symbol with SIC depends on previous decodings, errors will inevitably propagate and impact the system performance. This makes SIC residual error propagation an important parameter that must be considered while designing realistic massive MIMO-NOMA systems.

A. Related Works

A few NOMA-related works have considered the impact of imperfect SIC. For instance, in [10], a massive MIMO-NOMA system with non-orthogonal channel estimation and SIC error propagation was investigated. The work considered a single-cell downlink scenario, where a single multi-antenna BS communicates with multiple single-antenna users. In particular, the authors derived a lower bound expression for the spectral efficiency and developed iterative optimization algorithms for maximizing the weighted sum spectral efficiency. The provided numerical results validated the analytical approximation, although the gap between the bounds and simulation curves were not very tight. The work in [12] proposed a sub-optimum iterative algorithm for maximizing the sum-rate of a downlink MIMO-NOMA network. By equipping both BS and users with two antennas, the paper provided results for two very specific scenarios, in which a high and a low value of SIC residual error was considered. However, intermediate error levels were not investigated. In [13], the authors analyzed the outage probability and minimized the total transmit power of a multi-carrier NOMA system by modeling the SIC error propagation as a complex Gaussian random variable. Complementary geometric programming and arithmetic geometric mean approximation techniques were used to transform the non-convex formulated problem into a convex one. The heterogeneous networks case was considered in [14]. By taking into consideration various sources of interference, such as inter-cell interference, power disparity, and imperfect SIC, the work proposed user clustering and power-bandwidth allocation algorithms. The impact of imperfect SIC in the uplink of MIMO-NOMA systems employing the concept of virtualized wireless networks (VWN) was studied in [15], in which algorithms based on successive convex approximation and complementary geometric programming were proposed for power and sub-carrier allocation. A massive MIMO-NOMA system with distributed antenna arrays was investigated in [16]. In this contribution, a closed-form expression for the ergodic sum-rate was derived. In [17], by taking into consideration SIC error propagation and in-phase and quadrature-phase imbalance, the performance of a full-duplex relaying system was investigated. The study of α-μ fading channels in cooperative NOMA networks with hardware impairments was considered in [18], and the work in [19] addressed the application of deep learning techniques to MIMO-NOMA systems with imperfect SIC decoding.

Some contributions have addressed fairness in NOMA systems, although none of them have considered the effects of imperfect SIC. For example, by assuming that SIC can be carried out perfectly, the work in [20] investigated the impact of power allocation on the fairness of a simple system where a single-antenna BS serves multiple single-antenna users. The authors developed low-complexity bisection-based iterative algorithms to optimally solve the optimization problem. In [21], the fairness of user clustering in a multi-user MIMO-NOMA setup was considered. Bisection algorithms were also adopted to optimize the power of users within each cluster. In addition, three sub-optimum clustering algorithms have been proposed. A fair NOMA protocol, in which the user capacity is always at least equal to the capacity achieved with orthogonal multiple access (OMA), was proposed in [22]. The referred work pairs near and cell-edge single-antenna users to form NOMA groups, based on which the power allocation coefficients are determined. The outage probability was also investigated. The authors of [23] and [24] proposed user clustering algorithms based on proportional fairness to balance between throughput and fairness. [23] also presented an optimal power allocation for maximizing the system sum-rate such that the rate of weak users is guaranteed to be equal to that achieved with OMA. In [6], the authors developed dynamic resource allocation policies, which are optimally obtained via Lagrangian dual decomposition. The millimeter-wave MIMO-NOMA case was addressed in [25], in which spatial sparsity was exploited to propose sub-optimum power allocation solutions.

B. Motivation and Contributions

Even though there are numerous contributions showing that massive MIMO-NOMA systems can provide remarkable spectral gains and outperform the massive MIMO-OMA counterpart, the majority of these works do not consider the impact of imperfect SIC decoding. In addition, to the best of the authors' knowledge, only a very limited number of works investigates fairness in massive MIMO-NOMA networks, and none of them have considered SIC error propagation. Given the aforementioned research gap, this paper aims to design, analyze, and optimize the performance of a massive MIMO-NOMA network under the impact of residual error propagation from imperfect SIC. More details and the main original contributions provided in this work are summarized as follows.

- Inspired by the works in [3], [4], and assuming that the users are confined within multiple clusters of scatterers, we employ at the BS a two-stage precoder. Specifically, the first-stage precoder, which is intended to eliminate inter-cluster interference, is designed based only on the slowly varying covariance matrices of interfering clusters. By its turn, the second-stage precoder is responsible for directing the superposed symbols to the corresponding NOMA sub-groups, where each sub-group is formed by two users so that the computational complexity of SIC is reduced. This strategy provides attractive advantages to massive MIMO-NOMA setups, such as less processing overload and reduced feedback overhead.
- Assuming first a fixed power allocation policy, a novel analytical framework for the proposed massive MIMO-NOMA network is developed. In particular, by considering the impact of residual error from imperfect SIC, we derive the system signal-to-interference-plus-noise ratio (SINR) expression and carry out a statistical characterization of the effective channel gains. Then, based on this initial analysis, exact closed-form expressions for the outage probability and for the users' ergodic rates are derived, whose accuracies are validated through numerical and simulation examples. The obtained analytical results provide a practical alternative for designing massive MIMO-NOMA systems with imperfect SIC decoding.
- Next, we develop a more sophisticated dynamic power allocation that maximizes the achievable rates of users with worst channel conditions within each NOMA sub-group. More specifically, the optimization problem is formulated to guarantee that weaker users never experience a rate less than what is achieved by the stronger ones, and the optimal solution is obtained via Karush-Kuhn-Tucker (KKT) conditions. Then, to balance the data rates also among different sub-groups, we propose an iterative algorithm that extends the fairness concept to all users within the spatial clusters so that all terminals can reach identical performance levels, i.e., maximum fairness is provided.
- Simulation results alongside with insightful discussions are provided to investigate the impact of imperfect SIC and demonstrate the fairness superiority of the proposed dynamic power allocation policies. For example, our results show that if the residual error propagation levels are high, the employment of OMA is always preferable than NOMA. It is also shown that the proposed power allocation outperforms conventional massive MIMO-NOMA setups operating with fixed power allocation strategies in terms of outage probability.

Notation and Special Functions: Bold-faced lower-case letters denotes vectors and upper-case represent matrices. The ith element of a vector $\mathbf{a}$ is denoted by $[\mathbf{a}]_i$ and the (ij) entry of a matrix $\mathbf{A}$ by $[\mathbf{A}]_{ij}$. The Hermitian transposition of $\mathbf{A}$ is represented by $\mathbf{A}^H$ and the trace by $\text{tr}\{\mathbf{A}\}$. In addition, $\mathbf{0}_{M\times N}$ denotes the $M \times N$ matrix with all zero entries, $\mathbb{E}[\cdot]$ denotes expectation, $\Gamma(\cdot)$ is the Gamma function [26, eq. (8.310.1)], $\gamma(\cdot,\cdot)$ is the lower incomplete Gamma function [26, eq. (8.350.1)], and $\text{Ei}(\cdot)$ corresponds to the exponential integral [26, eq. (8.211.1)].

II. SYSTEM MODEL

We consider a single-cell scenario where one elevated BS is communicating in downlink mode with L multi-antenna users. The BS is equipped with a uniform linear array of M transmit antenna elements, which are separated by half a wavelength, i.e., $\lambda/2$. Moreover, each user is equipped with N receive antennas, in which we assume that M is much greater than N, i.e., $M \gg N$, which characterizes a typical massive MIMO setup. The users are considered to be uniformly distributed within S spatial clusters of scatterers, modeled by the one-ring scattering model [27]. Within each cluster, the BS subdivides the users into G smaller sub-groups, each one containing 2 users,[1] as illustrated in Fig. 1. Then, power-domain NOMA is employed within each sub-group. Given the described scenario, and applying the Karhunen-Loeve transform [27], the channel matrix for the kth user in the gth sub-group in the sth cluster, can be expressed by

$$\mathbf{H}_{sgk} = \sqrt{\Phi d_{sg}^{-\eta}}\,\mathbf{U}_s \mathbf{\Lambda}_s^{\frac{1}{2}} \mathbf{G}_{sgk} \in \mathbb{C}^{M\times N}, \tag{1}$$

which has covariance matrix given by $\mathbb{E}\{\mathbf{H}_{sgk}\mathbf{H}_{sgk}^H\} = \Phi d_{sg}^{-\eta}\mathbf{R}_s \in \mathbb{C}^{M\times M}$, with rank denoted by r_s. $\mathbf{\Lambda}_s \in \mathbb{R}_{>0}^{r_s^*\times r_s^*}$ represents a diagonal matrix formed by the first r_s^* dominant eigenvalues of $\mathbf{R}_s$, sorted out in decreasing order, in which $r_s^* \leq r_s$. $\mathbf{U}_s \in \mathbb{C}^{M\times r_s^*}$ is a matrix of eigenvectors corresponding to the dominant eigenvalues of $\mathbf{R}_s$, and $\mathbf{G}_{sgk} \in \mathbb{C}^{r_s^*\times N}$ is the fast varying channel matrix, which has complex Gaussian distributed entries with zero-mean and unit-variance. d_{sg} is the distance of the gth sub-group from the BS, η is the path-loss exponent, and Φ is a gain parameter that is adjusted based on the desired performance of the receivers [28]. Moreover, all users confined within the sth cluster are assumed to share identical[2] covariance matrices $\mathbf{R}_s$, whose entries can

---

[1] Given that SIC is an interference-limited technique, the consideration of a large number of users per sub-group can lead to performance degradation (due to decoding error propagation), increase in detection and hardware complexities, and higher energy consumption. Therefore, small sub-groups (usually of two users) are preferable in practical downlink NOMA systems [7].

[2] The assumption of users sharing identical covariance matrices cannot be exactly satisfied in real-world scenarios. However, as stated in [27], if users within the same cluster of scatterers are grouped properly, this condition can be efficiently approximated. Even though user grouping is an important topic and an active area of research [14], it goes beyond the scope of this work.

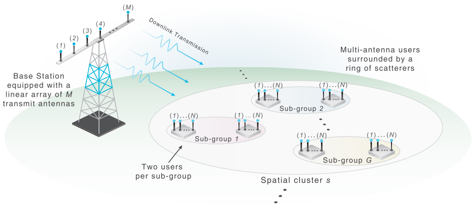

Fig. 1. System model. Users within each spatial cluster are organized into multiple sub-groups.

be generated by [27]

$$[\mathbf{R}_s]_{mm'} = \frac{1}{2\delta_s}\int_{-\delta_s}^{\delta_s} e^{-j\frac{2\pi}{\lambda}[\cos(\phi+\varphi_s),\sin(\phi+\varphi_s)](\mathbf{a}_m-\mathbf{a}_{m'})}d\phi, \tag{2}$$

where δ_s and φ_s are, respectively, the angular spread and the azimuth angle of the sth spatial cluster, ϕ corresponds to the angle of arrival of incident planar waves at the BS, and $\mathbf{a}_m, \mathbf{a}_{m'}$ are the Cartesian coordinates of the antenna elements m and m', for $1 \leq m, m' \leq M$.

At the BS, the symbols for users within each sub-group are superposed and transmitted through the wireless channels. Then, the kth user in the gth sub-group receives the following signal

$$\mathbf{y}_{sgk} = \mathbf{H}_{sgk}^H \sum_{n=1}^{S} \mathbf{B}_n \sum_{i=1}^{G} \mathbf{v}_{ni} \sum_{j=1}^{2} \sqrt{\alpha_{nij}} x_{nij} + \mathbf{n}_{sgk}, \tag{3}$$

where $\mathbf{n}_{gk} \in \mathbb{C}^{N\times 1}$ is a noise vector with entries following the complex Gaussian distribution with zero-mean and variance σ_n^2. The variable α_{nij} denotes the power coefficient, and x_{nij} is the symbol intended for the jth user in the ith sub-group at the nth cluster. $\mathbf{B}_n \in \mathbb{C}^{M\times V}$ is the beamforming matrix responsible for eliminating the interference from other clusters, where V is a parameter that defines the number of parallel effective transmissions, and $\mathbf{v}_{ni} \in \mathbb{C}^{V\times 1}$ is the precoding vector designed to assign the superposed symbols to the corresponding sub-groups.

A. Beamforming Design

The beamforming matrix $\mathbf{B}_s$ is designed to focus the signal transmission to a desired spatial cluster s, such that everywhere else outside the area of interest the propagation is nulled out. To achieve this spatial directivity, $\mathbf{B}_s$ is constructed based on the null space spanned by the nonzero eigenmodes of the covariance matrices of interfering clusters [27]. To this end, we define $\mathbf{U}_s^- = [\mathbf{U}_1, \cdots, \mathbf{U}_{s-1}, \mathbf{U}_{s+1}, \cdots, \mathbf{U}_S]$ and denote its last $M-(S-1)r_s^*$ left eigenvectors by $\mathbf{E}_s^0 \in \mathbb{C}^{M\times M-(S-1)r_s^*}$, which corresponds to the vanishing eigenmodes of $\mathbf{U}_s^-$. As a result, due to the dimension of $\mathbf{E}_s^0$, the constraint $M > (S-1)r_s^*$ must be satisfied.

Given that $(\mathbf{E}_s^0)^H\mathbf{U}_s^- = 0$, the matrix $\tilde{\mathbf{H}}_{sgk} = (\mathbf{E}_s^0)^H\mathbf{U}_s\mathbf{\Lambda}_s^{\frac{1}{2}}\mathbf{G}_{sgk}$ is orthogonal to the r_s^* dominant eigenmodes of interfering clusters, and it has covariance matrix given by $\tilde{\mathbf{R}}_s = \tilde{\mathbf{H}}_{sgk}\tilde{\mathbf{H}}_{sgk}^H = (\mathbf{E}_s^0)^H\mathbf{R}_s\mathbf{E}_s^0 = \mathbf{F}_s\mathbf{R}_s\mathbf{F}_s^H$, where $\mathbf{F}_s$ represents the left eigenvectors of $\tilde{\mathbf{R}}_s$. Then, by defining the first V eigenvectors of $\mathbf{F}_s$ by $\mathbf{F}_s^1 \in \mathbb{C}^{M-(S-1)r_s^*\times V}$, the beamforming matrix $\mathbf{B}_s$ is finally obtained, as follows

$$\mathbf{B}_s = \mathbf{E}_s^0\mathbf{F}_s^1 \in \mathbb{C}^{M\times V}, \tag{4}$$

where $S \leq V \leq (M-(S-1)r_s^*)$ and $V \leq r_s^* \leq r_s$.

It is noteworthy that the number of dominant eigenvalues r_s^* will determine the amount of interference that will leak from other clusters.[3] Specifically, the inter-cluster interference will approach zero as r_s^* approaches to the rank r_s, such that, when $r_s^* = r_s$, $\mathbf{H}_{sgk}^H\mathbf{B}_{s'} = \mathbf{0}, \forall s \neq s'$. However, since part of the eigenvalues can be very small, i.e., ≈ 0, the extreme choice $r_s^* = r_s$ is usually not efficient, and it does not result in significant performance improvements [4], [27]. In addition, given that $S < M/r_s^* + 1$, increasing r_s^* will reduce the maximum number of clusters S. In particular, due to the beamforming constraints, we set the dominant eigenvalues parameter to $r_s^* = \min\{r_s, \lfloor (M-V)/(S-1)\rfloor\}$.

More clarifications for the precoding vector $\mathbf{v}_{sg}$ are now provided. We design $\mathbf{v}_{sg}$ to assign the superimposed symbols to each corresponding NOMA sub-group, such that it should not introduce additional power, i.e., $\|\mathbf{v}_{sg}\|^2 = 1$. This can be accomplished by defining $\mathbf{v}_{sg}$ as

$$\mathbf{v}_{sg} = [\ \mathbf{0}_{1\times(g-1)}\ ,\ 1\ ,\ \mathbf{0}_{1\times(V-g)}\ ]^T, \quad \forall g = 1, \cdots, G. \tag{5}$$

Note that the above design associates the gth effective data stream to the gth NOMA sub-group, and it does not modify by any form the data messages. Besides, to construct the beamformers, it is not necessary to acquire the fast fading channel matrices $\mathbf{G}_{sgk}$ at the BS, that is, only the channel covariance matrices are required. And given that $\mathbf{R}_s$ varies slowly, the users only need to measure it once after several coherence intervals. Once this statistical information is obtained, users can feed it back to the BS with low feedback overhead [27]. As a result, it is reasonable to assume that all the channel information can be accurately estimated at the users' side through downlink training techniques.[4] Therefore, as in [3]–[5], we consider that $\mathbf{R}_s$ is known in the system (at both BS and users), and that $\mathbf{G}_{sgk}$ can be estimated perfectly[5] by the users' terminals. Also, since $\mathbf{B}_s$ only addresses the inter-cluster interference, the users still need to employ some reception technique for canceling the remaining intra-cluster interference. Details for signal reception are provided next.

---

[3] As discussed in [4] and [27], finding the optimum value of r_s^* depends on the parameters and requisites of each specific system, such as the number of antennas, desired number of clusters, and maximum interference level, which is not a trivial task and goes beyond the scope of this work. We configure this parameter not aiming its optimally, but to achieve a good system performance and to satisfy the beamforming design constraints.

[4] Channel estimation and acquisition are critical in massive MIMO and are topics of ongoing interest in the literature (see [29] and references therein, for example). However, the investigation of such topics goes beyond the scope of this work.

[5] In practice, the estimation of the fast varying channel matrices, $\mathbf{G}_{sgk}$, is usually not perfect. Therefore, the investigation of the impact of channel estimation errors on our proposed massive MIMO-NOMA design arises as an interesting future direction.

B. Signal Reception

For simplicity, from this point forward, we drop the subscript corresponding to the spatial cluster, e.g., we represent $\mathbf{y}_{sgk}$ as $\mathbf{y}_{gk}$. Accordingly, assuming that the beamforming matrix $\mathbf{B}_s$ successfully suppresses all inter-cluster interferences, the superposed signal observed by the kth user, $k \in \{1, 2\}$, in the gth sub-group can be rewritten as

$$\mathbf{y}_{gk} = \mathbf{H}_{gk}^H \mathbf{B} \sum_{i=1}^{G} \mathbf{v}_i \sum_{j=1}^{2} \sqrt{\alpha_{ij}} x_{ij} + \mathbf{n}_{gk}. \tag{6}$$

To eliminate the remaining inter-group interference, the users employ a zero-forcing receiver. Therefore, the detection matrix can be defined by $\mathbf{H}_{gk}^{\dagger} = [(\mathbf{H}_{gk}^H \mathbf{B})^H \mathbf{H}_{gk}^H \mathbf{B}]^{-1} (\mathbf{H}_{gk}^H \mathbf{B})^H$, which corresponds to the pseudo-inverse of the virtual channel. Note that, in order to construct the zero-forcing receiver, the users need to have access also to the beamforming matrices. Since, in our design, $\mathbf{B}$ is built based only on the channel covariance matrices, which vary slowly, such beamforming information can be efficiently informed back to the users, imposing low overhead.

After the received signal has been filtered through $\mathbf{H}_{gk}^{\dagger}$, the kth user in the gth group achieves the following data vector

$$\hat{\mathbf{x}}_{gk} = \begin{bmatrix} \sqrt{\alpha_{11}} x_{11} + \sqrt{\alpha_{12}} x_{12} \\ \vdots \\ \sqrt{\alpha_{G1}} x_{G1} + \sqrt{\alpha_{G2}} x_{G2} \end{bmatrix} + \mathbf{H}_{gk}^{\dagger} \mathbf{n}_{gk}. \tag{7}$$

Note that the zero-forcing receiver has decoupled the signal in (6) into G parallel symbols, each one belonging to a different sub-group. This enables the users within the gth NOMA sub-group to apply SIC to their corresponding superposed symbol, i.e., the gth element of $\hat{\mathbf{x}}_{gk}$.

III. PERFORMANCE ANALYSIS FOR FIXED POWER ALLOCATION

In this section, the performance of the proposed massive MIMO-NOMA system operating under fixed power allocation policy is investigated. Specifically, by considering the impact of residual error from imperfect SIC decoding, we derive the SINR experienced by the users and identify the statistical distributions of the effective channel gains, based on which closed-form analytical expressions for the outage probability and for the users' ergodic rates are obtained.

A. SINR Analysis

In our design, the users within each sub-group are organized by the BS in ascending order based on their effective channel gains, that is, the first user has the lowest gain and the second user the highest one. Following the SIC protocol, the weak user retrieves its data symbol directly from (7) and treats the message intended for the second user as interference, so no further processing is required. On the other hand, the second user, which has the best channel condition, first decodes the message intended for the first user and, subsequently, recovers its own data symbol [3]–[5]. Ideally, the strong user can recover its information without interference, but, as previously discussed, this is difficult to happen in practice. In real deployments, due to many impairments, the strong users may achieve an imperfect estimation of the symbols intended to the weak users and suffer from residual interference. On these grounds, as in [10], [14], [15], we model the effects of imperfect SIC as a function of the interfering power. More specifically, the kth user in the gth sub-group will recover the following symbol

$$\hat{x}_{gk} = \begin{cases} \underset{\substack{\uparrow \\ \text{symbol of interest}}}{\sqrt{\alpha_{g1}} x_{g1}} + \underset{\substack{\uparrow \\ \text{interference}}}{\sqrt{\alpha_{g2}} x_{g2}} + \underset{\substack{\uparrow \\ \text{noise}}}{[\mathbf{H}_{g1}^{\dagger} \mathbf{n}_{g1}]_g}, \\ \quad \text{if } k = 1, \\ \underset{\substack{\uparrow \\ \text{symbol of interest}}}{\sqrt{\alpha_{g2}} x_{g2}} + \underset{\substack{\uparrow \\ \text{residual SIC interference}}}{\sqrt{\mu \alpha_{g1}} x_{g1}} + \underset{\substack{\uparrow \\ \text{noise}}}{[\mathbf{H}_{g2}^{\dagger} \mathbf{n}_{g2}]_g}, \\ \quad \text{if } k = 2, \end{cases} \tag{8}$$

in which $\mu \in [0, 1]$ is the error propagation factor that models the impact of imperfect SIC, where $\mu = 1$ represents the scenario of maximum interference, and $\mu = 0$ corresponds to the ideal case of perfect SIC. As demonstrated in [30], [31], the error factor μ can be easily calculated at the receivers by dividing the variance of the interference term, which can be obtained by averaging a large number of samples, by the power allocated to the interfering user, e.g., supposing that $\tilde{x}_{g1}$ is the symbol intended for the user 1 estimated at user 2 during the SIC process, the error factor can be computed as[6] $\mu = \mathbb{E}\{|\sqrt{\alpha_{g1}}(x_1 - \tilde{x}_1)|^2\}/\alpha_{g1}$. In practice, the value of μ will depend on factors such as the type of the receiver, channel characteristics, and hardware sensibility [14], [15]. Considering the signal model in (8), the SINR achieved by each user during each NOMA decoding is defined in the following Lemma.

Lemma 1: Supposing that the users within each sub-group are sorted out in increasing order based on their effective channel gains, the SINR achieved at the current kth user, $1 \leq k \leq 2$, when decoding the symbol that belongs to the ith user, $1 \leq i \leq 2$, is obtained by

$$\gamma_{gk}^{i} = \frac{\rho \varrho_{gk} \alpha_{gi}}{\rho \varrho_{gk} \alpha_{gi}^{\star} + 1}, \quad \text{for } 1 \leq i \leq k \leq 2, \tag{9}$$

where $\varrho_{gk} = \frac{1}{[\mathbf{H}_{gk}^{\dagger} \mathbf{H}_{gk}^{\dagger H}]_{gg}}$ is the effective channel gain, $\rho = 1/\sigma_n^2$ denotes the signal-to-noise ratio (SNR), and $\alpha_{gi}^{\star}$ corresponds to the interference power, which is given by

$$\alpha_{gi}^{\star} = \begin{cases} \alpha_{g2}, & \text{for } i = 1, \\ \mu \alpha_{g1}, & \text{for } i = k = 2, \end{cases} \tag{10}$$

Proof: Please, see Appendix A. ■

Observe that, since users are ordered based on their effective channel gains, to enable NOMA, they are required to feed the gains ϱ_{gk} back to the BS at each coherence interval. However, since ϱ_{gk} is just a scalar parameter, such a task will result in low additional overhead only [32].

---

[6] Note that in our analysis, we model μ as a deterministic parameter. However, since the residual SIC interference term in (8) can be approximated by a Gaussian distribution [30], μ can also be modeled as a chi-squared random variable, as in [13]. This possibility arises as a potential extension of this work.

B. Statistical Characterization of the Effective Channel Gains

Before obtaining the desired outage probability and ergodic rate expressions, we need to statistically characterize the effective channel gains. As one can observe in (A-1), ϱ_{gk} is the inverse of the gth element on the main diagonal of the following matrix

$$\begin{aligned}\mathbf{H}_{gk}^{\dagger}\mathbf{H}_{gk}^{\dagger H} &= [(\mathbf{H}_{gk}^H\mathbf{B})^H\mathbf{H}_{gk}^H\mathbf{B}]^{-1}(\mathbf{H}_{gk}^H\mathbf{B})^H\mathbf{H}_{gk}^H\mathbf{B} \\ &\quad\times([(\mathbf{H}_{gk}^H\mathbf{B})^H\mathbf{H}_{gk}^H\mathbf{B}]^{-1})^H = (\mathbf{B}^H\mathbf{H}_{gk}\mathbf{H}_{gk}^H\mathbf{B})^{-1} \\ &= \left(\mathbf{B}^H\Phi d_g^{-\eta}(\mathbf{U}\mathbf{\Lambda}^{\frac{1}{2}}\mathbf{G}_{gk})(\mathbf{U}\mathbf{\Lambda}^{\frac{1}{2}}\mathbf{G}_{gk})^H\mathbf{B}\right)^{-1} \\ &= \frac{1}{\Phi d_g^{-\eta}}\left(\mathbf{B}^H\mathbf{R}\mathbf{B}\right)^{-1} \in \mathbb{C}^{V\times V}. \qquad (11)\end{aligned}$$

As demonstrated in [3], [4], since $\mathbf{G}_{gk}$ consists of a complex Gaussian distributed matrix, the resulting matrix $\left(\mathbf{B}^H\mathbf{R}\mathbf{B}\right)^{-1}$ is inverse Wishart distributed with $N \geq V-1$ degrees of freedom. Consequently, the unordered effective channel gain $\varrho_{gk} = \frac{1}{[\mathbf{H}_{gk}^{\dagger}\mathbf{H}_{gk}^{\dagger H}]_{gg}}$ follows a Gamma distribution with shape parameter $N-V+1$ and scale parameter given by $\Phi d_g^{-\eta}[(\mathbf{B}^H\mathbf{R}\mathbf{B})^{-1}]_{gg}$. However, since the BS sorts the users out in ascending order, we need to find the probability density function (PDF) of the ordered effective channel gains. To this end, we use the theory of order statistics, which allow us to achieve the desired PDF in the following way [33]

$$\begin{aligned}f_{\varrho_{gk}}(x) &= K\binom{K-1}{k-1}\sum_{i=0}^{K-k}(-1)^i\binom{K-k}{i}\tilde{f}_{\varrho_{gk}}(x) \\ &\quad\times\tilde{F}_{\varrho_{gk}}(x)^{k-1+i}, \qquad (12)\end{aligned}$$

where $\tilde{f}_{\varrho_{gk}}(x)$ and $\tilde{F}_{\varrho_{gk}}(x)$ are, respectively, the PDF and the cumulative distribution function (CDF) of unordered gains, which are provided in [3], [4]. Then, by using the fact that in our considered scenario $K=2$, the PDF for the ordered gain of user 1 can be achieved as

$$\begin{aligned}f_{\varrho_{g1}}(x) &= 2[\tilde{f}_{\varrho_{gk}}(x) - \tilde{f}_{\varrho_{gk}}(x)\tilde{F}_{\varrho_{gk}}(x)] \\ &= \frac{2\beta_g^{\vartheta}}{\Gamma(\vartheta)}\left[x^{\vartheta-1}e^{-\beta_g x} - x^{\vartheta-1}e^{-\beta_g x}\frac{\gamma(\vartheta,\beta_g x)}{\Gamma(\vartheta)}\right], \qquad (13)\end{aligned}$$

and for user 2 as

$$f_{\varrho_{g2}}(x) = 2\tilde{f}_{\varrho_{gk}}(x)\tilde{F}_{\varrho_{gk}}(x) = \frac{2\beta_g^{\vartheta}}{\Gamma(\vartheta)}x^{\vartheta-1}e^{-\beta_g x}\frac{\gamma(\vartheta,\beta_g x)}{\Gamma(\vartheta)}, \qquad (14)$$

in which, for notation simplicity, we have defined $\vartheta = N-V+1$ and $\beta_g = \Phi d_g^{-\eta}[(\mathbf{B}^H\mathbf{R}\mathbf{B})^{-1}]_{gg}$.

C. Outage Probability

The outage probability for the kth user, in the gth sub-group, represented by P_{gk}, is the probability of achieving a data rate less than the target rate, T_{gi}, required to decode the message intended to the ith user, $i \leq k \in \{1,2\}$, and it can be defined as [3], [4]

$$P_{gk} = P[\log_2(1+\gamma_{gk}^i) < T_{gi}], \quad \forall i = 1,\cdots,k. \qquad (15)$$

Note from (15) that user 1 (weak user) will face an outage event only when its achieved data rate is not enough to satisfy its own target rate, i.e., when $\log_2(1+\gamma_{g1}^1) < T_{g1}$. While user 2 (strong user) will experience outage either if $\log_2(1+\gamma_{g2}^1) < T_{g1}$ or $\log_2(1+\gamma_{g2}^2) < T_{g2}$. Also see that, due to (10), the outage probability of the strong user will be also impacted by residual SIC interference. Closed-form expressions for the outage probability are provided in the following proposition.

Proposition I: Assuming that $\varrho_{g1} < \varrho_{g2}$, and considering imperfect SIC, the exact closed-form expressions for the outage probability achieved by users 1 and 2, can be derived as follows:

- For user 1:

$$P_{g1} = \begin{cases}\frac{2\gamma(\vartheta,\rho^{-1}\beta_g\mathcal{L}_{g1})}{\Gamma(\vartheta)} - \left[\frac{\gamma(\vartheta,\rho^{-1}\beta_g\mathcal{L}_{g1})}{\Gamma(\vartheta)}\right]^2, & \text{if } \mathcal{L}_{g1} \geq 0, \\ 1, & \text{otherwise.}\end{cases} \qquad (16)$$

- For user 2:

$$P_{g2} = \begin{cases}\left[\frac{\gamma(\vartheta,\rho^{-1}\beta_g\max\{\mathcal{L}_{g1},\mathcal{L}_{g2}\})}{\Gamma(\vartheta)}\right]^2, & \text{if } \min\{\mathcal{L}_{g1},\mathcal{L}_{g2}\} \geq 0, \\ 1, & \text{otherwise,}\end{cases} \qquad (17)$$

where $\mathcal{L}_{g1} = \frac{2^{T_{g1}}-1}{\alpha_{g1}-\alpha_{g2}(2^{T_{g1}}-1)}$, and $\mathcal{L}_{g2} = \frac{2^{T_{g2}}-1}{\alpha_{g2}-\mu\alpha_{g1}(2^{T_{g2}}-1)}$.

Proof: Please, see Appendix B. ■

D. Ergodic Rates

In this subsection, we analyze the ergodic rates experienced by each user within the sub-groups. In particular, it is considered that the strong user cannot decode perfectly the symbol intended to the weak user. As a consequence, its achievable rate, which is resulted from the SINR observed while decoding its own data symbol, will be impacted by residual interference. Under this consideration, the instantaneous data rate achieved by the first user can be written as

$$R_{g1} = \log_2(1+\gamma_{g1}^1) = \log_2\left(1+\frac{\rho\varrho_{g1}\alpha_{g1}}{\rho\varrho_{g1}\alpha_{g2}+1}\right), \qquad (18)$$

and, for the second user, the data rate is given by

$$R_{g2} = \log_2(1+\gamma_{g2}^2) = \log_2\left(1+\frac{\rho\varrho_{g2}\alpha_{g2}}{\rho\varrho_{g2}\mu\alpha_{g1}+1}\right). \qquad (19)$$

From (18) and (19), exact closed-form expressions for the users' ergodic rates will be derived, which are presented in Proposition II.

Proposition II: In presence of residual error propagation from imperfect SIC, exact closed-form expressions for the ergodic rates of users 1 and 2 can be obtained as follows:

- For user 1:

$$\bar{R}_{g1} = \xi_1(\kappa_{g1}) - \xi_1(\tilde{\kappa}_{g1}), \qquad (20)$$

where $\kappa_{g1} = \rho(\alpha_{g1} + \alpha_{g2})$, $\tilde{\kappa}_{g1} = \rho\alpha_{g2}$, and

$$\xi_1(\kappa) = \begin{cases} \sum_{i=0}^{\vartheta-1} \frac{1}{2^{\vartheta+i-1}\ln(2)\Gamma(\vartheta)i!} \sum_{m=0}^{\vartheta+i-1} \frac{(\vartheta+i-1)!}{(\vartheta+i-m-1)!} \\ \times \left[\frac{(-1)^{\vartheta+i-m-2}}{\left(\frac{\kappa}{2\beta_g}\right)^{\vartheta+i-m-1}} e^{\frac{2\beta_g}{\kappa}} \mathrm{Ei}\left(-\frac{2\beta_g}{\kappa}\right) \right. \\ \quad \left. + \sum_{n=1}^{\vartheta+i-m-1} \frac{(n-1)!}{\left(-\frac{\kappa}{2\beta_g}\right)^{\vartheta+i-m-n-1}} \right], \\ \qquad\qquad\qquad \text{if } \vartheta > 1, \\ -\frac{1}{\ln(2)} e^{\frac{2\beta_g}{\kappa}} \mathrm{Ei}\left(-\frac{2\beta_g}{\kappa}\right), \quad \text{if } \vartheta = 1. \end{cases}$$

- For user 2:

$$\bar{R}_{g2} = \begin{cases} \xi_2(\kappa_{g2}) - \xi_2(\tilde{\kappa}_{g2}), & \text{if } \mu > 0, \\ \xi_2(\kappa_{g2}), & \text{if } \mu = 0, \end{cases} \tag{21}$$

where $\kappa_{g2} = \rho(\mu\alpha_{g1} + \alpha_{g2})$, $\tilde{\kappa}_{g2} = \rho\mu\alpha_{g1}$, and

$$\xi_2(\kappa) = \begin{cases} \frac{2}{\ln(2)} \sum_{m=0}^{\vartheta-1} \frac{1}{(\vartheta-m-1)!} \left[\frac{(-1)^{\vartheta-m-2}}{\left(\frac{\kappa}{\beta_g}\right)^{\vartheta-m-1}} e^{\frac{\beta_g}{\kappa}} \mathrm{Ei}\left(-\frac{\beta_g}{\kappa}\right) \right. \\ \quad \left. + \sum_{n=1}^{\vartheta-m-1} \frac{(n-1)!}{\left(-\frac{\kappa}{\beta_g}\right)^{\vartheta-m-n-1}} \right] - \xi_1(\kappa), \\ \qquad\qquad\qquad \text{if } \vartheta > 1, \\ -\frac{2}{\ln(2)} e^{\frac{\beta_g}{\kappa}} \mathrm{Ei}\left(-\frac{\beta_g}{\kappa}\right) - \xi_1(\kappa), \quad \text{if } \vartheta = 1. \end{cases}$$

Proof: Please, see Appendix C. ■

Note that as long as we have SIC error propagation, there will be a negative term in (21), i.e., $-\xi_2(\tilde{\kappa}_{g2})$, which indicates degradation in the rate of the strong user. In fact, numerical results show that $\xi_2(\kappa)$ is an increasing function of the SNR ρ. However, when $\rho \to \infty$, the negative term in (21) will make the expression to converge to a saturation point, which means that the achievable data rate at the strong user will be always capped if $\mu \neq 0$. Similar behavior can be observed in the expression for the weak user, in (20). Nevertheless, since it does not perform SIC, its rate ceiling will be independent of μ. More details are provided in Section V, where we perform an insightful numerical analysis.

IV. ENHANCING USER FAIRNESS THROUGH DYNAMIC POWER ALLOCATION

Even though fixed power allocation policy, which was considered in the previous section, is simpler to employ and has been widely adopted in several previous works [3], [4], [32], it can lead to low data rates at the weaker users. As mentioned before, such an unbalanced performance can be very detrimental to certain 5G applications with strict fairness requirements. Therefore, in this section, we develop dynamic power allocation protocols for enhancing user fairness within the proposed massive MIMO-NOMA network. More details are provided next.

A. Power Allocation Within the NOMA Sub-Groups

First, we focus on enhancing user fairness only within each NOMA sub-group. Specifically, the BS needs to distribute the power resources between the two users within the sub-groups in such a way that their rates become balanced. Given that the weak users face the worst channel conditions, we must ensure that their rates are greater than or equal to that achieved by the stronger ones, i.e., $\log_2\left(1 + \frac{\rho\varrho_{g1}\alpha_{g1}}{\rho\varrho_{g1}\alpha_{g2}+1}\right) \geq \log_2\left(1 + \frac{\rho\varrho_{g2}\alpha_{g2}}{\rho\varrho_{g2}\mu\alpha_{g1}+1}\right)$. With this in mind, our objective can be accomplished with the following optimization problem

$$\max_{\alpha_{g1},\alpha_{g2}} \quad \{R_{g2}\} \tag{22a}$$
$$\text{s.t. } R_{g1} \geq R_{g2}, \tag{22b}$$
$$\alpha_{g1} + \alpha_{g2} = \bar{\alpha}_g, \tag{22c}$$
$$\alpha_{g1} \geq 0, \alpha_{g2} \geq 0, \tag{22d}$$

where $\bar{\alpha}_g$ denotes the total transmit power available for the gth sub-group.

Given that $\log_2(\cdot)$ is a monotonic increasing function, from the constraint (22b), it follows that $\frac{\rho\varrho_{g1}\alpha_{g1}}{\rho\varrho_{g1}\alpha_{g2}+1} \geq \frac{\rho\varrho_{g2}\alpha_{g2}}{\rho\varrho_{g2}\mu\alpha_{g1}+1}$. As a result, the problem (22) can be simplified to

$$\max_{\alpha_{g1},\alpha_{g2}} \quad \left\{\log_2\left(1 + \frac{\rho\varrho_{g2}\alpha_{g2}}{\rho\varrho_{g2}\mu\alpha_{g1}+1}\right)\right\} \tag{23a}$$
$$\text{s.t. } \varrho_{g1}\varrho_{g2}\alpha_{g2}^2 - \mu\varrho_{g1}\varrho_{g2}\alpha_{g1}^2 + \varrho_{g2}\alpha_{g2}\rho^{-1} \leq \varrho_{g1}\alpha_{g1}\rho^{-1}, \tag{23b}$$
$$\alpha_{g1} + \alpha_{g2} = \bar{\alpha}_g, \tag{23c}$$
$$\alpha_{g1} \geq 0, \alpha_{g2} \geq 0. \tag{23d}$$

Then, by letting $\alpha_{g1} = \bar{\alpha}_g - \alpha_{g2}$, the constraint in (23b) becomes $\alpha_{g2}^2(\varrho_{g1}\varrho_{g2} - \mu\varrho_{g1}\varrho_{g2}) + \alpha_{g2}(\varrho_{g1}\rho^{-1} + \varrho_{g2}\rho^{-1} + 2\mu\varrho_{g1}\varrho_{g2}\bar{\alpha}_g) - (\varrho_{g1}\rho^{-1}\bar{\alpha}_g + \mu\varrho_{g1}\varrho_{g2}\bar{\alpha}_g^2) \leq 0$, and (23) can be rewritten as

$$\max_{\alpha_{g2}} \quad \left\{\log_2\left(1 + \frac{\rho\varrho_{g2}\alpha_{g2}}{\rho\varrho_{g2}\mu(\bar{\alpha}_g - \alpha_{g2})+1}\right)\right\} \tag{24a}$$
$$\text{s.t. } \alpha_{g2}^2(\varrho_{g1}\varrho_{g2} - \mu\varrho_{g1}\varrho_{g2}) + \alpha_{g2}(\varrho_{g1}\rho^{-1} + \varrho_{g2}\rho^{-1} + 2\mu\varrho_{g1}\varrho_{g2}\bar{\alpha}_g) - (\varrho_{g1}\rho^{-1}\bar{\alpha}_g + \mu\varrho_{g1}\varrho_{g2}\bar{\alpha}_g^2) \leq 0, \tag{24b}$$
$$\alpha_{g2} \geq 0. \tag{24c}$$

By using the fact that $\log_2\left(1 + \frac{\rho\varrho_{g2}\alpha_{g2}}{\rho\varrho_{g2}\mu(\bar{\alpha}_g-\alpha_{g2})+1}\right)$ increases monotonically with α_{g2}, the problem (24) can be reduced to the optimization of only α_{g2}, as follows

$$\min_{\alpha_{g2}} \quad -\{\alpha_{g2}\} \tag{25a}$$
$$\text{s.t. } \alpha_{g2}^2(\varrho_{g1}\varrho_{g2} - \mu\varrho_{g1}\varrho_{g2}) + \alpha_{g2}(\varrho_{g1}\rho^{-1} + \varrho_{g2}\rho^{-1} + 2\mu\varrho_{g1}\varrho_{g2}\bar{\alpha}_g) - (\varrho_{g1}\rho^{-1}\bar{\alpha}_g + \mu\varrho_{g1}\varrho_{g2}\bar{\alpha}_g^2) \leq 0, \tag{25b}$$
$$-\alpha_{g2} \leq 0, \tag{25c}$$

The optimal solution for (25) is given in the following proposition.

Proposition III: The optimization problem in (25) is convex and, consequently, has a global optimal solution, which is given in closed-form by (26), shown at the bottom of the next page, and

$$\alpha_{g1}^* = \bar{\alpha}_g - \alpha_{g2}^*. \tag{27}$$

Proof: Please, see Appendix D. ■

Algorithm 1 Iterative Algorithm for Fairness Among Sub-Groups

```
   Input: $\epsilon, \rho, \varrho_{g1}, \varrho_{g2}$.
1  Set the initial available power to $\bar{\alpha}_g = 1, \forall g$;
2  do
3      for $g = 1$ to $G$ do
4          Calculate $\alpha^*_{g2}$ and $\alpha^*_{g1}$ using (26) and (27), respectively;
5          Calculate the sub-group's sum-rate by $\mathcal{R}_g = R_{g1} + R_{g2}$;
6      end
7      $\hat{g} = \mathbf{argmax}(\mathcal{R}_g : \forall g \in \{1, 2, \cdots, G\})$;
8      $\check{g} = \mathbf{argmin}(\mathcal{R}_g : \forall g \in \{1, 2, \cdots, G\})$;
9      Calculate $\Delta_\alpha$ using (28);
10     Update $\bar{\alpha}_{\hat{g}} = \bar{\alpha}_{\hat{g}} - \Delta_\alpha$;
11     Update $\bar{\alpha}_{\check{g}} = \bar{\alpha}_{\check{g}} + \Delta_\alpha$;
12     $\epsilon^* = \mathcal{R}_{\hat{g}} - \mathcal{R}_{\check{g}}$;
13 while $\epsilon^* > \epsilon$;
```

Note that the calculation of the solution above requires knowledge of the error propagation factor μ and the effective channel gains $\varrho_{gk}, \forall g, k$. Since the gains ϱ_{gk} are already needed at the BS for enabling NOMA, they can be directly used in power allocation. On the other hand, as clarified in Subsection III-A, μ can be estimated at the receiver's side through long-term measurements. Therefore, this scalar parameter can be fed back to the BS with little impact on the feedback overhead, and the optimum power allocation in (26) and (27) can be computed.

B. Providing Fairness Among Sub-Groups

In the last subsection, we have developed a dynamic power allocation policy for providing fairness to the users within each NOMA sub-group. However, users located at different sub-groups can still experience different performance levels. This represents an unfair distribution of resources since some groups can achieve high data rates while others can be almost in a state of outage. In view of this, in this subsection, we develop a strategy for improving fairness also among different sub-groups. For achieving this goal, we propose an iterative algorithm that enables the BS to provide a fair power allocation for all users in all sub-groups within each cluster so that all terminals can reach identical data rates. The basic idea is to, at each iteration, transfer a certain amount of power, denoted by Δ_α, from the best to the worst sub-group, and to use the dynamic power allocation derived in the last subsection to iteratively rebalance each user's individual rate. This iterative solution is shown in Algorithm 1. As one can observe, in the first stage of the algorithm, we calculate the users' power allocation coefficients by using (26) and (27) and compute the resulting sum-rate, $\mathcal{R}_g$, for each sub-group. Then, in lines 7 and 8, the indexes of sub-groups with the highest and lowest sum-rate are selected, which are represented by $\hat{g}$ and $\check{g}$, respectively. After that, we calculate the amount of power Δ_α that needs to be reallocated from the group $\hat{g}$ to the group $\check{g}$. This process repeats until the sum-rate difference between the best and worst sub-group reaches a value lower than a predefined threshold ϵ. Observe that, since this iterative approach is computed based on the effective channel gains, $\varrho_{gk}, \forall g, k$, the BS will be required to execute Algorithm 1 at each coherence interval.

The value of Δ_α is determined by the amount of power that is required to balance the data rates of the strongest users from the best and worst sub-groups, in which, in this section, we assume that $\mu = 0$, i.e., SIC is carried out perfectly. Δ_α is calculated in the following proposition.

Proposition IV: The amount of power Δ_α needed to balance the rates of the strongest users from the sub-groups with the highest and lowest sum-rate, assuming perfect SIC,[7] is given by

$$\Delta_\alpha = \frac{-A_2 \pm \sqrt{A_2^2 - 4A_1A_3}}{2A_1}, \tag{28}$$

where

$$\begin{aligned} A_1 &= 4\varrho_{\check{g}1}^2\varrho_{\check{g}2}\rho^{-1} + 4K_1, \quad A_2 = 2A_1K_3 + 16K_2K_1, \\ A_3 &= K_3^2 - 4K_2\frac{\varrho_{\check{g}1}^2}{\varrho_{\hat{g}1}^2}(\varrho_{\hat{g}1}\rho^{-1} + \varrho_{\hat{g}2}\rho^{-1})^2 - 16K_2K_1\bar{\alpha}_{\hat{g}}, \end{aligned}$$

and

$$\begin{aligned} K_1 &= \frac{\varrho_{\check{g}1}^2}{\varrho_{\hat{g}1}^2}\varrho_{\hat{g}1}^2\varrho_{\hat{g}2}\rho^{-1}, \\ K_2 &= (\varrho_{\check{g}1}\rho^{-1} + \varrho_{\check{g}2}\rho^{-1} - \frac{\varrho_{\check{g}1}}{\varrho_{\hat{g}1}}(\varrho_{\hat{g}1}\rho^{-1} + \varrho_{\hat{g}2}\rho^{-1}))^2, \\ K_3 &= (\varrho_{\check{g}1}\rho^{-1} + \varrho_{\check{g}2}\rho^{-1})^2 + 4\varrho_{\check{g}1}^2\varrho_{\check{g}2}\rho^{-1}\bar{\alpha}_{\check{g}} \\ &\qquad - K_2 - \frac{\varrho_{\check{g}1}^2}{\varrho_{\hat{g}1}^2}(\varrho_{\check{g}1}\rho^{-1} + \varrho_{\check{g}2}\rho^{-1})^2 - 4K_1\bar{\alpha}_{\hat{g}}. \end{aligned}$$

Proof: Please, see Appendix E. ■

C. Computational Complexity of Algorithm 1

In this subsection, we provide the worst-case computational complexity of the proposed power allocation solution shown in Algorithm 1. As in [34], we consider summations, multiplications, comparisons, and square-roots as the most relevant

$$\alpha^*_{g2} = \begin{cases} \frac{1}{2(\varrho_{g1}\varrho_{g2} - \mu\varrho_{g1}\varrho_{g2})}\Big[-(\varrho_{g1}\rho^{-1} + \varrho_{g2}\rho^{-1} + 2\mu\varrho_{g1}\varrho_{g2}\bar{\alpha}_g) \\ \quad + \sqrt{(\varrho_{g1}\rho^{-1} + \varrho_{g2}\rho^{-1} + 2\mu\varrho_{g1}\varrho_{g2}\bar{\alpha}_g)^2 + 4\varrho_{g1}\varrho_{g2}(1-\mu)(\varrho_{g1}\rho^{-1}\bar{\alpha}_g + \mu\varrho_{g1}\varrho_{g2}\bar{\alpha}_g^2)}\Big], & \text{if } 0 \le \mu < 1, \\ (\varrho_{g1}\rho^{-1}\bar{\alpha}_g + \mu\varrho_{g1}\varrho_{g2}\bar{\alpha}_g^2)/(\varrho_{g1}\rho^{-1} + \varrho_{g2}\rho^{-1} + 2\mu\varrho_{g1}\varrho_{g2}\bar{\alpha}_g), & \text{if } \mu = 1. \end{cases} \tag{26}$$

---

[7] Due to the complicated expression in (26), obtaining a closed-form solution for Δ_α considering imperfect SIC becomes a very challenging task. Thus, a different approach for computing Δ_α is necessary when $\mu \neq 0$, but this is left for future works.

and time-consuming operations. The proposed algorithm is iterative, and the number of iterations, denoted here by I, depends on the predefined threshold ϵ. This shows a clear trade-off between the accuracy of the solutions and the computational complexity. Between lines 3 and 6 of Algorithm 1, at each iteration, the power allocation coefficients for strong and weak users are computed for each sub-group according to equations (26) and (27) and, then, the sum-rate of each sub-group is calculated. Note that, in (26), the variables ϱ_{g_1}, ϱ_{g_2}, μ and ρ do not change along the iterations. In fact, only the sub-group's power budget, $\bar{\alpha}$, changes. As a result, the number of summations, multiplications, and square-root operations performed at each algorithm iteration are $6G$, $8G$, and G, respectively. In line 5, we have G summations per iteration. In lines 7 and 8, we have the search for the maximum and minimum sub-group's data rate, respectively. Thereby, in each line, the algorithm performs $G-1$ comparisons. In the calculation of (28), in line 9, the number of summations, multiplications, and square-root operations are 7, 8, and 1 per iteration, respectively. Lastly, in lines from 10 to 12, we have 3 summations per iteration. To sum up, the total number of operations for a given number of iterations, I, is $17IG + 17I$. Consequently, we can conclude that the worst-case computational complexity of Algorithm 1 is $\mathcal{O}(IG)$.

V. SIMULATION RESULTS AND DISCUSSIONS

In this section, we investigate the performance of the proposed massive MIMO-NOMA system under the impact of imperfect SIC employing both fixed and dynamic power allocation policies. We also present performance comparisons with conventional massive MIMO-OMA scheme, whose implementation details can be found in [4]. We configure the BS with a uniform linear array of $M = 90$ antennas, which is transmitting information to users that are distributed among $S = 4$ spatial clusters, each one having a diameter of $D = 50$ m and an angular spread of $\delta = 10°$, which corresponds to a distance of $L = \frac{D}{2\tan(\delta)} \cong 141$ m from the BS to the center of the cluster. In addition, we configure the direction of the antenna array to the cluster that is being analyzed, i.e., the first cluster, which is located at the azimuth angle of $\varphi = 7°$, so that the array gain is maximized. Within each cluster, if not stated otherwise, there are $G = V = 2$ NOMA sub-groups with $K = 2$ users each, and we focus on the first sub-group, which is located at 115 m from the BS. The path-loss exponent is set to $\eta = 2$, and the array gain parameter to $\Phi = 4 \times 10^4$. Moreover, when fixed power allocation is considered, the power coefficients of users 1 and 2 are configured as $\alpha_1 = 5/8$ and $\alpha_2 = 3/8$, respectively. All provided simulation results are generated by averaging extensive random channel realizations.

A. *Fixed Power Allocation Results*

In this subsection, the performance analysis derived in Section III is validated, in which, in all figures, a perfect agreement between analytical and simulated curves can be visualized. Besides, all results provided in this subsection are generated by employing a fixed power allocation policy.

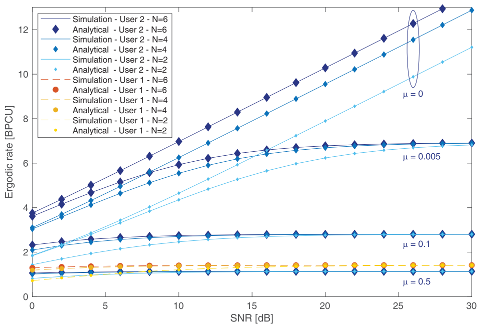

Fig. 2. Impact of imperfect SIC on the users' ergodic rates for different number of receive antennas.

Fig. 2 shows the ergodic rates in terms of transmit SNR for different levels of SIC error propagation and various numbers of receive antennas. As one can notice, when perfect SIC is considered, by increasing the number of receive antennas, the performance of the strong user is improved for all considered SNR range. However, when there is some residual error from imperfect SIC, the maximum achievable rate decreases as μ gets higher. For instance, for an error factor of $\mu = 0.005$, when $\rho = 30$dB and $N = 2$, the strong user's rate reaches a limit of 6.82 bits per channel use (BPCU), which represents a reduction of 4.4 BPCU if compared with the perfect SIC case considering the same value of transmit SNR. When $\mu = 0.5$, the impact on the performance of the strong user is even more severe, where regardless of how many antennas are employed, a rate of only 1.14 BPCU can be reached, which is lower than that achievable by the weak user. This behavior is justified by the fact that when $\rho \to \infty$, if $\mu > 0$, $R_{g2} \to \log_2\left(1 + \frac{\alpha_{g2}}{\mu\alpha_{g1}}\right)$. Therefore, if there is some residual SIC error and $\alpha_{g1} > 0$, there will be always a rate ceiling for the strong user, as anticipated in the Subsection III-D.

In Fig. 3, the ergodic sum-rate performance achieved with the proposed massive MIMO-NOMA system is compared with conventional massive MIMO-OMA counterpart, in which the impact of imperfect SIC is investigated. One can see that when the error factor is greater than zero, at some point the MIMO-OMA system outperforms the MIMO-NOMA design. This behavior show us that employing NOMA is not always advantageous when SIC imperfection is significant. For example, when $\mu = 0.005$ and $N = 2$, from 16dB onward, the OMA sum-rate performance becomes superior to that achieved by the NOMA scheme, which saturates at 8.33 BPCU. When $\mu = 0.1$, either for $N = 2$ and $N = 6$, the MIMO-OMA system always achieves higher performance than the massive MIMO-NOMA system, meaning that when error propagation is high, the employment of OMA is always preferable.

Figs. 4 and 5 show the outage probability curves for different numbers of receive antennas, target rates, and error propagation factors. In Fig. 4, by fixing the target rates of weak and strong users at 1.4 BPCU, one can see that when the error

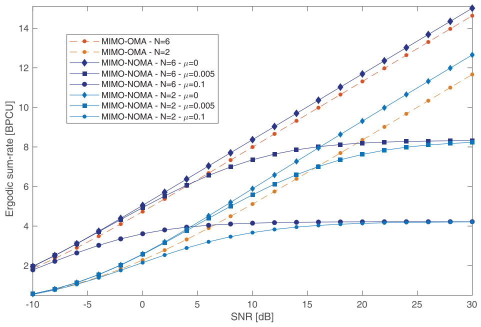

Fig. 3. Simulated ergodic sum-rate curves for massive MIMO-NOMA system with imperfect SIC and conventional massive MIMO-OMA counterpart.

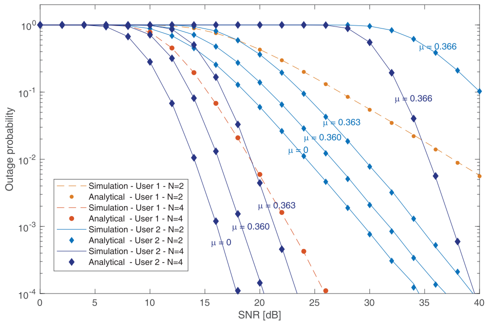

Fig. 4. Impact of imperfect SIC on the outage probability for different number of receive antennas ($T_1 = T_2 = 1.4$ BPCU).

factor gets higher than 0.36, with just a tiny error increase, the performance of the strong user is severely degraded. In particular, when $N = 4$ and μ is increased from 0.363 to 0.366, the outage probability of the strong user becomes worse even than that achieved by the weak user employing $N = 2$ receive antennas for SNR values lower than 36dB. This fast degradation happens because the maximum achievable rate of the strong user shifts very close to its target data rate when μ reaches values above 0.36, i.e., $R_{g2} \rightarrow \log_2\left(1 + \frac{\alpha_{g2}}{0.36\alpha_{g1}}\right) \approx$ 1.4 BPCU when $\rho \rightarrow \infty$. As a result, from low to moderate SNR ranges, the strong user will face an increased probability of achieving a throughput lower than its target rate, which explains the observed behavior. In Fig. 5, we can observe the impact of SIC error propagation for different sets of target rates. One can realize that for higher target values, the outage probability performance becomes more sensible to imperfect SIC. For example, by setting the target rates of both users to 1 BPCU, when μ is increased from 0 to 0.5, the outage curve of the strong user shifted only 6dB to the right. On the other hand, when $T_1 = 1.4$ and $T_2 = 2.8$ BPCU, for an error factor of only $\mu = 0.1$, the strong user requires approximately 12dB more SNR to reach the same performance of that achieved when perfect SIC is considered.

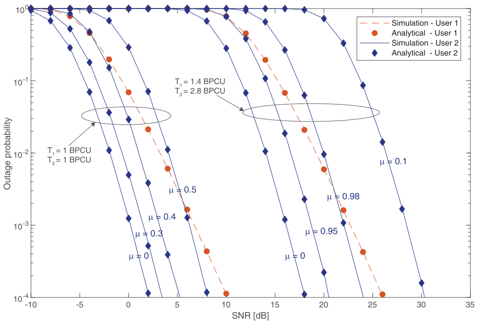

Fig. 5. Outage probability versus transmit SNR for different SIC interference levels and different target rates ($N = 4$).

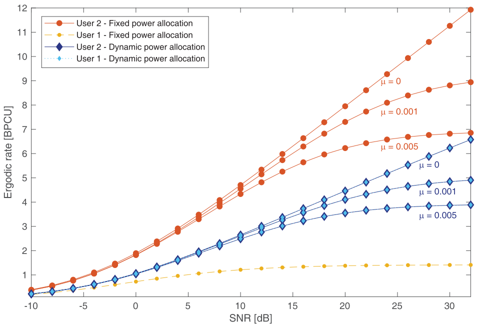

Fig. 6. Ergodic rates for strong and weak users in massive MIMO-NOMA system with dynamic and fixed power allocation policies ($N = 2$).

B. Dynamic Power Allocation Results

Now, the dynamic power allocation policies achieved in Section IV are investigated. Fig. 6 demonstrates the effectiveness of the optimum solution obtained in Proposition III, in which the ergodic rates of weak and strong users employing fixed and dynamic power allocation are shown. One can see that, with fixed power allocation, the performance of the weak user is strongly impacted, such that its ergodic rate reaches a very low limit for higher values of transmit SNR. In contrast, the strong user experiences high data rates even when SIC error propagation is present. This illustrates an unfair resource allocation. On the other hand, the dynamic policy provides great benefits to the weak user, improving fairness within the sub-group. As one can observe, the rates of the two users are balanced so that both achieve an acceptable performance. For instance, for an SNR of 22dB when perfect SIC is considered, both users can reach a rate of 4.82 BPCU with dynamic power allocation, what represents an improvement of 3.43 BPCU to the weak user if compared with that achieved with fixed policy of only 1.39 BPCU.

Considering perfect SIC, Fig. 7 brings the ergodic rate curves for various values of receive antennas, exclusively for the weak user within the considered sub-group. As one can see, in the fixed power allocation, regardless of how many

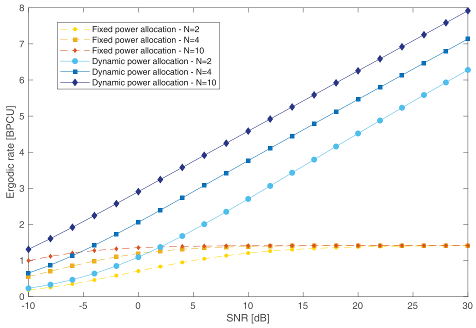

Fig. 7. Ergodic rates for the weak user in massive MIMO-NOMA system with dynamic and fixed power allocation policies ($\mu = 0$).

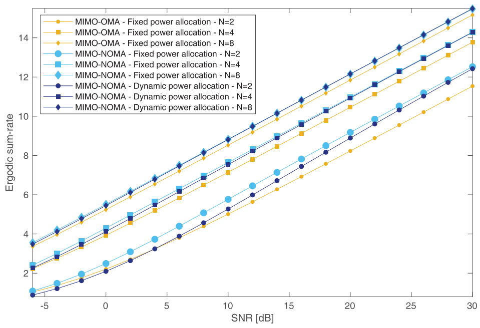

Fig. 8. Ergodic sum-rate curves for massive MIMO-NOMA and MIMO-OMA systems with dynamic and fixed power allocation policies ($\mu = 0$).

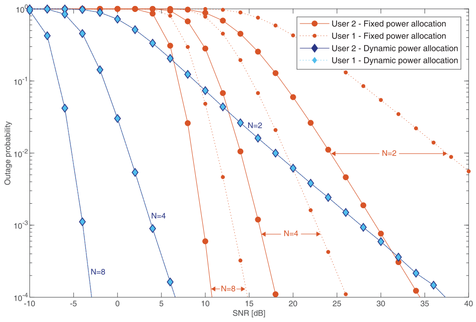

Fig. 9. Outage probabilities achieved with dynamic and fixed power allocation policies in massive MIMO-NOMA systems ($T_1 = T_2 = 1.4$ BPCU; $\mu = 0$).

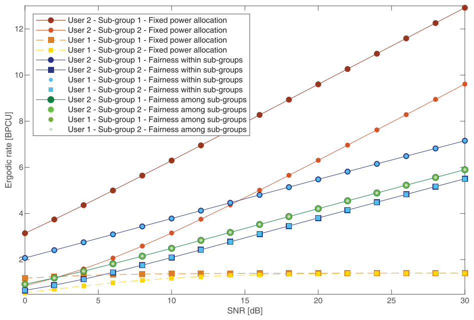

Fig. 10. Ergodic rates for users in different sub-groups employing different power allocation policies ($d_1 = 115$m; $d_2 = 150$m; $N = 4$; $\mu = 0$).

receive antennas are employed or how much the transmit SNR is improved, the achievable rate approaches a common limiting value. This does not happen with the proposed dynamic allocation. As it can be observed, the performance continues to increase even for higher SNR values. For example, considering a transmit SNR of 24dB and $N = 10$ receive antennas, the dynamic allocation can achieve a rate of 6.92 BPCU, which is almost 5 times greater than the achieved with the fixed policy. Fig. 8 compares the ergodic sum-rate curves achieved in MIMO-NOMA and MIMO-OMA systems. One can realize that dynamic allocation causes a slight decrease in the performance of the MIMO-NOMA scheme. This is because, in order to enhance fairness, the optimization problem in (22) decreases the strong users' rates, which impacts the system sum-rate. However, it is noteworthy that, for all values of receive antennas, the performance achieved in the MIMO-NOMA system employing dynamic power allocation can still outperform the conventional MIMO-OMA counterpart.

Fig. 9 demonstrates the benefits of the dynamic power allocation on the outage probability. It is interesting to observe that, in addition to the fairness improvements, the outage performance of both weak and strong users is remarkably improved. For instance, with $N = 4$ receive antennas, when employing the dynamic policy, the strong user requires roughly 12dB less SNR to reach the same outage level of that achieved with fixed power allocation. The performance gains obtained by the weak user with dynamic allocation are even more impressive, in which a remarkable gain of 20dB can be achieved.

At last, by considering different power allocation protocols, Fig. 10 plots the ergodic rates for users within two different sub-groups, one located at 115m and other at 150m from the BS. It becomes clear that, even though the optimization problem in (22) is capable of providing fairness to users within the same sub-group, users from other sub-groups can still experience different performance levels, which, in some applications, might not be desirable. This figure also illustrates the performance of the iterative algorithm proposed in Section IV-B, which provides fairness also among different sub-groups. We see that, when the referred algorithm is adopted, the rates of users from the worst sub-group are improved at the cost of reducing the performance of users from the best one. However, if we compare with fixed power allocation, Algorithm 1 is very beneficial to the weak users independently of the group. For example, for an SNR of 24dB, all users employing the iterative algorithm can reach a rate of 4.9 BPCU, which represents a gain of 3.5 BPCU for all weak users when adopting the fixed policy.

VI. CONCLUSION

In this paper, by modeling residual error propagation from imperfect SIC, the performance of a massive MIMO-NOMA network was investigated. In particular, the detailed design of beamformers and detection matrices were presented, an in-depth analytical analysis was carried out, and optimum power allocation for maximizing the rates of weak users within each sub-group was derived. An iterative algorithm for providing fairness among different sub-groups was also proposed. The simulation results demonstrated that the developed dynamic power allocation provides remarkable fairness enhancements and, at the same time, enormous performance gains in terms of outage probability. It also became evident that when SIC error propagation is present, the employment of NOMA is not always advantageous.

APPENDIX A
PROOF OF LEMMA I

From (8), it is straightforward to see that the current kth user, $1 \leq k \leq 2$, decodes the first message, i.e., the message intended to the first user, with the following SINR

$$\gamma_{gk}^{1} = \frac{|\sqrt{\alpha_{g1}}x_{g1}|^2}{|\sqrt{\alpha_{g2}}x_{g2}|^2 + |[\mathbf{H}_{gk}^{\dagger}\mathbf{n}_{gk}]_g|^2} = \frac{\frac{1}{[\mathbf{H}_{gk}^{\dagger}\mathbf{H}_{gk}^{\dagger H}]_{gg}}\alpha_{g1}}{\frac{1}{[\mathbf{H}_{gk}^{\dagger}\mathbf{H}_{gk}^{\dagger H}]_{gg}}\alpha_{g2} + \sigma_n^2}. \tag{A-1}$$

For convenience, let $\varrho_{gk} = \frac{1}{[\mathbf{H}_{gk}^{\dagger}\mathbf{H}_{gk}^{\dagger H}]_{gg}}$ be the effective channel gain, and let $\rho = 1/\sigma_n^2$ represent the transmit SNR. Given these definitions, (A-1) can be rewritten as

$$\gamma_{gk}^{1} = \frac{\rho\varrho_{gk}\alpha_{g1}}{\rho\varrho_{gk}\alpha_{g2} + 1}, \quad \text{for } 1 \leq k \leq 2. \tag{A-2}$$

Note that, since user 2 is the strongest one, it will decode its own message with some residual interference, resulting in the following SINR

$$\gamma_{g2}^{2} = \frac{\rho\varrho_{g2}\alpha_{g2}}{\rho\varrho_{g2}\mu\alpha_{g1} + 1}. \tag{A-3}$$

Then, for achieving a general SINR expression valid for both users, the following is defined

$$\alpha_{gi}^{\star} = \begin{cases} \alpha_{g2}, & \text{for } i = 1, \\ \mu\alpha_{g1}, & \text{for } i = k = 2. \end{cases} \tag{A-4}$$

Lastly, by combining (A-2), (A-3), and (A-4), the final SINR expression is obtained, as follows

$$\gamma_{gk}^{i} = \frac{\rho\varrho_{gk}\alpha_{gi}}{\rho\varrho_{gk}\alpha_{gi}^{\star} + 1}, \quad \text{for } 1 \leq i \leq k \leq 2, \tag{A-5}$$

which completes the proof. ■

APPENDIX B
PROOF OF PROPOSITION I

The outage probability expression in (15) can be rewritten as follows

$$P_{gk} = P\left[\log_2\left(1 + \frac{\rho\varrho_{gk}\alpha_{gi}}{\rho\varrho_{gk}\alpha_{gi}^{\star} + 1}\right) < T_{gi}\right] = P\left[\varrho_{gk} < \frac{2^{T_{gi}} - 1}{\rho(\alpha_{gi} - \alpha_{gi}^{\star}(2^{T_{gi}} - 1))}\right], \tag{B-1}$$

in which, for user 1 (the weak user), (B-1) can be simplified as

$$P_{g1} = P\left[\varrho_{g1} < \frac{\rho^{-1}(2^{T_{g1}} - 1)}{\alpha_{g1} - \alpha_{g2}(2^{T_{g1}} - 1)}\right] = P\left[\varrho_{g1} < \rho^{-1}\mathcal{L}_{g1}\right], \tag{B-2}$$

while, for user 2 (the strong user), (B-1) becomes

$$P_{g2} = P\left[\varrho_{g2} < \rho^{-1}\max\left\{\frac{2^{T_{g1}} - 1}{\alpha_{g1} - \alpha_{g2}(2^{T_{g1}} - 1)}, \frac{2^{T_{g2}} - 1}{\alpha_{g2} - \mu\alpha_{g1}(2^{T_{g2}} - 1)}\right\}\right] = P\left[\varrho_{g2} < \rho^{-1}\max\left\{\mathcal{L}_{g1}, \mathcal{L}_{g2}\right\}\right], \tag{B-3}$$

in which, for simplicity, we have defined $\mathcal{L}_{g1} = \frac{2^{T_{g1}}-1}{\alpha_{g1}-\alpha_{g2}(2^{T_{g1}}-1)}$ and $\mathcal{L}_{g2} = \frac{2^{T_{g2}}-1}{\alpha_{g2}-\mu\alpha_{g1}(2^{T_{g2}}-1)}$.

As one can observe, (B-2) and (B-3) are equivalent to the CDF of the effective channel gains of users 1 and 2, respectively. Consequently, the outage probability expressions can be obtained by integrating the PDFs in (13) and (14), in which, for user 1, it results in

$$P_{g1} = \frac{2\beta_g^{\vartheta}}{\Gamma(\vartheta)}\left[\int_0^{\rho^{-1}\mathcal{L}_{g1}} x^{\vartheta-1}e^{-\beta_g x}dx - \int_0^{\rho^{-1}\mathcal{L}_{g1}} x^{\vartheta-1}e^{-\beta_g x}\frac{\gamma(\vartheta, \beta_g x)}{\Gamma(\vartheta)}dx\right] = \begin{cases} \frac{2\gamma(\vartheta,\rho^{-1}\beta_g\mathcal{L}_{g1})}{\Gamma(\vartheta)} - \left[\frac{\gamma(\vartheta,\rho^{-1}\beta_g\mathcal{L}_{g1})}{\Gamma(\vartheta)}\right]^2, & \text{if } \mathcal{L}_{g1} \geq 0, \\ 1, & \text{otherwise,} \end{cases} \tag{B-4}$$

while, for user 2, the following is obtained

$$P_{g2} = \begin{cases} \left[\frac{\gamma(\vartheta,\rho^{-1}\beta_g\max\{\mathcal{L}_{g1},\mathcal{L}_{g2}\})}{\Gamma(\vartheta)}\right]^2, & \text{if } \min\left\{\mathcal{L}_{g1}, \mathcal{L}_{g2}\right\} \geq 0, \\ 1, & \text{otherwise,} \end{cases} \tag{B-5}$$

which completes the proof. ■

APPENDIX C
PROOF OF PROPOSITION II

The ergodic rates for users 1 and 2, can be obtained by calculating the expected value of their instantaneous rates. Then, firstly, let us rewrite the rate expression of user 1, in (18), as follows

$$R_{g1} = \log_2\left(\frac{1 + \rho(\alpha_{g1} + \alpha_{g2})\varrho_{g1}}{1 + \rho\alpha_{g2}\varrho_{g1}}\right) = \log_2\left(1 + \kappa_{g1}\varrho_{g1}\right) - \log_2\left(1 + \tilde{\kappa}_{g1}\varrho_{g1}\right), \tag{C-1}$$

and, for user 2, as

$$R_{g2} = \log_2\left(\frac{1 + \rho(\mu\alpha_{g1} + \alpha_{g2})\varrho_{g2}}{1 + \rho\mu\alpha_{g1}\varrho_{g2}}\right) = \log_2\left(1 + \kappa_{g2}\varrho_{g2}\right) - \log_2\left(1 + \tilde{\kappa}_{g2}\varrho_{g2}\right), \tag{C-2}$$

in which, for notation convenience, it has been defined $\kappa_{g1} = \rho(\alpha_{g1} + \alpha_{g2})$, $\tilde{\kappa}_{g1} = \rho\alpha_{g2}$,
$\kappa_{g2} = \rho(\mu\alpha_{g1} + \alpha_{g2})$, and $\tilde{\kappa}_{g2} = \rho\mu\alpha_{g1}$.

Given the expression in (C-1), the ergodic rate for user 1 can be expressed as

$$\begin{aligned}\bar{R}_{g1} &= \int_0^\infty \log_2\left(1+\kappa_{g1}x\right) f_{\varrho_{g1}}(x)dx \\ &\quad - \int_0^\infty \log_2\left(1+\tilde{\kappa}_{g1}x\right) f_{\varrho_{g1}}(x)dx \\ &= \xi_1(\kappa_{g1}) - \xi_1(\tilde{\kappa}_{g1}). \end{aligned} \tag{C-3}$$

Then, by invoking the PDF of ϱ_{g1}, provided in (13), $\xi_1(\kappa)$ can be calculated as follows

$$\begin{aligned}\xi_1(\kappa) = \frac{2\beta_g^\vartheta}{\Gamma(\vartheta)}\Bigg[&\int_0^\infty \log_2\left(1+\kappa x\right) x^{\vartheta-1}e^{-\beta_g x}dx \\ &- \int_0^\infty \log_2\left(1+\kappa x\right) x^{\vartheta-1}e^{-\beta_g x}\frac{\gamma(\vartheta,\beta_g x)}{\Gamma(\vartheta)}dx\Bigg]. \end{aligned} \tag{C-4}$$

Next, by applying the series representation of the incomplete gamma function to the second integral in (C-4), we obtain

$$\xi_1(\kappa) = \sum_{i=0}^{\vartheta-1}\frac{2\beta_g^{\vartheta+i}}{\Gamma(\vartheta)i!}\int_0^\infty \log_2\left(1+\kappa x\right) x^{\vartheta+i-1}e^{-2\beta_g x}dx. \tag{C-5}$$

Lastly, after some algebraic manipulation and applying results from [26], we achieve the desired solution, as follows

$$\xi_1(\kappa) = \begin{cases} \sum_{i=0}^{\vartheta-1}\frac{1}{2^{\vartheta+i-1}\ln(2)\Gamma(\vartheta)i!}\sum_{m=0}^{\vartheta+i-1}\frac{(\vartheta+i-1)!}{(\vartheta+i-m-1)!} \\ \times\left[\frac{(-1)^{\vartheta+i-m-2}}{\left(\frac{\kappa}{2\beta_g}\right)^{\vartheta+i-m-1}}e^{\frac{2\beta_g}{\kappa}}\mathrm{Ei}\left(-\frac{2\beta_g}{\kappa}\right)\right. \\ \quad\left.+\sum_{n=1}^{\vartheta+i-m-1}\frac{(n-1)!}{\left(-\frac{\kappa}{2\beta_g}\right)^{\vartheta+i-m-n-1}}\right], \\ \qquad\qquad\qquad \text{if } \vartheta > 1, \\ -\frac{1}{\ln(2)}e^{\frac{2\beta_g}{\kappa}}\mathrm{Ei}\left(-\frac{2\beta_g}{\kappa}\right), \quad \text{if } \vartheta = 1. \end{cases}$$

Now, we focus on the second user, in which, from (C-2), its ergodic rate can be obtained as

$$\begin{aligned}\bar{R}_{g2} &= \int_0^\infty \log_2\left(1+\kappa_{g2}x\right) f_{\varrho_{g2}}(x)dx \\ &\quad - \int_0^\infty \log_2\left(1+\tilde{\kappa}_{g2}x\right) f_{\varrho_{g2}}(x)dx \\ &= \xi_2(\kappa_{g2}) - \xi_2(\tilde{\kappa}_{g2}), \end{aligned} \tag{C-6}$$

where $\xi_2(\kappa)$ can be derived as

$$\begin{aligned}\xi_2(\kappa) &= \frac{2\beta_g^\vartheta}{\ln(2)\Gamma(\vartheta)}\int_0^\infty \ln\left(1+\kappa x\right) x^{\vartheta-1}e^{-\beta_g x}dx \\ &\quad -\sum_{i=0}^{\vartheta-1}\frac{2\beta_g^{\vartheta+i}}{\ln(2)\Gamma(\vartheta)i!}\int_0^\infty \ln\left(1+\kappa x\right) x^{\vartheta+i-1}e^{-2\beta_g x}dx \\ &= \frac{2\beta_g^\vartheta}{\ln(2)\Gamma(\vartheta)}\int_0^\infty \ln\left(1+\kappa x\right) x^{\vartheta-1}e^{-\beta_g x}dx - \xi_1(\kappa). \end{aligned} \tag{C-7}$$

Finally, by doing some manipulations in (C-7), and also using results from [26], we obtain the following solution

$$\xi_2(\kappa) = \begin{cases} \frac{2}{\ln(2)}\sum_{m=0}^{\vartheta-1}\frac{1}{(\vartheta-m-1)!}\left[\frac{(-1)^{\vartheta-m-2}}{\left(\frac{\kappa}{\beta_g}\right)^{\vartheta-m-1}}e^{\frac{\beta_g}{\kappa}}\mathrm{Ei}\left(-\frac{\beta_g}{\kappa}\right)\right. \\ \quad\left.+\sum_{n=1}^{\vartheta-m-1}\frac{(n-1)!}{\left(-\frac{\kappa}{\beta_g}\right)^{\vartheta-m-n-1}}\right] - \xi_1(\kappa), \\ \qquad\qquad\qquad \text{if } \vartheta > 1, \\ -\frac{2}{\ln(2)}e^{\frac{\beta_g}{\kappa}}\mathrm{Ei}\left(-\frac{\beta_g}{\kappa}\right) - \xi_1(\kappa), \quad \text{if } \vartheta = 1, \end{cases}$$

which completes the proof. ■

APPENDIX D
PROOF OF PROPOSITION III

Clearly, the objective function in (25a) is linear and the function on the left-hand-side of constraint (25b) consists in a quadratic polynomial. As $\varrho_{gk} \geq 0,\ \forall\ g,k$, the constraint in (25b) is convex. This makes (25) a convex optimization problem. Therefore, the KKT conditions are necessary and sufficient to determine the global optimal solution of the considered problem [35]. The Lagrangian function of (25) can be written as

$$\begin{aligned}\mathcal{L}(\alpha_{g2},\omega,\nu) &= -\alpha_{g2} + \omega[\alpha_{g2}^2(\varrho_{g1}\varrho_{g2} - \mu\varrho_{g1}\varrho_{g2}) \\ &\quad + \alpha_{g2}(\varrho_{g1}\rho^{-1} + \varrho_{g2}\rho^{-1} + 2\mu\varrho_{g1}\varrho_{g2}\bar{\alpha}_g) \\ &\quad - (\varrho_{g1}\rho^{-1}\bar{\alpha}_g + \mu\varrho_{g1}\varrho_{g2}\bar{\alpha}_g^2)] - \nu\alpha_{g2}, \end{aligned} \tag{D-1}$$

where $\omega \geq 0$ and $\nu \geq 0$ are, respectively, the Lagrangian multipliers associated with the constraints (25b) and (25c). The KKT conditions are summarized as follows

$$\nabla\mathcal{L}(\alpha_{g2},\omega,\nu) = 0, \tag{D-2a}$$

$$\begin{aligned}&\omega[\alpha_{g2}^2(\varrho_{g1}\varrho_{g2} - \mu\varrho_{g1}\varrho_{g2}) \\ &\quad + \alpha_{g2}(\varrho_{g1}\rho^{-1} + \varrho_{g2}\rho^{-1} + 2\mu\varrho_{g1}\varrho_{g2}\bar{\alpha}_g) \\ &\quad - (\varrho_{g1}\rho^{-1}\bar{\alpha}_g + \mu\varrho_{g1}\varrho_{g2}\bar{\alpha}_g^2)] = 0, \end{aligned} \tag{D-2b}$$

$$-\nu\alpha_{g2} = 0. \tag{D-2c}$$

Assuming that $\alpha_{g2} > 0$, from (D-2c) it can be concluded that $\nu = 0$. Then, from (D-2a), the value of ω is easily determined as follows

$$\begin{aligned}\omega &= (2\alpha_{g2}(\varrho_{g1}\varrho_{g2} - \mu\varrho_{g1}\varrho_{g2}) + \varrho_{g1}\rho^{-1} + \varrho_{g2}\rho^{-1} \\ &\quad + 2\mu\varrho_{g1}\varrho_{g2}\bar{\alpha}_g)^{-1}. \end{aligned} \tag{D-3}$$

Considering that the expression in (D-3) never reaches zero, and that $0 \leq \mu < 1$, the solution for (D-2b) can be obtained from the following quadratic equation

$$\begin{aligned}&\alpha_{g2}^2(\varrho_{g1}\varrho_{g2} - \mu\varrho_{g1}\varrho_{g2}) + \alpha_{g2}(\varrho_{g1}\rho^{-1} + \varrho_{g2}\rho^{-1} \\ &\quad + 2\mu\varrho_{g1}\varrho_{g2}\bar{\alpha}_g) - (\varrho_{g1}\rho^{-1}\bar{\alpha}_g + \mu\varrho_{g1}\varrho_{g2}\bar{\alpha}_g^2) = 0. \end{aligned} \tag{D-4}$$

If $\mu = 1$, (D-4) becomes the following linear equation

$$\begin{aligned}&\alpha_{g2}(\varrho_{g1}\rho^{-1} + \varrho_{g2}\rho^{-1} + 2\mu\varrho_{g1}\varrho_{g2}\bar{\alpha}_g) \\ &\quad - (\varrho_{g1}\rho^{-1}\bar{\alpha}_g + \mu\varrho_{g1}\varrho_{g2}\bar{\alpha}_g^2) = 0. \end{aligned} \tag{D-5}$$

$$\alpha^*_{g2} = \begin{cases} \frac{1}{2(\varrho_{g1}\varrho_{g2}-\mu\varrho_{g1}\varrho_{g2})} \Big[-(\varrho_{g1}\rho^{-1} + \varrho_{g2}\rho^{-1} + 2\mu\varrho_{g1}\varrho_{g2}\bar{\alpha}_g) \\ + \sqrt{(\varrho_{g1}\rho^{-1} + \varrho_{g2}\rho^{-1} + 2\mu\varrho_{g1}\varrho_{g2}\bar{\alpha}_g)^2 + 4\varrho_{g1}\varrho_{g2}(1-\mu)(\varrho_{g1}\rho^{-1}\bar{\alpha}_g + \mu\varrho_{g1}\varrho_{g2}\bar{\alpha}_g^2)}\ \Big], & \textit{if } 0 \leq \mu < 1, \\ (\varrho_{g1}\rho^{-1}\bar{\alpha}_g + \mu\varrho_{g1}\varrho_{g2}\bar{\alpha}_g^2)/(\varrho_{g1}\rho^{-1} + \varrho_{g2}\rho^{-1} + 2\mu\varrho_{g1}\varrho_{g2}\bar{\alpha}_g), & \textit{if } \mu = 1, \end{cases} \tag{D-6}$$

Therefore, the optimal power allocation for user 2 can be obtained by calculating the zeros of (D-4), if $0 \leq \mu < 1$, or solving (D-5), if $\mu = 1$, as in (D-6), shown at the top of this page, which completes the proof. ■

APPENDIX E
PROOF OF PROPOSITION IV

The amount of power Δ_α can be calculated by equalizing the rate expressions of the two strongest users of interest, in which, by considering that $\mu = 0$, the following is obtained

$$\begin{aligned} R_{\hat{g}2} = R_{\check{g}2} &\implies \log_2\left(1 + \rho\varrho_{\hat{g}2}\alpha^*_{\hat{g}2}\right) = \log_2\left(1 + \rho\varrho_{\check{g}2}\alpha^*_{\check{g}2}\right) \\ &\implies \alpha^*_{\hat{g}2}\varrho_{\hat{g}2} = \alpha^*_{\check{g}2}\varrho_{\check{g}2}. \end{aligned} \tag{E-1}$$

Next, by replacing $\alpha^*_{\hat{g}2}$ and $\alpha^*_{\check{g}2}$ by their corresponding closed-form expressions, (E-1) becomes

$$\begin{aligned} &-2\varrho_{\check{g}1}\varrho_{\hat{g}1}\rho^{-1} - 2\varrho_{\check{g}1}\varrho_{\hat{g}2}\rho^{-1} \\ &+ 2\varrho_{\check{g}1}\sqrt{(\varrho_{\hat{g}1}\rho^{-1} + \varrho_{\hat{g}2}\rho^{-1})^2 + 4\varrho^2_{\hat{g}1}\varrho_{\hat{g}2}\rho^{-1}(\bar{\alpha}_{\hat{g}} - \Delta_\alpha)} \\ &= -2\varrho_{\hat{g}1}\varrho_{\check{g}1}\rho^{-1} - 2\varrho_{\hat{g}1}\varrho_{\check{g}2}\rho^{-1} \\ &+ 2\varrho_{\hat{g}1}\sqrt{(\varrho_{\check{g}1}\rho^{-1} + \varrho_{\check{g}2}\rho^{-1})^2 + 4\varrho^2_{\check{g}1}\varrho_{\check{g}2}\rho^{-1}(\bar{\alpha}_{\check{g}} + \Delta_\alpha)}. \end{aligned} \tag{E-2}$$

Then, after some algebraic manipulation, and defining $K_1 = \frac{\varrho^2_{\check{g}1}}{\varrho^2_{\hat{g}1}}\varrho^2_{\hat{g}1}\varrho_{\hat{g}2}\rho^{-1}$, $K_2 = (\varrho_{\check{g}1}\rho^{-1} + \varrho_{\check{g}2}\rho^{-1} - \frac{\varrho_{\check{g}1}}{\varrho_{\hat{g}1}}(\varrho_{\hat{g}1}\rho^{-1} + \varrho_{\hat{g}2}\rho^{-1}))^2$, $K_3 = ((\varrho_{\check{g}1}\rho^{-1} + \varrho_{\check{g}2}\rho^{-1})^2 + 4\varrho^2_{\check{g}1}\varrho_{\check{g}2}\rho^{-1}\bar{\alpha}_{\check{g}} - K_2 - \frac{\varrho^2_{\check{g}1}}{\varrho^2_{\hat{g}1}}(\varrho_{\check{g}1}\rho^{-1} + \varrho_{\check{g}2}\rho^{-1})^2 - 4K_1\bar{\alpha}_{\hat{g}})$, $A_1 = 4\varrho^2_{\check{g}1}\varrho_{\check{g}2}\rho^{-1} + 4K_1$, $A_2 = 2A_1K_3 + 16K_2K_1$, and $A_3 = (K_3^2 - 4K_2\frac{\varrho^2_{\check{g}1}}{\varrho^2_{\hat{g}1}}(\varrho_{\hat{g}1}\rho^{-1} + \varrho_{\hat{g}2}\rho^{-1})^2 - 16K_2K_1\bar{\alpha}_{\hat{g}})$, we achieve the following quadratic equation

$$A_1\Delta^2_\alpha + A_2\Delta_\alpha + A_3 = 0. \tag{E-3}$$

The final result is obtained by calculating the zeros of (E-3). This completes the proof. ■

REFERENCES

[1] L. Lv, J. Chen, Q. Ni, Z. Ding, and H. Jiang, "Cognitive non-orthogonal multiple access with cooperative relaying: A new wireless frontier for 5G spectrum sharing," *IEEE Commun. Mag.*, vol. 56, no. 4, pp. 188–195, Apr. 2018.

[2] S.-Y. Lien, S.-L. Shieh, Y. Huang, B. Su, Y.-L. Hsu, and H.-Y. Wei, "5G new radio: Waveform, frame structure, multiple access, and initial access," *IEEE Commun. Mag.*, vol. 55, no. 6, pp. 64–71, Jun. 2017.

[3] Z. Ding and H. V. Poor, "Design of massive-MIMO-NOMA with limited feedback," *IEEE Signal Process. Lett.*, vol. 23, no. 5, pp. 629–633, May 2016.

[4] A. S. De Sena, D. B. da Costa, Z. Ding, and P. H. J. Nardelli, "Massive MIMO–NOMA networks with multi-polarized antennas," *IEEE Trans. Wireless Commun.*, vol. 18, no. 12, pp. 5630–5642, Dec. 2019.

[5] A. S. De Sena, D. B. da Costa, Z. Ding, P. H. J. Nardelli, U. S. Dias, and C. B. Papadias, "Massive MIMO-NOMA networks with successive sub-array activation," *IEEE Trans. Wireless Commun.*, vol. 19, no. 3, pp. 1622–1635, Mar. 2020.

[6] H. Xing, Y. Liu, A. Nallanathan, Z. Ding, and H. V. Poor, "Optimal throughput fairness tradeoffs for downlink non-orthogonal multiple access over fading channels," *IEEE Trans. Wireless Commun.*, vol. 17, no. 6, pp. 3556–3571, Jun. 2018.

[7] S. M. R. Islam, N. Avazov, O. A. Dobre, and K.-S. Kwak, "Power-domain non-orthogonal multiple access (NOMA) in 5G systems: Potentials and challenges," *IEEE Commun. Surveys Tuts.*, vol. 19, no. 2, pp. 721–742, 2nd Quart., 2017.

[8] A. S. de Sena *et al.*, "What role do intelligent reflecting surfaces play in non-orthogonal multiple access?" *TechRxiv*, Feb. 2020, doi: 10.36227/techrxiv.11791050.v1.

[9] H. D. R. Albonda and J. Perez-Romero, "An efficient RAN slicing strategy for a heterogeneous network with eMBB and V2X services," *IEEE Access*, vol. 7, pp. 44771–44782, 2019.

[10] X. Chen, Z. Zhang, C. Zhong, R. Jia, and D. W. K. Ng, "Fully non-orthogonal communication for massive access," *IEEE Trans. Commun.*, vol. 66, no. 4, pp. 1717–1731, Apr. 2018.

[11] M. Zeng, N.-P. Nguyen, O. A. Dobre, and H. V. Poor, "Securing downlink massive MIMO-NOMA networks with artificial noise," *IEEE J. Sel. Topics Signal Process.*, vol. 13, no. 3, pp. 685–699, Jun. 2019.

[12] H. Sun, B. Xie, R. Q. Hu, and G. Wu, "Non-orthogonal multiple access with SIC error propagation in downlink wireless MIMO networks," in *Proc. IEEE 84th Veh. Technol. Conf. (VTC-Fall)*, Sep. 2016, pp. 1–5.

[13] S. Li, M. Derakhshani, and S. Lambotharan, "Outage-constrained robust power allocation for downlink MC-NOMA with imperfect SIC," in *Proc. IEEE Int. Conf. Commun. (ICC)*, May 2018, pp. 1–7.

[14] A. Celik, M.-C. Tsai, R. M. Radaydeh, F. S. Al-Qahtani, and M.-S. Alouini, "Distributed cluster formation and power-bandwidth allocation for imperfect NOMA in DL-HetNets," *IEEE Trans. Commun.*, vol. 67, no. 2, pp. 1677–1692, Feb. 2019.

[15] D. Tweed and T. Le-Ngoc, "Dynamic resource allocation for uplink MIMO NOMA VWN with imperfect SIC," in *Proc. IEEE Int. Conf. Commun. (ICC)*, May 2018, pp. 1–6.

[16] Y. Li and G. Amarasuriya, "NOMA-aided massive MIMO downlink with distributed antenna arrays," in *Proc. IEEE Int. Conf. Commun. (ICC)*, May 2019, pp. 1–7.

[17] X. Li, M. Liu, C. Deng, P. T. Mathiopoulos, Z. Ding, and Y. Liu, "Full-duplex cooperative NOMA relaying systems with I/Q imbalance and imperfect SIC," *IEEE Wireless Commun. Lett.*, vol. 9, no. 1, pp. 17–20, Jan. 2020.

[18] X. Li, J. Li, Y. Liu, Z. Ding, and A. Nallanathan, "Residual transceiver hardware impairments on cooperative NOMA networks," *IEEE Trans. Wireless Commun.*, vol. 19, no. 1, pp. 680–695, Jan. 2020.

[19] J.-M. Kang, I.-M. Kim, and C.-J. Chun, "Deep learning-based MIMO-NOMA with imperfect SIC decoding," *IEEE Syst. J.*, early access, Sep. 10, 2019, doi: 10.1109/JSYST.2019.2937463.

[20] S. Timotheou and I. Krikidis, "Fairness for non-orthogonal multiple access in 5G systems," *IEEE Signal Process. Lett.*, vol. 22, no. 10, pp. 1647–1651, Oct. 2015.

[21] Y. Liu, M. Elkashlan, Z. Ding, and G. K. Karagiannidis, "Fairness of user clustering in MIMO non-orthogonal multiple access systems," *IEEE Commun. Lett.*, vol. 20, no. 7, pp. 1465–1468, Jul. 2016.

[22] J. A. Oviedo and H. R. Sadjadpour, "A fair power allocation approach to NOMA in multiuser SISO systems," *IEEE Trans. Veh. Technol.*, vol. 66, no. 9, pp. 7974–7985, Sep. 2017.

[23] M. M. Al-Wani, A. Sali, N. K. Noordin, S. J. Hashim, C. Y. Leow, and I. Krikidis, "Robust beamforming and user clustering for guaranteed fairness in downlink NOMA with partial feedback," *IEEE Access*, vol. 7, pp. 121599–121611, 2019.

[24] M. M. Al-Wani *et al.*, "On short term fairness and throughput of user clustering for downlink non-orthogonal multiple access system," in *Proc. IEEE 89th Veh. Technol. Conf. (VTC-Spring)*, Apr. 2019, pp. 1–6.

[25] Z. Xiao, L. Zhu, Z. Gao, D. O. Wu, and X.-G. Xia, "User fairness non-orthogonal multiple access (NOMA) for millimeter-wave communications with analog beamforming," *IEEE Trans. Wireless Commun.*, vol. 18, no. 7, pp. 3411–3423, Jul. 2019.

[26] I. S. Gradshteyn and I. M. Ryzhik, *Table of Integrals, Series, and Products*, 7th ed. Amsterdam, The Netherlands: Academic, 2007.

[27] A. Adhikary, J. Nam, J.-Y. Ahn, and G. Caire, “Joint spatial division and multiplexing—The large-scale array regime,” *IEEE Trans. Inf. Theory*, vol. 59, no. 10, pp. 6441–6463, Oct. 2013.

[28] H. Yin, D. Gesbert, and L. Cottatellucci, “Dealing with interference in distributed large-scale MIMO systems: A statistical approach,” *IEEE J. Sel. Topics Signal Process.*, vol. 8, no. 5, pp. 942–953, Oct. 2014.

[29] S. Bazzi and W. Xu, “Downlink training sequence design for FDD multi-user massive MIMO systems,” *IEEE Trans. Signal Process.*, vol. 65, no. 18, pp. 4732–4744, Sep. 2017.

[30] A. Hasan and J. Andrews, “Cancellation error statistics in a power-controlled CDMA system using successive interference cancellation,” in *Proc. 8th IEEE Int. Symp. Spread Spectr. Techn. Appl.*, Aug./Sep. 2004, pp. 419–423.

[31] A. Agrawal, J. G. Andrews, J. M. Cioffi, and T. Meng, “Iterative power control for imperfect successive interference cancellation,” *IEEE Trans. Wireless Commun.*, vol. 4, no. 3, pp. 878–884, May 2005.

[32] Z. Ding, F. Adachi, and H. V. Poor, “The application of MIMO to non-orthogonal multiple access,” *IEEE Trans. Wireless Commun.*, vol. 15, no. 1, pp. 537–552, Jan. 2016.

[33] H. A. David and H. N. Nagaraja, *Order Statistics* (Wiley Series in Probability and Statistics), 3rd ed. Hoboken, NJ, USA: Wiley, 2003.

[34] F. R. M. Lima, T. F. Maciel, W. C. Freitas, and F. R. P. Cavalcanti, “Improved spectral efficiency with acceptable service provision in multiuser MIMO scenarios,” *IEEE Trans. Veh. Technol.*, vol. 63, no. 6, pp. 2697–2711, Jul. 2014.

[35] S. Boyd and L. Vandenberghe, *Convex Optimization*. New York, NY, USA: Cambridge Univ. Press, 2004.

Arthur Sousa de Sena (Student Member, IEEE) received the B.Sc. degree in computer engineering and the M.Sc. degree in teleinformatics engineering from the Federal University of Ceará, Brazil, in 2017 and 2019, respectively. He is currently pursuing the Ph.D. degree with the School of Energy Systems, Lappeenranta University of Technology, Finland. From 2014 to 2015, he studied computer engineering as an Exchange Student with the Illinois Institute of Technology, USA. His research interests include signal processing, mobile communications systems, non-orthogonal multiple access techniques, and massive MIMO.

Francisco Rafael Marques Lima (Member, IEEE) received the B.Sc. degree (Hons.) in electrical engineering and the M.Sc. and D.Sc. degrees in telecommunications engineering from the Federal University of Ceará, Fortaleza, Brazil, in 2005, 2008, and 2012, respectively. In 2008, he was attended an internship with Ericsson Research in Lulea, Sweden, where he studied scheduling algorithms for LTE system. Since 2010, he has been a Professor with the Computer Engineering Department, Federal University of Ceará, Sobral, Brazil. He is currently a Senior Researcher with the Wireless Telecom Research Group (GTEL), Fortaleza, Brazil, where he also works on projects in cooperation with Ericsson Research. He has published several conference and journal articles as well as patents in the wireless telecommunications field. His research interests include radio resource allocation algorithms for QoS guarantees for 5G and beyond 5G networks in scenarios with multiple services, resources, antennas, and users. He is currently an Associate Editor of IEEE Access and reviewer of important IEEE journals.

Daniel Benevides da Costa (Senior Member, IEEE) was born in Fortaleza, Ceará, Brazil, in 1981. He received the B.Sc. degree in Telecommunications from the Military Institute of Engineering (IME), Rio de Janeiro, Brazil, in 2003, and the M.Sc. and Ph.D. degrees in Electrical Engineering, Area: Telecommunications, from the University of Campinas, SP, Brazil, in 2006 and 2008, respectively. His Ph.D. thesis was awarded the Best Ph.D. Thesis in Electrical Engineering by the Brazilian Ministry of Education (CAPES) at the 2009 CAPES Thesis Contest. From 2008 to 2009, he was a Postdoctoral Research Fellow with INRS-EMT, University of Quebec, Montreal, QC, Canada. Since 2010, he has been with the Federal University of Ceará, where he is currently an Associate Professor.

Prof. da Costa is currently Executive Editor of the IEEE Communications Letters and Area Editor of IEEE Open Journal of the Communication Society - Area: Green, Cognitive, and Intelligent Communications and Networks. He is also Editor of the IEEE Communications Surveys and Tutorials, IEEE Transactions on Communications, IEEE Transactions on Vehicular Technology, and IEEE Transactions on Cognitive Communications and Networking. From Jan. 2012 to May 2020, he served as Associate Technical Editor of the *IEEE Communications Magazine*. From 2012 to 2017 and from Mar. 2019 to Aug. 2019, he was Editor and Senior Editor, respectively, of the IEEE Communications Letters. He has served as Lead Guest Editor and Guest Editor of several Journal Special Issues. He has been involved on the Organizing Committee of several conferences. He is currently the Latin American Chapters Coordinator of the IEEE Vehicular Technology Society. Also, he acts as a Scientific Consultant of the National Council of Scientific and Technological Development (CNPq), Brazil, and he is a Productivity Research Fellow of CNPq. From 2012 to 2017, he was Member of the Advisory Board of the Ceará Council of Scientific and Technological Development (FUNCAP), Area: Telecommunications. Currently, he is Vice-Chair of Americas of the IEEE Technical Committee of Cognitive Networks (TCCN), Director of the TCCN Newsletter, and Chair of the Special Interest Group on “Energy-Harvesting Cognitive Radio Networks” in IEEE TCCN.

Prof. da Costa is the recipient of four conference paper awards. He received the Exemplary Reviewer Certificate of the IEEE Wireless Communications Letters in 2013 and 2019, the Exemplary Reviewer Certificate of the IEEE Communications Letters in 2016, 2017, and 2019, the Certificate of Appreciation of Top Associate Editor for outstanding contributions to IEEE Transactions on Vehicular Technology in 2013, 2015 and 2016, the Exemplary Editor Award of IEEE Communications Letters in 2016, and the Outstanding Editor Award of IEEE Access in 2017, and the Certificate of Appreciation for notable services and contributions to IEEE Access in 2018 and 2019. He is a Distinguished Lecturer of the IEEE Vehicular Technology Society. He is a Senior Member of IEEE, Member of IEEE Communications Society and IEEE Vehicular Technology Society.

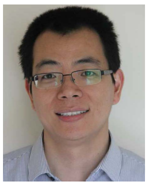

Zhiguo Ding (Fellow, IEEE) received the B.Eng. degree in electrical engineering from the Beijing University of Posts and Telecommunications in 2000, and the Ph.D. degree in electrical engineering from Imperial College London in 2005. From July 2005 to April 2018, he was worked with Queen’s University Belfast, Imperial College, Newcastle University, and Lancaster University. Since April 2018, he has been a Professor of communications with The University of Manchester. From October 2012 to September 2020, he has also been an Academic Visitor with Princeton University. His research interests are 5G networks, game theory, cooperative and energy harvesting networks, and statistical signal processing. He received the Best Paper Award in IET ICWMC-2009 and the IEEE WCSP-2014, the EU Marie Curie Fellowship from 2012 to 2014, the Top IEEE TVT Editor 2017, the IEEE Heinrich Hertz Award 2018, the IEEE Jack Neubauer Memorial Award 2018, the IEEE Best Signal Processing Letter Award 2018, and Web of Science Highly Cited Researcher 2019. He is currently serving as an Area Editor for the IEEE Open Journal of the Communications Society, an Editor for the IEEE Transactions on Communications, the IEEE Transactions on Vehicular Technology, and *the Journal of Wireless Communications and Mobile Computing*, and was an Editor for the IEEE Wireless Communications Letters, and the IEEE Communications Letters from 2013 to 2016.

Pedro H. J. Nardelli (Senior Member, IEEE) received the B.S. and M.Sc. degrees in electrical engineering from the State University of Campinas, Brazil, in 2006 and 2008, respectively, and the Ph.D. degree in communications engineering from the University of Oulu, Finland, and in electrical engineering from the State University of Campinas following a dual-degree agreement, in 2013. He is currently an Assistant Professor (tenure track) in the IoT in energy systems with the Laboratory of Control Engineering and Digital Systems, School of Energy Systems, Lappeenranta University of Technology, Finland, as well as an Adjunct Professor (docent) in information processing and communication strategies for energy systems with the Centre for Wireless Communications, University of Oulu. He is also a Research Fellow with the Academy of Finland.

Ugo Silva Dias (Senior Member, IEEE) was born in Belém, Pará, Brazil, in 1981. He received the B.Sc. degree in electrical engineering from The Federal University of Pará, Brazil, in 2004, and the M.Sc. and Ph.D. degrees in electrical engineering from The State University of Campinas, Brazil, in 2006 and 2010, respectively. Since March 2010, he has been an Assistant Professor with the University of Brasília (UnB), Brazil. He is currently a Faculty Member of the Department of Electrical Engineering. His main research interests include fading channels, field measurements, AI for future wireless networks, and wireless technologies in general. He is also an Editor of the *IET Electronics Letters* and *Communications* (ACTA Press). He has been involved on the Organizing Committee of several conferences. He was a recipient of four conference paper awards and one award from the IEEE R9 for the First Place in the IEEE R9 Success Story Contest-ComSoc Student Chapter 2017. He acts as a Scientific Consultant of the National Council of Scientific and Technological Development (CNPq), Brazil. He is a Productivity Research Fellow of CNPq. Besides the academic experiences, he also worked in several companies in the ICT industry. He serves as the Vice-President of the Brazilian Telecommunications Society, the Chair of the IEEE ComSoc CN Brazil Chapter, and an advisor of the IEEE ComSoc UnB Student Branch Chapter. He is a Senior Member of the Brazilian Telecommunications Society and a member of the IEEE Communications Society and Brazilian Communications Committee.

Constantinos B. Papadias (Fellow, IEEE) received the Diploma degree in electrical engineering from the National Technical University of Athens (NTUA) in 1991 and the Ph.D. degree (Hons.) in signal processing from the Ecole Nationale Supérieure des Télécommunications (ENST), Paris, France, in 1995.

He was a Researcher with the Institut Eurécom from 1992 to 1995, Stanford University from 1995 to 1997, Bell Labs (as a Member of Technical Staff from 1997 to 2001 and as a Technical Manager from 2001 to 2006). He was an Adjunct Professor with Columbia University from 2004 to 2005 and Carnegie Mellon University from 2006 to 2011. He was also a Professor with Athens Information Technology (AIT), in Athens, Greece, from 2006 to 2019, the Head of the Broadband Wireless and Sensor Networks (B-WiSE) Research Group, from 2013 to 2019, and the Dean from 2014 to 2019. He is currently the founding Executive Director of the Research, Technology, and Innovation Network (RTIN), The American College of Greece (ACG), where he has been a Professor of information technology, since February 2020. He also founded and the Head of RTIN's Smart Wireless Future Technologies (SWIFT) Lab. He holds an Adjunct Professorships with the ACG's Alba Graduate School of Business (AGBS), with Aalborg University, and with the University of Cyprus. He has published more than 200 articles and four books and has received more than 9400 citations for his work, with an H-index of 44. He has also made standards contributions and holds 12 patents.

Dr. Papadias was a member of the Steering Board of the Wireless World Research Forum (WWRF) from 2002 to 2006, a member and industrial liaison of the IEEE's Signal Processing for Communications Technical Committee from 2003 to 2008, and a National Representative of Greece to the European Research Council's IDEAS program from 2007 to 2008. He has served as a member of the IEEE Communications Society's Fellow Evaluation and Awards Committees, as well as an Associate Editor for various journals. He has contributed to the organization of several conferences as the General Chair including, the IEEE CTW 2016 and the IEEE SPAWC 2018 workshops. He has acted as a Technical Coordinator in several EU projects such as: CROWN in the area of cognitive radio, HIATUS in the area of interference alignment, HARP in the area of remote radio heads, and ADEL in the area of licensed shared access. He is also the Research Coordinator of the European Training Network project PAINLESS on the topic of energy autonomous infrastructure-less wireless networks and the Technical Coordinator of the EU CHIST-ERA project FIREMAN on the topic of predictive maintenance via machine type wireless communication systems. His distinctions include the Bell Labs President's Award in 2002, the IEEE Signal Processing Society's Young Author Best Paper Award in 2003, the Bell Labs Teamwork Award in 2004, his recognition as a Highly Cited Greek Scientist in 2011, two IEEE conference paper awards in 2013 and 2014 and a Best Booth Award at EUCNC in 2016. He has also been shortlisted twice for the Bell Labs Prize in 2014 and 2019. He was a Distinguished Lecturer of the IEEE Communications Society for 2012 and 2013. He was appointed as a fellow of the European Alliance of Innovation (EAI) in 2019.

Publication II

de Sena, A. S., Carrillo, D., Fang, F., Nardelli, P. H. J., da Costa, D. B., Dias, U. S.,
Ding, Z., Papadias, C. B., and Saad, W.

What Role Do Intelligent Reflecting Surfaces Play in Multi-Antenna Non-Orthogonal Multiple Access?

Reprinted with permission from
IEEE Wireless Communications
Vol. 27, no. 5, pp. 24–31, Oct. 2020

SPECTRUM AND ENERGY EFFICIENT WIRELESS COMMUNICATIONS

WHAT ROLE DO INTELLIGENT REFLECTING SURFACES PLAY IN MULTI-ANTENNA NON-ORTHOGONAL MULTIPLE ACCESS?

Arthur S. de Sena, Dick Carrillo, Fang Fang, Pedro H. J. Nardelli, Daniel B. da Costa, Ugo S. Dias, Zhiguo Ding,
Constantinos B. Papadias, and Walid Saad

ABSTRACT

Massive multiple-input multiple-output (MIMO) and non-orthogonal multiple access (NOMA) are two key techniques for enabling massive connectivity in future wireless networks. A massive MIMO-NOMA system can deliver remarkable spectral improvements and low communication latency. Nevertheless, the uncontrollable stochastic behavior of the wireless channels can still degrade its performance. In this context, the idea of an intelligent reflecting surface (IRS) has emerged as a promising technology for smartly overcoming the possibly detrimental effects of the wireless environment. The disruptive IRS concept of controlling the propagation channels via software can provide attractive performance gains to the communication networks, including higher data rates, improved user fairness, and possibly higher energy efficiency. In this article, we demonstrate the main roles of IRSs in MIMO-NOMA systems. Specifically, we identify key challenges and perform a comprehensive discussion of the main performance gains that can be achieved in IRS-assisted massive MIMO-NOMA (IRS-NOMA) networks. We outline exciting futuristic use case scenarios for IRS-NOMA and expose the main related challenges and future research directions. Furthermore, throughout the article, we support our in-depth discussions with representative numerical results.

INTRODUCTION

The fifth generation (5G) of wireless cellular systems will enable the deployment of demanding applications such as autonomous cars, massive sensor networks, telemedicine, smart homes, and more. To make these applications possible, stringent requirements such as massive connectivity, improved spectrum efficiency, and low communication latency must be fulfilled. Massive multiple-input multiple-output (MIMO) is one of 5G's key technologies for accomplishing these requirements. By exploiting the spatial domain with transmit beamforming techniques, and employing a large number of antennas, massive MIMO schemes enable resource-efficient parallel transmissions to multiple users using the same frequency and time slot. Non-orthogonal multiple access (NOMA) is another important technology envisioned to be part of future wireless systems. In particular, by employing superposition coding (SC) at the base station (BS) and successive interference cancellation (SIC) at the receivers, power-domain NOMA can simultaneously serve more than one user with a single resource block. This makes NOMA capable of providing significant connectivity improvements to communication networks. If massive MIMO and NOMA are properly combined, the features of the two techniques can be exploited to reach even higher spectral gains, which can outperform conventional systems employing orthogonal multiple access (OMA) [1].

Nevertheless, despite its potential advantage, a MIMO-NOMA system has several limitations. The random fluctuation of wireless channels, signal path loss, high user mobility, and atmospheric absorption are just a few examples of issues that can strongly impact the performance of MIMO-NOMA systems [2]. The impact of such impairments becomes even more severe at higher frequencies, that is, frequencies above 6 GHz, which are a key feature of 5G systems and beyond. Although an increase in the number of antennas can help overcome such kinds of performance degradation, this comes at the cost of increased energy consumption when the number of antenna elements becomes high. In view of this, while 5G is still being deployed, engineers and researchers have already started looking at new energy-efficient technologies to go beyond 5G and build the sixth generation (6G) [3]. In particular, due to recent advances in the field of electromagnetic metamaterials, the appealing concept of an intelligent reflecting surface (IRS) has been drawing significant attention from both academia and industry [4].

An IRS is an ultra-thin planar structure composed of a large number of reflecting elements, known as meta-atoms, whose size is smaller than the signal wavelength [5]. The key advantage of IRS structures is that each meta-atom can be dynamically tuned by software with distinct phases and amplitudes of reflection so that they can collaboratively forward the impinging waves with, ideally, any desired radiation pattern, like a hologram. This capability enables the deployment of smart wireless environments with optimized and

---

Arthur S. de Sena, Dick Carrillo, and Pedro H. J. Nardelli are with the Lappeenranta-Lahti University of Technology; Fang Fang is with Durham University; Zhiguo Ding is with the University of Manchester; Daniel B. da Costa is with the Federal University of Ceará; Ugo S. Dias is with the University of Brasília; Constantinos B. Papadias is with the American College of Greece; Walid Saad is with Virginia Tech and also with Kyung Hee University.

Digital Object Identifier:
10.1109/MWC.001.2000061

1536-1284/20/$25.00 © 2020 IEEE

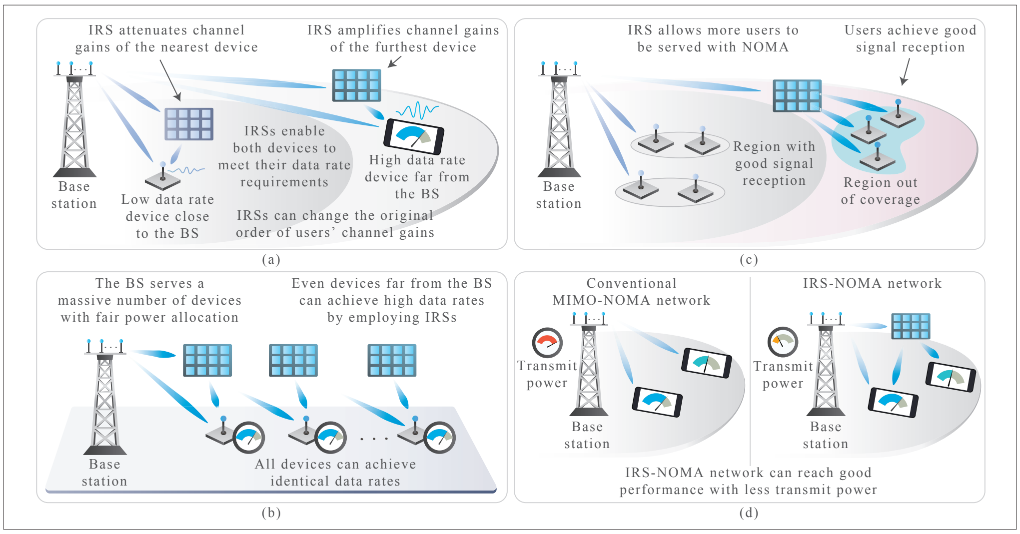

FIGURE 1. Illustration of potential achievements of IRS-NOMA networks: a) the IRSs can tune the channel gains to meet the data rate requirements of both near and far users; b) the IRSs can boost the performance of the network under fair resource allocation; c) by deploying an IRS at the cell edge, more users can be served with NOMA; d) the IRS-NOMA system can achieve similar rate performance as conventional MIMO-NOMA with less transmit power.

possibly energy-efficient signal propagation, thus paving the way toward a new wireless communication paradigm. For instance, by properly optimizing the IRS's reflection coefficients, signal beams can be formed to achieve goals such as enhancing the performance of a specific terminal, mitigating interference coming from other devices, or even completely nulling out information leakage at an eavesdropper [6, 7]. In addition to these advantageous features, an IRS has potential to exhibit near-zero energy consumption since it does not comprise the power-hungry components of conventional radio frequency chains. In general, an IRS design contains passive metamaterial parts and active control components with only ultra-low-power electronic circuitry that can be powered by energy harvesting wireless modules [4]. These features make IRSs a promising plug-and-play technology for improving the performance of future communication networks.

Although a number of surveys on the topic of IRS have recently appeared [4, 6, 8], and a few technical works on IRS and MIMO-NOMA exist [5, 9], there are no tutorials or surveys that overview and study these two subjects combined. As a result, it is still not completely clear what roles can IRSs play in MIMO-NOMA networks. Therefore, further studies for an in-depth understanding of the combination of these two promising technologies are required. In view of this, the main contribution of this article is to investigate the potential spectral and energy efficiency gains of IRS-assisted massive MIMO-NOMA (IRS-NOMA) systems in future wireless networks, as presented in Fig. 1. We also discuss the fundamental challenges pertaining to their effective deployment. In summary, this article makes the following key contributions:

- Four attractive potential achievements of IRS-NOMA networks are identified. Specifically, we show that IRS-NOMA can enable flexible control on users' channel gains, enhanced user fairness, enhanced scalability, and improved energy efficiency.
- Pervasive coverage via multiple IRSs, 3D coverage in unmanned aerial vehicle (UAV) networks, and massive grant-free transmissions are introduced as three promising applications that IRS-NOMA has potential to enable in future wireless systems beyond 5G.
- A comprehensive discussion of the main open problems, technical challenges, and possible future directions of IRS-NOMA is provided.

AN OVERVIEW OF IRS TECHNOLOGY

To shed light on the operation of an IRS system, in this section, we provide a fundamental background on the IRS hardware architecture and channel model, and a comparison with two different related technologies.

FUNDAMENTALS OF IRS ARCHITECTURE

There is no consensus on the most appropriate IRS architecture. Indeed, the available literature proposes a variety of IRS designs with different numbers of layers and different technologies, including liquid crystals, microelectromechanical systems, doped semiconductors, and electromechanical switches [4]. However, the majority of those architectures share at least three common layers:

- A meta-atom layer, comprising a larger number of passive conductor elements and low-power active switches
- A control layer, which is responsible for adjusting the amplitude and phase shift of each meta-atom element

- A gateway layer (or communication layer) that establishes the communication between the control layer and the BS

Each meta-atom acts as a sub-wavelength scatterer with reconfigurable electromagnetic properties. Such a feature enables them to collectively change the induced current patterns in the IRS so that a desired electromagnetic field response can be generated. This allows the IRS to manipulate the wavefronts to achieve objectives like steering, absorption, polarization, filtering, and collimation [8].

IRS's Channel Model, Estimation Strategies, and Associated Trade-offs

Propagation channels via an IRS behave differently from those observed in conventional communication systems. First, in a classical cellular network, users are usually considered to be located far from the transmit antennas. As a result, most conventional channel models rely on the assumption that the system is operating in the far-field regime (i.e., the impinging signals at the receive antennas are approximated as plane wavefronts). On the other hand, in IRS-assisted communication systems, one cannot guarantee that users are positioned far enough from an IRS, and the far-field assumption may not always hold. More specifically, depending on the distance between the user and its serving IRS, as well as on the size of the IRS, the system might operate instead in the near-field radiative regime. The mutual coupling effect among IRS elements is another important effect that differentiates IRS systems from classical counterparts. All of these characteristics make classical multi-path and path loss channel models not suitable and inaccurate for modeling IRS-assisted communications. Therefore, the development of more realistic models is necessary to capture the fundamental performance limits of IRS systems in practice. This is in fact known to be an important open problem in this area.

In a general IRS-aided MIMO design, the channel matrix from the BS to the user, via an IRS, conventionally includes the channel responses from the BS to the IRS, a diagonal matrix that models the IRS's signal reflection, and the channel responses between the IRS and the user. Specifically, the IRS receives the signal from the BS, and then reflects the impinging signal by inducing the amplitude and phase changes adjusted by the control layer. As a result, the BS-IRS-user link can be represented by a multiplicative channel model, which can be added coherently with the direct link from the BS to either boost or attenuate the signal strength at the receiver [6]. For a practical channel model, propagation phenomena as discussed above, that is, far-field effect, mutual coupling, path loss, and multi-path, should all be incorporated in these channel matrices.

To enable the real-time capabilities of an IRS, its control layer needs to optimize the meta-atom elements based on the channel state information (CSI) of the entire system, including all propagation links. To obtain this global CSI, different strategies with different trade-offs can be employed. For instance, it is possible to estimate the BS-IRS-user link directly on the IRSs, allowing them to reconfigure their elements autonomously. To accomplish this feature, each IRS needs to comprise at least low-power sensors and must have some processing capabilities. This distributed design can facilitate, to some extent, the channel estimation process if compared to other strategies. However, the IRS optimization complexity increases as the number of elements becomes high, which can result in high energy consumption at the IRSs. Moreover, hardware complexity and costs will also increase. Equipping the BS with a central controller and employing sophisticated channel estimation protocols is another common approach used to optimize the IRSs. In this centralized design, the estimation and optimization protocols are executed at the BS, which can afford high computational power. Once the estimation and optimization are completed, the BS only needs to send the result with the optimal set of coefficients to the IRS's control layer. The main advantage of a centralized design is that, without the need for sensing components, the IRS hardware can be further simplified, which can potentially lead to lower energy consumption. The downside is that, when the number of IRS elements grows, the channel estimation complexity and the signaling overhead from the BS to the IRSs will increase, which can be challenging in practical implementations.

IRS and Related Technologies

Next, we discuss some important features that distinguish IRSs from related technologies like amplify-and-forward (AF) relaying and ambient backscatter radio systems.

In AF relaying networks, when a relay node amplifies the received signals (which can be energy-consuming), it also amplifies noise, which consequently can degrade the system performance. Moreover, AF relays can only operate in full-duplex mode if efficient self-interference cancellation techniques are employed. This impairment can increase the implementation cost and system complexity [6]. In contrast, IRSs operate in passive reflecting mode and do not require a dedicated energy source to retransmit the impinging signals. This characteristic enables the IRSs to work in full-duplex mode without generating self-interference and noise amplification. Ambient backscatter communication [10] is another technology that operates recycling the impinging electromagnetic waves. However, the working principle and objectives of such systems are very distinct from the IRS concept. While IRSs are designed to only reflect transmitted signals, passive backscatter devices harvest energy from the received analog waves coming from different active sources to transmit its own information. Furthermore, backscatter systems are susceptible to strong direct interference generated from active sources, an issue that is not present in IRS networks. A comparison of the features of IRS and the aforementioned technologies is summarized in Table 1.

IRS-NOMA Networks: Potential Improvements

In this section, we identify four important performance gains that IRS-NOMA systems can potentially provide, namely tuned channel gains, improved fair resource allocation, enhanced coverage range, and high energy efficiency. These attractive achievements are illustrated in Fig. 1. For each of the illustrated gains, we perform a comprehensive and in-depth discussion that is supported by numerical results generated from IRS-NOMA Monte Carlo simulations. In particular, we consider the downlink transmissions of a cellular network having a single BS equipped with a uniform linear array of 80 transmit antennas that serves users with 4 receive antennas. Unless stated otherwise, an IRS with 20 reflecting elements is installed nearby to each user. Given that an IRS can forward the impinging signals with high directivity and considering that users are separated far enough, we assume that the IRS of a given user does not interfere with other IRSs. Furthermore, we present results considering both fixed and optimized reflection coefficients. In the optimized IRS results, depending on the system objectives, we dynamically tune the reflecting elements to either maximize or attenuate the instantaneous rates achieved by each user, and, on the fixed setups, all reflection phases and amplitudes are adjusted to 0° and 1, respectively. To realize these capabilities, we assume a centralized architecture where the IRSs are coordinated by a central controller installed at the BS, which can accurately estimate the CSI of all propagation links. Moreover, analogous to [1, 2], the multi-antenna users are considered to be distributed among multiple clusters, in which the users are sub-divided into multiple NOMA groups. In order to cancel inter-cluster interference, the BS employs a precoder that is constructed based on the null-space spanned by the channel matrices of interfering clusters, and each user adopts a zero-forcing receiver to eliminate the remaining inter-group interference. More details about this transmission and reception strategy can be found in [1].

TUNED CHANNEL GAINS

In order for NOMA to be effective, during the SC process at the BS, the users are sorted in an ascending or descending order based on their channel gains so that, relying on this information, the users can successfully employ SIC to recover the transmitted messages. This renders the performance of MIMO-NOMA systems highly dependent on the users' channel conditions. In particular, it has been shown that NOMA can achieve higher spectral efficiency than OMA only if the channel gains of different users are significantly distinct and if their spatial directions are not orthogonal to each other [9]. The challenge of these constraints in conventional networks is that they cannot be always satisfied. This is because the highly stochastic propagation paths are determined almost exclusively by the scattering environment and the location of the receivers, in which classical communication systems have no control. This scenario completely changes when it comes to IRS-assisted networks. By deploying IRSs, the propagation environment can be smartly tuned according to the desired objectives, potentially enabling the network to finely adjust its users' channel gains so that NOMA can always achieve good spectral efficiency. For instance, the recent work in [9] has shown that, with the help of IRSs, it is possible to force the channels to become quasi-degraded — a condition in which MIMO-NOMA can achieve the same performance of dirty paper coding (DPC), that is, where it can approach the capacity region of the downlink channel.

The IRS technology introduces a new paradigm to MIMO-NOMA networks by providing it with flexibility in multiplexing users. By employing IRSs, it can become possible even to change the original order of the users' channel gains. This capability enables the network to sort its users based on their particular data rate requirements rather than on the uncontrollable random environment of classical communication systems. For instance, in conventional NOMA deployments with fixed power allocation, when a user with high capacity requirements faces highly unfavorable channel conditions (e.g., when the user is very far from the BS), it will inevitably fall in an outage state (a state where its minimum performance requirements are not met). This is a difficult situation to be solved by traditional approaches since, independent of the power allocated, the weak user's rate will always be limited due to interference from the strong user. Figure 2 shows the simulation results for the scenario illustrated in Fig. 1a, where user 1 is located at 200 m and user 2 at 100 m from the BS. We see that the conventional MIMO-NOMA system is not able to deliver the required rate of 4 bits per channel use (BPCU) for user 1. By employing IRSs in this scenario, the system performance can be efficiently optimized. As one can notice, by properly adjusting the reflection coefficients of the IRSs, user 1, which was originally experiencing bad channel conditions, can achieve high performance and meet its required data rate. In contrast, the channel gains of the nearer user 2 are optimized to provide just the necessary capacity.

Technology	Operation mode	Characters	Drawbacks
IRS	Full duplex	Low hardware cost Potential to exhibit low energy consumption	Short range of implementation Difficult to estimate CSI
AF relay	Half/full duplex	Actively regenerate and transmit signals	High hardware cost High energy consumption
Ambient backscatter	Half duplex	Low hardware cost Low energy consumption	Limited data rate Strong interference from active source

TABLE 1. Comparison of IRS with other technologies.

IMPROVED FAIR POWER ALLOCATION

In some emerging applications, such as the Industrial Internet of Things, it can be important that all devices experience similar data rates. It has been demonstrated that, by properly performing power allocation, MIMO-NOMA systems can achieve this interesting capability. Specifically, the performance of different devices can be balanced by maximizing the minimum achievable rate in the network so that everyone can experience similar rate levels. The main disadvantage of such approaches is that to increase the performance of a weak device, the ones with good channel conditions can be excessively penalized. In addition, if the channel conditions of the weak device are too degraded, the data rates achieved under fair power allocation can be not enough to meet the quality of service requirements of other devices, leading to poor network performance. As illustrated in Fig. 1b, installing IRSs in such deployments can be very beneficial. Theoretically, all devices could reach the same data rate with the help of dynamic fair power allocation, while the IRSs could boost the channel gains to guarantee high network performance.

This above achievement can be visualized in the simulation results presented in Fig. 3, where we employ to MIMO-NOMA and IRS-NOMA both fixed and the fair power allocation policy developed in [11]. Here, we consider the existence of two users per NOMA group, one located at 100 m and another at 200 m from the BS. One can see that the fair power allocation in the MIMO-NOMA system can successfully balance the users' rates. However, the strong user pays a high price for enabling this capability. For instance, when the SNR is 36 dB, the rate achieved by both users in MIMO-NOMA under fair power allocation is 4 BPCU. This represents an expressive reduction of almost 3 BPCU to the strong user's rate. On the other hand, IRS-NOMA, in which we consider fixed reflection coefficients, can provide high data rate performance for all users. The rate curves become superior even to that achieved by the strong one with fixed allocation for the majority of the considered SNR range. This confirms that IRS-NOMA can bring high-performance fair networks to reality in the future.

ENHANCED COVERAGE RANGE

In conventional MIMO-NOMA networks, it is difficult to provide uniform signal coverage to all existing devices. Users that are far from a BS or are suffering heavy blockage may experience poor or no signal reception. This issue becomes more relevant at the higher frequency bands of 5G, 6G, and beyond. The short wavelengths of the millimeter-wave and terahertz spectrum can resonate with atmospheric oxygen and water molecules, causing a significant part of the radiated energy to be dissipated through kinetic absorption, bringing about strong signal attenuation. Such a harmful characteristic can be detrimental to the practical implementation of MIMO-NOMA. Specifically, serving users that are facing too degraded signal reception with NOMA can lead to a substantial decrease in the system sum-rate. One could increase the power allocated to strong users to improve the sum-rate, but this strategy intensifies the interference at weak users, making their performance even worse. Consequently, users that are suffering from severe channel attenuation usually end up being disconnected, which limits the coverage range of practical MIMO-NOMA networks. Fortunately, IRSs are capable of enabling long-range communication to NOMA systems. As shown in Fig. 1c, an IRS could be installed close to users that are located in regions with no signal reception. As a result, more users are allowed to be served with NOMA, thereby enhancing the connectivity capacity of such systems.

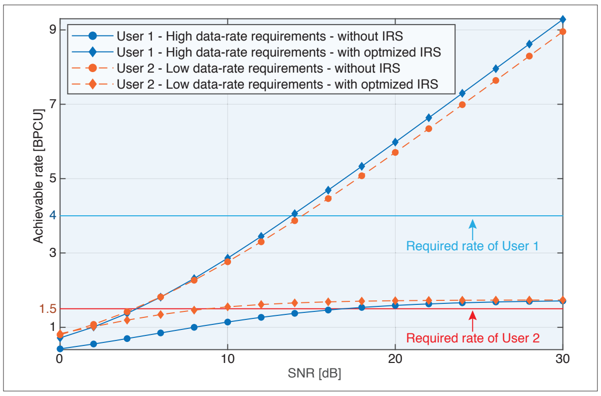

FIGURE 2. Achievable rates vs. signal-to-noise ratio (SNR) for MIMO-NOMA and IRS-NOMA systems under fixed power allocation where user 1 is located at 200 m and user 2 at 100 m from the BS. The power allocation coefficients of users 1 and 2 are 7/10 and 3/10, respectively.

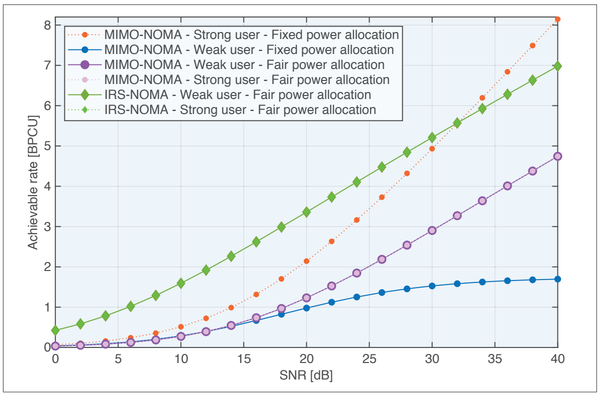

FIGURE 3. Achievable rates vs. SNR for MIMO-NOMA and IRS-NOMA systems under fixed and fair power allocation, where the weak user is located at 200 m and the strong one at 100 m from the BS. When fixed allocation is employed, the power coefficients for the weak and strong users are 7/10 and 3/10, respectively.

A practical demonstration of the aforementioned IRS capability can be seen in Fig. 4 This simulation example shows the achievable rates for MIMO-NOMA and IRS-NOMA networks under fixed power allocation when the SNR is 26 dBm. Here, we consider three users in the group of interest. Two users are closer to the BS, with the nearest user located at 100 m and the intermediate one at 200 m, while the third user is very far from the BS, located at 1500 m. As one can observe, in the conventional MIMO-NOMA system, due to the long distance from the BS, the far user experiences a weak signal reception that allows a data rate of only 0.188 BPCU. When the same user is assisted by an IRS, its rate is improved to 1.185 BPCU, which represents a gain of more than 6 times when compared to that achieved in MIMO-NOMA and incredibly almost the same rate obtained by the intermediate user. This result clearly demonstrates another attractive improvement that can be achieved with IRS-NOMA systems.

HIGH ENERGY EFFICIENCY

Because NOMA exploits the power domain, the achievable rates of served users become highly coupled with their power allocation coefficients. For example, a direct way to improve the data rate of a weak user in a conventional MIMO-NOMA system can be achieved by increasing its power coefficient and decreasing the coefficients of other users. However, since too much power can be spent to achieve just a modest increase in the data rate of one particular user, and since the system sum-rate is actually decreased, this strategy renders low energy efficiency to MIMO-NOMA systems.

On the other hand, as demonstrated in the previous subsection, IRSs can improve the data rates of weak users without requiring more transmit power. Achieving this benefit and not increasing the energy consumption of the network is another potential advantage of IRS-NOMA systems. Specifically, if we consider a centralized IRS deployment as explained earlier, the only energy required will be to enable the IRS's reconfigurability capability, which can be implemented with the help of ultra-low-power electronics. In consequence, the use of energy harvesting components can be enough to supply all the necessary power, providing the IRS technology with an opportunity to become truly energy-neutral. As shown in Fig. 1d, if this attractive feature becomes a reality, we can achieve higher performance gains with less transmit power, significantly improving the energy efficiency of IRS-NOMA networks. Nevertheless, it is noteworthy that if the energy neutrality assumption cannot be satisfied, the energy efficiency will inevitably be decreased.

In Fig. 5, we present the energy efficiency curves vs. transmit power for MIMO-NOMA and IRS-NOMA schemes. In order to show how energy-efficient IRSs can become, we consider the scenario in which energy neutrality can be achieved, as well as scenarios where the IRS contributes to the power consumption of the network. As one can see, when energy neutrality is considered, the IRS-NOMA system can offer remarkable energy efficiency improvements that outperform the conventional MIMO-NOMA counterpart. For example, when the transmit power is 10 dBm, the conventional MIMO-NOMA system can reach a maximum energy efficiency of 159.6 BPCU/W, while with the IRS-NOMA scheme, the maximum energy efficiency increases up to an incredible 427.2 BPCU/W, and at the same time, the transmit power required to reach this point decreases to 6 dBm. However, when the IRS's energy consumption is taken into account, the energy efficiency is strongly impacted. For instance, if we consider that each reflecting element introduces an additional 0.5 mW to the total power consumption, the maximum energy efficiency is decreased to approximately 253 BPCU/W, and when the power consumption per element is 3 mW, the energy efficiency becomes inferior to that achieved in the conventional MIMO-NOMA system.

SCENARIOS AND OPPORTUNITIES

In this section, we identify and discuss potential IRS-NOMA use case scenarios for future wireless networks.

MULTIPLE IRSS FOR PERVASIVE COVERAGE

With the continuous growth of the global population, crowded environments are expected to become ever more common in the upcoming years. However, the majority of the existing IRS-NOMA related works consider system models where users are assisted by a single IRS, which are not suitable for these crowded scenarios of future networks. It can be extremely difficult, or even impractical, to optimize the meta-atoms of a single IRS to assist a large number of NOMA users with different channel gains and diverse requirements. Also, since users can be highly mobile, they might not always dispose of an IRS in range. To address this challenging use case scenario, one can envision a widescale deployment of multiple IRSs for pervasive coverage. In such scenarios, the IRSs could be jointly coordinated to deliver multiple independent beams to each user so that their channel gains could be flexibly tuned. This would enable the formation of small NOMA groups in crowded environments (a difficult task to accomplish relying solely on conventional MIMO-NOMA schemes), rendering low SIC complexity to the users' devices. This large-scale IRS-NOMA network could provide massive access, ultra-high data rates, and ubiquitous signal coverage, enabling the deployment of futuristic applications such as holographic augmented reality and telepresence. For instance, in the future, large-scale IRS-NOMA can be deployed in crowded environments, like shopping malls, to attend the massive number of connections and provide ultra-high throughput to the users' sophisticated holographic enabled smartphones.

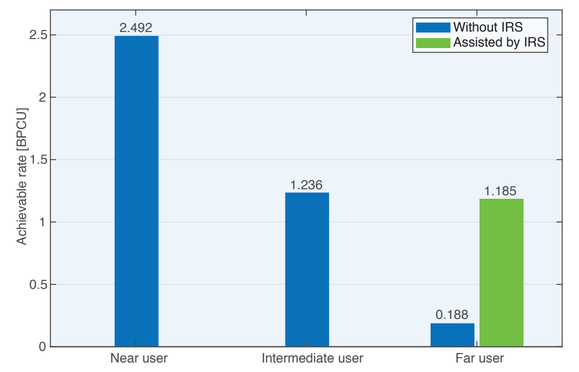

FIGURE 4. Achievable rates when the SNR is 26 dBm for MIMO-NOMA and IRS-NOMA systems serving three users with fixed power allocation. The near user is located at 100 m, the intermediate user at 200 m, and the far user at 1500 m from the BS. The power coefficients for the near, intermediate, and far users are 1/10, 3/10, and 6/10, respectively.

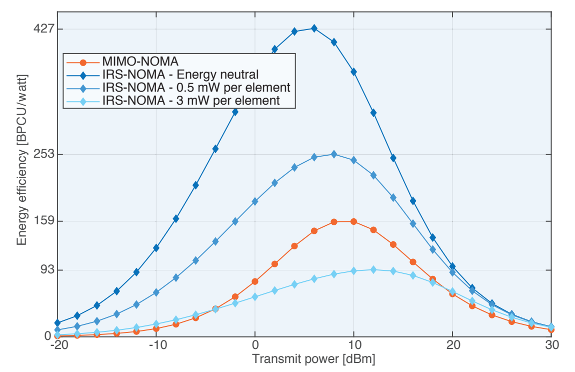

FIGURE 5. Energy efficiency vs. transmit power for MIMO-NOMA and IRS-NOMA systems under fixed power allocation. Two users are considered in this simulation, one located at 100 m and another at 200 m from the BS. The power coefficients for the far and near users are 7/10 and 3/10, respectively.

3D COVERAGE IN NOMA-UAV NETWORKS

The deployment of UAVs as aerial BSs is another appealing approach for improving signal coverage of communication networks. The intelligent arrangement of multiple UAVs combined with the use of high operating altitude enables them to enhance the coverage area through efficient dynamic 3D beamforming. UAV networks can offer

> Grant-free protocols have arisen as efficient approaches for reducing the high signaling overhead faced in traditional cellular networks [13]. In particular, NOMA-based grant-free transmissions allow multiple devices to transmit information in the uplink using the same spectrum, and without requiring grant to radio resources from the BS.

many advantages, such as flexibility in increasing the number of transmit antennas (with any array pattern), the ability to avoid obstacles (avoiding signal blockage), and more [12]. In addition to that, if NOMA is applied to UAV networks, it becomes possible to serve multiple devices with a single 3D beam, which is attractive for enabling massive access in ultra-dense dynamic environments.

Despite the above advantages, it can be challenging for a NOMA-enabled UAV to serve multiple geographically dispersed user groups. Specifically, if the NOMA groups are separated far apart, providing satisfactory performance to everyone can demand an excessive amount of energy. This can be a major impairment since a UAV hasonly a limited power supply (i.e., an onboard battery). Therefore, strategies for reducing energy consumption in NOMA-UAV networks are crucial for their successful implementation. The employment of IRSs can be very effective for accomplishing this objective as well. For instance, instead of deploying all UAVs as active transmitters, we could implement hybrid networks where some of the UAVs work as active, and others operate as smart reflective devices equipped with only lightweight passive IRSs. A UAV-assisted IRS-NOMA system would provide extended signal coverage by exploiting a combination of passive and active 3D beamforming, enabling enhanced communication performance even to NOMA groups far from active UAVs. By relaxing the need for high transmit power, such systems could present low energy consumption (if IRS energy neutrality is satisfied), prolonging the UAVs' lifetimes.

Massive NOMA-Based Grant-Free Transmissions

Grant-free protocols have emerged as efficient approaches for reducing the high signaling overhead faced by traditional cellular networks [13]. In particular, NOMA-based grant-free transmissions allow multiple devices to transmit information in the uplink using the same spectrum, and without requiring grant to radio resources from the BS. Such schemes can efficiently tackle collision issues and reduce communication delays, making them ideal for enabling critical applications with ultra-low latency requirements. However, when the number of connected devices grows, the probability of achieving similar channel gains at the BS also increases. This characteristic can lead to poor multiuser detection performance. For example, in massive machine-type communication applications like in a car factory, such impairment could lead to a failure in the production line. The installation of IRSs in this scenario can reduce the likelihood of this serious issue arising. IRS-NOMA-based grant-free transmissions could guarantee that the BS is always able to distinguish different devices so that the network can operate with stable performance even when the number of connections becomes large.

Research Challenges and Future Directions

Previously, we have shown with a simple two-user example that the order of users in IRS-NOMA networks can be controlled by properly configuring the IRS's meta-atoms, providing more flexibility for optimizing the network performance. Despite the advantages of this capability, determining the optimal user ordering in a multi-user NOMA scenario can be challenging. This is because the IRSs must be dynamically optimized based on the instantaneous realizations of combined channels of direct and BS-IRS-user links, which are also dependent on the current set of meta-atoms. As a result, the users' effective channel gains (and consequently the user ordering) become coupled with the IRS coefficients. The resulting optimization problem becomes highly complex as the number of users and the number of reflecting elements increase, which imposes major challenges for the practical implementation of IRS-NOMA networks. Therefore, the development of efficient low-complexity algorithms for jointly optimizing the IRS coefficients and user ordering is mandatory, and therefore a promising research direction.

User clustering schemes also play an important role in the performance of IRS-NOMA systems. For instance, in [9], it was shown that if users with certain channel conditions are grouped, IRS-NOMA can be outperformed by the IRS-OMA counterpart. This demonstrates that the design of efficient user clustering algorithms is also essential to exploit at maximum the benefits of IRS-NOMA systems. Given that only a few works have investigated this subject, there are excellent opportunities for future work in this domain. Furthermore, the fact that IRS-OMA can outperform IRS-NOMA also raises another issue: when should we use NOMA, and when should we use OMA? Such a fundamental question is not yet totally clarified and deserves further investigation.

Most of the contributions of this article are focused on the downlink. However, as demonstrated above with the practical example of NOMA-based grant-free transmissions, IRSs can also find useful applications in uplink MIMO-NOMA scenarios. For example, IRSs could be installed close to the users to amplify uplink transmissions, and as well as at the BS to ensure that the channel gains of the different users are always distinct. One could also deploy IRSs at BSs in shield mode to mitigate inter-cell interference in multi-cell uplink NOMA scenarios. Nevertheless, the challenges and tradeoffs associated with these tempting use case scenarios are still unclear and demand further studies.

The idea of a large-scale deployment of IRSs, as suggested earlier, can also bring challenges to the network. Transmissions coming from one IRS can leak to others and cause strong inter-IRS interference, impacting network performance. Such impairment could be mitigated if those IRSs with exceeding levels of interference could work in cooperative mode, as in [14], instead of operating independently. However, the joint coordination of multiple IRSs can trigger an explosion in signaling and processing overhead, which can potentially impact communication latency. In addition, since the channel gains observed at the receivers will be the result of the combination of all links from all IRSs, achieving the optimal set of reflection coefficients for determining the best user ordering for the entire IRS-NOMA network can become extremely difficult. Nevertheless, this is an interesting topic worth studying that is still lacking in the literature.

Finally, the concept of hybrid IRS-NOMA UAV networks (with some of the UAVs active and some passive) is another subject that can find attractive applications in 5G and beyond, but that also leads to new unsolved problems. For example, UAV-to-ground and UAV-to-UAV channels are highly dynamic and have specific features that differ from those of conventional systems [15]. As a result, the channels of IRSs mounted on UAVs will also exhibit unique characteristics that are still unknown. The accurate channel characterization of IRSs in the air, the development of specialized optimization frameworks, and the in-depth understanding of the application of NOMA in such scenarios arise as promising research possibilities.

Since the channel gains observed at the receivers will be the result of the combination of all links from all IRSs, achieving the optimal set of reflection coefficients for determining the best user ordering for the entire IRS-NOMA network can become extremely difficult. Nevertheless, this is an interesting topic worth studying that is still lacking in the literature.

ACKNOWLEDGMENTS

This work is partly supported by the Academy of Finland via: (a) ee-IoT project under Grant no. 319009, (b) FIREMAN consortium under Grant CHIST-ERA/no. 326270, and (c) EnergyNet research fellowship under Grant nos. 321265 and 328869.

REFERENCES

[1] A. S. de Sena *et al.*, "Massive MIMO-NOMA Networks with Multi-Polarized Antennas," *IEEE Trans. Wireless Commun.*, vol. 18, no. 12, Dec. 2019, pp. 5630–42.

[2] A. S. de Sena *et al.*, "Massive MIMO-NOMA Networks with Successive Sub-Array Activation," *IEEE Trans. Wireless Commun.*, vol. 19, no. 3, Mar. 2020, pp. 1622–35.

[3] W. Saad, M. Bennis, and M. Chen, "A Vision of 6G Wireless Systems: Applications, Trends, Technologies, and Open Research Problems," *IEEE Network*, vol. 34, no. 3, May/June 2020, pp. 134–42.

[4] C. Huang *et al.*, "Holographic MIMO Surfaces for 6G Wireless Networks: Opportunities, Challenges, and Trend"; https://arxiv.org/abs/1911.12296, accessed Jan. 2020.

[5] G. Yang, X. Xu, and Y.-C. Liang, "Intelligent Reflecting Surface Assisted Non-Orthogonal Multiple Access"; http://arxiv.org/abs/1907.03133, accessed Jan. 2020.

[6] Q. Wu *et al.*, "Toward Smart and Reconfigurable Environment: Intelligent Reflecting Surface Aided Wireless Network," *IEEE Commun. Mag.*, vol. 58, no. 1, Jan. 2020, pp. 106–12.

[7] M. Jung *et al.*, "On the Optimality of Reconfigurable Intelligent Surfaces (RISs): Passive Beamforming, Modulation, and Resource Allocation"; https://arxiv.org/abs/1910.00968, accessed Jan. 2020.

[8] C. Liaskos *et al.*, "A New Wireless Communication Paradigm through Software-Controlled Metasurfaces," *IEEE Wireless Commun.*, vol. 56, no. 4, Aug.. 2018, pp. 162–69.

[9] J. Zhu *et al.*, "Power Efficient IRS Assisted NOMA"; https://arxiv.org/abs/1912.11768, accessed Jan. 2020.

[10] N. V. Huynh *et al.*, "Ambient Backscatter Communications: A Contemporary Survey," *IEEE Commun. Surveys & Tutorials*, vol. 20, no. 4, 2018, pp. 2889–2922.

[11] A. S. de Sena *et al.*, "Massive MIMO-NOMA Networks with Imperfect SIC: Design and Fairness Enhancement," *IEEE Trans. Wireless Commun.*, vol. 19, no. 9, Sept. 2020, pp. 6100–15.

[12] M. Mozaffari *et al.*, "A Tutorial on UAVs for Wireless Networks: Applications, Challenges, and Open Problems," *IEEE Commun. Surveys & Tutorials*, 2019, pp. 2334–60.

[13] Z. Ding *et al.*, "Simple Semi-Grant-Free Transmission Strategies Assisted by Non-Orthogonal Multiple Access," *IEEE Trans. Commun.*, vol. 67, no. 6, June 2019, pp. 4464–78.

[14] Y. Han *et al.*, "Cooperative Double-IRS Aided Communication: Beamforming Design and Power Scaling," *IEEE Wireless Commun. Lett.*, vol. 9, no. 8, Aug. 2020, pp. 1206–10.

[15] Q. Zhang *et al.*, "Reflections in the Sky: Millimeter Wave Communication with UAV-Carried Intelligent Reflectors," *Proc. IEEE GLOBECOM*, Waikoloa, HI, Dec. 2019.

BIOGRAPHIES

ARTHUR SOUSA DE SENA [M] (arthur.sena@lut.fi) received his B.Sc. degree in computer engineering and M.Sc. degree in teleinformatics engineering from the Federal University of Ceará, Brazil, in 2017 and 2019, respectively. From 2014 to 2015, he studied computer engineering as an exchange student at Illinois Institute of Technology. He is currently working toward a Ph.D. degree at the School of Energy Systems at LUT University, Finland. He is also a researcher in the Cyber-Physical Systems Group at LUT. His research interests include signal processing, mobile communications systems, non-orthogonal multiple access techniques, intelligent metasurfaces, and massive MIMO.

DICK CARRILLO MELGAREJO [M] (dick.carrillo.melgarejo@lut.fi) received his M.Sc. degree in electrical engineering from Pontifical Catholic University of Rio de Janeiro, Brazil, in 2008. Between 2008 and 2010, he has worked as a research engineer on several research projects and standardization activities on cellular networks. From 2010 to 2018, he worked with the design and implementation of development projects based on LTE-Advanced and LTE-Advanced Pro. Since 2018 he has been a researcher at Lappeenranta — Lahti University of Technology, where he is also pursuing a Ph.D. degree in electrical engineering. His research interests are cellular networks beyond 5G supporting industrial verticals, and deep learning in communications.

FANG FANG [M] (fang.fang@durham.ac.uk) received her Ph.D. degree in electrical engineering from the University of British Columbia, Canada, in 2017. From 2018 to 2020, she was a research associate with the Department of Electrical and Electronic Engineering, University of Manchester, United Kingdom. Since August 2020, she has been with the Department of Engineering at Durham University, United Kingdom, as an assistant professor.

PEDRO H. J. NARDELLI [SM] (pedro.nardelli@lut.fi) is an assistant professor (tenure track) and Academy Research Fellow at LUT University. He currently leads the Cyber-Physical Systems Group at LUT and is project coordinator of the FIREMAN European consortium. He is also an adjunct professor at the University of Oulu. His research focuses on wireless communications, particularly applied in industrial automation and energy systems.

DANIEL BENEVIDES DA COSTA [SM] (danielbcosta@ieee.org) received his B.Sc. degree in telecommunications from the Military Institute of Engineering, Rio de Janeiro, Brazil, in 2003, and his M.Sc. and Ph.D. degrees in electrical engineering, area: telecommunications, from the University of Campinas, Sao Paolo, Brazil, in 2006 and 2008, respectively. His Ph.D thesis was awarded the Best Ph.D. Thesis in Electrical Engineering by the Brazilian Ministry of Education (CAPES) at the 2009 CAPES Thesis Contest. Since 2010, he has been with the Federal University of Ceará, where he is currently an associate professor.

UGO SILVA DIAS [SM] (ugodias@ieee.org) received his B.Sc. degree in electrical engineering from the Federal University of Pará, Brazil, in 2004, and his M.Sc. and Ph.D. degrees in electrical engineering, from the State University of Campinas, Brazil, in 2006 and 2010, respectively. Since March 2010, he has been an assistant professor at University of Brasilia, Brazil. He is a faculty member of the Department of Electrical Engineering. His main research interests include fading channels, field measurements, AI for future wireless networks, and wireless technologies in general. He is currently an Editor of *IET Electronics Letters* and ACTA Press — Communications.

ZHIGUO DING [F] (zhiguo.ding@manchester.ac.uk) is currently a professor at the University of Manchester. From September 2012 to September 2020, he was also an academic visitor at Princeton University. His research interests are 5G networks, signal processing, and statistical signal processing. He has been serving as an Editor for *IEEE TCOM* and *IEEE TVT*, and served as an Editor for *IEEE WCL* and *IEEE CL*. He received the EU Marie Curie Fellowship 2012–2014, *IEEE TVT* Top Editor 2017, the 2018 IEEE ComSoc Heinrich Hertz Award, 2018 IEEE VTS Jack Neubauer Memorial Award, and 2018 IEEE SPS Best Signal Processing Letter Award.

CONSTANTINOS B. PAPADIAS [F] (cpapadias@acg.edu) is the executive director of the Research, Technology and Innovation Network at the American College of Greece (ACG). He is also a professor of information technology at ACG's Deree College and Alba Graduate Business School, and an adjunct professor at Aalborg University and the University of Cyprus. Prior to these, he was a researcher at Institut Eurécom (1992–1995), Stanford University (1995–1997), and Lucent Bell Labs (1997–2006), where he also served as technical manager (2001–2006). He was an adjunct professor at Columbia University (2004–2005) and Carnegie Mellon University (2006–2011), and a professor at Athens Information Technology (2006–2019), where he also served as Dean (2014–2019). He has been a Fellow of the European Alliance of Innovation since 2019.

WALID SAAD [F] (walids@vt.edu) received his Ph.D. degree from the University of Oslo in 2010. Currently, he is a professor in the Department of Electrical and Computer Engineering at Virginia Tech where he leads the Network sciEnce, Wireless, and Security (NEWS) laboratory. His research interests include wireless networks, machine learning, game theory, cybersecurity, unmanned aerial vehicles, cellular networks, and cyber-physical systems. He was the author/co-author of 10 conference best paper awards and of the 2015 IEEE ComSoc Fred W. Ellersick Prize. He is an IEEE Distinguished Lecturer.

Publication III

de Sena, A. S., Nardelli, P. H. J., da Costa, D. B., Lima, F. R. M., Yang, L., Popovski, P.,
Ding, Z., and Papadias, C. B.
IRS-Assisted Massive MIMO-NOMA Networks: Exploiting Wave Polarization

Reprinted with permission from
IEEE Transactions on Wireless Communications
Vol. 20, no. 11, pp. 7166–7183, May 2021

IRS-Assisted Massive MIMO-NOMA Networks: Exploiting Wave Polarization

Arthur Sousa de Sena, *Student Member, IEEE*, Pedro H. J. Nardelli, *Senior Member, IEEE*,
Daniel Benevides da Costa, *Senior Member, IEEE*, Francisco Rafael Marques Lima, *Senior Member, IEEE*,
Liang Yang, *Member, IEEE*, Petar Popovski, *Fellow, IEEE*, Zhiguo Ding, *Fellow, IEEE*,
and Constantinos B. Papadias, *Fellow, IEEE*

***Abstract*—A dual-polarized intelligent reflecting surface (IRS) can contribute to a better multiplexing of interfering wireless users. In this paper, we use this feature to improve the performance of dual-polarized massive multiple-input multiple-output (MIMO) with non-orthogonal multiple access (NOMA) under imperfect successive interference cancellation (SIC). By considering the downlink of a multi-cluster scenario, the IRSs assist the base station (BS) to multiplex subsets of users in the polarization domain. Our novel strategy alleviates the impact of imperfect SIC and enables users to exploit polarization diversity with near-zero inter-subset interference. To this end, the IRSs are optimized to mitigate transmissions originated at the BS from the interfering polarization. The formulated optimization is transformed into quadratically constrained quadratic sub-problems, which makes it possible to obtain the optimal solution via interior-points methods. We also derive analytically a closed-form expression for the users' ergodic rates by considering large numbers of reflecting elements. This is followed by representative simulation examples and comprehensive discussions. The results show that when the IRSs are large enough, the proposed scheme always outperforms conventional massive MIMO-NOMA and MIMO-OMA systems even if SIC error propagation is present. It is also confirmed that dual-polarized IRSs can make cross-polar transmissions beneficial to the users, allowing them to improve their performance through diversity.**

***Index Terms*—Multi-polarization, intelligent reflecting surfaces, massive MIMO, NOMA.**

I. INTRODUCTION

THE fifth-generation (5G) wireless systems are already being deployed worldwide. The novel technologies and infrastructures of 5G provide support to unprecedented applications with diverse requirements, such as high data rates, high reliability, and low latency. One key technology is massive multiple-input multiple-output (MIMO), where a large number of antennas at the base station (BS) is used to transmit parallel data streams to multiple users through spatially separated beams. Conventionally, orthogonal multiple access (OMA) techniques are combined with massive MIMO to guarantee zero inter-beam interference in scenarios where it is difficult to multiplex users solely in the space domain. Even though such schemes can effectively cope with the interference issue, they may perform poorly in terms of spectral efficiency and latency as the number of users increases. Therefore, MIMO-OMA systems are not ideal for ultra-dense deployments, and this motivates the use of non-orthogonal multiple access (NOMA), such that MIMO-NOMA can serve simultaneously several users with non-separable beams.

The performance of a massive MIMO-NOMA network scales up with the increase of transmit and receive antennas. However, due to physical space constraints, the number of antennas installed in practical systems is limited at both the BS and user's devices. One efficient strategy to alleviate such a limitation can be achieved by arranging the antenna elements into co-located pairs with orthogonal polarizations, forming a dual-polarized antenna array. With such an approach, it becomes possible to install twice the number of antennas of a single-polarized array utilizing the

Manuscript received December 6, 2020; revised March 14, 2021; accepted May 14, 2021. Date of publication May 25, 2021; date of current version November 11, 2021. The work of Arthur Sousa de Sena and Pedro H. J. Nardelli was supported in part by the Academy of Finland via ee-IoT Project under Grant 319009, in part by the Framework for the Identification of Rare Events via Machine Learning and IoT Networks (FIREMAN) Consortium under Grant CHIST-ERA-17-BDSI-003 Grant 326270, and in part by the EnergyNet Research Fellowship under Grant 321265 and Grant 328869. The work of Francisco Rafael Marques Lima was supported by Ceará Council of Scientific and Technological Development (FUNCAP) (edital BPI) under Grant BP4-0172-00245.01.00/20. The work of Petar Popovski was supported in part by EU H2020 RISE-6G Project. This article was presented in part at the IEEE International Conference on Communications (ICC), Montreal, QC, Canada, June 2021. The associate editor coordinating the review of this article and approving it for publication was V. Sciancalepore. *(Corresponding author: Daniel Benevides da Costa.)*

Arthur Sousa de Sena and Pedro H. J. Nardelli are with the Department of Electrical Engineering, Lappeenranta-Lahti University of Technology, 53850 Lappeenranta, Finland (e-mail: arthurssena@ieee.org; pedro.nardelli@lut.fi).

Daniel Benevides da Costa is with the Future Technology Research Center, National Yunlin University of Science and Technology, Douliu 64002, Taiwan, and also with the Department of Computer Engineering, Federal University of Ceará (UFC), Sobral 62010-560, Brazil (e-mail: danielbcosta@ieee.org).

Francisco Rafael Marques Lima is with the Department of Computer Engineering, Federal University of Ceará (UFC), Sobral 62010-560, Brazil, and also with the Wireless Telecommunications Research Group (GTEL), UFC, Fortaleza 60416-200, Brazil (e-mail: rafaelm@gtel.ufc.br).

Liang Yang is with the College of Information Science and Engineering, Hunan University, Changsha 410082, China (e-mail: liangy@hnu.edu.cn).

Petar Popovski is with the Department of Electronic Systems, Aalborg University, 9220 Aalborg, Denmark (e-mail: petarp@es.aau.dk).

Zhiguo Ding is with the School of Electrical and Electronic Engineering, The University of Manchester, Manchester M13 9PL, U.K. (e-mail: zhiguo.ding@manchester.ac.uk).

Constantinos B. Papadias is with the Research, Technology and Innovation Network (RTIN), The American College of Greece, 15342 Athens, Greece (e-mail: cpapadias@acg.edu).

Color versions of one or more figures in this article are available at https://doi.org/10.1109/TWC.2021.3081419.

Digital Object Identifier 10.1109/TWC.2021.3081419

same physical space. In addition, since antennas with orthogonal polarizations exhibit a low correlation, dual-polarization enables massive MIMO-NOMA systems to exploit diversity in the polarization domain, which can significantly outperform conventional single-polarized schemes [1]. Due to these attractive features, dual-polarized antenna arrays have been adopted as standard in the 3rd generation partnership project (3GPP) long-term evolution advanced (LTE-A) and 5G New Radio (NR) specifications [2].

Despite the mentioned advantages, a dual-polarized massive MIMO-NOMA system still has numerous limitations. For instance, the mutual coupling between antennas and the stochastic nature of the scatterer environment can depolarize the transmitted signals and generate cross-polar interference at the receivers. As demonstrated in [1], these depolarization phenomena can deteriorate the system performance. Furthermore, in power-domain NOMA, the users need to employ successive interference cancellation (SIC) to decode their received data symbols, which also has some drawbacks. An increase in the number of users leads to higher interference and a more complex SIC decoding process, potentially resulting in excessive decoding errors, lowered system throughput, and increased usage of the device battery. It was shown in [3] that SIC errors severely impact the performance of massive MIMO-NOMA systems, making them less spectrally efficient than massive MIMO-OMA schemes. This harmful characteristic limits the maximum number of users served with NOMA in practical systems.

This implies that the benefits of dual-polarized MIMO-NOMA systems can be harvested if there is an increased control of the (de)polarization properties of the propagation environment. In this sense, the recent concept of an intelligent reflecting surface (IRS) [4]–[7] holds a great potential. An IRS is an engineered device that comprises multiple sub-wavelength reflecting elements with reconfigurable electromagnetic properties. The phases and amplitudes of reflections induced by the IRS elements are controlled independently via software, which enables them to, collectively, forward the impinging waves with an optimized radiation pattern and reach diverse objectives like beam steering, collimation, absorption, and control of polarization [8]. Such appealing features unlock countless new possibilities for manipulating the random phenomena of electromagnetic propagation, a critical issue in any wireless communication system. This is discussed in several recent works, some of them dealing specifically with MIMO-OMA and MIMO-NOMA.

A. Related Works

The majority of recent IRS-MIMO related works are concentrated on the study of point-to-point or OMA-based schemes. For example, the authors of [9] investigated the performance of IRS-assisted point-to-point narrow-band and orthogonal frequency division multiplexing (OFDM) MIMO systems. Specifically, transmit beamforming and IRS reflecting elements were optimized to maximize the ergodic rates of the considered systems. In the simulation examples, the proposed optimization algorithms outperformed conventional MIMO schemes with and without IRSs. The minimization of the symbol error rate (SER) of an IRS-assisted point-to-point MIMO system was addressed in [10]. The IRS reflecting elements and beamforming matrix were optimized alternatively, in which four different methods were investigated. All methods achieved superior performance than conventional systems without IRS in terms of SER. A single-cell multi-user OMA-based network was considered in [11]. The authors of this work minimized the total transmit power of an IRS-MIMO system under users' individual SINR constraints. An asymptotic analysis with a large number of reflecting elements was also performed. The multi-cell IRS-MIMO case was addressed in [12]. In this work, an IRS was exploited to improve the performance of cell-edge users, in which two algorithms based on majorization-minimization and the complex circle manifold methods were proposed to optimize the IRS reflecting elements. The authors of [13] employed an IRS to assist multi-user MIMO cognitive radio systems, where a block coordinate descent algorithm was proposed to maximize the achievable weighted sum rate. The employment of IRSs for improving the performance of simultaneous wireless information and power transfer (SWIPT) in MIMO systems was investigated in [14], and for addressing security issues in [15].

A few contributions have investigated IRSs in MIMO-NOMA schemes. For instance, the work in [16] addressed a simple IRS-assisted MIMO-NOMA network, in which near and far users were paired to be served with NOMA with the aid of IRSs. The energy efficiency of a two-user IRS-MIMO-NOMA network was investigated in [17]. In this work, the IRS reflecting elements and the beamforming vectors at the BS were jointly optimized to minimize the total power consumption of the system. In [18], by considering both continuous and discrete phase shifters, the authors maximized the sum-rate of a IRS-MIMO-NOMA system in a scenario with multiple users. The proposed scheme outperformed conventional NOMA and OMA-based systems in the presented simulation examples. A multi-cluster IRS-assisted MIMO-NOMA network was considered in [19]. By relaxing the need for active beamforming at the BS, the authors focused on the design of an IRS for canceling inter-cluster interference. The application of IRSs to millimeter-wave NOMA systems was studied in [20]. With the objective of maximizing the system sum-rate, this work developed an algorithm for optimizing power allocation, reflecting elements, and active beamforming. The scenario with IRSs mounted on unmanned aerial vehicles (UAV) to assist a MIMO-NOMA network was investigated in [21]. In this work, by optimizing the position of the UAV, the transmit beamforming, and the IRS reflecting elements, the rate of the strong user was maximized while guaranteeing the target rate of the weak user.

B. Motivation and Contributions

To the best of our knowledge, all related works are limited to only single-polarized systems, and there are no works that exploit the capabilities of IRSs for manipulating wave polarization in dual-polarized MIMO-NOMA networks. Motivated by this, and given the great potential of IRSs for improving the performance of communication systems, we harness the attractive features of dual-polarized IRSs for tackling the interference limitation issue of NOMA from a perspective that has not been addressed so far. Specifically, in this work, multiple dual-polarized IRSs are optimized to reduce the interference observed during the SIC decoding process of users in a massive dual-polarized MIMO-NOMA network. The study of interference mitigation via an IRS in MIMO-NOMA systems was only considered in [19]. However, [19] optimized a single IRS to diminish inter-cluster interference in a small-scale single-polarized MIMO-NOMA system, which is different from the objectives and system model of this work. Furthermore, the approach in [19] imposes strict restrictions on the minimum number of reflecting elements, which makes it not scalable for massive MIMO-NOMA systems, whereas our scheme is compatible with IRSs of any size (at the cost of an IRS optimization with higher complexity than in [19]). In addition to alleviating the impact of imperfect SIC, our novel scheme enables users to exploit polarization diversity. Further details and the main contributions of this work are summarized as follows:

- By considering a scenario where the BS and the users employ multiple dual-polarized antennas and assuming imperfect SIC, we propose a novel strategy that exploits the functionalities of dual-polarized IRSs to assist the BS to subdivide each group of users into two polarization subsets. For users in the first subset, the BS transmits the data symbols using vertically polarized antennas and, for users in the second one, the BS transmits using the horizontally polarized antennas. With this strategy, SIC can be executed by users from each subset separately. As a result, each user will experience less SIC interference when decoding its message. Moreover, the IRSs transform depolarization phenomena into an advantage and enable the users to exploit polarization diversity with near-zero inter-subset interference.
- By assuming that the users and the IRSs are distributed among different spatial clusters and aiming to focus the transmissions to the users and IRSs of interest and null out anywhere else, we first exploit the second-order statistics of the channels, i.e., the channel covariance matrices, to construct the active beamforming matrices at the BS. We then concatenate the beamforming matrix for spatial interference cancellation with a low-complexity precoding vector that is designed to multiplex the users and form the polarization subsets.
- The dual-polarized reflecting elements of each IRS are optimized to mitigate the transmissions originated at the BS from the interfering polarization. The formulated optimization problem is challenging to solve. To overcome the complex formulation, we transform the original problem into quadratically constrained quadratic subproblems, and we show that their optimal solutions can be obtained via interior-points methods in polynomial time.
- An in-depth performance analysis is carried out, where, by modeling polarization interference and errors from imperfect SIC, we derive the signal-to-interference-plus-noise ratio (SINR) experienced by the users and investigate the statistical distributions of the effective channel gains. Because the reflecting elements of the IRSs change rapidly with the fast fading channels, identifying the exact distributions for arbitrary numbers of reflecting elements becomes difficult. As an alternative, we characterize the approximate distributions for the asymptotic case with a large number of reflecting elements. Based on this asymptotic statistical analysis, we derive a closed-form expression for the ergodic rates observed by each user, which provides a practical tool for verifying the fundamental limits of the proposed system when large IRSs are employed.
- Last, by presenting representative numerical simulation results, we validate the analysis and supplement it with discussions. We show that when the IRSs are large enough, the proposed scheme always outperforms conventional massive MIMO-NOMA and MIMO-OMA systems even if SIC error propagation is present. We also confirm that the dual-polarized IRSs can make cross-polar transmissions beneficial to the users, allowing them to improve their performance through diversity.

Notation and Special Functions: Bold-faced lower-case letters denote vectors and upper-case represent matrices. The ith element of a vector $\mathbf{a}$ is denoted by $[\mathbf{a}]_i$, the (ij) entry of a matrix $\mathbf{A}$ by $[\mathbf{A}]_{ij}$, and the transpose and the Hermitian transpose of $\mathbf{A}$ are represented by $\mathbf{A}^T$ and $\mathbf{A}^H$, respectively. The symbol $\otimes$ represents the Kronecker product, $\odot$ is the Khatri-Rao product [22], $\mathbf{I}_M$ represents the identity matrix of dimension $M \times M$, and $\mathbf{0}_{M,N}$ denotes the $M \times N$ matrix with all zero entries. The operator *vec*$\{\cdot\}$ transforms a matrix of dimension $M \times N$ into a column vector of length MN, the operator *vecd*$\{\cdot\}$ converts the diagonal elements of an $M \times M$ square matrix into a column vector of length M, and *diag*$\{\cdot\}$ transforms a vector of length M into an $M \times M$ diagonal matrix. In addition, $\Re\{\cdot\}$ returns the real part of a complex number, $(\cdot)^*$ is the complex conjugate, $\mathbb{E}[\cdot]$ denotes expectation, $\Gamma(\cdot)$ is the Gamma function [23, eq. (8.310.1)], $\gamma(\cdot,\cdot)$ is the lower incomplete Gamma function [23, eq. (8.350.1)], and $G_{p,q}^{m,n}\left(\begin{smallmatrix}\mathbf{a}\\ \mathbf{b}\end{smallmatrix} \mid x\right)$ corresponds to the Meijer's G-function [23, eq. (9.301)].

II. FUNDAMENTALS OF A DUAL-POLARIZED IRS

The design of dual-polarized IRSs and their potential capabilities have been well studied in the field of antennas and electromagnetic theory [24]–[26]. In addition to phase/amplitude control, also possible with a single-polarized IRS, a dual-polarized IRS can perform polarization beam splitting, independent control of impinging polarizations, and polarization conversion [26]. For instance, by properly tuning the IRS reflecting elements, it is possible to convert a vertically polarized wave into a horizontally polarized one, and vice-versa, or reflect it with its original polarization [24], [25]. These features can find useful applications in dual-polarized communication systems, such as interference mitigation or polarization diversity. Specifically, by considering linear vertical-horizontal polarization, the transformations

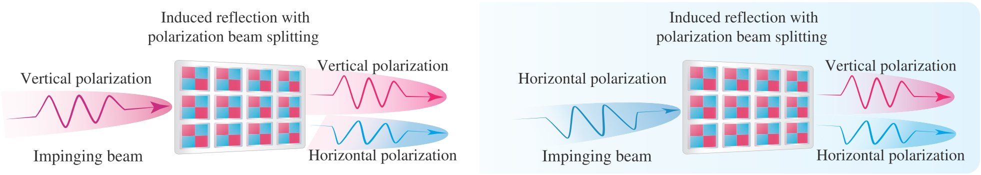

Fig. 1. Simplified capabilities of a dual-polarized IRS. Linearly polarized impinging signals are split into two beams with orthogonal polarizations.

induced by each reflecting element of a dual-polarized IRS can be modeled by a reflection matrix:

$$\mathbf{\Psi} = \begin{bmatrix} \omega^{vv} e^{-j\phi^{vv}} & \omega^{hv} e^{-j\phi^{hv}} \\ \omega^{vh} e^{-j\phi^{vh}} & \omega^{hh} e^{-j\phi^{hh}} \end{bmatrix}, \tag{1}$$

where $\phi_l^{pq} \in [0, 2\pi]$ and $\omega_l^{pq} \in [0, 1]$ represent, respectively, the phase and amplitude of reflection induced by the IRS element from polarization p to polarization q, with $p, q \in \{v, h\}$, in which v stands for vertical and h for horizontal. A simplified illustration of the capabilities of the dual-polarized IRS considered in this work is shown in Fig. 1.

We illustrate these concepts through a simple example. Suppose that a transmitter that is equipped with a single vertically polarized antenna sends information to a receiver that employs a pair of dual-polarized antennas, with a vertically and a horizontally polarized antenna element, respectively. In an ideal scenario without any depolarization, the transmitted information would only be received in the matching vertically polarized receive antenna, becoming impossible to explore polarization diversity at the receiver. By deploying a dual-polarized IRS, the transmitted vertically polarized wave can be split into two independent beams, one with vertical polarization and another with horizontal polarization, as shown in Fig. 1. This would enable the receiver to exploit polarization diversity and improve its performance. Specifically, assume that the IRS has only a single dual-polarized reflecting element. Then, by recalling the dyadic backscatter channel model [7], [27], and using the reflection matrix in (1), the noiseless signal propagated through the reflected IRS link, observed at the vertically and horizontally polarized receive antennas is:

$$\begin{aligned} \begin{bmatrix} y^v \\ y^h \end{bmatrix} &= \frac{1}{\sqrt{2}} \begin{bmatrix} (s^{vv})^* & 0 \\ 0 & (s^{hh})^* \end{bmatrix} \begin{bmatrix} \omega^{vv} e^{-j\phi^{vv}} & \omega^{hv} e^{-j\phi^{hv}} \\ \omega^{vh} e^{-j\phi^{vh}} & \omega^{hh} e^{-j\phi^{hh}} \end{bmatrix} \\ &\times \begin{bmatrix} g^{vv} \\ 0 \end{bmatrix} x = \begin{bmatrix} \frac{1}{\sqrt{2}} (s^{vv})^* \omega^{vv} e^{-j\phi^{vv}} g^{vv} x \\ \frac{1}{\sqrt{2}} (s^{hh})^* \omega^{vh} e^{-j\phi^{vh}} g^{vv} x \end{bmatrix}, \end{aligned} \tag{2}$$

where x is the transmitted data symbol, g^{vv} is the channel coefficient between the transmitter and the IRS, and s^{pq} is the channel coefficient between the IRS and the receiver corresponding to the signal that was reflected with polarization p and arrived with polarization q, in which $p, q \in \{v, h\}$. Since an IRS is a passive device, we introduce a normalization factor of $\frac{1}{\sqrt{2}}$. As one can observe in (2), by performing polarization beam splitting, the IRS was capable of delivering two replicas with independent phases and amplitudes of the transmitted data symbol. Hence, a range of new possibilities can be enabled by properly optimizing the IRS reflecting elements. For instance, if the transmitter in this example is instead sending interference, one could easily switch the IRS to an absorption mode, i.e., set the coefficients ω^{vv} and ω^{vh} to zero, so that no interfering transmissions would arrive at the receiver.

In this work, we consider a generalization of the signal model in (2) in a more complex setup containing several IRSs with a large number of dual-polarized reflecting elements. Despite the more complex system model and the greater number of reflecting elements, the capabilities of the larger IRSs considered in the proposed scheme are the same as the presented in this section, i.e., capabilities of manipulating wave polarization, clearly illustrated in Fig. 1. Since the basic background for understanding this work's proposal has been provided, we can now dive into the detailed system model.

III. System Model

Consider a single cell MIMO-NOMA network where a single BS is communicating in downlink mode with multiple users. Both users and the BS comprise dual-polarized antenna elements that are arranged into multiple co-located pairs, each one containing one vertically and one horizontally polarized antenna element. More specifically, users are equipped with $N/2$ pairs of dual-polarized receive antennas, and the BS with $M/2$ pairs of dual-polarized transmit antennas that are organized in a uniform linear array. It is considered that M and N are even, and that $M \gg N$. Moreover, within the cell, users are assumed to be distributed among different geographical areas, forming K spatial clusters with Q users each. Users within each cluster are organized into G groups, each one containing U users, i.e, $Q = GU$. In conventional MIMO-NOMA systems, the uth user from a given group performs SIC by considering interference from all the other $U - 1$ users within the same group. However, since SIC is an interference-limited technique, such an approach can lead to performance degradation, which here is tackled by a novel strategy that exploits the polarization domain. Specifically, we program the BS to further subdivide each of the G groups into two polarization subsets, namely vertical subset and horizontal subset, each one containing U^p users, $p \in \{v, h\}$, i.e., U^v users are served with vertically polarized transmit antennas, and U^h users are served with horizontally polarized antennas, such that $U^v + U^h = U$. To enable this scheme, we exploit the capabilities of dual-polarized IRSs to ensure that signals transmitted from one polarization impinge only

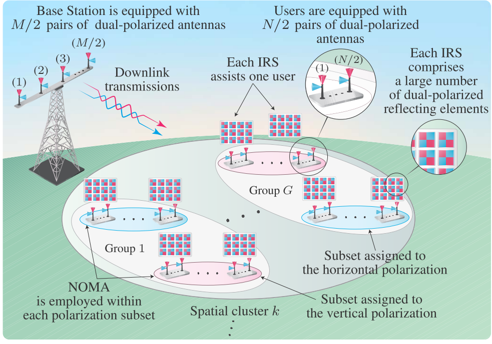

Fig. 2. System model. Dual-polarized IRSs enable users to exploit polarization diversity by mitigating polarization interference.

at users assigned to that specific polarization. For instance, if a user is assigned to the vertical polarization, its serving IRS should cancel out all signals coming from horizontally polarized BS antennas. For this, we assume that there are U IRSs with L dual-polarized reflecting elements installed within each group and that each IRS assists exactly one user,[1] as illustrated in Fig. 2. A comparison of the main characteristics and highlights between our proposal and those from conventional schemes is provided in Fig. 3. As more details will be provided later, in addition to reducing interference and SIC decoding errors, our IRS-MIMO-NOMA scheme naturally enables users to exploit polarization diversity with only a low computational complexity.

Following the proposed strategy, after the users have been properly grouped, the BS applies superposition coding to each polarization subset and transmit the superimposed messages through the assigned polarization. More specifically, the BS sends the following signal

$$\mathbf{x}=\sum_{k=1}^{K}\mathbf{P}_k\begin{bmatrix}\mathbf{x}^v\\ \mathbf{x}^h\end{bmatrix}=\sum_{k=1}^{K}\mathbf{P}_k\sum_{g=1}^{G}\sum_{u=1}^{U}\mathbf{v}_{kgu}\alpha_{kgu}x_{kgu}\in\mathbb{C}^{M\times 1}, \tag{3}$$

where $\mathbf{x}^p$ is the data vector transmitted in the polarization $p\in\{v,h\}$. x_{kgu} and α_{kgu} are, respectively, the symbol and the power coefficient for the uth user in the gth group within the kth cluster. $\mathbf{P}_k\in\mathbb{C}^{M\times\bar{M}}$ is a precoding matrix intended to eliminate inter-cluster interference, in which $\bar{M}$ is a parameter that controls the number of effective data streams transmitted from the BS, and $\mathbf{v}_{kgu}=\left[(\mathbf{v}_{kgu}^v)^T,(\mathbf{v}_{kgu}^h)^T\right]^T\in\mathbb{C}^{\bar{M}\times 1}$ is an inner precoding vector responsible for multiplexing the users in the polarization domain, satisfying $\|\mathbf{v}_{kgu}\|^2=1$.

As the phases and amplitudes of reflections induced by a single dual-polarized reflecting element can be modeled by the 2×2 matrix in (1), the reflection matrix for an IRS with L reflecting elements can be generalized to a $2L\times 2L$ matrix. This matrix is partitioned into four $L\times L$ diagonal submatrices.[2] Thus, the reflection matrix for the dual-polarized IRS that assists the uth user in the gth group of the kth spatial cluster is:

$$\mathbf{\Theta}_{kgu}=\begin{bmatrix}\mathbf{\Phi}_{kgu}^{vv} & \mathbf{\Phi}_{kgu}^{hv}\\ \mathbf{\Phi}_{kgu}^{vh} & \mathbf{\Phi}_{kgu}^{hh}\end{bmatrix}\in\mathbb{C}^{2L\times 2L}, \tag{4}$$

where $\mathbf{\Phi}_{kgu}^{pq}=diag\{[\omega_{kgu,1}^{pq}e^{-j\phi_{kgu,1}^{pq}},\omega_{kgu,2}^{pq}e^{-j\phi_{kgu,2}^{pq}},\cdots,\omega_{kgu,L}^{pq}e^{-j\phi_{kgu,L}^{pq}}]\}\in\mathbb{C}^{L\times L}$, with $\phi_{kgu,l}^{pq}$ and $\omega_{kgu,l}^{pq}$ representing, respectively, the phase and amplitude of reflection induced by the lth IRS element from polarization p to polarization q, with $p,q\in\{v,h\}$, in which we must have $|\omega_{kgu,l}^{pq}|^2\leq 1$ for passive reflection. By using the multi-polarized and the dyadic backscatter channel models [1], [7], [27], the composite full dual-polarized channel matrix for the uth user in the gth group of the kth cluster can represented by

$$\begin{aligned}&\mathbf{H}_{kgu}^{H}\\&=\sqrt{\zeta_{kgu}^{\text{BS-IRS}}\zeta_{kgu}^{\text{IRS-U}}}\frac{1}{\sqrt{2}}\begin{bmatrix}\bar{\mathbf{S}}_{kgu}^{vv} & \mathbf{0}_{L,\frac{N}{2}}\\ \mathbf{0}_{L,\frac{N}{2}} & \bar{\mathbf{S}}_{kgu}^{hh}\end{bmatrix}^{H}\begin{bmatrix}\mathbf{\Phi}_{kgu}^{vv} & \mathbf{\Phi}_{kgu}^{hv}\\ \mathbf{\Phi}_{kgu}^{vh} & \mathbf{\Phi}_{kgu}^{hh}\end{bmatrix}\\&\quad\times\begin{bmatrix}\bar{\mathbf{G}}_{kgu}^{vv} & \sqrt{\chi^{\text{BS-IRS}}}\bar{\mathbf{G}}_{kgu}^{hv}\\ \sqrt{\chi^{\text{BS-IRS}}}\bar{\mathbf{G}}_{kgu}^{vh} & \bar{\mathbf{G}}_{kgu}^{hh}\end{bmatrix}\\&\quad+\sqrt{\zeta_{kgu}^{\text{BS-U}}}\begin{bmatrix}\bar{\mathbf{D}}_{kgu}^{vv} & \sqrt{\chi^{\text{BS-U}}}\bar{\mathbf{D}}_{kgu}^{vh}\\ \sqrt{\chi^{\text{BS-U}}}\bar{\mathbf{D}}_{kgu}^{hv} & \bar{\mathbf{D}}_{kgu}^{hh}\end{bmatrix}^{H}\\&\quad\in\mathbb{C}^{N\times M},\end{aligned} \tag{5}$$

where $\bar{\mathbf{D}}_{kgu}^{pq}\in\mathbb{C}^{\frac{M}{2}\times\frac{N}{2}}$, $\bar{\mathbf{S}}_{kgu}^{pq}\in\mathbb{C}^{L\times\frac{N}{2}}$, and $\bar{\mathbf{G}}_{kgu}^{pq}\in\mathbb{C}^{L\times\frac{M}{2}}$ model, respectively, the fast fading channels between the BS and the uth user (link BS-U), the uth IRS and the uth user (link IRS-U), and the BS and the uth IRS (link BS-IRS), from the polarization p to the polarization q, in which $p,q\in\{v,h\}$, with $\chi^{\text{BS-U}}$ and $\chi^{\text{BS-IRS}}\in[0,1]$ denoting the inverse of the cross-polar discrimination parameter (iXPD) that measures the power leakage between polarizations in the links BS-U and BS-IRS. Moreover, $\frac{1}{\sqrt{2}}$ is the energy normalization factor, and $\zeta_{kgu}^{\text{BS-U}}$, $\zeta_{kgu}^{\text{IRS-U}}$, and $\zeta_{kgu}^{\text{BS-IRS}}$ represents the large-scale fading coefficients for the links BS-U, IRS-U, and BS-IRS, respectively. Observe that, the channel in (5) consists of a generalization of that introduced in Section II, with the difference that now both the transmitter, i.e., the BS, and receivers employ multiple dual-polarized antennas. Also, notice that we model depolarization phenomena in the links BS-U and BS-IRS, but not in the link IRS-U.[3] This means

---

[1] In practice, more than one user can be connected simultaneously to an IRS. However, as stated in [8], as the number of connected users increases, the complexity for optimizing the IRS reflecting elements also increases. Because of this, the number of users is usually maintained small. Despite that, investigating the performance of the proposed system with multiple users connected to each IRS is also interesting, but this possibility is left for future works.

[2] The proposed system model considers that the IRSs' reflecting elements are uncoupled and that the induced phases and amplitudes of reflections do not depend on the inter-element distance. This ideal consideration is reasonable when the reflecting elements are spaced by at least half of the wavelength [28], i.e., $\geq\lambda/2$, which is the case assumed in this paper. The study of more realistic models arises as a possible extension of this work.

[3] Although depolarization phenomena are not considered in the link IRS-U, we would like to emphasize that the proposed model can be easily extended to this more general case. However, such consideration would lead to a more intricate mathematical formulation of difficult interpretation. Therefore, we choose not to address this issue in this work.

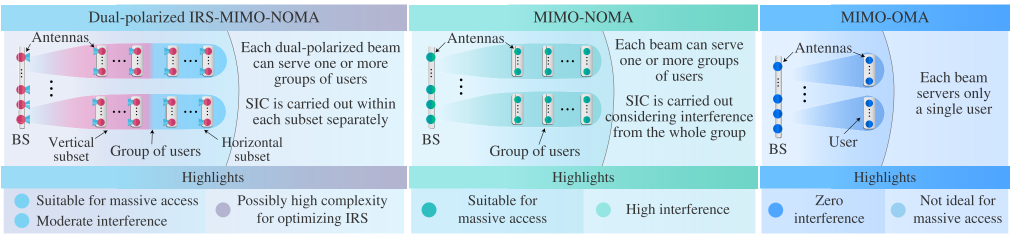

Fig. 3. Main differences between the proposed dual-polarized IRS-MIMO-NOMA and other conventional schemes.

that only negligible power leaks between polarizations in the propagation channels between the IRSs and users.

Furthermore, due to the closely spaced antennas at the BS and due to the scattering environment surrounding each spatial cluster, we assume that $\bar{\mathbf{D}}_{kgu}^{pq}$, and $\bar{\mathbf{G}}_{kgu}^{pq}$ are correlated, i.e., are rank deficient. On the other hand, we model $\bar{\mathbf{S}}_{kgu}^{pq}$ as a full rank channel matrix. Under such assumptions, the covariance matrices of the links BS-IRS and BS-U can be calculated as [1]

$$\mathbf{R}_k^{\text{BS-IRS}} = \zeta_{kgu}^{\text{BS-IRS}}(\chi^{\text{BS-IRS}} + 1)\mathbf{I}_2 \otimes \mathbf{R}_k, \tag{6}$$

$$\mathbf{R}_k^{\text{BS-U}} = \zeta_{kgu}^{\text{BS-U}}(\chi^{\text{BS-U}} + 1)\mathbf{I}_2 \otimes \mathbf{R}_k, \tag{7}$$

where $\mathbf{R}_k$ is the covariance matrix observed in each polarization, with rank denoted by r_k. Note that, we have assumed that the links BS-U and BS-IRS share the same covariance matrix $\mathbf{R}_k$. This is valid for the scenario where both IRS and users are located within the same cluster of scatterers, which in our model is reasonable since the user is located nearby its serving IRS.

Recalling the Karhunen–Loève representation [29], the channel in (5) can be rewritten as

$$\begin{aligned}\mathbf{H}_{kgu}^H &= \left(\begin{bmatrix} \mathbf{S}_{kgu}^{vv} & \mathbf{0}_{L,\frac{N}{2}} \\ \mathbf{0}_{L,\frac{N}{2}} & \mathbf{S}_{kgu}^{hh} \end{bmatrix}^H \begin{bmatrix} \mathbf{\Phi}_{kgu}^{vv} & \mathbf{\Phi}_{kgu}^{hv} \\ \mathbf{\Phi}_{kgu}^{vh} & \mathbf{\Phi}_{kgu}^{hh} \end{bmatrix} \begin{bmatrix} \mathbf{G}_{kgu}^{vv} & \mathbf{G}_{kgu}^{hv} \\ \mathbf{G}_{kgu}^{vh} & \mathbf{G}_{kgu}^{hh} \end{bmatrix} \right. \\ &\quad \left. + \begin{bmatrix} \mathbf{D}_{kgu}^{vv} & \mathbf{D}_{kgu}^{vh} \\ \mathbf{D}_{kgu}^{hv} & \mathbf{D}_{kgu}^{hh} \end{bmatrix}^H \right) \left(\mathbf{I}_2 \otimes \left(\mathbf{\Lambda}_k^{\frac{1}{2}} \mathbf{U}_k^H \right) \right) \\ &= \left(\mathbf{S}_{kgu}^H \mathbf{\Theta}_{kgu} \mathbf{G}_{kgu} + \mathbf{D}_{kgu}^H \right) \left(\mathbf{I}_2 \otimes \left(\mathbf{\Lambda}_k^{\frac{1}{2}} \mathbf{U}_k^H \right) \right), \end{aligned} \tag{8}$$

where $\mathbf{\Lambda}_k \in \mathbb{R}_{>0}^{r_k^\star \times r_k^\star}$ is a diagonal matrix that collects $r_k^\star$ nonzero eigenvalues of $\mathbf{R}_k$, sorted in descending order, $\mathbf{U}_k \in \mathbb{C}^{\frac{M}{2} \times r_k^\star}$ is a unitary matrix containing the first $r_k^\star$ left eigenvectors of $\mathbf{R}_k$, corresponding to the eigenvalues in $\mathbf{\Lambda}_k$, $\mathbf{S}_{kgu}^{pq} \in \mathbb{C}^{L \times \frac{N}{2}}$ is the full rank channel matrix of the link IRS-U, and $\mathbf{D}_{kgu}^{pq} \in \mathbb{C}^{r_k^\star \times \frac{N}{2}}$ and $\mathbf{G}_{kgu}^{pq} \in \mathbb{C}^{L \times r_k^\star}$ represent, respectively, the reduced-dimension fast fading channels of the links BS-U and BS-IRS, from the polarization p to the polarization q, with $p, q \in \{v, h\}$, whose entries follow the complex Gaussian distribution with zero mean and unit variance. Note that, for notation simplicity, the iXPD, the large scale fading coefficients, and the normalization factor $\frac{1}{\sqrt{2}}$ have been absorbed in the corresponding channel matrices.

With the above channel model, after the superimposed symbols have propagated through all wireless links, the uth user in the gth group within the kth cluster observes the following signal

$$\begin{aligned}\mathbf{y}_{kgu} &= \left(\mathbf{S}_{kgu}^H \mathbf{\Theta}_{kgu} \mathbf{G}_{kgu} + \mathbf{D}_{kgu}^H \right) \left(\mathbf{I}_2 \otimes \left(\mathbf{\Lambda}_k^{\frac{1}{2}} \mathbf{U}_k^H \right) \right) \\ &\quad \times \sum_{m=1}^{K} \mathbf{P}_m \sum_{n=1}^{G} \sum_{i=1}^{U} \mathbf{v}_{mni} \alpha_{mni} x_{mni} + \begin{bmatrix} \mathbf{n}_{kgu}^v \\ \mathbf{n}_{kgu}^h \end{bmatrix}, \end{aligned} \tag{9}$$

where $\mathbf{n}_{kgu}^p \in \mathbb{C}^{\frac{N}{2} \times 1}$ is the noise vector observed at the receive antennas of polarization $p \in \{v, h\}$, whose entries follow the complex Gaussian distribution with zero mean and variance σ_n.

Next, we provide details on the design of the precoding matrices, IRS optimization, and detection strategy.

IV. PRECODING, IRS OPTIMIZATION, AND RECEPTION MATRICES

A. Spatial Interference Cancellation

As mentioned before, the precoding matrix $\mathbf{P}_k$ is intended to remove the interference of different spatial clusters. From the signal model in (9), it is clear that this objective can be accomplished if $\left[\mathbf{I}_2 \otimes \left(\mathbf{\Lambda}_k^{\frac{1}{2}} \mathbf{U}_k^H \right) \right] \mathbf{P}_k = \mathbf{0}, \forall k' \neq k$, i.e., $\mathbf{P}_k$ should be orthogonal to the subspace spanned by the left eigenvectors of interfering clusters. Therefore, $\mathbf{P}_k$ can be computed from the null space of the matrix $\mathbf{\Omega}_k = [\mathbf{U}_1, \cdots, \mathbf{U}_{k-1}, \mathbf{U}_{k+1}, \cdots, \mathbf{U}_K] \in \mathbb{C}^{\frac{M}{2} \times \sum_{k' \neq k} r_{k'}^\star}$. This task can be performed by exploiting the singular value decomposition (SVD) of $\mathbf{\Omega}_k$. Specifically, the left eigenvectors of $\mathbf{\Omega}_k$ obtained from its SVD can be partitioned as $\tilde{\mathbf{U}}_k = \left[\tilde{\mathbf{U}}_k^{(1)} \; \tilde{\mathbf{U}}_k^{(0)} \right]$, with $\tilde{\mathbf{U}}_k^{(0)} \in \mathbb{C}^{\frac{M}{2} \times \frac{M}{2} - \sum_{k' \neq k} r_{k'}^\star}$ being a unitary matrix composed by the left eigenvectors of $\mathbf{\Omega}_k$ associated with its last $\frac{M}{2} - \sum_{k' \neq k} r_{k'}^\star$ vanishing eigenvalues. Since the columns of $\tilde{\mathbf{U}}_k^{(0)}$ form a set of orthonormal basis vectors for the null space of $\mathbf{\Omega}_k$, we have that $\mathbf{H}_{k'gu}^H (\mathbf{I}_2 \otimes \tilde{\mathbf{U}}_k^{(0)}) = 0$, $\forall k' \neq k$. Therefore, the goal of nulling out inter-cluster interference can be already fulfilled by constructing $\mathbf{P}_k$ from the columns of $\tilde{\mathbf{U}}_k^{(0)}$. However, following the strategy proposed in [30], and given (9), we can further improve the performance of the system by matching $\mathbf{P}_k$ to the dominant eigenmodes of the matrix $\mathbf{\Pi}_k = \mathbf{I}_2 \otimes \left[\left(\tilde{\mathbf{U}}_k^{(0)} \right)^H \left(\mathbf{U}_k \mathbf{\Lambda}_k^{\frac{1}{2}} \right) \right]$. This can be accomplished by multiplying $\tilde{\mathbf{U}}_k^{(0)}$ by a unitary matrix constructed from the dominant eigenvectors of the covariance matrix of $\mathbf{\Pi}_k$, i.e., from $\mathbf{\Pi}_k(\mathbf{\Pi}_k)^H = \mathbf{I}_2 \otimes \left[\left(\tilde{\mathbf{U}}_k^{(0)}\right)^H \mathbf{R}_k \tilde{\mathbf{U}}_k^{(0)}\right] = \mathbf{I}_2 \otimes \tilde{\mathbf{\Xi}}_k$. To be more specific, by representing the left eigenvectors of $\tilde{\mathbf{\Xi}}_k$ by $\bar{\mathbf{U}}_k = \left[\bar{\mathbf{U}}_k^{(1)} \ \bar{\mathbf{U}}_k^{(0)}\right]$, with $\bar{\mathbf{U}}_k^{(1)} \in \mathbb{C}^{\left(\frac{M}{2} - \sum_{k' \neq k} r_{k'}^\star\right) \times \frac{\bar{M}}{2}}$ collecting the first $\frac{\bar{M}}{2}$ columns of $\bar{\mathbf{U}}_k$, the desired precoding matrix can be finally computed by $\mathbf{P}_k = \mathbf{I}_2 \otimes \left(\tilde{\mathbf{U}}_k^{(0)} \bar{\mathbf{U}}_k^{(1)}\right) = \mathbf{I}_2 \otimes \tilde{\mathbf{P}}_k \in \mathbb{C}^{M \times \bar{M}}$, in which, due to the dimensions of $\tilde{\mathbf{U}}_k$ and $\bar{\mathbf{U}}_k$, the constraints $K \leq \bar{M} \leq \left(M - 2\sum_{k' \neq k} r_{k'}^\star\right)$ and $\bar{M} \leq 2r_k^\star$ must be satisfied.

B. Polarization Assignment and Formation of Subsets

In this subsection, we provide details on the strategy adopted for the formation of the polarization subsets and on the construction of the inner precoding vector $\mathbf{v}_{kgu}$. First, the BS divides arbitrarily the users within each spatial cluster into G groups. Then, the users within each group are sorted in ascending order based on their large-scale fading coefficients observed in the link BS-U, such that $\zeta_{kg1}^{\text{BS-U}} < \zeta_{kg2}^{\text{BS-U}} < \cdots < \zeta_{kgU}^{\text{BS-U}}$. Then, without loss of generality, by assuming that U is an even number, and aiming to form subsets with relatively balanced performance, users associated with odd indexes are assigned to the vertical polarization, and users associated with even indexes to the horizontal polarization, resulting in two disjoint subsets, the vertical subset $\mathcal{U}^v = \{1, 3, \cdots, U-1\}$, containing $U^v = U/2$ users, and the horizontal subset $\mathcal{U}^h = \{2, 4, \cdots, U\}$, containing $U^h = U - U^v = U/2$ users. As a result, users within vertical subsets will be sorted as $\zeta_{kg1}^{\text{BS-U}} < \zeta_{kg3}^{\text{BS-U}} < \cdots < \zeta_{kg(U-1)}^{\text{BS-U}}$, and the ones within horizontal subsets as $\zeta_{kg2}^{\text{BS-U}} < \zeta_{kg4}^{\text{BS-U}} < \cdots < \zeta_{kgU}^{\text{BS-U}}$. In order to implement this strategy, for $1 \leq g \leq G$ and $1 \leq u \leq U$, the BS employs the following precoding vector

$$\mathbf{v}_{kgu} = \begin{bmatrix} \mathbf{v}_{kgu}^v \\ \mathbf{v}_{kgu}^h \end{bmatrix} = \begin{bmatrix} \left[\mathbf{0}_{1,g-1}, \mathbf{1}_{\mathcal{U}^v}(u), \mathbf{0}_{1,\frac{\bar{M}}{2}-g}\right]^T \\ \left[\mathbf{0}_{1,g-1}, \mathbf{1}_{\mathcal{U}^h}(u), \mathbf{0}_{1,\frac{\bar{M}}{2}-g}\right]^T \end{bmatrix}, \tag{10}$$

where $\mathbf{1}_{\mathcal{A}}(i)$ is the indicator function of a subset $\mathcal{A}$, which results 1 if $i \in \mathcal{A}$, and 0 if $i \notin \mathcal{A}$. Note that, due to the structure of $\mathbf{v}_{kgu}$, the constraint $G \leq \bar{M}/2$ must be satisfied.

Note that more sophisticated strategies for creating the polarization subsets can be easily employed with the above precoding choice. In addition, it is noteworthy that the investigation of advanced approaches for forming the NOMA groups goes beyond the scope of this paper. Although user grouping in NOMA has been widely studied in the literature [31], [32], this paper does not aim to develop an optimal user grouping strategy but to shed light on the fundamental performance gains that our proposed scheme can render.

C. IRS Optimization

With the precoding matrix designed in the Section IV-A, all inter-cluster interference can be effectively eliminated. Therefore, from now on, by focusing on the first cluster, we can drop the cluster subscript and simplify the signal in (9) as in (11), shown at the bottom of the page.

As can be observed in (11), in both the BS-U and the BS-IRS-U links, the symbols intended to the subsets assigned to the vertical polarization propagate through the channels modeled by the left blocks of the channel matrices, while the symbols for subsets assigned to the horizontal polarization propagate through the right blocks. Therefore, the IRSs of users assigned to the vertical polarization should be optimized to null out the right channel blocks, and the IRSs for users assigned to the horizontal polarization should null out the left channel blocks. More specifically, we aim to achieve in subsets assigned to the vertical polarization:

$$\begin{bmatrix} (\mathbf{S}_{gu}^{vv})^H \mathbf{\Phi}_{gu}^{vv} \mathbf{G}_{gu}^{hv} + (\mathbf{S}_{gu}^{vv})^H \mathbf{\Phi}_{gu}^{hv} \mathbf{G}_{gu}^{hh} \\ (\mathbf{S}_{gu}^{hh})^H \mathbf{\Phi}_{gu}^{vh} \mathbf{G}_{gu}^{hv} + (\mathbf{S}_{gu}^{hh})^H \mathbf{\Phi}_{gu}^{hh} \mathbf{G}_{gu}^{hh} \end{bmatrix} + \begin{bmatrix} (\mathbf{D}_{gu}^{hv})^H \\ (\mathbf{D}_{gu}^{hh})^H \end{bmatrix} \approx \begin{bmatrix} \mathbf{0}_{\frac{N}{2}, r_k^\star} \\ \mathbf{0}_{\frac{N}{2}, r_k^\star} \end{bmatrix}, \tag{12}$$

and in subsets assigned to the horizontal polarization:

$$\begin{bmatrix} (\mathbf{S}_{gu}^{vv})^H \mathbf{\Phi}_{gu}^{vv} \mathbf{G}_{gu}^{vv} + (\mathbf{S}_{gu}^{vv})^H \mathbf{\Phi}_{gu}^{hv} \mathbf{G}_{gu}^{vh} \\ (\mathbf{S}_{gu}^{hh})^H \mathbf{\Phi}_{gu}^{vh} \mathbf{G}_{gu}^{vv} + (\mathbf{S}_{gu}^{hh})^H \mathbf{\Phi}_{gu}^{hh} \mathbf{G}_{gu}^{vh} \end{bmatrix} + \begin{bmatrix} (\mathbf{D}_{gu}^{vv})^H \\ (\mathbf{D}_{gu}^{vh})^H \end{bmatrix} \approx \begin{bmatrix} \mathbf{0}_{\frac{N}{2}, r_k^\star} \\ \mathbf{0}_{\frac{N}{2}, r_k^\star} \end{bmatrix}. \tag{13}$$

Note that, by mitigating the transmissions originated from the interfering polarization, we can transform depolarization phenomena, which usually are harmful, into an advantage. More specifically, this strategy should enable users to receive their intended messages, transmitted from a single polarization (or vertical, or horizontal), in both receive polarizations, ideally, interference-free. Take a user within a vertical subset, for instance. If all interference from the horizontal subset can be canceled, the message transmitted from the vertical polarization at the BS will reach this user through both vertical-to-vertical co-polar transmissions and vertical-to-horizontal

$$\mathbf{y}_{gu} = \left(\begin{bmatrix} \left[(\mathbf{S}_{gu}^{vv})^H \mathbf{\Phi}_{gu}^{vv} \mathbf{G}_{gu}^{vv} + (\mathbf{S}_{gu}^{vv})^H \mathbf{\Phi}_{gu}^{hv} \mathbf{G}_{gu}^{vh}\right] & \left[(\mathbf{S}_{gu}^{vv})^H \mathbf{\Phi}_{gu}^{vv} \mathbf{G}_{gu}^{hv} + (\mathbf{S}_{gu}^{vv})^H \mathbf{\Phi}_{gu}^{hv} \mathbf{G}_{gu}^{hh}\right] \\ \left[(\mathbf{S}_{gu}^{hh})^H \mathbf{\Phi}_{gu}^{vh} \mathbf{G}_{gu}^{vv} + (\mathbf{S}_{gu}^{hh})^H \mathbf{\Phi}_{gu}^{hh} \mathbf{G}_{gu}^{vh}\right] & \left[(\mathbf{S}_{gu}^{hh})^H \mathbf{\Phi}_{gu}^{vh} \mathbf{G}_{gu}^{hv} + (\mathbf{S}_{gu}^{hh})^H \mathbf{\Phi}_{gu}^{hh} \mathbf{G}_{gu}^{hh}\right] \end{bmatrix} + \begin{bmatrix} (\mathbf{D}_{gu}^{vv})^H & (\mathbf{D}_{gu}^{hv})^H \\ (\mathbf{D}_{gu}^{vh})^H & (\mathbf{D}_{gu}^{hh})^H \end{bmatrix} \right) \times \begin{bmatrix} \mathbf{\Lambda}^{\frac{1}{2}} \mathbf{U}^H \tilde{\mathbf{P}} & \mathbf{0}_{\frac{M}{2}, \frac{\bar{M}}{2}} \\ \mathbf{0}_{\frac{M}{2}, \frac{\bar{M}}{2}} & \mathbf{\Lambda}^{\frac{1}{2}} \mathbf{U}^H \tilde{\mathbf{P}} \end{bmatrix} \sum_{n=1}^{G} \sum_{i=1}^{U} \begin{bmatrix} \mathbf{v}_{ni}^v \\ \mathbf{v}_{ni}^h \end{bmatrix} \alpha_{ni} x_{ni} + \begin{bmatrix} \mathbf{n}_{gu}^v \\ \mathbf{n}_{gu}^h \end{bmatrix}. \tag{11}$$

cross-polar transmissions.[4] In other words, the proposed scheme enables polarization diversity, as anticipated in previous sections.

Given that the objectives for the IRSs of vertical and horizontal polarization subsets are similar, i.e., to null out co-polar and cross-polar transmissions from interfering subsets, the optimization procedure for both subsets will be also similar. For this reason, and also due to space constraints, we focus on the optimization of IRSs for subsets assigned for vertical polarization. Specifically, based on (12), the reflecting coefficients for users assigned to the vertical polarization can be optimized by solving the problem in (14), as shown at the bottom of the page,[5] where (14b) is the constraint for ensuring a passive reflection. The problem above can be seen as a generalization of the unconstrained least squares problem for matrix equations, in which some studies have been carried out in [33]. However, due to the element-wise quadratic constraint and the diagonal matrices constraint, it becomes difficult to solve (14) in its current form. To overcome this challenge, next, we transform (14) in an equivalent tractable problem.

Using the Khatri-Rao identity $(\mathbf{C}^T \odot \mathbf{A})\mathit{vecd}\{\mathbf{B}\} = \mathit{vec}\{\mathbf{ABC}\}$ [22], we define:

$$\begin{aligned}
\boldsymbol{\theta}_{gu}^{pq} &= \mathit{vecd}\{\boldsymbol{\Phi}_{gu}^{pq}\} \in \mathbb{C}^{L\times 1},\\
\mathbf{d}_{gu}^{hv} &= \mathit{vec}\left\{(\mathbf{D}_{gu}^{hv})^H\right\} \in \mathbb{C}^{\frac{N}{2}r_k^\star \times 1},\\
\mathbf{d}_{gu}^{hh} &= \mathit{vec}\left\{(\mathbf{D}_{gu}^{hh})^H\right\} \in \mathbb{C}^{\frac{N}{2}r_k^\star \times 1},\\
\mathbf{K}_{gu}^{hv,vv} &= [(\mathbf{G}_{gu}^{hv})^T \odot (\mathbf{S}_{gu}^{vv})^H] \in \mathbb{C}^{\frac{N}{2}r_k^\star \times L},\\
\mathbf{K}_{gu}^{hh,vv} &= [(\mathbf{G}_{gu}^{hh})^T \odot (\mathbf{S}_{gu}^{vv})^H] \in \mathbb{C}^{\frac{N}{2}r_k^\star \times L},\\
\mathbf{K}_{gu}^{hv,hh} &= [(\mathbf{G}_{gu}^{hv})^T \odot (\mathbf{S}_{gu}^{hh})^H] \in \mathbb{C}^{\frac{N}{2}r_k^\star \times L},\\
\mathbf{K}_{gu}^{hh,hh} &= [(\mathbf{G}_{gu}^{hh})^T \odot (\mathbf{S}_{gu}^{hh})^H] \in \mathbb{C}^{\frac{N}{2}r_k^\star \times L}.
\end{aligned}$$

Then, we can transform (14) into the following two subproblems

$$\min_{\boldsymbol{\theta}_{gu}^{vv},\boldsymbol{\theta}_{gu}^{hv}} \left\| \left[\mathbf{K}_{gu}^{hv,vv}\ \mathbf{K}_{gu}^{hh,vv}\right] \left[(\boldsymbol{\theta}_{gu}^{vv})^T, (\boldsymbol{\theta}_{gu}^{hv})^T\right]^T + \mathbf{d}_{gu}^{hv} \right\|^2 \tag{15a}$$

$$\text{s.t.} \quad \left\| \left[(\boldsymbol{\theta}_{gu}^{vv})^T, (\boldsymbol{\theta}_{gu}^{hv})^T\right]^T \right\|_\infty^2 \leq 1, \tag{15b}$$

$$\min_{\boldsymbol{\theta}_{gu}^{vh},\boldsymbol{\theta}_{gu}^{hh}} \left\| \left[\mathbf{K}_{gu}^{hv,hh}\ \mathbf{K}_{gu}^{hh,hh}\right] \left[(\boldsymbol{\theta}_{gu}^{vh})^T, (\boldsymbol{\theta}_{gu}^{hh})^T\right]^T + \mathbf{d}_{gu}^{hh} \right\|^2 \tag{16a}$$

$$\text{s.t.} \quad \left\| \left[(\boldsymbol{\theta}_{gu}^{vh})^T, (\boldsymbol{\theta}_{gu}^{hh})^T\right]^T \right\|_\infty^2 \leq 1. \tag{16b}$$

which consist of least squares problems with $\mathcal{L}_\infty$ norm constraints. Before we can solve the problems above, let us denote $\bar{\mathbf{K}}_{gu} = \left[\mathbf{K}_{gu}^{hv,vv}\ \mathbf{K}_{gu}^{hh,vv}\right]$, $\bar{\mathbf{C}}_{gu} = \bar{\mathbf{K}}_{gu}^H \bar{\mathbf{K}}_{gu}$, and $\tilde{\mathbf{K}}_{gu} = \left[\mathbf{K}_{gu}^{hv,hh}\ \mathbf{K}_{gu}^{hh,hh}\right]$, $\tilde{\mathbf{C}}_{gu} = \tilde{\mathbf{K}}_{gu}^H \tilde{\mathbf{K}}_{gu}$, and rewrite the left-hand side of the constraints in (15b) and (15c), respectively, as

$$\left\| \left[(\boldsymbol{\theta}_{gu}^{vv})^T, (\boldsymbol{\theta}_{gu}^{hv})^T\right]^T \right\|_\infty^2 = \left[(\boldsymbol{\theta}_{gu}^{vv})^H, (\boldsymbol{\theta}_{gu}^{hv})^H\right] \mathbf{B}_l \left[(\boldsymbol{\theta}_{gu}^{vv})^T, (\boldsymbol{\theta}_{gu}^{hv})^T\right]^T,$$

and

$$\left\| \left[(\boldsymbol{\theta}_{gu}^{vh})^T, (\boldsymbol{\theta}_{gu}^{hh})^T\right]^T \right\|_\infty^2 = \left[(\boldsymbol{\theta}_{gu}^{vh})^H, (\boldsymbol{\theta}_{gu}^{hh})^H\right] \mathbf{B}_l \left[(\boldsymbol{\theta}_{gu}^{vh})^T, (\boldsymbol{\theta}_{gu}^{hh})^T\right]^T,$$

where $\mathbf{B}_l = \mathit{diag}\{\mathbf{e}_l\}, l = 1, \cdots, L$, with $\mathbf{e}_l$ representing the standard basis vector that contains 1 in the lth position and zeros elsewhere. Then, by expanding the objective functions

$$\min_{\substack{\boldsymbol{\Phi}_{gu}^{vv},\boldsymbol{\Phi}_{gu}^{vh},\\ \boldsymbol{\Phi}_{gu}^{hv},\boldsymbol{\Phi}_{gu}^{hh}}} \left\| \begin{bmatrix} (\mathbf{S}_{gu}^{vv})^H \boldsymbol{\Phi}_{gu}^{vv} \mathbf{G}_{gu}^{hv} \\ (\mathbf{S}_{gu}^{hh})^H \boldsymbol{\Phi}_{gu}^{vh} \mathbf{G}_{gu}^{hv} \end{bmatrix} + \begin{bmatrix} (\mathbf{S}_{gu}^{vv})^H \boldsymbol{\Phi}_{gu}^{hv} \mathbf{G}_{gu}^{hh} \\ (\mathbf{S}_{gu}^{hh})^H \boldsymbol{\Phi}_{gu}^{hh} \mathbf{G}_{gu}^{hh} \end{bmatrix} + \begin{bmatrix} (\mathbf{D}_{gu}^{hv})^H \\ (\mathbf{D}_{gu}^{hh})^H \end{bmatrix} \right\|^2 \tag{14a}$$

$$\text{s.t.} \ |\omega_{gu,l}^{pq}|^2 \leq 1, \quad \forall l \in [1, L], \forall p, q \in \{v, h\}, \tag{14b}$$

$$\boldsymbol{\Phi}_{gu}^{vv}, \boldsymbol{\Phi}_{gu}^{vh}, \boldsymbol{\Phi}_{gu}^{hv}, \boldsymbol{\Phi}_{gu}^{hh} \ \text{diagonal.} \tag{14c}$$

$$\min_{\boldsymbol{\theta}_{gu}^{vv},\boldsymbol{\theta}_{gu}^{hv}} \left\{ \begin{bmatrix} \boldsymbol{\theta}_{gu}^{vv} \\ \boldsymbol{\theta}_{gu}^{hv} \end{bmatrix}^H \bar{\mathbf{C}}_{gu} \begin{bmatrix} \boldsymbol{\theta}_{gu}^{vv} \\ \boldsymbol{\theta}_{gu}^{hv} \end{bmatrix} + 2\Re\left\{ (\mathbf{d}_{gu}^{hv})^H \bar{\mathbf{K}}_{gu} \begin{bmatrix} \boldsymbol{\theta}_{gu}^{vv} \\ \boldsymbol{\theta}_{gu}^{hv} \end{bmatrix} \right\} + (\mathbf{d}_{gu}^{hv})^H \mathbf{d}_{gu}^{hv} \right\} \tag{17a}$$

$$\text{s.t.} \ \begin{bmatrix} \boldsymbol{\theta}_{gu}^{vv} \\ \boldsymbol{\theta}_{gu}^{hv} \end{bmatrix}^H \mathbf{B}_l \begin{bmatrix} \boldsymbol{\theta}_{gu}^{vv} \\ \boldsymbol{\theta}_{gu}^{hv} \end{bmatrix} \leq 1, \tag{17b}$$

$$\min_{\boldsymbol{\theta}_{gu}^{vh},\boldsymbol{\theta}_{gu}^{hh}} \left\{ \begin{bmatrix} \boldsymbol{\theta}_{gu}^{vh} \\ \boldsymbol{\theta}_{gu}^{hh} \end{bmatrix}^H \tilde{\mathbf{C}}_{gu} \begin{bmatrix} \boldsymbol{\theta}_{gu}^{vh} \\ \boldsymbol{\theta}_{gu}^{hh} \end{bmatrix} + 2\Re\left\{ (\mathbf{d}_{gu}^{hh})^H \tilde{\mathbf{K}}_{gu} \begin{bmatrix} \boldsymbol{\theta}_{gu}^{vh} \\ \boldsymbol{\theta}_{gu}^{hh} \end{bmatrix} \right\} + (\mathbf{d}_{gu}^{hh})^H \mathbf{d}_{gu}^{hh} \right\} \tag{18a}$$

$$\text{s.t.} \ \begin{bmatrix} \boldsymbol{\theta}_{gu}^{vh} \\ \boldsymbol{\theta}_{gu}^{hh} \end{bmatrix}^H \mathbf{B}_l \begin{bmatrix} \boldsymbol{\theta}_{gu}^{vh} \\ \boldsymbol{\theta}_{gu}^{hh} \end{bmatrix} \leq 1. \tag{18b}$$

---

[4] Given the randomness of scatterers in real-world scenarios, it is possible (even though very unlikely) that the cross-polarized transmissions superimpose destructively at the receivers, making them unable to exploit polarization diversity with the proposed scheme. Such a research direction goes beyond the scope of this paper and is left to future works, where an in-depth investigation can be carried out.

[5] Note that the IRSs are optimized in this work only to cancel polarization interference. It is possible, however, to further improve the system performance by jointly maximizing the system data rates (see [18] and [20] for instance). This interesting possibility shall be considered in future works.

in (15a) and (15c), we obtain (17) and (18), as shown at the bottom of the previous page.

It is straightforward to see that (17) and (18) are quadratically constrained quadratic problems. Given that the entries of $\bar{\mathbf{K}}_{gu}$ and $\tilde{\mathbf{K}}_{gu}$ are independent complex Gaussian random variables, $\bar{\mathbf{C}}_{gu}$ and $\tilde{\mathbf{C}}_{gu}$ will be positive semidefinite matrices with probability one. Furthermore, since $\mathbf{z}^H\mathbf{B}_l\mathbf{z} = |[\mathbf{z}]_l|^2 \geq 0, \forall \mathbf{z} \in \mathbb{C}^{L\times 1}$, the matrix $\mathbf{B}_l$ is also positive semidefinite. As a result, the problems (17) and (18) are convex and, consequently, have global optimal solutions that can be efficiently computed via interior-points methods in polynomial time [34]. Then, by denoting the optimal vectors of reflection coefficients by $\dot{\boldsymbol{\theta}}_{gu}^{pq}$, obtained by solving (17) and (18), the reflection matrices that minimizes (14) are obtained as $\boldsymbol{\Phi}_{gu}^{pq} = diag\left\{\dot{\boldsymbol{\theta}}_{gu}^{pq}\right\}, \forall p, q \in \{v, h\}$.

Since the optimization problems in (17) and (18) depend on the fast fading channel matrices observed in all propagation links, one can wonder how the IRSs can be configured in a real-time manner in practical systems. In fact, there are different approaches to perform such optimizations, which may require the knowledge of the channel stated information (CSI) on the IRSs, as explained in [8]. For instance, if the installed IRSs have sensing capabilities, i.e., if the IRSs comprise also active sensor elements, the channels in the reflected link BS-IRS-U can be estimated directly on them. Channel estimation approaches based on augmented Lagrangian methods, channel quantization, compressive sensing, and deep learning techniques have been recently proposed considering these hybrid active/passive IRSs [35], [36]. In such architectures, the optimization can run in the IRSs' local controllers in a distributed fashion. To this end, the BS needs to inform the CSI of the direct link BS-U to the IRSs. The disadvantage is that when the number of transmit/receive antennas and reflecting elements increases, the optimization becomes excessively complex for the limited processing power of the IRSs. Moreover, since these IRSs have also active components, the energy efficiency of the network can be impacted, and the IRSs' hardware becomes more complex.

As an alternative, it is possible to simplify the IRSs' hardware by removing the sensing components and move the computation of the channel estimations and the IRSs optimization entirely to the BS, which disposes of abundant computational resources. Time-division duplexing (TDD) is usually employed in these centralized setups, in which the CSI of both BS-IRS-U and BS-U links are obtained through uplink training at the BS. Different strategies exist for estimating the composite reflected channel BS-IRS-U, including sequential element-wise estimation, discrete Fourier transform-based estimation, minimum mean squared error-based estimation, among others [37]–[39]. Obtaining the global CSI in this centralized fashion allows the BS itself to compute the optimal sets of reflection coefficients, which are later sent to the IRSs through an ultra-fast backhaul link. Such centralized channel estimation and optimization demand a simpler IRS hardware than the distributed counterpart. However, it may lead to an excessive signaling overhead at the BS when the number of users and IRSs gets larger.[6] Therefore, there are pros and cons with both architectures. Choosing the best one will depend on factors such as the numbers of transmit and receive antennas, the size of the IRSs, and the network load, which require further studies on this topic. In particular, since we consider an IRS to be a nearly passive device with low computational capabilities, here we assume a centralized approach.[7]

D. Signal Reception

Since we have already provided details on the optimization of the IRSs, for the sake of simplicity, hereinafter the links BS-IRS-U and BS-U are absorbed into a single channel matrix, and (8) is rewritten in a more compact structure, as follows

$$\mathbf{H}_{gu}^H = \begin{bmatrix} \tilde{\mathbf{H}}_{gu}^{vv} & \tilde{\mathbf{H}}_{gu}^{vh} \\ \tilde{\mathbf{H}}_{gu}^{hv} & \tilde{\mathbf{H}}_{gu}^{hh} \end{bmatrix}^H, \tag{19}$$

where $\tilde{\mathbf{H}}_{gu}^{pq}$ accounts for both direct and reflected transmissions that depart the BS from polarization p and arrive at the user's devices on polarization q, with $p, q \in \{v, h\}$, e.g., the effective vertical-to-vertical channel matrix is defined by $\tilde{\mathbf{H}}_{gu}^{vv} = \mathbf{U}_k\boldsymbol{\Lambda}_k^{\frac{1}{2}}\left[(\mathbf{S}_{gu}^{vv})^H\boldsymbol{\Phi}_{gu}^{vv}\mathbf{G}_{gu}^{vv} + (\mathbf{S}_{gu}^{vv})^H\boldsymbol{\Phi}_{gu}^{hv}\mathbf{G}_{gu}^{vh}\right]^H + \mathbf{U}_k\boldsymbol{\Lambda}_k^{\frac{1}{2}}\mathbf{D}_{gu}^{vv}$. With this notation, the signal in (11) can be simplified to

$$\begin{aligned}\mathbf{y}_{gu} = &\begin{bmatrix} (\tilde{\mathbf{H}}_{gu}^{vv})^H\tilde{\mathbf{P}} & (\tilde{\mathbf{H}}_{gu}^{hv})^H\tilde{\mathbf{P}} \\ (\tilde{\mathbf{H}}_{gu}^{vh})^H\tilde{\mathbf{P}} & (\tilde{\mathbf{H}}_{gu}^{hh})^H\tilde{\mathbf{P}} \end{bmatrix} \sum_{n=1}^{G}\sum_{i=1}^{U} \begin{bmatrix} \mathbf{v}_{ni}^v \\ \mathbf{v}_{ni}^h \end{bmatrix} \alpha_{ni}x_{ni} \\ &+ \begin{bmatrix} \mathbf{n}_{gu}^v \\ \mathbf{n}_{gu}^h \end{bmatrix}. \end{aligned} \tag{20}$$

Then, in order to explain our detection strategy, without loss of generality, we focus on subsets assigned to the vertical polarization. Remember that the IRSs of users assigned to the vertical polarization are optimized to mitigate all transmissions originated at the BS from the horizontal polarization. Therefore, by relying on the effectiveness of the IRS, we exploit the left blocks of the channel matrix in (20) to construct our detection matrix. More specifically, in order to remove the remaining interference from other subsets also assigned to the vertical polarization, the uth user exploits the virtual channels $\underline{\mathbf{H}}_{gu}^{vv} = (\tilde{\mathbf{H}}_{gu}^{vv})^H\tilde{\mathbf{P}}$ and $\underline{\mathbf{H}}_{gu}^{vh} = (\tilde{\mathbf{H}}_{gu}^{vh})^H\tilde{\mathbf{P}}$ to construct the following detection matrix

$$\begin{aligned} &\mathbf{H}_{gu}^{\dagger} \\ &= \begin{bmatrix} \mathbf{H}_{gu}^{\dagger v} & \mathbf{0}_{\frac{\bar{M}}{2},\frac{N}{2}} \\ \mathbf{0}_{\frac{\bar{M}}{2},\frac{N}{2}} & \mathbf{H}_{gu}^{\dagger h} \end{bmatrix} \\ &= \begin{bmatrix} [(\underline{\mathbf{H}}_{gu}^{vv})^H\underline{\mathbf{H}}_{gu}^{vv}]^{-1}(\underline{\mathbf{H}}_{gu}^{vv})^H & \mathbf{0}_{\frac{\bar{M}}{2},\frac{N}{2}} \\ \mathbf{0}_{\frac{\bar{M}}{2},\frac{N}{2}} & [(\underline{\mathbf{H}}_{gu}^{vh})^H\underline{\mathbf{H}}_{gu}^{vh}]^{-1}(\underline{\mathbf{H}}_{gu}^{vh})^H \end{bmatrix}, \end{aligned} \tag{21}$$

---

[6] Configuring IRSs with polarization capabilities may be relatively more complex than configuring conventional single-polarized counterparts. However, further investigations are still necessary on this topic, which goes beyond the scope of this paper.

[7] Note that, in order for the proposed scheme to be effective, the channels must be estimated and the IRSs optimized at least at each coherence interval. Channel estimation in IRS-assisted communication systems is an important and active topic of research [35]–[39], which arises as an interesting subject to be investigated in future works.

where $\mathbf{H}_{gu}^{\dagger p}$ is a left Moore–Penrose inverse intended to detect the signals impinging on the receive antennas with polarization p, in which it is assumed that $N \geq \bar{M}$. Then, after multipliying the signal in (20) by $\mathbf{H}_{gu}^{\dagger}$, the uth user obtains the following data vector

$$\hat{\mathbf{x}}_{gu} = \begin{bmatrix} \hat{\mathbf{x}}_{gu}^{v} \\ \hat{\mathbf{x}}_{gu}^{h} \end{bmatrix} = \begin{bmatrix} \mathbf{x}^{v} + \mathbf{H}_{gu}^{\dagger v}\underline{\mathbf{H}}_{gu}^{hv}\mathbf{x}^{h} \\ \mathbf{x}^{v} + \mathbf{H}_{gu}^{\dagger h}\underline{\mathbf{H}}_{gu}^{hh}\mathbf{x}^{h} \end{bmatrix} + \begin{bmatrix} \mathbf{H}_{gu}^{\dagger v}\mathbf{n}_{gu}^{v} \\ \mathbf{H}_{gu}^{\dagger h}\mathbf{n}_{gu}^{h} \end{bmatrix}, \tag{22}$$

where, due to the precoding vector in (10), $\mathbf{x}^{v}$ is given by

$$\mathbf{x}^{v} = \begin{bmatrix} \sum_{i\in\mathcal{U}^{v}} \alpha_{1i}x_{1i} \\ \vdots \\ \sum_{i\in\mathcal{U}^{v}} \alpha_{Gi}x_{Gi} \end{bmatrix}. \tag{23}$$

Note in (22) that, by employing $\mathbf{H}_{gu}^{\dagger}$, users will obtain in both receive polarizations corrupted replicas of the vector of superimposed symbols that was transmitted by the BS from the vertical polarization. Moreover, as one can observe in (23), each element of $\mathbf{x}^{v}$ consists of a superimposed symbol intended to a specific user subset. Therefore, a user within the gth vertical subset is able to decode its symbol from the gth element of both $\hat{\mathbf{x}}_{gu}^{v}$ and $\hat{\mathbf{x}}_{gu}^{h}$. In particular, inspired by the strategy proposed in [1], the data symbols will be decoded from the polarization that renders the highest effective channel gain, denoted in this work as the polarization $\ddot{p}$. As a result, the superimposed symbol recovered by the uth user in the gth vertical subset before carrying out SIC is given by

$$[\hat{\mathbf{x}}_{gu}^{\ddot{p}}]_{g} = \sum_{i\in\mathcal{U}^{v}} \alpha_{gi}x_{gi} + [\mathbf{H}_{gu}^{\dagger\ddot{p}}\underline{\mathbf{H}}_{gu}^{h\ddot{p}}\mathbf{x}^{h}]_{g} + [\mathbf{H}_{gu}^{\dagger\ddot{p}}\mathbf{n}_{gu}^{\ddot{p}}]_{g}. \tag{24}$$

Users within horizontal subsets employ the same strategy. However, differently from vertical subsets, the matrix $\mathbf{H}_{gu}^{\dagger}$ is constructed based on the right blocks of the channel matrix in (20).

V. PERFORMANCE ANALYSIS

In this section, we carry out an in-depth study of the performance of the proposed system. By taking into account polarization interference and errors from imperfect SIC, we first provide a general expression for the SINR observed by each user during the SIC process. A statistical analysis is then performed to identify the distribution of the channel gains, which turns out to be challenging to find for general values of reflecting elements. We then investigate the limiting case for $L \to \infty$, in which the asymptotic distribution is determined. Lastly, by considering large values of L, a closed-form analytical expression for the ergodic rates is derived.

A. SINR Analysis

Before the users can read their messages, they still need to decode the superimposed symbol in (24) through SIC. Recall that due to the polarization assignment strategy proposed in the Section IV-B, users within each subset are sorted in ascending order based on their large scale coefficients, e.g., in vertical subsets $\zeta_{kg1}^{\text{BS-U}} < \zeta_{kg3}^{\text{BS-U}} < \cdots < \zeta_{kgU^{v}}^{\text{BS-U}}$. As a result, following the NOMA protocol, before the uth user in the polarization subset $\mathcal{U}^{p}$, $p \in \{v,h\}$, can retrieve its own message, it carries out SIC to decode the symbol intended for the mth weaker user, $\forall m < u$, $m \in \mathcal{U}^{p}$, and treats the message to the nth stronger user as interference, $\forall n > u, n \in \mathcal{U}^{p}$. Ideally, the symbols intended for weaker users can be perfectly removed by SIC. However, as clarified in Section I, due to many factors, SIC errors are inevitable in practice. Therefore, users suffer from SIC error propagation in the proposed system, and this is modeled as a linear function of the power of decoded symbols, as in [3]. Then, after all SIC decodings, the uth user assigned to the polarization subset $\mathcal{U}^{p}$ in the gth group observes the following symbol

$$\begin{aligned} \hat{x}_{gu} = {} & \underbrace{\alpha_{gu}x_{gu}}_{\text{Desired symbol}} + \underbrace{\sum_{m\in\{a|a>u,a\in\mathcal{U}^{p}\}} \alpha_{gm}x_{gm}}_{\text{Interference of stronger users}} \\ & \underbrace{+\sqrt{\xi} \sum_{n\in\{b|b<u,b\in\mathcal{U}^{p}\}} \alpha_{gn}x_{gn}}_{\text{Residual SIC interference}} \\ & + \underbrace{[\mathbf{H}_{gu}^{\dagger\ddot{p}}\underline{\mathbf{H}}_{gu}^{t\ddot{p}}\mathbf{x}^{t}]_{g}}_{\text{Polarization interference}} + \underbrace{[\mathbf{H}_{gu}^{\dagger\ddot{p}}\mathbf{n}_{gu}^{\ddot{p}}]_{g}}_{\text{Noise}}, \end{aligned} \tag{25}$$

where the superscript t represents the interfering polarization that is defined by $t = h$, if $u \in \mathcal{U}^{v}$, or $t = v$, if $u \in \mathcal{U}^{h}$, and $\xi \in [0,1]$ is the SIC error propagation factor, in which $\xi = 0$ corresponds to the perfect SIC case, and $\xi = 1$ represents the scenario of maximum error. Moreover, note that if the IRS of the uth can completely eliminate the transmissions coming from the horizontally polarized BS antennas, the polarization interference term in (25) will disappear.

The SINR observed during each SIC decoding is defined in the following lemma.

Lemma I: Under the assumption of imperfect SIC, the uth user in the gth group decodes the data symbol intended to the ith user, $\forall i \leq u$, $i \in \mathcal{U}^{p}$, with the following SINR

$$\gamma_{gu}^{i} = \frac{\rho\ddot{\langle}_{gu}\alpha_{gi}^{2}}{\rho\ddot{\langle}_{gu}\mathfrak{I}_{gi} + \rho\ddot{\langle}_{gu}\mathfrak{X}_{gu} + 1}, \tag{26}$$

where $\ddot{\langle}_{gu} = \max\{\langle_{gu}^{v}, \langle_{gu}^{h}\}$, with $\langle_{gu}^{p} = [1/\mathbf{H}_{gu}^{\dagger p}(\mathbf{H}_{gu}^{\dagger p})^{H}]_{gg}$ being the effective channel observed in the polarization p, $\mathfrak{X}_{gu} = \left|[\mathbf{H}_{gu}^{\dagger\ddot{p}}\underline{\mathbf{H}}_{gu}^{t\ddot{p}}\mathbf{x}^{t}]_{g}\right|^{2}$ represents the residual polarization interference left by the IRS, in which, if $u \in \mathcal{U}^{v}$, $t = h$, and if $u \in \mathcal{U}^{h}$, $t = v$. The symbol $\rho = 1/\sigma_{n}^{2}$ represents the SNR, and $\mathfrak{I}_{gi}$ is the total SIC interference given by (27), as shown at the bottom of the next page.

Proof: Please, see Appendix A. $\square$

B. Statistical Analysis of Channel Gains

In order to proceed with the theoretical analysis, it is crucial to identify the statistical distribution of the gains $\ddot{\langle}_{gu} = \max\{1/[\mathbf{H}_{gu}^{\dagger v}(\mathbf{H}_{gu}^{\dagger v})^{H}]_{gg}, 1/[\mathbf{H}_{gu}^{\dagger h}(\mathbf{H}_{gu}^{\dagger h})^{H}]_{gg}\}$ and $\mathfrak{X}_{gu} = \left|[\mathbf{H}_{gu}^{\dagger\ddot{p}}\underline{\mathbf{H}}_{gu}^{t\ddot{p}}\mathbf{x}^{t}]_{g}\right|^{2}$. This task will be performed in this subsection. By turning our attention to the uth user in the gth vertical subset, let us identify the distribution of $[\mathbf{H}_{gu}^{\dagger v}(\mathbf{H}_{gu}^{\dagger v})^{H}]_{gg}$. In particular, by recalling (8) and (19), the matrix $\mathbf{H}_{gu}^{\dagger v}(\mathbf{H}_{gu}^{\dagger v})^{H}$

can be expanded as

$$\begin{aligned}&\mathbf{H}^{\dagger v}_{gu}(\mathbf{H}^{\dagger v}_{gu})^H\\&=[\tilde{\mathbf{P}}^H\tilde{\mathbf{H}}^{vv}_{gu}(\tilde{\mathbf{H}}^{vv}_{gu})^H\tilde{\mathbf{P}}]^{-1}\\&=\Big(\tilde{\mathbf{P}}^H\mathbf{U}\boldsymbol{\Lambda}^{\frac{1}{2}}(\mathbf{G}^{vv}_{gu})^H(\boldsymbol{\Phi}^{vv}_{gu})^H\mathbf{S}^{vv}_{gu}(\mathbf{S}^{vv}_{gu})^H\boldsymbol{\Phi}^{vv}_{gu}\mathbf{G}^{vv}_{gu}\boldsymbol{\Lambda}^{\frac{1}{2}}\mathbf{U}^H\tilde{\mathbf{P}}\\&\quad+\tilde{\mathbf{P}}^H\mathbf{U}\boldsymbol{\Lambda}^{\frac{1}{2}}(\mathbf{G}^{vh}_{gu})^H(\boldsymbol{\Phi}^{hv}_{gu})^H\mathbf{S}^{vv}_{gu}(\mathbf{S}^{vv}_{gu})^H\boldsymbol{\Phi}^{hv}_{gu}\mathbf{G}^{vh}_{gu}\boldsymbol{\Lambda}^{\frac{1}{2}}\mathbf{U}^H\tilde{\mathbf{P}}\\&\quad+\tilde{\mathbf{P}}^H\mathbf{U}\boldsymbol{\Lambda}^{\frac{1}{2}}\mathbf{D}^{vv}_{gu}(\mathbf{D}^{vv}_{gu})^H\boldsymbol{\Lambda}^{\frac{1}{2}}\mathbf{U}^H\tilde{\mathbf{P}}\Big)^{-1}.\end{aligned}\tag{28}$$

Given that $\mathbf{S}^{pq}_{gu}$ is a full rank channel matrix, we have that $\mathbb{E}\{\mathbf{S}^{vv}_{gu}(\mathbf{S}^{vv}_{gu})^H\}=\zeta^{\text{IRS-U}}_{gu}\mathbf{I}_{L,L}$. Then, by using (5), the matrix in (28) is further simplified as

$$\begin{aligned}&\mathbf{H}^{\dagger v}_{gu}(\mathbf{H}^{\dagger v}_{gu})^H\\&\quad=\Big(\frac{1}{2}\zeta^{\text{BS-IRS}}_{gu}\zeta^{\text{IRS-U}}_{gu}\tilde{\mathbf{P}}^H(\bar{\mathbf{G}}^{vv}_{gu})^H(\boldsymbol{\Phi}^{vv}_{gu})^H\boldsymbol{\Phi}^{vv}_{gu}\bar{\mathbf{G}}^{vv}_{gu}\tilde{\mathbf{P}}\\&\qquad+\frac{1}{2}\zeta^{\text{BS-IRS}}_{gu}\zeta^{\text{IRS-U}}_{gu}\tilde{\mathbf{P}}^H(\bar{\mathbf{G}}^{vh}_{gu})^H(\boldsymbol{\Phi}^{hv}_{gu})^H\boldsymbol{\Phi}^{hv}_{gu}\bar{\mathbf{G}}^{vh}_{gu}\tilde{\mathbf{P}}\\&\qquad+\zeta^{\text{BS-U}}_{gu}\tilde{\mathbf{P}}^H\bar{\mathbf{D}}^{vv}_{gu}(\bar{\mathbf{D}}^{vv}_{gu})^H\tilde{\mathbf{P}}\Big)^{-1}.\end{aligned}\tag{29}$$

As can be observed, the entries of the matrix above will be the result of the inverse of the sum of three independent matrices. Therefore, one could fully characterize $\mathbf{H}^{\dagger v}_{gu}(\mathbf{H}^{\dagger v}_{gu})^H$ by identifying the distributions of the virtual channels $\tilde{\mathbf{P}}^H\bar{\mathbf{D}}^{vv}_{gu}$, $\tilde{\mathbf{P}}^H(\bar{\mathbf{G}}^{vv}_{gu})^H(\boldsymbol{\Phi}^{vv}_{gu})^H$, and $\tilde{\mathbf{P}}^H(\bar{\mathbf{G}}^{hv}_{gu})^H(\boldsymbol{\Phi}^{hv}_{gu})^H$. However, since the elements of $\boldsymbol{\Phi}^{vv}_{gu}$ and $\boldsymbol{\Phi}^{hv}_{gu}$ result from the optimization problem in (17), which change rapidly with the fast fading channels, determining the exact distribution of (29), with L assuming any value in $\mathbb{N}_{>0}$, becomes a difficult task.

In face of this mathematical challenge, we study next the limiting case with large number of reflecting elements, i.e., $L\to\infty$, which is also important since it provides a bound to the maximum achievable performance of the proposed system. As one can observe in (29), the key step to proceed with the analysis is to study the behavior of $(\boldsymbol{\Phi}^{pq}_{gu})^H\boldsymbol{\Phi}^{pq}_{gu}$ in the large-scale regime of L. The following lemma performs this task.

Lemma II: If the matrices $\boldsymbol{\Phi}^{pq}_{gu}$, $p,q\in\{v,h\}$, are optimized to cancel out co-polar and cross-polar interference, like in (14), when the number of reflecting elements L becomes large, the magnitude of the reflection coefficients becomes arbitrarily small, i.e., $(\boldsymbol{\Phi}^{pq}_{gu})^H\boldsymbol{\Phi}^{pq}_{gu}\to\mathbf{0}_{L,L}$ as $L\to\infty$, $\forall p,q\in\{v,h\}$.

Proof: Please, see Appendix B. ☐

Based on Lemma II, it becomes clear that the channel matrices corresponding to the reflected link BS-IRS-U in (29) will be attenuated with the increase of the number of reflecting elements L. Therefore, in the limiting case with $L\to\infty$, (29) can be approximated by

$$\mathbf{H}^{\dagger v}_{gu}(\mathbf{H}^{\dagger v}_{gu})^H\approx\Big(\zeta^{\text{BS-U}}_{gu}\tilde{\mathbf{P}}^H\bar{\mathbf{D}}^{vv}_{gu}(\bar{\mathbf{D}}^{vv}_{gu})^H\tilde{\mathbf{P}}\Big)^{-1},\tag{30}$$

which can be characterized as follows. First, remember that $\tilde{\mathbf{P}}$ is an unitary matrix and $\bar{\mathbf{D}}^{vv}_{gu}$ follows a complex Gaussian distribution. Consequently, the product $\tilde{\mathbf{P}}^H\bar{\mathbf{D}}^{vv}_{gu}\in\mathbb{C}^{\frac{\bar{M}}{2}\times\frac{N}{2}}$ will also follow a complex Gaussian distribution. This leads us to conclude that, when $L\to\infty$, $\mathbf{H}^{\dagger v}_{gu}(\mathbf{H}^{\dagger v}_{gu})^H$ will converge in distribution to an inverse Wishart distribution with $\frac{N}{2}$ degrees of freedom, and covariance matrix given by $\mathbb{E}\{\mathbf{H}^{\dagger v}_{gu}(\mathbf{H}^{\dagger v}_{gu})^H\}=\Big(\zeta^{\text{BS-U}}_{gu}\tilde{\mathbf{P}}^H\mathbf{R}\tilde{\mathbf{P}}\Big)^{-1}$, which is a diagonal matrix. Therefore, given the dimensions of $\tilde{\mathbf{P}}^H\bar{\mathbf{D}}^{vv}_{gu}$, the channel gain $1/[\mathbf{H}^{\dagger v}_{gu}(\mathbf{H}^{\dagger v}_{gu})^H]_{gg}$ will converge to the Gamma distribution with shape parameter $(N-\bar{M})/2+1$ and rate parameter $(\zeta^{\text{BS-U}}_{gu}[\tilde{\mathbf{P}}^H\mathbf{R}\tilde{\mathbf{P}}]_{gg})^{-1}$. A similar analysis can be carried out for the effective channel gain observed in the horizontal polarization. However, its corresponding covariance matrix will be also multiplied by the iXPD factor experienced in the link BS-U, i.e., $\mathbb{E}\{\mathbf{H}^{\dagger h}_{gu}(\mathbf{H}^{\dagger h}_{gu})^H\}=\Big(\zeta^{\text{BS-U}}_{gu}\chi^{\text{BS-U}}\tilde{\mathbf{P}}^H\mathbf{R}\tilde{\mathbf{P}}\Big)^{-1}$. Before we continue, for the sake of simplicity, let $\lambda_{gu}=(\zeta^{\text{BS-U}}_{gu}[\tilde{\mathbf{P}}^H\mathbf{R}\tilde{\mathbf{P}}]_{gg})^{-1}$ and $\kappa=(N-\bar{M})/2+1$. Then, by recalling that the channel coefficients observed in both polarizations are independent, the cumulative distribution function (CDF) for the effective channel gain $\ddot{\langle}_{gu}$ can be derived as

$$\begin{aligned}F_{\ddot{\langle}_{gu}}(x)&=F_{\langle^{v}_{gu}}(x)F_{\langle^{h}_{gu}}(x)\\&=\frac{\gamma\left(\kappa,(\chi^{\text{BS-U}})^{-1}\lambda_{gu}x\right)\gamma\left(\kappa,\lambda_{gu}x\right)}{\Gamma\left(\kappa\right)^2},\end{aligned}\tag{31}$$

and the respective probability density function (PDF) can be obtained from the derivative of $F_{\ddot{\langle}_{gu}}(x)$, resulting in

$$\begin{aligned}f_{\ddot{\langle}_{gu}}(x)=\frac{(\lambda_{gu})^{\kappa}x^{\kappa-1}}{\Gamma\left(\kappa\right)^2}&\left(e^{-\lambda_{gu}x}\gamma\left(\kappa,(\chi^{\text{BS-U}})^{-1}\lambda_{gu}x\right)\right.\\&\left.+(\chi^{\text{BS-U}})^{-\kappa}e^{-(\chi^{\text{BS-U}})^{-1}\lambda_{gu}x}\gamma\left(\kappa,\lambda_{gu}x\right)\right).\end{aligned}\tag{32}$$

Note that the effective channel gains of users from horizontal subsets will also have an identical distribution as the above.

Another implication of Lemma II is that, for large values of L, the magnitude of the reflection coefficients required for cancelling out all polarization interference will

$$\mathfrak{I}_{gi}=\begin{cases}\displaystyle\sum_{m=i+1}^{\max\{\mathcal{U}^p\}}\alpha^2_{gm}, & \text{if } i=\min\{\mathcal{U}^p\},\\ \displaystyle\sum_{m=i+1}^{\max\{\mathcal{U}^p\}}\alpha^2_{gm}+\xi\sum_{n=\min\{\mathcal{U}^p\}}^{i-1}\alpha^2_{gn}, & \text{if } \min\{\mathcal{U}^p\}<i\leq u<\max\{\mathcal{U}^p\},\\ \displaystyle\xi\sum_{n=1}^{i-1}\alpha^2_{gn}, & \text{if } i=u=\max\{\mathcal{U}^p\}.\end{cases}\tag{27}$$

be always less than one. Therefore, when $L \to \infty$, the solution obtained through the optimization problems (17) and (18) should converge to that obtained via standard unconstrained least squares problem, as in (B-1), and, consequently, the polarization interference term in (26) will be extinguished, i.e., $\lim_{L\to\infty} \mathfrak{X}_{gu} \to 0$. The ergodic rates for this limiting case are derived in the next subsection.

C. Ergodic Rates for the Large-Scale Regime of L

Now, we derive the ergodic rates for users within each polarization subset. Specifically, we consider a scenario in which the users are assisted by IRSs with a large number of reflecting elements. Therefore, as a consequence of Lemma II, the data rates will not be impacted by polarization interference, but only from errors due to imperfect SIC. Under such considerations, a closed-form expression for the ergodic rates is derived in the following proposition.

Proposition I: When the uth user in the gth polarization subset is assisted by an IRS with a large number of reflecting elements, i.e., $L \to \infty$, and considering degradation from imperfect SIC, it will experience the ergodic rate in (33), as shown at the bottom of the page, where $\bar{\alpha}_{gu} = \rho(\alpha_{gu}^2 + \Im_{gu})$, and $\tilde{\alpha}_{gu} = \rho\Im_{gu}$.

Proof: Please, see Appendix C. $\square$

Even though (33) may look complex to interpret, by knowing that all terms with Meijer's G-functions are increasing functions of the SNR ρ, which have been numerically verified, we can still extract some insights. First, note that the terms that are functions of $\tilde{\alpha}_{gu}$, which accounts only for interference, are negative. This suggests that such terms are expected to degrade the ergodic rates of the users as long as they experience some interference. On the other hand, the positive term that depends on $\chi^{\text{BS-U}}$ and $\bar{\alpha}_{gu}$ indicates that the cross-polar transmissions will improve the rate performance of the users. This behavior is indeed expected since the IRSs enables polarization diversity by recycling cross-polar transmissions.

VI. SIMULATION RESULTS AND DISCUSSIONS

In this section, by presenting representative numerical simulation examples, we validate the theoretical analysis carried out in the last section and demonstrate the potential performance gains that the proposed dual-polarized IRS-MIMO-NOMA scheme can achieve over conventional systems. Specifically, the theoretical results have been obtained through (33), while the simulation ones have been generated by averaging a large number random channel realizations, in which we use as baseline schemes the classical MIMO-OMA system, where users are served via time division multiple access, and the conventional single-polarized and dual-polarized MIMO-NOMA systems, whose implementation details can be found in [1].

For a fair performance comparison, in both single and dual-polarized schemes, we employ at the BS a linear array with $M = 90$ transmit antennas. However, as explained in the System Model Section, the antenna elements in the dual-polarized systems are arranged into co-located pairs, thereby, resulting in $\frac{M}{2} = 45$ pairs of dual-polarized antennas spaced by half of the wavelength, i.e., $\lambda/2$ (the inter-antenna spacing in the single-polarized systems is also set to $\lambda/2$). The operating frequency is set up to 3 GHz, and for modeling the scattering environment and the correlation between transmit antennas, we generate the covariance matrices in (6) and (7) through the one-ring geometrical model [1], [29], [30], where we consider the existence of $K = 4$ spatial clusters, each with 30 m of radius and located at 120 m from the BS. In addition, the BS's antenna array is directed to the center of the first cluster that is positioned at the azimuth angle of 30°. This is the cluster from which the simulation results are generated, which comprises $G = \bar{M} = 4$ groups, each one containing $U = 4$ users.[8] For simplicity, we assume that users within each group share a common spatial direction, in which users in groups 1, 2, 3 and 4 have azimuth angles of 20°, 24°, 36°, and 40°, respectively. In particular, we focus on the first group, where the users 1, 2, 3 and 4 are located, respectively, at 135 m, 125 m, 115 m, and 105 m from the BS, resulting in an inter-user distance of 10 m. A fixed power allocation is adopted, in which we set $\alpha_1^2 = 0.4, \alpha_2^2 = 0.35, \alpha_3^2 = 0.2, \alpha_4^2 = 0.05$. Moreover, we assume that the distances from the BS to each IRS are the same as that from the BS to its connected user, and that $\chi^{\text{BS-U}} = \chi^{\text{BS-IRS}} = \chi$. Under these assumptions, the fading coefficients for the links BS-U and BS-IRS are configured as $\zeta_u^{\text{BS-U}} = \zeta_u^{\text{BS-IRS}} = \varrho d_u^{-\eta}$, where d_u is the distance between the BS and the uth user and its serving IRS, $\varrho = 2 \times 10^4$ is an array gain parameter that is configured at the BS according to the desired receivers' performance [3], and $\eta = 2$ is the path-loss exponent. Regarding the link IRS-U, since an IRS is a passive device, we discard the array gain and model the corresponding fading coefficient as $\zeta_{gu}^{\text{IRS-U}} = \tilde{d}^{-\eta}$, where $\tilde{d} = 20$ m for all IRSs, i.e., users are positioned 20 m apart from its serving IRS. Other parameters that have not

$$
\begin{aligned}
\bar{R}_{gu} = \frac{1}{\ln(2)\Gamma(\kappa)} \Bigg\{ & G_{3,2}^{1,3}\left({}^{1-\kappa,1,1}_{\quad 1,0} \,\middle|\, \frac{\bar{\alpha}_{gu}}{\lambda_{gu}} \right) + G_{3,2}^{1,3}\left({}^{1-\kappa,1,1}_{\quad 1,0} \,\middle|\, \frac{\chi^{\text{BS-U}}\bar{\alpha}_{gu}}{\lambda_{gu}} \right) - G_{3,2}^{1,3}\left({}^{1-\kappa,1,1}_{\quad 1,0} \,\middle|\, \frac{\tilde{\alpha}_{gu}}{\lambda_{gu}} \right) \\
& - G_{3,2}^{1,3}\left({}^{1-\kappa,1,1}_{\quad 1,0} \,\middle|\, \frac{\chi^{\text{BS-U}}\tilde{\alpha}_{gu}}{\lambda_{gu}} \right) - \sum_{n=0}^{\kappa-1} \frac{(\chi^{\text{BS-U}})^{\kappa} + (\chi^{\text{BS-U}})^{n}}{n!(\chi^{\text{BS-U}}+1)^{\kappa+n}} \Bigg[- G_{3,2}^{1,3}\left({}^{1-\kappa-n,1,1}_{\quad 1,0} \,\middle|\, \frac{\chi^{\text{BS-U}}\bar{\alpha}_{gu}}{(\chi^{\text{BS-U}}+1)\lambda_{gu}} \right) \\
& - G_{3,2}^{1,3}\left({}^{1-\kappa-n,1,1}_{\quad 1,0} \,\middle|\, \frac{\chi^{\text{BS-U}}\tilde{\alpha}_{gu}}{(\chi^{\text{BS-U}}+1)\lambda_{gu}} \right) \Bigg] \Bigg\}, \qquad 1 \le u \le U. \qquad (33)
\end{aligned}
$$

---

[8] Due to the interference-limited behavior of NOMA-based schemes, the number of users served in practical systems is usually maintained small [3].

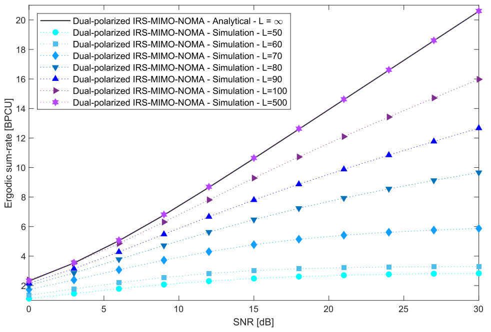

Fig. 4. Simulated and analytical ergodic sum-rates considering perfect SIC. Effect of the increase in the number of dual-polarized reflecting elements $(N = 4, \chi = 0.5, \xi = 0)$.

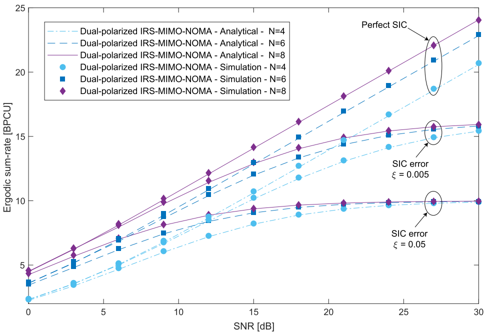

Fig. 5. Simulated and analytical ergodic sum-rates for various levels of SIC error propagation $(L = 500, \chi = 0.5)$.

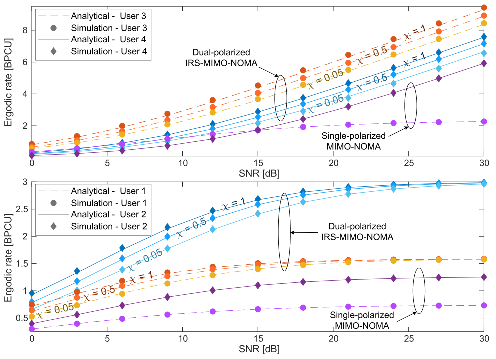

Fig. 6. Simulated and analytical ergodic rates for different values of iXPD $(L = 500, N = 4, \xi = 0)$.

been mentioned will assume different values throughout the simulation examples.

Fig. 4 brings the simulated and analytical ergodic sum-rate curves, generated by $\sum_{i=1}^{U} \bar{R}_{gi}$, for various values of dual-polarized reflecting elements L, and considering perfect SIC decoding. As one can see, for small numbers of reflecting elements, when optimizing the IRSs through (17) and (18), the simulated ergodic sum-rate curves reach values lower than that from the analytical curve obtained by solving (33). This behavior is explained by the fact that the IRS cannot eliminate all polarization interference when the number of reflecting elements is small, which degrades the system sum-rate. However, as the number of reflecting elements increases, the polarization interference decreases, and the sum-rate improves, approaching the analytical one. For instance, when 500 dual-polarized elements are considered, the simulated sum-rate matches perfectly the analytical curve. Such performance is in total agreement with Lemma II and the analytical derivation of Section V-C, therefore, providing the first validation to our analysis.

To further corroborate the analysis for large values of L, we present in Fig. 5 the sum-rates and in Fig. 6 the individual ergodic rates for 500 reflecting elements, in which, in all considered cases, a perfect agreement between simulated and analytical curves can be observed. Specifically, Fig. 5 shows the effects of SIC error propagation on the system performance for different numbers of receive antennas. As one can notice, when the users face imperfect SIC, their sum-rate curves become limited to a saturation point that deteriorates with the increase of the error factor ξ. This happens due to the fact that all users, even the strongest one, experience interference when $\xi \neq 0$, thereby, leading to the observed limited performance. Such behavior confirms the insights raised in the last paragraph of Section V-C.

Fig. 6 depicts the impact of the level of cross-polar transmissions in the users' ergodic rates considering perfect SIC, in which results for different values for the iXPD parameter χ are shown. In addition to validating the theoretical analysis, this figure shows how beneficial the proposed scheme can be to improve the performance of each user. It also becomes clear that, with the help of IRSs, depolarization phenomena can be transformed into an advantage, e.g., the higher the iXPD, the greater the performance gains. For instance, in the conventional single-polarized system, when the SNR is 30 dB, the rate of user 3 is limited to only 2.27 bits per channel use (BPCU). On the other hand, when this same user is served via the IRS-MIMO-NOMA scheme, for a low iXPD of $\chi = 0.05$, and an SNR of 30 dB, its rate can reach 8.44 BPCU, which is more than three times greater than that achieved in the single-polarized scheme. When we consider a high iXPD of $\chi = 1$, the achievable ergodic rate of the user 3 becomes even more remarkable, reaching up to 9.42 BPCU. Impressive performance gains can be also observed in all the other users, with their rates remarkably outperforming those achievable in the conventional single-polarized scheme. These improvements are mainly due to two features of the proposed IRS-MIMO-NOMA system, already explained in previous sections. That is, firstly, the IRSs enable the users to exploit polarization diversity, and, secondly, the users are able to perform SIC considering interference only from their own polarization subset. Therefore, in addition to benefit

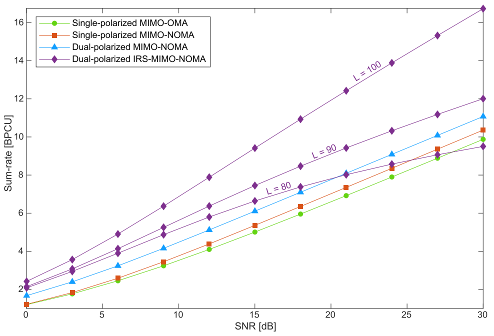

Fig. 7. Simulated ergodic sum-rates. Comparison between proposed dual-polarized IRS-MIMO-NOMA and conventional schemes ($N = 4, \chi = 0.5, \xi = 0$).

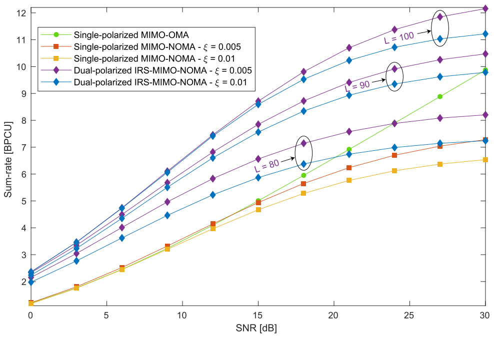

Fig. 8. Simulated ergodic sum-rates. Comparison between proposed dual-polarized IRS-MIMO-NOMA and conventional schemes under imperfect SIC ($N = 4, \chi = 0.5$).

from diversity, users in the IRS-MIMO-NOMA system are impacted by less interference than they are in the conventional MIMO-NOMA counterpart.

In Fig. 7, we compare the sum-rate performance of the proposed IRS-MIMO-NOMA scheme and other conventional systems assuming perfect SIC. As one can notice, when $L = 80$, from 21 dB onward, the proposed scheme is outperformed by the dual-polarized MIMO-NOMA counterpart, and when the SNR reaches 30 dB, the MIMO-OMA system is the one that achieves the best performance. However, with a slight increase in the number of reflecting elements, from $L = 80$ to $L = 90$, the IRS-MIMO-NOMA scheme can already outperform all the other baseline schemes, in all considered SNR range. Finally, Fig. 8 shows how well the dual-polarized IRS-MIMO-NOMA system performs in comparison with the single-polarized MIMO-OMA and MIMO-NOMA counterparts in the presence of SIC error propagation. As can be seen, even though the sum-rate of all NOMA-based schemes are caped in the high-SNR regime, the proposed IRS-MIMO-NOMA system is significantly more robust to SIC errors than the conventional single-polarized MIMO-NOMA. For instance, for a SIC error factor of $\xi = 0.005$, the single-polarized MIMO-NOMA can only slightly outperform the MIMO-OMA scheme for SNR values lower than 15 dB. When the error is $\xi = 0.01$, the sum-rate degradation becomes so severe that, in the whole SNR range, the MIMO-OMA system outperforms the MIMO-NOMA counterpart. On the other hand, even when considering $L = 80$ reflecting elements, and an error of $\xi = 0.01$, the IRS-MIMO-NOMA can reach sum-rates remarkably higher than those achieved by the conventional schemes, being outperformed by the MIMO-OMA scheme only in SNR values above 20 dB. Moreover, for $L = 90$ and $L = 100$, the IRS-MIMO-NOMA scheme always achieves the best performance. For example, when $\xi = 0.005$, $L = 100$ and the SNR is 18 dB, the IRS-MIMO-NOMA scheme reaches an expressive sum-rate of 9.81 BPCU, which is an increase of 3.86 BPCU over the MIMO-OMA system and 4.17 BPCU over the single-polarized MIMO-NOMA.

VII. CONCLUSION

In this work, by exploiting the capabilities of dual-polarized IRSs, we proposed and investigated a novel strategy for improving the performance of dual-polarized massive MIMO-NOMA networks under the impact of imperfect SIC. The detailed construction of the beamforming and reception matrices was provided, and an efficient procedure for optimizing the IRS reflecting elements was developed. Moreover, we carried out an insightful mathematical analysis, in which the ergodic rates for large numbers of reflecting elements were derived. Our numerical results revealed that the proposed dual-polarized IRS-MIMO-NOMA scheme can achieve remarkable performance gains over conventional single-polarized and dual-polarized systems and that cross-polar transmissions can further improve the ergodic rates of the users.

APPENDIX A
PROOF OF LEMMA I

Given the data symbol in (25), when the uth user in the polarization subset $\mathcal{U}^p$, $p \in \{v, h\}$, of the gth group decodes the message intended to the ith user, $\min\{\mathcal{U}^p\} < i < u$, $i \in \mathcal{U}^p$, it experiences the following SINR

$$
\begin{aligned}
\gamma_{gu}^{i} \\
&= |\alpha_{gi} x_{gi}|^2 \Bigg(\sum_{m \in \{a|\, a>i,\, a \in \mathcal{U}^p\}} |\alpha_{gm} x_{gm}|^2 + \xi \sum_{n \in \{b|\, b<i,\, b \in \mathcal{U}^p\}} |\alpha_{gn} x_{gn}|^2 \\
&\quad + \left| [\mathbf{H}_{gu}^{\dagger \ddot{p}} \underline{\mathbf{H}}_{gu}^{t \ddot{p}} \mathbf{x}^t]_g \right|^2 + |[\mathbf{H}_{gu}^{\dagger \ddot{p}} \mathbf{n}_{gu}^{\ddot{p}}]_g|^2 \Bigg)^{-1} \\
&= \alpha_{gi}^2 \Bigg(\sum_{m \in \{a|\, a>i,\, a \in \mathcal{U}^p\}} \alpha_{gm}^2 + \quad \xi \sum_{n \in \{b|\, b<i,\, b \in \mathcal{U}^p\}} \alpha_{gn}^2 + \left| [\mathbf{H}_{gu}^{\dagger \ddot{p}} \underline{\mathbf{H}}_{gu}^{t \ddot{p}} \mathbf{x}^t]_g \right|^2 \\
&\quad + \sigma_n^2 [\mathbf{H}_{gu}^{\dagger \ddot{p}} (\mathbf{H}_{gu}^{\dagger \ddot{p}})^H]_{gg} \Bigg)^{-1}. \qquad \text{(A-1)}
\end{aligned}
$$

By defining $\rho = 1/\sigma_n^2$ as the SNR, and denoting the effective channel gain by $\ddot{\zeta}_{gu} = \max\{\zeta_{gu}^v, \zeta_{gu}^h\} = \max$

$\{1/[\mathbf{H}_{gu}^{\dagger v}(\mathbf{H}_{gu}^{\dagger v})^H]_{gg}, 1/[\mathbf{H}_{gu}^{\dagger h}(\mathbf{H}_{gu}^{\dagger h})^H]_{gg}\}$, the SINR can be rewritten as

$$\gamma_{gu}^i = \rho\ddot{\langle}_{gu}\alpha_{gi}^2\left[\rho\ddot{\langle}_{gu}\left(\sum_{m=i+1}^{\max\{\mathcal{U}^p\}}\alpha_{gm}^2 + \xi\sum_{n=\min\{\mathcal{U}^p\}}^{i-1}\alpha_{gn}^2 + \left|[\mathbf{H}_{gu}^{\dagger\ddot{p}}\underline{\mathbf{H}}_{gu}^{t\ddot{p}}\mathbf{x}^t]_g\right|^2\right) + 1\right]^{-1}. \quad \text{(A-2)}$$

Note that when the weakest user, i.e., the 1st user corresponding to $\min\{\mathcal{U}^p\}$, detects its symbol, it will experience interference from everyone else, but it will not face imperfect SIC. On the other hand, when the user with the best channel gain, i.e., the user corresponding to the maximum index in $\mathcal{U}^p$, decodes its symbol, there will be no interference from higher-order users, but only from imperfect SIC. Under these observations, we denote the polarization interference by $\mathfrak{X}_{gu} = \left|[\mathbf{H}_{gu}^{\dagger\ddot{p}}\underline{\mathbf{H}}_{gu}^{t\ddot{p}}\mathbf{x}^t]_g\right|^2$, and the total SIC interference by (A-3), as shown at the bottom of the page. Then, by applying these definitions in (A-2), we can achieve the final SINR expression, as in (26), which completes the proof. □

APPENDIX B
PROOF OF LEMMA II

First, note that $(\mathbf{\Phi}_{gu}^{pq})^H\mathbf{\Phi}_{gu}^{pq}$ is a diagonal matrix whose entries are the squared magnitude of the reflection coefficients, i.e., $(\omega_{gu,l}^{pq})^2$. Therefore, we aim to investigate the behavior of $(\omega_{gu,l}^{pq})^2$ when $L \to \infty$. For this, let us start by relaxing the unity $\mathcal{L}_\infty$ norm constraint (15b), and rewriting the problem in (15) as

$$\min_{\boldsymbol{\theta}_{gu}^{vv},\boldsymbol{\theta}_{gu}^{hv}} \left\|\bar{\mathbf{K}}_{gu}\left[(\boldsymbol{\theta}_{gu}^{vv})^T, (\boldsymbol{\theta}_{gu}^{hv})^T\right]^T + \mathbf{d}_{gu}^{hv}\right\|^2, \quad \text{(B-1)}$$

which consists of a standard least squares problem that, by assuming $L \geq Nr_k^\star$, has optimal solution given by

$$\left[(\dot{\boldsymbol{\theta}}_{gu}^{vv})^T, (\dot{\boldsymbol{\theta}}_{gu}^{hv})^T\right]^T = \bar{\mathbf{K}}_{gu}^H(\bar{\mathbf{K}}_{gu}\bar{\mathbf{K}}_{gu}^H)^{-1}\mathbf{d}_{gu}^{hv}, \quad \text{(B-2)}$$

which is the solution with minimum $\mathcal{L}_2$ norm. Then, it follows that $\bar{\mathbf{K}}_{gu}\left[(\dot{\boldsymbol{\theta}}_{gu}^{vv})^T, (\dot{\boldsymbol{\theta}}_{gu}^{hv})^T\right]^T + \mathbf{d}_{gu}^{hv} = 0$, which implies

$$\sum_{l=1}^{2L}[\bar{\mathbf{K}}_{gu}]_{il}\begin{bmatrix}\dot{\boldsymbol{\theta}}_{gu}^{vv}\\ \dot{\boldsymbol{\theta}}_{gu}^{hv}\end{bmatrix}_l = -\left[\mathbf{d}_{gu}^{hv}\right]_i, \quad \forall i = 1, \cdots, \frac{N}{2}r_k^\star. \quad \text{(B-3)}$$

Recall that $\left[\mathbf{d}_{gu}^{hv}\right]_i$ is a complex Gaussian random variable with zero mean and unit variance. Consequently, the sum on the left-hand side of (B-3) will also have zero mean and unity variance $\forall L \geq Nr_k^\star \in \mathbb{N}_{>0}$. Therefore, we can exploit the independence of $[\bar{\mathbf{K}}_{gu}]_{il}$ and $\left[\left[(\dot{\boldsymbol{\theta}}_{gu}^{vv})^T, (\dot{\boldsymbol{\theta}}_{gu}^{hv})^T\right]^T\right]_l$ and write

$$\sum_{l=1}^{2L}\mathbb{E}\left\{\left|[\bar{\mathbf{K}}_{gu}]_{il}\right|^2\right\}\mathbb{E}\left\{\left|\begin{bmatrix}\dot{\boldsymbol{\theta}}_{gu}^{vv}\\ \dot{\boldsymbol{\theta}}_{gu}^{hv}\end{bmatrix}_l\right|^2\right\} = \mathbb{E}\left\{\left|\left[\mathbf{d}_{gu}^{hv}\right]_i\right|^2\right\} = 1. \quad \text{(B-4)}$$

As long as the reflection coefficients are optimized based on (B-2), the sum in (B-4) will always converge to 1, independently of L. By knowing this beforehand, we need to check the convergence behavior of each term of the above sum separately. First, recall that the entries of $\bar{\mathbf{K}}_{gu}$ also result from independent complex Gaussian random variables with unity variance. Because of this, we have that $\lim_{L\to\infty}\sum_{l=1}^{2L}\mathbb{E}\{|[\bar{\mathbf{K}}_{gu}]_{il}|^2\} \to \infty$. Therefore, the sum in (B-4) will only converge if $\left|\left[\left[(\dot{\boldsymbol{\theta}}_{gu}^{vv})^T, (\dot{\boldsymbol{\theta}}_{gu}^{hv})^T\right]^T\right]_l\right|^2 = (\omega_{gu,l}^{pq})^2 \to 0$, $\forall l = 1, \cdots, 2L$, and we can conclude that $(\mathbf{\Phi}_{gu}^{pq})^H\mathbf{\Phi}_{gu}^{pq} \to \mathbf{0}_{L,L}$, as $L \to \infty, \forall p, q \in \{v, h\}$,, which completes the proof. □

APPENDIX C
PROOF OF PROPOSITION I

By relying on Lemma II, when $L \to \infty$, the uth user experiences the following data rate

$$R_{gu} = \log_2\left(\rho\ddot{\langle}_{gu}(\alpha_{gu}^2 + \mathfrak{I}_{gu}) + 1\right) - \log_2\left(\rho\ddot{\langle}_{gu}\mathfrak{I}_{gu} + 1\right), \quad 1 \leq u \leq U. \quad \text{(C-1)}$$

The ergodic rate can be then derived from the expectation of R_{gu}, i.e.,

$$\bar{R}_{gu} = \int_0^\infty \left[\log_2\left(\rho(\alpha_{gu}^2 + \mathfrak{I}_{gu})x + 1\right) - \log_2\left(\rho\mathfrak{I}_{gu}x + 1\right)\right] f_{\ddot{\langle}_{gu}}(x)dx. \quad \text{(C-2)}$$

Next, by denoting $\bar{\alpha}_{gu} = \rho(\alpha_{gu}^2 + \mathfrak{I}_{gu})$ and $\tilde{\alpha}_{gu} = \rho\mathfrak{I}_{gu}$, and replacing the PDF of $\ddot{\langle}_{gu}$ in (C-2), we obtain

$$\begin{aligned}\bar{R}_{gu} &= \frac{(\lambda_{gu})^\kappa}{\Gamma(\kappa)^2}\int_0^\infty \left[\log_2\left(\bar{\alpha}_{gu}x + 1\right) - \log_2\left(\tilde{\alpha}_{gu}x + 1\right)\right] x^{\kappa-1}e^{-\lambda_{gu}x}\gamma\left(\kappa, (\chi^{\text{BS-U}})^{-1}\lambda_{gu}x\right)dx \\ &+ \frac{(\lambda_{gu})^\kappa}{\Gamma(\kappa)^2(\chi^{\text{BS-U}})^\kappa}\int_0^\infty \left[\log_2\left(\bar{\alpha}_{gu}x + 1\right)\right.\end{aligned}$$

$$\mathfrak{I}_{gi} = \begin{cases}\displaystyle\sum_{m=i+1}^{\max\{\mathcal{U}^p\}}\alpha_{gm}^2, & \text{if } i = \min\{\mathcal{U}^p\},\\ \displaystyle\sum_{m=i+1}^{\max\{\mathcal{U}^p\}}\alpha_{gm}^2 + \xi\sum_{n=\min\{\mathcal{U}^p\}}^{i-1}\alpha_{gn}^2, & \text{if } \min\{\mathcal{U}^p\} < i \leq u < \max\{\mathcal{U}^p\},\\ \displaystyle\xi\sum_{n=1}^{i-1}\alpha_{gn}^2, & \text{if } i = u = \max\{\mathcal{U}^p\}.\end{cases} \quad \text{(A-3)}$$

$$
\begin{aligned}
&- \log_2\left(\tilde{\alpha}_{gu}x + 1\right)\Big] x^{\kappa-1} e^{-(\chi^{\text{BS-U}})^{-1}\lambda_{gu}x} \gamma\left(\kappa, \lambda_{gu}x\right) dx \\
&\triangleq I_1 + I_2. \qquad \text{(C-3)}
\end{aligned}
$$

First, let us focus on solving I_1. By applying the Meijer's G-function representation for $\ln(x+1)$ [40, eq. (2.6.6)] and exploiting the series representation of the incomplete gamma function in [23, eq. (8.352.6)], we can rewrite I_1 as follows

$$
\begin{aligned}
I_1 = \frac{(\lambda_{gu})^{\kappa}}{\ln(2)\Gamma(\kappa)} \Bigg[\int_0^{\infty} \Big[& G_{2,2}^{1,2}\left({}^{1,1}_{1,0} \middle| \bar{\alpha}_{gu}x \right) \\
& - G_{2,2}^{1,2}\left({}^{1,1}_{1,0} \middle| \tilde{\alpha}_{gu}x \right) \Big] x^{\kappa-1} e^{-\lambda_{gu}x} dx \\
& - \sum_{n=0}^{\kappa-1} \frac{(\lambda_{gu})^{n}}{n!(\chi^{\text{BS-U}})^{n}} \int_0^{\infty} \Big[G_{2,2}^{1,2}\left({}^{1,1}_{1,0} \middle| \bar{\alpha}_{gu}x \right) \\
& - G_{2,2}^{1,2}\left({}^{1,1}_{1,0} \middle| \tilde{\alpha}_{gu}x \right) \Big] x^{\kappa+n-1} e^{-\lambda_{gu}(1+(\chi^{\text{BS-U}})^{-1})x} dx \Bigg]. \\
& \qquad \text{(C-4)}
\end{aligned}
$$

Then, by exploiting the Laplace transform property for Meijer's G-functions [41, eq. (5.6.3.1)], and performing some manipulations in (C-4), I_1 can be derived as

$$
\begin{aligned}
I_1 = \frac{1}{\ln(2)\Gamma(\kappa)} \Bigg\{ & \left({}^{1-\kappa,1,1}_{1,0} \middle| \frac{\bar{\alpha}_{gu}}{\lambda_{gu}} \right) \\
& - G_{3,2}^{1,3}\left({}^{1-\kappa,1,1}_{1,0} \middle| \frac{\tilde{\alpha}_{gu}}{\lambda_{gu}} \right) - \sum_{n=0}^{\kappa-1} \frac{(1+(\chi^{\text{BS-U}})^{-1})^{-\kappa-n}}{n!(\chi^{\text{BS-U}})^{n}} \\
& \times \Bigg[G_{3,2}^{1,3}\left({}^{1-\kappa-n,1,1}_{1,0} \middle| \frac{\bar{\alpha}_{gu}}{\lambda_{gu}(1+(\chi^{\text{BS-U}})^{-1})} \right) \\
& - \left({}^{1-\kappa-n,1,1}_{1,0} \middle| \frac{\tilde{\alpha}_{gu}}{\lambda_{gu}(1+(\chi^{\text{BS-U}})^{-1})} \right) \Bigg] \Bigg\}. \qquad \text{(C-5)}
\end{aligned}
$$

A similar analysis can be carried out to solve I_2, which is not shown here due to space constraints. Then, after replacing I_1 and I_2 in (C-3), and performing some manipulations, the final ergodic rate expression can be obtained as in (33), which completes the proof. □

REFERENCES

[1] A. Sousa De Sena, D. Benevides da Costa, Z. Ding, and P. H. J. Nardelli, "Massive MIMO–NOMA networks with multi-polarized antennas," *IEEE Trans. Wireless Commun.*, vol. 18, no. 12, pp. 5630–5642, Dec. 2019.

[2] H. Asplund, *Advanced Antenna Systems for 5G Network Deployments*. New York, NY, USA: Academic, 2020.

[3] A. S. de Sena *et al.*, "Massive MIMO-NOMA networks with imperfect SIC: Design and fairness enhancement," *IEEE Trans. Wireless Commun.*, vol. 19, no. 9, pp. 6100–6115, Sep. 2020.

[4] N. Kaina, M. Dupré, G. Lerosey, and M. Fink, "Shaping complex microwave fields in reverberating media with binary tunable metasurfaces," *Sci. Rep.*, vol. 4, no. 1, pp. 1–8, Oct. 2014.

[5] P. del Hougne, M. Fink, and G. Lerosey, "Optimally diverse communication channels in disordered environments with tuned randomness," *Nature Electron.*, vol. 2, no. 1, pp. 36–41, Jan. 2019.

[6] M. D. Renzo *et al.*, "Smart radio environments empowered by reconfigurable AI meta-surfaces: An idea whose time has come," *EURASIP J. Wireless Commun. Netw.*, vol. 2019, no. 1, pp. 1–20, May 2019.

[7] M. Di Renzo *et al.*, "Smart radio environments empowered by reconfigurable intelligent surfaces: How it works, state of research, and the road ahead," *IEEE J. Sel. Areas Commun.*, vol. 38, no. 11, pp. 2450–2525, Nov. 2020.

[8] A. S. D. Sena *et al.*, "What role do intelligent reflecting surfaces play in multi-antenna non-orthogonal multiple access?" *IEEE Wireless Commun.*, vol. 27, no. 5, pp. 24–31, Oct. 2020.

[9] S. Zhang and R. Zhang, "Capacity characterization for intelligent reflecting surface aided MIMO communication," *IEEE J. Sel. Areas Commun.*, vol. 38, no. 8, pp. 1823–1838, Aug. 2020.

[10] J. Ye, S. Guo, and M.-S. Alouini, "Joint reflecting and precoding designs for SER minimization in reconfigurable intelligent surfaces assisted MIMO systems," *IEEE Trans. Wireless Commun.*, vol. 19, no. 8, pp. 5561–5574, Aug. 2020.

[11] Q. Wu and R. Zhang, "Intelligent reflecting surface enhanced wireless network via joint active and passive beamforming," *IEEE Trans. Wireless Commun.*, vol. 18, no. 11, pp. 5394–5409, Nov. 2019.

[12] C. Pan *et al.*, "Multicell MIMO communications relying on intelligent reflecting surfaces," *IEEE Trans. Wireless Commun.*, vol. 19, no. 8, pp. 5218–5233, Aug. 2020.

[13] L. Zhang, Y. Wang, W. Tao, Z. Jia, T. Song, and C. Pan, "Intelligent reflecting surface aided MIMO cognitive radio systems," *IEEE Trans. Veh. Technol.*, vol. 69, no. 10, pp. 11445–11457, Jul. 2020.

[14] C. Pan *et al.*, "Intelligent reflecting surface aided MIMO broadcasting for simultaneous wireless information and power transfer," *IEEE J. Sel. Areas Commun.*, vol. 38, no. 8, pp. 1719–1734, Aug. 2020.

[15] W. Jiang, Y. Zhang, J. Wu, W. Feng, and Y. Jin, "Intelligent reflecting surface assisted secure wireless communications with Multiple- transmit and multiple-receive antennas," *IEEE Access*, vol. 8, pp. 86659–86673, 2020.

[16] Z. Ding and H. V. Poor, "A simple design of IRS-NOMA transmission," *IEEE Commun. Lett.*, vol. 24, no. 5, pp. 1119–1123, May 2020.

[17] F. Fang, Y. Xu, Q.-V. Pham, and Z. Ding, "Energy-efficient design of IRS-NOMA networks," *IEEE Trans. Veh. Technol.*, vol. 69, no. 11, pp. 14088–14092, Nov. 2020.

[18] X. Mu, Y. Liu, L. Guo, J. Lin, and N. Al-Dhahir, "Exploiting intelligent reflecting surfaces in NOMA networks: Joint beamforming optimization," *IEEE Trans. Wireless Commun.*, vol. 19, no. 10, pp. 6884–6898, Oct. 2020.

[19] T. Hou, Y. Liu, Z. Song, X. Sun, and Y. Chen, "MIMO-NOMA networks relying on reconfigurable intelligent surface: A signal cancellation-based design," *IEEE Trans. Commun.*, vol. 68, no. 11, pp. 6932–6944, Nov. 2020.

[20] J. Zuo, Y. Liu, E. Basar, and O. A. Dobre, "Intelligent reflecting surface enhanced millimeter-wave NOMA systems," *IEEE Commun. Lett.*, vol. 24, no. 11, pp. 2632–2636, Nov. 2020.

[21] S. Jiao, F. Fang, X. Zhou, and H. Zhang, "Joint beamforming and phase shift design in downlink UAV networks with IRS-assisted NOMA," *J. Commun. Inf. Netw.*, vol. 5, no. 2, pp. 138–149, Jun. 2020.

[22] J. Brewer, "Kronecker products and matrix calculus in system theory," *IEEE Trans. Circuits Syst.*, vol. CS-25, no. 9, pp. 772–781, Sep. 1978.

[23] I. S. Gradshteyn and I. M. Ryzhik, *Table of Integrals, Series, and Products*, 7th ed. New York, NY, USA: Academic, 2007.

[24] S. Sun, W. Jiang, S. Gong, and T. Hong, "Reconfigurable linear-to-linear polarization conversion metasurface based on PIN diodes," *IEEE Antennas Wireless Propag. Lett.*, vol. 17, no. 9, pp. 1722–1726, Sep. 2018.

[25] J. Wang, R. Yang, R. Ma, J. Tian, and W. Zhang, "Reconfigurable multifunctional metasurface for broadband polarization conversion and perfect absorption," *IEEE Access*, vol. 8, pp. 105815–105823, 2020.

[26] H. F. Ma, G. Z. Wang, G. S. Kong, and T. J. Cui, "Independent controls of differently-polarized reflected waves by anisotropic metasurfaces," *Sci. Rep.*, vol. 5, no. 1, p. 1, Sep. 2015.

[27] Y.-C. Liang, R. Long, Q. Zhang, J. Chen, H. V. Cheng, and H. Guo, "Large intelligent surface/antennas (LISA): Making reflective radios smart," *J. Commun. Inf. Netw.*, vol. 4, no. 2, pp. 40–50, Jun. 2019.

[28] X. Qian and M. Di Renzo, "Mutual coupling and unit cell aware optimization for reconfigurable intelligent surfaces," *IEEE Wireless Commun. Lett.*, early access, Feb. 23, 2021, doi: 10.1109/LWC.2021.3061449.

[29] J. Park and B. Clerckx, "Multi-user linear precoding for multi-polarized massive MIMO system under imperfect CSIT," *IEEE Trans. Wireless Commun.*, vol. 14, no. 5, pp. 2532–2547, May 2015.

[30] A. Adhikary, J. Nam, J.-Y. Ahn, and G. Caire, "Joint spatial division and multiplexing—The large-scale array regime," *IEEE Trans. Inf. Theory*, vol. 59, no. 10, pp. 6441–6463, Oct. 2013.

[31] W. Chen, S. Zhao, R. Zhang, and L. Yang, "Generalized user grouping in NOMA based on overlapping coalition formation game," *IEEE J. Sel. Areas Commun.*, vol. 39, no. 4, pp. 969–981, Apr. 2021.

[32] D.-T. Do, T.-L. Nguyen, S. Ekin, Z. Kaleem, and M. Voznak, "Joint user grouping and decoding order in uplink/downlink MISO/SIMO-NOMA," *IEEE Access*, vol. 8, pp. 143632–143643, 2020.

[33] S.-Y. Shim and Y. Chen, "Least squares solution of matrix equation $AXB^* + CYD^* = E$," *SIAM J. Matrix Anal. Appl.*, vol. 24, no. 3, pp. 802–808, 2003.

[34] Z.-Q. Luo, W.-K. Ma, A. So, Y. Ye, and S. Zhang, "Semidefinite relaxation of quadratic optimization problems," *IEEE Signal Process. Mag.*, vol. 27, no. 3, pp. 20–34, May 2010.

[35] A. Taha, Y. Zhang, F. B. Mismar, and A. Alkhateeb, "Deep reinforcement learning for intelligent reflecting surfaces: Towards standalone operation," in *Proc. IEEE 21st Int. Workshop Signal Process. Adv. Wireless Commun. (SPAWC)*, May 2020, pp. 1–5.

[36] G. C. Alexandropoulos and E. Vlachos, "A hardware architecture for reconfigurable intelligent surfaces with minimal active elements for explicit channel estimation," in *Proc. IEEE Int. Conf. Acoust., Speech Signal Process. (ICASSP)*, May 2020, pp. 9175–9179.

[37] Z. Wang, L. Liu, and S. Cui, "Channel estimation for intelligent reflecting surface assisted multiuser communications: Framework, algorithms, and analysis," *IEEE Trans. Wireless Commun.*, vol. 19, no. 10, pp. 6607–6620, Oct. 2020.

[38] Q.-U.-A. Nadeem, H. Alwazani, A. Kammoun, A. Chaaban, M. Debbah, and M.-S. Alouini, "Intelligent reflecting surface-assisted multi-user MISO communication: Channel estimation and beamforming design," *IEEE Open J. Commun. Soc.*, vol. 1, pp. 661–680, 2020.

[39] B. Zheng, C. You, and R. Zhang, "Intelligent reflecting surface assisted multi-user OFDMA: Channel estimation and training design," *IEEE Trans. Wireless Commun.*, vol. 19, no. 12, pp. 8315–8329, Dec. 2020.

[40] A. M. Mathai and R. K. Saxena, *Generalized Hypergeometric Functions With Applications in Statistics and Physical Sciences*, 1st ed. Berlin, Germany: Springer-Verlag, 1973.

[41] Y. L. Keke, *The Special Functions and Their Approximations*, vol. 1, 1st ed. New York, NY, USA: Academic, 1969.

Arthur Sousa de Sena (Student Member, IEEE) received the B.Sc. degree in computer engineering and the M.Sc. degree in teleinformatics engineering from the Federal University of Ceará, Brazil, in 2017 and 2019, respectively. He is currently pursuing the Ph.D. degree in electrical engineering with the School of Energy Systems, LUT University, Finland. From 2014 to 2015, he studied computer engineering as an Exchange Student at the Illinois Institute of Technology, USA. He is also a Researcher with the Cyber-Physical Systems Group, LUT University, where he has been actively working in the wireless communication field, having already published several articles in prestigious journals and conferences. His research interests include signal processing, mobile communications systems, non-orthogonal multiple access techniques, intelligent metasurfaces, and massive MIMO.

Pedro H. J. Nardelli (Senior Member, IEEE) received the B.S. and M.Sc. degrees in electrical engineering from the State University of Campinas, Brazil, in 2006 and 2008, respectively, and the dual Ph.D. degree from the University of Oulu, Finland, and the State University of Campinas, in 2013. He is currently an Associate Professor (tenure track) in the IoT in energy systems with LUT University, Finland, and holds a position of the Academy of Finland Research Fellow with a project called Building the Energy Internet as a large-scale IoT-based cyber-physical system that manages the energy inventory of distribution grids as discretized packets via machine-type communications (EnergyNet). He leads the Cyber-Physical Systems Group, LUT University. He is also the Project Coordinator of the CHIST-ERA European Consortium Framework for the Identification of Rare Events via Machine Learning and IoT Networks (FIREMAN) and the project Swarming Technology for Reliable and Energy-aware Aerial Missions (STREAM) supported by Jane and Aatos Erkko Foundation. He is also the Docent with the University of Oulu in the topic of "communications strategies and information processing in energy systems." His research interests include wireless communications particularly applied in industrial automation and energy systems. He received the Best Paper Award of IEEE PES Innovative Smart Grid Technologies Latin America 2019 in the track "Big Data and the Internet of Things."

Daniel Benevides da Costa (Senior Member, IEEE) was born in Fortaleza, Ceará, Brazil, in 1981. He received the B.Sc. degree in Telecommunications from the Military Institute of Engineering (IME), Rio de Janeiro, Brazil, in 2003, and the M.Sc. and Ph.D. degrees in Electrical Engineering, Area: Telecommunications, from the University of Campinas, SP, Brazil, in 2006 and 2008, respectively. His Ph.D. thesis was awarded the Best Ph.D. Thesis in Electrical Engineering by the Brazilian Ministry of Education (CAPES) at the 2009 CAPES Thesis Contest. From 2008 to 2009, he was a Postdoctoral Research Fellow with INRS-EMT, University of Quebec, Montreal, QC, Canada. In 2019, he was awarded with the prestigious grant of Nokia Visiting Professor. Since 2010, he has been with the Federal University of Ceará, where he is currently an Associate Professor. Recently, he joined as Full Professor the National Yunlin University of Science and Technology (YunTech), Taiwan.

Prof. da Costa is currently Executive Editor of the IEEE COMMUNICATIONS LETTERS, Area Editor of IEEE OPEN JOURNAL OF THE COMMUNICATION SOCIETY - Area: Green, Cognitive, and Intelligent Communications and Networks, Editor at Large of the IEEE TRANSACTIONS ON COMMUNICATIONS, Area: Communication Theory & Systems II, and Specialty Chief Editor of the *Frontiers in Communications and Networks* - Wireless Communications Section. He is also Editor of the IEEE TRANSACTIONS ON VEHICULAR TECHNOLOGY and IEEE TRANSACTIONS ON COGNITIVE COMMUNICATIONS AND NETWORKING. He has served as Lead Guest Editor and Guest Editor of several Journal Special Issues. He has been involved on the Organizing Committee of several conferences. He is currently the Latin American Chapters Coordinator of the IEEE Vehicular Technology Society. Also, he acts as a Scientific Consultant of the National Council of Scientific and Technological Development (CNPq), Brazil, and he is a Productivity Research Fellow of CNPq. He was Vice-Chair of Americas of the IEEE Technical Committee of Cognitive Networks (TCCN) and Director of the TCCN Newsletter in the 2019-2020 biennium. Currently, he is Vice-Chair of the SIG on "REconFigurabLE Intelligent Surfaces for Signal Processing and CommunicatIONS" (REFLECTIONS) in Signal Processing and Computing for Communications Technical Committee (SPCC).

Prof. da Costa is the recipient of four conference paper awards. He received the Exemplary Reviewer Certificate of the IEEE WIRELESS COMMUNICATIONS LETTERS in 2013 and 2019, the Exemplary Reviewer Certificate of the IEEE COMMUNICATIONS LETTERS in 2016, 2017, and 2019, the Certificate of Appreciation of Top Associate Editor for outstanding contributions to IEEE TRANSACTIONS ON VEHICULAR TECHNOLOGY in 2013, 2015 and 2016, the Exemplary Editor Award of IEEE COMMUNICATIONS LETTERS in 2016, and the Outstanding Editor Award of IEEE ACCESS in 2017, and the Certificate of Appreciation for notable services and contributions to IEEE ACCESS in 2018 and 2019. He is a World's Top 2% Scientist from Stanford University (2020) and a Distinguished Lecturer of the IEEE Vehicular Technology Society. He is a Senior Member of IEEE, Member of IEEE Communications Society, IEEE Vehicular Technology Society, and Brazilian Telecommunications Society.

Francisco Rafael Marques Lima (Senior Member, IEEE) received the B.Sc. degree (Hons.) in electrical engineering and the M.Sc. and D.Sc. degrees in telecommunications engineering from the Federal University of Ceará, Fortaleza, Brazil, in 2005, 2008, and 2012, respectively. In 2008, he was an Internship at Ericsson Research, Lulea, Sweden, where he studied scheduling algorithms for LTE systems. Since 2010, he has been a Professor with the Computer Engineering Department, Federal University of Ceará, Sobral, Brazil. He is currently a Senior Researcher with the Wireless Telecom Research Group (GTEL), Fortaleza, where he works in projects in cooperation with Ericsson Research. He has published several conference papers and journal articles as well as patents in wireless telecommunications field. His research interests include radio resource allocation algorithms for QoS guarantees for 5G and beyond 5G networks in scenarios with multiple services, resources, antennas, and users. He is also an Associate Editor of IEEE ACCESS and a reviewer of important IEEE journals.

Liang Yang (Member, IEEE) was born in Hunan, China. He received the Ph.D. degree in electrical engineering from Sun Yat-sen University, Guangzhou, China, in 2006. From 2006 to 2013, he was a Faculty Member with Jinan University, Guangzhou. He joined the Guangdong University of Technology in 2013. He is currently a Professor with Hunan University, Changsha, China. His current research interest includes the performance analysis of wireless communications systems.

Petar Popovski (Fellow, IEEE) received the Dipl.-Ing. and M.Sc. degrees in communication engineering from the University of Ss. Cyril and Methodius, Skopje, and the Ph.D. degree from Aalborg University in 2005. He is currently a Professor with Aalborg University, where he heads the section on connectivity. He has authored the book *Wireless Connectivity: An Intuitive and Fundamental Guide* (Wiley, 2020). His research interests include wireless communication and communication theory. He received an ERC Consolidator Grant in 2015, the Danish Elite Researcher Award in 2016, the IEEE Fred W. Ellersick Prize in 2016, the IEEE Stephen O. Rice Prize in 2018, the Technical Achievement Award from the IEEE Technical Committee on Smart Grid Communications in 2019, and the Danish Telecommunication Prize in 2020. He is also a member at Large with the Board of Governors in the IEEE Communication Society, and the Vice-Chair of the IEEE Communication Theory Technical Committee and IEEE TRANSACTIONS ON GREEN COMMUNICATIONS AND NETWORKING. He was the General Chair of IEEE SmartGridComm 2018 and IEEE Communication Theory Workshop 2019. He is also an Area Editor of the IEEE TRANSACTIONS ON WIRELESS COMMUNICATIONS.

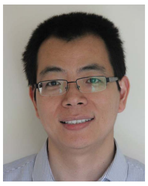

Zhiguo Ding (Fellow, IEEE) received the B.Eng. degree in electrical engineering from the Beijing University of Posts and Telecommunications in 2000, and the Ph.D. degree in electrical engineering from Imperial College London in 2005. From July 2005 to April 2018, he was with Queen's University Belfast, Imperial College London, Newcastle University, and Lancaster University. Since April 2018, he has been with The University of Manchester as a Professor of Communications. From October 2012 to September 2021, he was an Academic Visitor with Princeton University. His research interests include 5G networks, game theory, cooperative and energy harvesting networks, and statistical signal processing. He recently received the EU Marie Curie Fellowship 2012–2014, the Top IEEE TVT Editor 2017, the IEEE Heinrich Hertz Award 2018, the IEEE Jack Neubauer Memorial Award 2018, the IEEE Best Signal Processing Letter Award 2018, and the Friedrich Wilhelm Bessel Research Award 2020. He is also serving as an Area Editor for the IEEE OPEN JOURNAL OF THE COMMUNICATIONS SOCIETY, and an Editor for IEEE TRANSACTIONS ON VEHICULAR TECHNOLOGY and *Journal of Wireless Communications and Mobile Computing*. He was an Editor for IEEE WIRELESS COMMUNICATION LETTERS, IEEE TRANSACTIONS ON COMMUNICATIONS, and IEEE COMMUNICATION LETTERS from 2013 to 2016. He is also a Distinguished Lecturer of IEEE ComSoc, and a Web of Science Highly Cited Researcher in two categories 2020.

Constantinos B. Papadias (Fellow, IEEE) received the diploma degree in electrical engineering from the National Technical University of Athens (NTUA), in 1991, and the Ph.D. degree (Hons.) in signal processing from the Ecole Nationale Supérieure des Télécommunications (ENST), Paris, France, in 1995. He was a Researcher with the Institut Eurécom from 1992 to 1995, Stanford University from 1995 to 1997, and Bell Labs (as a member of Technical Staff from 1997 to 2001 and as a Technical Manager from 2001 to 2006). He was also an Adjunct Professor with Columbia University from 2004 to 2005 and Carnegie Mellon University from 2006 to 2011. He has been the founding Executive Director of the Research, Technology and Innovation Network (RTIN), The American College of Greece (ACG), Athens, Greece, and the Head of the RTIN's Smart Wireless Future Technologies (SWIFT) Lab, since 2020. He is currently a Professor of Information Technology with the ACG's Deree College and the Alba Graduate Business School, and the Scientific Director of the American College of Greece Research Center (ACG-RC). Prior to these, he was the Dean of Athens Information Technology (AIT), Athens, where he was also the Head of the Broadband Wireless and Sensor Networks (B-WiSE) Research Group. He also holds Adjunct Professorships with Aalborg University and the University of Cyprus. He has published over 215 articles and four books and has received over 9800 citations for his work, with an H-index of 45. He has also made standards contributions and holds 12 patents. He was a member of the Steering Board of the Wireless World Research Forum (WWRF) from 2002 to 2006, a member and an Industrial Liaison of the IEEE's Signal Processing for Communications Technical Committee from 2003 to 2008, and a National Representative of Greece to the European Research Council's IDEAS program from 2007 to 2008. He has served as a member for the IEEE Communications Society's Fellow Evaluation and Awards Committees, as well as an associate editor for various journals. He has contributed to the organization of several conferences, including, as the General Chair of the IEEE CTW 2016, and the IEEE SPAWC 2018 workshops. He has acted as a Technical Coordinator in several EU projects, such as: CROWN in the area of cognitive radio; HIATUS in the area of interference alignment; and HARP in the area of remote radio heads and ADEL in the area of licensed shared access. He is also the Research Coordinator of the European Training Network project PAINLESS on the topic of energy autonomous infrastructure-less wireless networks and the Technical Coordinator of the EU CHIST-ERA project FIREMAN on the topic of predictive maintenance via machine type wireless communication systems. He is also a fellow of the European Alliance of Innovation (EAI) since 2019. He is also a member of Greece's Sectorial Scientific Council of Engineering Sciences, which supports the country's National Council for Research and Innovation. His distinctions include the Bell Labs President's Award in 2002, the IEEE Signal Processing Society's Young Author Best Paper Award in 2003, a Bell Labs Teamwork Award in 2004, his recognition as a "Highly Cited Greek Scientist" in 2011, two IEEE conference paper awards in 2013 and 2014 and the "Best Booth" Award at EUCNC in 2016. He had been shortlisted twice for the Bell Labs Prize from 2014 to 2019. He was a Distinguished Lecturer of the IEEE Communications Society for 2012–2013.

Publication IV

de Sena, A. S., Nardelli, P. H. J., da Costa, D. B., Dias, U. S., Popovski, P.,
and Papadias, C. B.

Dual-Polarized IRSs in Uplink MIMO-NOMA Networks: An Interference Mitigation Approach

Reprinted with permission from
IEEE Wireless Communications Letters
Vol. 10, no. 10, pp. 2284–2288, Jul. 2021

Dual-Polarized IRSs in Uplink MIMO-NOMA Networks: An Interference Mitigation Approach

Arthur S. de Sena, *Graduate Student Member, IEEE*, Pedro H. J. Nardelli, *Senior Member, IEEE*,
Daniel B. da Costa, *Senior Member, IEEE*, Ugo S. Dias, *Senior Member, IEEE*,
Petar Popovski, *Fellow, IEEE*, and Constantinos B. Papadias, *Fellow, IEEE*

***Abstract*—In this work, intelligent reflecting surfaces (IRSs) are optimized to manipulate signal polarization and improve the uplink performance of a dual-polarized multiple-input multiple-output (MIMO) non-orthogonal multiple access (NOMA) network. By multiplexing subsets of users in the polarization domain, we propose a strategy for reducing the interference load observed in the successive interference cancelation (SIC) process. To this end, dual-polarized IRSs are programmed to mitigate interference impinging at the base station (BS) in unsigned polarizations, in which the optimal set of reflecting coefficients are obtained via conditional gradient method. We also develop an adaptive power allocation strategy to guarantee rate fairness within each subset, in which the optimal power coefficients are obtained via a low-complexity alternate approach. Our results show that all users can reach high data rates with the proposed scheme, substantially outperforming conventional systems.**

***Index Terms*—IRS, multi-polarization, MIMO, NOMA.**

I. Introduction

Dual-polarized antenna arrays are effective for overcoming physical space limitations in multiple-input multiple-output (MIMO) systems [1]. Dual-polarized MIMO systems can also deliver improved user multiplexing and higher spectral efficiency than that achieved in single-polarized counterparts [2]. Power-domain non-orthogonal multiple access (NOMA) is another promising technique envisioned for enabling massive access in future wireless systems. In the uplink, through successive interference cancelation (SIC), NOMA enables the base station (BS) to decode the messages coming simultaneously from different users, thereby leading to latency and spectral improvements. NOMA and dual-polarized MIMO combined render even larger gains that substantially outperform conventional systems [3]. Nevertheless, the rates of strong users are always capped due to interference from the weak ones. Besides limiting the sum-rate, this behavior leads to unbalanced individual rates, which is not suitable for applications where multiple devices require a uniform performance. One can alleviate this issue by balancing the users' rates through adaptive power allocation [4]. However, since these schemes usually lead to excessive penalties for some users, the sum-rate is also impacted. Therefore, new strategies for alleviating SIC interference are necessary.

Fortunately, a dual-polarized intelligent reflecting surface (IRS) has recently emerged as a disruptive technology for optimizing the propagation environment [5]. In this work, we exploit dual-polarized IRSs to propose a novel approach for reducing the interference levels of the SIC process in the uplink. Our results show that all users can reach high data rates with the proposed scheme, substantially outperforming conventional systems.

Notation: Bold-faced lower-case letters denote vectors and upper-case denote matrices. The transpose and the Hermitian transpose of $\mathbf{A}$ are represented by $\mathbf{A}^T$ and $\mathbf{A}^H$, respectively. The symbol $\odot$ represents the Khatri-Rao product [6], $\mathbf{I}_M$ is the identity matrix of dimension $M \times M$, and $\mathbf{0}_{M,N}$ is the $M \times N$ matrix with all zero entries. The operator $\text{vec}(\cdot)$ transforms a $M \times N$ matrix into a column vector of length MN, $\text{vecd}(\cdot)$ converts the diagonal elements of an $M \times M$ square matrix into a column vector of length M, and $\text{diag}(\cdot)$ transforms a vector of length M into an $M \times M$ diagonal matrix.

II. System Model

Consider that multiple users are communicating in uplink mode with a single BS in a MIMO-NOMA network. The BS and the users employ multiple antennas organized into co-located pairs, with each pair comprising antenna elements with orthogonal polarizations, i.e., vertical and horizontal polarizations. The number of antenna pairs at the BS is denoted by $M/2$, and at the users by $N/2$, in which, due to the dual-polarized antenna structure, we assume that M and N are even and greater than 2. Moreover, the users are clustered into G groups with U users each. As mentioned, the performance of NOMA is limited by interference. To alleviate this major issue, we exploit the concepts of a dual-polarized IRS to propose a novel strategy. First, we assume that one IRS with L dual-polarized reflecting elements is installed between each group and the BS, i.e., there are G IRSs. Second, the BS subdivides each group into 2 subsets, in which vertically polarized antennas are assigned to receive the messages from the first subset, that contains U^v users, and horizontally polarized antennas are assigned to the second subset, that contains U^h users, such that $U^v + U^h = U$. Then, the IRSs are optimized to ensure that the signals coming from each subset impinge only

Manuscript received June 23, 2021; accepted July 21, 2021. Date of publication July 26, 2021; date of current version October 7, 2021. This work was supported in part by the Academy of Finland under Grant 319009, Grant 321265, Grant 328869, and Grant CHIST-ERA-17-BDSI-003/326270. The associate editor coordinating the review of this article and approving it for publication was H. Zhang. *(Corresponding author: Pedro H. J. Nardelli.)*

Arthur S. de Sena and Pedro H. J. Nardelli are with the Department of Electrical Engineering, Lappeenranta–Lahti University of Technology, 53850 Lappeenranta, Finland (e-mail: arthur.sena@lut.fi; pedro.nardelli@lut.fi).

Daniel B. da Costa is with the Future Technology Research Center, National Yunlin University of Science and Technology, Douliou 64002, Taiwan, and also with the Department of Computer Engineering, Federal University of Ceará, Sobral 62010-560, Brazil (e-mail: danielbcosta@ieee.org).

Ugo S. Dias is with the Department of Electrical Engineering, University of Brasília, Brasília 70910-900, Brazil (e-mail: ugodias@ieee.org).

Petar Popovski is with the Department of Electronic Systems, Aalborg University, 9220 Aalborg, Denmark (e-mail: petarp@es.aau.dk).

Constantinos B. Papadias is with the Research, Technology and Innovation Network, ALBA, The American College of Greece, 153 42 Athens, Greece (e-mail: cpapadias@acg.edu).

Digital Object Identifier 10.1109/LWC.2021.3099867

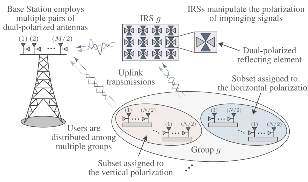

Fig. 1. System model. Each dual-polarized IRS mitigates polarization interference from one group of users.

at antennas corresponding to the assigned polarization. This scheme is illustrated in Fig. 1.

The phases and amplitude of reflection induced by the dual-polarized IRS for the *g*th group can be organized in the following block diagonal matrix [5]

$$\boldsymbol{\Theta}_g = \begin{bmatrix} \boldsymbol{\Phi}_g^{vv} & \boldsymbol{\Phi}_g^{hv} \\ \boldsymbol{\Phi}_g^{vh} & \boldsymbol{\Phi}_g^{hh} \end{bmatrix} \in \mathbb{C}^{2L\times 2L}, \tag{1}$$

where $\boldsymbol{\Phi}_g^{pq} = \mathrm{diag}\{[\alpha_{g,1}^{pq} e^{-j\phi_{g,1}^{pq}}, \dots, \alpha_{g,L}^{pq} e^{-j\phi_{g,L}^{pq}}]\} \in \mathbb{C}^{L\times L}$, with $\phi_{g,l}^{pq}$ and $\alpha_{g,l}^{pq}$ representing, respectively, the phase and amplitude of reflection induced by the *l*th IRS element[1] from polarization *p* to polarization *q*, with $p, q \in \{v, h\}$ (v stands for vertical and h for horizontal). Given the matrix in (1), we can represent the full channel matrix obtained at the BS by

$$\begin{aligned}\mathbf{H}_{gu} = &\begin{bmatrix} \mathbf{F}_g^{vv} & \mathbf{0}_{L,\frac{M}{2}} \\ \mathbf{0}_{L,\frac{M}{2}} & \mathbf{F}_g^{hh} \end{bmatrix}^H \begin{bmatrix} \boldsymbol{\Phi}_g^{vv} & \boldsymbol{\Phi}_g^{hv} \\ \boldsymbol{\Phi}_g^{vh} & \boldsymbol{\Phi}_g^{hh} \end{bmatrix} \begin{bmatrix} \mathbf{G}_{gu}^{vv} & \sqrt{\chi^{\text{U-IRS}}}\mathbf{G}_{gu}^{hv} \\ \sqrt{\chi^{\text{U-IRS}}}\mathbf{G}_{gu}^{vh} & \mathbf{G}_{gu}^{hh} \end{bmatrix} \\ &+ \begin{bmatrix} \mathbf{D}_{gu}^{vv} & \sqrt{\chi^{\text{U-BS}}}\mathbf{D}_{gu}^{hv} \\ \sqrt{\chi^{\text{U-BS}}}\mathbf{D}_{gu}^{vh} & \mathbf{D}_{gu}^{hh} \end{bmatrix} \in \mathbb{C}^{M\times N}, \end{aligned} \tag{2}$$

where $\mathbf{D}_{gu}^{pq} = \sqrt{\zeta_{gu}^{\text{U-BS}}}\tilde{\mathbf{D}}_{gu}^{pq} \in \mathbb{C}^{\frac{M}{2}\times\frac{N}{2}}$, $\mathbf{G}_{gu}^{pq} = \sqrt{\frac{\zeta_{gu}^{\text{U-IRS}}}{2}}\tilde{\mathbf{G}}_{gu}^{pq} \in \mathbb{C}^{L\times\frac{N}{2}}$, and $\mathbf{F}_g^{pq} = \sqrt{\zeta_{gu}^{\text{IRS-BS}}}\tilde{\mathbf{F}}_g^{pq} \in \mathbb{C}^{L\times\frac{M}{2}}$, with $\tilde{\mathbf{D}}_g^{pq}$, $\tilde{\mathbf{G}}_g^{pq}$ and $\tilde{\mathbf{F}}_g^{pq}$ modeling, respectively, the fast-fading channels between the *u*th user and the BS (link U-BS), the *u*th user and the *g*th IRS (link U-IRS), and the *g*th IRS and the BS (link IRS-BS), from the polarization *p* to the polarization *q*, in which the entries of $\tilde{\mathbf{D}}_g^{pq}$, $\tilde{\mathbf{G}}_g^{pq}$ and $\tilde{\mathbf{F}}_g^{pq}$ follow the complex Gaussian distribution with zero mean and unity variance. Moreover, $\zeta_{gu}^{\text{U-BS}}$, $\zeta_{gu}^{\text{U-IRS}}$, and $\zeta_{gu}^{\text{IRS-BS}}$ represent, respectively, the large-scale fading coefficients for the links U-BS, U-IRS, and IRS-BS, the normalization factor $\frac{1}{\sqrt{2}}$ ensures a passive beam splitting at the IRS, and $\chi^{\text{U-IRS}}$, and $\chi^{\text{U-BS}} \in [0, 1]$ denote the inverse of the cross-polar discrimination parameter (iXPD) that measures the power leakage between polarizations. Note that, for mathematical convenience, depolarization phenomena are not considered in the link IRS-BS. Further details for the channel modeling of dual-polarized IRSs can be found in [5].

Given the channel model in (2), the signal received at BS coming from all user groups can be expressed by

$$\mathbf{y} = \sum_{m=1}^{G}\sum_{n=1}^{U} \mathbf{H}_{mn}\mathbf{x}_{mn} + \mathbf{n} \in \mathbb{C}^M, \tag{3}$$

where $\mathbf{x}_{mn} = \mathbf{p}_{mn}\sqrt{P\beta_{mn}}x_{mn} \in \mathbb{C}^N$, in which $\mathbf{p}_{mn}$ is a precoding vector to be explained later, *P* is the transmit power budget, $\beta_{mn} \in [0, 1]$ is the power allocation coefficient, x_{mn} represents the transmitted data symbol, and $\mathbf{n} = [(\mathbf{n}^v)^T, (\mathbf{n}^h)^T]^T \in \mathbb{C}^M$ is the noise vector observed at the BS, whose entries follow the complex Gaussian distribution with zero mean and variance σ_n.

III. IRS Optimization, Precoding, and Reception

A. IRS Optimization

In this section, we focus on the optimization of the IRSs. Firstly, let us represent each subset by the index set $\mathcal{G}_g^p = \{1, 2, \dots, U^p\}$, in which $p \in \{v, h\}$, and let:

$$\mathbf{G}_{gu}^v = \left[\mathbf{G}_{gu}^{vv}\sqrt{\chi^{\text{U-IRS}}}\mathbf{G}_{gu}^{hv}\right], \mathbf{G}_{gu}^h = \left[\sqrt{\chi^{\text{U-IRS}}}\mathbf{G}_{gu}^{vh}\mathbf{G}_{gu}^{hh}\right]$$

$$\mathbf{D}_{gu}^v = \left[\mathbf{D}_{gu}^{vv}\sqrt{\chi^{\text{U-IRS}}}\mathbf{D}_{gu}^{hv}\right], \mathbf{D}_{gu}^h = \left[\sqrt{\chi^{\text{U-IRS}}}\mathbf{D}_{gu}^{vh}\mathbf{D}_{gu}^{hh}\right].$$

Then, we can expand the signal model in (3) as follows

$$\begin{aligned}\mathbf{y} = \sum_{m=1}^{G}\Bigg[&\sum_{n=1}^{U}\left(\begin{bmatrix}(\mathbf{F}_m^{vv})^H\boldsymbol{\Phi}_m^{vv}\mathbf{G}_{mn}^v \\ (\mathbf{F}_m^{hh})^H\boldsymbol{\Phi}_m^{vh}\mathbf{G}_{mn}^v\end{bmatrix} + \begin{bmatrix}(\mathbf{F}_m^{vv})^H\boldsymbol{\Phi}_m^{hv}\mathbf{G}_{mn}^h \\ (\mathbf{F}_m^{hh})^H\boldsymbol{\Phi}_m^{hh}\mathbf{G}_{mn}^h\end{bmatrix}\right)\mathbf{x}_{mn} \\ &+ \sum_{s\in\mathcal{G}_m^v}\begin{bmatrix}\mathbf{D}_{ms}^v \\ \mathbf{D}_{ms}^h\end{bmatrix}\mathbf{x}_{ms} + \sum_{t\in\mathcal{G}_m^h}\begin{bmatrix}\mathbf{D}_{mt}^v \\ \mathbf{D}_{mt}^h\end{bmatrix}\mathbf{x}_{mt}\Bigg] + \mathbf{n}. \end{aligned} \tag{4}$$

Following the proposed strategy, the messages transmitted from users in subset $\mathcal{G}_g^v$ should arrive at the BS only through the channels modeled by the upper blocks of the matrices in (4), while the messages from $\mathcal{G}_g^h$ should arrive only through the lower blocks, in both reflected, U-IRS-BS, and direct, U-BS, links. To this end, the IRS associated with the *g*th group must mitigate all transmissions from subset $\mathcal{G}_g^v$ that impinges the BS with horizontal polarization, and all transmissions from $\mathcal{G}_g^h$ that impinges the BS with vertical polarization.

Therefore, we can formulate the optimization problem as in (5), shown at the bottom of the page. Due to the complicated matricial objective function, and the diagonal matrices constraint, solving problem (5) in its original form is challenging. Therefore, we recall the Khatri-Rao property $(\mathbf{C}^T \odot \mathbf{A})\mathrm{vecd}(\mathbf{B}) = \mathrm{vec}(\mathbf{ABC})$ [6] to transform (5) into a simpler equivalent problem. More specifically, we define:

$$\theta_g^{pq} = \mathrm{vecd}(\boldsymbol{\Phi}_g^{pq}), \mathbf{z}_g^v = \sum_{t\in\mathcal{G}_g^h}\mathbf{D}_{gt}^v\mathbf{x}_{gt}, \mathbf{z}_g^h = \sum_{s\in\mathcal{G}_g^v}\mathbf{D}_{gs}^h\mathbf{x}_{gs},$$

$$\mathbf{W}_g^{vv} = \left[\sum_{n=1}^{U}\mathbf{G}_{gn}^v\mathbf{x}_{gn}\right]^T \odot (\mathbf{F}_g^{vv})^H, \tilde{\mathbf{W}}_g^{vv} = \left[\sum_{n=1}^{U}\mathbf{G}_{gn}^h\mathbf{x}_{gn}\right]^T \odot (\mathbf{F}_g^{vv})^H,$$

$$\mathbf{W}_g^{hh} = [\sum_{n=1}^{U}\mathbf{G}_{gn}^h\mathbf{x}_{gn}]^T \odot (\mathbf{F}_g^{hh})^H, \tilde{\mathbf{W}}_g^{hh} = [\sum_{n=1}^{U}\mathbf{G}_{gn}^v\mathbf{x}_{gn}]^T \odot (\mathbf{F}_g^{hh})^H.$$

Then, (5) is transformed into the following sub-problems

$$\underset{\boldsymbol{\theta}_g^{vv}, \boldsymbol{\theta}_g^{hv}}{\arg\min} \left\| \left[\mathbf{W}_g^{vv}\ \tilde{\mathbf{W}}_g^{vv}\right]\begin{bmatrix}\boldsymbol{\theta}_g^{vv} \\ \boldsymbol{\theta}_g^{hv}\end{bmatrix} + \mathbf{z}_g^v \right\|^2 \tag{6a}$$

$$\text{s.t.} \quad \left\|\begin{bmatrix}\boldsymbol{\theta}_g^{vv} \\ \boldsymbol{\theta}_g^{hv}\end{bmatrix}\right\|_\infty \leq 1, \tag{6b}$$

$$\underset{\boldsymbol{\theta}_g^{vh}, \boldsymbol{\theta}_g^{hh}}{\arg\min} \left\| \left[\tilde{\mathbf{W}}_g^{hh}\ \mathbf{W}_g^{hh}\right]\begin{bmatrix}\boldsymbol{\theta}_g^{vh} \\ \boldsymbol{\theta}_g^{hh}\end{bmatrix} + \mathbf{z}_g^h \right\|^2 \tag{7a}$$

$$\text{s.t.} \quad \left\|\begin{bmatrix}\boldsymbol{\theta}_g^{vh} \\ \boldsymbol{\theta}_g^{hh}\end{bmatrix}\right\|_\infty \leq 1. \tag{7b}$$

---

[1] Discrete reflection coefficients shall be considered in future works.

The objective functions of the problems above are of the form $f(\boldsymbol{\theta}) = \|\mathbf{W}\boldsymbol{\theta} + \mathbf{z}\|^2$, which has gradient $\nabla f(\boldsymbol{\theta}) = 2\mathbf{W}^H(\mathbf{W}\boldsymbol{\theta} + \mathbf{z})$, and Hessian given by $2\mathbf{W}^H\mathbf{W}$. Consequently, since the Hessian matrix of $f(\boldsymbol{\theta})$ is positive semidefinite, the functions in (6a) and (7a) are convex. Moreover, the ℓ_∞ norm constraints in (6b) and (7b) define convex compact subsets in the Hilbert space. As a result, problems (6) and (7) can be solved via the Conditional Gradient method [7], which is implemented in Algorithm 1. The algorithm converges to the optimal solutions at a rate of $\mathcal{O}(\frac{1}{k})$, with k representing its iterations. Furthermore, since the optimization happens over the ℓ_∞ space, each iteration has linear time complexity [8].

In this letter, the BS is responsible for executing Algorithm 1 and sending the optimized reflecting coefficients to the IRSs (e.g., through a backhaul link). To this end, we assume perfect knowledge of the global channel state information (CSI).

B. Precoding for Intra-Group Channel Alignment

We build $\mathbf{p}_{gu}$ to align the channels of users within each subset. Specifically, we design $\mathbf{p}_{gu}$ to align only the channels corresponding to the assigned polarization of the link U-BS. For notation simplicity, let $\tilde{\mathbf{D}}^v_{gu} = (\sqrt{\zeta^{\text{U-BS}}_{gu}})^{-1}\mathbf{D}^v_{gu}$ and $\tilde{\mathbf{D}}^h_{gu} = (\sqrt{\zeta^{\text{U-BS}}_{gu}})^{-1}\mathbf{D}^h_{gu}$ be the block matrices corresponding to the fast-fading arriving at the BS antennas with vertical and horizontal polarizations, respectively. Then, for users in subset $\mathcal{G}^p_g$, with $p \in \{v, h\}$, the following must be achieved

$$\tilde{\mathbf{D}}^p_{g1}\mathbf{p}_{g1} = \tilde{\mathbf{D}}^p_{g2}\mathbf{p}_{g2} = \cdots = \tilde{\mathbf{D}}^p_{gU^p}\mathbf{p}_{gU^p}. \tag{8}$$

This goal can be obtained by solving the following problem

$$\begin{bmatrix} \mathbf{I}_{\frac{M}{2}} & -\tilde{\mathbf{D}}^p_{g1} & \mathbf{0}_{\frac{M}{2},N} & \cdots & \mathbf{0}_{\frac{M}{2},N} \\ \mathbf{I}_{\frac{M}{2}} & \mathbf{0}_{\frac{M}{2},N} & -\tilde{\mathbf{D}}^p_{g2} & \cdots & \mathbf{0}_{\frac{M}{2},N} \\ \vdots & \vdots & \vdots & \ddots & \vdots \\ \mathbf{I}_{\frac{M}{2}} & \mathbf{0}_{\frac{M}{2},N} & \mathbf{0}_{\frac{M}{2},N} & \cdots & -\tilde{\mathbf{D}}^p_{gU^p} \end{bmatrix} \begin{bmatrix} \bar{\mathbf{d}}^p_g \\ \mathbf{p}_{g1} \\ \vdots \\ \mathbf{p}_{gU^p} \end{bmatrix} = \mathbf{0}_{(U^p\frac{M}{2}),1}, \tag{9}$$

where $\bar{\mathbf{d}}^p_g \in \mathbb{C}^{\frac{M}{2}}$ is the aligned channel vector obtained by the BS at polarization p from users in subset $\mathcal{G}^p_g$, i.e., $\bar{\mathbf{d}}^p_g = \tilde{\mathbf{D}}^p_{gu}\mathbf{p}_{gu}, \forall u \in \mathcal{G}^p_g$. Moreover, note that since the matrix in the leftmost side of (9) has dimension $(\frac{M}{2}U^p) \times (\frac{M}{2} + NU^p)$, the constraint $2NU^p > M(U^p - 1)$ must be obeyed.

C. Inter-Group Interference Cancelation

Since the channels of users assigned to the same polarization have been aligned, now we can compute the reception vector intended to remove inter-group interference. The desired vector for the receive polarization $p \in \{v, h\}$ can be derived as

$$\mathbf{q}^p_g = \text{null}\left\{\left[\bar{\mathbf{d}}^p_1, \ldots, \bar{\mathbf{d}}^p_{(g-1)}, \bar{\mathbf{d}}^p_{(g+1)}, \ldots, \bar{\mathbf{d}}^p_G\right]^H\right\} \in \mathbb{C}^{\frac{M}{2}}, \tag{10}$$

where, to ensure the existence of a nontrivial null space, $M > 2(G - 1)$ must be satisfied.

D. Signal Reception

After filtering the signals received in both polarizations through the vector in (10), all inter-group interference vanishes. Therefore, from (4), the superimposed symbol from the gth group detected by the BS can be written as

$$\begin{aligned} \hat{\mathbf{x}}_g = & \begin{bmatrix} (\mathbf{q}^v_g)^H \bar{\mathbf{d}}^v_g \sum_{s \in \mathcal{G}^v_g} \sqrt{\zeta^{\text{U-BS}}_{gs} P \beta_{gs}} x_{gs} \\ \left(\mathbf{q}^h_g\right)^H \bar{\mathbf{d}}^h_g \sum_{t \in \mathcal{G}^h_g} \sqrt{\zeta^{\text{U-BS}}_{gt} P \beta_{gt}} x_{gt} \end{bmatrix} + \begin{bmatrix} I^v_g \\ I^h_g \end{bmatrix} \\ & + \begin{bmatrix} (\mathbf{q}^v_g)^H \mathbf{n}^v \\ (\mathbf{q}^h_g)^H \mathbf{n}^h \end{bmatrix} \in \mathbb{C}^2, \end{aligned} \tag{11}$$

where I^p_g is the polarization interference left by the gth IRS, which is defined by

$$\begin{aligned} \begin{bmatrix} I^v_g \\ I^h_g \end{bmatrix} = & \sum_{n=1}^{U} \begin{bmatrix} (\mathbf{q}^v_g)^H (\mathbf{F}^{vv}_g)^H \boldsymbol{\Phi}^{vv}_g \mathbf{G}^v_{gn} \mathbf{x}_{gn} \\ \left(\mathbf{q}^h_g\right)^H \left(\mathbf{F}^{hh}_g\right)^H \boldsymbol{\Phi}^{vh}_g \mathbf{G}^v_{gn} \mathbf{x}_{gn} \end{bmatrix} \\ & + \sum_{n=1}^{U} \begin{bmatrix} (\mathbf{q}^v_g)^H (\mathbf{F}^{vv}_g)^H \boldsymbol{\Phi}^{hv}_g \mathbf{G}^h_{gn} \mathbf{x}_{gn} \\ \left(\mathbf{q}^h_g\right)^H \left(\mathbf{F}^{hh}_g\right)^H \boldsymbol{\Phi}^{hh}_g \mathbf{G}^h_{gn} \mathbf{x}_{gn} \end{bmatrix} \\ & + \begin{bmatrix} (\mathbf{q}^v_g)^H \sum_{t \in \mathcal{G}^h_g} \mathbf{D}^v_{gt} \mathbf{x}_{gt} \\ \left(\mathbf{q}^h_g\right)^H \sum_{s \in \mathcal{G}^v_g} \mathbf{D}^h_{gs} \mathbf{x}_{gs} \end{bmatrix}. \end{aligned} \tag{12}$$

As one can observe, after filtering the received signals through the detection vectors, the BS retrieves two superimposed symbols, i.e., one symbol from each polarization. Observe that, if the IRSs completely eliminate the signals in unassigned polarizations, the interference term in (12) will vanish. Next, the BS employs SIC to recover the messages of users assigned to their corresponding polarization.

IV. SINR ANALYSIS

Since both inter-group and inter-subset interference have been addressed, now the BS can securely apply SIC to each polarization separately. For this, the BS first sorts users from each subset in a descending order based on their large scale fading coefficient observed in the link U-BS, such that $\zeta^{\text{U-BS}}_{g1} > \zeta^{\text{U-BS}}_{g2} > \cdots > \zeta^{\text{U-BS}}_{gU^p}$. Then, the SIC decoding process is carried out following this order, i.e., the symbol from the uth user received in polarization p is decoded by treating

$$\underset{\substack{\boldsymbol{\Phi}^{vv}_g, \boldsymbol{\Phi}^{vh}_g, \\ \boldsymbol{\Phi}^{hv}_g, \boldsymbol{\Phi}^{hh}_g}}{\arg\min} \left\| \begin{bmatrix} (\mathbf{F}^{vv}_g)^H \boldsymbol{\Phi}^{vv}_g \sum_{n=1}^{U} \mathbf{G}^v_{gn} \mathbf{x}_{gn} \\ \left(\mathbf{F}^{hh}_g\right)^H \boldsymbol{\Phi}^{vh}_g \sum_{n=1}^{U} \mathbf{G}^v_{gn} \mathbf{x}_{gn} \end{bmatrix} + \begin{bmatrix} (\mathbf{F}^{vv}_g)^H \boldsymbol{\Phi}^{hv}_g \sum_{n=1}^{U} \mathbf{G}^h_{gn} \mathbf{x}_{gn} \\ \left(\mathbf{F}^{hh}_g\right)^H \boldsymbol{\Phi}^{hh}_g \sum_{n=1}^{U} \mathbf{G}^h_{gn} \mathbf{x}_{gn} \end{bmatrix} + \begin{bmatrix} \sum_{t \in \mathcal{G}^h_g} \mathbf{D}^v_{gt} \mathbf{x}_{gt} \\ \sum_{s \in \mathcal{G}^v_g} \mathbf{D}^h_{gs} \mathbf{x}_{gs} \end{bmatrix} \right\|^2 \tag{5a}$$

$$\text{s.t.} \quad \left|\omega^{pq}_{g,l}\right|^2 \leq 1, \forall l \in [1, L], \forall p, q \in \{v, h\} \tag{5b}$$

$$\boldsymbol{\Phi}^{vv}_g, \boldsymbol{\Phi}^{vh}_g, \boldsymbol{\Phi}^{hv}_g, \boldsymbol{\Phi}^{hh}_g \text{ diagonal} \tag{5c}$$

Algorithm 1: Algorithm for Optimizing the Dual Polarized IRSs Based on the Conditional Gradient Method

```
Input: $K, \mathbf{z}_g^v, \mathbf{z}_g^h, [\mathbf{W}_g^{vv}\ \tilde{\mathbf{W}}_g^{vv}], [\tilde{\mathbf{W}}_g^{hh}\ \mathbf{W}_g^{hh}]$.
Output: $\mathbf{\Phi}_g^{vv}, \mathbf{\Phi}_g^{hv}, \mathbf{\Phi}_g^{vh}, \mathbf{\Phi}_g^{hh}$.
Initialize $c = 1, \boldsymbol{\theta}_g^{(1)} = \mathbf{0}_{2L,1}, \tilde{\boldsymbol{\theta}}_g^{(1)} = \mathbf{0}_{2L,1}$;
for $k = 1$ to $K - 1$ do
    Compute the gradients of (6a) and (7a):
      $\nabla f(\boldsymbol{\theta}_g^{(k)}) = 2[\mathbf{W}_g^{vv}\ \tilde{\mathbf{W}}_g^{vv}]^H([\mathbf{W}_g^{vv}\ \tilde{\mathbf{W}}_g^{vv}]\boldsymbol{\theta}_g^{(k)} + \mathbf{z}_g^v)$,
      $\nabla f(\tilde{\boldsymbol{\theta}}_g^{(k)}) = 2[\tilde{\mathbf{W}}_g^{hh}\ \mathbf{W}_g^{hh}]^H([\tilde{\mathbf{W}}_g^{hh}\ \mathbf{W}_g^{hh}]\tilde{\boldsymbol{\theta}}_g^{(k)} + \mathbf{z}_g^h)$;
    Construct the direction-finding vectors $\mathbf{s}^{(k)}$ and $\tilde{\mathbf{s}}^{(k)}$ by
      computing: $[\mathbf{s}^{(k)}]_i = -c \cdot \nabla f(\boldsymbol{\theta}_g^{(k)})$, and
      $[\tilde{\mathbf{s}}^{(k)}]_i = -c \cdot \nabla f(\tilde{\boldsymbol{\theta}}_g^{(k)})$;
    Compute the step size: $\nu^{(k)} = \frac{2}{2+k}$;
    Update the vectors of reflecting coefficients:
      $\boldsymbol{\theta}_g^{(k+1)} = (1 - \nu^{(k)})\boldsymbol{\theta}_g^{(k)} + \nu^{(k)}\mathbf{s}^{(k)}$,
      $\tilde{\boldsymbol{\theta}}_g^{(k+1)} = (1 - \nu^{(k)})\tilde{\boldsymbol{\theta}}_g^{(k)} + \nu^{(k)}\tilde{\mathbf{s}}^{(k)}$;
end
Obtain the final set of coefficients: $\mathbf{\Phi}_g^{vv} = \mathrm{diag}\left(\left[\boldsymbol{\theta}_g^{(K)}\right]_{1:L}\right)$,
  $\mathbf{\Phi}_g^{vh} = \mathrm{diag}\left(\left[\tilde{\boldsymbol{\theta}}_g^{(K)}\right]_{1:L}\right)$, $\mathbf{\Phi}_g^{hv} = \mathrm{diag}\left(\left[\boldsymbol{\theta}_g^{(K)}\right]_{(L+1):2L}\right)$,
  $\mathbf{\Phi}_g^{hh} = \mathrm{diag}\left(\left[\tilde{\boldsymbol{\theta}}_g^{(K)}\right]_{(L+1):2L}\right)$.
```

the messages from the $U^p - u$ weaker users as interference. More specifically, the recovered symbol that was transmitted from the *u*th user in subset $\mathcal{G}_g^p$, can be written as

$$\hat{x}_{gu}^p = \underbrace{(\mathbf{q}_g^p)^H \bar{\mathbf{d}}_g^p \sqrt{\zeta_{gu}^{\text{U-BS}} P \beta_{gu}} x_{gu}}_{\text{Desired symbol}} + \underbrace{(\mathbf{q}_g^p)^H \bar{\mathbf{d}}_g^p \sum_{n=u+1}^{U^p} \sqrt{\zeta_{gn}^{\text{U-BS}} P \beta_{gn}} x_{gn}}_{\text{Interference from weaker users}} + \underbrace{I_g^p}_{\text{Polarization interference}} + \underbrace{(\mathbf{q}_g^p)^H \mathbf{n}^p}_{\text{Noise}}. \quad (13)$$

By knowing that $|(\mathbf{q}_g^p)^H \mathbf{n}^p|^2 = (\mathbf{q}_g^p)^H \mathbf{n}^p (\mathbf{n}^p)^H \mathbf{q}_g^p = \sigma_n^2$, and defining $\rho = \frac{P}{\sigma_n^2}$, the SINR for the *u*th in $\mathcal{G}_g^p$ is given by

$$\gamma_{gu}^p = \frac{\left|(\mathbf{q}_g^p)^H \bar{\mathbf{d}}_g^p\right|^2 \zeta_{gu}^{\text{U-BS}} \beta_{gu}}{\left|(\mathbf{q}_g^p)^H \bar{\mathbf{d}}_g^p\right|^2 \sum_{n=u+1}^{U^p} \zeta_{gn}^{\text{U-BS}} \beta_{gn} + \left|I_g^p\right|^2 / P + 1/\rho}. \quad (14)$$

V. POWER ALLOCATION FOR RATE FAIRNESS

In this section, we develop an adaptive power allocation policy for balancing the data rates of users within each subset. Our aim is to show that the proposed dual-polarized IRS-MIMO-NOMA scheme can achieve a high throughput even when fair power allocation is employed.

Since in practical systems only small groups of users are served with NOMA, we assume that each subset is formed by only two users, i.e., there is a total of 4 users per group. Moreover, we consider that the polarization interference term in (13) is negligible so that $I_g^p \approx 0$. As a result, the data rate observed when decoding the symbol of the first user from the *g*th subset assigned to polarization *p* can be written as

$$R_{g1}^p = \log_2\left(1 + \frac{\left|(\mathbf{q}_g^p)^H \bar{\mathbf{d}}_g^p\right|^2 \zeta_{g1}^{\text{U-BS}} \rho \beta_{g1}}{\left|(\mathbf{q}_g^p)^H \bar{\mathbf{d}}_g^p\right|^2 \zeta_{g2}^{\text{U-BS}} \rho \beta_{g2} + 1}\right), \quad (15)$$

and for the second user as

$$R_{g2}^p = \log_2\left(1 + \left|(\mathbf{q}_g^p)^H \bar{\mathbf{d}}_g^p\right|^2 \zeta_{g2}^{\text{U-BS}} \rho \beta_{g2}\right). \quad (16)$$

Then, our goal can be accomplished by solving the following optimization problem:

$$\begin{aligned} \underset{\beta_{g1}, \beta_{g2}}{\arg\max} \quad & R_{g1}^p && (17a) \\ \text{s.t.} \quad & R_{g2}^p \geq R_{g1}^p, && (17b) \\ & 0 \leq \beta_{g1} \leq 1, && (17c) \\ & 0 \leq \beta_{g2} \leq 1, && (17d) \end{aligned}$$

where the objective function in (17a) aims at the maximization of the rate of the strong user, while the constraint (17b) ensures that the rate of the weak user does not drop below that achieved for the strong one, i.e., it guarantees fairness. Moreover, constraints (17c) and (17d) define the feasible set for the power allocation coefficients β_{g1} and β_{g2}.

Since the objective function in (17a) is an increasing function of β_{g1}, if we consider a fixed β_{g2}, (17) will be maximized when β_{g1} reaches the maximum value in the feasible set. Also, since $\log_2(\cdot)$ is a monotonic increasing function of its argument, the constraint (17b) can be equivalently represented by $|(\mathbf{q}_g^p)^H \bar{\mathbf{d}}_g^p|^2 \zeta_{g2}^{\text{U-BS}} \rho \beta_{g2} \geq \frac{|(\mathbf{q}_g^p)^H \bar{\mathbf{d}}_g^p|^2 \zeta_{g1}^{\text{U-BS}} \rho \beta_{g1}}{|(\mathbf{q}_g^p)^H \bar{\mathbf{d}}_g^p|^2 \zeta_{g2}^{\text{U-BS}} \rho \beta_{g2} + 1}$. With these observations, first, we consider β_{g1} to be a constant and optimize (17) in terms of only β_{g2}. More specifically, after simplifying (17b), we can write

$$\begin{aligned} \underset{\beta_{g2}}{\arg\max} \quad & \log_2\left(1 + \frac{\left|(\mathbf{q}_g^p)^H \bar{\mathbf{d}}_g^p\right|^2 \zeta_{g1}^{\text{U-BS}} \rho \beta_{g1}}{\left|(\mathbf{q}_g^p)^H \bar{\mathbf{d}}_g^p\right|^2 \zeta_{g2}^{\text{U-BS}} \rho \beta_{g2} + 1}\right) && (18a) \\ \text{s.t.} \quad & \left(\left|(\mathbf{q}_g^p)^H \bar{\mathbf{d}}_g^p\right|^2 \zeta_{g2}^{\text{U-BS}} \rho\right)^2 \beta_{g2}^2 + \left(\left|(\mathbf{q}_g^p)^H \bar{\mathbf{d}}_g^p\right|^2 \zeta_{g2}^{\text{U-BS}} \rho\right) \beta_{g2} \\ & - \left(\left|(\mathbf{q}_g^p)^H \bar{\mathbf{d}}_g^p\right|^2 \zeta_{g1}^{\text{U-BS}} \rho\right) \beta_{g1} \geq 0, && (18b) \\ & 0 \leq \beta_{g2} \leq 1. && (18c) \end{aligned}$$

One can verify that the second derivative of the objective function in (18a) is positive $\forall \beta_{g2} > 0$, which means convexity. Moreover, (18a) is a decreasing function of β_{g2}, which tells us that, if the constraint (18b) is relaxed, the global maximum within the feasible set is reached when $\beta_{g2} \to 0$. Also, note that (18b) is a concave upward quadratic function that increases with β_{g2}. Therefore, the solution for (18) can be obtained by computing the minimum possible value for β_{g2}, which clearly can be accomplished through the roots of (18b). However, for computing the desired roots, we need first to determine the value of β_{g1} in a way that β_{g2} can satisfy (18c).

$$\Delta_{g2} = \left(-\left|(\mathbf{q}_g^p)^H \bar{\mathbf{d}}_g^p\right|^2 \zeta_{g2}^{\text{U-BS}} \rho + \sqrt{\left(\left|(\mathbf{q}_g^p)^H \bar{\mathbf{d}}_g^p\right|^2 \zeta_{g2}^{\text{U-BS}} \rho\right)^2 + 4\left(\left|(\mathbf{q}_g^p)^H \bar{\mathbf{d}}_g^p\right|^2 \zeta_{g2}^{\text{U-BS}} \rho\right)^2 \left|(\mathbf{q}_g^p)^H \bar{\mathbf{d}}_g^p\right|^2 \zeta_{g1}^{\text{U-BS}} \rho \beta_{g1}}\right) \left(2\left(\left|(\mathbf{q}_g^p)^H \bar{\mathbf{d}}_g^p\right|^2 \zeta_{g2}^{\text{U-BS}} \rho\right)^2\right)^{-1} \quad (19)$$

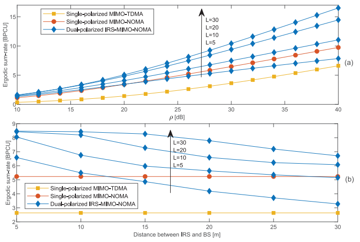

Fig. 2. Ergodic sum-rates with fixed power allocation when the IRS is located at $\bar{d} = 15$ m from the BS (a), and when ρ is fixed to 26 dB (b).

By noticing that (18b) is a decreasing function of β_{g1}, we optimize both coefficients with a simple alternate approach: first, aiming the maximization of R_{g1}^{p}, we initialize β_{g1} with 1. Then, we calculate the positive root of (18b) as in (19), shown at the bottom of the page, and test if $\Delta_{g2} \leq 1$. If this is satisfied, then $\beta_{g2}^{*} = \Delta_{g2}$, and $\beta_{g1}^{*} = 1$. Otherwise, $\beta_{g2}^{*} = 1$, and β_{g1}^{*} is computed with (19) by setting $\Delta_{g2} = 1$.

VI. SIMULATION RESULTS AND DISCUSSIONS

In this section, we evaluate the performance of the proposed IRS-MIMO-NOMA system. The conventional single-polarized MIMO-NOMA and MIMO with time division multiple access (TDMA) are used as baseline schemes. We consider a scenario with $G = 2$ groups of $U = 4$ users, in which, in both dual-polarized and single-polarized systems, the BS and the users employ $M = N = 4$ antennas. Given that the signal alignment approach from Section III successfully eliminates all inter-group interference, without loss of generality, we focus on the first group, and we assume that users 1, 2, 3, and 4 are located, respectively, at $d_1 = 20$ m, $d_2 = 40$ m, $d_3 = 80$ m, and $d_4 = 120$ m from the BS. Users 1 and 2 are assigned to the vertical polarization, and users 3 and 4 to the horizontal polarization. For simplicity, we assume that the distances between the users and the connected IRS are the same as that from the users to the BS. On the other hand, the distance between the IRS and the BS, denoted by $\bar{d}$, varies throughout the simulation examples. As a result, the large scale fading coefficients for the links U-BS and U-IRS are obtained by $\zeta_u^{\text{U-BS}} = \zeta_u^{\text{U-IRS}} = \delta d_u^{-\eta}$, and for the link IRS-BS by $\zeta_u^{\text{IRS-BS}} = \bar{d}^{-\eta}$, where δ is a gain set to 30 dB, and η is the path-loss exponent set to 2. Moreover, we set $\chi^{\text{U-BS}} = \chi^{\text{U-IRS}} = 0.5$, $P = 1$, and, in results with fixed power allocation, we assume that all users transmit using their total power, i.e., $\beta_1 = \beta_2 = \beta_3 = \beta_4 = 1$.

Fig. 2(a) compares the ergodic sum-rates of conventional MIMO-NOMA and MIMO-TDMA systems with those obtained with the dual-polarized IRS-MIMO-NOMA scheme for different numbers of reflecting elements when the IRS is deployed at 15 m from the BS. We can see that impressive gains can be achieved over the baseline schemes when the IRS becomes large enough. Fig. 2(b) shows the impact of the distance between the IRS and the BS on the system sum-rate for $\rho = 26$ dB. As can be noticed, the sum-rate of the IRS-MIMO-NOMA system decreases with the increase of the distance. Such behavior is explained by the fact that the IRS's ability to cancel polarization interference worsens when the distance increases. Despite that, for $L = 20$ and $L = 30$, the proposed scheme is able to outperform the conventional systems even when $\bar{d} = 30$ m.

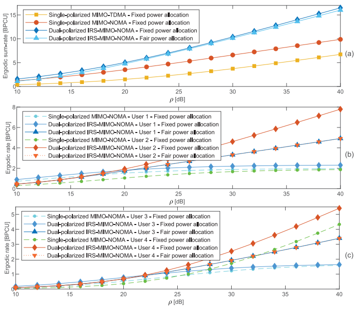

Fig. 3. Ergodic sum-rates (a) and rates (b)–(c) with fixed and fair power allocation for $L = 30$ and $\bar{d} = 10$ m.

Fig. 3(a) shows how the fair power allocation policy performs in terms of sum-rate. As one can see, because the fair policy decreases the data rates of some users to improve the rates of others, the fair IRS-MIMO-NOMA scheme experiences a sum-rate slightly inferior to the achieved with the fixed policy. Nevertheless, the fair scheme can still outperform all the baseline systems. For instance, the proposed scheme under fair power allocation surpasses 16 bits per channel use (BPCU) when $\rho = 40$ dB, which is more than 6 BPCU higher than that achieved by the single-polarized MIMO-NOMA, and incredibly 9 BPCU above that of MIMO-TDMA. Finally, Figs. 3(b) and 3(c) reveal the behavior of the rates observed for each user with fixed and fair power allocation. One can see that, in the IRS-MIMO-NOMA scheme, the rates of all users are improved, remarkably outperforming the conventional systems. The main reason for these improvements is that SIC is employed in each subset separately, which leads users to experience less interference in the decoding process. We can also verify that fair power allocation is highly beneficial to strong users. For instance, when $\rho = 40$ dB, while the rate of user 3 is limited to 1.63 BPCU in the IRS-MIMO-NOMA scheme with fixed policy, with fair power allocation, the same user can improve its rate to 3.39 BPCU.

REFERENCES

[1] H. Asplund *et al.*, *Advanced Antenna Systems for 5G Network Deployments*. London, U.K.: Academic, 2020.

[2] J. Park and B. Clerckx, "Multi-user linear precoding for multi-polarized massive MIMO system under imperfect CSIT," *IEEE Trans. Wireless Commun.*, vol. 14, no. 5, pp. 2532–2547, May 2015.

[3] A. S. de Sena *et al.*, "Massive MIMO-NOMA networks with multi-polarized antennas," *IEEE Trans. Wireless Commun.*, vol. 18, no. 12, pp. 5630–5642, Dec. 2019.

[4] A. S. de Sena *et al.*, "Massive MIMO-NOMA networks with imperfect SIC: Design and fairness enhancement," *IEEE Trans. Wireless Commun.*, vol. 19, no. 9, pp. 6100–6115, Sep. 2020.

[5] A. S. de Sena *et al.*, "IRS-assisted massive MIMO-NOMA networks: Exploiting wave polarization," *IEEE Trans. Wireless Commun.*, early access, May 25, 2021, doi: 10.1109/TWC.2021.3081419.

[6] J. Brewer, "Kronecker products and matrix calculus in system theory," *IEEE Trans. Circuits Syst.*, vol. 25, no. 9, pp. 772–781, Sep. 1978.

[7] D. Liu *et al.*, "Frank-Wolfe network: An interpretable deep structure for non-sparse coding," *IEEE Trans. Circuits Syst. Video Technol.*, vol. 30, no. 9, pp. 3068–3080, Sep. 2020.

[8] M. Jaggi, "Revisiting Frank-Wolfe: Projection-free sparse convex optimization," in *Proc. Int. Conf. Mach. Learn.*, vol. 28, 2013, pp. 427–435.

Publication V

de Sena, A. S., Nardelli, P. H. J., da Costa, D. B., Popovski, P., and Papadias, C. B.
Rate-Splitting Multiple Access and Its Interplay with Intelligent Reflecting Surfaces

Reprinted with permission from
IEEE Communications Magazine
Vol. 60, no. 7, pp. 52–57, Jul. 2022

MOBILE COMMUNICATIONS AND NETWORKS

Rate-Splitting Multiple Access and Its Interplay with Intelligent Reflecting Surfaces

Arthur S. de Sena, Pedro H. J. Nardelli, Daniel B. da Costa, Petar Popovski, and Constantinos B. Papadias

The authors present the potential of synergy between IRS and RSMA. Three important improvements achievable by IRS-RSMA schemes are identified, supported by insightful numerical examples, and mapped to beyond-5G use cases, along with future research directions.

ABSTRACT

Rate-splitting multiple access (RSMA) has recently appeared as a powerful technique for improving the downlink performance of multiple-input multiple-output systems. By flexibly managing interference, RSMA can deliver high spectral and energy efficiency, as well as robustness to imperfect channel state information. In another development, an intelligent reflecting surface (IRS) has emerged as a method to control the wireless environment through software-configurable, near-passive, sub-wavelength reflecting elements. This article presents the potential of synergy between IRS and RSMA. Three important improvements achievable by IRS-RSMA schemes are identified, supported by insightful numerical examples, and mapped to beyond 5G use cases, along with future research directions.

INTRODUCTION

A multiple-input multiple-output (MIMO) system can implement spatial-division multiple access (SDMA) to communicate with multiple spatially separated users simultaneously and at the same frequency. This can improve system rate, scalability, reliability, and latency, making MIMO an indispensable technology for fifth-generation (5G) communication systems. Nevertheless, by relying solely on SDMA, severe inter-user interference can be experienced when users have overlapping spatial directions or are located close to one another in overload scenarios. To tackle this issue, strategies exploiting different domains have been combined in MIMO systems, from conventional orthogonal multiple access (OMA) techniques, such as time-division multiple access (TDMA) and orthogonal frequency-division multiple access (OFDMA), to non-orthogonal multiple access (NOMA) techniques, such as power-domain and code-domain NOMA. Under ideal conditions, all these techniques efficiently mitigate inter-user interference. However, they are underpinned by an assumption of perfect channel state information (CSI), which is difficult to achieve in real-world deployments. In practice, CSI inaccuracies can diminish the data rates of MIMO, MIMO-OMA, and MIMO-NOMA schemes [1, 2].

Rate-splitting multiple access (RSMA) addresses the drawbacks of OMA and NOMA under imperfect CSI [1]. Unlike SDMA and OMA techniques, which treat residual multi-user interference as noise, or NOMA, which, by relying on successive interference cancellation (SIC), fully decodes the interference, the innovative RSMA technique combines the two approaches and flexibly treats one fraction of the interference as noise and addresses the other fraction through SIC. The RSMA technique unlocks a flexible interference management framework that can deliver high spectral and energy efficiencies, optimality in terms of degrees of freedom (DoF), and robustness to imperfect CSI [2].

Even though RSMA has numerous benefits, establishing reliable communication links through fast-varying wireless channels continues to be a challenge. As an attempt to overcome channel issues, a promising technology called an intelligent reflecting surface (IRS) has been proposed [3]. An IRS can be seen as a cluster of controllable scatterers, where each scatterer (i.e., a reflecting element) can be configured independently to generate distinct amplitude and phase responses. Collectively, the reflecting elements of an IRS are able to manipulate and reflect impinging electromagnetic waves with an optimized radiation pattern, creating a large number of possibilities for tuning the propagation medium. Conventionally, these reflections are performed without active amplification. As a result, an IRS does not require amplifiers or other components of conventional radio frequency (RF) chains, which gives IRSs the potential to enable ubiquitous connectivity in beyond 5G at low energy costs. Furthermore, several other advantages have been reported, including advanced control of users' channel gains, extended coverage range, and improved fairness [4]. Due to these features, several works investigating the application of IRS to diverse systems have appeared recently, some of which have focused on the IRS-RSMA topic [5].

Nevertheless, few technical contributions have been presented, and the full possibilities of the combination of IRS and RSMA remain to be investigated. This major literature lacuna motivates the work reported in this article. Specifically, we perform an in-depth investigation of the possible benefits that combined RSMA and IRS can provide. On one hand, we show that IRSs can enable a more flexible precoding design and make RSMA resilient to imperfect SIC. On the other hand, we show that RSMA can contribute to robust

---

Arthur S. de Sena and Pedro H. J. Nardelli are with Lappeenranta-Lahti University of Technology, Finland.; Daniel B. da Costa is with the Technology Innovation Institute (TII), United Arab Emirates and the National Yunlin University of Science and Technology, Taiwan; Petar Popovski is with Aalborg University, Denmark; Constantinos B. Papadias is with the American College of Greece, Greece.

Digital Object Identifier:
10.1109/MCOM.004.2100956

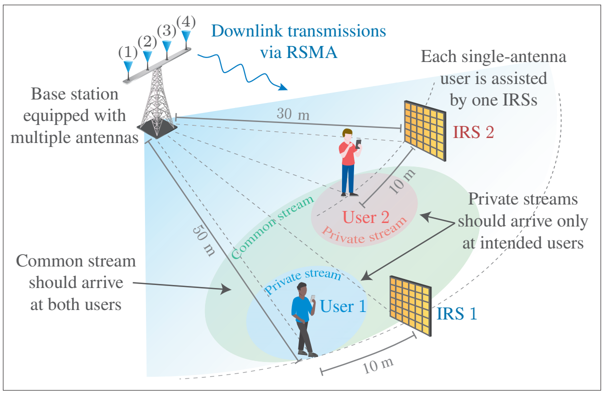

FIGURE 1. IRS-RSMA setup. Single-antenna users are assisted by IRSs..

IRS optimizations even under imperfect CSI. We demonstrate through simulations that these features unleash performance gains unreachable with other multiple access (MA) techniques. We also present future use case scenarios enabled by IRS-RSMA in beyond 5G networks. The article concludes by considering existing challenges and promising research directions.

AN OVERVIEW OF RSMA AND IRS TECHNOLOGY

INTRODUCTION TO THE RSMA TECHNIQUE

The work in [6] can be seen as one of the first studies to demonstrate that superior rate regions are achievable through rate-splitting (RS) strategies in broadcast channels of single-antenna systems. The goal of achieving new rate regions motivated subsequent works investigating further RS approaches. For instance, the RS strategies presented in [7, 8] indicated that if users are being served through interfering channels, it can be beneficial to convey part of the information in a shared common stream and decode part of the inter-user interference. This feature was recently found useful for improving the performance of modern MIMO systems.

Practical MIMO-OMA systems conventionally rely on linear precoding, such as zero-forcing (ZF) precoding, to mitigate inter-user interference. The adoption of these precoding techniques is mainly motivated by their low computational complexity and their optimality in terms of DoF under perfect CSI. In practice, however, the CSI estimate is inevitably imperfect, which makes linear precoding unable to cancel the interference completely and ultimately results in residual noise at the receivers. Such an issue can reduce the system's DoF and limit the achievable data rates. As an attempt to alleviate this limitation, researchers have recently exploited the RS concepts proposed in [6–8] to develop a new robust MA technique for MIMO systems, called RSMA. The technique can be seen as an implementation of the *divide-and-conquer* concept where part of the inter-user interference is addressed at the base station (BS), for example, through ZF precoding, and part by the users, through SIC. Consequently, it becomes possible to manage how much interference (not canceled by precoding due to imperfect CSI) is treated as noise and how much is decoded. This flexibility makes the technique powerful even in scenarios with inaccurate CSI.

In its simplest form, RSMA splits the data messages of different users into two parts. One part of each message is encoded into a common symbol and the remaining part into private symbols. The common symbol is multiplied by a common precoder (intended for all users), and the private symbols are multiplied by private precoders (each designed for a particular user). The obtained streams are superimposed in the power domain and then transmitted towards the users. At the receivers' side, all users first decode the common stream, while treating the private streams as noise, and perform SIC to subtract the retrieved messages from the superimposed stream. After SIC, the data in the private streams is finally decoded, ideally interference-free. Note that unlike NOMA, in which the number of SIC layers increases with the increase of users, RSMA requires that all users (independent of the number) execute SIC only once. Due to this feature, the technique is commonly called single-layer RSMA. Recent results have demonstrated that single-layer RSMA can outperform all conventional OMA, NOMA, and SDMA counterparts [2]. Advanced techniques with multiple common streams and multiple layers of SIC have also been proposed (e.g., called generalized RSMA [1]). However, more complicated schemes are beyond the scope of this article.

BASICS OF THE IRS TECHNOLOGY

An IRS consists of a thin two-dimensional structure that comprises multiple reflecting elements with adjustable electromagnetic properties. The reflecting elements, made of passive conductive materials, are tuned by a low-power control layer, which can be implemented through diverse technologies. Existing designs propose the use of PIN diodes, varactors, graphene, and liquid-crystal-based solutions [3]. Moreover, the reflecting elements usually have dimensions much smaller than the carrier wavelength [9]. Comprising such tiny components enables IRSs to steer signals ideally in any direction and achieve various goals, such as to maximize signal-to-noise ratio (SNR), assist interference cancellation, or operate in absorption mode for security purposes.

The fast-fading channels of an IRS-assisted system can be represented by the addition of a matrix modeling the direct link between the BS and users and a channel matrix corresponding to the reflected link via the IRS, which in turn is usually represented by the dyadic channel model [10]. The dyadic model is a multiplicative channel representation containing three matrices: a matrix for the link between the BS and IRS, a matrix for the link between the IRS and users, and a diagonal matrix with complex-valued elements that model the induced reflections, with amplitudes and phases limited to $[0, 1]$ and $[0, 2\pi]$, respectively. This model is used in the simulation examples given in this article.

IRS-RSMA: POTENTIAL IMPROVEMENTS

In this section, we discuss three potential performance improvements that the combined use of IRSs and RSMA offers. Each improvement is

The concept introduced by RSMA of conveying part of the information through a common stream brings a novel DoF for configuring IRSs, which makes this synergy unique and distinct from what is achievable with classic MA solutions. Specifically, IRSs can assist the design of efficient precoders for broadcasting common messages, which is known to be a challenge in RSMA.

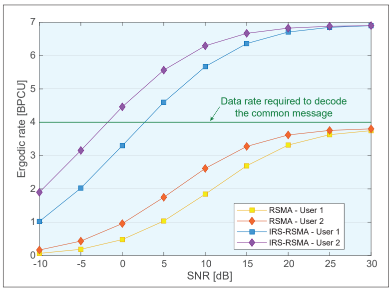

FIGURE 2. Ergodic rates vs. SNR for the common message in RSMA schemes ($\alpha_c = 0.9$, $\alpha_1 = \alpha_2 = 0.05$).

supported by representative simulation examples, where we compare the downlink performance of MIMO systems in combination with different MA solutions, including TDMA, NOMA, and RSMA. In all implemented systems, we consider a narrowband block-fading channel model, where the channel coefficients remain constant during a time slot but change independently over different time slots, such that time dispersion and fading correlation are not modeled. For illustration purposes, in the RSMA schemes, random precoders are employed for broadcasting the common messages, and ZF precoding is used for transmitting the private ones. In the baseline schemes, matched filter (MF) precoding is adopted in the NOMA systems and ZF precoding in the TDMA counterpart. We consider a scenario with two single-antenna users, where user 1 is located at 50 m and user 2 at 30 m from a BS equipped with 4 antennas, as shown in Fig. 1. Each user is assisted by one IRS containing 50 reflecting elements, with each IRS located 10 m apart from its connected user. For simplicity, the distances from the IRSs to the BS are the same as those from the connected users to the BS, and the path loss exponent is set to 2.5 in all links. Moreover, the precoders are normalized to unity, and fixed power allocation policies are employed in all systems. The power coefficients for users 1 and 2 in the NOMA schemes are configured as $\alpha_1 = 7/8$ and $\alpha_2 = 1/8$, whereas in TDMA all available power is allocated in each time slot to the scheduled user (i.e., $\alpha_1 = \alpha_2 = 1$). In turn, in the RSMA systems, the power coefficients for the private messages are set as $\alpha_1 = \alpha_2 = (1 - \alpha_c)/2$, where α_c represents the coefficient for the common message. It is noteworthy that even though we consider a narrowband channel model in the simulations, the gains presented in this section should also be applicable to other system setups. We recognize, though, that new insights could be achieved with different models, such as frequency-selective channels. However, this possibility is left for future work where an in-depth investigation can be carried out.

Enhanced Rate of the Common Message

The concept introduced by RSMA of conveying part of the information through a common stream brings a novel DoF for configuring IRSs, which makes this synergy unique and distinct from what is achievable with classic MA solutions. Specifically, IRSs can assist the design of efficient precoders for broadcasting common messages, which is known to be a challenge in RSMA. Several approaches have been proposed for addressing this issue in conventional RSMA systems [1]. However, most strategies usually favor some users more than others or result in complex optimization problems. Moreover, constructing a single precoder capable of meeting the rate requirement for the common message for all users may be an infeasible task. On the other hand, by assisting common stream transmissions with IRSs, it could be possible to deliver strong signal beams to users even when employing simple precoders at the BS.

The above gain is illustrated in Fig. 2, where the ergodic rates for the common message achieved with RSMA and IRS-RSMA are presented. The IRS of each user is optimized to match (to add constructively) the channel gains of the common stream achieved in the reflected link with the gains observed in the direct link. As can be seen, due to the interference generated by the private streams, the data rates of the common message become limited in the high-SNR regime in both RSMA and IRS-RSMA schemes. Note, however, that only the two users served via conventional RSMA are not able to meet the minimum rate required to decode the common message. In contrast, when the IRSs are optimized to boost the common message, the users in the IRS-RSMA system become able to achieve a rate higher than the requirement of 4 bpcu (ergodic rate) after 5 dB, reaching almost 7 bpcu at 30 dB. This higher rate represents an impressive improvement of more than 3 bpcu when compared to the rate observed in the RSMA counterpart for the same SNR value.

Robustness to Imperfect SIC

One key feature shared by NOMA and RSMA is that both techniques rely on SIC to decode part of the transmitted messages. In ideal conditions, it is possible to decode the messages perfectly through SIC without any errors. In practice, however, as a result of hardware imperfections and other impairments, even if the CSI can be perfectly estimated, decoding errors may still occur during the SIC process. It has been demonstrated in the literature [11] that imperfect SIC can severely harm the performance of NOMA systems and make them less spectrally efficient than conventional OMA schemes. An in-depth investigation of the impacts of imperfect SIC on RSMA schemes is still missing in the literature. Nevertheless, it is evident that despite the benefits of RSMA, its performance can deteriorate as a result of SIC errors. The deployment of IRSs could be highly beneficial to alleviate this issue in RSMA. Specifically, by assisting the RSMA scheme with IRSs and properly splitting the data symbols between common and private messages, high performance can be achieved even under the constraint of imperfect SIC.

The robustness of IRS-RSMA to residual SIC errors is illustrated in Fig. 3, where the IRSs are optimized to boost the users' channel gains and mitigate interference through a constrained least-squares approach. As in [11, Sec. III], a deterministic error factor is used to model the residual interference left by imperfect SIC. It can be seen that both the NOMA and IRS-NOMA systems are strongly impacted by residual SIC errors, with sum-rates limited to only 6.9 bpcu in the high-SNR regime, which is inferior to that achieved by the TDMA counterpart after 20 dB. In contrast, despite the presence of SIC errors, the sum-rates of the RSMA schemes can outperform the TDMA counterpart in the entire considered SNR range. For SNR values below 10 dB, the RSMA system can, however, still be outperformed by its NOMA and IRS-TDMA counterparts. On the other hand, the IRS-RSMA system can overcome this issue and boost the sum-rate over almost all the SNR range. For instance, when the SNR is 25 dB and the power allocated to the common message is $\alpha_c = 0.5$, the IRS-RSMA scheme can achieve a sum-rate of 14 bpcu, which is superior to that achieved by the RSMA counterpart for all values of α_c, and more than 6 bpcu higher than the sum-rate achieved by the TDMA and NOMA-based schemes.

Robustness to Imperfect CSI

As IRSs comprise only nearly passive components, accurately estimating the channels of the cascade-reflected link (i.e., the channels between the BS and the IRS, and the IRS and users) has been one of the main challenges of IRS-assisted systems, and different strategies have been proposed. Most common approaches try to estimate the full concatenated channel entirely at the BS through uplink training techniques, and some other approaches try to simplify the estimation process by installing scattered active sensors in the IRS [9]. Nevertheless, independent of the IRS hardware or estimation strategy, perfectly obtaining the global CSI remains a complicated task. Consequently, in practice, the optimization of the IRSs is usually performed based on imperfect CSI, which might result in sub-optimal performance. Fortunately, unlike other conventional MA techniques, RSMA has the advantage of being robust in scenarios with inaccurate channel estimation. Therefore, RSMA is a good fit for realistic IRS-assisted systems with imperfect CSI.

Figure 4 plots the ergodic sum-rates of various IRS-assisted systems under perfect and imperfect CSI. In this figure, the reflecting elements of the IRSs are also optimized to boost the users' channel gains and mitigate interference. Note that because ZF precoding is unable to cancel the inter-user interference completely when the CSI is imperfect, IRS-TDMA is the most impacted scheme, with its sum-rate saturating slightly above 5 bpcu at high SNR, which is almost 10 bpcu lower than the IRS-TDMA scheme can reach at 40 dB under perfect CSI. On the other hand, the IRS-RSMA system can achieve high sum-rate levels with perfect and imperfect CSI, outperforming all the baseline schemes. For instance, when the SNR is 30 dB, the IRS-RSMA scheme with perfect CSI can obtain a sum-rate of 21.7 bpcu, while under imperfect CSI it can still achieve an impressive 20.2 bpcu, which is approximately 6 bpcu higher than that achieved by the IRS-NOMA counterpart with imperfect CSI, and 15 bpcu higher than that of the IRS-TDMA counterpart with imperfect CSI. These results confirm that by combining RSMA and IRS technology, it becomes possible to deploy robust communication systems even when the channel estimation is poor.

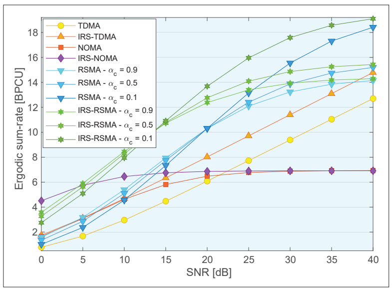

FIGURE 3. Impact of imperfect SIC on the ergodic sum-rates of various MA systems (SIC error factor = 0.01).

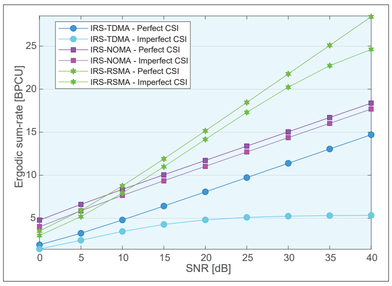

FIGURE 4. Ergodic sum-rate curves for various MA systems under imperfect CSI (channel error variance = 0.5, $\alpha_c = 0.9$, $\alpha_1 = \alpha_2 = 0.05$).

Potential Use Cases in Beyond 5G

In this section, we present use case scenarios that can be enabled with the aid of IRS-RSMA schemes.

CSI-Robust UAV Networks

Unmanned aerial vehicles (UAVs) will play an important role in beyond 5G [12]. UAVs have been envisioned as executing diverse tasks, ranging from goods deliveries, surveillance and military applications, to working as BSs, where UAVs can provide flexible and dynamic coverage. For instance, with the help of UAVs, it will be possible to temporarily support high-performance connectivity in hyper-crowded environments, such as in stadiums and at festivals, or extend signal coverage to remote rural areas and during natural disasters. The deployment of swarms of UAVs is another promising application for future communication systems. In a swarm, by sensing the environment, a large number of UAVs can intercommunicate, reorganize, and adapt autonomously in the air, allowing them to execute even the most complex tasks.

Nevertheless, there are unsolved issues that need to be tackled before UAV networks become everyday reality. IRS-RSMA schemes can efficiently address some of these challenges. In particular, channel interference and the overhead generated by multiple UAVs and their fast 3D motion make channel estimation a complicated process, which can potentially result in imperfect CSI. As noted earlier, in addition to being effective at managing interference, IRS-RSMA schemes are robust to imperfect CSI, which makes them very suitable

The deployment of swarms of UAVs is another promising application for future communication systems. In a swarm, by sensing the environment, a large number of UAVs can intercommunicate, reorganize and adapt autonomously in the air, allowing them to execute even the most complex tasks.

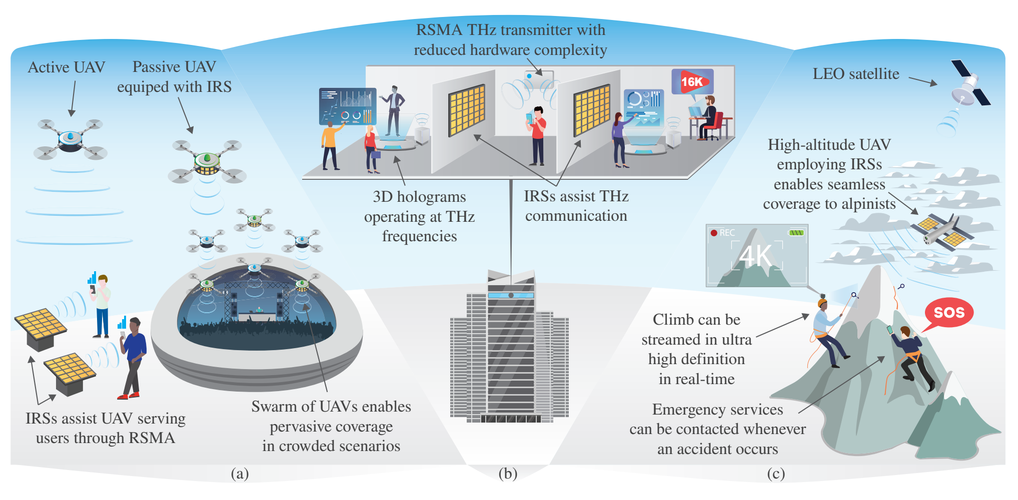

FIGURE 5. Potential use case scenarios enabled by IRS-RSMA in future wireless networks beyond 5G.

for employment in UAV networks. For instance, RSMA could enable multiple UAVs to communicate efficiently with multiple ground users, whereas IRSs pointed to the sky could guarantee a strong communication link between users and UAVs. One can also envision a CSI-robust swarm of UAVs equipped with IRSs, with some UAVs active and others passive, interacting with each other via RSMA. As illustrated in Fig. 5a, in both examples, the UAVs would be able to deliver high data rates seamlessly with low impact from a possibly degraded CSI.

ENHANCED HIGH-FREQUENCY COMMUNICATION

5G has expanded its operating bandwidth by adopting higher frequency bands above 6 GHz, known as the millimeter-wave (mmWave) spectrum. While 5G is expected to operate at frequencies not higher than 100 GHz, 6G and beyond generations are foreseen to go further and operate from the upper band of the mmWave spectrum (100 GHz to 300 GHz), up to the terahertz (THz) spectrum (up to 3 THz) [13]. However, due to the high signal attenuation and absorption, operating at such high frequencies becomes very challenging. The coverage range of mmWave and THz communication can be improved by deploying a large number of transmit antennas (hundreds or thousands). Nevertheless, the large number of RF chains required in these large-scale arrays may lead to complicated precoding design, excessive feedback overhead, and increased energy consumption.

On the other hand, by deploying IRSs to induce sharp beams directed toward the users, it becomes possible to mitigate signal attenuation and extend signal coverage. In turn, by leveraging the RSMA technique, due to its robustness to imperfect CSI, the required CSI feedback overhead can be reduced without significantly deteriorating the system performance. These capabilities suggest that IRS-RSMA schemes can help to reduce the required number of active antennas and RF chains at the BS and still deliver good communication performance with the benefits of reducing the BS hardware complexity. Moreover, since IRSs comprise only low-power components, the energy required for optimizing the reflecting elements should be less than the energy savings achieved with a lower number of power-hungry RF chains at the BS. Therefore, as another benefit, IRS-RSMA could also reduce the overall energy consumption of mmWave and THz systems. As illustrated in Fig. 5b, a BS of an indoor THz IRS-RSMA system could support real-time 3D holographic meetings in multiple rooms of a commercial building and, at the same time, stream 16K resolution video to users' laptops and advanced smartphones.

SEAMLESS SATELLITE COMMUNICATION

Enabling seamless connectivity across the entire Earth's surface, from high altitude mountain ranges to the middle of the oceans, by relying on terrestrial and UAV networks alone may be unrealizable or too costly. On the other hand, low Earth orbit (LEO) satellite networks can cover vast geographical areas and potentially deliver high data rates to the most remote and inhospitable regions of the globe [14, 15]. However, LEO networks come with some drawbacks. Specifically, due to atmospheric gases, rain, and cloud coverage, the signals transmitted and received by satellites can suffer strong attenuation. Moreover, due to long-distance signal travel, the CSI available in satellites can become outdated.

IRS-RSMA strategies are also suited to cope with these satellite-related communication issues. First, by employing the RSMA technique, LEO satellites become able to deliver high data rates to multiple users even when the CSI is outdated. Second, by deploying IRSs to boost the signal transmissions, it is possible to mitigate the effects of atmospheric phenomena. For example, high-altitude UAVs equipped with IRSs could be deployed near cloud cover to assist a LEO network to serve multiple alpinists via RSMA in remote mountainous regions. This IRS-assisted RSMA-LEO network would ensure high data rates and reduce the probability of alpinists finding themselves out of coverage. Such capabilities would enable alpinists to stream their climb in real time even under adverse weather conditions. These features could also save lives following accidents. Figure 5c illustrates this extreme scenario.

Challenges, Future Directions, and Concluding Remarks

We have demonstrated that the use of IRSs and RSMA can bring mutual benefits, in that IRSs can help to address issues related to precoding design and imperfect SIC in RSMA, and reciprocally, RSMA can bring robustness to the imperfect CSI that is unavoidable in IRS-assisted communications. However, both RSMA and IRS technology are still in their infancy, and there are still several open problems that need to be solved before practical deployment can happen. Specifically, more extensive studies need to be carried out to determine the best optimization strategies, the most appropriate IRS architecture, and associated trade-offs. Frequency-selective fading in IRS-RSMA still needs to be better investigated. Furthermore, due to the more complex encoding, IRS-RSMA schemes require new signaling strategies to coordinate users, IRSs and the BS, and extensive tests need to be performed in real-world testbeds to confirm the claimed gains.

The combination of IRS and RSMA is a research area with exciting possibilities for future work. IRS-RSMA contributions investigating the application of different modulation techniques, aerial networks, and THz communications, spanning from performance analysis and resource allocation to channel estimation strategies, are interesting and exciting future directions. All in all, the full potential of the interplay of IRSs and RSMA has yet to be realized.

Acknowledgments

This article is partly supported by the Academy of Finland via (a) FIREMAN consortium n.326270 as part of CHIST-ERA-17-BDSI-003, and (b) EnergyNet Research Fellowship n.321265/n.328869, and by Jane and Aatos Erkko Foundation via STREAM project.

References

[1] Y. Mao, B. Clerckx, and V.O. Li, “Rate-Splitting Multiple Access for Downlink Communication Systems: Bridging, Generalizing, and Outperforming SDMA and NOMA,” *EURASIP J. Wireless Commun. Network*, May 2018.

[2] B. Clerckx *et al.*, “Is NOMA Efficient in Multi-Antenna Networks? A Critical Look at Next Generation Multiple Access Techniques,” *IEEE Open J. Commun. Soc.*, vol. 2, 2021, pp. 1310–43.

[3] M. Di Renzo *et al.*, “Smart Radio Environments Empowered by Reconfigurable Intelligent Surfaces: How It Works, State of Research, and the Road Ahead,” *IEEE JSAC*, vol. 38, no. 11, Nov. 2020, pp. 2450–2525.

[4] A. S. de Sena *et al.*, “What Role Do Intelligent Reflecting Surfaces Play in Multi-Antenna Non-Orthogonal Multiple Access?,” *IEEE Wireless Commun.*, vol. 27, no. 5, Oct. 2020, pp. 24–31.

[5] A. Bansal, K. Singh, and C. -P. Li, “Analysis of Hierarchical Rate Splitting for Intelligent Reflecting Surfaces-Aided Downlink Multiuser MISO Communications,” *IEEE Open J. Commun. Soc.*, vol. 2, 2021, pp. 785–98.

[6] T. Cover, “Broadcast Channels,” *IEEE Trans. Info. Theory*, vol. 18, no. 1, Jan. 1972, pp. 2–14.

[7] A. Carleial, “Interference Channels,” *IEEE Trans. Info. Theory*, vol. 24, no. 1, Jan. 1978, pp. 60-70.

[8] T. Han and K. Kobayashi, “A New Achievable Rate Region for the Interference Channel,” *IEEE Trans. Info. Theory*, vol. 27, no. 1, Jan. 1981, pp. 49–60.

[9] M. Dajer *et al.*, “Reconfigurable Intelligent Surface: Design the Channel — A New Opportunity for Future Wireless Networks,” *Digital Commun. Networks*, 2021.

[10] Y. Liang *et al.*, “Large Intelligent Surface/Antennas (LISA): Making Reflective Radios Smart,” *J. Commun. Info. Networks*, vol. 4, no. 2, June 2019, pp. 40–50.

[11] A. S. de Sena *et al.*, “Massive MIMO-NOMA Networks with Imperfect SIC: Design and Fairness Enhancement,” *IEEE Trans. Wireless Commun.*, vol. 19, no. 9, June 2020, pp. 6100–15.

[12] W. Jaafar *et al.*, “Multiple Access in Aerial Networks: From Orthogonal and Non-Orthogonal to Rate-Splitting,” *IEEE Open J. Vehic. Tech.*, vol. 1, 2020, pp. 372–92.

[13] K. Rikkinen *et al.*, “THz Radio Communication: Link Budget Analysis Toward 6G,” *IEEE Commun. Mag.*, vol. 58, no. 11, Nov. 2020, pp. 22–27.

[14] L. You *et al.*, “Massive MIMO Transmission for LEO Satellite Communications,” *IEEE JSAC*, vol. 38, no. 8, Aug. 2020, pp. 1851–65.

[15] B. Matthiesen *et al.*, “Intelligent Reflecting Surface Operation Under Predictable Receiver Mobility: A Continuous Time Propagation Model,” *IEEE Wireless Commun. Lett.*, vol. 10, no. 2, Feb. 2021, pp. 216–20.

Biographies

Arthur Sousa de Sena [M] (arthur.sena@lut.fi) is with Lappeenranta-Lahti University of Technology, Finland.

Pedro H. J. Nardelli [SM] (pedro.nardelli@lut.fi) is with Lappeenranta-Lahti University of Technology.

Daniel Benevides da Costa [SM] (danielbcosta@ieee.org) is with the Technology Innovation Institute (TII), Abu Dhabi, United Arab Emirates, and also with the National Yunlin University of Science and Technology, Taiwan.

Petar Popovski [F] (petarp@es.aau.dk) is with Aalborg University, Denmark.

Constantinos B. Papadias [F] (cpapadias@acg.edu) is with the American College of Greece.

Publication VI

de Sena, A. S., Nardelli, P. H. J., da Costa, D. B., Popovski, P., Papadias, C. B.,
and Debbah, M.

Dual-Polarized RSMA for Massive MIMO Systems

Reprinted with permission from
IEEE Wireless Communications Letters
Vol. 11, no. 9, pp. 2000–2004, Sep. 2022

Dual-Polarized RSMA for Massive MIMO Systems

Arthur S. de Sena, *Graduate Student Member, IEEE*, Pedro H. J. Nardelli, *Senior Member, IEEE*,
Daniel B. da Costa, *Senior Member, IEEE*, Petar Popovski, *Fellow, IEEE*,
Constantinos B. Papadias, *Fellow, IEEE*, and Mérouane Debbah

***Abstract*—This letter proposes a novel dual-polarized rate-splitting multiple access (RSMA) technique for massive multiple-input multiple-output (MIMO) networks. The proposed strategy transmits common and private symbols in parallel through dynamic polarization multiplexing, and it does not require successive interference cancellation (SIC) in the reception. For assisting the design of dual-polarized MIMO-RSMA systems, we propose a deep neural network (DNN) framework for predicting the ergodic sum-rates. An efficient DNN-aided adaptive power allocation policy is also developed for maximizing the ergodic sum-rates. Simulation results validate the effectiveness of the DNNs for sum-rate prediction and power allocation and reveal that the dual-polarized MIMO-RSMA strategy can impressively outperform conventional baseline schemes.**

***Index Terms*—Dual-polarized MIMO, RSMA, deep learning.**

I. INTRODUCTION

RATE-SPLITTING multiple access (RSMA) has recently appeared as a powerful downlink transmission technique for multiple-input multiple-output (MIMO) systems. At the base station (BS), RSMA encodes the data messages of different users into common and private symbols and transmits them through linear precoding. Upon reception, users rely on successive interference cancellation (SIC) to recover the original message. The features of RSMA enable attractive performance improvements, such as higher data rates and robustness to imperfect channel state information (CSI). When RSMA is combined with massive MIMO systems, with a large number of antennas at the BS, further improvements can be achieved, outperforming conventional techniques like time-division multiple access (TDMA), space-division multiple access (SDMA), and non-orthogonal multiple access (NOMA) [1], [2].

Despite the advantages of RSMA, there are still unsolved issues and room for improvement. In particular, SIC introduces interference in the decoding process of RSMA, which is detrimental to the system spectral efficiency. Moreover, SIC error propagation can happen in practice, which also deteriorates the system performance. The recent work in [3] has shown that dual-polarized antenna arrays can be harnessed to alleviate SIC issues and improve user multiplexing. Moreover, dual-polarized antenna arrays are widely employed in commercial cellular systems and have been adopted as the standard in the 3rd generation partnership project (3GPP) long-term evolution advanced (LTE-A) and 5G New Radio (NR) specifications [3]. These facts imply that the polarization domain is a practical resource that is abundantly available and offers promising opportunities for enhancing the performance of next-generation communication systems. Under such motivations, we propose an appealing dual-polarized RSMA strategy for dual-polarized massive MIMO systems, a concept not yet reported in the technical literature. With the goal of maximizing the system sum-rate, common and private symbols are multiplexed dynamically in the polarization domain. Our low-complexity strategy enables users to detect common and private symbols simultaneously from orthogonal polarizations without SIC, which reduces the overall interference experienced in the system. Due to the dynamic nature of the system model, classical performance analysis and optimization become unfeasible. Alternatively, we propose a deep neural network (DNN) framework for predicting the ergodic sum-rates of the proposed scheme. The DNN sum-rate prediction framework can be used as an efficient tool for assisting the design of dual-polarized MIMO-RSMA systems. To improve the ergodic sum-rate further, we also develop a DNN-aided adaptive power allocation framework, which smartly splits the transmit power between common and private symbols. Simulation results validate the effectiveness of the DNN frameworks and confirm that remarkable performance improvements are achievable with the dual-polarized MIMO-RSMA strategy.

Notation: The transpose and the Hermitian transpose of a matrix $\mathbf{A}$ are represented by $\mathbf{A}^T$ and $\mathbf{A}^H$, respectively. $\mathbf{I}_M$ is the $M \times M$ identity matrix, $\mathbf{0}_{M,N}$ is the $M \times N$ matrix with all zero entries, and $\otimes$ is the Kronecker product. Moreover, the cardinality of a set $\mathcal{A}$ is represented by $|\mathcal{A}|$, $\circ$ represents the function composition, and $\mathrm{E}[\cdot]$ denotes expectation.

II. SYSTEM MODEL

We consider a downlink single-cell scenario in which one base station (BS) employing $M/2$ co-located pairs of dual-polarized antennas (with vertical (v) and horizontal (h) polarizations) communicates with multiple users equipped with a single pair of dual-polarized antennas. The BS clusters the users into G groups, with each group containing N_g users. Users within a given group are assumed to share a common covariance matrix given by $\mathbf{R}_g = \mathbf{I}_2 \otimes \boldsymbol{\Sigma}_g = \mathbf{I}_2 \otimes (\mathbf{Q}_g \boldsymbol{\Delta}_g \mathbf{Q}_g^H)$, where $\boldsymbol{\Sigma}_g \in \mathbb{C}^{\frac{M}{2} \times \frac{M}{2}}$ denotes the covariance matrix of rank r_g observed in each polarization, $\boldsymbol{\Delta}_g$ is a real-valued $\bar{r}_g \times \bar{r}_g$ diagonal matrix containing $\bar{r}_g < r_g$ nonzero eigenvalues of $\boldsymbol{\Sigma}_g$, and $\mathbf{Q}_g$ is a matrix comprising its corresponding eigenvectors.

Manuscript received 15 June 2022; accepted 12 July 2022. Date of publication 15 July 2022; date of current version 9 September 2022. This work was supported in part by the Academy of Finland under Grant 321265, Grant 328869, and Grant 326270; and in part by CHIST-ERA-17-BDSI-003. The associate editor coordinating the review of this article and approving it for publication was X. Lei. *(Corresponding author: Pedro H. J. Nardelli.)*

Arthur S. de Sena and Pedro H. J. Nardelli are with the Department of Electrical Engineering, Lappeenranta-Lahti University of Technology, 53850 Lappeenranta, Finland (e-mail: arthur.sena@lut.fi; pedro.nardelli@lut.fi).

Daniel B. da Costa and Mérouane Debbah are with the Digital Science Research Center, Technology Innovation Institute, Abu Dhabi, UAE (e-mail: danielbcosta@ieee.org; merouane.debbah@tii.ae).

Petar Popovski is with the Department of Electronic Systems, Aalborg University, 9220 Aalborg, Denmark (e-mail: petarp@es.aau.dk).

Constantinos B. Papadias is with the Research, Technology and Innovation Network, ALBA, The American College of Greece, 153 42 Athens, Greece (e-mail: cpapadias@acg.edu).

Digital Object Identifier 10.1109/LWC.2022.3191547

As a result, the dual-polarized channel matrix for the *n*th user in the *g*th group can be structured as

$$\mathbf{H}_{gn} = \begin{bmatrix} \mathbf{h}_{gn}^{vv} & \mathbf{h}_{gn}^{vh} \\ \mathbf{h}_{gn}^{hv} & \mathbf{h}_{gn}^{hh} \end{bmatrix} = \left[\mathbf{I}_2 \otimes \left(\mathbf{Q}_g \boldsymbol{\Delta}_g^{\frac{1}{2}}\right)\right] \begin{bmatrix} \mathbf{g}_{gn}^{vv} & \sqrt{\chi}\mathbf{g}_{gn}^{vh} \\ \sqrt{\chi}\mathbf{g}_{gn}^{hv} & \mathbf{g}_{gn}^{hh} \end{bmatrix}, \quad (1)$$

where $\mathbf{g}_{gn}^{ij} \in \mathbb{C}^{\bar{r}_g}$ denotes the reduced-dimension fast-fading channel vector from polarization *i* to *j*, with $i, j \in \{v, h\}$, and $\chi \in [0, 1]$ is the inverse cross-polar discrimination which measures the ratio of cross-polar to co-polar signal powers.

A. CSI Estimation and Acquisition

Due to quantization errors and other issues, the acquisition of $\mathbf{g}_{gn}^{ij}$ at the BS is imperfect. As in [2], we model the corrupted estimate of $\mathbf{g}_{gn}^{ij}$ by

$$\hat{\mathbf{g}}_{gn}^{ij} = \sqrt{1 - \tau^2}\mathbf{g}_{gn}^{ij} + \tau\mathbf{z}_{gn}^{ij}, \quad (2)$$

where $\mathbf{z}_{gn}^{ij}$ is a complex standard Gaussian random vector independent of $\mathbf{g}_{gn}^{ij}$, and τ is a factor that informs the quality of the CSI estimation, such that $\tau = 0$ corresponds to the perfect CSI case, and $\tau = 1$ models the extreme scenario where the estimate $\hat{\mathbf{g}}_{gn}^{ij}$ is statistically independent of $\mathbf{g}_{gn}^{ij}$.

On the other hand, we assume that $\boldsymbol{\Sigma}_g$ is perfectly known at the BS. In particular, the one-ring model [3] is adopted for generating $\boldsymbol{\Sigma}_g$ in this letter.

B. Dual-Polarized Rate-Splitting Multiple Access

The proposed dual-polarized MIMO-RSMA strategy can be explained as follows. First, each user's message is split into a common and a private part. Then, the BS encodes the common parts into a single super-symbol, which we denote by x_g^c, and the private parts into private symbols, denoted by x_{gn}^p. The symbol x_g^c is intended for all users within the *g*th group, whereas x_{gn}^p should be decoded by the intended *n*th user only. In the original RSMA technique, x_g^c and x_{gn}^p are linearly precoded and superimposed in the power domain for transmission, which requires SIC in the reception. In contrast to conventional RSMA, our proposed technique transmits common and private symbols in parallel data streams via the polarization domain. More specifically, the BS transmits

$$\mathbf{x} = \sum_{g=1}^{G} \mathbf{P}_g \left(\sum_{n=1}^{N_g} \mathbf{w}_{gn}^p \sqrt{P\zeta_{gn}\alpha_{gn}^p} x_{gn}^p + \mathbf{w}_g^c \sqrt{P\zeta_{gn}\alpha_g^c} x_g^c \right), \quad (3)$$

where $\mathbf{P}_g \in \mathbb{C}^{M \times \bar{\bar{M}}}$ is the precoding matrix for cancelling inter-group interference, in which $\bar{\bar{M}}$ determines the dimension of the transformed channel. The parameter *P* denotes the total transmit power, ζ_{gn} is the large-scale fading coefficient for the *n*th user in the *g*th group, and α_g^c and α_{gn}^p are the power allocation coefficients for the common and private symbols, with the constraint $\alpha_g^c + \sum_{n=1}^{N_g} \alpha_{gn}^p = 1$. In turn, $\mathbf{w}_g^c \in \mathbb{C}^{\bar{\bar{M}}}$ and $\mathbf{w}_{gn}^p \in \mathbb{C}^{\bar{\bar{M}}}$ are precoding vectors responsible for multiplexing the common and private symbols in polarizations i_g^c and i_g^p, respectively, such that $i_g^c \neq i_g^p \in \{v, h\}$, which are defined by

$$\mathbf{w}_g^c = \begin{bmatrix} \mathbf{w}_g^{c,v} \\ \mathbf{0} \end{bmatrix}, \mathbf{w}_{gn}^p = \begin{bmatrix} \mathbf{0} \\ \mathbf{w}_{gn}^{p,h} \end{bmatrix}, \text{ if } i_g^c = v, \text{ and } i_g^p = h, (4)$$

$$\mathbf{w}_g^c = \begin{bmatrix} \mathbf{0} \\ \mathbf{w}_g^{c,h} \end{bmatrix}, \mathbf{w}_{gn}^p = \begin{bmatrix} \mathbf{w}_{gn}^{p,v} \\ \mathbf{0} \end{bmatrix}, \text{ if } i_g^c = h, \text{ and } i_g^p = v. (5)$$

The polarizations i_g^c and i_g^p are assigned dynamically at each coherence interval by the BS. To this end, based on the estimated CSI modeled by (2), the BS predicts the instantaneous rates of the common and private symbols experienced by the users, denoted by $\hat{R}_{gn}^c$ and $\hat{R}_{gn}^p$, and determines the desired polarizations based on the following criteria

$$\underset{i_g^c, i_g^p}{\arg\max} \sum_{n=1}^{N_g} \left[\hat{R}_{gn}^p + \min_{l \in \{1, \ldots, N_g\}} \hat{R}_{gl}^c \right]. \quad (6)$$

After computing (6), the BS feeds back i_g^c and i_g^p to the users. In the reception, users within the *g*th group detects the common message from polarization i_g^c and the private messages from polarization i_g^p. A simplified diagram of the proposed scheme is presented in Fig. 1.

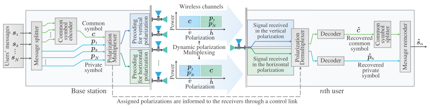

Fig. 1. Dual-polarized MIMO-RSMA transceiver. Private and common streams are transmitted in parallel via the polarization domain.

C. Precoding for Inter-Group Interference Cancellation

After the signal in (3) has passed through the channel in (1), the *n*th user in the *g*th group receives:

$$\mathbf{y}_{gn} = \begin{bmatrix} \mathbf{g}_{gn}^{vv} & \sqrt{\chi}\mathbf{g}_{gn}^{vh} \\ \sqrt{\chi}\mathbf{g}_{gn}^{hv} & \mathbf{g}_{gn}^{hh} \end{bmatrix}^H \left[\mathbf{I}_2 \otimes (\boldsymbol{\Delta}_g^{\frac{1}{2}} \mathbf{Q}_g^H)\right] \sum_{k=1}^{G} \mathbf{P}_k \times \left(\sum_{u=1}^{N_g} \mathbf{w}_{ku}^p \sqrt{P\zeta_{ku}\alpha_{ku}^p} x_{ku}^p + \mathbf{w}_k^c \sqrt{P\zeta_{ku}\alpha_k^c} x_k^c \right) + \begin{bmatrix} n_{gn}^v \\ n_{gn}^h \end{bmatrix}, \quad (7)$$

where n_{gn}^i denotes the additive noise observed by the *n*th user in polarization $i \in \{v, h\}$, which follows the complex Gaussian distribution with zero mean and variance σ^2.

From (7), it is clear that the inter-group interference can be cancelled if, $\forall g \neq g'$, the following is satisfied

$$\left[\mathbf{I}_2 \otimes \left(\boldsymbol{\Delta}_{g'}^{\frac{1}{2}} \mathbf{Q}_{g'}^H\right)\right] \mathbf{P}_g = \left[\mathbf{I}_2 \otimes \left(\boldsymbol{\Delta}_{g'}^{\frac{1}{2}} \mathbf{Q}_{g'}^H\right)\right] \left(\mathbf{I}_2 \otimes \bar{\mathbf{P}}_g\right) = \mathbf{0}, \quad (8)$$

where $\bar{\mathbf{P}}_g \in \mathbb{C}^{\frac{M}{2} \times \bar{M}}$ is the precoding matrix for each polarization, in which $\bar{M} \triangleq \bar{\bar{M}}/2$. To this end, $\bar{\mathbf{P}}_g$ can be constructed by concatenating $\bar{M}$ basis vectors of the null space of the matrix $\underline{\mathbf{Q}} = [\mathbf{Q}_1, \ldots, \mathbf{Q}_{g-1}, \mathbf{Q}_{g+1}, \ldots, \mathbf{Q}_G] \in \mathbb{C}^{\frac{M}{2} \times \sum_{g'=1, g' \neq g}^{G} \bar{r}_{g'}}$, where $\bar{M} < M/2 - \sum_{g'=1, g' \neq g}^{G} \bar{r}_{g'}$. With this design, the signal in (7) can be simplified as

$$\mathbf{y}_{gn} = \begin{bmatrix} (\mathbf{g}_{gn}^{vv})^H \boldsymbol{\Delta}_g^{\frac{1}{2}} \mathbf{Q}_g^H \bar{\mathbf{P}}_g & \sqrt{\chi}(\mathbf{g}_{gn}^{hv})^H \boldsymbol{\Delta}_g^{\frac{1}{2}} \mathbf{Q}_g^H \bar{\mathbf{P}}_g \\ \sqrt{\chi}(\mathbf{g}_{gn}^{vh})^H \boldsymbol{\Delta}_g^{\frac{1}{2}} \mathbf{Q}_g^H \bar{\mathbf{P}}_g & (\mathbf{g}_{gn}^{hh})^H \boldsymbol{\Delta}_g^{\frac{1}{2}} \mathbf{Q}_g^H \bar{\mathbf{P}}_g \end{bmatrix} \times \left(\sum_{u=1}^{N_g} \mathbf{w}_{gu}^p \sqrt{P\zeta_{gu}\alpha_{gu}^p} x_{gu}^p + \mathbf{w}_g^c \sqrt{P\zeta_{gu}\alpha_g^c} x_g^c \right) + \begin{bmatrix} n_{gn}^v \\ n_{gn}^h \end{bmatrix}. \quad (9)$$

As a result, the *n*th user decodes the common message with following signal-to-interference-plus-noise ratio (SINR)

$$\gamma_{gn}^c = \frac{|(\mathbf{g}_{gn}^{i^c i^c})^H \boldsymbol{\Delta}_g^{\frac{1}{2}} \mathbf{Q}_g^H \bar{\mathbf{P}}_g \mathbf{w}_g^{c, i_g^c}|^2 \rho\zeta_{gn}\alpha_g^c}{\chi \sum_{u=1}^{N_g} |(\mathbf{g}_{gn}^{i_g^p i_g^c})^H \boldsymbol{\Delta}_g^{\frac{1}{2}} \mathbf{Q}_g^H \bar{\mathbf{P}}_g \mathbf{w}_{gu}^{p, i_g^p}|^2 \rho\zeta_{gn}\alpha_{gu}^p + 1}, (10)$$

where $\rho = P/\sigma^2$ denotes the signal-to-noise ratio (SNR), and the first term in the denominator models the cross-polar interference from polarization i_g^p to polarization i_g^c.

In turn, the SINR observed by the *n*th user in the *g*th group when decoding its private message can be represented by

$$\gamma_{gn}^p = \frac{|(\mathbf{g}_{gn}^{i_g^p i_g^p})^H \boldsymbol{\Delta}_g^{\frac{1}{2}} \mathbf{Q}_g^H \bar{\mathbf{P}}_g \mathbf{w}_{gn}^{p, i_g^p}|^2 \rho\zeta_{gn}\alpha_{gn}^p}{\chi|(\mathbf{g}_{gn}^{i^c i^p})^H \boldsymbol{\Delta}_g^{\frac{1}{2}} \mathbf{Q}_g^H \bar{\mathbf{P}}_g \mathbf{w}_g^{c, i_g^c}|^2 \rho\zeta_{gn}\alpha_g^c + \Psi_{gn}^{i_g^p} + 1}. \quad (11)$$

where the first term in the denominator corresponds to the cross-polar interference, and the term $\Psi_{gn}^{i_g^p} = \sum_{u=1,u\neq n}^{N_g} |(\mathbf{g}_{gn}^{i_g^p i_g^p})^H \mathbf{\Delta}_g^{\frac{1}{2}} \mathbf{Q}_g^H \bar{\mathbf{P}}_g \mathbf{w}_{gu}^{p,i_g^p}|^2 \rho\zeta_{gn}\alpha_{gu}^p$ is the interference generated by imperfect CSI.

D. Precoding for the Common and Private Symbols

The precoding vector $\mathbf{w}_{gn}^{p,i_g^p} \in \mathbb{C}^{\bar{M}}$ should be designed to cancel the remaining inter-user interference observed in the assigned polarization $i_g^p \in \{v,h\}$ within each group. Mathematically, we must have $[(\mathbf{g}_{gn'}^{i_g^p i_g^p})^H \mathbf{\Delta}_g^{\frac{1}{2}} \mathbf{Q}_g^H \bar{\mathbf{P}}_g]\mathbf{w}_{gn}^{p,i_g^p} \approx 0$, for $\forall n' \neq n \in \{1,\ldots,N_g\}$, i.e., the private precoder for one user must be near-orthogonal (orthogonal with perfect CSI) to the effective channels of other users. By defining $\hat{\mathbf{H}}_g^{i_g^p} = [\bar{\mathbf{P}}_g^H \mathbf{Q}_g \mathbf{\Delta}_g^{\frac{1}{2}} \hat{\mathbf{g}}_{g1}^{i_g^p i_g^p}, \ldots, \bar{\mathbf{P}}_g^H \mathbf{Q}_g \mathbf{\Delta}_g^{\frac{1}{2}} \hat{\mathbf{g}}_{gN_g}^{i_g^p i_g^p}] \in \mathbb{C}^{\bar{M}\times N_g}$, the private precoder for the *n*th user can be computed as the zero-forcing precoder $\mathbf{w}_{gn}^{p,i_g^p} = [\hat{\mathbf{H}}_g^{i_g^p}((\hat{\mathbf{H}}_g^{i_g^p})^H \hat{\mathbf{H}}_g^{i_g^p})^{-1}]_{:n}$, where $\bar{M} \geq N_g$ should be satisfied.

In turn, aiming at maximizing the worst observed SINR, $\mathbf{w}_g^{c,i_g^c}$ can be obtained as follows:

$$\max_{\mathbf{w}_g^{c,i_g^c}} \min_{\forall l\in\{1,\ldots,N_g\}} \gamma_{gn}^c,$$
$$\text{s.t. } \|\mathbf{w}_g^{c,i_g^c}\|^2 = 1. \tag{12}$$

However, the problem in (12) is non-convex and NP-hard for general numbers of transmit antennas [4]. Fortunately, when $M \to \infty$, the asymptotic optimal $\mathbf{w}_g^{c,i_g^c}$ is given by a linear combination of the effective channel vectors, as follows [5]

$$\mathbf{w}_g^{c,i_g^c} = \sum_{n=1}^{N_g} \mu_{gn} \bar{\mathbf{P}}_g^H \mathbf{Q}_g \mathbf{\Delta}_g^{\frac{1}{2}} \hat{\mathbf{g}}_{gn}^{i^c i^c}, \tag{13}$$

which consists of a weighted matched filter (MF) precoder for the channels of polarization $i_g^c \in \{v,h\}$, where μ_{gn} is the weight for the *n*th user in the *g*th group. As in [5], we employ an equally-weighted MF precoder, i.e., $\mu_{g1} = \cdots = \mu_{gN_g} = \mu_g$. By defining $\boldsymbol{\omega}_g = \frac{1}{N_g}\sum_{n=1}^{N_g} \bar{\mathbf{P}}_g^H \mathbf{Q}_g \mathbf{\Delta}_g^{\frac{1}{2}} \hat{\mathbf{g}}_{gn}^{i^c i^c}$, μ_g is computed as $\mu_g^2 = 1/N_g^2(\boldsymbol{\omega}_g^H \bar{\mathbf{P}}_g^H \bar{\mathbf{P}}_g \boldsymbol{\omega}_g)$, which satisfies the unity norm constraint in (12).

III. ERGODIC SUM-RATE ANALYSIS AND ADAPTIVE POWER ALLOCATION WITH DEEP NEURAL NETWORKS

A. Ergodic Sum-Rate

The instantaneous data rate for the *n*th user in the *g*th group is given by the sum of its private and common rates, which are calculated as $R_{gn}^p = \log_2(1+\gamma_{gn}^p)$ and $R_{gn}^c = \min_{\forall l\in\{1,\ldots,N_g\}}\{\log_2(1+\gamma_{gl}^c)\}$, respectively. Thus, the ergodic sum-rate for the *g*th group can be obtained analytically through

$$\bar{R}_g = \sum_{n=1}^{N_g}\left(\int_0^\infty \log_2(1+x) f_{\gamma_{gn}^p}(x)\,dx + \int_0^\infty \log_2(1+y) f_{\gamma_{g(1)}^c}(y)\,dy\right), \tag{14}$$

where $f_{\gamma_{gn}^p}(x)$ is the probability density function (PDF) of γ_{gn}^p, and $f_{\gamma_{g(1)}^c}(y)$ denotes the PDF of the first order statistic of γ_{gn}^c, i.e., the PDF of $\min_{\forall l}\{\gamma_{gl}^c\}$. However, due to the correlated gains in the SINRs in (10) and (11), obtaining the exact expressions of $f_{\gamma_{gn}^p}(x)$ and $f_{\gamma_{g(1)}^c}(y)$ becomes a convoluted task. This complication makes the derivation of (14) intractable. Alternatively, we exploit the powerful capabilities of DNNs to approximate the desired sum-rate.

Given that the input parameters for $\bar{R}_g$ form a compact subset, denoted by $\mathcal{X}_g$, and that $\bar{R}_g$ is a real-valued continuous function, the universal approximation theorem [6, Th. 2.2] ensures that a DNN with at least one hidden layer can approximate $\bar{R}_g$ to any degree of accuracy, i.e.,

$$\sup_{\mathbf{x}_g\in\mathcal{X}_g} |\hat{\hat{\bar{R}}}_g - \bar{R}_g| < \epsilon, \tag{15}$$

for every $\epsilon > 0$, where $\hat{\hat{\bar{R}}}_g$ is the function that models the DNN, and $\mathbf{x}_g \in \mathcal{X}_g \subseteq \mathbb{R}^{b_{\mathcal{X}_g}}$ represents the feature vector with $b_{\mathcal{X}_g}$ input parameters of the sum-rate function. This theorem provides theoretical support for the adoption of DNNs as predictors for the intricate multivariate expression in (14).

B. DNN for Ergodic Sum-Rate Prediction

We consider a DNN model with L dense layers, in which there are one input layer, one output layer, and $L-2$ hidden layers, where the *l*th layer has Q_l neurons. For reducing the training complexity, we address the ergodic sum-rate for each spatial group separately. More specifically, the training dataset for users within the *g*th group is represented by $\mathcal{D}_g = \{(\mathbf{x}_{g,i}, \bar{R}_{g,i})|\mathbf{x}_{g,i} \in \mathcal{X}_g, \bar{R}_{g,i} \in \mathbb{R}, i = 1,\ldots,|\mathcal{D}_g|\}$, where $\bar{R}_{g,i}$ is the target output, i.e., the actual ergodic sum-rate, of the *i*th training sample in $\mathcal{D}_g$, and $\mathbf{x}_{g,i}$ is the *i*th input sample vector containing $b_{\mathcal{X}_g} = 2N_g + 7$ system parameters, which are structured as $\mathbf{x}_{g,i} = [M, \bar{M}, N_g, \chi, \tau, \alpha_g^c, [\alpha_{g1}^p, \ldots, \alpha_{gN_g}^p], [\zeta_{g1}, \ldots, \zeta_{gN_g}], \rho]^T$. Note that the entries of $\mathbf{x}_{g,i}$ are within different ranges and that $\bar{R}_{g,i}$ can assume values from a broad interval, which can lead to an unstable and slow training convergence. To avoid this limitation, the training samples are scaled to the unity range. Under such considerations, ergodic sum-rate prediction function for the *g*th group can be expressed by

$$\hat{\hat{\bar{R}}}_g(\mathbf{x}_{g,i}) = \mathbf{r}_{L-1} \circ \mathbf{r}_{L-2} \circ \cdots \circ \mathbf{r}_1(\mathbf{x}_{g,i}), \tag{16}$$

where $\mathbf{r}_l(\cdot)$ maps the transformation applied to the input data in the *l*th layer, which is defined by

$$\mathbf{r}_l(\mathbf{x}) = \pi_l(\mathbf{W}_l\mathbf{x} + \mathbf{b}_l), \forall l \in \{1,\ldots,L-1\}, \tag{17}$$

in which $\mathbf{x}$ is the input for the *l*th layer, $\mathbf{W}_l \in \mathbb{R}^{Q_l\times Q_{l-1}}$ is the weight matrix connecting the *l*th and $(l-1)$th layers, and $\mathbf{b}_l \in \mathbb{R}^{Q_l}$ and $\pi_l : \mathbb{R}^{Q_l} \to \mathbb{R}^{Q_l}$ represent, respectively, the bias vector and activation function for the *l*th layer. In the hidden layers, we use as the activation function the rectified linear unity (ReLU), i.e., $\pi_l(\mathbf{x}) = \max(0,\mathbf{x})$, $\forall l \in \{1,\ldots,L-2\}$, and in the output layer, a linear activation function is adopted.

For training, the data samples in $\mathcal{D}_g$ are randomly selected and partitioned into J batches. As a result, the mean-squared error (MSE) loss function for the *j*th batch, $\forall j \in \{1,\ldots,J\}$, to be minimized, can be written as

$$\mathcal{L}_{\mathcal{D}_{g,j}}(\tilde{}_g) = \frac{1}{S}\sum_{s=1}^{S} |\hat{\hat{\bar{R}}}_g(\mathbf{x}_{g,s}) - \bar{R}_{g,s}|^2, \tag{18}$$

where $\mathcal{D}_{g,j} = \{(\mathbf{x}_{g,s}, \bar{R}_{g,s})|s = 1,\ldots,S\} \subseteq \mathcal{D}_g$ represents the subset corresponding to the *j*th data batch, in which S denotes the carnality of $\mathcal{D}_{g,j}$, i.e., the batch size.

C. DNN-Aided Adaptive Power Allocation

Following the work in [5], the power allocation adopted for the private symbols is computed by $\alpha_{gu}^p = (1-\alpha_g^c)/N_g$, which consists of a uniform allocation policy given as a function of the power coefficient for the common symbol. Therefore, the challenge with this strategy remains in determining the coefficient α_g^c. In particular, our goal is to maximize the ergodic

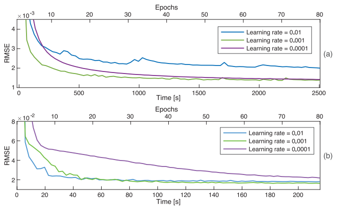

Fig. 2. Training convergence behavior in terms of RMSE for: (a) DNN for ergodic sum-rate prediction, and (b) DNN for adaptive power allocation.

sum-rate, which can be formulated as

$$\underset{\alpha_g^c}{\arg\max} \sum_{n=1}^{N_g} \mathrm{E}\big[\log_2(1+\gamma_{gn}^p) + \min_{\forall l}\{\log_2(1+\gamma_{gl}^c)\}\big], \quad \text{s.t.} \;\; \alpha_g^c \le 1. \tag{19}$$

However, due to the dynamic polarization multiplexing, the coupled SNRs in (10) and (11), and the coupled coefficients α_g^c and α_{gu}^p, a closed-form optimal solution for (19) cannot be obtained. Determining the desired coefficient through an exhaustive search is also a possibility. However, brute-force strategies can be computationally expensive, which is not ideal for real-time communication. On the other hand, DNNs offer a short run-time after trained. With this motivation, we propose a DNN framework for approximating the optimal power coefficient. To this end, for each spatial group, we train a DNN model with one input layer, one output layer, and $D-2$ hidden layers, with the dth layer having V_d neurons.

Specifically, for training the DNN for power allocation, we use the dataset $\mathcal{M}_g = \{(\mathbf{z}_{g,i}, \alpha_{g,i}^{c*}) | \mathbf{z}_{g,i} \in \mathcal{Z}_g, \alpha_{g,i}^{c*} \in \mathbb{R}, i = 1, \ldots, |\mathcal{M}_g|\}$, where $\alpha_{g,i}^{c*}$ is the target power coefficient that maximizes the ergodic sum-rate for the ith input vector $\mathbf{z}_{g,i} \in \mathcal{Z}_g \subseteq \mathbb{R}^{b_{\mathcal{Z}_g}}$, which is defined by $\mathbf{z}_{g,i} = [M, \bar{M}, N_g, \chi, \tau, [\zeta_{g1}, \ldots, \zeta_{gN_g}], \rho]^T$. Both $\mathbf{z}_{g,i}$ and $\alpha_{g,i}^{c*}$ are achieved by exploiting the existing datasets $\mathcal{D}_g$. That is, for each sample $\mathbf{z}_{g,i}$, we select the power coefficient that maximizes the corresponding sum-rate in $\mathcal{D}_g$ and create the new dataset $\mathcal{M}_g$. As in Section III-B, the vectors $\mathbf{z}_{g,i}$ are scaled to the unity range. As a result, the function that predicts the optimal power allocation coefficient can be written as

$$\hat{\Lambda}_g(\mathbf{z}_{g,i}) = \mathbf{r}_{D-1} \circ \mathbf{r}_{D-2} \circ \cdots \circ \mathbf{r}_1(\mathbf{z}_{g,i}), \tag{20}$$

where $\mathbf{r}_d(\cdot)$ is defined as in (17), in which ReLU activation functions are employed in the hidden layers and a linear function in the output layer. We also adopt the MSE loss function in this model. Moreover, for satisfying the constraint in (19), the power coefficient is computed by $\hat{\alpha}_g^{c*} = \min\{1, \hat{\Lambda}_g(\mathbf{z}_{g,i})\}$.

D. Complexity Remarks

Note that we implement one DNN model for each spatial group. The main implication of this choice is that the covariance matrices, which have large dimensions, are not required for designing and training the DNNs. Consequently, we can considerably simplify the model architecture and decrease the training complexity. In practice, DNNs can be trained very efficiently in specialized hardware. Therefore, the complexity of the testing phase is more relevant for the practical operation of the proposed scheme. Specifically, the computational complexity of one forward pass can be expressed in terms of floating-point operations [7]. Under this analysis, the DNN for sum-rate prediction has a complexity of $\mathcal{O}(\sum_{l=1}^{L} Q_{l-1} Q_l)$. For the DNN-aided power allocation strategy, on the other hand, it is also important to mention the complexity associated with the generation of the dataset with optimal power coefficients. More specifically, we need to perform an exhaustive search on the dataset $\mathcal{D}_g$ to construct $\mathcal{M}_g$, which imposes additional complexity. Nevertheless, this search needs to be executed only once before the training, thus, it is a computationally affordable task. After the dataset $\mathcal{M}_g$ is properly generated and the DNN is trained, the desired power coefficient is computed with a complexity of $\mathcal{O}(\sum_{d=1}^{D} V_{d-1} V_d)$ in the testing phase.[1]

E. Datasets Generation and DNN Implementation

Due to the unknown PDFs of γ_{gn}^p and $\min_{\forall l}\{\gamma_{gl}^c\}$, we cannot generate the datasets $\mathcal{D}_g$ and $\mathcal{M}_g$, $g \in \{1, \ldots, G\}$, with the expression in (14). Due to this reason, instead, we used Monte Carlo simulations for obtaining the required data samples, in which the high-performance Julia Programming Language [8] has been used for implementing the proposed MIMO-RSMA network. For generating the training data, we adjusted the number of groups to $G = 3$, and the number of users within each group to $N_1 = \cdots = N_g = 3$. Consequently, the resulting number of features in the ith input vectors $\mathbf{x}_{g,i}$ and $\mathbf{z}_{g,i}$ were $b_{\mathcal{X}_g} = 13$ and $b_{\mathcal{Z}_g} = 9$, respectively. Then, we have extensively varied the system parameters and generated for each group a total of 6,561,000 samples for $\mathcal{D}_g$, and 72.900 samples for $\mathcal{M}_g$, where each sample was generated by averaging 2×10^3 random channel realizations. Moreover, 90% of the samples were used for training and 10% for testing.

The DNN models were implemented and trained in Python 3.9.11 using Tensor Flow Metal 2.8.0. The DNN for sum-rate prediction was implemented with five hidden layers, with the first and last hidden layers comprising 128 neurons and the remaining layers comprising 256 neurons each. In turn, the DNN for power allocation was implemented with four hidden layers, with the first and last hidden layers also containing 128 neurons and the remaining layers containing 256 neurons. For training the DNNs, we adopted the adaptive moment estimation (ADAM) optimizer. Moreover, the batch sizes for sum-rate prediction and power allocation were adjusted to 1000 and 100 samples, respectively, and both DNNs were trained for 80 epochs. Fig. 2 presents the training convergence in terms of root mean squared error (RMSE) for the two DNNs. As can be seen, the learning rate of 0.001 achieves the lowest RMSE. Thus, this value is adopted in the next section.

IV. SIMULATION RESULTS

The DNNs for sum-rate prediction and power allocation are evaluated in this section. The performance superiority of the proposed dual-polarized MIMO-RSMA scheme is also demonstrated over conventional baseline systems, including the single-polarized MIMO-RSMA, MIMO-TDMA, MIMO-SDMA, MIMO-NOMA, and the dual-polarized MIMO-NOMA approach proposed in [9]. In all systems, we configure the BS with $M = 64$ transmit antennas, and we consider that users are distributed within $G = 3$ spatial groups. Without loss of generality, we present results for the first group, which contains $N = 3$ users, is located at the azimuth angle of 20°, and has an angular spread of 11°. Moreover, the distances from the BS to users 1, 2, and 3 are set to $d_1 = 115$ m, $d_2 = 100$ m, and $d_3 = 85$ m, respectively. Under this setting, the large-scale

---

[1] The complexity trade-offs between the proposed dual-polarized MIMO-RSMA with the DNN-aided power allocation and the conventional MIMO-RSMA still need to be better investigated, which arises as a potential future research direction.

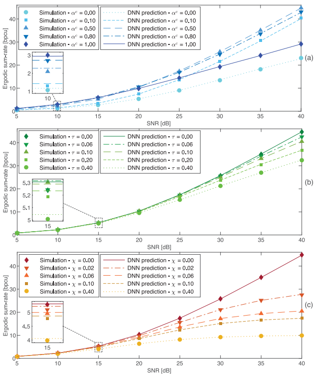

Fig. 3. Simulated and predicted ergodic sum-rates: (a) for different values of α^c, with $\chi = 0$ and $\tau = 0$, (b) for different values of τ, with $\alpha^c = 0.5$ and $\chi = 0$, and (c) for different values of χ, with $\alpha^c = 0.5$ and $\tau = 0$.

fading coefficient for each user is modeled by $\zeta_n = \delta d_n^{-\eta}$, where δ is an array gain parameter adjusted to 40 dB, and η is the path-loss exponent set to 2.7. Furthermore, we set $\bar{M} = 6$ and adjust the total transmit power to $P = 1$ W. Unless otherwise stated, when fixed power allocation is employed, we set $\alpha^c = 0.5$ and $\alpha_n^p = (1 - \alpha^c)/N \approx 0.17$ for the MIMO-RSMA schemes, whereas, for the MIMO-NOMA counterpart, we set the coefficients of users 1, 2, and 3 to 5/8, 2/8, and 1/8, respectively. In turn, a uniform power allocation is employed in the MIMO-SDMA systems, and in the MIMO-TDMA, the full transmit power, P, is used at each time slot.

Fig. 3 validates the DNN framework for ergodic sum-rate prediction under fixed power allocation. As can be seen, the predicted curves can follow the simulated ones with high accuracy in all considered cases. This figure also provides the first insights into the performance behavior of the proposed dual-polarized MIMO-RSMA scheme. Fig. 3(a), for instance, shows that the power coefficient for the common message plays an important role in the ergodic sum-rate performance and that the optimal power coefficient changes with the observed SNR. Fig. 3(b) reveals how imperfect CSI impacts the sum-rate of the proposed strategy. As can be seen, even though the system performance deteriorates with the increase of τ, a remarkable sum-rate of more than 30 bits per channel use (bpcu) can be achieved even when $\tau = 0.4$, which confirms robustness to imperfect CSI. On the other hand, as can be seen in Fig. 3(c), the dual-polarized MIMO-RSMA is more severely impacted by polarization interference (with fixed power allocation).

The ergodic sum-rates achieved with the dual-polarized MIMO-RSMA scheme and with the conventional systems are compared in Fig. 4. As we can see in Fig. 4(a), when $\chi = 0$, the dual-polarized MIMO-RSMA systems always achieve the best performance. However, with $\chi = 0.2$, the dual-polarized MIMO-RSMA scheme with fixed power allocation becomes less spectrally efficient than the single-polarized MIMO-RSMA and MIMO-SDMA counterparts. In contrast, by smartly splitting the transmit power between private and common streams, the proposed dual-polarized approach with the DNN-aided power allocation can impressively outperform all conventional baseline schemes despite the high interference. The effectiveness of our proposal is further corroborated in Fig. 4(b), where we plot the ergodic sum-rates versus the CSI quality factor τ. As can be seen, the dual-polarized MIMO-RSMA scheme with the DNN power allocation achieves the highest sum-rates for all values of τ and χ. The reason for such robustness is that the DNN mitigates the effects of both imperfect CSI and cross-polar interference by smartly adjusting α_g^c. For instance, the DNN assigns power only to one polarization if χ becomes excessively high for tackling cross-polar interference or allocates more power to the common stream when the CSI becomes degraded. Last, Fig. 4(c) compares the sum-rate performance of the dual-polarized MIMO-RSMA and of SIC-based schemes under the effects of SIC error propagation. The sum-rates of the schemes that rely on SIC are strongly degraded when the SIC error factor increases. On the other hand, the robust dual-polarized MIMO-RSMA is unaffected by SIC issues.

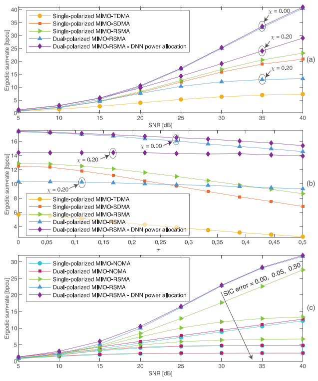

Fig. 4. Simulated ergodic sum-rates: (a) versus SNR for different levels of χ, with $\tau = 0.1$, (b) versus τ for a SNR of 25 dB and different levels of χ, and (c) versus SNR for different levels of SIC error, with $\chi = 0.01$ and $\tau = 0$.

V. CONCLUSION

We have proposed a novel low-complexity dual-polarized massive MIMO-RSMA scheme, which is free from the interference issues of SIC and robust to imperfect CSI. We have also developed DNN frameworks for ergodic sum-rate prediction and efficient power allocation, which ensured high performance even under strong cross-polar interference.

REFERENCES

[1] B. Clerckx *et al.*, "Is NOMA efficient in multi-antenna networks? A critical look at next generation multiple access techniques," *IEEE Open J. Commun. Soc.*, vol. 2, pp. 1310–1343, 2021.
[2] O. Dizdar *et al.*, "Rate-splitting multiple access to mitigate the curse of mobility in (massive) MIMO networks," *IEEE Trans. Commun.*, vol. 69, no. 10, pp. 6765–6780, Oct. 2021.
[3] A. S. de Sena *et al.*, "IRS-assisted massive MIMO–NOMA networks: Exploiting wave polarization," *IEEE Trans. Wireless Commun.*, vol. 20, no. 11, pp. 7166–7183, Nov. 2021.
[4] Z. Xiang *et al.*, "Massive MIMO multicasting in noncooperative cellular networks," *IEEE J. Sel. Areas Commun.*, vol. 32, no. 6, pp. 1180–1193, Jun. 2014.
[5] M. Dai *et al.*, "A rate splitting strategy for massive MIMO with imperfect CSIT," *IEEE Trans. Wireless Commun.*, vol. 15, no. 7, pp. 4611–4624, Jul. 2016.
[6] K. Hornik *et al.*, "Multilayer feedforward networks are universal approximators," *Neural Netw.*, vol. 2, no. 5, pp. 359–366, Jan. 1989.
[7] Y. Yang *et al.*, "Deep transfer learning-based downlink channel prediction for FDD massive MIMO systems," *IEEE Trans. Commun.*, vol. 68, no. 12, pp. 7485–7497, Dec. 2020.
[8] J. Bezanson *et al.*, "Julia: A fresh approach to numerical computing," *SIAM Rev.*, vol. 59, no. 1, pp. 65–98, 2017.
[9] A. S. de Sena *et al.*, "Massive MIMO–NOMA networks with multi-polarized antennas," *IEEE Trans. Wireless Commun.*, vol. 18, no. 12, pp. 5630–5642, Dec. 2019.

ACTA UNIVERSITATIS LAPPEENRANTAENSIS

1004. ELFVING, JERE. Direct capture of CO2 from air using amine-functionalized resin - Effect of humidity in modelling and evaluation of process concepts. 2021. Diss.

1005. KOMLEV, ANTON. Magnetism of metal-free graphene-based materials. 2021. Diss.

1006. RISSANEN, MATTI. EcoGame and Ecosystem Profiler: solutions for business ecosystem management. 2021. Diss.

1007. VANHAMÄKI, SUSANNA. Implementation of circular economy in regional strategies. 2021. Diss.

1008. LEHTINEN, VESA. Organisaation emergentti itseohjautuvuus, case sinfoniaorkesteri: ”Miksi orkesteri soittaa hyvin, vaikka sitä johdettaisiin huonosti?”. 2022. Diss.

1009. KÄHKÖNEN, TIINA. Employee trust repair in the context of organizational change – identification and measurement of active trust repair practices. 2022. Diss.

1010. AHONEN, AILA. Challenges in sport entrepreneurship: cases in team sport business. 2022. Diss.

1011. LEVIKARI, SAKU. Acoustic emission testing of multilayer ceramic capacitors. 2022. Diss.

1012. ZAHEER, MINHAJ. Evaluation of open-source FEM software performance in analysing converter-fed induction machine losses. 2022. Diss.

1013. HAAPANIEMI, JOUNI. Power-based electricity distribution tariffs providing an incentive to enhance the capacity effectiveness of electricity distribution grids. 2022. Diss.

1014. BUAH, ERIC. Artificial intelligence technology acceptance framework for energy systems analysis. 2022. Diss.

1015. GIVIROVSKIY, GEORGY. In situ hydrogen production in power-to-food applications. 2022. Diss.

1016. SOMMARSTRÖM, KAARINA. Teachers’ practices of entrepreneurship education in cooperation with companies. 2022. Diss.

1017. KAN, YELENA. Coherent anti-stokes raman scattering spectromicroscopy in biomedical and climate research. 2022. Diss.

1018. MÄNDMAA, SIRLI. Financial literacy in perspective – evidence from Estonian and Finnish students. 2022. Diss.

1019. QORRI, ARDIAN. Measuring and managing sustainable development in supply chains. 2022. Diss.

1020. MARTIKAINEN, SUVI-JONNA. Meaningful work and eudaimonia: contributing to social sustainability in the workplace. 2022. Diss.

1021. MANNINEN, KAISA. Conducting sustainability target-driven business. 2022. Diss.

1022. LI, CHANGYAN. Design, development, and multi-objective optimization of robotic systems in a fusion reactor. 2022. Diss.

1023. CHOUDHURY, TUHIN. Simulation-based methods for fault estimation and parameter identification of rotating machines. 2022. Diss.

1024. DUKEOV, IGOR. On antecedents of organizational innovation: How the organizational learning, age and size of a firm impact its organizational innovation. 2022. Diss.

1025. BREIER, MATTHIAS. Business model innovation as crisis response strategy. 2022. Diss.

1026. FADEEV, EGOR. Magnetotransport properties of nanocomposites close to the percolation threshold. 2022. Diss.

1027. KEPSU, DARIA. Technology analysis of magnetically supported rotors applied to a centrifugal compressor of a high-temperature heat pump. 2022. Diss.

1028. CHAUHAN, VARDAAN. Optimizing design and process parameters for recycled thermoplastic natural fiber composites in automotive applications. 2022. Diss.

1029. RAM, MANISH. Socioeconomic impacts of cost optimised and climate compliant energy transitions across the world. 2022. Diss.

1030. AMADI, MIRACLE. Hybrid modelling methods for epidemiological studies. 2022. Diss.

1031. RAMÍREZ ANGEL, YENDERY. Water-energy nexus for waste minimisation in the mining industry. 2022. Diss.

1032. ZOLOTAREV, FEDOR. Computer vision for virtual sawing and timber tracing. 2022. Diss.

1033. NEPOVINNYKH, EKATERINA. Automatic image-based re-identification of ringed seals. 2022. Diss.

1034. ARAYA GÓMEZ, Natalia Andrea. Sustainable management of water and tailings in the mining industry. 2022. Diss.

1035. YAHYA, MANAL. Augmented reality based on human needs. 2022. Diss.

1036. KARUPPANNAN GOPALRAJ, SANKAR. Impacts of recycling carbon fibre and glass fibre as sustainable raw materials for thermosetting composites. 2022. Diss.

1037. UDOKWU, CHIBUZOR JOSEPH. A modelling approach for building blockchain applications that enables trustable inter-organizational collaborations. 2022. Diss.

1038. INGMAN, JONNY. Evaluation of failure mechanisms in electronics using X-ray imaging. 2022. Diss.

1039. LIPIÄINEN, SATU. The role of the forest industry in mitigating global change: towards energy efficient and low-carbon operation. 2022. Diss.

1040. AFKHAMI, SHAHRIAR. Laser powder-bed fusion of steels: case studies on microstructures, mechanical properties, and notch-load interactions. 2022. Diss.

1041. SHEVELEVA, NADEZHDA. NMR studies of functionalized peptide dendrimers. 2022. Diss.

LUT University

ISBN 978-952-335-859-1
ISBN 978-952-335-860-7 (PDF)
ISSN 1456-4491 (Print)
ISSN 2814-5518 (Online)
Lappeenranta 2022